

A \$20 billion boon
for U.S. R&D p. 1447

Frogs amp up resistance to
chytridiomycosis pp. 1458 & 2137

Antibodies lock "kill me" signals
onto tumors pp. 1460 & 2137

Science

\$15
30 MARCH 2018
sciencemag.org

AAAS

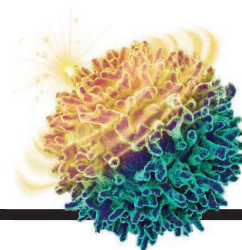
SHOCKING SYNTHESIS

Making multimetallic
nanoparticles
pp. 1467 & 1489



CONTENTS

30 MARCH 2018 • VOLUME 359 • ISSUE 6383



1454

A new way to rein in hyperactive immune cells

1451

NEWS

IN BRIEF

1444 News at a glance

IN DEPTH

1447 CONGRESS GIVES SCIENCE A RECORD FUNDING BOOST

Lawmakers largely reject deep cuts proposed by President Donald Trump for 2018 *By J. Mervis*

1448 U.K. TRIALS OF AIRWAY TRANSPLANTS ARE IN LIMBO

Studies are based on flawed evidence and could harm patients, scientists say *By M. Warren*

1450 U.S. BLAMES 'MASSIVE' HACK OF RESEARCH DATA ON IRAN

Targets included nearly 8000 professors in 22 countries *By J. Cohen*

1451 METEORITE DIVIDE POINTS TO SOLAR SYSTEM CHAOS

"Warren gap" validates models that suggest early wanderings for the giant planets *By P. Voosen*

1452 X-RAY 'GHOST IMAGES' COULD CUT RADIATION DOSES

Technique points to safer medical imaging done with cheap, single-pixel cameras *By S. Chen*

► PODCAST

1453 NEW MISSIONS AIM TO MAKE A SHORT LIST OF EXO-EARTHS

Ground- and space-based searches seek Earth-like targets for the next great space telescope *By D. Clery*

FEATURE

1454 PUTTING IMMUNE CELLS ON A DIET

To treat immune illnesses, researchers are probing drugs that could starve troublemaker cells *By M. Leslie*

INSIGHTS

PERSPECTIVES

1458 CHANGE IS KEY TO FROG SURVIVAL

Changes in host traits help amphibian populations to survive chytrid infection *By J. P. Collins*

► REPORT P. 1517

1460 NATURAL KILLERS JOIN THE FIGHT AGAINST CANCER

An antibody overcomes cancer cell immune evasion and activates natural killer cells *By A. Cerwenka and L. L. Lanier*

► REPORT P. 1537

1461 MAKING ROOM FOR NEW MEMORIES

Clearing neuronal networks from transient memory engrams during sleep consolidates memories

By A. Draguhn

► REPORT P. 1524

1463 LI METAL BATTERY, HEAL THYSELF

Intermittent high-current pulses prevent battery failure

By A. Mukhopadhyay and M. K. Jangid

► REPORT P. 1513

1464 FORCE MATTERS IN HOSPITAL-ACQUIRED INFECTIONS

Extremely strong forces help staphylococci to colonize biomaterials and infect humans

By P. Herman-Bausier and Y. F. Dufrène

► REPORT P. 1527

1465 NEURONAL-IMMUNE SYSTEM CROSS-TALK IN HOMEOSTASIS

Interactions between immune and neuronal cells are pillars in tissue homeostasis

By H. Veiga-Fernandes and D. Artis

1467 MASHING UP METALS WITH CARBOTHERMAL SHOCK

Many elements can be combined in the formation of high-entropy-alloy nanoparticles *By S. E. Skrabalak*

► RESEARCH ARTICLE P. 1489

POLICY FORUM

1468 ANATOMY OF STEM TEACHING IN NORTH AMERICAN UNIVERSITIES

Lecture is prominent, but practices vary *By M. Stains et al.*

BOOKS ET AL.

1472 WHAT'S IN A NAME?

A taxonomist contemplates the implications involved in naming new species *By G. R. Goldsmith*

1474 QUESTIONING QUANTUM MECHANICS

In a critique of the Copenhagen dogma, a physicist gives voice to "quantum dissidents" *By M. Frappier*

LETTERS

1475 MINING THREATENS COLOMBIAN ECOSYSTEMS

By O. A. Pérez-Escobar et al.

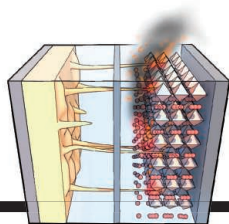
1475 OCEAN DEOXYGENATION: TIME FOR ACTION

By S. A. Earle et al.

1476 AMAZON SUGAR CANE: A THREAT TO THE FOREST

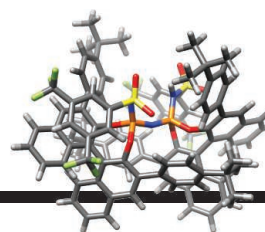
By L. Ferrante and P. M. Fearnside

1476 TECHNICAL COMMENT ABSTRACTS



1463 & 1513

Dendrite demolition



1501

Asymmetric acid
for alkenes

RESEARCH

IN BRIEF

1480 From *Science* and other journals

RESEARCH ARTICLES

1483 BIOCHEMISTRY

Structure of the nucleotide exchange factor eIF2B reveals mechanism of memory-enhancing molecule

J. C. Tsai et al.

RESEARCH ARTICLE SUMMARY; FOR FULL TEXT:
[dx.doi.org/10.1126/science.aag0939](https://doi.org/10.1126/science.aag0939)

► REPORT P. 1533

1484 NITROGEN FIXATION

A bound reaction intermediate sheds light on the mechanism of nitrogenase

D. Sippel et al.

1489 NANOMATERIALS

Carbothermal shock synthesis of high-entropy-alloy nanoparticles

Y. Yao et al.

► PERSPECTIVE P. 1467



1458 & 1517

1495 MATERIALS SCIENCE

Adaptive infrared-reflecting systems inspired by cephalopods

C. Xu et al.

REPORTS

1501 ORGANIC CHEMISTRY

Activation of olefins via asymmetric Brønsted acid catalysis

N. Tsuji et al.

1505 APPLIED PHYSICS

Nanofluidic rocking Brownian motors

M. J. Skaug et al.

1509 MATERIALS SCIENCE

Chameleon-like elastomers with molecularly encoded strain-adaptive stiffening and coloration

M. Vatankehah-Varnosfaderani et al.

1513 BATTERIES

Self-heating-induced healing of lithium dendrites

L. Li et al.

► PERSPECTIVE P. 1463

1517 AMPHIBIAN DISEASE

Shifts in disease dynamics in a tropical amphibian assemblage are not due to pathogen attenuation

J. Voyles et al.

► PERSPECTIVE P. 1458

1520 IRON HOMEOSTASIS

Erythrocytic ferroportin reduces intracellular iron accumulation, hemolysis, and malaria risk

D.-L. Zhang et al.

1524 NEUROSCIENCE

Hippocampal ripples down-regulate synapses

H. Norimoto et al.

► PERSPECTIVE P. 1461

1527 BIOPHYSICS

Molecular mechanism of extreme mechanostability in a pathogen adhesin

L. F. Milles et al.

► PERSPECTIVE P. 1464

1533 BIOCHEMISTRY

Binding of ISRIB reveals a regulatory site in the nucleotide exchange factor eIF2B

A. F. Zyryanova et al.

► RESEARCH ARTICLE P. 1483

1537 CANCER IMMUNOLOGY

Antibody-mediated inhibition of MICA and MICB shedding promotes NK cell-driven tumor immunity

L. Ferrari de Andrade et al.

► PERSPECTIVE P. 1460

1542 VIRAL EVOLUTION

Destabilizing mutations encode nongenetic variation that drives evolutionary innovation

K. L. Petrie et al.

DEPARTMENTS

1443 EDITORIAL

Keeping science honest

By Josefin Sundin and Fredrik Jutfelt

1558 WORKING LIFE

Figuring out how I belong

By Malin L. Nording

ON THE COVER



A diverse array of multimetallic alloy nanoparticles (large multicolored spheres) can be achieved via high-temperature shocking of metal salts on carbon nanofibers (small spheres represent individual metal atoms). This method enables homogeneous mixing of up to eight different metals to form single-phase solid solutions and presents a viable platform for nanometallurgical studies with a wide range of applications. See pages 1467 and 1489. *Image: Jiaqi Dai*

Science Staff	1442
AAAS News & Notes	1478
New Products	1549
Science Careers	1550

SCIENCE (ISSN 0036-8075) is published weekly on Friday, except last week in December, by the American Association for the Advancement of Science, 1200 New York Avenue, NW, Washington, DC 20005. Periodicals mail postage (publication No. 484460) paid at Washington, DC, and additional mailing offices. Copyright © 2018 by the American Association for the Advancement of Science. The title SCIENCE is a registered trademark of the AAAS. Domestic individual membership, including subscription (12 months): \$165 (\$74 allocated to subscription). Domestic institutional subscription (51 issues): \$1808; Foreign postage extra: Mexico, Caribbean (surface mail) \$55; other countries (air assist delivery): \$89. First class, airmail, student, and emeritus rates on request. Canadian rates with GST available upon request. GST #R125488122. Publications Mail Agreement Number 1069624. Printed in the U.S.A. Change of address: Allow 4 weeks, giving old and new addresses and 8-digit account number. Postmaster: Send change of address to AAAS, P.O. Box 96178, Washington, DC 20090-6178. Single-copy sales: \$15 each plus shipping and handling; bulk rate on request. Authorization to reproduce material for internal or personal use under circumstances not falling within the fair use provisions of the Copyright Act is granted by AAAS to libraries and others who use Copyright Clearance Center (CCC) Pay-Per-Use services provided that \$35.00 per article is paid directly to CCC, 222 Rosewood Drive, Danvers, MA 01923. The identification code for Science is 0036-8075. Science is indexed in the Reader's Guide to Periodical Literature and in several specialized indexes.

Editor-in-Chief Jeremy Berg

Executive Editor Monica M. Bradford **News Editor** Tim Appenzeller

Deputy Editors Lisa D. Chong, Andrew M. Sugden(UK), Valda J. Vinson, Jake S. Yeston

Research and Insights

DEPUTY EDITOR, EMERITUS Barbara R. Jasny **SR. EDITORS** Gemma Alderton(UK), Caroline Ash(UK), Julia Fahrenkamp-Uppenbrink(UK), Pamela J. Hines, Stella M. Hurtlely(UK), Paula A. Kiberstis, Marc S. Lavine(Canada), Steve Mao, Ian S. Osborne(UK), Beverly A. Purnell, L. Bryan Ray, H. Jesse Smith, Helena Stajic, Peter Stern(UK), Phillip D. Szuroni, Sacha Vignieri, Brad Wible, Laura M. Zahn **ASSOCIATE EDITORS** Michael A. Funk, Brent Grocholski, Priscilla N. Kelly, Seth Thomas Scanlon(UK), Keith T. Smith(UK) **ASSOCIATE BOOK REVIEW EDITOR** Valerie B. Thompson **LETTERS EDITOR** Jennifer Sills **LEAD CONTENT PRODUCTION EDITORS** Harry Jach, Lauren Kmec **CONTENT PRODUCTION EDITORS** Amelia Beyna, Jeffrey E. Cook, Amber Esplin, Chris Filiatreau, Cynthia Howe, Catherine Wolner **SR. EDITORIAL COORDINATORS** Carolyn Kyle, Beverly Shields **EDITORIAL COORDINATORS** Aneera Dobbins, Joi S. Granger, Jeffrey Hearn, Lisa Johnson, Maryrose Madrid, Scott Miller, Jerry Richardson, Anita Wynn **PUBLICATIONS ASSISTANTS** Ope Martins, Nida Masiulis, Dona Mathieu, Hilary Stewart(UK), Alana Warnke, Alice Whaley(UK), Brian White **EXECUTIVE ASSISTANT** Jessica Slater **ADMINISTRATIVE SUPPORT** Janet Clements(UK), Lizzanne Newton(UK)

News

NEWS MANAGING EDITOR John Travis **INTERNATIONAL EDITOR** Richard Stone **DEPUTY NEWS EDITORS** Elizabeth Culotta, Martin Enserink(Europe), David Grimm, Eric Hand, David Malakoff, Leslie Roberts **SR. CORRESPONDENTS** Daniel Clery(UK), Jeffrey Mervis, Elizabeth Pennisi **ASSOCIATE EDITORS** Jeffrey Brainard, Catherine Matatic **NEWS WRITERS** Adrian Cho, Jon Cohen, Jennifer Couzin-Frankel, Jocelyn Kaiser, Kelly Servick, Robert F. Service, Erik Stokstad(Cambridge, UK), Paul Voosen, Meredith Wadman **INTERNS** Roni Dengler, Katie Langin, Matt Warren **CONTRIBUTING CORRESPONDENTS** John Bohannon, Warren Cornwall, Ann Gibbons, Mara Hvistendahl, Sam Kean, Eli Kintisch, Kai Kupferschmidt(Berlin), Andrew Lawler, Mitch Leslie, Eliot Marshall, Virginia Morell, Dennis Normile(Shanghai), Charles Piller, Tania Rabesandratana(London), Emily Underwood, Gretchen Vogel(Berlin), Lizzie Wade(Mexico City) **CAREERS** Donisha Adams, Rachel Bernstein(Editor), Maggie Kuo **COPY EDITORS** Dorie Cheveln, Julia Cole (Senior Copy Editor), Cyra Master (Copy Chief) **ADMINISTRATIVE SUPPORT** Meagan Weiland

Executive Publisher Rush D. Holt

Publisher Bill Moran **Chief Digital Media Officer** Josh Freeman

DIRECTOR, BUSINESS STRATEGY AND PORTFOLIO MANAGEMENT Sarah Whalen **DIRECTOR, PRODUCT AND CUSTOM PUBLISHING** Will Schweitzer **MANAGER, PRODUCT DEVELOPMENT** Hannah Heckner **BUSINESS SYSTEMS AND FINANCIAL ANALYSIS** DIRECTOR Randy Yi **DIRECTOR, BUSINESS OPERATIONS & ANALYST** Eric Knott **SENIOR SYSTEMS ANALYST** Nicole Mehmedovich **SENIOR BUSINESS ANALYST** Cory Lipman **MANAGER, BUSINESS OPERATIONS** Jessica Tierney **BUSINESS ANALYSTS** Meron Kebede, Sandy Kim, Jourdan Stewart **FINANCIAL ANALYST** Julian Iriarte **ADVERTISING SYSTEM ADMINISTRATOR** Tina Burks **SALES COORDINATOR** Shirley Young **DIRECTOR, COPYRIGHT, LICENSING, SPECIAL PROJECTS** Emilie David **DIGITAL PRODUCT ASSOCIATE** Michael Hardesty **RIGHTS AND PERMISSIONS ASSOCIATE** Elizabeth Sandler **RIGHTS, CONTRACTS, AND LICENSING ASSOCIATE** Lili Catlett **RIGHTS & PERMISSIONS ASSISTANT** Alexander Lee

MARKETING MANAGER, PUBLISHING Shawana Arnold **MARKETING ASSOCIATE** Steven Goodman **SENIOR ART ASSOCIATES** Paula Fry **ART ASSOCIATE** Kim Huynh

INTERIM DIRECTOR, INSTITUTIONAL LICENSING Iquo Edim **ASSOCIATE DIRECTOR, RESEARCH & DEVELOPMENT** Elisabeth Leonard **SENIOR INSTITUTIONAL LICENSING MANAGER** Ryan Rexroth **INSTITUTIONAL LICENSING MANAGERS** Marco Castellani, Chris Murawski **SENIOR OPERATIONS ANALYST** Lana Guz **MANAGER, AGENT RELATIONS & CUSTOMER SUCCESS** Judy Lillibridge

WEB TECHNOLOGIES TECHNICAL DIRECTOR David Levy **TECHNICAL MANAGER** Chris Coleman **PORTFOLIO MANAGER** Trista Smith **PROJECT MANAGER** Tara Kelly, Dean Robbins **DEVELOPERS** Elissa Heller, Ryan Jensen, Brandon Morrison

DIGITAL MEDIA DIRECTOR OF ANALYTICS Enrique Gonzales **SR. MULTIMEDIA PRODUCER** Sarah Crespi **MANAGING DIGITAL PRODUCER** Kara Estelle-Powers **PRODUCER** Liana Birke **VIDEO PRODUCERS** Chris Burns, Nguyễn Khôi Nguyễn **DIGITAL SOCIAL MEDIA PRODUCER** Brice Russ

DIGITAL/PRINT STRATEGY MANAGER Jason Hillman **QUALITY TECHNICAL MANAGER** Marcus Spiegler **DIGITAL PRODUCTION MANAGER** Lisa Stanford **ASSISTANT MANAGER DIGITAL/PRINT** Rebecca Doshi **SENIOR CONTENT SPECIALISTS** Steve Forrester, Antoinette Hodal, Lori Murphy, Anthony Rosen **CONTENT SPECIALISTS** Jacob Hedrick, Kimberley Oster

DESIGN DIRECTOR Beth Rakouskas **DESIGN MANAGING EDITOR** Marcy Atarod **SENIOR DESIGNER** Chrystal Smith **DESIGNER** Christina Aycock **GRAPHICS MANAGING EDITOR** Alberto Cuadra **GRAPHICS EDITOR** Nirja Desai **SENIOR SCIENTIFIC ILLUSTRATORS** Valerie Altounian, Chris Bickel, Katharine Sutfill **SCIENTIFIC ILLUSTRATOR** Alice Kitterman **INTERACTIVE GRAPHICS EDITOR** Jia You **SENIOR GRAPHICS SPECIALISTS** Holly Bishop, Nathalie Cary **PHOTOGRAPHY MANAGING EDITOR** William Douthitt **PHOTO EDITOR** Emily Petersen **IMAGE RIGHTS AND FINANCIAL MANAGER** Jessica Adams **INTERN** Mike Shanahan

SENIOR EDITOR, CUSTOM PUBLISHING Sean Sanders: 202-326-6430 **ASSISTANT EDITOR, CUSTOM PUBLISHING** Jackie Oberst: 202-326-6463 **ASSOCIATE DIRECTOR, BUSINESS DEVELOPMENT** Justin Sawyers: 202-326-7061 science_advertising@aaas.org **ADVERTISING PRODUCTION OPERATIONS MANAGER** Deborah Tompkins **SR. PRODUCTION SPECIALIST/GRAPHIC DESIGNER** Amy Hardcastle **SR. TRAFFIC ASSOCIATE** Christine Hall **DIRECTOR OF BUSINESS DEVELOPMENT AND ACADEMIC PUBLISHING RELATIONS, ASIA** Xiaoying Chu: +86-131 6136 3212, xchu@aaas.org **COLLABORATION/CUSTOM PUBLICATIONS/JAPAN** Adarsh Sandhu + 81532-81-5142 asandhu@aaas.org **EAST COAST/E. CANADA** Laurie Faraday: 508-747-9395, FAX 617-507-8189 **WEST COAST/W. CANADA** Lynne Stickrod: 415-931-9782, FAX 415-520-6940 **MIDWEST** Jeffrey Dembski: 847-498-4520 x3005, Steven Loerch: 847-498-4520 x3006 **UK EUROPE/ASIA** Roger Goncalves: TEL/FAX +41 43 243 1358 **JAPAN** Kaoru Sasaki (Tokyo): + 81 (3) 6459 4174 ksasaki@aaas.org

GLOBAL SALES DIRECTOR ADVERTISING AND CUSTOM PUBLISHING Tracy Holmes: +44 (0) 1223 326525 **CLASSIFIED** advertise@sciencecareers.org **SALES MANAGER, US, CANADA AND LATIN AMERICA** SCIENCE CAREERS Claudia Paulsen-Young: 202-326-6577 **EUROPE/ROW SALES** Sarah Lelege **SALES ADMIN ASSISTANT** Kelly Grace +44 (0)1223 326528 **JAPAN** Miyuki Tani(Osaka): +81 (6) 6202 6272 mtani@aaas.org **CHINA/TAIWAN** Xiaoying Chu: +86-131-636 3212, xchu@aaas.org **GLOBAL MARKETING MANAGER** Allison Pritchard **DIGITAL MARKETING ASSOCIATE** Aimee Aponte

AAAS BOARD OF DIRECTORS, CHAIR Susan Hockfield **PRESIDENT** Margaret A. Hamburg **PRESIDENT-ELECT** Steven Chu **TREASURER** Carolyn N. Ainslie **CHIEF EXECUTIVE OFFICER** Rush D. Holt **BOARD** Cynthia M. Beall, May R. Berenbaum, Rosina M. Bierbaum, Kaye Husbands Fealing, Stephen P.A. Fodor, S. James Gates, Jr., Michael S. Gazzaniga, Laura H. Greene, Robert B. Millard, Mercedes Pascual, William D. Provine

SUBSCRIPTION SERVICES For change of address, missing issues, new orders and renewals, and payment questions: 866-434-AAAS (2227) or 202-326-6417, FAX 202-842-1065. Mailing addresses: AAAS, P.O. Box 96178, Washington, DC 20090-6178 or AAAS Member Services, 1200 New York Avenue, NW, Washington, DC 20005

INSTITUTIONAL SITE LICENSES 202-326-6730 **REPRINTS:** Author Inquiries 800-635-7181 **COMMERCIAL INQUIRIES** 803-359-4578 **PERMISSIONS** 202-326-6765, permissions@aaas.org **AAAS Member Central Support** 866-434-2227 www.aaas.org/membercentral

Science serves as a forum for discussion of important issues related to the advancement of science by publishing material on which a consensus has been reached as well as including the presentation of minority or conflicting points of view. Accordingly, all articles published in Science—including editorials, news and comment, and book reviews—are signed and reflect the individual views of the authors and not official points of view adopted by AAAS or the institutions with which the authors are affiliated.

INFORMATION FOR AUTHORS See www.sciencemag.org/authors/science-information-authors

BOARD OF REVIEWING EDITORS (Statistics board members indicated with \$)

Adriano Aguzzi, U. Hospital Zürich
Takuzo Aida, U. of Tokyo
Leslie Aiello, Wenner-Gren Foundation
Judith Allen, U. of Manchester
Sebastian Amigorena, Institut Curie
Meinrat O. Andrae, Max Planck Inst. Mainz
Paola Ariotti, Harvard U.
Johan Auwerx, EPFL
David Awschalom, U. of Chicago
Clare Baker, U. of Cambridge
Nenad Ban, ETH Zürich
Franz Bauer, Pontificia Universidad Católica de Chile
Ray H. Baughman, U. of Texas at Dallas
Carlo Beenakker, Leiden U.
Kamran Behnia, ESPCI
Yasmine Belkaid, NIAID, NIH
Philip Benfey, Duke U.
Gabriele Bergers, VIB
Bradley Bernstein, Massachusetts General Hospital
Peer Bork, EMBL
Chris Bowler, École Normale Supérieure
Ian Boyd, U. of St. Andrews
Emily Brodsky, U. of California, Santa Cruz
Ron Brookmeyer, U. of California, Los Angeles (\$) **\$**
Christian Büchel, UKE Hamburg
Dennis Burton, The Scripps Res. Inst.
Carter Tribley Butts, U. of California, Irvine
Gyorgy Buzsáki, New York U. School of Medicine
Blanche Capel, Duke U.
Mats Carlsson, U. of Oslo
Ib Chorkendorff, Denmark TU
James J. Collins, MIT
Robert Cook-Deegan, Arizona State U.
Lisa Coussens, Oregon Health & Science U.
Alan Cowman, Walter & Eliza Hall Inst.
Roberta Croce, VU Amsterdam
Janet Currie, Princeton U.
Jeff L. Dangl, U. of North Carolina
Tom Daniel, U. of Washington
Chiara Daraio, Caltech
Nicolas Daughas, U. of Chicago
Frans de Waal, Emory U.
Stanislas Dehaene, Collège de France
Robert Desimone, MIT
Claude Desplan, New York U.
Sandra Díaz, Universidad Nacional de Córdoba
Dennis Discher, U. of Penn.
Gerald W. Dorn II, Washington U. in St. Louis
Jennifer A. Doudna, U. of California, Berkeley
Bruce Dunn, U. of California, Los Angeles
William Dunphy, Caltech
Christopher Dye, WHO
Todd Ehlers, U. of Tübingen
Jennifer Elisseeff, Johns Hopkins U.
Tim Elston, U. of North Carolina at Chapel Hill
Barry Everitt, U. of Cambridge
Vanessa Ezenwa, U. of Georgia
Ernst Fehr, U. of Zürich
Anne C. Ferguson-Smith, U. of Cambridge
Michael Feuer, The George Washington U.
Toren Finkel, NHLBI, NIH
Kate Fitzgerald, U. of Massachusetts
Peter Fratzl, Max Planck Inst. Potsdam
Elaine Fuchs, Rockefeller U.
Eileen Furlong, EMBL
Jay Gallagher, U. of Wisconsin
Daniel Geschwind, U. of California, Los Angeles
Karl-Heinz Glassmeier, TU Braunschweig
Ramon Gonzalez, Rice U.
Elizabeth Grove, U. of Chicago
Nicolas Gruber, ETH Zürich
Kip Guy, U. of Kentucky College of Pharmacy
Taekjip Ha, Johns Hopkins U.
Christian Haass, Ludwig Maximilians U.
Sharon Hammes-Schiffer, U. of Illinois at Urbana-Champaign
Wolf-Dietrich Hardt, ETH Zürich
Michael Hasselmo, Boston U.
Martin Heimann, Max Planck Inst. Jena
Ykä Helariutta, U. of Cambridge
Janet G. Hering, Ewag
Kai-Uwe Hinrichs, U. of Bremen
David Hodell, U. of Cambridge
Lora Hooper, UT Southwestern Medical Ctr. at Dallas
Fred Hughson, Princeton U.
Randall Hulet, Rice U.
Auke Ijspeert, EPFL
Akiko Iwasaki, Yale U.
Stephen Jackson, USGS SW Climate Science Ctr.
Seema Jayachandran, Northwestern U.
Kai Johnsson, EPFL
Peter Jonas, Inst. of Science & Technology Austria
Matt Kaebberlein, U. of Washington
William Kaelin Jr., Dana-Farber Cancer Inst.
Daniel Kammen, U. of California, Berkeley
Abby Kavner, U. of California, Los Angeles
Hitoshi Kawakatsu, U. of Tokyo
Masashi Kawasaki, U. of Tokyo
V. Narry Kim, Seoul Nat. U.
Robert Kingston, Harvard Medical School
Etienne Koechlin, École Normale Supérieure
Alexander Kolodkin, Johns Hopkins U.
Thomas Langer, U. of Cologne
Mitchell A. Lazar, U. of Penn.

David Lazer, Harvard U.
Thomas Lecuit, IBDM
Virginia Lee, U. of Penn.
Stanley Lemon, U. of North Carolina at Chapel Hill
Ottoline Leyser, U. of Cambridge
Wendell Lim, U. of California, San Francisco
Marcia C. Linn, U. of California, Berkeley
Jianguo Liu, Michigan State U.
Luis Liz-Marzán, CIC biomaGUNE
Jonathan Losos, Harvard U.
Ke Lu, Chinese Acad. of Sciences
Christian Lüscher, U. of Geneva
Laura Machesky, Cancer Research UK Beatson Inst.
Anne Magurran, U. of St. Andrews
Oscar Marín, King's College London
Charles Marshall, U. of California, Berkeley
Christopher Marx, U. of Idaho
C. Robertson McClung, Dartmouth College
Rodrigo Medellín, U. of Mexico
Graham Medley, London School of Hygiene & Tropical Med.
Jane Memmott, U. of Bristol
Tom Misteli, NCI, NIH
Yasushi Miyashita, U. of Tokyo
Mary Ann Moran, U. of Georgia
Richard Morris, U. of Edinburgh
Alison Motsinger-Reif, NC State U. (\$) **\$**
Daniel Neumark, U. of California, Berkeley
Kitty Nijmeijer, TU Eindhoven
Helga Nowotny, Austrian Council
Rachel O'Reilly, U. of Warwick
Joe Orenstein, U. of California, Berkeley & Lawrence Berkeley Nat. Lab.
Harry Orr, U. of Minnesota
Pilar Ossorio, U. of Wisconsin
Andrew Oswald, U. of Warwick
Isabella Pagano, Istituto Nazionale di Astrofisica
Margaret Palmer, U. of Maryland
Steve Palumbi, Stanford U.
Jane Parker, Max Planck Inst. Cologne
Giovanni Parmigiani, Dana-Farber Cancer Inst. (\$) **\$**
John H. J. Petrini, Memorial Sloan Kettering
Samuel Pfaff, Salk Inst. for Biological Studies
Kathrin Plath, U. of California, Los Angeles
Martin Plenio, Ulm U.
Albert Polman, FOM Institute for AMOLF
Elvira Poloczanska, Alfred-Wegener-Inst.
Philippe Poulin, CNRS
Jonathan Pritchard, Stanford U.
David Randall, Colorado State U.
Sarah Reisman, Caltech
Félix A. Rey, Institut Pasteur
Trevor Robbins, U. of Cambridge
Amy Rosenzweig, Northwestern U.
Mike Ryan, U. of Texas at Austin
Mitinori Saitou, Kyoto U.
Shimon Sakaguchi, Osaka U.
Miquel Salmeron, Lawrence Berkeley Nat. Lab
Jürgen Sandkühler, Medical U. of Vienna
Alexander Schier, Harvard U.
Wolfram Schlenker, Columbia U.
Susannah Scott, U. of California, Santa Barbara
Vladimir Shalaev, Purdue U.
Beth Shapiro, U. of California, Santa Cruz
Jay Shendure, U. of Washington
Brian Shoichet, U. of California, San Francisco
Robert Siliciano, Johns Hopkins U. School of Medicine
Uri Simonsohn, U. of Penn.
Alison Smith, John Innes Centre
Richard Smith, U. of North Carolina at Chapel Hill (\$) **\$**
Mark Smyth, QIMR Berghofer
Pam Solts, U. of Florida
John Speakman, U. of Aberdeen
Allan C. Spradling, Carnegie Institution for Science
Eric Steig, U. of Washington
Paula Stephan, Georgia State U.
V. S. Subrahmanian, U. of Maryland
Ira Tabas, Columbia U.
Sarah Teichmann, U. of Cambridge
Shubha Tole, Tata Inst. of Fundamental Research
Wim van der Putten, Netherlands Inst. of Ecology
Bert Vogelstein, Johns Hopkins U.
David Wallach, Weizmann Inst. of Science
Jane-Ling Wang, U. of California, Davis (\$) **\$**
David Waxman, Fudan U.
Jonathan Weissman, U. of California, San Francisco
Chris Wickle, U. of Missouri (\$) **\$**
Terrie Williams, U. of California, Santa Cruz
Ian A. Wilson, The Scripps Res. Inst. (\$) **\$**
Timothy D. Wilson, U. of Virginia
Yu Xie, Princeton U.
Jan Zaenen, Leiden U.
Kenneth Zaret, U. of Penn. School of Medicine
Jonathan Zehr, U. of California, Santa Cruz
Len Zon, Boston Children's Hospital
Maria Zuber, MIT

Keeping science honest

We are the whistle-blowers. Our ethical obligations as scientists made it impossible for us to accept a publication of fabricated results, even though it could have cost us our scientific careers. The process was slow and arduous, but worked nevertheless. Would we do it again? Yes. It was something we had to do to retain our trust in science.

The Research Article, published in *Science* in June 2016, made headlines around the world: Fish prefer microplastics to live prey. But we witnessed the experiments and knew that this paper was fraudulent. We reported the scientific misconduct and thereby set in motion an 18-month investigation that has had numerous repercussions for many. The paper was eventually retracted, and a final investigation concluded that the results were fabricated. The guilty scientists lost their research grants, and the university's decisions regarding potential reprimands are forthcoming.

The case severely influenced our personal and professional lives. The time and energy that we devoted to it can never be replaced. We naively thought that the “science police” would ride in, secure evidence, and make a swift declaration of misconduct. Despite a catalog of overwhelming evidence, the outcome was never certain, especially given the initial “not guilty” verdict by the preliminary investigation. That report almost caused us to lose trust in science and change careers altogether. We were attacked by the accused, who said that jealousy motivated our sole intention to discredit their work. We were told that our behavior was distasteful and unethical.

Yet, despite this, we have been encouraged by a process that ultimately worked. What lessons can we pass on to others who may find themselves in a similarly unfortunate situation? Gather a team of dedicated collaborators, because you're going to need help and support. Be prepared for a prolonged battle. Collect evidence, but don't contact the accused with questions if you are certain that they fabricated data, because they may then hide their tracks. Identify the appropriate authority where miscon-

duct should be reported; this could be at your own or the accused's institution. If no obvious channels exist, your own institution should be able to provide guidance. Be professional, stick to factual concerns, and ask trusted colleagues to critically assess the evidence and how you have presented your case. Put everything in writing, from correspondence with the university to contacts with any organization or government body that may be of assistance by, for example, providing documents.

What can be done by research institutions to help whistle-blowers? Universities could be associated with a central organization that handles reports of misconduct. This organization would convene an independent investigative committee, because universities might be more interested in protecting their reputation than protecting good science. This would reduce the potential for a conflict of interest and ensure that credible claims of misconduct are handled professionally. Once an investigation is initiated, it must be performed by independent, critical people with the appropriate expertise. A person with training in investigative journalism, police work, and/or law would also benefit the investigative team. The central organization, as well as the whistle-blower's home institution, should offer

her/him support and protection from personal attacks during the process. For example, a whistle-blower's identity could be kept anonymous. Whistle-blowers who were mistaken in their report should not be punished if they are deemed as acting in good faith. However, when they are correct in their claims, their institutions, as well as the institutions of the guilty scientists, should consider mechanisms to compensate the whistle-blowers for their service to the scientific community. This could include supporting contract extension and/or reducing teaching and administrative duties to make up for lost time.

Ideally, whistle-blowing should not be necessary. The scientific community must enforce a culture of honesty. Sometimes that takes courage.

—Josefin Sundin and Fredrik Jutfelt



Josefin Sundin is a postdoctoral fellow at the University of Science and Technology in Trondheim, Norway. josefin@teamsundin.se



Fredrik Jutfelt is an associate professor at the University of Science and Technology in Trondheim, Norway. fredrik.jutfelt@ntnu.no



“...we have been encouraged by a process that ultimately worked.”

“Sunrise and sunset
Cracking, creaking, and rumbling
The Moon never rests”

Haiku by Renee Weber in a presentation about moonquakes
at last week's Lunar and Planetary Science Conference.

IN BRIEF

Edited by Jeffrey Brainard

CONSERVATION

Alarm over land degradation



Asia is losing wetlands the fastest. A nature preserve protects this Chinese marsh that reddens in autumn.

More than 75% of terra firma has been altered by humans, a figure that will likely rise to more than 90% by 2050, according to the first comprehensive assessment of land degradation and its impacts. The report, released this week by the Intergovernmental Science-Policy Platform on Biodiversity and Ecosystem Services, was prepared by more than 100 experts from around the world. Crops and livestock affect the greatest area—a third of all land—by contributing to soil erosion and water pollution, for example. Wetlands are among the most impacted of ecosystems; 87% have been destroyed over the past 3 centuries. All told, the authors estimate damage to terrestrial ecosystems costs up to a 10th of global gross domestic product annually (by harming ecosystem services such as pollination and water purification), makes life worse for 3.2 billion people, and contributes significantly to climate change. They call for an “urgent step-change” in efforts to restore degraded land and prevent further damage. The report also identifies top priorities for further research.

Trump picks new CDC director

PUBLIC HEALTH | U.S. President Donald Trump's administration this week appointed Robert Redfield, an HIV/AIDS specialist who has weathered his share of controversies, as director of the Centers for Disease Control and Prevention (CDC) in Atlanta. Redfield worked at the University of Maryland's Institute of Human Virology in Baltimore, which he co-founded. Before that, he spent 20 years in the U.S. Army's Medical Corps, heading its department of retroviral research. The appointment has won praise from many colleagues, but several critics—including Senator Patty Murray (WA), the top Democrat on the Senate health committee—have raised concerns about his past. More than 2 decades ago, Redfield was criticized for how he presented data from an AIDS vaccine trial and for views he then held about how best to contain HIV's spread. Anne Schuchat has been interim CDC director since Brenda Fitzgerald resigned in January.

A new forum for genome editing

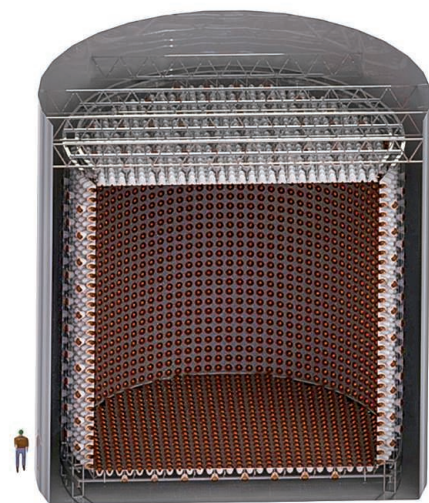
BIOTECHNOLOGY | Dozens of meetings and reports have considered the promise and perils of genome editing, a technique that could transform science, health, and agriculture. But an association launched on 23 March at a meeting in Paris promises to be something new: a permanent global discussion forum on the topic. The Association for Responsible Research and Innovation in Genome Editing (ARRIGE) was conceived by a small group of European researchers with support from the French biomedical research agency INSERM. It will be open to individuals and organizations and seeks to involve not just scientists, but also patient advocates, environmental groups, funders, and industry. The more than 150 participants at last week's event came from 35 countries. ARRIGE is “multi-disciplinary, and broader than what you'd get from a national academy or a professional society,” says Peter Mills of the Nuffield Council on Bioethics in London, who spoke at the meeting but is not involved in ARRIGE. “If it gets a good following and adequate resources, it could be a useful forum.”

European grants promote patents

RESEARCH FUNDING | A grant program started by the European Research Council (ERC) in Brussels to spur commercialization of basic research is showing success, an independent survey released by the council last week found. With a budget of €1.8 billion in 2017, ERC awards basic research grants to individual researchers that typically pay €1.5 million to €2.5 million over 5 years. But in 2011 the agency started adding €150,000 supplemental grants to cover the initial costs of commercial development. Among recipients of these Proof of Concept (PoC) grants who responded to the survey, 42% reported filing at least one patent application, compared with only 17% of a control group who had unsuccessfully applied for PoC funding. And 20% of respondents said their project led to the creation of a company, compared with 6% in a control group. For example, a PoC grantee raised €1 million in private seed funding and created a company that develops supermirror coatings for ultraprecise laser measurements. In all, the council has provided about 800 PoC grants, totaling 1% of its budget.

Detecting secret bombmaking

NUCLEAR WEAPONS | A nuclear reactor radiates scads of nearly undetectable subatomic particles called antineutrinos, and scientists from the United States and the United Kingdom hope they might use them to detect reactors used secretly to make fuel for nuclear weapons. As a test of this strategy, they will place a detector called the Water Cherenkov Monitor of Antineutrinos (WATCHMAN) at Boulby Underground Laboratory on the northeast coast of England, 25 kilometers from a pair



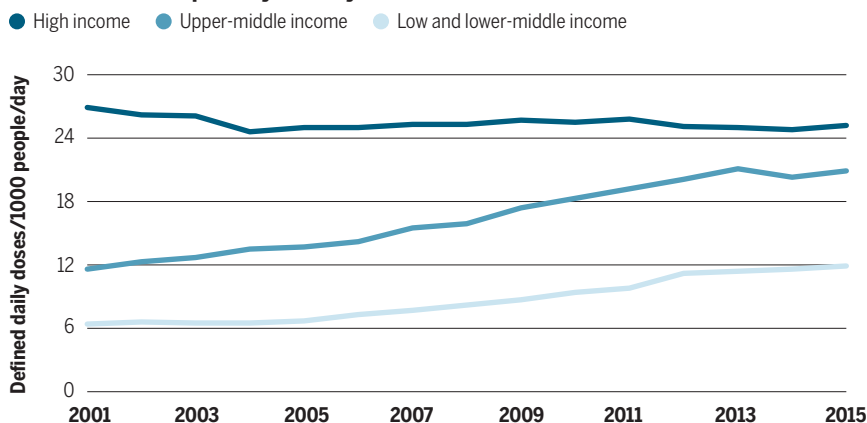
A 16-meter-tall antineutrino detector could glimpse clues to secret weapons development.

PUBLIC HEALTH

More wealth, more antibiotics

Low- and middle-income countries are rapidly increasing their consumption of antibiotics as economic growth has enabled people of modest means to afford the life-saving drugs, a new study says. But the trend also raises concerns about overuse, which could accelerate the emergence of drug-resistant strains of bacteria, researchers write this week in the *Proceedings of the National Academy of Sciences*. The study, which covered 76 countries, found that Turkey, Tunisia, and Romania had some of the largest increases in consumption rates from 2000 to 2015. Many lower-income countries face a higher burden of bacterial disease than wealthier countries do, and authorities there should support judicious use of antibiotics and alternatives such as building water supply systems to improve sanitation and reduce bacterial infections, the authors say.

Antibiotic consumption by country income, 2000–2015



of reactors at the Hartlepool Nuclear Power Station. From the antineutrinos it detects, they hope to track the reactors as they cycle on and off. WATCHMAN, which will contain 3200 metric tons of gadolinium-doped water, should detect about six antineutrinos per month from the reactors. Physicists have detected antineutrinos from reactors many times before, sometimes over long ranges, but the new collaboration aims eventually to spot them at distances of thousands of kilometers, across national borders.

Census to ask about citizenship

DEMOGRAPHICS | U.S. Commerce Secretary Wilbur Ross decided this week that the 2020 census should include a question about citizenship, putting the decennial headcount in the middle of the country's fierce debate about immigration. Ross was responding to a December 2017 request from the Justice Department, which argued that it needed data from the question to help enforce federal voting laws. Civil rights groups and immigration advocates say the new question will make minorities less likely to answer the questionnaire, leading to an undercount that will undermine the accuracy of the 2020 census.

They also say the question would weaken, not strengthen, voter protections. In his eight-page memo, Ross says he reviewed the issue and was “not able to determine definitively how inclusion of a citizenship question ... will impact responsiveness.” If it were to do so, he adds, “the value of more complete and accurate data ... outweighs such concerns.” Democrats in both chambers of Congress have introduced a bill blocking any last-minute questions on the 2020 census that have not been tested thoroughly.

New effort to sequence microbes

GENOMICS | Microbiologists last week outlined a plan already underway to sequence the genomes of 10,000 distinct strains of prokaryotes—bacteria and other microorganisms with a single, nucleus-free cell—to accelerate understanding of their virulence and antibiotic resistance. The new effort, called the Global Catalogue of Microorganisms 10K Type Strain Sequencing Project, involves at least 16 microbial culture collections from 11 countries, with Chinese institutions taking the financial and logistical lead. The project is another indication that “China is taking

more responsibility” for global scientific collaborations, says Liu Shuang-Jiang, director of the Institute of Microbiology in Beijing, which hosts the World Data Centre for Microorganisms, one of the project organizers. It’s the most ambitious sequencing effort to focus primarily on prokaryotes, and it should “accelerate the discovery of new natural products and drugs,” the organizers wrote online last week in *GigaScience*. Sequencing 10,000 genomes will barely dent the estimated inventory of 1 million prokaryotic species, but “it is a very good place to start,” says Martin Blaser, a microbiologist at New York University in New York City, who calls it “a very worthwhile project.”

NIH scrutinizes Duke research

BIOMEDICINE | The U.S. National Institutes of Health (NIH) has imposed unusual new requirements on NIH-funded researchers at Duke University in Durham, North Carolina, citing concerns about how the institution handled recent cases involving research misconduct and grant management. In a letter sent last week to faculty members, university administrators said the incidents, dating back to 2010, include that of Anil Potti, a once-rising star in cancer research who was found to have fabricated data. According to a Duke spokesperson, starting 1 April NIH will require Duke researchers to obtain prior approval for any

modifications to new and existing NIH grants. And any Duke researcher submitting a so-called modular application for a grant worth less than \$250,000 per year must include “detailed budgets” justifying the costs. “Duke has already addressed many of the concerns that prompted this change through enhanced internal controls, education and training, and new information systems, and will continue to look for opportunities to improve our oversight,” the spokesperson said.

Space telescope delayed again

ASTRONOMY | Delays in the testing and integration of NASA’s next space observatory, the James Webb Space Telescope (JWST), will push its launch back by nearly a year to May 2020, the second schedule slip in recent months. NASA’s acting administrator, Robert Lightfoot, said in a press briefing on 27 March that the project’s cost may exceed the ceiling of \$8 billion imposed by Congress in 2011. The agency will provide a confirmed schedule and cost estimate in the summer, and Congress will have to give its approval if the cap has been breached. Delays in testing the telescope’s sunshield and problems with its in-space propulsion system have slowed work, and an independent review commissioned by NASA and released at the briefing suggested that testing of the completed spacecraft will take longer than predicted. The review predicted a 70% probability the JWST would be ready for a May 2020 launch.

A new journal for African science

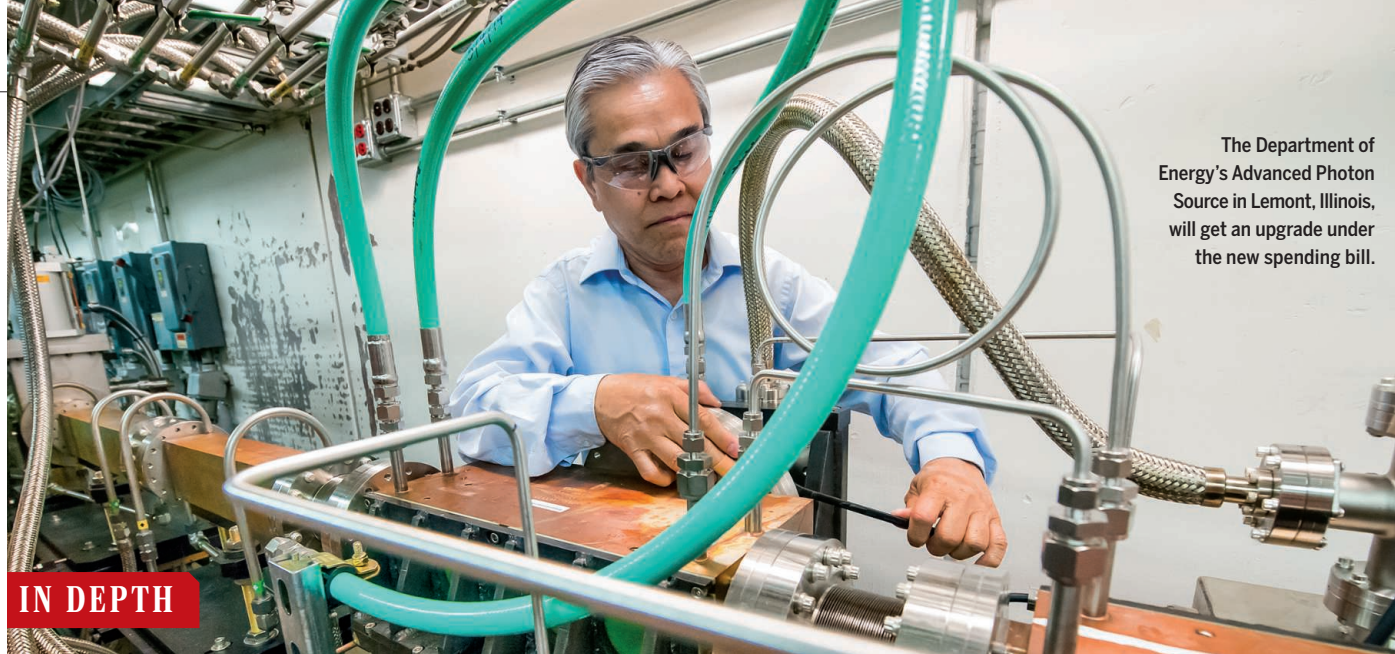
PUBLISHING | The Next Einstein Forum, which advocates for African science, and Elsevier, the publishing and analytics company, announced this week that they are starting an open-access journal, *Scientific African*, to feature research in all scientific disciplines from the continent. The announcement came in Kigali, Rwanda, at the Next Einstein Forum Global Gathering, a biannual meeting held to promote African science. Elsevier presented data at the meeting showing that the number of African authors of published scientific research grew by 43% from 2012 to 2016, and Rwandan President Paul Kagame spoke on his nation’s recent emphasis on education and technology, stressing the need for gender equity in science. “As Africa catches up to the rest of the world,” he said, “we cannot afford to leave our women and girls out of the equation.”



ANIMAL RESEARCH

Famed chimps enter sanctuary

Two of the world’s most famous research chimpanzees—Hercules and Leo—retired last week to Project Chimps, a 95-hectare sanctuary in the wooded hills of Morganton, Georgia. The 11-year-old apes had spent years bouncing between research facilities and were the subject of failed efforts by an animal rights group to grant them legal “personhood.” They had also become the face of a tortuously slow effort to move hundreds of the United States’s remaining research chimpanzees to wildlife refuges (*Science*, 16 June 2017, p. 1114). Their arrival at Project Chimps suggests plans to retire these animals—which can live up to 50 years in captivity—may be back on track. “For the first time, there are more chimpanzees in sanctuaries than there are in labs,” says Stephen Ross, director of the Lester E. Fisher Center for the Study and Conservation of Apes at the Lincoln Park Zoo in Chicago, Illinois, and board chair of Chimp Haven, the National Chimpanzee Sanctuary, in Keithville, Louisiana. “Hercules and Leo are representative of a movement that’s finally bearing fruit.”



The Department of Energy's Advanced Photon Source in Lemont, Illinois, will get an upgrade under the new spending bill.

IN DEPTH

U.S. SCIENCE FUNDING

Congress gives science a record funding boost

Lawmakers largely reject deep cuts proposed by President Donald Trump for 2018

By Jeffrey Mervis

Researchers are ecstatic over the \$4.8 billion increase that the U.S. Congress showered on nine leading civilian science agencies last week. But their joy may be short-lived.

The hikes, including \$3 billion more for the National Institutes of Health (NIH), are part of a \$1.3 trillion spending package for 2018 that includes a record \$176.8 billion for federal spending on R&D—a 12.8%, or \$20.1 billion, increase over 2017. The spending bill, which President Donald Trump signed last Friday, has put the scientific community “over the moon,” Rush Holt, CEO of AAAS (publisher of *Science*) in Washington, D.C., said in a statement. “We applaud congressional leaders ... for recognizing that funding science and technology continues to be a sound investment.”

The good news stems largely from a government-wide budget deal that allowed lawmakers to lift mandatory spending caps on discretionary accounts by a cumulative \$300 billion over 2 years. But there's a string attached: Most of the additional civilian spending occurs in the first year, 2018, meaning that researchers shouldn't expect a repeat of this year's windfall in fiscal 2019, which starts on 1 October 2018.

Another concern is the lopsided allocation, with NIH getting about two-thirds of the raise given to the top civilian science agencies (see graphic, p. 1448). That could reignite a long-simmering debate over

whether federal investments have tipped too far toward the biomedical sciences.

Still, passage of the legislation marked a happy ending to a year of fiscal angst and political wrangling. Many scientists had seen Trump's 2018 budget request as a slap in the face. Released last May, it called for massive cuts to research—22% less for NIH, an 11% reduction at the National Science Foundation (NSF), 17% less for the Office of Science at the Department of Energy (DOE), and a 24% cut at the National Institute of Standards and Technology (NIST). The White House also wanted to ax the Advanced Research Projects Agency-Energy (ARPA-E) and numerous climate and environmental science programs. A modest 1% dip in NASA science was a rare exception to the proposed bloodletting.

Congressional appropriators largely ignored the cuts Trump requested as they began writing their spending bills. Still, they were constrained by annual spending caps set by a 2011 law aimed at reducing the federal deficit over the next decade. In practice, the caps meant that any boost for one program required offsetting cuts elsewhere.

Those trade-offs reflected ideological and personal preferences. At NASA, for instance, Representative John Culberson (R-TX), a science fan who leads the House of Representatives spending committee that oversees NASA, NSF, and other science agencies, proposed cutting the space agency's climate research—which he thinks falls outside NASA's charter. At the same time, he wanted to expedite a proposed mission to Jupiter's wa-

tery moon Europa, which he and some scientists see as a promising place to find alien life.

Culberson and other appropriators also noted that many science agencies might benefit if Congress and the White House could agree on raising the caps. That is exactly what happened. A February budget deal, which also prevented a government shutdown, provided \$63 billion more for civilian discretionary spending in 2018, with an additional \$18 billion available in 2019. (The military got \$80 billion and \$18 billion, respectively.)

With the new money in hand, Congress went to work. NASA science got an 8% boost, to \$6.22 billion, and the Europa mission—including a lander—got an even bigger hike than initially planned. The agency's \$1.92 billion earth sciences budget avoided the ax, as did several climate missions. NSF's budget grew by 4%, to \$7.767 billion, and NIST's research account gained 5%, to \$724 million.

At DOE, the final bill not only rejected the proposed Trump cuts but also raised the Office of Science budget by \$868 million—or 16%—to \$6.26 billion. The total will enable the agency to continue U.S. support for ITER, the international fusion reactor under construction in France, and accelerate work on several shovel-ready projects at DOE's national laboratories, including upgrading the Spallation Neutron Source at the Oak Ridge National Laboratory (ORNL) in Tennessee. In addition, ARPA-E survived and received a \$47 million bump, to \$353 million. Overall, DOE's raise should allow the agency to fund “a lot of timely, well-vetted ideas that are

champing at the bit,” says Thom Mason, a former ORNL director who is vice president for laboratory operations at Battelle in Columbus, which runs six DOE labs.

NIH, the biggest winner, cashed in on its traditional popularity among legislators and the potent pleas of disease advocacy organizations. No one expected Congress to go along with Trump’s proposed deep cut. Instead, the question was how much more NIH, which received \$2 billion increases in both 2016 and 2017, would get this time around.

Last summer, before the budget caps were lifted, the House came in at the low end, with a \$1 billion raise for 2018. The Senate countered with \$2 billion. In the end, the two bodies “compromised” at \$3 billion, an 8.7% boost. That’s the largest annual increase for NIH since a massive 2009 economic recovery bill gave it \$10 billion.

the agency received in the late 1990s and early 2000s, when its budget doubled in just 5 years. The doubling triggered concern that federal spending had tilted too far toward biomedicine and was neglecting the physical sciences. In response, in 2006, then-President George W. Bush and his science adviser, John Marburger, hatched an initiative to double the budgets of NSF, NIST, and DOE science over a similarly short time span. Congress liked the idea but never delivered the money.

At the same time, the NIH doubling left a mixed legacy. NIH’s budget stagnated for the next decade as legislators felt they had taken care of the agency for years to come. Meanwhile, the boom created an expanded cohort of young, well-trained scientists, leading to increasingly stiff competition for funding. Community leaders lamented this “hard landing,” and some said that smaller, steadier

REGENERATIVE MEDICINE

U.K. trials of airway transplants are in limbo

Studies are based on flawed evidence and could harm patients, scientists say

By **Matt Warren**, in *Liverpool, U.K.*

Replacing a failing windpipe, or trachea, with one partially made from a patient’s own stem cells once looked like the cutting edge of regenerative medicine. But the concept took a severe blow in 2016 with the dramatic fall of Paolo Macchiarini, a surgeon at the Karolinska Institute (KI) in Stockholm. Macchiarini was fired by KI for scientific negligence and has been found guilty of misconduct in more than half a dozen papers. Most of his patients have died, and Swedish prosecutors are considering whether to reopen a criminal case against him that was closed last October.

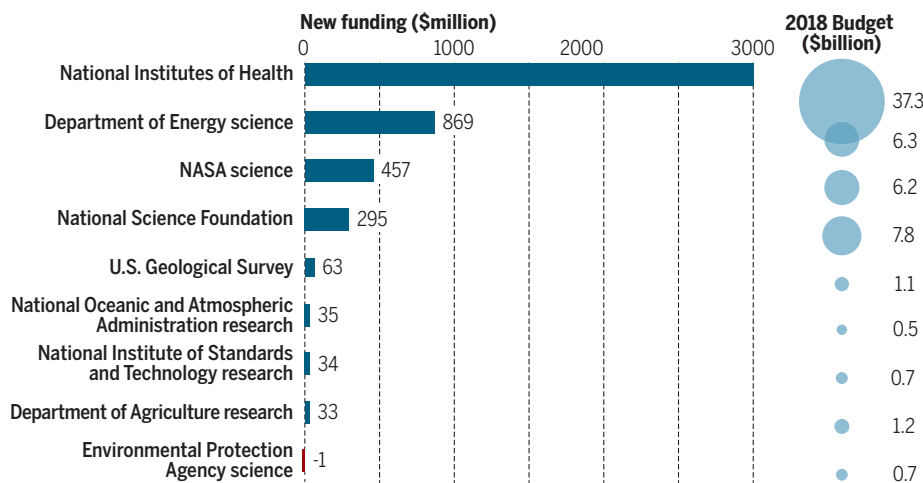
But is the idea underlying Macchiarini’s work—“seeding” a scaffold with a patient’s own stem cells, in hopes of regenerating a healthy, functional organ—still worth testing in patients? That’s the question facing scientists in the United Kingdom, where two trials of stem cell–based larynx (voice box) and trachea transplants are planned but on hold in the wake of the scandal.

Both studies, led by former Macchiarini collaborator and University College London (UCL) laryngologist Martin Birchall, received approval from the Medicine and Healthcare Products Regulatory Agency more than 2 years ago and have obtained close to £5 million from U.K. funding agencies. An independent inquiry last year concluded there was no reason to cancel the trials, and UCL says they can proceed.

But some scientists say the studies, like Macchiarini’s operations, are based on flimsy evidence and could harm patients. In November 2017, cellular and molecular biologist Patricia Murray and biochemist Raphaël Lévy of the University of Liverpool filed a detailed complaint with the U.K. Parliament’s Science and Technology Committee, which is holding an inquiry into research integrity, in an effort to stop the studies. (They followed

The National Institutes of Health leads the way

Biomedical research won about two-thirds of the \$4.8 billion increase given to nine civilian science agencies.



The total includes a 30%, \$414 million increase for Alzheimer’s disease research. The Brain Research through Advancing Innovative Neurotechnologies Initiative gets a \$140 million boost, to \$400 million. The All of Us precision medicine study receives a \$60 million increase, to \$290 million. At least \$500 million in new funds will go to research on opioid addiction. The bill also orders NIH to delay implementing a new, broader definition of clinical trials that basic behavioral and brain researchers had warned could stifle their research.

Even NIH advocates were stunned by the outcome. “Beyond words, folks,” tweeted Benjamin Corb, director of public affairs at the American Society for Biochemistry and Molecular Biology in Rockville, Maryland.

But outside the biomedical community the news stirred some quiet grumbling. NIH’s success recalls the large spending increases

increases would have been better for NIH.

Congress may not have the fiscal wherewithal for another big boost in civilian research in 2019, however. And there’s also reason to question its overall commitment to continued growth. In touting the omnibus bill, for instance, many top appropriators didn’t even mention research. Those that did mentioned just medical research.

The White House has also ignored the research boost, emphasizing the big increases for the military and denigrating civilian science programs. Trump responded to the news of a final deal by tweeting that he “had to waste money on Dem giveaways” to get the \$700 billion he wanted for national security. Of course, those “giveaways” include every dollar spent on civilian science. ■

With reporting by Jeffrey Brainard, Adrian Cho, Jocelyn Kaiser, and Kelly Servick.



Martin Birchall (far left), Paolo Macchiarini (second from right), and collaborators in 2010, after the first transplant of a stem cell–seeded trachea into a child.

up with a second submission in January.) “I’d really like to see [the trials] taken off the table completely,” Murray says. So would head and neck surgeon Pierre Delaere of the Catholic University of Leuven in Belgium, a ferocious critic of the trachea transplants long before Macchiarini’s downfall.

Birchall did not respond to requests for comment; UCL has submitted a response to Parliament but said it could not answer questions pending the completion of the inquiry.

In the studies, a larynx or trachea would be taken from a donor and all its cells removed using detergents and enzymes. The outside of the structure would be repopulated with mesenchymal stem cells from the patient’s own bone marrow, and the inside seeded with their epithelial cells. Then it would be grafted into the patient.

Birchall and Macchiarini first used this procedure to replace one of the bronchi—the ducts leading from the trachea to the lungs—in a patient in Barcelona, Spain, in 2008, a case globally publicized as heralding a new era of regenerative medicine. The duo replaced a child’s trachea with the technique in 2010 before going their separate ways, reportedly amid a patent conflict. Macchiarini operated on more than a dozen other patients, but switched to using tracheas made from a polymer instead of donor organs in 2011. Meanwhile, the UCL team gave donor tracheas to two more children in the United Kingdom, and a UCL surgeon attended when Macchiarini operated in Italy on a U.K. adult.

So far, the operations occurred under “compassionate use” guidelines, which allow doctors to try untested treatments in patients with a serious or life-threatening illness when there are no other options. The clinical trials are designed to examine safety and effectiveness more rigorously. INSPIRE, a collaboration between UCL and regenera-

tive medicine company Videregen, intends to recruit four patients suffering from narrowing or softening of the trachea, while a study named RegenVox would recruit 10 patients with similar defects in the larynx. Later, UCL and Videregen plan to lead a Europe-wide trial in 48 patients, which was awarded €6.8 million under Europe’s Horizon 2020 funding program in 2015.

Delaere has long claimed that there is no evidence that stem cells can grow into new tissues on a decellularized or polymer trachea, calling the idea “completely unrealistic.” In 2015, he accused Macchiarini and Birchall of misconduct in an eight-page document sent to UCL, KI, and two scientific journals, suggesting the pair was guilty of “the biggest lie in medical history.”

UCL SET UP A PANEL to examine Delaere’s claims. Its 2015 report has not been made public, but a draft version seen by *Science* cleared Birchall and a UCL collaborator. But the report did cite a “misleading element” in a 2012 paper in *The Lancet* describing a patient given a tissue-engineered trachea. It said that, although there was no “deliberate fraud or intent to mislead,” Birchall did not sufficiently acknowledge that the patient’s recovery may have been aided by procedures not directly related to the stem cells, namely the introduction of a stent and a “tissue wrap” to support the transplant. The report also said Birchall had failed to present evidence that the stem cells “played any therapeutic role,” and that he should be more careful in his papers and receive “education and training,” lest he “jeopardise his future research efforts and subject both himself and UCL to reputational risk.”

After Macchiarini’s firing the next year, UCL put the trials on hold while another panel investigated UCL’s relationship with

Macchiarini. In September 2017, that group concluded that the trials had the appropriate approvals in place and should go ahead. It didn’t examine the preclinical evidence underlying the studies in detail, however.

Murray and Lévy’s submissions to the parliamentary committee echo Delaere’s concerns and add several accusations. They say the five compassionate-use cases show that the procedure doesn’t work and isn’t safe. In two patients the transplanted trachea collapsed, and one died soon afterward; the other required further surgery and died some months later. Neither was in immediate danger of losing their lives before the transplants, the duo says, based on evidence from UCL’s 2017 inquiry and a BBC documentary featuring one of the patients.

The duo also charges that Birchall’s team provided inaccurate descriptions of its patients to funders and regulators. For example, in an application to the U.K. Medical Research Council obtained by German blogger Leonid Schneider, the researchers write that one of their patients “died of non-graft related causes,” but in a recent case study in *Stem Cells Translational Medicine*, the team concludes that the death may have been the result of a failure of the transplant.

Animal studies underlying the procedure have problems as well, Murray and Lévy say. One key paper investigating the procedure in pigs provides “insufficient evidence to support the authors’ claims,” they write. They also assert that identical images showing transplanted larynxes appear to have been used in two separate papers, even though the papers describe distinct surgical procedures. Murray says the duo has referred the case to UCL as potential research misconduct, and that the university has told her it will look into the matter.

Birchall’s statements on what the stem cells actually do contradict each other, Murray and Lévy add. Some documents, including the RegenVox trial’s entry on ClinicalTrials.gov, state that they form new cartilage, but in one of the pig studies of larynx transplants, the authors acknowledge that they were unable to follow the fate of the stem cells and found “no evidence of regeneration of the de-cellularised cartilage.”

UCL’s response to the Science and Technology Committee, which is public, says that the deceased patients would also have died without treatment, and that the transplants offered them a chance to live longer. That three of five patients remain alive today supports the case for formal clinical trials, UCL says. When introducing new technologies, “It

is rare for everything to work perfectly [the] first time,” the university writes, “and the introduction of tissue engineered treatments is no exception.” As to the animal studies, UCL doesn’t address many of the issues raised by Murray and Lévy but says its researchers “have done as much as they can already to show safety and efficacy in animals,” and further animal work would be unethical.

Other scientists say the jury is still out on the effects of stem cells in these kinds of grafts. “The impact of seeded cells for us is unclear at this point,” says Tendy Chiang, a pediatric otolaryngologist at Nationwide Children’s Hospital and The Ohio State University in Columbus, who is conducting preclinical research into tissue-engineered trachea transplants.

John Rasko, a clinical haematologist and pathologist at Royal Prince Alfred Hospital in Sydney, Australia, says U.K. funding bodies have a “declared enthusiasm” for research on stem cell therapy. But given the issues raised by critics, “to now have this substantial investment in Birchall and others’ trials in the U.K. is something of concern,” says Rasko, who was recently elected president of the International Society for Cellular Therapy but says he’s speaking in a personal capacity. “I just don’t see why there’s a need to rush into these things until clear evidence is brought to bear,” he adds.

The parliamentary committee is expected to publish its report in the next few months, but it appears unlikely to render any judgment about Birchall’s trials. A source at the committee says the inquiry’s intention is to examine how institutions respond to allegations of research misconduct, rather than to investigate any particular case.

What will happen to the studies remains unclear. In the wake of UCL’s 2017 inquiry, the INSPIRE consortium decided to conduct a further risk assessment. As a result, say spokespeople for the Cell and Gene Therapy Catapult, a nonprofit center that serves as the trial’s sponsor, the group has decided to “gather more data” and “will only recommend the restart of any trials ... if supported by expert opinion with regulatory and ethical approval.” UCL did not respond to questions about the future of the RegenVox trial, but for now it remains listed as “suspended” on the university’s website.

Murray says Macchiarini and Birchall both rode on the high hopes for stem cells. Media stories about their operations—sometimes with photos of patients taken shortly after surgery—projected an air of success that blinded even respected institutes and funders to potential flaws in the research, she says: “Once people were seeing pictures of the patients, maybe no one’s really looking at the hard evidence so much anymore.” ■

CYBERSECURITY

U.S. blames ‘massive’ hack of research data on Iran

Targets included nearly 8000 professors in 22 countries

By Jon Cohen

A “massive and brazen cyberassault” revealed last week by the U.S. Department of Justice (DOJ) showed that academics are easy targets for hacking. In “one of the largest state-sponsored hacking campaigns” it has ever prosecuted, DOJ alleges that nine Iranians working on behalf of the Islamic Revolutionary Guard Corps stole data from 7998 professors at 320 universities around the world over the past 5 years.

The indictment, filed by a federal grand jury in New York City and unsealed on 23 March, alleges that the hackers pilfered 31.5 terabytes of documents and data, including scientific research, journals, and disser-

tations. Their targets also included the United Nations, 30 U.S. companies, and five U.S. government agencies. The indictment does not name the hacked academic institutions or companies, but it notes that the victims included

academic publishers, a biotechnology company, and IT technology companies.

“This is not an isolated breach—it’s hundreds if not thousands of breaches,” says Anthony Ferrante, who heads cybersecurity at FTI Consulting in Washington, D.C., and formerly worked as a cyber expert for the White House’s National Security Council. Ferrante says academia is particularly vulnerable because of its open, collaborative ethos. “It really becomes a target for malicious cyberactivity.”

The hacks came to light through investigations by the Federal Bureau of Investigation and reports from victims. “The hackers targeted innovations and intellectual property from our country’s greatest minds,” said U.S. Attorney Geoffrey Berman of the Southern District of New York, where the indictment was filed.

Bahram Ghasemi, spokesperson for Iran’s Ministry of Foreign Affairs, countered that the accusations were false and “yet another clear sign of the U.S. ruling elite’s inherent hostility and enmity towards the Iranian nation.” Some U.S. cyber and policy analysts also see political moti-

uations behind the indictment and suggest the actual harm was modest.

According to the indictment, the attack targeted 3768 professors at 144 U.S. universities and stole data that cost the institutions about \$3.4 billion to “procure and access.” The accused allegedly set up an institute in Iran called Mabna that coordinated and paid for the hacks. The institute, the indictment says, aimed to “assist Iranian universities, as well as scientific and research organizations, to obtain access to non-Iranian scientific resources.” The stolen data were sold through two websites, Gigapaper and Megapaper.

The indictment says the university breaches involved “spearfishing,” in which the accused sent emails that tricked targets

into providing their login credentials. The emails supposedly came from professors who had read articles by the targets and asked for access to more of their work, helpfully providing links. Clicking a link took the victim to a fake

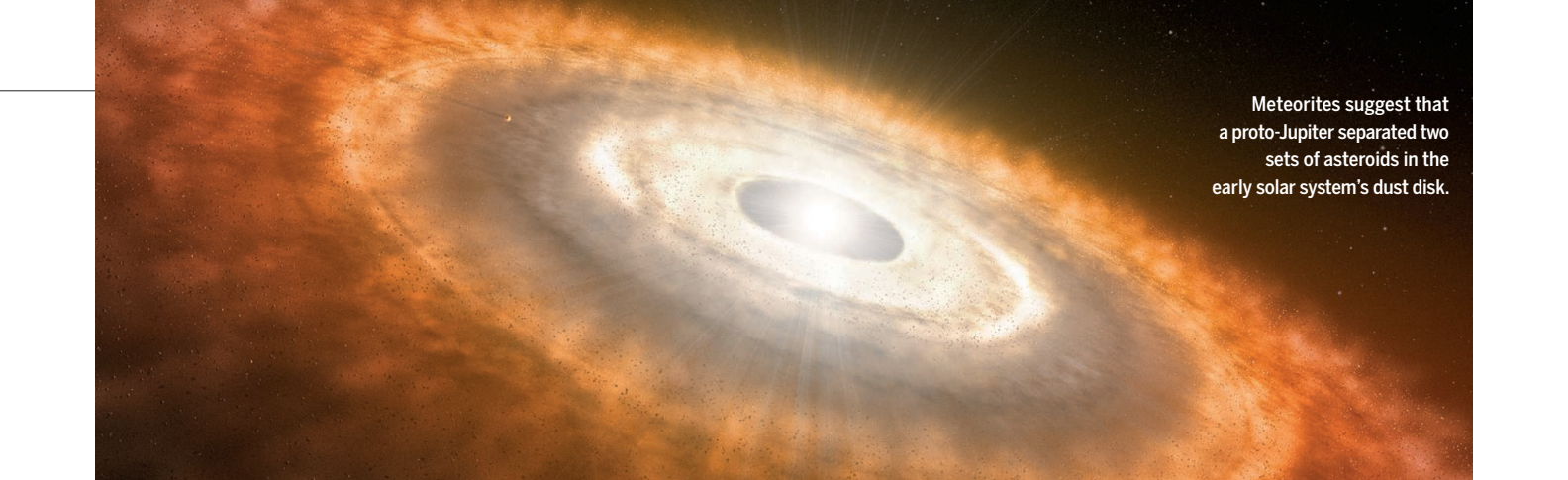
internet domain that resembled their own university’s website and asked them to log in.

With the harvested credentials, documents and other resources were easy pickings. “College professors are like shooting fish in a barrel,” says Max Kilger, a social psychologist at University of Texas in San Antonio who studies motivations of cyber-terrorists. “For the most part, they’re pretty unassuming and they leave valuable data on personal machines and university machines that aren’t very well protected.” (For the private sector, the indictment says hackers used “password spraying,” cracking into accounts with commonly used passwords.)

The charges against the accused include wire fraud, aggravated identity theft, and conspiracy to commit computer intrusions. The U.S. Department of the Treasury separately announced sanctions against the alleged perpetrators. They “are no longer free to travel outside of Iran without the fear of being arrested and extradited to the United States,” Berman said. “The only way they can see the rest of the world is through their computer screen, but now stripped of their greatest asset, anonymity.” ■

“College professors are like shooting fish in a barrel.”

Max Kilger, University of Texas



Meteorites suggest that a proto-Jupiter separated two sets of asteroids in the early solar system's dust disk.

PLANETARY SCIENCE

Meteorite divide points to solar system chaos

“Warren gap” validates models that suggest early wanderings for the giant planets

By **Paul Voosen**, in *The Woodlands, Texas*

The stately solar system of today was in turmoil in its first several million years, theorists believe, with giant planets sowing chaos as they strayed far from their current orbits. But corroborating evidence has been thin—until now.

Scientists have found a new window into the early dynamics: a curious chemical divide in the dozens of species of meteorites. The picture has emerged over several years, but in work presented last week at the Lunar and Planetary Science Conference here, a group of German geochemists reported clinching evidence. They tested 32 meteorites representing nearly all known types and found that “any meteorite you take, it belongs to either one of these groups,” says Thorsten Kleine, a geochemist at the University of Münster in Germany who led the work.

Those divergent chemistries imply distinct origin stories for asteroids, the parent bodies of most meteorites. One group formed from grist that began near the current location of the asteroid belt. The others coalesced much farther out, beyond a proto-Jupiter, near where Saturn orbits today. Only later, pushed and pulled by the wandering giant planets, did these immigrant asteroids find their home in today’s asteroid belt. Bill Bottke, a planetary dynamicist at the Southwest Research Institute (SwRI) in Boulder, Colorado, thinks the chemical divide holds other clues to the timing and formation of the planets. “It really seems to be a powerful mechanism for understanding our solar system.”

Paul Warren, a meteoriticist at the University of California, Los Angeles, was the first to notice what has come to be called the Warren gap. He gathered measurements of chromium and titanium isotopes for two

meteorite types. Those metals, forged by the explosions of dying stars, were mixed throughout the disk of gas and dust from which planets and asteroids took shape. Warren expected his meteorites to display a continuum of isotopic abundances, because he assumed they had formed across the one broad region of the asteroid belt. Instead, he found that, in one meteorite type, called carbonaceous chondrites, the isotope levels were starkly different from other types. “I knew a good thing when I saw it,” he says.

In a 2011 study, Warren argued that such a dichotomy could exist only if the two groups were separated for millions of years at formation. The most plausible source of that split was a void created by the gravity of a proto-Jupiter. But carbonaceous chondrites are known to have formed later than other meteorites—so it was possible that their peculiar isotopic chemistry reflected changes over time in the disk, rather than a distinct place of origin.

A few years ago, Kleine’s group began looking at isotopes of molybdenum, another metal, and found a Warren gap there, too. It also found that iron meteorites fell into two populations even though they must all have formed at about the same time. That meant a physical barrier. “And the most obvious one would be Jupiter,” Kleine says.

Kleine’s team began spelling out the implications: By 1 million years after the solar system’s start, Jupiter’s core had grown large enough to sweep up dust in its path, creating a barrier. A new influx of metal-rich dust to the solar system, perhaps from a nearby supernova, would have augmented isotopes in the outer asteroids but not the inner ones. Then, 3 million to 4 million years later, Jupiter migrated inward, mixing the two reservoirs. The Warren gap is both

a validation of dynamic solar system models that predict a similar scenario, and a constraint they must reckon with, says Kevin Walsh, a SwRI dynamicist.

Now, scientists are gleaning other clues about the early solar system from the meteorites. One group is studying rare meteorites that mix up carbonaceous and noncarbonaceous components, a hint that they formed just after Jupiter’s migration, in an effort to date when the two reservoirs combined. And by comparing molybdenum isotopes in rocks from Earth’s mantle with those in meteorites, Kleine’s team has found preliminary signs that Earth’s water was partially delivered by a shower of impactors from the more distant asteroid population.

The meteorite studies could even set back the clock on the age of the 4.6-billion-year-old solar system itself. That date comes from the decay of uranium in calcium-aluminum-rich inclusions in meteorites. These little metal snowflakes, created by the sun’s heat, are thought to have arisen in the earliest years of the solar system. But scientists have long wondered why carbonaceous meteorites are richer in these snowflakes. It appears that the inclusions are also isotopically similar to the outer solar system meteorites. Researchers now speculate that they formed far from the sun, driven by heat from a proto-Jupiter. If so, some inclusions must have formed after Jupiter took shape, meaning they are at least 1 million years younger than the solar system. “A huge advance,” Bottke said. “My jaw was on the floor about that.”

Meanwhile, the hunt is on to interpret other meteorites in this new light. It’s amazing to think that samples on Earth originated near Saturn, Bottke says. “A few years ago if you had said that you would have had people laugh at you.” ■

OPTICS

X-ray 'ghost images' could cut radiation doses

Technique points to safer medical imaging done with cheap, single-pixel cameras

By **Sophia Chen**

On its own, a single-pixel camera captures pictures that are pretty dull: squares that are completely black, completely white, or some shade of gray in between. All it does, after all, is detect brightness.

Yet by connecting a single-pixel camera to a patterned light source, a team of physicists in China has made detailed x-ray images using a statistical technique called ghost imaging, first pioneered 20 years ago in infrared and visible light. Researchers in the field say future versions of this system could take clear x-ray photographs with cheap cameras—no need for lenses and multipixel detectors—and less cancer-causing radiation than conventional techniques.

“Our system is much smaller and cheaper, and it could even be portable if you needed to take it into the field,” says Wu Ling-An, a physicist at the Chinese Academy of Sciences in Beijing whose work with her colleagues was published on 28 March in *Optica*.

The researchers’ system still isn’t ready to be used in medicine. But they have lowered the x-ray dose by about a million times compared with earlier attempts, says Daniele Pelliccia, who in 2015 made some of the first x-ray ghost images. A physicist at Instru-

ments & Data Tools, an optics startup near Melbourne, Australia, he used a building-size source of intense x-rays called a synchrotron, but Wu’s group made do with a compact tabletop source. And whereas early x-ray ghost images were simple pictures of slits cut into metal, the Chinese group produced outlines of a seashell and of initials etched into metal plates. They have made “images that look like images,” Pelliccia says. “The potential payback, if it works for medical images, is big.”

The key to ghost imaging is to illuminate an object with light that has passed through a filter with a known pattern, says Miles Padgett, a physicist at the University of Glasgow in the United Kingdom. On the other side of the object, the single-pixel camera takes a picture—nothing more than a gray square. To end up with an image, you do this thousands of times, swapping out the filter pattern for a different one after each exposure. Wu’s group used a piece of sandpaper, which is partially transparent to x-rays, and rotated it to create a different pattern after each exposure.

A computer produces the final image. Because the computer knows the filter pattern for each exposure, it can calculate the image from variations in the sequence of gray pixels captured by the camera. The result, in theory, is an x-ray image as good as any

today, but without a high-resolution camera or the intense x-rays needed for conventional imaging.

Researchers have already demonstrated simple ghost imaging systems for optical and infrared light, which rely on programmable filters, says Jeffrey Shapiro, a physicist at the Massachusetts Institute of Technology in Cambridge. A computer records and resets the filter pattern as the light source projects it onto the object and the single-pixel detector.

Using an infrared system, Padgett’s group has shown it can ghost-image a methane gas leak. The group’s industry collaborator, M Squared Lasers, based in Glasgow, is working to commercialize the system and hoping to sell detectors to the oil and gas industry as a cheaper way to detect leaky pipelines, Padgett says.

Making a computer-programmable filter for x-rays is a bigger challenge, Wu says, because x-rays simply stream through most materials. Because her group resorted to unprogrammable sandpaper, it had to use a high-resolution camera to measure the patterns. But you could imagine a commercial x-ray system in which the manufacturer prerecords all the sandpaper patterns, Padgett says. Then, only the manufacturer would need the high-resolution camera, and individual users could simply buy a single-pixel camera and use the sandpaper filters in a specified sequence.

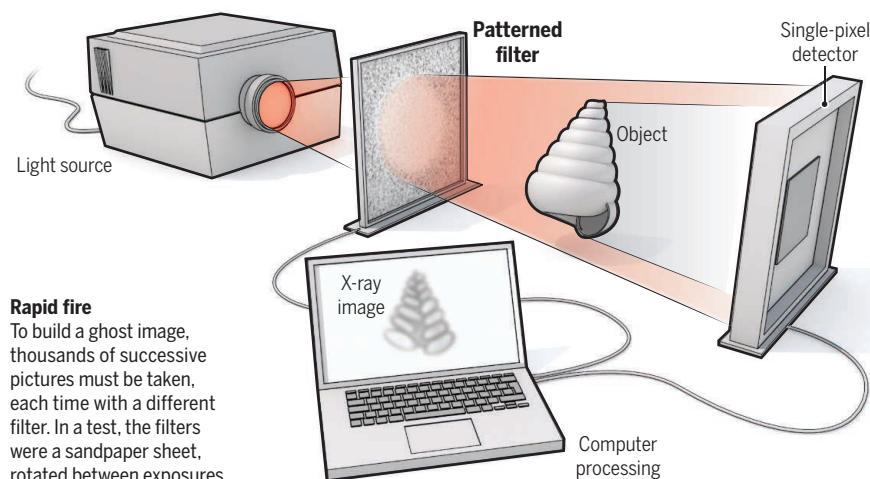
In order for ghost imaging to be viable in medicine, Wu says, researchers must show that the total x-ray dose needed for an image is lower than with a conventional system. One ghost image requires thousands of exposures, and the x-rays add up. In addition, the more detailed the object—for example, a human body—the more exposures you need. However, Wu says the x-ray intensity per exposure can be made low enough that ghost imaging may come out ahead.

Doing so would be important, Shapiro says. “If you could reduce the amount of x-ray exposure that women suffer in getting mammograms, or in chest exams, that would be a big deal,” he says. But image quality still needs to be improved, he says. “It’s got to be a good image.” ■

Sophia Chen is a journalist in Tucson, Arizona.

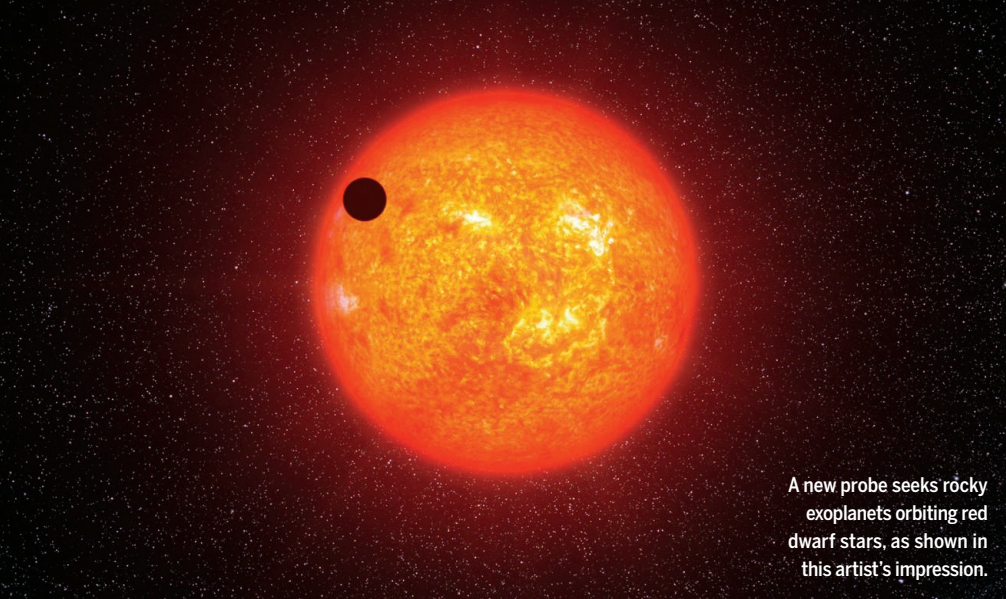
Seeing ghosts

Using a patterned light filter and a single-pixel detector, researchers can make crisp pictures of objects, even though the detector only captures unresolved, gray squares.



Rapid fire

To build a ghost image, thousands of successive pictures must be taken, each time with a different filter. In a test, the filters were a sandpaper sheet, rotated between exposures.



A new probe seeks rocky exoplanets orbiting red dwarf stars, as shown in this artist's impression.

ASTRONOMY

New missions aim to make a short list of *exo-Earths*

Ground- and space-based searches seek Earth-like targets for the next great space telescope

By Daniel Clery

Thanks to NASA's pioneering Kepler probe, we know our galaxy is teeming with exoplanets. Now, a new generation of exoplanet hunters is set to home in on rocky worlds closer to home.

Over 9 years in space, Kepler has found more than 2600 confirmed exoplanets, implying hundreds of billions in the Milky Way. The new efforts sacrifice sheer numbers and target Earth-size planets whose composition, atmosphere, and climate—factors in whether they might be hospitable to life—could be studied. Leading the charge is the Transiting Exoplanet Survey Satellite (TESS), a NASA mission due for launch on 16 April.

The brainchild of researchers at the Massachusetts Institute of Technology (MIT) in Cambridge, the \$337 million TESS project aims to identify at least 50 rocky exoplanets—Earth-size or bigger—close enough for their atmospheres to be scrutinized by the much larger James Webb Space Telescope (JWST), due for launch in 2020 (*Science*, 19 February 2016, p. 804). “Where do we point Webb?” TESS Principal Investigator George Ricker asked rhetorically at the American Astronomical Society annual meeting at National Harbor in Maryland in January. “This is the finder scope.”

Like Kepler, TESS finds planets by staring at stars and looking for a dip in brightness as a planet passes in front, blocking some of the

star's light in a so-called transit. But whereas Kepler kept a fixed view, watching just 0.25% of the sky out to a distance of 3000 light-years, TESS will maneuver to observe 85% of it, out to about 300 light-years.

The spacecraft carries four telescopes that together will survey a strip of sky extending from the solar system's pole to its equator, known as the ecliptic. The scopes will watch a strip for 27 days, then shift sideways and repeat the process. After observing 13 such strips over a year, covering almost an entire hemisphere of sky, TESS will flip over and survey the other hemisphere.

Over 2 years, TESS should measure the brightness of some 2 million stars, says project scientist Stephen Rinehart of NASA's Goddard Space Flight Center in Greenbelt, Maryland. “If there is one planet per star [as Kepler predicts], we will see many. It'll be a firehose of data.”

TESS's primary targets are red dwarf stars, the most common stars in our neighborhood. Red dwarfs weigh less than half as much as the sun, so they do not burn brightly, offering several advantages to exoplanet hunters. A planet passing in front of a small, dim red dwarf blocks more of its light, yielding a stronger transit signal. Moreover, planets can whip around red dwarfs in orbits closer than Mercury's, and still have hospitable climates. More orbits mean more opportunities for transit detections. TESS researchers are targeting speedsters that would circle

the star at least twice during a 27-day TESS watch. Spotting two transits is key because it tells astronomers the length of the planet's orbit. Other features of the transit—its duration, how much light is blocked, and how quickly the brightness dips—provide additional details such as the planet's diameter.

Transits don't reveal a planet's mass, however, which is vital to determining its density—a clue to whether it is made of iron, rock, or ice. For this, TESS is relying on follow-up studies by ground-based telescopes, which can watch for tiny periodic Doppler shifts in the frequency of a star's light caused by an orbiting planet tugging on it. The shift is a clue to the planet's mass (*Science*, 5 January, p. 18). Of the 5000 transitlike signals that the TESS team expects to detect, the clearest will be chosen for ground-based follow-up, says MIT's Sara Seager, the mission's deputy science director. The aim is to identify and weigh 50 planets to serve up to the JWST.

Although detecting planets around red dwarfs is easier, life may be less likely to arise there. Red dwarfs are erratic, prone to blasts of lethal radiation, and because the planets are so close, “they feel the effects of the star,” says astronomer Elisa Quintana of NASA Goddard. Close-in planets are also likely to be “tidally locked,” with one side always facing the star in an eternal scorching day while the other side freezes in an endless night. “Can they be habitable?” Quintana asks. “The debate goes back more than 10 years.”

Later this year, the European Space Agency will launch another eye on exoplanets: the Characterising Exoplanets Satellite. Rather than searching for new worlds, it will take a second, much longer look at transits of known planets to pin down their sizes more precisely. In combination with mass measurements from the ground, that should provide a better fix on planets' densities.

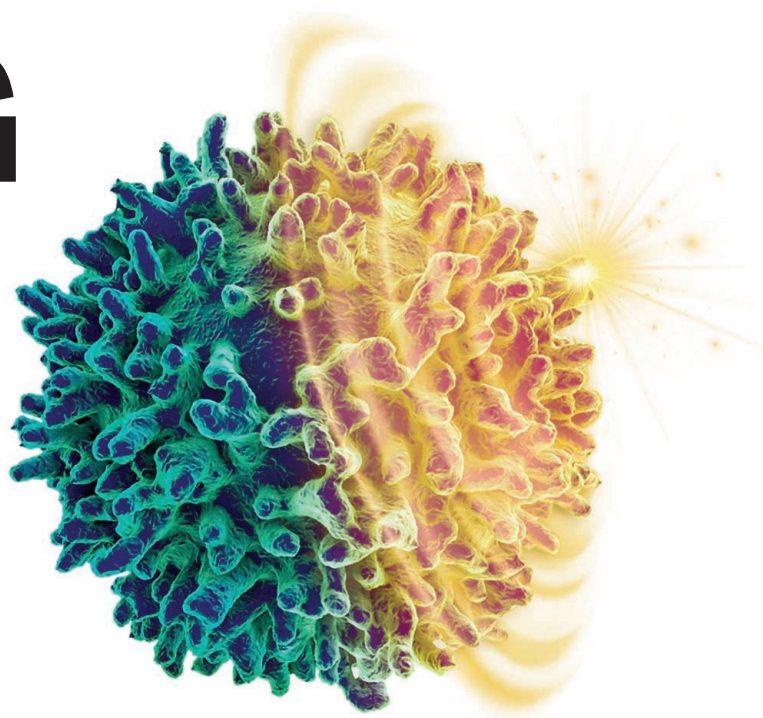
Also debuting in the next few months is a ground-based search in Chile: SPECULOOS, the search for habitable planets eclipsing ultra-cool stars. The project's four 1-meter telescopes have near-infrared sensors to detect transits of the very dimmest, coolest stars; a similar array in the Canary Islands will survey the northern sky. These stars are too faint for TESS's small telescopes to see, but they could give the JWST valuable targets, says Michaël Gillon of the University of Liège in Belgium, which is leading the project.

SPECULOOS may be especially sensitive to small planets, because even small bodies will block noticeable amounts of light from the dim target stars. “TESS will find many more planets, but in the temperate—and potentially habitable—Earth-size regime, SPECULOOS's detection potential should be significantly better,” Gillon says. “The next years are going to be very exciting!” ■

FEATURES

PUTTING IMMUNE CELLS ON A DIET

To treat immune illnesses, researchers are probing drugs that could starve troublemaker cells



By **Mitch Leslie**

About 12 years ago, Gary Glick and his wife noticed something wrong with their son, Jeremy. He seemed to be lagging behind his twin sister, recalls the immunologist and chemical biologist at the University of Michigan in Ann Arbor. “They were growing in unison, and he sort of stopped.” Jeremy, who was 9 or 10 at the time, also looked sickly and pale and began complaining of nagging pains in his stomach and elsewhere.

Rachel Lipson Glick, a physician, was stumped by their son’s mysterious ailment. So were other doctors. It took about 3 years to rule out myriad cancers, endocrine malfunctions, and other potential causes and to determine that Jeremy had Crohn disease, an inflammation of the digestive tract stoked by misbehaving immune cells.

The diagnosis made life harder for Jeremy, now 22 and a senior at college. To control the symptoms, he injects the antibody drug adalimumab (Humira). He will likely need it, or another immune-inhibiting treatment, for the rest of his life.

By coincidence, one of those alternatives might stem from his father’s work. Gary Glick, like an increasing number of other researchers, is convinced that the immune cells driving conditions such as Crohn disease share a feature that could be their undoing: their metabolism. He has spent the past 2 decades searching for drugs that target metabolic adaptations of immune cells. Clinical trials by Lycera, a company Glick founded, are now assessing the first of those drugs for psoriasis and ulcerative colitis, an intestinal illness related to Crohn disease.

Drug companies are working to develop other candidates. Researchers are also look-

Once triggered into action, an immune cell overhauls its metabolism in ways that could be exploited for treatment.

ing to deploy existing drugs that tamper with metabolism, such as the diabetes treatments metformin and 2-deoxyglucose (2DG). “It’s a very exciting time,” says immunologist Jonathan Powell of Johns Hopkins University’s School of Medicine in Baltimore, Maryland. “Potentially, all immunologic diseases are targets for metabolic therapy.”

Cancer researchers have also tried to disrupt cell metabolism, even testing some of the same drugs immunologists are investigating. But many scientists are convinced the strategy will work better for immune diseases than for tumors because drugs to treat those illnesses need only to suppress a relatively small number of overexuberant cells, not eliminate them. And whereas existing drugs that restrain immune cells, such as adalimumab, can compromise our defenses against pathogens, Glick and other scientists think that drawback won’t affect their strategy. Focusing on the metabolism of overactive immune cells, he says, offers “a way to directly target these cells while sparing immune function.”

IN THE 1920s, the German doctor and chemist Otto Warburg was the first to realize that immune cells have a distinctive way of fueling themselves. To power their activities, cells need to produce the molecule adenosine triphosphate (ATP). They can make it directly through glycolysis, a biochemical pathway that dismembers glucose. Or they can generate ATP through a more involved process called oxidative phosphorylation, which requires energy-laden molecules produced by glycolysis but also enlists other biochemical reactions that break down fatty acids and amino acids such as glutamine (see graphic, p. 1456).

Normal body cells typically rely on oxidative phosphorylation for most of their energy needs, but Warburg discovered that cancer cells ramped up glycolysis. He also noticed that some healthy cells depended on glycolysis: immune cells.

Warburg was on the right track, but researchers now know that when immune cells aren’t fighting pathogens, they set their metabolism to low and produce ATP mainly through oxidative phosphorylation. The arrival of a threat, such as a flu virus reproducing in the lungs, activates the cells, galvanizing them to combat the invader. At that point, “they undergo these massive metabolic changes,” says

immunologist Erika Pearce of the Max Planck Institute of Immunobiology and Epigenetics in Freiburg, Germany. The stimulated cells don’t just require more energy, she notes. An activated T cell can divide several times per day, quickly spawning an army of millions of descendants. To sustain that mobilization, the cells also require large amounts of raw materials, such as the precursors of DNA, proteins, and lipids.

How exactly an activated immune cell satisfies its massive demand for energy and molecular material depends on what type of cell it is. Activated helper T cells, which serve as immune commanders, seem to follow Warburg’s paradigm. They guzzle glucose and crank up glycolysis, although they also boost the rate of oxidative phosphory-

serve as cellular power plants, Pearce and her colleagues reported 2 years ago.

Although memory T cells “have these beautiful, intact, threadlike mitochondria,” she says, effector T cells mince their mitochondria. The organelles are where oxidative phosphorylation takes place, and breaking them up may make that metabolic pathway less efficient and promote glycolysis, the researchers suggest.

Metabolic adaptations permit immune cells to perform their protective roles, but sometimes they lead cells to malfunction. In rheumatoid arthritis, for instance, activated T cells slip into the joints, says immunologist Cornelia Weyand of Stanford University in Palo Alto, California. “They like it there, and they stay and they cause chronic tissue inflammation.”

That behavior reflects a change in metabolism. Like other activated T cells, the T cells implicated in rheumatoid arthritis rely on glycolysis. But they tweak that pathway to make less ATP and more of the molecular precursors needed to support their rapid division. As a result, the T cells run short of reactive oxygen species—key signaling molecules that control their behavior—and go rogue. They speed up their reproduction and specialize into varieties that promote inflammation.

The cells also become better gymnasts, skilled at slithering through narrow spaces into the joints. Weyand and her colleagues found that the abnormal T cells sprouted ruffles on their cell membranes that enabled them to penetrate

deeper into tissues. Within the joint, the mobile T cells help stimulate other cells to form a lesion that resembles a non-healing wound, Weyand says, and that causes pain and further joint deterioration. “The metabolism of the cell controls its behavior, and its behavior is not good for the patient,” she says.

PEARCE SAYS the prospect of meddling with immune cell metabolism to treat diseases frightens some of her colleagues, who fear crippling the body’s entire defense system or harming other vital cells. “If you give an inhibitor of glycolysis, isn’t that going to kill someone?” they ask her. But immunologist Jeff Rathmell of Vanderbilt University Medical Center in Nashville says that only a small fraction of immune cells—and of body cells in general—boost their use of those pathways and would



Gary Glick (left) discovered a drug that could lead to a treatment for the autoimmune illness that affects his son Jeremy (right).

lation by a lesser amount and consume more glutamine. Cytotoxic T cells, which kill tumor cells and cells commandeered by viruses, take a similar tack. In contrast, immune-suppressing regulatory T cells continue to get most of their energy from oxidative phosphorylation, even after they swing into action, and they prefer fatty acids to amino acids and glucose.

Immune cells also make different metabolic choices depending on whether they are memory cells, which persist for years and protect us from getting sick from the same pathogen more than once, or shorter-lived effector cells specialized to attack microbes immediately. Memory T cells, for instance, typically favor oxidative phosphorylation and consume fatty acids. Effector T cells, by contrast, turn up glycolysis and are heavy glucose users—a difference reflected in their mitochondria, the organelles that

be affected by metabolism-altering drugs. “Most cells don’t care.”

Work in animals suggests that targeting immune metabolism is a promising approach. In one 2015 study, immunologist Laurence Morel of the University of Florida in Gainesville and colleagues dosed mice that were genetically modified to develop a lupuslike condition with metformin and 2DG. Metformin curtails oxidative phosphorylation, whereas 2DG squelches glycolysis. Together, the molecules reversed lupus

glutamine to mice that had received skin grafts or heart transplants. The skin grafts survived about four times longer in the treated mice than in control animals, which quickly rejected the tissue. Transplanted hearts also worked much longer in mice that received the drug trio, the team reported in 2015 in *Cell Reports*.

THE FEW CLINICAL TRIALS TESTING the concept in people have mostly used already approved compounds such as metformin. Two

of the University of Texas Southwestern Medical Center in Dallas. “We shouldn’t be surprised if they don’t have the potency or specificity to have a significant effect.”

Some scientists think talk of treatments is premature. Inhibiting immune cells’ energy-producing reactions in a chronic disease “is an appealing idea,” says mitochondrial biologist Navdeep Chandel of Northwestern University’s Feinberg School of Medicine in Chicago, Illinois. But he contends that researchers don’t understand immune cell metabolism well enough to know how to intervene safely and effectively.

Yet a study published online this week in *Science* provides more support that inhibiting immune metabolism can quell human diseases. The work centers on a drug, dimethyl fumarate, that has already received approval from the U.S. Food and Drug Administration as a treatment for multiple sclerosis. Although researchers knew that the drug suppresses immune cells, they weren’t sure how. A team led by scientists at Johns Hopkins now reports that the compound cripples an enzyme necessary for glycolysis, bolstering the idea that the pathway can be targeted by drugs.

Glick is confident that he and others are on to something. The compound he discovered dates to research he began in the mid-1990s. “I sort of backed into it,” he says. Glick and his colleagues were looking for compounds that would kill B cells, the antibody-producing cells that help cause the symptoms of lupus. After testing several compounds, they found one that stymies an enzyme necessary for oxidative phosphorylation.

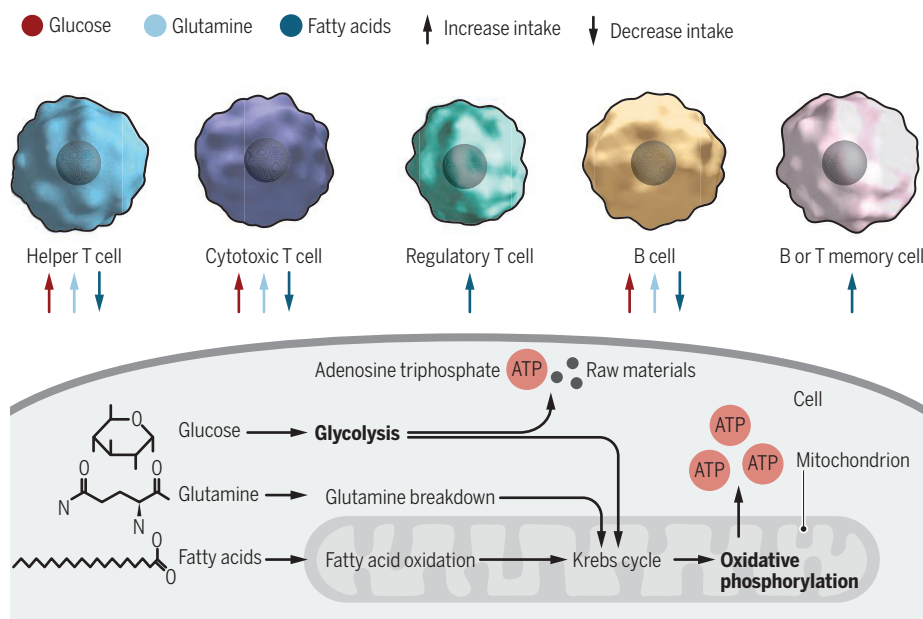
Lycera is evaluating an improved version of that molecule in people with psoriasis or ulcerative colitis in part because it’s easier to test drugs on those diseases than on lupus, whose symptoms affect more organs and are harder to track. Unlike the adalimumab that Jeremy Glick injects, this drug can be taken in pill form. Lycera plans to announce the results of its two trials later this year.

This month, a new company founded by Gary Glick started clinical trials of an existing antiparasite drug, niclosamide, in patients with ulcerative colitis. Niclosamide, which kills tapeworms by inhibiting oxidative phosphorylation, has a long safety record, Glick notes. “It’s approved for children and pregnant women,” he says.

Glick was searching for compounds that tinker with immune cell metabolism years before his son was diagnosed with Crohn disease, but he says Jeremy’s illness furnished extra motivation. “If he could wake up every morning and take a pill that dad invented, he’d be thrilled,” Glick says. ■

Alternative energy sources

Activated immune cells change what they consume and which metabolic pathway they use to break down that fuel to produce energy-carrying ATP. Some types load up on glucose, increasing glycolysis, and they consume more glutamine. Fatty acids remain a staple for other cells, which still depend on oxidative phosphorylation.



symptoms in the animals. Lupus patients, for example, pump out antibodies that attack their own DNA. But in the mice, the levels of those antibodies fell by about 50% after treatment began. The researchers detected no signs that the rodents became more vulnerable to infections.

In another study, Rathmell and colleagues added dichloroacetate, which suppresses glycolysis, to the drinking water of mice that have a condition that mimics multiple sclerosis, in which the immune system attacks nerves’ insulating myelin sheath. The compound prevented myelin destruction in the animals and reduced neurological symptoms such as muscle weakness, the scientists reported in 2014.

Impeding cellular metabolism also could curb the immune system’s attacks on transplanted organs, Powell and colleagues have found. They gave metformin, 2DG, and a third drug that blocks the metabolism of

years ago, Argentine researchers reported fewer new brain lesions in 30 patients with multiple sclerosis who took metformin or another drug that short-circuits oxidative phosphorylation. A clinical trial by Chinese researchers is testing whether metformin can quell lupus flares. And so far, such drugs seem safe. “Metformin on its own does very little to impair immunity, for example, but can reduce chronic inflammation,” Rathmell says.

Skeptics note that researchers also have tried to repurpose metformin and 2DG to block metabolism in cancer cells, with inconsistent results. However, Powell and other scientists say they aren’t discouraged. In contrast to cancer cells, “You don’t actually have to kill an [immune] cell to modify its metabolism,” Rathmell says.

These hand-me-down drugs weren’t designed to tweak immune cell metabolism, adds cancer biologist Ralph DeBerardinis

INSIGHTS

PERSPECTIVES



ECOLOGY

Change is key to frog survival

Changes in host traits help amphibian populations to survive chytrid infection

By James P. Collins

Outbreaks of infectious wildlife diseases often reduce host population size, but rarely cause extinction. An exception is the ongoing global decline of amphibians (1). A pathogenic chytrid fungus, *Batrachochytrium dendrobatidis* (Bd), may affect amphibian species little to not at all, predictably reduce population size, or have a role in extinction (2). On page 1517 of this issue, Voyles *et al.* (3) report that at three sites in Panamá, amphibian population sizes declined substantially, and most species went missing after the chytrid fungus emerged in their habitats. However, other frog species survived as Bd became endemic (see the figure). Only 9 frog species to date (~12% of species before the fungus arrived) returned to population levels approaching those estimated before Bd emerged (4). Voyles *et al.* show that the frog species that recovered did so as a result of changes in their traits and not due to a decrease in Bd's pathogenicity.

The stage for this research was set in 2004, when Bd's arrival triggered an outbreak of the infectious disease chytridiomycosis that coincided with frog declines and extinctions at El Copé, Panamá (see the photos) (5). More outbreaks followed at El Valle in 2006 and Campana in 2007. The wave-like declines echoed patterns seen in South America (6) and from Mexico to Costa Rica (7). After the frog population sizes reached low points between 2006 and 2010, ongoing observations revealed increases in the populations of some species (3, 8), a pattern that has also been reported in Australia (9). What caused the populations of some species to recover at the three study sites?

Voyles *et al.* predicted that hosts would recover because of a decrease in Bd pathogenicity, an increase in host resistance, or

A white-spotted Cochran frog (*Sachatamia albomaculata*) in Parque Nacional Omar Torrijos, El Copé, Panamá.

Downloaded from <http://science.sciencemag.org/> on March 29, 2018

PHOTO: SCOTT CONNELLY

both. Bd isolates cryopreserved in 2004 as the fungus emerged in the region provided a historical baseline. In their experiments, the authors paired these samples with Bd isolates collected in 2012 to 2013, after some frog populations had increased in size. This pairing allowed the team to ask whether the pathogenicity of Bd collected recently had changed compared to Bd collected nearly a decade before. Traits assessed included changes in Bd reproductive rate, size of infective zoospores, immune evasion, outcome of infection in live hosts, and genomic structure. By all these measures, Bd was as pathogenic in 2012 to 2013 as it was nearly a decade before. Bd isolates cryopreserved in 2004 and those collected in 2012 to 2013 clustered within the Global Pandemic Lineage (Bd-GPL) (10). There was no strong phylogenetic divergence between isolates over 10 years—long enough for pathogenicity to decrease *in vitro* (11).

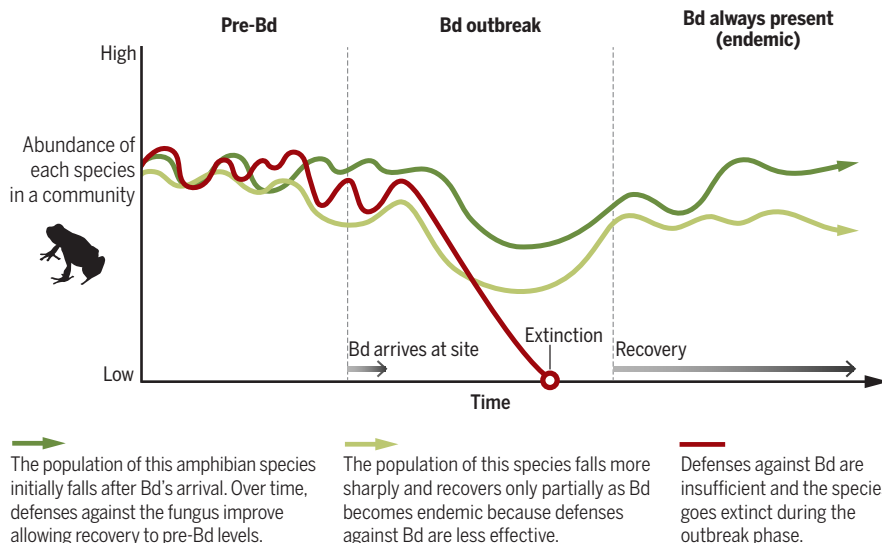
Voyles *et al.* next used two approaches to determine whether the frogs changed. The first approach was based on previous research, which analyzed whole-skin secretions to show that innate immune defenses vary substantially among rainforest stream species (12). Voyles *et al.* compared the effectiveness of whole-skin secretions at inhibiting the amphibian chytrid, using samples collected from frogs at locations where Bd was endemic and at sites where Bd was absent. The capacity of skin secretions to inhibit Bd varied substantially among species and was much greater in frogs from sites where the amphibian chytrid was endemic. A change in antimicrobial secretions appears to confer improved defense against the fungus, causing a shift from an outbreak phase to an endemic phase, in which hosts and pathogen coexist.

Second, the authors studied clown frogs (*Atelopus varius*), a species susceptible to Bd. Some clown frogs had been collected near El Copé before Bd emerged and bred in an off-site facility. The team tested the inhibitory effectiveness against Bd of skin secretions from these frogs, which had never been exposed to the pathogen. They then compared it with *A. varius* collected from sites where Bd is now endemic. The inhibitory effectiveness against Bd was greater in the latter frogs than in captive-bred individuals. Frogs never exposed to Bd thus had a reduced capacity to defend against it.

It remains to be shown how skin secretions came to be more effective after Bd invaded. If the capacity to resist epidermal fungi existed before Bd emerged, then its

Surviving a fungal killer

In amphibian communities, population sizes and number of species vary with time. When Bd's arrival triggers a chytridiomycosis outbreak, populations fall below the lower limits of their pre-Bd population sizes. Some species go extinct, but others recover partially or fully as the amphibian chytrid becomes endemic (always present) in the community.



arrival perhaps stimulated in individuals a standing physiological capacity to respond to microscopic fungi in general, a capacity that varies among species (12). Alternatively, mutations in host genomes favoring a capacity to resist Bd may have occurred over the ~10 years of the study. That would be rapid, given that these frog species likely have a generation time of more than 6 months. Finally, the capacity to resist a Bd-like fungus may have been a polymorphic trait, in place in these frogs before Bd invaded. If so, selection by Bd presumably shifted allele frequencies to those favoring a defense against Bd, a novel fungal threat

but one perhaps within the scope of variation in antimicrobial secretions that could be produced. Other host defense traits (such as behavior or life history characters) could be as important as skin secretions.

Why do infectious disease outbreaks in tropical frogs end? In Panamá and at other sites, host extinction, or in general death of susceptible individuals, is part of the answer. Based on the study by Voyles *et al.*, another part of the answer is that initially susceptible hosts become less susceptible through changes in their capacity to tolerate or resist Bd, fostering a transition from an emergent to endemic epidemiological phase. To understand fully why some Neotropical frog species are unaffected by Bd, others decline and recover, and yet others go extinct, scientists must learn a lot more about how frogs react to pathogens. ■

REFERENCES AND NOTES

1. J. P. Collins, M. L. Crump, *Extinction in Our Times*. Global Amphibian Decline (Oxford Univ. Press, 2009).
2. *Batrachochytrium salamandrivorans* is associated with declines in Europe.
3. J. Voyles *et al.*, *Science* **359**, 1517 (2018).
4. A. J. Crawford *et al.*, *Proc. Natl. Acad. Sci. U.S.A.* **107**, 13777 (2010).
5. K. R. Lips *et al.*, *Proc. Natl. Acad. Sci. U.S.A.* **103**, 3165 (2006).
6. K. R. Lips *et al.*, *PLOS Biol.* **6**, e72 (2008).
7. T. L. Cheng *et al.*, *Proc. Natl. Acad. Sci. U.S.A.* **108**, 9502 (2011).
8. N. F. Angeli *et al.*, *J. Herpet.* **49**, 388 (2015).
9. D. A. Newell *et al.*, *PLOS ONE* **8**, e58559 (2013).
10. E. B. Rosenblum *et al.*, *Proc. Natl. Acad. Sci. U.S.A.* **110**, 9385 (2013).
11. P. F. Langhammer *et al.*, *PLOS ONE* **8**, e77630 (2013).
12. D. C. Woodhams *et al.*, *J. Wildl. Dis.* **42**, 207 (2006).



A stream in Parque Nacional Omar Torrijos, El Copé, Panamá, where Bd has caused amphibian declines.

Arizona State University, School of Life Sciences, Tempe, AZ 85287, USA. Email: jcollins@asu.edu

CANCER IMMUNOTHERAPY

Natural killers join the fight against cancer

An antibody overcomes cancer cell immune evasion and activates natural killer cells

By **Adelheid Cerwenka**¹ and
Lewis L. Lanier²

Immunotherapy represents one of the major breakthroughs in the treatment of cancer patients. Current therapies focus on harnessing the adaptive immune system, with great success achieved by interfering with immune checkpoints to unleash antitumor CD8⁺ T cell responses. There is emerging evidence that cancers develop multiple strategies to escape CD8⁺ T cell recognition. These tumors, however, can be preferentially attacked by natural killer (NK) cells. NK cells are innate lymphocytes that express activating receptors, including the NK group 2D (NKG2D) receptor, which recognize ligands displayed on the surface of tumor cells and pathogen-infected cells. On page 1537 of this issue, Ferrari de Andrade *et al.* (7) present an elegant approach to improve NK cell recognition of tumor cells, extending the range of immunotherapies beyond T cells.

The NKG2D-NKG2D ligand axis represents a major activating pathway for human NK cell-mediated recognition of tumor cells and virus-infected cells (2–4). Several strategies targeting NKG2D ligands (5, 6) expressed on cancer cells or the NKG2D receptor (7) on NK cells and certain other immune cells (including CD8⁺ T cells) have been reported and are now under evaluation in preclinical studies. These approaches are challenging because tumors have evolved mechanisms to escape NK cell surveillance. One major mechanism of tumor escape is the shedding of the NKG2D ligands, major histocompatibility complex (MHC) class I polypeptide-related sequence A (MICA) and MICB, from the tumor cell surface by matrix

metalloproteinases (MMPs) and ADAMs (a disintegrin and metalloproteinases), thus impairing NK cell recognition (8–10). Moreover, shed MICA and MICB that might block NKG2D receptor interaction with its cellular ligands are found in the sera of cancer patients, which frequently correlates with poor prognosis and impaired NK cell function.

To circumvent tumor immune escape and to efficiently target NK cells to tumors, Ferrari de Andrade *et al.* generated a monoclonal antibody (mAb) against MICA and MICB that masks the region of their extracellular domains that is cleaved by MMPs and ADAMs. The use of a mAb that binds to

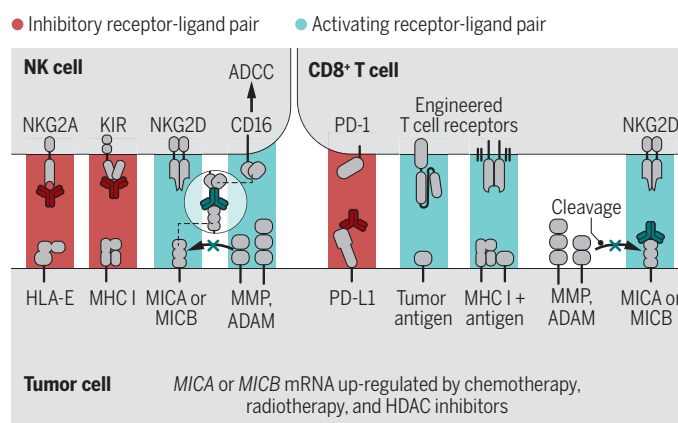
The biology of NKG2D ligands is complex (4, 10). The *MICA* and *MICB* genes are highly polymorphic, and different alleles of these ligands vary in expression and their affinity for the NKG2D receptor. The mAb generated in this study recognizes the most common MICA and MICB variants, which are expressed in many tumors but rarely by healthy cells. Expression of MICA and MICB can be enhanced at the transcriptional level by radiotherapy, histone deacetylase (HDAC) inhibitors, or chemotherapy. The present approach, however, is more specific. Moreover, tumor cells often evolve strategies to down-regulate NKG2D on NK

cells or T effector cells in the host. In this respect, tumor cell-produced transforming growth factor β (TGF- β) and kynurenine were shown to transcriptionally down-regulate NKG2D expression on NK cells (11). These effects are transient, and NKG2D expression can be restored by activation of NK cells with cytokines, for example, interleukin-2 (IL-2) and IL-15. Thus, a combination of the MICA-MICB mAb with cytokines that are now being used in the clinic might further increase the therapeutic efficiency of this approach. Additional combinatorial strategies could involve the blockade of inhibitory NK cell pathways such as killer cell inhibitory receptors (KIRs) or NKG2A, which are now in clinical trials in different types of cancer (12) (see the figure).

In humans, NKG2D is not only expressed by NK cells but also by all CD8⁺ T cells in which a costimulatory function of the NKG2D-NKG2D ligand axis has been reported (13). Ferrari de Andrade *et al.* used a poorly immunogenic metastatic melanoma model to show that after application of the MICA-MICB mAb, tumor growth control was mainly mediated by NK cells and not by CD8⁺ T cells. It will be important to assess whether blocking MICA and MICB shedding in more immunogenic tumor models will also elicit an antigen-specific CD8⁺ T cell response. Accordingly, it is feasible to combine the MICA-MICB mAb with immune checkpoint inhibitors such

Combinatorial strategies with MICA-MICB mAb

The MICA-MICB mAb stabilizes these NKG2D ligands on tumor cells, inducing tumor cell killing by NK and CD8⁺ T cells. Combinations with immune checkpoint inhibitors (anti-PD-1 or anti-PD-L1), engineered immune cells, or antibodies blocking NKG2A or KIR could amplify antitumor activity. HLA-E, human leukocyte antigen E.



the cleavage site, but does not interfere with the sites for NKG2D receptor binding, preserves the expression of MICA and MICB on tumor cells and allows NKG2D-dependent activation of NK cell effectors. Additionally, the Fc portion of this mAb can mediate antibody-dependent cellular cytotoxicity (ADCC), triggering target-cell killing by NK cells. The application of this mAb greatly reduced the growth of subcutaneous tumors and metastases in an immune-competent mouse model and in an immunocompromised xenograft mouse model in which human NK cells were administered. The study introduces an exciting concept for a therapeutic mAb with the potential to improve NK cell-based cancer immunotherapy.

¹Centre for Biomedicine and Medical Technology (CBTM) and European Center for Angioscience (ECAS), Heidelberg University, Medical Faculty Mannheim, Ludolf-Krehl-Strasse 13–17, D-68167 Mannheim, Germany. ²Department of Microbiology and Immunology and Parker Institute for Cancer Immunotherapy, University of California, San Francisco, San Francisco, CA 94143, USA. Email: adelheid.cerwenka@medma.uni-heidelberg.de

as anti-programmed cell death protein 1 (PD-1), anti-PD-1 ligand 1 (PD-L1), or other T cell-based therapies, including the adoptive transfer of engineered T cells to further enhance T cell activation. These combinations would not only enhance both CD8⁺ T cell and NK cell activation against cancer cells but, in addition, broaden the spectrum of tumor cells that can be attacked.

MICA and MICB expression has been reported in healthy individuals in barrier tissues such as the gut. It is unknown whether these cells also shed NKG2D ligands. Expression and stabilization of MICA and MICB in these tissues could cause excessive inflammation resulting from aberrant immune cell activation and might lead to serious side effects. Additionally, circulating monocytes and tumor-infiltrating myeloid cells in some cancer patients express MICB. Activated T cells can express NKG2D ligands as well (14). Moreover, under homeostatic conditions, NKG2D ligands were detected on mouse endothelial cells and might modulate NK cell function (15). Whether NKG2D ligands on myeloid cells, T cells, and endothelial cells are also stabilized by the MICA-MICB mAb, potentially promoting inflammation, has not been addressed. Undoubtedly, future studies are needed to provide a comprehensive analysis of MICA and MICB expression in homeostatic conditions and during disease.

Bispecific mAbs targeting additional antitumor effector cells, such as CD3⁺ T cells (which infiltrate solid tumors at higher numbers than NK cells), to MICA- and MICB-bearing tumors could be generated. Moreover, the MICA-MICB mAb could also be engineered into T cells or NK cells for adoptive cell transfer, potentially resulting in efficient tumor cell targeting, provided there is no toxic off-target cell killing. Ferrari de Andrade *et al.* reveal an innovative approach to counteract a major mechanism of cancer immune escape from NK cell recognition that, if safe in patients, harbors high potential and versatility for future clinical application. ■

REFERENCES

1. L. Ferrari de Andrade *et al.*, *Science* **359**, 1537 (2018).
2. S. Bauer *et al.*, *Science* **285**, 727 (1999).
3. J. Wu *et al.*, *Science* **285**, 730 (1999).
4. L. L. Lanier *et al.*, *Cancer Immunol. Res.* **3**, 575 (2015).
5. E. P. von Strandmann *et al.*, *Blood* **107**, 1955 (2006).
6. J. Steinbacher *et al.*, *Int. J. Cancer* **136**, 1073 (2015).
7. C. Godbersen *et al.*, *Mol. Cancer Ther.* **16**, 1335 (2017).
8. H. R. Salih *et al.*, *J. Immunol.* **169**, 4098 (2002).
9. V. Groh *et al.*, *Nature* **419**, 734 (2002).
10. N. Nausch *et al.*, *Oncogene* **27**, 5944 (2008).
11. M. Della Chiesa *et al.*, *Blood* **108**, 4118 (2006).
12. L. Chiossone *et al.*, *Sem. Immunol.* **31**, 55 (2017).
13. A. I. Roberts *et al.*, *J. Immunol.* **167**, 5527 (2001).
14. C. Cerboni *et al.*, *Blood* **113**, 2955 (2009).
15. T. W. Thompson *et al.*, *eLife* **6**, e30881 (2017).

10.1126/science.aat2184

NEUROSCIENCE

Making room for new memories

Clearing neuronal networks from transient memory engrams during sleep consolidates memories

By Andreas Draguhn

What are our memories made of? Plato suggested imagining a block of wax in our soul, where perceptions and thoughts leave impressions that we can remember as long as they have not been erased. This historic metaphor captures the transience of some memories and the stability of others, and it illustrates the brain's plasticity. The mechanisms of memory formation and retention remain a key question in neuroscience. Groundbreaking work on the rodent hippocampus (a network in the temporal lobe) revealed that certain neurons form transiently stable representations of places (1). Hence, this brain region has become an important focus for

“...how can we remember an almost infinite number of items with the limited storage capacity of the hippocampus?...neuronal activity during sleep plays a major role...”

studying spatial memory (or engram) formation. It also serves as an experimentally accessible proxy for declarative (knowledge) and episodic (experience) memory in humans, which involves the same brain structures and mechanisms. However, how can we remember an almost infinite number of items with the limited storage capacity of the hippocampus? There is good evidence that relevant representations are transferred to neocortical networks before forming long-lasting engrams. The hippocampus is then reset for acquisition of new memories. Studies in animals (2) and humans (3) show that neuronal activity during sleep plays a major role in these processes. The underlying mechanisms,

however, have remained mostly enigmatic. On page 1524 of this issue, Norimoto *et al.* (4) show how sleep-associated activity patterns induce “negative” neuronal plasticity in the hippocampus, erasing remote memories. A previous, related paper by Khodagholy *et al.* (5) reveals similar activity patterns in the neocortex, which, hence, may mediate long-term consolidation of transient engrams at their final location.

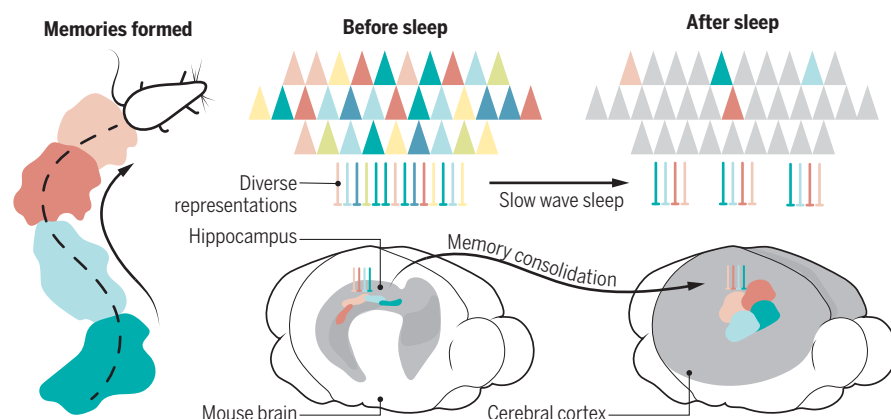
Norimoto *et al.* show that excitatory synapses between hippocampal neurons are weakened by sharp wave-ripple (SWR) complexes, patterns of coordinated network activity that typically occur during sleep (6) (see the figure). Surprisingly, neurons contributing to recently acquired engrams are excluded from this weakening and remain stably active. Behavioral tests suggest that this mechanism supports the formation of new memories, in line with the idea that the hippocampal memory system must be regularly cleared. This requires, however, that “old” memories (if relevant) must be stored elsewhere, fostering the idea of engram transfer from the hippocampus to the neocortex (7).

The representation of spatial contexts in hippocampal networks involves three major mechanisms. First, special neurons called “place cells” are selectively activated when the animal is in a certain spot of its environment (1). Second, exploring an environment strengthens the coupling of sequentially activated place cells, which then form neuronal ensembles representing the spatial experience (8). Third, coherent membrane potential oscillations of all local neurons provide a common time frame for coordinating the activation of coupled neurons (9). The resulting spatio-temporal activity patterns form transiently stable representations of spatial experience. A key observation from multineuronal recordings in rats links such coactive neuronal ensembles to memory consolidation: Sequences of place cell activity that were formed during spatial exploration are replayed in the same order during phases of immobility or slow-wave sleep (2). This sleep state, better known as deep or non-REM (rapid eye movement) sleep, is exactly the phase where humans stabilize recently formed memories (3). Compared to memory acquisition, however, replay of

Institute of Physiology and Pathophysiology, Heidelberg University, Im Neuenheimer Feld 326, 69120 Heidelberg, Germany. Email: andreas.draguhn@physiologie.uni-heidelberg.de

Processing of engrams in the rodent brain

Firing of place cells during spatial exploration leads to the formation of coactive neuronal ensembles. During subsequent sleep, engrams of old ensembles are erased, which increases the distinction of newly formed ensembles. Memory consolidation occurs through hippocampal-cortical cross-talk, indicated by SWR-like activity patterns during sleep.



activity sequences occurs on top of a much faster pattern of network oscillations—hippocampal SWRs.

Norimoto *et al.* first confirmed two properties of slow-wave sleep in mice: Synaptic coupling strength between hippocampal neurons declines (10), and hippocampal networks produce spontaneous SWR activity (6). They then asked whether there is a causal link between both phenomena, using an elegant optogenetic closed-loop technique to silence neuronal activity during SWRs with pulses of light. Indeed, aborting the patterns prevented the decay of synaptic coupling and, at the same time, blocked hippocampus-dependent spatial memory formation. How do slow-wave sleep, SWRs, and the related synaptic plasticity support spatial memory? Recordings from multiple single neurons revealed that the decline in activity was selective for those place cells that represent old, well-known environments, whereas recently formed place cells remained fully active. Reducing the strength of recently unchanged synapses may prevent saturation of synaptic strength and ensure homeostasis of excitability in the network (10). It separates newly formed ensembles from old, established engrams (4) and clears the stage for “positive” synaptic plasticity during future experiences.

The underlying cellular and molecular mechanisms involve changes in dendritic spine size and depend on activation of NMDA (*N*-methyl-D-aspartate) receptors, both typical for activity-dependent synaptic plasticity (11). At present, it remains unclear how newly potentiated synapses (or memory-relevant neurons) are distinguished from established connections (or

memory-irrelevant neurons). The findings by Norimoto *et al.* and the precise timing of neuronal activity during SWR events (6) suggest a role for spike-timing-dependent plasticity (11)—lasting changes in synaptic strength upon near-coincident activation of pre- and postsynaptic neurons.

Thus, as time progresses, old impressions are progressively erased from Plato’s block of wax, avoiding confusion by superimposed engrams. But where and how are representations preserved to form long-lived memories for the many places and objects we (and rodents) know? The prevailing view is that during SWRs, replayed neuronal activity patterns are transferred from the hippocampus into distributed

“The findings also underline the important role of slow-wave sleep for the consolidation of spatial (and declarative) memories.”

neocortical networks (7). There, some unknown process of plasticity is induced that forms stable representations. Indeed, hippocampal SWRs coincide with defined patterns of sleep-related neocortical network activity (12, 13). However, the precise nature and location of neocortical long-term engrams remain elusive. Important progress comes from Khodagholy *et al.* They used dense, large-scale electrode arrays to study multineuronal activity patterns in rats subjected to a hippocampus-dependent memory task. With this de-

vice, they detected fast oscillations in the “ripple” frequency band (typical for SWRs) in several circumscribed neocortical areas (see the figure). Neocortical ripples are restricted to prefrontal or parietal “association” cortices, i.e., areas with rich intracortical connections that are involved in cognitive functions like action planning and spatial navigation. The pattern occurs coincidentally with hippocampal SWRs, and coupling between both areas is increased by previous spatial learning episodes. Given that the highly coincident neuronal activation during SWRs facilitates synaptic potentiation (14), neocortical ripples are a strong candidate mechanism for the induction of long-lasting engrams. The findings also underline the important role of slow-wave sleep for the consolidation of spatial (and declarative) memories.

Together, the two studies mark considerable progress in understanding the network-level mechanisms of spatial memory formation. Both groups made elegant use of recent methodological advances: Khodagholy *et al.* performed massively parallel recordings from large numbers of neurons, establishing new correlations between multineuronal patterns, vigilance states, and behavioral performance. Norimoto *et al.* used an interventionist approach to unravel causal relationships between network activity, synaptic plasticity, and memory. It should be kept in mind, however, that we are far from a complete reconstruction of all elements and causal interactions linking molecular events, neuronal coupling, local network oscillations, whole-brain information processing, memory formation, and behavior—provided this can ever be achieved (15). Crucial future steps include identifying the (sub)cellular events that couple neurons within ensembles, elucidating the mechanisms that determine the transience or stability of engrams, and pinpointing the location and nature of neocortical memory-related ensembles. ■

REFERENCES

1. J. O’Keefe, J. Dostrovsky, *Brain Res.* **34**, 171 (1971).
2. A. K. Lee, M. A. Wilson, *Neuron* **36**, 1183 (2002).
3. L. Marshall *et al.*, *Nature* **444**, 610 (2006).
4. H. Norimoto *et al.*, *Science* **359**, 1524 (2018).
5. D. Khodagholy *et al.*, *Science* **358**, 369 (2017).
6. G. Buzsáki *et al.*, *Science* **256**, 1025 (1992).
7. G. Buzsáki, *Hippocampus* **25**, 1073 (2015).
8. L. M. Frank *et al.*, *Hippocampus* **16**, 775 (2006).
9. G. Buzsáki, A. Draguhn, *Science* **304**, 1926 (2004).
10. V. V. Vyazovskiy *et al.*, *Nat. Neurosci.* **11**, 200 (2008).
11. Q. Zhou *et al.*, *Neuron* **44**, 749 (2004).
12. A. G. Siapas, M. A. Wilson, *Neuron* **21**, 1123 (1998).
13. A. Sirota *et al.*, *Proc. Natl. Acad. Sci. U.S.A.* **100**, 2065 (2003).
14. J. H. L. P. Sadowski *et al.*, *Cell Rep.* **14**, 1916 (2016).
15. Y. Frégnac, *Science* **358**, 470 (2017).

10.1126/science.aat1493

Li metal battery, heal thyself

Intermittent high-current pulses prevent battery failure

By **Amartya Mukhopadhyay** and
Manoj K. Jangid

In the 1970s, scientists first developed a promising class of rechargeable batteries in which lithium (Li) metal served as the anode and compounds that could reversibly host Li ions inside the lattice formed the cathode (1). Because Li is the lightest and most electropositive metal, this setup allows very high energy and power densities. However, repeated discharge-charge cycles cause growth of Li dendrites from the anode toward the cathode. Such dendrites can eventually penetrate the separator (placed to prevent contact between the electrodes) and touch the cathode, causing short circuiting of the cell and potentially leading to safety hazards (2–5). On page 1513 of this issue, Li *et al.* (6) show that Li dendrite growth can be suppressed by applying short, intermittent high-current pulses during battery use. These pulses lead to self-healing of the dendrites.

The growth of Li dendrites not only causes failure and overheating of the cell because of short circuiting but also consumes Li irreversibly from the electrolyte, resulting in irreversible cell capacity loss and electrolyte degradation. To circumvent these problems, scientists have developed graphite-based anode materials that can host Li ions reversibly inside the lattice at electrochemical potentials close to that of Li metal (2). This arrangement can address the Li dendrite problem to some extent but lowers the cell voltage and charge storage capacity of the battery, thus substantially reducing the energy and power densities of such batteries relative to Li metal-based batteries. Furthermore, even graphite-based anodes may sometimes suffer from dendrite formation because Li plating and stripping can still occur on the graphite surface (7), especially when the cell is operated at high current densities for applications demanding high power densities.

Other anode materials have also generated interest. For example, silicon (Si) can reversibly alloy with Li at higher operating potentials than that of Li metal and even than that of graphite, thus preventing Li dendrite formation. Furthermore, Si anodes have Li storage capacities similar to that of Li metal.

However, they are mechanically unstable upon repeated alloying and dealloying, leading to a rapid fade in capacity with discharge-charge cycles (8).

In recent years, interest in renewable-energy storage, grid storage, and batteries for electric vehicles has led to efforts toward increasing the energy and power density of rechargeable batteries. This has led to renewed interest in Li metal anodes. Previous studies aimed at suppressing the Li dendrite problem mainly attempted to contain the growing dendrites (9, 10) or change their growth direction (11). However, these approaches did not prevent dendrite growth and thus merely delayed the inevitable; that is, dendrites eventually touch the cathode (4, 5, 9–11).

This is where the work by Li *et al.* stands out because they use simple physical concepts to enable the dendrites to heal themselves before they even reach the separator. They do so by using a higher current density of optimized magnitude, which leads to the formation of finer, more densely populated dendrites on the Li surface (5) and in turn results in considerable heating of the dendrites. This heat does not melt the Li and is safe for the other cell components but increases the “mobility” of the Li atoms and causes rapid migration of the surface atoms from the dendrite tips to the valleys between them. This migration blunts the tips and smoothenes the

dendrites (see the figure). The smoothening also suppresses further dendrite growth. This suppression of dendrite growth and smoothening of the Li metal surface not only prevents short circuiting but also reduces irreversible capacity loss during operation.

Li *et al.* demonstrate this approach in a cell with a Li anode and sulfur (S) cathode (a Li-S cell). Upon application of intermittent high-current pulses, the cell did not fail after a finite number of cycles. Furthermore, the cell showed improved reversibility as compared with that of most Li-S cells reported to date (12). In a control experiment without high-current pulses, short circuiting did take place because of dendrite-induced cell shorting.

Li *et al.*'s successful demonstration of this concept may lead to a paradigm shift in Li-based rechargeable battery technology. It should encourage researchers and engineers to investigate this aspect with a range of Li-based cells, using different cathode materials and larger cells, so that the scientific approach developed in the laboratory can be translated to technological application in the near future. The faster that happens, the sooner we shall have lighter batteries for greater energy and power output. ■

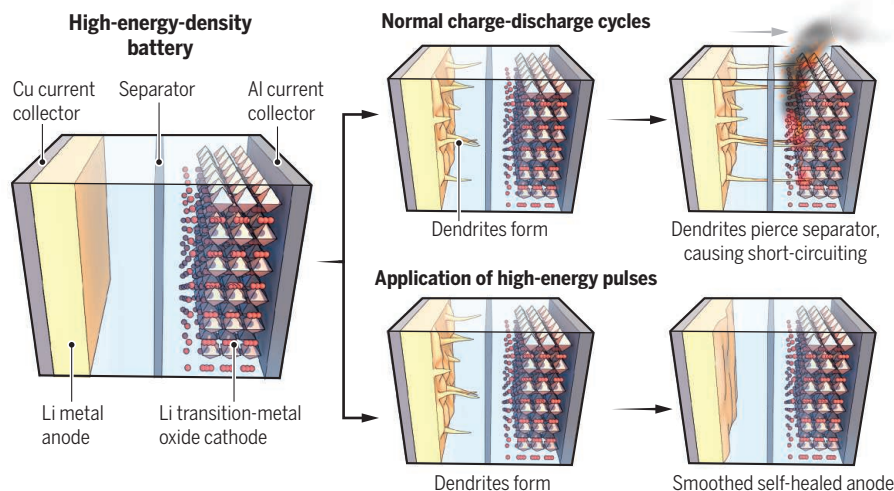
REFERENCES

1. M. S. Whittingham, *Science* **192**, 1126 (1976).
2. K. Brandt, *Sci. State Ion.* **69**, 173 (1994).
3. D. Lin, Y. Liu, Y. Cui, *Nature Nanotech.* **12**, 194 (2017).
4. H. Kim *et al.*, *Chem. Soc. Rev.* **42**, 9011 (2013).
5. A. Pei, G. Zheng, F. Shi, Y. Li, Y. Cui, *Nano Lett.* **17**, 1132 (2017).
6. L. Li *et al.*, *Science* **359**, 1513 (2018).
7. D. R. Ely, R. E. Garcia, *J. Electrochem. Soc.* **160**, A662 (2013).
8. A. Mukhopadhyay, B. W. Sheldon, *Prog. Mater. Sci.* **63**, 58 (2014).
9. R. Mukherjee *et al.*, *Nature Commun.* **5**, 3710 (2014).
10. G. Zheng *et al.*, *Nature Nanotech.* **9**, 618 (2014).
11. Y. Liu *et al.*, *Nature Energy* **2**, 17083 (2017).
12. R. Fang *et al.*, *Adv. Mater.* **29**, 1606823 (2017).

10.1126/science.aat2452

Preventing Li metal battery failure

Use of Li metal anodes allows high energy densities in rechargeable batteries, but Li dendrite formation leads to short-circuiting. Li *et al.* report that application of intermittent high-current pulses heals the dendrites and prevents short-circuiting, as shown here for a simple Li/LiMO₂ cell (TM, transition metal).



High Temperature and Energy Materials Laboratory,
Department of Metallurgical Engineering and Materials
Science, Indian Institute of Technology Bombay, Mumbai,
India. Email: amartya_mukhopadhyay@iitb.ac.in

BIOPHYSICS

Force matters in hospital-acquired infections

Extremely strong forces help staphylococci to colonize biomaterials and infect humans

By **Philippe Herman-Bausier**¹ and

Yves F. Dufrène^{1,2}

Bacterial pathogens show a remarkable capacity to stick to host tissues and implanted biomaterials, grow, and form biofilms on these surfaces (1). These multicellular communities protect the bacteria from the host immune system and from drugs, thereby causing infections that are difficult to eradicate. Today, biofilms are estimated to be involved in half of all infections acquired in hospitals. On page 1527 of this issue, Milles *et al.* (2) combine single-molecule experiments and molecular dynamics simulations to study the forces involved in the adhesion of bacterial pathogens to host proteins, the first step of biofilm formation.

Biofilm infections commonly involve *Staphylococcus epidermidis* and *S. aureus* strains, including methicillin-resistant *S. aureus* (MRSA). These microbes are decorated with adhesins that mediate both attachment to host proteins and cell-cell association (3). The structural features and molecular biology of staphylococcal adhesins have been widely investigated, but their binding forces are poorly understood because of a lack of ultrasensitive biophysical force probes. However, recent progress in single-molecule techniques (4) has provided new opportunities for studying forces in bacterial proteins (5).

Unlike traditional methods that probe large ensembles of cells and molecules, atomic force microscopy (AFM) makes it possible to study bacterial components one molecule at a time (5). The technology has enabled researchers to understand the nanoscale biophysical properties of bacteria, unravel the binding mechanisms of their individual surface molecules, and decipher the forces guiding cell-cell and cell-substrate interactions (5).

Milles *et al.* elegantly combine single-molecule AFM and steered molecular dynamics (SMD) simulations to investigate the molecular mechanism by which the prototypical staphylococcal adhesin SD-repeat protein G (SdrG) binds to fibrinogen (Fg), a host

protein that rapidly coats implanted biomedical devices. They show that the extreme mechanical stability of the SdrG-Fg complex originates from an intricate hydrogen bond network between the ligand peptide backbone and the adhesin. The study represents an important step toward understanding how hospital-acquired pathogens use their surface adhesins to guide cell adhesion and trigger infections.

SdrG binds to Fg via a dock, lock, and latch (DLL) mechanism that involves dynamic conformational changes of the protein, resulting in a greatly stabilized

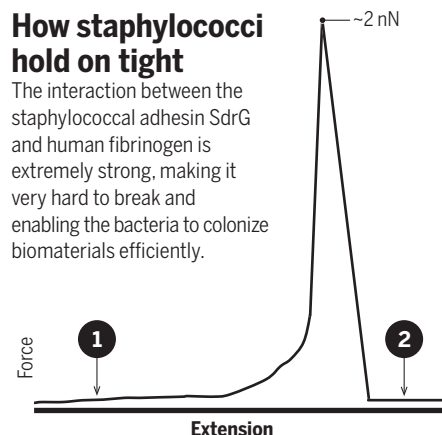
adhesin-ligand complex (6). The N2 and N3 subdomains of SdrG bind to a short peptide sequence in the Fg molecule (see the figure). Milles *et al.* used single-molecule AFM to quantify the mechanical strength of the SdrG-Fg complex. By immobilizing the SdrG subdomains on the AFM tip and the ligand peptides on a substrate, the authors could probe the forces between the interacting molecules in their native configuration. Consistent with earlier AFM experiments on living bacteria (7), these *in vitro* measurements revealed that the SdrG-Fg interaction is ultrastrong, with a strength of ~2 nN, similar to that of covalent bonds (8).

Sophisticated simulations enabled Milles *et al.* to unravel the mechanism behind this extreme mechanostability. They found that the target peptide is confined in a screwlike manner in the binding pocket of SdrG and that the binding strength of the complex results from numerous hydrogen bonds between the peptide backbone and SdrG, independent of peptide side chains. Rupture of the complex requires all hydrogen bonds to be broken simultaneously. The authors observed similar side-chain-independent mechanical stability in experiments and simulations of clumping factor B (ClfB), a protein from *S. aureus* that is structurally and functionally related to SdrG. This finding suggests that this hydrogen bond mechanism may be generalized to other adhesins.

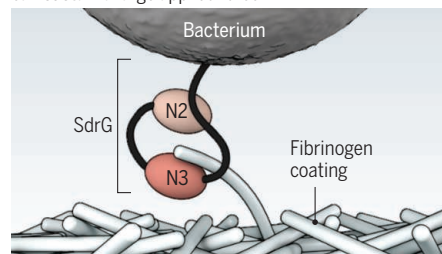
The extreme mechanical stability of SdrG explains at the molecular scale how staphylococci colonize biomaterials so efficiently while sustaining high mechanical stresses (9). The 2-nN force is much larger than that reported for other cell adhesion molecules, as well as for the mechanically strong biotin-streptavidin and cohesin-dockerin complexes. However, this ultrahigh binding strength is in contrast with biochemical data showing that SdrG binds its ligand with moderate affinity (6). This discrepancy shows that binding forces measured at nonequilibrium are uncorrelated with the equilibrium binding affinity. Given that in nature, most surface-attached bacteria are subjected to physical stresses (9), force measurements are likely to be more relevant than traditional bioassays for properly describing cell adhesion. This is particularly true for staphylococci, which are constantly exposed to fluid shear forces during colonization of implanted biomaterials.

How staphylococci hold on tight

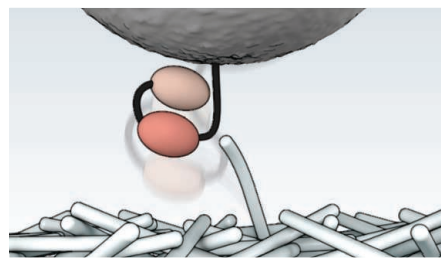
The interaction between the staphylococcal adhesin SdrG and human fibrinogen is extremely strong, making it very hard to break and enabling the bacteria to colonize biomaterials efficiently.



1 The N2 and N3 subdomains of SdrG bind to fibrinogen through an intricate hydrogen-bonding network that can sustain a large applied force.



2 The tight binding is only broken by application of a large force, equivalent to that needed to break a covalent bond.



¹Institute of Life Sciences, Université catholique de Louvain, 1348 Louvain-la-Neuve, Belgium. ²Walloon Excellence in Life Sciences and Biotechnology (WELBIO), 1300 Wavre, Belgium. Email: yves.dufrene@uclouvain.be

The authors also speculate that SdrG may bind its ligand through a catch bond—that is, a bond strengthened by tensile force, as observed with the *Escherichia coli* adhesin FimH (10). Supporting this idea, a recent single-molecule study demonstrated that the mechanical strength of ClfB increases dramatically as mechanical force is applied (11). The results suggested that ClfB-mediated adhesion is enhanced through force-induced conformational changes in the adhesin, which changes from a weakly binding folded state to a strongly binding extended state. This force-dependent ligand-binding mechanism may help *S. aureus* to attach firmly to biomaterials under high shear stress, and to detach under low shear stress to colonize new sites.

The study by Milles *et al.* has important implications for many fields. In molecular microbiology, the combined use of AFM experiments and SMD simulations should greatly contribute to the identification of new binding mechanisms in bacterial adhesins, thus helping to show how they regulate biofilm formation. In diagnosis and therapy, this combined approach could represent a powerful platform for the treatment of microbial infections. For instance,

“The extreme mechanical stability of SdrG explains... how staphylococci colonize biomaterials so efficiently...”

correlative single-molecule experiments and simulations could be used to screen antiadhesion compounds for their potential to prevent or treat biofilm-associated infections (12). The binding mechanism reported here may also serve as a basis for the development of bioinspired glues that stick under water and outperform traditional adhesives. ■

REFERENCES

1. J. W. Costerton, P. S. Stewart, E. P. Greenberg, *Science* **284**, 1318 (1999).
2. L. F. Milles, K. Schulten, H. E. Gaub, R. C. Bernardi, *Science* **359**, 1527 (2018).
3. T. J. Foster, J. A. Geoghegan, V. K. Ganesh, M. Höök, *Nat. Rev. Microbiol.* **12**, 49 (2014).
4. K. C. Neuman, A. Nagy, *Nat. Methods* **5**, 491 (2008).
5. J. Xiao, Y. F. Dufrêne, *Nat. Microbiol.* **1**, 16186 (2016).
6. K. Ponnuraj *et al.*, *Cell* **115**, 217 (2003).
7. P. Herman *et al.*, *Mol. Microbiol.* **93**, 356 (2014).
8. M. Grandbois, M. Beyer, M. Rief, H. Clausen-Schaumann, H. E. Gaub, *Science* **283**, 1727 (1999).
9. A. Persat *et al.*, *Cell* **161**, 988 (2015).
10. E. V. Sokurenko, V. Vogel, W. E. Thomas, *Cell Host Microbe* **4**, 314 (2008).
11. P. Vitry *et al.*, *mBio* **8**, e01748 (2017).
12. C. Feuille *et al.*, *Proc. Natl. Acad. Sci. U.S.A.* **114**, 3738 (2017).

10.1126/science.aat3764

NEUROIMMUNOLOGY

Neuronal-immune system cross-talk in homeostasis

Interactions between immune and neuronal cells are pillars in tissue homeostasis

By **Henrique Veiga-Fernandes¹** and **David Artis²**

Maintenance of mammalian tissue homeostasis and function requires coordinated actions of multiple cellular and molecular networks. This complexity is reflected in the immune system, which is composed of a plethora of cells that constitute the innate and adaptive immune system and which can sense multiple endogenous and exogenous factors. Similarly, the nervous system includes a myriad of distinct neurons that perceive, integrate, and respond to ever-changing environmental conditions. Functional interactions between the neuronal and immune systems have been reported in health and disease, such as in multiple sclerosis, autism, cancer, and chronic inflammatory disorders (1). More recently, a number of studies have revealed that discrete neuronal and immune cells share anatomical localization and interact functionally, forming neuroimmune cell units (NICUs) that orchestrate tissue homeostasis and integrity (2). These findings are provoking a fundamental paradigm shift in our understanding of neuronal-immune cell interactions. A recent noteworthy example is the finding that the nervous system can have a major regulatory effect on multiple innate immune cells with functional impact in several physiological processes (3–8).

Earlier studies established that signals from the parasympathetic vagus nerve, which connects the brainstem with peripheral organs, can have an anti-inflammatory effect via tuning the activity of macrophages, innate immune cells that engulf pathogens and cell debris, leading to the production of macrophage-derived immunomodulatory molecules (9). Bidirectional neuronal-macrophage interactions were also shown to regulate important aspects of intestinal

physiology. Notably, intestinal macrophages control myenteric neuron activity and small intestine peristalsis (muscular contractions that move food down the intestine) in response to microbial signals in the intestines (3), whereas intestinal pathogenic bacterial infections activate neurons to produce norepinephrine that induces a tissue-protective program in enteric macrophages (4). Notably, neuron-associated macrophages are also present in adipose tissue and were shown to buffer sympathetic neuronal activity and fat tissue physiology, thus controlling obesity and organismal metabolism (10). Dendritic cells and mast cells (both components of the innate immune system) also interact with peripheral neurons (1). For example, upon chemical irritation or infection with fungi, sensory neurons in the skin instruct dermal dendritic cells to produce the cytokine interleukin-23 (IL-23), which activates adaptive T lymphocytes to produce pro-inflammatory cytokines (11). Reciprocally, lymphocyte-derived type 2 cytokines—such as IL-4, IL-5, and IL-13—were also shown to induce chronic itch via sensory neuron activation (12). Together, these findings demonstrate that neurons can trigger functional molecular cascades that lead to the activation of innate and adaptive immune cells, influencing immunity to infection, chronic inflammation, and restoration of tissue homeostasis. Nevertheless, defining additional pathways that operate in the opposing direction, whereby immune cells can modulate neuronal activity, requires further study.

But how widespread and biologically important is this neuronal-immune interaction? Over the past decade, we have witnessed the formal discovery of innate lymphoid cells (ILCs) and their roles in development, infection, inflammation, metabolic disease, and cancer (13). ILCs are a relatively rare cell type, but they are particularly abundant at barrier surfaces that are exposed to the external environment, which are also densely populated with neuronal cells. Group 2 ILCs (ILC2s) are associated with allergy and parasitic worm infections and were reported to respond to vasoactive intestinal peptide signals that were presumably derived from neuronal cells (14), suggesting that neuronal-

¹Champalimaud Research, Champalimaud Centre for the Unknown, 1400-038 Lisboa, Portugal. ²Jill Roberts Institute for Research in Inflammatory Bowel Disease, Joan and Sanford I. Weill Department of Medicine, Department of Microbiology and Immunology, Weill Cornell Medicine, Cornell University, New York, NY 10021, USA. Email: henrique.veigafernandes@research.fchampalimaud.org; dartis@med.cornell.edu

Neuroimmune cell units (NICUs) at barrier surfaces

NICUs modulate immune responses. For example, reciprocal neuron-macrophage and neuron-ILC interactions occur in the lungs (not shown) and intestines.

Macrophages

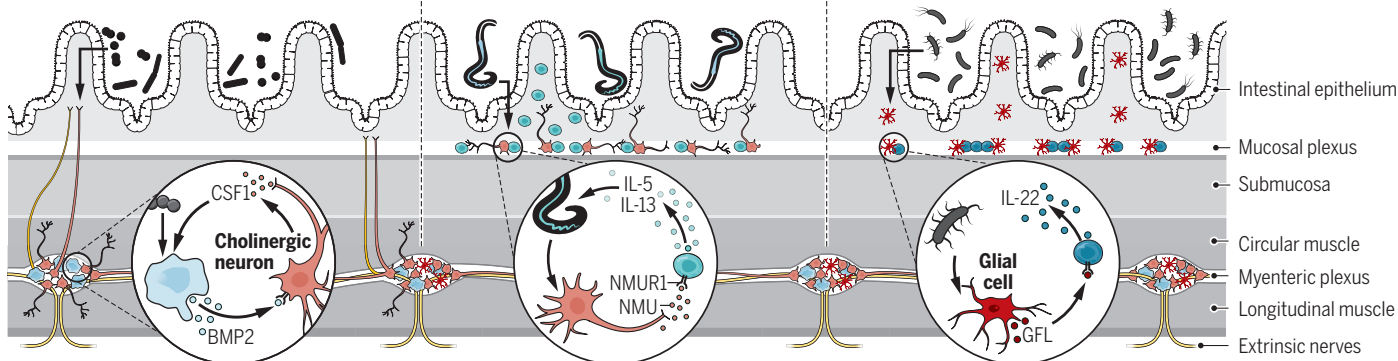
Microbiota signals induce macrophages to release bone morphogenetic protein 2 (BMP2), leading to neurons secreting colony-stimulating factor 1 (CSF1), which makes macrophages grow.

ILC2s

Allergy and parasitic worm infection lead to cholinergic neuron production of NMU, which activates ILC2s and leads to the production of type 2 cytokines and tissue protection.

ILC3s

Bacterial and tissue damage activate glial cells to secrete GFL neurotrophic factors, which induce ILC3s to release the tissue-protective cytokine IL-22.



ILC interactions could also occur at mucosal barriers. Consistent with this concept, group 3 ILCs (ILC3s) were shown to control intestinal health as part of a glial cell-ILC3 unit orchestrated by neurotrophic factors (5). Glial cells, considered to provide support and protection to neurons, are adjacent to ILC3s and integrate microbial-derived and host alarmin (danger molecules that are released upon tissue damage)-derived signals to control neurotrophic factor production (5). In turn, these neuroregulatory molecules activate RET-expressing ILC3s that produce the tissue-protective cytokine IL-22 (5). Thus, glial cells translate microbial and host cues into neurotrophic factor production, which target coordinated neuronal and ILC3 functions to promote intestinal tissue repair after exposure to infectious and inflammatory stimuli (see the figure).

Adding to the growing understanding of NICUs, other recent studies revealed that mucosal neurons regulate the production of ILC-derived type 2 cytokines via the production of the neuropeptide neuromedin U (NMU) (6–8). NMU-producing cholinergic neurons are adjacent to intestinal and pulmonary ILC2s, whereas NMU receptor 1 (NMUR1) is selectively expressed by ILC2s (6–8). Notably, activation of ILC2s with this neuropeptide leads to a rapid and potent production of type 2 inflammatory and tissue-protective cytokines (6, 7). Consistent with this, activation of this signaling axis in ILC2s in vivo leads to rapid type 2 cytokine responses after exposure to parasite infections or allergens (6–8). The capacity of neuronal-derived signals to rapidly trigger ILC2 responses may also explain in part why, despite their relatively low numbers, ILC2s can be rapidly activated and have profound effects across large barrier surfaces.

In addition to the activating functions of cholinergic nerve-derived NMU, catecholaminergic neurons—a component of the sympathetic nervous system that is a potent source of molecules such as norepinephrine that binds the β_2 -adrenergic receptor (β_2 AR)—were shown to act as a potent “off switch” that dampens ILC2 responses (15). β_2 AR deficiency resulted in exaggerated ILC2 responses and type 2 inflammation in intestinal and lung tissues, whereas β_2 AR agonist treatment, a frontline therapy for asthma patients, was associated with impaired ILC2 responses and reduced inflammation in vivo (15). Together, these new findings demonstrate that neuronal-ILC units are poised to trigger immediate barrier tissue protection programs through a neuronal-immune “fast track” response that can both switch on and switch off ILC2 responses, whereas activation by cytokines and alarmins appears to follow a “regular track,” inducing and sustaining ILC2 function with comparatively delayed kinetics.

How do neuronal cells sense environmental perturbations to instruct immune responses? Enteric neurons and glial cells can sense microbial products, parasites, and host alarmins through myeloid differentiation primary response 88 (MYD88) signaling in the neuronal cells to produce ILC-activating neuroregulators (5, 6). Although this local neuronal-innate immune cell interaction is critical during pathogen insults (5, 6), the nature of the efferent nervous signals (impulses emerging from the central nervous system) that may also regulate peripheral immune cells remain elusive. Nevertheless, perhaps local neural networks function as relay stations of environmental stimuli, amplifying these local insults through the increased expression of

neuroregulators that maximize rapid tissue-protective responses of immune cells.

Understanding the broader roles of NICUs in the regulation of tissue homeostasis in the context of health and disease is certainly a major challenge ahead. Notably, clarifying cellular and molecular players of NICUs could identify new putative therapeutic targets in the context of chronic inflammation, cancer, metabolic health, and beyond. Because pathogens and other environmental triggers have been major drivers of mammalian evolution, connecting immune and neuronal responses may therefore be considered a paradigm of coordinated multi-tissue physiology, suggesting that throughout evolution, neuroimmune networks may have also been selected at an organismal level. The neuroimmune system is out there to be explored. ■

REFERENCES AND NOTES

1. H. Veiga-Fernandes et al., *Cell* **165**, 801 (2016).
2. H. Veiga-Fernandes et al., *Nat. Immunol.* **18**, 116 (2017).
3. P. A. Muller et al., *Cell* **158**, 300 (2014).
4. I. Gabanyiet al., *Cell* **164**, 378 (2016).
5. S. Ibiza et al., *Nature* **535**, 440 (2016).
6. V. Cardoso et al., *Nature* **549**, 277 (2017).
7. C. S. N. Klose et al., *Nature* **549**, 282 (2017).
8. A. Wallrapp et al., *Nature* **549**, 351 (2017).
9. M. Rosas-Ballina et al., *Science* **334**, 98 (2011).
10. R. M. Pirzgalska et al., *Nat. Med.* **23**, 1309 (2017).
11. L. Riol-Blanco et al., *Nature* **510**, 157 (2014).
12. L. K. Oetjen et al., *Cell* **171**, 217 (2017).
13. C. S. Klose, D. Artis, *Nat. Immunol.* **17**, 765 (2016).
14. J. C. Nussbaum et al., *Nature* **502**, 245 (2013).
15. S. Moriyama et al., *Science* **359**, 1056 (2018).

ACKNOWLEDGMENTS

H.V.-F. is supported by the European Research Council, EU; Crohn's and Colitis Foundation of America, USA; and Fundação para a Ciência e Tecnologia, Portugal. D.A. is supported by the U.S. National Institutes of Health (grants AI061570, AI087990, AI074878, AI083480, AI095466, AI095608, AI02942, and AI097333), the Burroughs Wellcome Fund, and the Crohn's & Colitis Foundation of America.

10.1126/science.aap9598

Mashing up metals with carbothermal shock

Many elements can be combined in the formation of high-entropy-alloy nanoparticles

By Sara E. Skrabalak

Different materials and the capabilities they enabled have marked the ages of civilization. For example, the malleable copper alloys of the Bronze Age provided harder and more durable tools. Most exploration of new alloys has focused on random alloys, in which the alloying metal sites have no metal preference. In binary and ternary metal systems, dissimilar elements do not mix readily at high concentrations, which has limited alloying studies to intermetallics (ordered multimetallic phases) and random alloys, in which minor components are added to a principal element. In 2004, crystalline metal alloys consisting of five or more principal elements in equal or nearly equal amounts (1, 2) were reported that were stabilized by their high configurational entropy. Unlike most random alloys, the “high-entropy” alloys (3, 4) reside in the centers of their multidimensional phase diagrams (see the figure, right). On page 1489 of this issue, Yao *et al.* (5) present an innovative and general route to high-entropy alloys that can mix up to eight elements into single-phase, size-controlled nanoparticles (NPs).

High-entropy alloys usually have a minimum of five elements in nearly equal proportions. Synthesis of these compositions is challenging and not typically compatible with methods that yield well-defined nanoparticles. Such integration would enable the nanoscale properties of these complex compositions to be studied and potentially leveraged in diverse applications. For example, high-entropy alloys are being studied as structural materials and for their superparamagnetic and superconducting properties (4).

High-entropy alloys were initially synthesized through high-temperature melting or plasma routes that could produce atomi-

cally mixed phases before solidification (1, 3). By contrast, nanoscale alloys are often made in solution by co-reducing metal salts along with capping agents that control crystal growth and aggregation (6, 7). However, the compositional space of such alloys is often limited because the precursors react at different rates (8). The high surface energy of NPs can be exploited to access new metal phases, but only simple compositions have been reported (9). Even recent printing methods for synthesizing multimetallic NPs

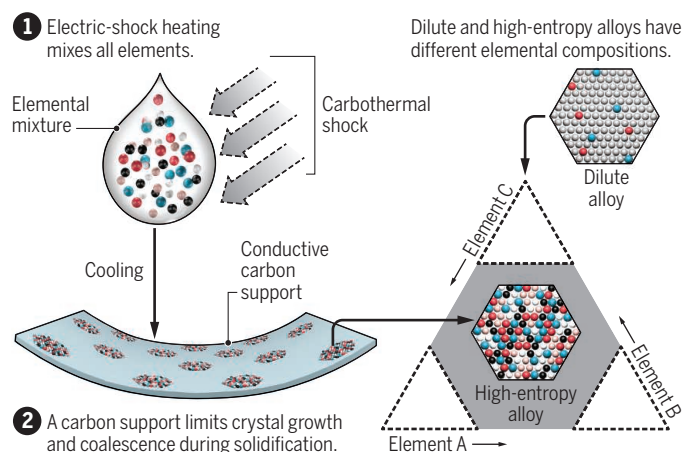
solutes. This observation gives insight into the formation mechanism of high-entropy alloyed NPs, in which a mixed phase must be achieved before solidification and then preserved through cooling at an optimal rate so that neither phase separation nor glass formation occurs (see the figure, left). This observation also suggests that this approach could yield new types of nanoscale heterostructures with further development.

Distinctive properties can emerge when new alloys undergo electron confinement at the nanoscale materials. For example, Yao *et al.* showed that their PtPdRhRuCe NPs were effective catalysts for ammonia oxidation, and this synthetic approach has the potential to yield additional new catalysts. An exceptionally high number of possible compositions and nanostructures can be envisioned, which introduces some fundamental challenges (4). In particular, identification of high-entropy alloys with useful properties by trial-and-error methods is unsatisfactory given the large phase space. High-throughput characterization of composition, nanoscale features, and properties are critically needed (12, 13). These advances should be coupled with theory so that a deeper

understanding of phase formation and the emergence of new properties can be achieved and enable materials by design. ■

Nanoscale high-entropy alloys

The synthesis route of Yao *et al.* makes mixtures of many elements.



yield phase-segregated multicomponent NPs when the input composition becomes too complex (10, 11). This observation is consistent with varied precursor reactivity and slow cooling rates.

By electrically shocking mixed-metal salt precursors dispersed on conductive carbon supports, Yao *et al.* accessed high-entropy alloys as size-controlled NPs. This method provided the high reaction temperatures (~2000 K) and rapid heating and cooling rates (~10⁵ K/s) necessary for high-entropy-alloy formation, while the underlying carbon support inhibited coalescence of the NPs. Conveniently, the input ratio of metal was replicated in the final product, and the method is scalable.

The NP size could be tuned through the shock conditions. Interestingly, phase segregated multicomponent NPs were produced by slowing the cooling rate to facilitate diffusion and partitioning of the

REFERENCES

1. J.-W. Yeh *et al.*, *Adv. Eng. Mater.* **6**, 299 (2004).
2. B. Cantor, I. T. H. Change, P. Knight, A. J. B. Vincent, *Mater. Sci. Eng. A* **375–377**, 213 (2004).
3. D. B. Miracle, O. N. Senkov, *Acta. Mater.* **122**, 448 (2017).
4. Y. F. Ye, Q. Wang, J. Lu, C. T. Liu, Y. Yang, *Mater. Today* **19**, 349 (2016).
5. Y. Yao *et al.*, *Science* **359**, 1489 (2018).
6. R. Ferrando, J. Jellinek, R. L. Johnston, *Chem. Rev.* **108**, 845 (2008).
7. K. D. Gilroy, A. Ruditskiy, H.-C. Peng, D. Qin, Y. Xia, *Chem. Rev.* **116**, 10414 (2016).
8. N. Ortiz, R. G. Weiner, S. E. Skrabalak, *ACS Nano* **8**, 12461 (2014).
9. V. F. Puentes, K. M. Krishnan, P. Alivisatos, *Appl. Phys. Lett.* **78**, 2187 (2001).
10. P.-C. Chen *et al.*, *Science* **352**, 1565 (2016).
11. P.-C. Chen *et al.*, *J. Am. Chem. Soc.* **137**, 9167 (2015).
12. M. A. Payne, J. B. Miller, A. J. Gellman, *ACS Comb. Sci.* **18**, 559 (2016).
13. S. Ding, Y. Liu, Y. Li, Z. Liu, S. Sohn, F. J. Walker, J. Schroers, *Nat. Mater.* **13**, 494 (2014).

10.1126/science.aat1471

Chemistry Department, Indiana University–Bloomington, 800 East Kirkwood Avenue, Bloomington, IN 47405, USA.
Email: sskrabalak@indiana.edu



POLICY FORUM

SCIENCE EDUCATION

Anatomy of STEM teaching in North American universities

Lecture is prominent, but practices vary

By M. Stains, J. Harshman, M. K. Barker, S. V. Chasteen, R. Cole, S. E. DeChenne-Peters, M. K. Eagan Jr., J. M. Esson, J. K. Knight, F. A. Laski, M. Levis-Fitzgerald, C. J. Lee, S. M. Lo, L. M. McDonnell, T. A. McKay, N. Michelotti, A. Musgrove, M. S. Palmer, K. M. Plank, T. M. Rodela, E. R. Sanders, N. G. Schimpf, P. M. Schulte, M. K. Smith, M. Stetzer, B. Van Valkenburgh, E. Vinson, L. K. Weir, P. J. Wendel, L. B. Wheeler, A. M. Young

A large body of evidence demonstrates that strategies that promote student interactions and cognitively engage students with content (1) lead to gains in learning and attitudinal outcomes for students in science, technology, engineering, and mathematics (STEM) courses (1, 2). Many educational

and governmental bodies have called for and supported adoption of these student-centered strategies throughout the undergraduate STEM curriculum. But to the extent that we have pictures of the STEM undergraduate instructional landscape, it has mostly been provided through self-report surveys of faculty members, within a particular STEM discipline [e.g., (3–6)]. Such surveys are prone to reliability threats and can underestimate the complexity of classroom environments, and few are implemented nationally to provide valid and reliable data (7). Reflecting the limited state of these data, a report from the U.S. National Academies of Sciences, Engineering, and Medicine called for improved data collection to understand the use of evidence-based instructional practices (8). We report here a major step toward a characteriza-

Despite numerous calls to improve student engagement, supported by a large body of evidence, STEM classes are often still dominated by lectures.

tion of STEM teaching practices in North American universities based on classroom observations from over 2000 classes taught by more than 500 STEM faculty members across 25 institutions.

Our study used the Classroom Observation Protocol for Undergraduate STEM (COPUS) (9), which can provide consistent assessment of instructional practices and document impacts of educational initiatives. COPUS requires documenting the co-occurrence of 13 student behaviors (e.g., listening, answering questions) and 12 instructor behaviors (e.g., lecturing, posing questions) during each 2-min interval of a class. Our large-scale COPUS data allow generalizations beyond institution-level descriptions and suggest an opportunity to resolve inconsistent findings from recent discipline-based education research (DBER) studies. For example, STEM faculty report that it is more difficult to use student-centered techniques in large classrooms or less amenable physical layouts (10),

The list of author affiliations is provided in the supplementary materials. Email: mstains2@unl.edu

but this has not been borne out in practice (11). Previous studies also disagree on the relationship between course level (introductory or upper division) and instructional practices (11–13). Also, although classroom observations are often used for evaluative (e.g., promotion and tenure) purposes, as well as to document the impact of educational initiatives, more data are needed to guide such use of observational protocols to collect data in a valid way (11).

DIDACTIC, INTERACTIVE, AND MORE

We observed 2008 STEM classes from 709 courses taught by 548 individual faculty members across 24 doctorate-granting universities and one primarily undergraduate institution (table S3). Faculty members were observed teaching on average 1.3 courses and 3.2 times. Observations covered seven STEM disciplines: 71.4% from lower-level courses, 19.8% from upper-level courses, 4.7% from graduate courses, 0.3% from cross-listed courses, and 3.7% from courses with unspecified levels (table S4). COPUS, which was adapted from the Teaching Dimensions Observation Protocol (14), was selected for this study as it is broadly used and has been demonstrated to provide valid characterization of instructional practices in STEM classrooms (see supplementary materials). The high level of inter-rater reliability consistently achieved across studies employing COPUS ensures that it can provide a reliable and valid characterization of STEM instruction on a large scale.

The most common instructor behaviors were lecture (an average of $74.9 \pm 27.8\%$ of the total 2-min intervals of a given class), writing in real time ($35.0 \pm 35.2\%$), posing nonrhetorical questions ($25.0 \pm 21.4\%$), following-up on questions ($14.3 \pm 18.9\%$), answering student questions ($11.5 \pm 12.8\%$), and administering clicker questions ($10.0 \pm 16.5\%$). Students primarily listened to the instructor ($87.1 \pm 20.8\%$), answered instructor questions ($21.6 \pm 19.8\%$), and asked questions ($10.4 \pm 12.1\%$).

Simply documenting the prevalence of instructor and student behaviors does not accurately reflect what strategies are being implemented alongside or instead of one another. To address this issue, we conducted latent profile analysis, creating clusters based on four instructor behaviors (lecture, posing questions, clicker questions, and one-on-one work with students) and four student behaviors (group work on clicker questions, group work on worksheets, other group work, and asking questions). We chose these eight behaviors because they were observed with adequate heterogeneity, were not highly correlated with each other, and were likely to be key strategies in active or nonactive learning environments.

The solution consisted of seven clusters, each representing a unique instructional profile (fig. S4).

The first group of instructional profiles, which we labeled “Didactic” (clusters 1 and 2), depicts classrooms in which 80% or more of class time consists of lecturing. Fifty-five percent of the observations belonged to this broad instructional style. Cluster 1 has no observed student involvement except sporadic questions from and to the students, whereas cluster 2 has clicker questions that are sometimes associated with group work.

The second group of profiles, which we named “Interactive Lecture” (clusters 3 and 4), represents instructors who supplement lecture with more student-centered strategies such as “Other group activities” (cluster 3) and “Clicker questions with group work” (cluster 4). Twenty-seven percent of the observations were classified in this instructional style.

Finally, clusters 5, 6, and 7 depict instructors who incorporate student-centered strategies into large portions of their classes.

“...institutions should revise ...policies to incentivize and reward...evidence-based instructional practices...”

Eighteen percent of observations were in this “Student-Centered” style. Cluster 5 represents a variety of group work strategies consistently used, whereas cluster 7 represents a similar variety but with less consistent usage. Some in cluster 6 may resemble a popular style of instruction, Process Oriented Guided Inquiry Learning (15), but others (due to a higher proportion of lecture) likely represent strategies that incorporate group worksheets and one-on-one assistance from the instructor. Although we are unable to claim that our data are entirely representative, the sample size and diversity of courses and disciplines represented in our data suggest that these profiles and broad instructional styles provide a reliable snapshot of the current instructional landscape in undergraduate STEM courses taught at North American institutions.

We leveraged the identification of the three broad instructional styles to address discrepancies among prior DBER studies (see the graphic). Observations in large courses were classified in the didactic instructional style more than expected by random chance and in the student-centered instructional style less than expected by

chance, whereas the opposite occurred for small courses [χ^2 (4, $N = 1753$) = 56.5, $P < 0.001$, $V = 0.13$]. Classrooms with flexible seating were more likely to be classified in the student-centered instructional style [χ^2 (2, $N = 1137$) = 55.9, $P < 0.001$, $V = 0.22$]. But simply providing infrastructure or small class size does not necessarily change instructional practices, as about half of the classes with flexible seating and about half of the small- and medium-size courses were classified as didactic. We found no significant relationships between instructional style and course level, suggesting that instructional style is similar throughout the curriculum [χ^2 (8, $N = 1927$) = 11.0, $P = 0.20$].

We were interested in differences by discipline because content, disciplinary teaching conventions, and educational research traditions are different for each. Relative to chance, mathematics and geology have more student-centered styles than expected, biology has more interactive styles than expected, and chemistry has more didactic styles than expected [χ^2 (12, $N = 1994$) = 101.3, $P < 0.001$, $V = 0.16$].

As in previous research (11), we found that individual instructors vary their teaching from day to day. Only about half of the courses (53.7%) from which two or more observations were collected had their observations classified into only one of the three broad instructional styles; 41.9% of these courses had their observations classified in two styles, and 9.1% of the courses that were observed three or more times had observations classified in all three styles. The more frequently an instructor was observed within the same course, the greater the number of instructional styles under which her or his teaching was classified. Our data thus suggest that at least four observations are necessary for reliable characterization of teaching (see the graphic, bottom).

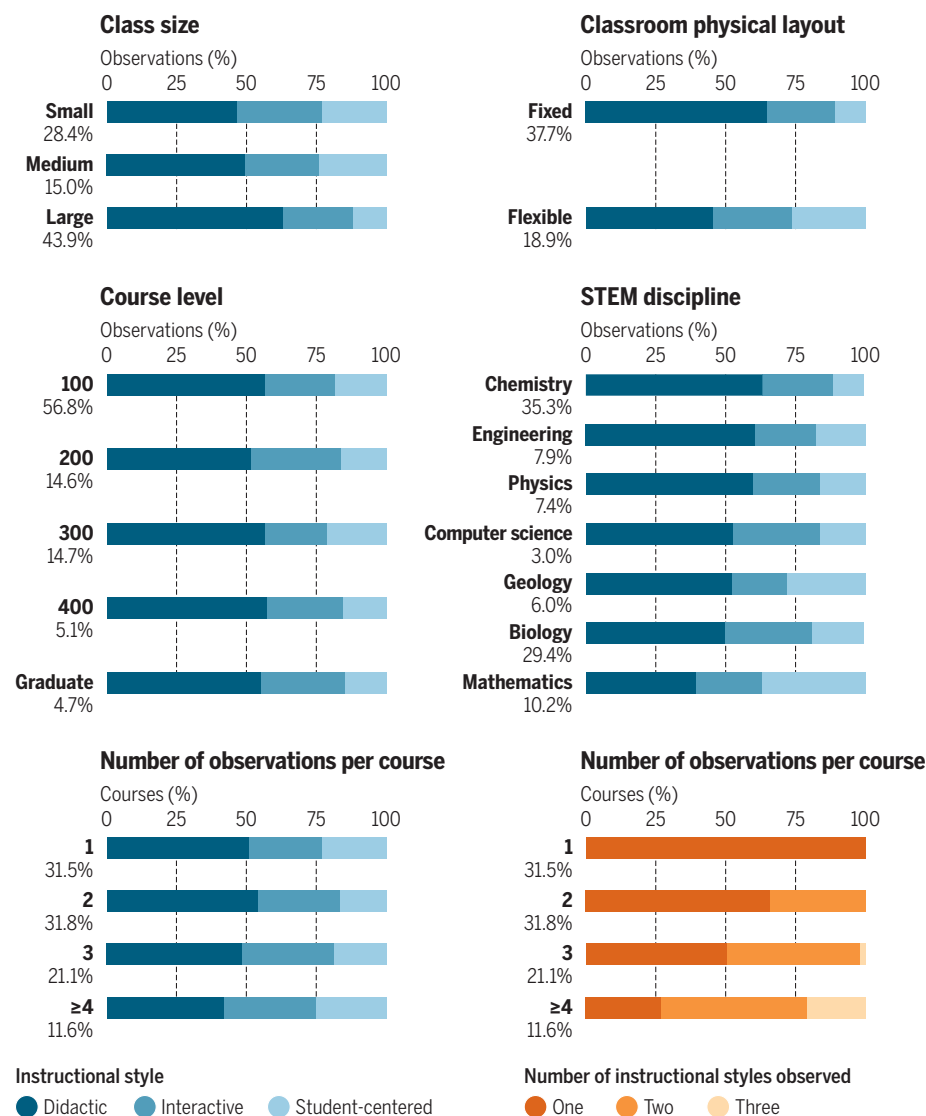
DATA, INCENTIVES, TRAINING

Three main findings emerge from this report: (i) Didactic practices are prevalent throughout the undergraduate STEM curriculum despite ample evidence for the limited impact of these practices and substantial interest on the part of institutions and national organizations in education reform. (ii) Although faculty survey-based studies have suggested classroom layouts and course size as barriers to instructional innovation, flexible classroom layouts and small course sizes do not necessarily lead to an increase in student-centered practices. (iii) Reliable characterization of instructional practices requires at least four visits.

These findings challenge institutions and STEM disciplines to reflect on practices and policies that sustain the status

Distributions of instructional styles

Distributions of the three broad instructional styles across class size (small, 0 to 50 students; medium, 51 to 100; large, more than 100), classroom physical layout, course level, STEM discipline, and number of observations per course. The lower-right panel represents the relationship between the number of observations per course and the classification of observations in one, two, and all three broad instructional styles. The percentages appearing to the left of each bar represent the proportion of the observations in a particular graph that are reflected in a given bar.



quo. Specifically, institutions should revise their tenure, promotion, and merit-recognition policies to incentivize and reward implementation of evidence-based instructional practices for all academic ranks. Ideally, implementation of these practices would be an expectation for promotion and tenure to be obtained and factored into annual merit decisions. These policy changes would require institutions and STEM professional organizations to provide effective pedagogical training for the current and future professoriate, similar to the level provided for research. Further, these policy changes cannot be meaningfully implemented without research-based

guidelines for measuring effective teaching practices. Funding agencies should prioritize the development of such guidelines.

This report provides specific baseline data for comparison for determining the impact of educational interventions, for professional development facilitators to inform the design of their programs, and for faculty when they receive COPUS data. The seven instructional profiles allow these comparisons to move beyond the binary teacher- or student-centered teaching classification and to inform incremental and diverse paths toward student-centered teaching. However, this baseline is limited because the sample is focused on doctorate-

granting universities in North America and only seven STEM disciplines. Moreover, the analytical tool used (i.e., COPUS) focuses on frequencies and not quality of behaviors, does not capture the quality of the content being conveyed, and only focuses on the classroom portion of STEM courses, not other components such as laboratory, field work, or online experiences. To fully characterize the STEM instructional landscape, funding agencies should support large-scale studies that include a representative sample of institutions and/or STEM disciplines, as well as multiple sources of data that characterize type and quality of instructional practices experienced by students in all components of a course. ■

REFERENCES AND NOTES

1. National Research Council, *Discipline-Based Education Research: Understanding and Improving Learning in Undergraduate Science and Engineering*, S. R. Singer, N. R. Nielsen, H. A. Schweingruber, Eds. (The National Academies Press, Washington, DC, 2012).
2. S. Freeman *et al.*, Active learning increases student performance in science, engineering, and mathematics. *Proc. Natl. Acad. Sci. U.S.A.* **111**, 8410 (2014).
3. C. Henderson, M. H. Dancy, *Phys. Rev. Spec. Top. Phys. Educ. Res.* **5**, 020107 (2009).
4. M. Borrego, J. E. Froyd, T. S. Hall, *J. Eng. Educ.* **99**, 185 (2010).
5. R. H. Macdonald, C. A. Manduca, D. W. Mogk, B. J. Tewksbury, *J. Geosci. Educ.* **53**, 237 (2005).
6. A. Zieffler, J. Park, J. Garfield, R. Delmas, A. Bjornsdottir, *J. Stat. Educ.* **20**, 1 (2012).
7. C. T. Williams, E. M. Walter, C. Henderson, A. L. Beach, *Int. J. STEM Educ.* **2**, 18 (2015).
8. National Academies of Sciences, and Medicine, "Indicators for monitoring undergraduate STEM Education" (The National Academies Press, Washington, DC, 2018).
9. M. K. Smith, F. H. M. Jones, S. L. Gilbert, C. E. Wieman, *CBE Life Sci. Educ.* **12**, 618 (2013).
10. S. E. Shadle, A. Marker, B. Earl, *Int. J. STEM Educ.* **4**, 8 (2017).
11. T. J. Lund *et al.*, *CBE Life Sci. Educ.* **14**, ar18 (2015).
12. K. Akiha *et al.*, *Front. Educ.* **2**, 68 (2018).
13. R. Teasdale *et al.*, *Geosphere* **13**, 608 (2017).
14. M. T. Hora, A. Oleson, J. J. Ferrare, "Teaching Dimensions Observation Protocol (TDOP) User's Manual" (Wisconsin Center for Education Research, University of Wisconsin-Madison, Madison, 2013).
15. R. S. Moog, J. N. Spencer, A. R. Straumanis, *Metrop. Univ.* **17**, 41 (2006).

ACKNOWLEDGMENTS

The authors acknowledge support from the U.S. National Science Foundation under grant nos. DUE 1347243 (J.M.E., K.M.P., P.J.W., A.M.Y.), DUE 1432804 (E.R.S., M.K.E., F.A.L., M.L.F., B.V.V.), DUE 1525331 (S.V.C.), DUE 1323022 (J.K.K.), DUE 1432728 (R.C.), DUE 1347577 (M.K.S., M.R.S., E.L.V.), DUE 1347578 (M.K.S.), DUE 1322851 (M.K.S.), DRL 0962805 (M.K.S., M.R.S., E.L.V.), DUE 1347697 (T.M., N.M.), DUE 1256003 (M.S.), DUE 1347814 (M.S.), CAREER 1552448 (M.S., J.H.); the NIH under award nos. 1R25GM114822-01 (C.J.L.) and 5R25GM114822 (C.J.L.); the John Templeton Foundation grant FP053369-G via a subaward from the University of Chicago Knowledge Lab (C.J.L.); The Carl Wieman Science Education Initiative, University of British Columbia (M.K.B., L.M.M., T.M.R., N.G.S., P.M.S., L.K.W.); the University of Northern Colorado: Faculty Research and Publications Board (S.E.D.P.); the Flexible Learning Initiative, University of British Columbia (A.M.); Howard Hughes Medical Institute award no. 52006934 (S.M.L.) and no. 52008380 (C.J.L.). All COPUS coders are acknowledged in the supplementary materials.

SUPPLEMENTARY MATERIALS

www.sciencemag.org/content/359/6382/1468/suppl/DC1

10.1126/science.aap8892



The gecko *Uroplatus phantasticus* is so named for its “flat tail” and its almost “imaginary” appearance.

BOOKS *et al.*

TAXONOMY

What's in a name?

A taxonomist contemplates the implications involved in naming new species

By Gregory R. Goldsmith

For those so inclined, taxonomy provides considerable material for dinner-party conversation. There is the species *Agra schwarzeneggeri*, the beetle with the “biceps-like” appendage named in honor of the physique of the famous Austrian bodybuilder (turned actor, turned politician) (1). The genus of flatworms named *Obama*, however, does not refer to the former president. It is actually derived from the words for leaf and animal in the indigenous language Tupi (2).

Then there are species names for which the meaning only becomes apparent when read aloud, such as is the case for the wasp species *Heerz lukenatcha*. Some names require less effort to understand. There is a genus of beetle that includes the species *Gelae baen*, *Gelae donut*, *Gelae fish*, and *Gelae belae*. Finally, there are those species that seem destined to twist the tongue, such as the tropical plant species *Rhodostemonodaphne crenaticupula*.

Such names can make light of a discipline that actually calls for a heavy knowledge of biology, as well as of linguistics, philosophy,

and information science. Michael Ohl's new book, *The Art of Naming*, intersects these unusual and amusing examples with more serious considerations of the craft. Ohl's is hardly the first book to explore taxonomy, but few others consider so many different aspects of it.

Unsurprisingly, Ohl, a taxonomist at the National History Museum in Berlin, devotes a considerable portion of the book to the process of choosing a name for a new species. At the heart of this matter is deciding on the intended semantics and the resultant morphology of a name. In turn, the linguistics behind a name intersect with philosophical considerations. What, exactly, is being named, after all? A proper name is supposed to refer to a specific object, but species names also refer to species as a collective whole.

Writing about such topics demands precision, and Ohl's theses are not always clear. For example, his discussion of why common names are unsuitable for distinguishing among species is confounded with a discussion of etymology. The book does, however, benefit from an admirable translation from the original German by Elisabeth Lauffer.

Of course, neither the linguistics nor the philosophy of naming a new species can be divorced from biology. In particular, there is the vexing question of what makes a



The Art of Naming

Michael Ohl

Translated by
Elisabeth Lauffer

MIT Press, 2018. 310 pp.

The reviewer is at Schmid College of Science and Technology, Chapman University, Orange, CA 92866, USA.
Email: goldsmith@chapman.edu

species a species. These delineations often draw from incomplete observations of the morphology, behavior, and distribution of individuals. Even with the advent of molecular phylogenetics, there will always be questions as to where one species ends and another begins. The biology, in turn, has linguistic implications (e.g., what happens when a behavioral observation used to form a name is refuted?) and philosophical ramifications (e.g., what happens when the name refers to only a single specimen that does not represent the variation observed across the entirety of the species?).

All of these considerations are arguably secondary to our ability to reliably store and retrieve standardized species descriptions. Ohl, in his role at the Natural History Museum, recognizes that much of the painstaking time spent describing species is devoted to comparing a new specimen with what is in the existing literature. The most common errors (e.g., assigning two different names to the same species) are likely to be considerably reduced simply by increasing access to taxonomic information.

Ohl is at his best in the book's final chapters, where he merges linguistics, philosophy, and biology together in a consideration of some particularly unusual matters of taxonomy. A chapter devoted in part to Nessie the Loch Ness Monster raises interesting questions of the implications of naming an object that may not exist. Similarly, a chapter devoted to the eternal question of how many species exist leads to interesting thinking about how the field compiles and updates catalogs. These are the most profitable parts of the book, because in looking at the past, they hint at the future.

In focusing his discussion on a retrospective of the discipline, Ohl misses poignant opportunities to consider what bearing fields like linguistics, philosophy, biology, and information science may have on the future of taxonomy. The unprecedented rates of land use and climate change we are imposing on the planet mean that much of its current biodiversity may become extinct before we will even be able to describe it. This is therefore a perfect time to consider where taxonomy could use insights from other disciplines to meet the challenges of the times. If such an endeavor provides us with a few more interesting dinner conversations along the way, all the better. ■

REFERENCES

1. T.L. Erwin, *Zootaxa* **119**, 1 (2002).
2. F. Carbayo et al., *Zool. Scripta* **42**, 508 (2013).

10.1126/science.aat1491

PHYSICS

Questioning quantum mechanics

In a critique of the Copenhagen dogma, a physicist gives voice to “quantum dissidents”

By **Mélanie Frappier**

A century after its inception, quantum mechanics continues to puzzle us with dead-and-alive cats, waves “collapsing” into particles, and “spooky action at a distance.” In his first book, *What Is Real?*, science writer and astrophysicist Adam Becker sets out to explore why the physics community is still arguing today about quantum mechanics’s true meaning.

For Becker, this lack of progress is unsurprising: Most physicists still frame quantum problems through the sole lens of the so-called “Copenhagen interpretation,” the loose set of assumptions Niels Bohr and his colleagues developed to make sense of the strange quantum phenomena they discovered in the 1920s and 1930s. However, he warns, the apparent success of the Copenhagen interpretation hides profound failures.

The approach of Bohr and his followers, Becker argues, was ultimately rooted in logical positivism, an early-20th-century philosophical movement that attempted to limit science to what is empirically verifiable. By the mid-20th century, philosophers such as Thomas Kuhn and W. V. O. Quine had completely discredited this untenable view of science, Becker continues. The end of logical positivism, he concludes, should have led to the demise of the Copenhagen interpretation. Yet, physicists maintain that it is the only viable approach to quantum mechanics.

As Becker demonstrates, the physics community’s faith in Bohr’s wisdom rapidly transformed into a pervasive censorship that stifled any opposition. Advisers steered Ph.D. students away from questioning the “orthodox” interpretation of quantum mechanics, and journals systematically rejected papers that did so. It became difficult to obtain funding and apparatuses to test contested claims. Those who dared discuss possible alternatives to the “dogma” were ostracized.

A riveting storyteller, Becker brings to life physicists who have too long remained in the

shadow of Bohr and Einstein. Drawing on a vast literature and scores of interviews, he weaves an engaging narrative in which Nazi science, communist sympathies, science-fiction magazines, Cold War strategists, hippies, and institutional feuds fueled heated disputes over alternative interpretations.

The book shows that more than mere philosophical disagreements explain why David Bohm was exiled to Brazil after proposing that electrons were guided by pilot waves, why Hugh Everett III preferred to run nuclear war simulations for the Pentagon rather than defend the possibility of “parallel” worlds, and why so few of John Bell’s CERN co-workers knew about his groundbreaking work in quantum physics.

Unfortunately, in his eagerness to defend the critiques of the “Copenhagen dogma,” Becker fails to give a fair hearing to Bohr and his colleagues. He admits that the Copenhagen interpretation is not a monolithic doctrine but nevertheless usually presents it as one.

Of course, nontechnical primers are not the place for fastidious philosophical distinctions. They should, however, be careful not to create straw men. Eugene Wigner may have claimed that only conscious observers collapse quantum wave functions, but Bohr did not. Grete Hermann argued that definite paths could be ascribed to electrons between measurements, but Werner

Heisenberg dismissed such claims as “matters of personal preference.”

By suggesting that, for all practical purposes, these physicists defended the same position, Becker—like so many before him—ends up portraying the Copenhagen interpretation as a single, internally inconsistent doctrine. His uncharitable account makes it difficult not to conclude that these physicists were at best unsophisticated instrumentalists, at worst self-serving hypocrites.

The defense Bohr and his students gave of their positions drew from many philosophical traditions, including Aristotelian metaphysics, neo-Kantianism, and analytic philosophy of language. They were especially intrigued by how these schools of thought dared to ask if “what is real?” can be meaningfully answered. By failing to engage the Copenhagen physicists on their own terms, Becker is unsuccessful in addressing the fundamental philosophical question hiding behind the title of his work, a question that remains at the heart of quantum interpretation debates.

Despite an oversimplified treatment of the philosophical issues at play, *What Is Real?* offers an engaging and accessible overview of the debates surrounding the interpretation of quantum mechanics. It will appeal to those who wonder whether instantaneous actions at a distance are logically—let alone physically—possible, as well as to those who, like Einstein, wonder if the Moon is still there when no one is looking. ■

10.1126/science.aas9190



What Is Real?
The Unfinished Quest
for the Meaning
of Quantum Physics
Adam Becker
Basic Books, 2018.
381 pp.

PODCAST

First in Fly
Drosophila Research
and Biological Discovery
Stephanie Elizabeth Mohr
Harvard University Press,
2018. 270 pp.

Valued for its short life cycle, prolific reproductive potential, and easily detected mutations, *Drosophila melanogaster* has been critical to advancing our understanding of health, disease, and genetic inheritance. This week on the *Science* podcast, Stephanie Elizabeth Mohr shares highlights from the tiny fruitfly’s major contributions to science.

10.1126/science.aat1629



From genetic breakthroughs to developmental biology insights, the unassuming fruitfly has proved invaluable to research.

The reviewer is director of the History of Science and Technology Programme, University of King’s College, Halifax, Nova Scotia B3H 2A1, Canada. Email: melanie.frappier@ukings.ca

LETTERS

Edited by **Jennifer Sills**

Mining threatens Colombian ecosystems

The American tropics are home to about 10% of Earth's species and several biodiversity hotspots of global importance for conservation (1, 2), including high-elevation tropical alpine ecosystems (páramos) and Andean forests. These ecosystems deliver numerous services, such as providing water to millions of people (3). They are also extremely sensitive to perturbations and difficult to restore (4). Despite their importance and fragility, a goldmining company has proposed a project that will put Colombia's montane and páramos environments at risk.

Minesa goldmining company plans to build one of the world's largest underground mines in Santurbán, Santander, Colombia (5, 6). The goal of the megamining project is to extract 255 million grams of gold over 20 years, and the extractive company claims that the sale of this gold will bring about U.S.\$2 billion in taxes to Colombia (7). However, an environmental impact assessment (8) shows that those benefits come with a cost: The study forecasts involuntary displacement of human settlements and large-scale habitat fragmentation and loss (8), thus threatening endemic flora and fauna with extinction. Similar large-scale extractive projects in Latin America have produced a severe negative impact on farming communities, affected water and air quality, and led to violent social conflicts (9).

Recent environmental policies in Colombia have fostered unparalleled conservation of remote and species-rich areas (10). However, the biodiverse sites threatened by deforestation and mining, including most of the Andean cloud forests and páramos, are disproportionately excluded from the country's protected areas (10). We urge environmental authorities to take the necessary action to stop the Santurbán goldmining project and instead promote the active preservation and restoration of the páramos and Andean forests, particularly in this biologically important area of the country.

Oscar Alejandro Pérez-Escobar,^{1,2*} Rodrigo Cámara-Leret,³ Alexandre Antonelli,^{1,2,4,5} Richard Bateman,⁶ Sidonie Bellot,⁷ Guillaume Chomicki^{8,9} Antoine Cleef,¹⁰ Mauricio Diazgranados,¹¹ Steven Dodsworth,¹² Carlos Jaramillo,¹³ Santiago Madriñán,¹⁴ Ingrid Olivares,¹⁵ Alejandro Zuluaga,¹⁶ Rodrigo Bernal¹⁷

¹Gothenburg Global Biodiversity Centre, SE-405 30 Gothenburg, Sweden. ²Department of Biological and Environmental Sciences, University of Gothenburg, 405 30 Gothenburg, Sweden. ³London SW8 3PF, UK. ⁴Gothenburg Botanical Garden, Gothenburg, Sweden. ⁵Department of Organismic and Evolutionary Biology, Harvard University, Cambridge, MA 02139, USA. ⁶London TW9 2DX, UK. ⁷Plant Biodiversity Research, Department Ecology & Ecosystem Management, Technical University of Munich, 85354 Freising, Germany. ⁸Department of Plant Sciences, University of Oxford, Oxford OX1 3RB, UK. ⁹The Queen's College, Oxford OX1 4AW, UK. ¹⁰Institute for Biodiversity and Ecosystem Dynamics, University of Amsterdam, Amsterdam, Netherlands. ¹¹West Sussex RH16 4ST, UK. ¹²School of Life Sciences, University of Bedfordshire, Luton LU1 3JU, UK. ¹³Smithsonian Tropical Research Institute, 9100 Panama City, Panama. ¹⁴Universidad de los Andes, DC 01 Bogotá, Colombia. ¹⁵University of Zurich, 8008 Zurich, Switzerland. ¹⁶Universidad de Valle, Ciudadela

Universitaria Melendez, Cali, Colombia. ¹⁷Jardín Botánico del Quindío, Calarcá, Colombia.
*Corresponding author. Email: opereze@yahoo.com

REFERENCES

1. N. Myers, R. A. Mittermeier, C. G. Mittermeier, G. A. B. Fonseca, J. Kent, *Nature* **403**, 853 (2000).
2. C. U. Ulloa *et al.*, *Science* **358**, 1614 (2017).
3. S. Díaz *et al.*, *Science* **359**, 270 (2018).
4. C. Murcia, *For. Ecol. Manage.* **99**, 163 (1997).
5. P. Harris, "Minesa to use TBM at Soto Norte," *Mining Journal* (2017); www.mining-journal.com/feasibility/news/1309067/minesa-tbm-soto-norte.
6. P. Harris, "California dreaming in Colombia," *Mining Journal* (2017); www.mining-journal.com/site-visits/news/1177651/california-dreaming-colombia.
7. S. M. de Santander, "Our project," Minesa (2016); www.minesa.com/en/nuestro-proyecto [in Spanish].
8. Ingetec, "Estudio de impacto ambiental para el proyecto de explotación subterránea de minerales auroargentíferos 'Soto Norte'" (2017); <https://imgcdn.larepublica.co/cms/2017/10/25072925/MINESA-EIA-Res-Ejecutivo-final-Ag-28.pdf> [in Spanish].
9. A. Bebbington, *Commun. Dev. J.* **48**, 501 (2013).
10. G. Forero-Medina, L. Joppa, *PLOS One* **5**, 1 (2010).

10.1126/science.aat4849

Ocean deoxygenation: Time for action

In their Review "Declining oxygen in the global ocean and coastal waters" (5 January, p. 46), D. Breitburg *et al.* summarize evidence showing that oxygen has declined in the open ocean and in coastal waters over the past 50 years as a result of increased greenhouse gas emissions and nutrient discharges to coastal waters. We also urgently need more data on the role and speed of microbial engagement, including how deoxygenation is altering microbial pathways and rates of processes within the water column and the deep ocean (1). Given that more than half of

the oxygen produced on Earth is derived from phytoplankton, decline of oxygen in the ocean concerns life on land as well. We cannot afford to wait before taking action.

Breitbart *et al.* call for a “raised awareness” of the deoxygenation phenomenon. We contend that such awareness must extend to all facets of society, beyond the pages of scientific journals. Intuitive, interactive, dynamic online maps and visualizations (2, 3) will be key to generating the societal and political will toward the effective management needed to ultimately reverse deoxygenation. The global trend by nations of securing large areas of ocean as “blue parks” (4) is cause for hope because protecting nature protects our existence.

Sylvia A. Earle,^{1,2} Dawn J. Wright,^{3,4}

Samantha Joye,⁵ Dan Laffoley,⁶ John

Baxter,⁶ Carl Safina,⁷ Patty Elkus²

¹National Geographic Society Explorer-in-Residence, Washington, DC 20036, USA. ²Mission Blue, Napa, CA 94581, USA. ³Environmental Systems Research Institute, Redlands, CA 92373, USA. ⁴College of Earth, Ocean, and Atmospheric Sciences, Oregon State University, Corvallis, OR 97331, USA. ⁵Department of Marine Sciences, University of Georgia, Athens, GA 30602, USA. ⁶International Union for Conservation of Nature–World Commission on Protected Areas, Gland, Switzerland. ⁷School of Marine and Atmospheric Sciences, Stony Brook University, Setauket, NY 11733, USA.

*Corresponding author. Email: saearle@aol.com

REFERENCES

1. D. Laffoley, J. M. Baxter, Eds., *Ocean Deoxygenation – Everyone’s Problem: Causes, Impacts, Consequences and Solutions* (International Union for Conservation of Nature and Natural Resources, Gland, Switzerland, 2018).
2. A. Witze, *Nature* **541**, 10 (2017).
3. R. Sayre *et al.*, *Oceanography* **30**, 90 (2017).
4. N. Gray *et al.*, *Coastal Management* **45**, 407 (2017).

10.1126/science.aat0167

Amazon sugar cane: A threat to the forest

Amazonia’s vegetation ranges from dense forests to savanna areas, and the region’s forests and their biodiversity are vulnerable to the ongoing advance of land-use change for agriculture and ranching (1). In Brazil, cultivation of sugar cane is currently prohibited in the Mato Grosso wetlands (pantanal) and Amazonia regions (2). The number of sugar cane plantations has vastly increased during the past decade, and Brazil is the world’s largest sugar cane producer (3). The cane plantations are projected to increase due to demand for biofuels (4). Sugar cane plantations have been shown to threaten biodiversity, their effects extending beyond the cultivated areas to adjacent forests (5). The Brazilian Senate has scheduled a decision for 2018 on a bill that proposes opening the Amazon

region to sugar cane (6). This crop would supposedly be planted in degraded fields, in natural Amazonian grasslands, and in the biodiversity hotspots of the central Brazilian savannas (cerrado). Because of the potential catastrophic effects on the Amazonian forest, the biodiversity and ecosystem services of South America, and the agricultural productivity of Brazil, we urge the President to veto this bill.

The threat of sugar cane is just one among Amazonia’s many strong drivers of destruction (4). Amazonian forests play an important role in the climate of South America, with substantial rainfall



Brazil may decide to expand sugar cane production.

contributions to agriculture in southeastern Brazil (7, 8). In the medium and long term, forest loss would threaten Brazil’s own agricultural and biofuel production, given that the area with the greatest agricultural production is in the south and southeast of the country (9) and depends on water vapor from the Amazon region (7, 8). Political decision-makers and national and international institutions that fund large agricultural enterprises should not be fooled by the sweet taste of a new agricultural frontier to be exploited. They should instead be guided by the need to avoid loss of Amazonia’s biodiversity, genetic heritage, and valuable ecosystem services, including climate regulation for the area with the largest population and agricultural production in South America (9, 10).

L. Ferrante* and P. M. Fearnside

National Institute for Research in the Amazon (INPA), 69067-375, Manaus, AM, Brazil.

*Corresponding author.

E-mail: lucasferrante@hotmail.com

REFERENCES

1. P. M. Fearnside, in *Oxford Research Encyclopedia of Environmental Science*, H. Shugart, Ed. (Oxford University Press, New York, 2017).
2. Brazil, Presidência da República, Decreto Nº 6.961, DE (17 September 2009). [in Portuguese].
3. Food and Agriculture Organization of the United Nations, *Commodities by Country* (2018); www.fao.org/faostat/en/#rankings/commodities_by_country.
4. P. M. Fearnside, in *Biofuels and Neotropical Forests: Trends, Implications, and Emerging Alternatives*, E. J. Garen, J. Mateo-Vega, Eds. (Environmental Leadership & Training Initiative, Yale University, New Haven, CT, 2009), pp. 29–36.
5. L. Ferrante *et al.*, *J. Biogeogr.* **44**, 1911 (2017).
6. Brazil, Senado Federal, Projeto de Lei do Senado Nº 626 (2011) [in Portuguese].
7. P. M. Fearnside, *Ciênc. Hoje* **34**, 63 (2004) [in Portuguese].
8. D. C. Zemp *et al.*, *Atmos. Chem. Phys.* **14**, 13337 (2014).
9. IBGE, Levantamento Sistemático da Produção Agrícola (2018); <https://sidra.ibge.gov.br/home/lspa/brasil> [in Portuguese].
10. IBGE, Coordenação de População e Indicadores Sociais, Estimativas da população residente para os municípios e para as unidades da federação brasileiros com data de referência em 1º de julho de 2017 (2017); <https://biblioteca.ibge.gov.br/index.php/biblioteca-catalogo?view=detalhes&id=2100923> [in Portuguese].

Published online 26 March 2018

10.1126/science.aat4208

TECHNICAL COMMENT ABSTRACTS

Comment on “Enhanced water permeability and tunable ion selectivity in subnanometer carbon nanotube porins”

Andreas Horner and Peter Pohl

Tunuguntla *et al.* (Reports, 25 August 2017, p. 792) report that permeation of single-file water occurs faster through carbon nanotubes than through aquaporins. We show that this conclusion violates fundamental thermodynamic laws: Because of its much lower activation energy, aquaporin-mediated water transport must be orders of magnitude faster. Leakage at the nanotube-membrane interface may explain the discrepancy.

Full text: [dx.doi.org/10.1126/science.aap9173](https://doi.org/10.1126/science.aap9173)

Response to Comment on “Enhanced water permeability and tunable ion selectivity in subnanometer carbon nanotube porins”

Ramya H. Tunuguntla, Yuliang Zhang, Robert Y. Henley, Yun-Chiao Yao, T. Anh Pham, Meni Wanunu, Aleksandr Noy

Horner and Pohl argue that high water transport rates reported for carbon nanotube porins (CNTPs) originate from leakage at the nanotube-bilayer interface. Our results and new experimental evidence are consistent with transport through the nanotube pores and rule out a defect-mediated transport mechanism. Mechanistic origins of the high Arrhenius factor that we reported for narrow CNTPs at pH 8 require further investigation.

Full text: [dx.doi.org/10.1126/science.aaq1241](https://doi.org/10.1126/science.aaq1241)

TECHNICAL COMMENT

MEMBRANES

Comment on “Enhanced water permeability and tunable ion selectivity in subnanometer carbon nanotube porins”

Andreas Horner and Peter Pohl*

Tunuguntla *et al.* (Reports, 25 August 2017, p. 792) report that permeation of single-file water occurs faster through carbon nanotubes than through aquaporins. We show that this conclusion violates fundamental thermodynamic laws: Because of its much lower activation energy, aquaporin-mediated water transport must be orders of magnitude faster. Leakage at the nanotube-membrane interface may explain the discrepancy.

Tunuguntla *et al.* mistakenly concluded that single-file water flow through narrow carbon nanotubes is responsible for the observed acceleration of osmotic vesicle deflation upon nanotube insertion into vesicular lipid membranes (1). Calculation of the unitary nanotube water permeability $p_f = 6.8 \times 10^{-13} \text{ cm}^3 \text{ s}^{-1}$ was performed by estimating the integral permeability P_f of the lipid vesicle and taking into account the total number of carbon nanotubes per vesicle. The latter was estimated by measuring the total proton conductivity across the vesicular membrane (pH 7.5 inside versus pH 6.9 outside) and using a previously published value for the proton conductivity of a single nanotube.

These results leave open the possibility that instead of being channeled through the nanotube, water moves through defects at the nanotube-bilayer interface (Fig. 1). To exclude this possibility, experiments with a molecule that could occlude the tubes would be required. In the absence of such an inhibitor, measurements of the Gibbs activation energy barrier ΔG_t^\ddagger constitute the traditional way of showing the pres-

ence of an aqueous pore: $\Delta G_t^\ddagger \sim 5 \text{ kcal/mol}$ represents the hallmark for water movement through protein water channels (2). This value is close to the activation energy for the self-diffusion of water (3). When plotting vesicular water permeability as a function of $1/T$, where T is absolute temperature, Tunuguntla *et al.* found $\Delta G_t^\ddagger = 24.1 \text{ kcal/mol}$. Such a large ΔG_t^\ddagger value is incompatible with diffusion through a water-conducting pore.

To bolster the fact that p_f and ΔG_t^\ddagger are intricately linked in single-file transport, we transform p_f into the “hopping rate” r with which the water chain moves forward or backward (4):

$$r = p_f \frac{N_A}{V_w} \quad (1)$$

where V_w is the molecular volume of water and N_A is Avogadro's constant. The water molecule loses two of its four neighbors when entering the pore. This lifts the water molecule from its energetic ground state to a state of higher energy. Moieties of wall-lining residues in proteinaceous channels may act as surrogates

for the lost waters (5). Yet constraints in both abundance and strength of the newly formed hydrogen bonds serve to keep the energy difference between bulk and intraluminal water molecules at ambient temperatures on the order of the thermal energy $k_B T$, where k_B is the Boltzmann constant. Equilibration between the individual jumps is ensured by the short hydrogen bond lifetime, which is $\sim 2 \text{ ps}$ in neat water. A much longer lifetime for pore waters (as sometimes observed for waters of hydration) seems doubtful because they retain bulk diffusibility (6). The theory of water permeation through nanotubes describes an analogous situation with imaginary water-binding sites (4). We thus may apply transition state theory and describe the hopping of the water file by linking r to ΔG_t^\ddagger :

$$r = v_0 \exp\left(\frac{-\Delta G_t^\ddagger}{k_B T}\right) \quad (2)$$

where $v_0 \approx 10^{13} \text{ s}^{-1}$ is the universal transition state theory attempt frequency. Using Eqs. 1 and 2 to calculate p_f as

$$p_f = \frac{v_0 V_w}{N_A} \exp\left(\frac{-\Delta G_t^\ddagger}{k_B T}\right) \quad (3)$$

we find a satisfactory match to experimentally obtained p_f values for aquaporin-1, aquaporin-Z, the bacterial potassium channel KcsA, and the pore-forming peptide gramicidin A (Table 1). In contrast, the large activation energy of 24.1 kcal/mol , now reported for carbon nanotubes (1), corresponds to a p_f value 15 orders of magnitude smaller than the p_f value derived from the rate of vesicle deflation.

Extending Table 1 to other channels may reveal additional discrepancies. First, it is important to exclude channels that may accommodate more than one water molecule in their cross section, because widening of the channel is likely to increase p_f (7), whereas ΔG_t^\ddagger cannot adopt values that are smaller than those measured for the self-diffusion of water (3). Second, it is important to keep in mind that direct p_f measurements are subject to large inherent technical difficulties: They may be hampered by stagnant water layers in the membrane vicinity or uncertainties in the actual channel density (6). Water-conducting ion channels, such as the bacterial potassium channel KcsA, may be miscounted when deriving the channel number from conductivity measurements (8), as this procedure does not account for water transport by electrically silent channels (i.e., by channels that are in their inactivated state) (9). Other obstacles arise when the precise analytical solution (5) that allows calculation of p_f from the time course of vesicle volume decrease is substituted for a more simple but inaccurate expression (1, 9). Such miscalculations may partly explain the dependence of the vesicular osmotic permeability P_f on the osmotic gradient [figure S2

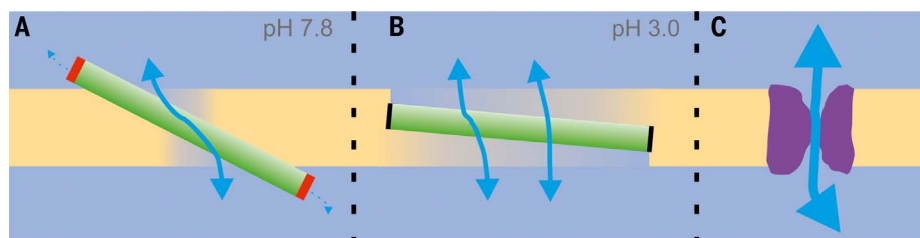


Fig. 1. Comparison of the water pathways across membranes with embedded carbon nanotubes and reconstituted aquaporins. (A) Conceivably, water leaks at the interface between the nanotubes and lipid membrane. (B) Altering the position of the nanotubes in the membrane by neutralizing the charged carboxylate groups at their ends (red to black) alters leak size and thus membrane water permeability. (C) Aquaporins offer aqueous pores that efficiently channel water. Protein-lipid interactions prevent any water from passing along the outer channel wall.

Johannes Kepler University, 4020 Linz, Austria.
*Corresponding author. Email: peter.pohl@jku.at

Table 1. The unitary pore water permeability p_f and the Gibbs activation energy barrier ΔG_t^\ddagger are intricately linked (Eq. 3).

Membrane pore	p_f (cm ³ s ⁻¹) (measured)	ΔG_t^\ddagger (kcal/mol) (measured)	r (s ⁻¹) (calculated from ΔG_t^\ddagger)	$p_{f,c}$ (cm ³ s ⁻¹) (calculated from ΔG_t^\ddagger)	$p_{f,c}/p_f$
Aquaporin-1	5.3×10^{-13} (5)	3.1 (12)	5.3×10^{10}	1.6×10^{-12}	3.0
Aquaporin-Z	2.9×10^{-13} (5)	4.0 (13)	1.2×10^{10}	3.5×10^{-13}	1.2
KcsA	5.3×10^{-14} (5)	5.1 (8)	1.8×10^9	5.4×10^{-14}	1.0
Gramicidin A	1.6×10^{-14} (14)	6.1 (15)	3.3×10^8	1×10^{-14}	0.6
Carbon nanotubes	6.8×10^{-13} (1)	24.1 (1)	2.1×10^{-5}	6.2×10^{-28}	9.1×10^{-16}

in (1)]. Alternative methods confirm that P_f is independent of the osmotic gradient (8, 10), thereby supporting this conclusion.

The bilayer may be permeated not only by water, but also by whole nanotubes (11). The first step is the transient protonation of one of their carboxylated ends, which facilitates membrane insertion of the nanotube. Water and ions may pass along the interface between lipids and the nanotube (Fig. 1). Permanent removal of the charge by switching pH from 7.8 to 3.0 should increase the probability of nanotube partition into in the bilayer. ΔG_t^\ddagger drops

from 24.1 kcal/mol at pH 7.8 to only 10.6 kcal/mol at pH 3.0. This suggests that at acidic pH, the nanotube may bury both ends within the bilayer. Lipid packing defects along the whole length of the nanotube represent a water pathway that offers less resistance than an unperturbed bilayer. At elevated temperatures, the pH difference vanishes because the thermal energy partly compensates for the additional expense in Born energy that is required for membrane portioning of a charged moiety.

We conclude that the large ΔG_t^\ddagger is incompatible with the presence of water-filled channels. Con-

ceivably, water leaks at the nanotube-bilayer interface, which is supported by the reported pH dependence of the water flux.

REFERENCES AND NOTES

1. R. H. Tunuguntla et al., *Science* **357**, 792–796 (2017).

2. P. Agre et al., *J. Physiol.* **542**, 3–16 (2002).

3. J. H. Wang, C. V. Robinson, I. S. Edelman, *J. Am. Chem. Soc.* **75**, 466–470 (1953).

4. A. Berezhkovskii, G. Hummer, *Phys. Rev. Lett.* **89**, 064503 (2002).

5. A. Horner et al., *Sci. Adv.* **1**, e1400083 (2015).

6. M.-C. Bellissent-Funel et al., *Chem. Rev.* **116**, 7673–7697 (2016).

7. G. Portella, B. L. de Groot, *Biophys. J.* **96**, 925–938 (2009).

8. S. M. Saparov, P. Pohl, *Proc. Natl. Acad. Sci. U.S.A.* **101**, 4805–4809 (2004).

9. T. Hoomann, N. Jahnke, A. Horner, S. Keller, P. Pohl, *Proc. Natl. Acad. Sci. U.S.A.* **110**, 10842–10847 (2013).

10. P. Y. Chen, D. Pearce, A. S. Verkman, *Biochemistry* **27**, 5713–5718 (1988).

11. K. Kostarelos et al., *Nat. Nanotechnol.* **2**, 108–113 (2007).

12. M. L. Zeidel, S. V. Ambudkar, B. L. Smith, P. Agre, *Biochemistry* **31**, 7436–7440 (1992).

13. P. Pohl, S. M. Saparov, M. J. Borgnia, P. Agre, *Proc. Natl. Acad. Sci. U.S.A.* **98**, 9624–9629 (2001).

14. P. Pohl, S. M. Saparov, *Biophys. J.* **78**, 2426–2434 (2000).

15. B. A. Boehler, J. De Gier, L. L. M. Van Deenen, *Biochim. Biophys. Acta* **512**, 480–488 (1978).

ACKNOWLEDGMENTS

Supported by Austrian Science Fund grant P23679.

9 September 2017; accepted 28 February 2018
10.1126/science.aap9173

TECHNICAL RESPONSE

MEMBRANES

Response to Comment on “Enhanced water permeability and tunable ion selectivity in subnanometer carbon nanotube porins”

Ramya H. Tunuguntla,^{1,*} Yuliang Zhang,¹ Robert Y. Henley,^{1,2†} Yun-Chiao Yao,^{1,3}
T. Anh Pham,¹ Meni Wanunu,² Aleksandr Noy^{1,3‡}

Horner and Pohl argue that high water transport rates reported for carbon nanotube porins (CNTPs) originate from leakage at the nanotube-bilayer interface. Our results and new experimental evidence are consistent with transport through the nanotube pores and rule out a defect-mediated transport mechanism. Mechanistic origins of the high Arrhenius factor that we reported for narrow CNTPs at pH 8 require further investigation.

At this point, high water permeability of small-diameter carbon nanotubes is hardly a surprise. The unitary permeability of 0.8-nm-diameter carbon nanotube porins (CNTPs) that we report for water transport at pH 7.8 (1), 6.8×10^{-13} cm³/s, is comparable to the 5.1×10^{-13} cm³/s value predicted by molecular dynamics simulations for a carbon nanotube of similar diameter (2). Horner and Pohl (3) themselves predicted that transport through a narrow carbon nanotube pore should be faster than transport through aquaporins and they have estimated the water diffusion coefficient in these pores to be on the order of 3×10^{-5} cm²/s (4), which is comparable to the values of 0.9×10^{-5} cm²/s and 4.4×10^{-5} cm²/s that we report for water transport at pH 7.8 and 3.0, respectively (1). Barati Farimani and Aluru (5) predicted a diffusion coefficient of 1.2×10^{-5} cm²/s for (7,7) carbon nanotubes, which also accommodate a single-file arrangement of water; again, this is close to our reported values. High water transport efficiency has been measured for larger-diameter carbon nanotubes (6, 7) and for 1.36-nm stacked graphene nanochannels (8). Thus, our reported unitary CNTP water permeabilities are consistent with the broad range of fast transport predictions and observations in the literature.

Horner and Pohl suggest that water transport through the carbon nanotubes can be verified by using a species that can obstruct the water transport through the pore. To follow this suggestion,

we measured water transport through 0.8-nm-diameter CNTPs in the presence of Ca²⁺ ions. We previously reported that Ca²⁺ ions obstruct proton transport through the narrow CNTP pore by binding to the negatively charged groups at the CNTP mouth (9); thus, it was reasonable to expect that the same mechanism could slow down water transport. Indeed, the measured unitary water permeability of 0.8-nm-diameter CNTPs decreased by a factor of >5 in the presence of 10 mM CaCl₂ (Fig. 1A). We also note that our previous measurements showed that wider 1.5-nm-diameter CNTPs can be partially obstructed by single-stranded DNA molecules (10), with the magnitude of the blockade matching the value expected for a 1.5-nm channel; this finding again

supports the idea that molecular transport occurs through the interior of the nanotube.

The suggested mechanism of transport mediated by the pH-dependent defects in the lipid bilayer created by fully or partially buried nanotubes in the bilayer interior is also incompatible with a number of observations reported in our past and present work. First, larger-diameter nanotubes should create more (and larger) defects; however, we observed substantially smaller unitary permeability for wider 1.5-nm-diameter CNTPs. This observation is again consistent with predictions that single-file water transport in subnanometer carbon nanotube pores should be faster than the more bulk-like transport in larger-diameter nanotube channels. Second, the defect-mediated transport mechanism is largely incompatible with the ionic conductance properties that we reported (1). An increased number of defects at a lower pH, as suggested by Horner and Pohl, would simply lead to an increase in overall conductance at all ionic strengths. Instead, we observed a qualitative transition from a saturating conductance characteristic at pH 7.8 to a nearly linear conductance characteristic at pH 3.0, which is fully consistent with ion transport through a narrow pore with charged groups at the entrance that neutralize at a lower pH. Our previous measurements of proton transport showed that Ca²⁺ ions are less effective in blocking the transport through 1.5-nm CNTPs than through smaller 0.8-nm CNTPs (9), again consistent with transport through the CNTP interior.

We have previously studied the configuration of CNTPs in lipid bilayers by means of cryo-transmission electron microscopy (cryo-TEM) (10) and high-speed atomic force microscopy (HS-AFM) (11). HS-AFM data show that CNTPs protrude above the bilayer plane, and cryo-TEM data indicate that the nanotubes are tilted with respect to the normal axis of the bilayer by an average of only 15°; furthermore, we do not find

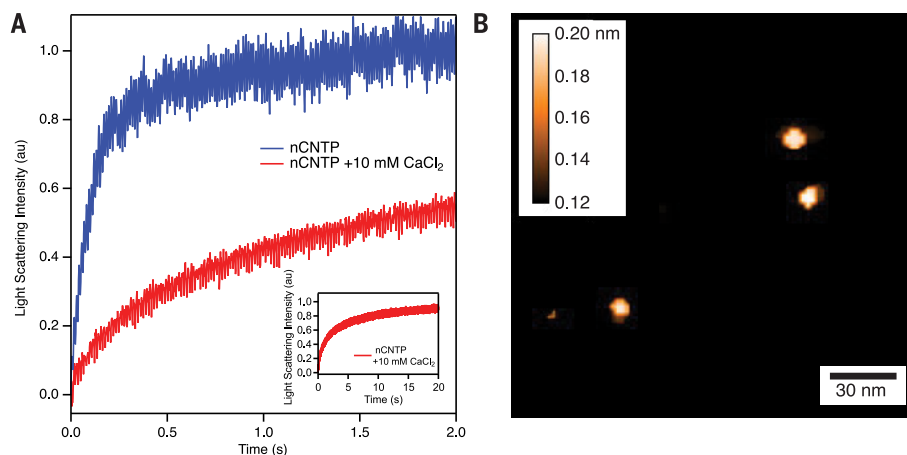


Fig. 1. Water transport obstruction by Ca²⁺ ions in CNTPs, and topography of CNTP in lipid bilayers. (A) Stopped-flow kinetics of osmotically driven size change of vesicles containing 0.8-nm-diameter CNTPs in the presence and absence of 10 mM CaCl₂. Inset shows the full range of transport kinetics in the presence of CaCl₂. Experiments followed the methodology described in (1). (B) HS-AFM image of CNTPs functionalized with a neutral moiety in a lipid bilayer supported on mica. Experiments followed the methodology described in (11).

¹Physical and Life Sciences Directorate, Lawrence Livermore National Laboratory, Livermore, CA 94550, USA. ²Physics Department, Northeastern University, Boston, MA 02115, USA. ³School of Natural Sciences, University of California, Merced, CA 94343, USA.

*Present address: PACT Pharma, Hayward, CA 94545, USA.

†Present address: Salk Institute for Biological Studies, La Jolla, CA 92037, USA.

‡Corresponding author. Email: noy1@llnl.gov

experimental evidence of a prevalent highly tilted configuration, as suggested by Horner and Pohl. Figure 1B shows a HS-AFM image of a supported bilayer containing these CNTPs functionalized with neutral methylamide groups; in preliminary experiments, they display water permeability and an activation energy at pH 8 comparable to those of unfunctionalized CNTPs at pH 3. Such findings indicate that CNTPs are still protruding from the bilayer plane, with an average surface density matching the expected CNTP loading of the vesicles. These observations do not support the suggestion by Horner and Pohl that increased permeability observed at pH 3 is due to complete burial of the nanotubes within the bilayer and creation of associated lipid packing defects. Taken together, these data strongly argue that transport in our system occurs through the carbon nanotube pores, not through defects in the nanotube-bilayer interface.

Horner and Pohl also raise an issue with the method we used to analyze our stopped-flow kinetics. We relied on a widely used approach by the groups of Zeidel (12) and Agre (13) and have reproduced literature-reported water permeability and activation energy values for aquaporin pores and background lipid bilayer water permeability in control experiments (1). We have also tried to use the analytical solution suggested by Horner and Pohl (4) and found that it fits our data poorly.

A wider survey of the literature shows that the relationship between unitary water permeability of biological channels and activation energy is more complicated than what a simple transition

state theory approach suggests; for example, the permeability of the GlpF protein, $1.1 \times 10^{-12} \text{ cm}^3/\text{s}$ (3), is more than 5×10^3 times the value expected on the basis of its activation energy of 7 kcal/mol (14). In 2001, de Groot and Grubmüller also commented that for water transport in protein channels, “considerable mismatch is seen between measured rates and corresponding activation energies”; they suggested that “observed high water-permeation rate is achieved through the highly collective motion of water molecules” (15). Similar collective motion of water molecules has also been observed in water transport simulations in carbon nanotubes (2). Simulations and recent experiments also reported unusual temperature-dependent effects and structural transitions for water in carbon nanotube pores (16, 17), although corresponding effects on activation energy are much less well understood. Even though carbon nanotube pores are often compared to aquaporins, they are not identical. Simulations show that the aquaporin structure is engineered to offer “replacement interactions” by two specialized amino acid motifs whenever the water-water bonds are broken (18). There is no reason to believe that the more primitive structure of the carbon nanotube rim can lower the activation energy to the same extent. Instead, fast transport is enabled by the smooth graphitic nanotube walls (2, 19). We believe that unraveling the details of the energy barriers for water transport through small-diameter carbon nanotubes requires additional studies, and we are actively pursuing them.

REFERENCES AND NOTES

1. R. H. Tunuguntla *et al.*, *Science* **357**, 792–796 (2017).
2. G. Hummer, J. C. Rasaiah, J. P. Noworyta, *Nature* **414**, 188–190 (2001).
3. A. Horner, P. Pohl, *Science* **359**, eaap9173 (2018).
4. A. Horner *et al.*, *Sci. Adv.* **1**, e1400083 (2015).
5. A. Barati Farimani, N. R. Aluru, *J. Phys. Chem. B* **115**, 12145–12149 (2011).
6. J. K. Holt *et al.*, *Science* **312**, 1034–1037 (2006).
7. E. Secchi *et al.*, *Nature* **537**, 210–213 (2016).
8. B. Radha *et al.*, *Nature* **538**, 222–225 (2016).
9. R. H. Tunuguntla, F. I. Allen, K. Kim, A. Belliveau, A. Noy, *Nat. Nanotechnol.* **11**, 639–644 (2016).
10. J. Geng *et al.*, *Nature* **514**, 612–615 (2014).
11. Y. Zhang, R. H. Tunuguntla, P.-O. Choi, A. Noy, *Philos. Trans. R. Soc. B* **372**, 20160226 (2017).
12. J. C. Mathai, G. D. Sprott, M. L. Zeidel, *J. Biol. Chem.* **276**, 27266–27271 (2001).
13. M. J. Borgnia, D. Kozono, G. Calamita, P. C. Maloney, P. Agre, *J. Mol. Biol.* **291**, 1169–1179 (1999).
14. M. J. Borgnia, P. Agre, *Proc. Natl. Acad. Sci. U.S.A.* **98**, 2888–2893 (2001).
15. B. L. de Groot, H. Grubmüller, *Science* **294**, 2353–2357 (2001).
16. T. A. Pascal, W. A. Goddard, Y. Jung, *Proc. Natl. Acad. Sci. U.S.A.* **108**, 11794–11798 (2011).
17. K. V. Agrawal, S. Shimizu, L. W. Drahushuk, D. Kilcoyne, M. S. Strano, *Nat. Nanotechnol.* **12**, 267–273 (2017).
18. B. L. de Groot, H. Grubmüller, *Curr. Opin. Struct. Biol.* **15**, 176–183 (2005).
19. S. Joseph, N. R. Aluru, *Nano Lett.* **8**, 452–458 (2008).

ACKNOWLEDGMENTS

Additional experiments performed for this response were supported by the U.S. Department of Energy, Office of Basic Energy Sciences, Division of Materials Sciences and Engineering. Author contributions: A.N., R.H.T., and Y.Z. designed additional experiments, which were performed by R.H.T. (transport measurements) and Y.Z. (HS-AFM). All authors participated in writing and editing the response.

17 October 2017; accepted 28 February 2018
10.1126/science.aag1241



AAAS NEWS & NOTES

The Annual Meeting's
Family Science Days offer
hands-on experiences.

AAAS Annual Meeting examines need for diversity in science

Workplace homogeneity and implicit bias continue to impede progress

By **Michaela Jarvis**

At a time when society needs innovation and technical solutions from as broad a scientific workforce as possible, AAAS convened a comprehensive range of presentations and discussions on diversity and inclusion at its 2018 AAAS Annual Meeting.

With sessions addressing issues from gender and racial imbalance to disability accommodation and combating discrimination against sexual orientation, the 15–19 February meeting provided a forum for diversity experts to share research findings on what works best to create an environment in science education and practice that is welcoming to all. The sessions were sprinkled throughout the 5 days of the annual event, known for its enormous range of cutting-edge science, as well as for presentations on science communication, policy, and culture.

Speakers at several sessions on diversity in science reported that the image of a scientist as an older white male persists.

“How dangerous is this normalization of what a scientist looks like, whether that’s about gender or race?” said Melissa Creary, advisory board member for 500 Women Scientists.

Ryan Kish, senior program manager at Arconic Foundation, said that some manufacturing companies struggle to retain women and people of color because they feel unwelcome in a mostly white, male environment.

“These people who are trained in STEM are leaving because of cultural issues,” Kish said. At the same time, Kish said, companies face a “retirement cliff” within the next 5 years, and the pipeline of STEM professionals to replace those retirees is inadequate.

Speakers in a number of sessions pointed to implicit bias as a main reason that the science workforce fails to reflect the diversity of society. Amy Landis of the Colorado School of Mines reported that resumes bearing men’s names are preferred two to one in studies investigating such bias in STEM.

“John is perceived to be twice as good as Jane, even if they have the exact same CV,” Landis said. She also reported that research has shown that white-sounding names receive 50 percent more callbacks for interviews, and applicants who identify as LGBTQ+ receive less consideration by search committees and more negative appraisals.

Landis and others recommended that members of the science community conduct self-appraisals of their own implicit bias using the tools

available at the Harvard University (implicit.harvard.edu) and American Association of University Women (aaup.org/resource/iat) websites.

Overall, speakers also strongly recommended getting the word out to students in underrepresented groups that technical careers can be well paid and can offer an excellent quality of life.

NASA scientist Kartik Sheth, who has begun several successful programs to mentor students from underrepresented populations in science, said that inviting his students to dinner at the home he had built in Charlottesville, Va., was an “aha” moment for them.

“It’s important for the students to see your life and see you as a real person and know that science is a viable career,” he said, adding that other mentors he has worked with have also adopted the practice of inviting students to their homes. “We need to open up our doors.”

Other news from the Annual Meeting

Outgoing AAAS President Susan Hockfield said in a meeting presentation that U.S. federal funding is necessary to support basic research “as the fundamental building block of all innovations.” Referring to the science advisory positions that remain unfilled in the Trump Administration, Hockfield said, “Our current government has not celebrated or appreciated the role of science. Bottom line, I think it is terrifying that our government is operating without the advice of scientists.”

Another presentation explained that researchers are able to grow cells specific to a vital organ—such as a liver or lung—and reproduce the environment of the organ on a small polymer chip. The chips can then be used to test drug treatments on a particular organ. “They are more true-to-life than cells in dishes and more humanlike than animal models,” said Geraldine Hamilton, president of Emulate, Inc.

A meeting briefing reported that people 80 or older with memory performance as good as people in their 50s or 60s showed less cortical thinning, reported lead researcher Emily Rogalski of the Northwestern University Feinberg School of Medicine. The “superagers” also had developed increased thickness in an area of the brain associated with decision-making, impulse control, and emotions. Superagers were more likely to report close, meaningful relationships with people in their lives. “There are brain benefits of having good friends,” Rogalski said.

Becky Ham, Andrea Korte, and Kathleen O’Neil contributed to this article.

SciLine scores successes in first five months of operation

Reporters and science experts work together to provide evidence-based news

By **Michaela Jarvis**

Reporter Mary Landers was puzzled when she received a press release in the fall announcing that the deaths of up to 24 green sea turtles would be considered allowable in an operation to deepen Savannah's harbor, raising an earlier limit that had already been reached with three green turtle deaths.

"I needed to find an outside expert who was conversant with how those numbers are set," she said, acknowledging that she wondered why when the first limit—set by the National Oceanic and Atmospheric Administration Fisheries and presumably based on biological evidence—was surpassed, a new, higher limit was allowed.

Landers, who works for the *Savannah Morning News*, contacted SciLine, a AAAS-hosted initiative aimed at incorporating more scientific evidence into the news. Within a day or two, she had spoken with three wildlife experts who were recommended by SciLine, learning that accurate reporting on the situation would indicate that this was an example not of controversial practices but of competing interests working together.

"All three of the researchers said pretty much the same thing," Landers said, explaining that while no one wants the turtles to die, she learned that protection efforts are based on whether the population, which in this case is threatened but recovering, will be affected by a certain number of deaths caused by operations such as harbor dredging. "They'll look at the number that were 'taken,' and then they'll figure out whether a new limit can be set."

"They told me this is a common practice," Landers said. Her resulting article also explained that the wildlife researchers were impressed with the efforts in place to protect the turtles, including requiring trawls to scoop them up and move them to safer ground before dredging began.

In this era of budget-constrained newsrooms, specialized science reporters are increasingly rare, and general-assignment and free-lance reporters cover more science news, often without networks of good science sources and while facing multiple deadlines per day. The idea behind SciLine is to help journalists quickly get to scientifically derived evidence by building a community of articulate science experts who are available to the journalists on deadline.

Launched in late October 2017, the initiative required a certain leap of faith that both writers and scientific experts would take part, according to SciLine Director Rick Weiss.

"If we built it," Weiss said, "would they come?"

In fact, the service has been very successful, attracting reporters from publications such as the *Pittsburgh Post-Gazette*, *The New York Times*, and *National Geographic* and from regional and smaller media outlets. SciLine has provided referrals of more than 140 scientists from 33 states and the District of Columbia, with most of the resulting stories featuring quotes from those experts. At the same time, the number of scientists who have connected with SciLine as potential sources has reached nearly 6,500.

"Each interaction with a reporter is a chance not only to get the science right in a particular story," said AAAS CEO Rush Holt, "but to help thousands of readers gain appreciation of the importance of evidence over unsubstantiated assertions."

Financial support for SciLine is provided by the Quadrivium Foundation, with additional funding from the Chan Zuckerberg Initiative, the Heinz Endowments, the John S. and James L. Knight Foundation, and the Rita Allen Foundation. AAAS provides in-kind support.

Since SciLine began, requests have been surprisingly specific, Weiss said. One reporter asked for a source with expertise in marine geology who was familiar with a flood theorized to have moved through the Mediterranean Sea about 6 million years ago. SciLine provided two such experts.

Researcher Caitlin Pepperell said she joined SciLine's list of expert sources because she thinks communicating with journalists broadens the impact of her work.

"We need the support and engagement of the general public and of course government and private funding agencies, and it's always useful to practice articulating what is interesting and important in our research," said Pepperell, who works at the University of Wisconsin-Madison. "I also saw it as an opportunity to raise the profile of women in science, to increase the diversity of voices and perspectives that make up the 'face' of science—my hope is that all young people have the opportunity to see themselves as scientists, to consider science as a career and pursue it if that's where their passions and skills lie."

With Weiss and his colleagues planning for more growth, SciLine will soon launch a virtual media briefing service to get reporters up to speed on advances in certain areas of science by offering presentations by panels of experts, who will also take reporters' questions. The SciLine staff, which has already gone from three to five in its first 5 months, will also continue to develop easy-to-use and meticulously vetted fact sheets for reporters on topical science subjects such as gravitational waves and lead in drinking water.

The staff will also visit newsrooms across the country to talk with journalists about how they cover science, and plans for SciLine also include a nationwide survey of newsrooms, "which should help SciLine understand the fast-changing landscape and make any needed course corrections to make sure we are doing the most we can to help reporters enrich their stories with scientifically derived facts," said Weiss.

Landers, at the *Savannah Morning News*, said she intends to make a habit of using SciLine.

"I got a great response from SciLine," Landers said. "I had three different academics, and they were all great. They got it. They understood what the needs were for a newspaper and responded perfectly."

For more information or to register with SciLine as an expert source or a journalist, please go to www.sciline.org.

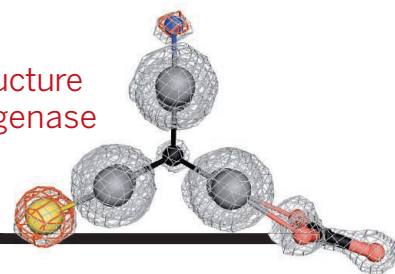
AAAS annual election: Preliminary announcement

The 2018 AAAS election of general and section officers will be held in the fall. Names may be placed in nomination for any office by petition submitted to the Chief Executive Officer no later than 31 May 2018. Petitions nominating candidates for president-elect, members of the Board, or members of the Committee on Nominations must bear the signatures of at least 100 members of the Association. Petitions nominating candidates for any section office must bear the signatures of at least 50 members of the section. A petition to place an additional name in nomination for any office must be accompanied by the nominee's curriculum vitae as well as a statement of acceptance of nomination.

RESEARCH

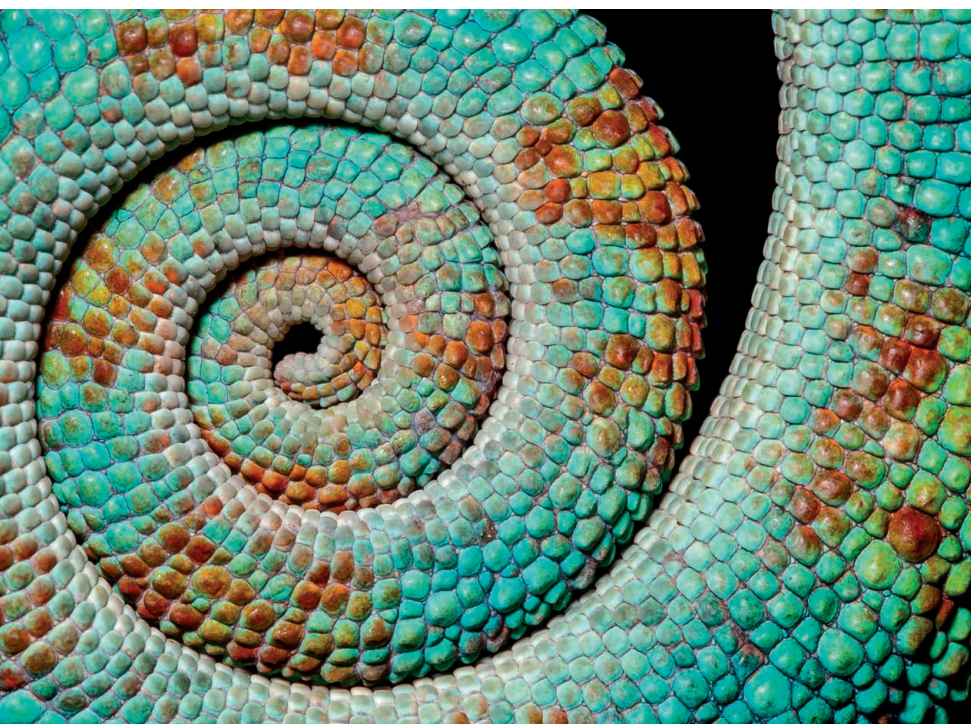
High-resolution structure of vanadium nitrogenase

Sippel et al., p. 1484



IN SCIENCE JOURNALS

Edited by Stella Hurtley



MATERIALS SCIENCE

Active camouflage from a polymer

Human skin is soft and compliant, but it can quickly become stiff when deformed to prevent injury. Chameleon skin can change color when the animal goes from a relaxed to an excited state. Although these properties can be captured individually in synthetic materials, the combination of different dynamic responses can be hard to control. Vatankeh-Varnosfaderani *et al.* created triblock copolymers of the ABA variety, where the A blocks have a linear structure and the B blocks are like bottle-brushes. When strained, these polymers stiffened like human skin and changed color, thus giving the materials a range of adaptive properties. —MSL

Science, this issue p. 1509

A new material, like chameleon skin, responds to stress.

ORGANIC CHEMISTRY

Attacking olefins with chiral acids

A little acid can accelerate a wide range of chemical reactions. The advent of chiral phosphoric acid derivatives has been useful for biasing these reactions toward just one of two mirror-image products. For the most part, though, these chiral catalysts have interacted with basic sites such as carbonyl groups. Tsuji *et al.* now extend asymmetric acid catalysis to simple carbon-carbon double bonds. Their custom imidodiphosphate forms a pocket that orients olefins to achieve mainly intramolecular alkoxylation on just one face after protonation. —JSY

Science, this issue p. 1501

NEUROSCIENCE

Rebalancing mechanisms during sleep

Synapses are often strengthened during wake periods and thus need to be homeostatically readjusted during sleep. During slow-wave sleep, synaptic depression is dominant. Sharp wave and ripple events are transient high-frequency field oscillations that occur spontaneously during slow-wave sleep in the brain. Norimoto *et al.* found that these events induced long-term depression of hippocampal synapses and may thus help to refine recently acquired memories (see the Perspective by Draguhn). —PRS

Science, this issue p. 1524;
see also p. 1461

CANCER IMMUNOLOGY

Helping NK cells find their way

MICA and MICB proteins can be expressed on tumors and act as “kill me” signals to the immune system. But tumors often disguise themselves by shedding these proteins, which prevents specialized natural killer (NK) cells from recognizing and destroying the cancer. Ferraride Andrade *et al.* engineered antibodies directed against the site responsible for the proteolytic shedding of MICA and MICB (see the Perspective by Cerwenka and Lanier). The approach effectively locked MICA and MICB onto tumors so that NK cells could spot them for elimination. The antibodies exhibited preclinical efficacy in

multiple tumor models, including humanized melanoma. Furthermore, the strategy reduced lung cancer metastasis after NK cell-mediated tumor lysis. —PNK

Science, this issue p. 1537;
see also p. 1460

GENETICS

Genetic clines and climate change

Marine species exhibit strong genetic variation in relation to oceanographic conditions, but the extent to which entire assemblages of species respond in concert is unknown. Stanley *et al.* document genetic clines of native cod, lobster, scallop, and shrimp and an introduced crab—species

that differ widely in ecology—from North Carolina, USA, to Labrador, Canada. All five species exhibit strikingly similar genetic clines, with a sharp biogeographic break between northern and southern populations centered east of Nova Scotia. The genetic break closely coincides with steep gradients in oceanographic conditions, most importantly seasonal minimum temperature. —JJ

Sci. Adv. 10.1126/sciadv.aag0929 (2018).

EPIDEMIOLOGY

The problem of pertussis

The recent rise of pertussis in developed countries has generated controversy as to its cause. Domenech de Cellès *et al.* modeled pertussis transmission by using incidence data from Massachusetts. They found little evidence that the switch to the acellular vaccine contributed to the Massachusetts outbreaks. Instead, waning vaccine-conferred immunity, as opposed to vaccine failure to mount a full or even partial immune response, best explained the local rise in pertussis cases, along with a historical gap in vaccination coverage. Simulations suggested that administering existing boosters to children may be an effective strategy to halt pertussis transmission. —CAC

Sci. Transl. Med. 10, eaaj1748 (2018).

APPLIED PHYSICS

Shaking the small from the even smaller

Gently oscillate a can of mixed nuts, and eventually the larger Brazil nuts will rise to the top. Skaug *et al.* created three-dimensional patterned surfaces to which they applied electric fields. Combined with gentle shaking to induce a rocking Brownian motion, they were able to guide particles smaller than 100 nm along

complicated paths. They could also quickly separate particles with different sizes and shapes. —MSL

Science, this issue p. 1505

BIOCHEMISTRY

ISRIB mechanism of action

In rodents, a druglike small molecule named ISRIB enhances cognition and reverses cognitive deficits after traumatic brain injury. ISRIB activates a protein complex called eIF2B that is required for the synthesis of new proteins. Tsai *et al.* report the visualization of eIF2B bound to ISRIB at near-atomic resolution by cryo-electron microscopy. Biochemical studies revealed that ISRIB is a “molecular staple” that promotes assembly of the fully active form of eIF2B. Zyryanova *et al.* report similar structures together with information on the binding of ISRIB analogs and their effects on protein translation. —SMH

Science, this issue p. 1483, p. 1533

AMPHIBIAN DISEASE

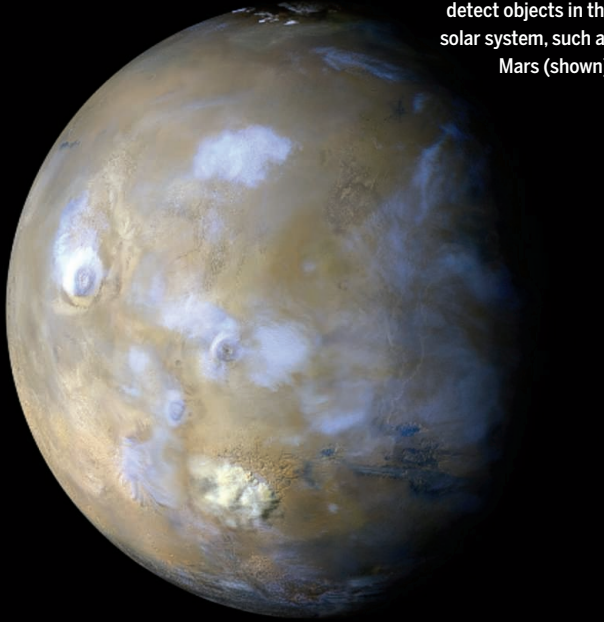
Resistance is not futile

The fungal disease chytridiomycosis has wreaked havoc on amphibians worldwide. The disease is caused by the organism *Batrachochytrium dendrobatidis* and was first identified in the late 1990s. Voyles *et al.* revisited protected areas in Panama where catastrophic amphibian losses were recorded a decade ago (see the Perspective by Collins). Although disease theory predicts that epidemics should result in reduced pathogenicity, they found no evidence for such a reduction. Despite this, the amphibian community is displaying signs of recovery—including some species presumed extinct after the outbreak. Increased host resistance may be responsible for this recovery. —SNV

Science, this issue p. 1517; see also p. 1458

IN OTHER JOURNALS

Edited by **Sacha Vignieri** and **Jesse Smith**



Radio waves from pulsars can be used to detect objects in the solar system, such as Mars (shown).

SOLAR SYSTEM

Searching the solar system with pulsars

Pulsar timing arrays (PTAs) monitor the arrival times of radio pulses from numerous pulsars to search for shifts caused by passing long-wavelength gravitational waves. Reaching the necessary level of precision requires correcting the data for small perturbations in Earth's orbit owing to the other planets in our solar system. Guo *et al.* have switched that process around: Instead of correcting for known planets, they show that PTAs can be used to search for undiscovered massive bodies in the solar system. Existing PTAs should be sufficient to recover the known planets and measure their masses, but more sensitive PTAs will be required to search the outer solar system for objects such as the proposed Planet Nine. —KTS

Mon. Not. R. Astron. Soc. 475, 3644 (2018).

CANCER

Blood biomarkers for melanoma therapy

Immunotherapy using checkpoint inhibitors has dramatically improved melanoma treatment response. However, only a subset of patients show durable remissions. Hong *et al.* studied circulating tumor cells (CTCs) from the blood of 49 melanoma patients to identify biomarkers

that may predict therapeutic outcomes. They developed a two-part test, wherein an RNA digital PCR (polymerase chain reaction) gene signature was combined with microfluidic enrichment for CTCs. A reduced CTC score within the first 7 weeks of therapy correlated with progression-free survival and overall survival in the small cohort studied. Liquid biopsy strategies may provide a means

IMMUNOLOGY

A bat's STING is less potent

Bats have evolved enhanced oxidative phosphorylation pathways in response to the increased metabolic demands of flight. One effect of this is DNA damage and release. Additionally, bats serve as reservoirs for a multitude of viruses, which raises the question of how these animals are able to tune cytosolic DNA sensing and innate immune activation. Xie *et al.* report that STING (stimulator of interferon genes)—the main adaptor in several DNA-sensing pathways—is mutated in bats at the serine-358 residue, which is critical for downstream interferon (IFN) activation. They found that bat STING was less effective at inducing IFN production and viral inhibition. These findings add to previous work showing bat-specific changes in other DNA sensors such as AIM2, IFI16, and TLR9 that elicit more harmonious immune responses to pathogens. —STS

Cell Host Microbe **23**, 297 (2018).

Bat immune responses to viruses are compromised.



to distinguish which patients are the best candidates for immunotherapy using checkpoint blockade. —PNK

Proc. Natl. Acad. Sci. U.S.A. 10.1073/pnas.1719264115 (2018).

NEUROSCIENCE

We choose what we want to hear

To make sense of the outside world, the brain must organize and group information that arrives at our sensory organs. Can we consciously influence this perception process? Billig *et al.* measured brain activity while subjects listened to sequences of pure tones that could be interpreted as individual sounds or as an integrated percept. Listeners indicated when their perception changed between these two interpretations. These changes were associated with changes in auditory cortex activity. Participants could also consciously control how many objects they perceived in an ambiguous auditory scene. This led to similar changes in neural activity. Listeners can thus use attention not only to enhance

the representation of a subset of sounds, but also to intentionally alter the number of distinct objects heard. —PRS

J. Neurosci. **38**, 2844 (2018).

CELL BIOLOGY

Right time, right speed, right size

Centrioles are microtubule-based organelles composed of an archetypal cylindrical arrangement of tubulin. Centrioles duplicate when a daughter centriole grows from the side of the mother, but it has been unclear how daughters grow to the right size. Aydogan *et al.* used live-cell imaging to quantify the dynamics of daughter centriole assembly in developing *Drosophila* embryos. They found that Polo-like kinase 4 (Plk4) promoted incorporation of a centriole component, Sas-6, into the proximal end of the growing daughter at a linear rate during the early S phase. However, growth abruptly stopped when centrioles reached the correct size in the mid- to late S phase. Plk4 is a “suicidal” enzyme that promotes its own degradation,

and it acted as a homeostatic clock to set the size of centrioles: The higher the centriolar Plk4 activity, the faster the centrioles would grow, but the faster Plk4 would become degraded and centriole growth would cease. —SMH

J. Cell Biol. 10.1083/jcb.201801014 (2018).

STRUCTURAL BIOLOGY

A scaffold for small proteins

Reconstruction of atomic-resolution structures in cryo-electron microscopy is limited by the ability to select, align, and average individual particles in the underlying images. Small biomolecules pose a particular challenge because they are hard to distinguish from the surrounding amorphous ice. Liu *et al.* combined a large, computationally designed protein cage with a small, modular domain containing a protein-binding surface that can be evolved separately to bind other small proteins for structure determination. The cage serves as a rigid scaffold that allows for accurate particle

selection and alignment. The 17-kDa protein-binding domain was well resolved in the electron density maps at near-atomic resolution. —MAF

Proc. Natl. Acad. Sci. U.S.A. 10.1073/pnas.1718825115 (2018).

ORGANIC CHEMISTRY

Enacting a program's plans for synthesis

How does a chemist plan a synthesis? In principle, it is an exercise in breaking down the targeted product into smaller pieces that look feasible to stitch together. Computer programs that offer such advice on the basis of a set of reaction precedents have been around for decades, but they have seldom proven broadly useful. Klucznik *et al.* now report a validation test of their Chematica program, which charts a course to products by using reactivity rules coded by human experts. Eight compounds were targeted, and all of them were successfully prepared in accord with routes devised by the software, often with improved yields relative to prior routes. —JSY

Chem **4**, 522 (2018).

ALSO IN SCIENCE JOURNALS

Edited by Stella Hurtley

NITROGEN FIXATION

Sulfur steps aside for nitrogen

Enzymatic conversion of molecular nitrogen to ammonia requires a dance of electrons and protons. The stage for that dance is the nitrogenase cofactor, a carefully constructed cluster of iron, sulfur, and carbon with homocitrate and, in some cases, bicarbonate appendages, as well as a secondary metal ion that defines the class of enzyme. The question of how this cofactor binds nitrogen has been vexingly difficult to answer. Sippel *et al.* report a high-resolution structure of the vanadium nitrogenase with a light atom, interpreted as nitrogen, bound to the FeV cofactor. A sulfur atom is displaced from the cofactor in this structure and is observed resting in a holding site formed by rearrangement of a glutamine residue. The putative bridging nitrogen atom suggests that diatomic nitrogen may bind to the cluster in a head-on manner, with the glutamine side chain stabilizing protonated intermediates as they are reduced. —MAF

Science, this issue p. 1484

BATTERIES

Healing away the dendrites

The formation of lithium dendrites during charge-discharge cycles limits the development of lithium metal batteries, because the dendrites can cause electrical shorting of the cells. A number of tricks have been used to try to prevent dendrite formation. Li *et al.* took the opposite approach (see the Perspective by Mukhopadhyay and Jangid). They operated their cells at higher current densities, under which one would expect dendrites to form owing to the higher nucleation rates. However, under these conditions, the dendrites that started to form heated up and

annealed, leading to their disappearance. —MSL

Science, this issue p. 1513;
see also p. 1463

NANOMATERIALS

Nanoparticle synthesis gets a shock

Nanoparticles are useful in a wide range of applications such as catalysis, imaging, and energy storage. Yao *et al.* developed a method for making nanoparticles with up to eight different elements (see the Perspective by Skrabalak). The method relies on shocking metal salt-covered carbon nanofibers, followed by rapid quenching. The “carbo-thermal shock synthesis” can be tuned to select for nanoparticle size as well. The authors successfully created PtPdRhRuCe nanoparticles to catalyze ammonia oxidation. —BG

Science, this issue p. 1489;
see also p. 1467

IRON HOMEOSTASIS

Iron's grip on malaria

Malaria parasites have coevolved with their human and mammalian hosts. These *Plasmodium* species invade the iron-rich environment of red blood cells. Zhang *et al.* found that the iron transporter ferroportin persists on the surface of mature mammalian red blood cells. Red blood cells are at risk of oxidative damage if their hemoglobin releases its iron; ferroportin is thus important to expel this iron. The authors also found that the transporter can deprive malaria parasites of the iron they need for proliferation. The Q248H mutation in the human ferroportin gene enhances ferroportin expression during development and seems to provide protection against malaria. This effect may explain the enrichment of the Q248H mutation among African populations. —CA

Science, this issue p. 1520

BIOPHYSICS

How a pathogen holds on to its host

Staphylococcus epidermidis and *Staphylococcus aureus* are pathogens that can form biofilms on implants and medical devices. Central to biofilm formation is a very tight interaction between microbial surface proteins called adhesins and components of the extracellular matrix of the host. Milles *et al.* used atomic force microscopy-based single-molecule force spectroscopy combined with steered molecular dynamics to explore how the bond between staphylococcal adhesin SdrG and its target fibrinogen peptide can withstand forces greater than 2 newtons (see the Perspective by Herman-Bausier and Dufrêne). The peptide is confined in a coiled geometry in a deep and rigid pocket through hydrogen bonds between SdrG and the peptide backbone. If pulled, the load is distributed over all hydrogen bonds so that all bonds must be broken at once to break the interaction. —VV

Science, this issue p. 1527;
see also p. 1464

VIRAL EVOLUTION

Nongenetic variation drives viral evolution

Bacteriophage λ is a virus that infects bacteria by exploiting various membrane proteins in a well-characterized manner. Petrie *et al.* show how the evolution of variable folding conformations of isogenic proteins, which do not differ in their genetic sequences, contributed to λ 's ability to exploit an additional host receptor for infection. Because the protein can take on two shapes, this genotype can have two phenotypes. Natural selection may thus be able to act on this nongenetic heterogeneity to connect phenotypic heterogeneity, evolvability, and protein stability. —LMZ

Science, this issue p. 1542

NEUROIMMUNOLOGY

Neuro-immune cell cross-talk

An emerging mechanism of tissue homeostasis involves cross-talk between neuronal and immune cells. In a Perspective, Veiga-Fernandes and Artis discuss how neuronal and immune cells can jointly coordinate gross tissue immune responses, particularly at barrier tissues such as the intestinal and lung epithelia. They describe how neuronal cells regulate immune cells at these sites and ask whether immune cells can, in turn, regulate neuronal cells. Furthermore, the authors describe the implications of this cross-talk for diseases including chronic inflammation, cancer, and metabolic syndrome. —GKA

Science, this issue p. 1465

CANCER

Messaging by oncogenic kinase

Cancer cells signal to non-transformed cells and to other transformed cells to generate an environment that is amenable for their growth. Zhang *et al.* noticed that the longest isoform of the growth-promoting kinase S6K1, unlike shorter isoforms, has a six-arginine motif similar to one that enables HIV TAT protein to be released from cells and enter surrounding cells. In cultured breast cancer or nontransformed cells, adding the long S6K1 isoform to the medium enhanced the phosphorylation of S6K1 targets, as well as cell size and migration. Injection of this S6K1 isoform into mice increased the growth and metastasis of breast cancer cell xenografts. —WW

Sci. Signal. **11**, eaao1052 (2018).

AUTOIMMUNITY

Infiltration inhibition

Type 1 diabetes (T1D) is associated with the infiltration of islet-specific autoreactive cytotoxic CD8⁺ T cells (CTLs) into pancreatic islets. This process leads to islet destruction and loss of insulin production. Most of the CTLs in islets are non-islet-specific, and their contribution to T1D is not well understood. Christoffersson *et al.* observed that the accumulation of these “bystander” CTLs was associated with decreased activation and proliferation of islet-specific CTLs. The abundance of non-islet-specific CTLs in islets reduced the access of islet-specific CTLs to autoantigens, which led to a state of unresponsiveness. A similar form of nonspecific suppression by CTLs was observed in a viral meningitis model. —CNF

Sci. Immunol. **3**, eaam6533 (2018).

MATERIALS SCIENCE

Now you see it, now you don't

Thermal vision cameras detect differences in temperature by sensing infrared wavelengths. If a coating could be developed that showed dynamic tuning of the effective temperature, it might be possible to hide objects from infrared sensing. Xu *et al.* started with a basic Bragg reflector made up of multiple layers of alternating materials with varying refractive index. The authors designed structures that were wavy to begin with so that they could be flattened out by electrical activation. This changed the infrared reflectivity and, thus, the effective temperature of the object observed in its infrared profile. —MSL

Science, this issue p.1495

RESEARCH ARTICLE SUMMARY

BIOCHEMISTRY

Structure of the nucleotide exchange factor eIF2B reveals mechanism of memory-enhancing molecule

Jordan C. Tsai,* Lakshmi E. Miller-Vedam,* Aditya A. Anand,* Priyadarshini Jaishankar, Henry C. Nguyen, Adam R. Renslo, Adam Frost,† Peter Walter†

INTRODUCTION: Regulation by the integrated stress response (ISR) converges on the phosphorylation of translation initiation factor eIF2 in response to a variety of stresses. Phosphorylation converts eIF2 from a substrate to a competitive inhibitor of its dedicated guanine nucleotide exchange factor, eIF2B, inhibiting translation. ISRIB is a drug-like eIF2B activator that reverses the effects of eIF2 phosphorylation, enhances cognition, and corrects cognitive deficits after brain injury in rodents. Because ISRIB shows promise for treating neurological disorders a deeper understanding of its mechanism of action is crucial. Previous work identified eIF2B as a target of ISRIB and suggested that the molecule stabilizes and activates the enzyme. However, the molecule's mode of binding and means of activation remain unknown.

RATIONALE: To identify the binding site and mechanism of action of ISRIB, we used cryo-electron microscopy (cryo-EM) to determine an atomic-resolution structure of decameric human eIF2B bound to ISRIB. We validated the structural model using mutational analysis and the synthesis of ISRIB analogs. Combined with pre-steady-state kinetic analysis of eIF2B complex assembly, these findings enabled us to derive a functional model of ISRIB action.

RESULTS: A robust recombinant expression and purification protocol for all subunits of human eIF2B produced a stable eIF2B holoenzyme that sedimented as a decamer. Under conditions of elevated ionic strength, an eIF2B α dimer [eIF2B(α_2)] dissociated from the remainder of the decamer, whereas ISRIB prevented disassembly. Sedimentation velocity experiments

determined that in the absence of eIF2B α , the remaining subunits form tetrameric complexes [eIF2B($\beta\gamma\delta\epsilon$)]. Loss of eIF2B(α_2) largely abolished eIF2B's nucleotide exchange activity. To explain these findings, we determined a structure of human eIF2B bound to ISRIB at 2.8 Å average resolution. The structure revealed that ISRIB binds within a deep cleft at a two-fold symmetry interface between the eIF2B β and eIF2B δ subunits in the decamer.

Greater resolution within the binding pocket enabled precise positioning of ISRIB, which we validated by probing with designed ISRIB analogs

and mutational analysis.

ON OUR WEBSITE

Read the full article at <http://dx.doi.org/10.1126/science.aag0939>

For example, stereospecific addition of a methyl group to ISRIB abrogated activity, whereas an eIF2B(δ L179A) mutation accommodated this analog and restored

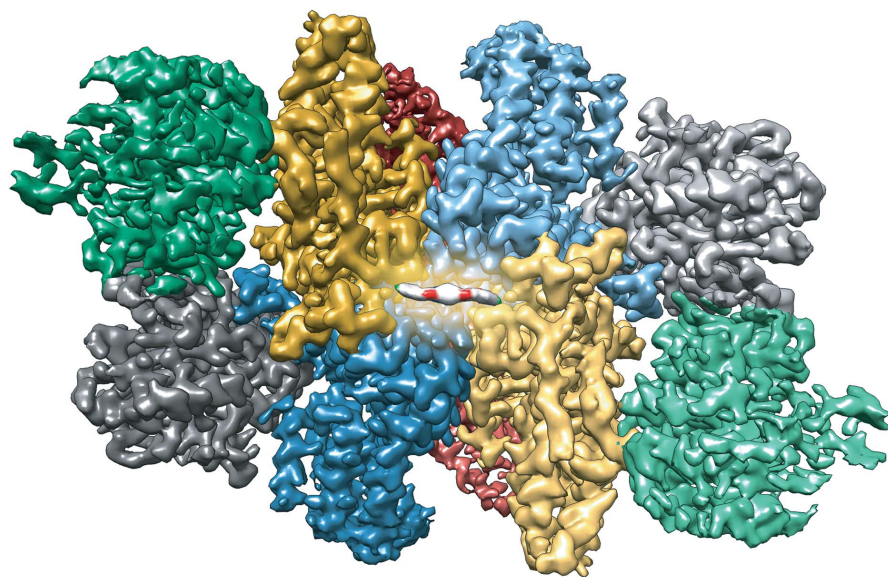
activity. Further, a predicted C-H π interaction between eIF2B(β H188) and ISRIB was confirmed by mutation of β H188 to other aromatic residues, which resulted in enhanced stability of the complex. To determine how ISRIB enhances incorporation of eIF2B(α_2) into the complex, we analyzed the eIF2B($\beta\gamma\delta\epsilon$) tetramer structurally and functionally. Cryo-EM imaging and analytical ultracentrifugation revealed that ISRIB staples two eIF2B($\beta\gamma\delta\epsilon$) tetramers together to form an octamer across its two-fold symmetry axis. The resulting octamer displays a composite surface for avid eIF2B(α_2) binding, explaining ISRIB's mechanism of action. Consistent with this model, saturating half-binding sites in the tetramer with ISRIB prevented dimerization and failed to activate the enzyme. Additional loss-of-function and gain-of-function dimerization mutants produced complexes that were insensitive to ISRIB.

CONCLUSION: From this work, the regulation of eIF2B assembly from stable subcomplexes emerges as a rheostat for eIF2B activity that tunes translation during the ISR and can be further modulated by ISRIB acting as a “molecular staple.” As a two-fold symmetric small molecule, ISRIB bridges a central symmetry axis of the decameric eIF2B complex, stabilizing it in an activated state. ISRIB's action as an assembly-promoting enzyme activator provides a plausible model for its ability to ameliorate the inhibitory effects of eIF2 α phosphorylation. Understanding the different modes of regulation of this vital translational control point will be of particular importance in the nervous system where ISRIB has been shown to have a range of effects, and will further enable ISRIB's development as a promising therapeutic agent in combating cognitive disorders. ■

The list of author affiliations is available in the full article online.
*These authors contributed equally to this work.

†Corresponding author. Email: peter@walterlab.ucsf.edu (P.W.); adam.frost@ucsf.edu (A.F.)

Cite this article as J. C. Tsai et al., *Science* 359, eaaq0939 (2018). DOI: 10.1126/science.aag0939



ISRIB bound to human eIF2B. View of cryo-EM density for eIF2B($\alpha\beta\gamma\delta\epsilon$) $_2$, colored in distinct shades for each subunit copy: (red, α ; blue, β ; green, γ ; gold, δ ; gray, ϵ). Density assigned to ISRIB is depicted in CPK coloring (red, O; blue, N; green, C) and artistically contrasted from its target protein.

RESEARCH ARTICLE

BIOCHEMISTRY

Structure of the nucleotide exchange factor eIF2B reveals mechanism of memory-enhancing molecule

Jordan C. Tsai,^{1,2*} Lakshmi E. Miller-Vedam,^{2,3*} Aditya A. Anand,^{1,2*} Priyadarshini Jaishankar,⁴ Henry C. Nguyen,^{2,3} Adam R. Renslo,⁴ Adam Frost,^{2,3†} Peter Walter^{1,2†}

Regulation by the integrated stress response (ISR) converges on the phosphorylation of translation initiation factor eIF2 in response to a variety of stresses. Phosphorylation converts eIF2 from a substrate to a competitive inhibitor of its dedicated guanine nucleotide exchange factor, eIF2B, thereby inhibiting translation. ISRIB, a drug-like eIF2B activator, reverses the effects of eIF2 phosphorylation, and in rodents it enhances cognition and corrects cognitive deficits after brain injury. To determine its mechanism of action, we solved an atomic-resolution structure of ISRIB bound in a deep cleft within decameric human eIF2B by cryo-electron microscopy. Formation of fully active, decameric eIF2B holoenzyme depended on the assembly of two identical tetrameric subcomplexes, and ISRIB promoted this step by cross-bridging a central symmetry interface. Thus, regulation of eIF2B assembly emerges as a rheostat for eIF2B activity that tunes translation during the ISR and that can be further modulated by ISRIB.

Protein quality control is essential to the maintenance of cellular and organismal health. To prevent the production of deleterious proteins, such as those from invading viruses or those produced in misfolding-prone environments, cells regulate protein synthesis. By arresting or accelerating the cardinal decision of translation initiation, cells effect proteome-wide changes that drive organismal functions such as development, memory, and immunity (1–3).

A key enzyme in the regulation of protein synthesis is eukaryotic translation initiation factor 2B (eIF2B), a dedicated guanine nucleotide exchange factor (GEF) for translation initiation factor 2 (eIF2). eIF2B is composed of five subunits (α , β , γ , δ , ϵ) that assemble into a decamer composed of two copies of each subunit (4–8). The eIF2B ϵ subunit contains the enzyme's catalytic center and associates closely with eIF2B γ (9). Two copies each of the structurally homologous eIF2B α , β , and δ subunits form the regulatory core that modulates eIF2B's catalytic activity (10–12). eIF2B's substrate, eIF2, is composed of three subunits (α , β , γ) and binds methionine initiator tRNA and guanosine triphosphate (GTP) to form the ternary complex required to initiate translation on AUG

start codons. eIF2's γ subunit contains the GTP-binding pocket [reviewed in (13, 14)].

In response to various inputs, many of which are cell stresses, phosphorylation of eIF2 α at Ser⁵¹ converts eIF2 from a substrate for nucleotide exchange into a competitive inhibitor of eIF2B. Phosphorylated eIF2 binds to eIF2B with enhanced affinity, effectively sequestering the limiting eIF2B complex from engaging unphosphorylated eIF2 for nucleotide exchange (10–12). Such inhibition leads to an attenuation of general translation and, paradoxically, the selective translation of stress-responsive mRNAs that contain small upstream open reading frames. This latter set includes mRNAs that encode transcriptional activators such as ATF4 (15, 16). In this way, eIF2 phosphorylation elicits an intricate gene expression program. This pathway was termed the “integrated stress response” after the discovery of several kinases that all phosphorylate eIF2 α at Ser⁵¹ to integrate different physiological signals, such as the accumulation of misfolded proteins in the lumen of the endoplasmic reticulum, the accumulation of double-stranded RNA indicative of viral infection, the cell's redox status, and nutrient availability (17).

We previously identified an ISR inhibitor (ISRIB) that reverses the effects of eIF2 α phosphorylation, restoring translation in stressed cells and blocking translation of ISR-activated mRNAs such as ATF4 (18, 19). When administered systemically to wild-type rodents, ISRIB enhances cognition, leading to significant improvements in spatial and fear-associated learning (18). This effect relies on translation-dependent remodeling of neuronal synapses (20). eIF2 phosphorylation

correlates with diverse neurodegenerative diseases and cancers as well as normal aging (21–24). In addition, a number of mutations that impair eIF2B activity lead to a neurodegenerative disorder of childhood known as vanishing white matter disease (VWMD), which is marked by cerebellar ataxia, spasticity, hypersensitivity to head trauma and infection, coma, and premature death (25). As a well-characterized small molecule with rapid cross-blood-brain barrier equilibration, reasonable bioavailability, and good tolerability in rodent efficacy models, ISRIB and related analogs offer great potential for treating VWMD and a range of other devastating diseases lacking therapeutic options (18, 26). Indeed, in rodents, ISRIB entirely reverses cognitive deficits associated with traumatic brain injuries (27) and protects against neurodegeneration (26).

Previous work identified eIF2B as the molecular target of ISRIB (28, 29). ISRIB enhances eIF2B GEF activity by a factor of 3, stabilizes a decameric form of the enzyme when analyzed in high-salt conditions, and increases thermostability of the eIF2B δ subunit (28). Mutations that render cells insensitive to ISRIB have been found to cluster in the N-terminal region of eIF2B δ (29); when projected onto the crystal structure of *Schizosaccharomyces pombe* eIF2B, two of the mutated residues map to its symmetric interface (8). These data hinted that ISRIB may activate eIF2B by binding near adjacent δ subunits to exert its blunting effects on the ISR. Here, we report mechanistic and structural insights into ISRIB's mechanism of action.

ISRIB stabilizes decameric eIF2B, thereby accelerating GEF activity

To investigate the mechanism by which ISRIB enhances the GEF activity of eIF2B, we engineered a recombinant *Escherichia coli* expression system for coexpression of all five subunits of human eIF2B (Fig. 1A). eIF2B purified as a monodisperse complex that sedimented at 13.6S, corresponding to the size of a decamer containing two copies of each subunit (Fig. 1B and fig. S1A).

We adapted a fluorescent guanosine diphosphate (GDP) exchange assay (29) to assess the enzymatic activity of recombinant eIF2B. We purified the substrate, nonphosphorylated human eIF2, from a *Saccharomyces cerevisiae* expression system genetically edited to lack the only yeast eIF2 kinase (*gcn2 Δ*) (30) (fig. S2, A and B). First, in a “GDP loading assay,” we added fluorescent Bodipy-GDP to GDP-bound eIF2. We observed an eIF2B concentration-dependent increase in fluorescence corresponding to the dislodging of bound GDP and subsequent binding of Bodipy-GDP to eIF2 (fig. S2, C and D). Second, in a “GDP unloading assay,” we chased with a 1000-fold excess of unlabeled GDP and measured a decrease in fluorescence corresponding to the eIF2B-catalyzed dissociation of Bodipy-GDP from eIF2 (fig. S2E). GEF activities were fit to a single-exponential curve (fig. S2F) for calculating the observed rate constants (k_{obs}). Titrating substrate concentration to saturating levels in GDP unloading assays yielded Michaelis constant (K_m)

¹Howard Hughes Medical Institute, University of California, San Francisco, CA, USA. ²Department of Biochemistry and Biophysics, University of California, San Francisco, CA, USA.

³Chan Zuckerberg Biohub, San Francisco, CA, USA.

⁴Department of Pharmaceutical Chemistry and Small Molecule Discovery Center, University of California, San Francisco, CA, USA.

*These authors contributed equally to this work.

†Corresponding author. Email: peter@walterlab.ucsf.edu (P.W.); adam.frost@ucsf.edu (A.F.)

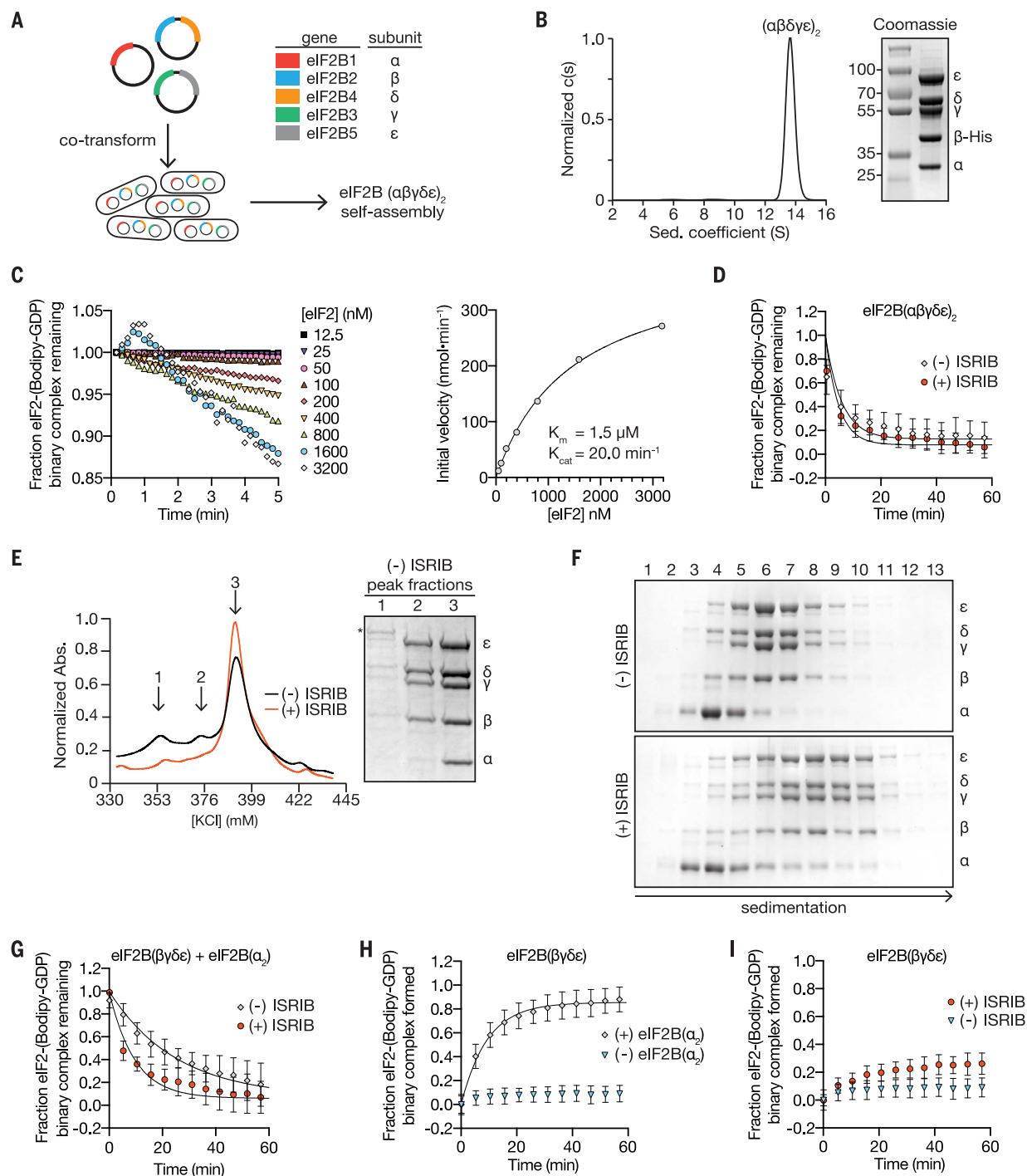


Fig. 1. ISIRIB stabilizes decameric eIF2B, accelerating GEF activity.

(A) Schematic diagram for three-plasmid expression of all five eIF2B genes in *E. coli*. (B) Characterization of eIF2B(αβγδε)₂ by sedimentation velocity analytical ultracentrifugation and SDS-polyacrylamide gel electrophoresis (PAGE) followed by Coomassie Blue staining. (C) Initial rate of nucleotide exchange (right) plotted as a function of substrate concentration. Note that at high eIF2 concentrations, we reproducibly observed a transient increase in fluorescence that peaked at the 1-min time point (left). Such an increase was reported previously (29) and remains unexplained. (D) GEF activity of eIF2B(αβγδε)₂ as measured by unloading of fluorescent GDP from eIF2 in the presence and absence of ISIRIB (mean ± SD; *n* = 3). (E) Representative absorbance 280-nm traces from an anion exchange column used in the purification of eIF2B in the presence (red) and absence

(black) of ISIRIB (*n* = 3). Traces were normalized to total protein eluted in respective runs. Peak fractions from the -ISIRIB purification were analyzed by SDS-PAGE and Coomassie-stained. eIF2B subunits are labeled α to ε; an asterisk denotes the presence of a contaminating protein that contributes to peak 1. (F) Stability of eIF2B(αβγδε)₂ was assessed by sedimentation velocity on a 5 to 20% sucrose gradient in 400 mM salt buffer. eIF2B(βγδε) and eIF2B(α₂) were combined with and without 500 nM ISIRIB. Fractions were analyzed by SDS-PAGE and Coomassie staining. (G) GEF activity of eIF2B assembled from purified eIF2B(βγδε) and eIF2B(α₂) in the presence and absence of ISIRIB (mean ± SD; *n* = 3). (H) GEF activity of eIF2B(βγδε) in the presence and absence of eIF2B(α₂) (mean ± SD; *n* = 3). (I) GEF activity of eIF2B(βγδε) in the presence and absence of ISIRIB (mean ± SD; *n* = 3).

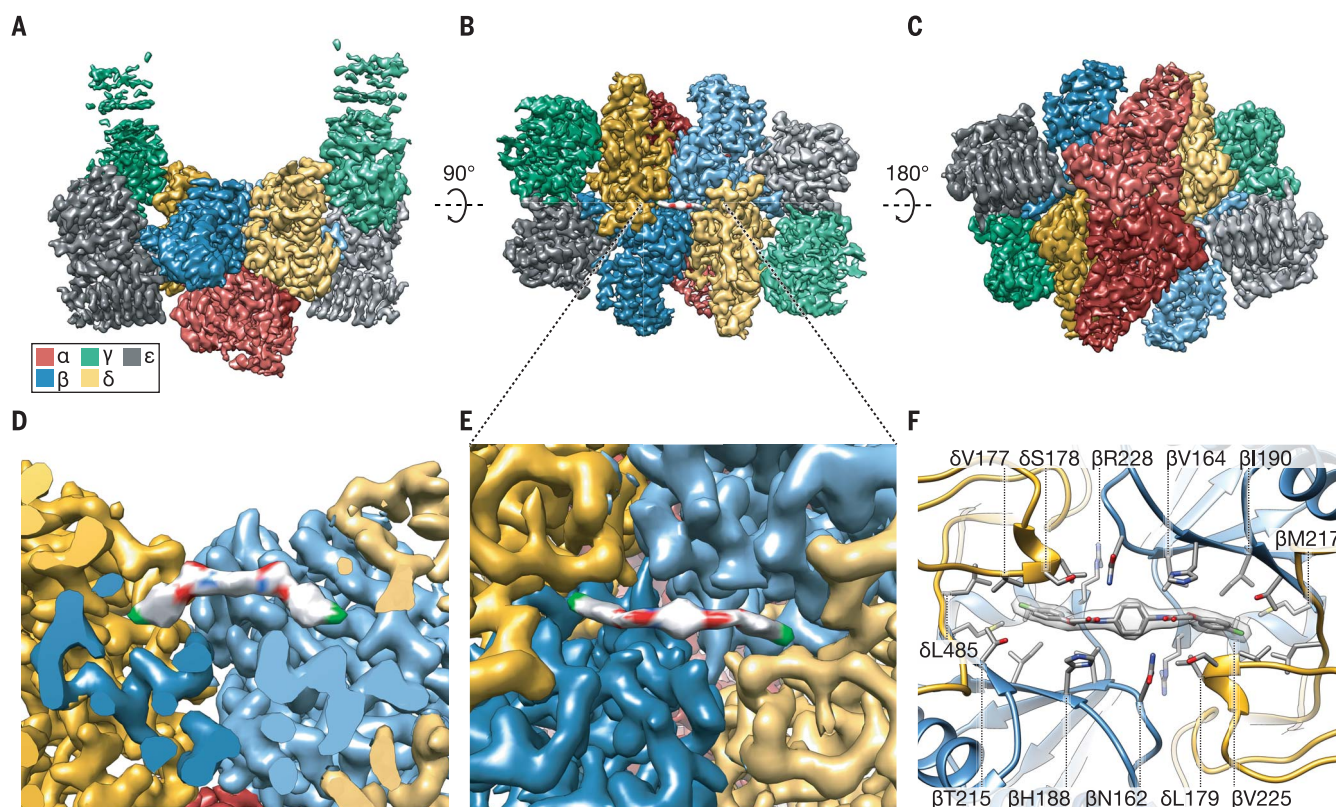


Fig. 2. Atomic-resolution reconstruction of ISRIB-bound eIF2B.

(A to C) Three views of cryo-EM density for eIF2B(αβγδε)₂, colored in distinct shades for each subunit copy (red, α; blue, β; green, γ; gold, δ; gray, ε). Density assigned to ISRIB is depicted in CPK coloring (red, O; blue, N; green, Cl). The rotational relationships between the views depicted in (A), (B), and (C) are indicated. (D) Cross section of (A), revealing the

ISRIB binding pocket at the central decamer symmetry interface and density assigned to ISRIB CPK-colored by element. (E) Close-up view of density assigned to ISRIB and its binding pocket in (B) at the intersection of two β and two δ subunits. (F) Two conformers of ISRIB modeled into the density. All residues within 3.7 Å of the ligand are rendered as sticks.

and catalytic rate constant (k_{cat}) values similar to those of eIF2B previously purified from mammalian cells (Fig. 1C) (31).

To investigate how ISRIB activates eIF2B, we fixed eIF2B and eIF2 in a multi-turnover regime at concentrations of 10 nM and 1 μM, respectively. Under these conditions, eIF2 is subsaturating given its K_m of 1.5 μM (Fig. 1C). Previously, a factor of 3 stimulation of nucleotide exchange by ISRIB was seen under similar conditions (28). Surprisingly, ISRIB only marginally activated the recombinant eIF2B decamer by a factor of 1.2 (Fig. 1D; -ISRIB, $k_{obs} = 0.17 \pm 0.006 \text{ min}^{-1}$; +ISRIB, $k_{obs} = 0.21 \pm 0.005 \text{ min}^{-1}$).

ISRIB stabilizes eIF2B decamers in lysates of human embryonic kidney (HEK) 293T cells (28), suggesting a role during assembly of the active complex. To test this notion and its implications for ISRIB's mechanism of action, we purified eIF2B in the presence or absence of ISRIB. Under both conditions, we obtained the fully assembled decamer (Fig. 1E, peak 3); however, in the absence of ISRIB, we also obtained a partially assembled complex lacking the α subunit that eluted from the anion exchange column at a lower ionic strength (Fig. 1E, peak 2). These data suggest that ISRIB enhances the stability of the decamer. To test this idea, we expressed eIF2B(βγδε) and eIF2Bα separately (Fig.

S1, B and C). Surprisingly, eIF2B(βγδε) purified as a heterotetramer, as determined by analytical ultracentrifugation (fig. S1D), whereas eIF2Bα purified as a homodimer, as previously observed (fig. S1E) (6). We then combined eIF2B(βγδε) and eIF2B(α₂) under stringent conditions of elevated ionic strength (400 mM) to assess ISRIB's contribution to the stability of the decameric complex. When analyzed by velocity sedimentation in the absence of ISRIB, eIF2B(βγδε) sedimented as a tetramer (peak fractions 6 and 7), whereas eIF2B(α₂) peaked in fraction 4 (Fig. 1F, top). By contrast, in the presence of ISRIB, eIF2B(βγδε) and eIF2B(α₂) sedimented together as a higher-molecular weight complex deeper in the gradient (peak fractions 7 to 9) (Fig. 1F, bottom). As we discuss below, the stabilized decamer peaked in fraction 10 of the gradient, indicating that under these conditions, the decamer partially dissociates during sedimentation. We surmise that dissociation during centrifugation led to the broad sedimentation profiles observed. Thus, ISRIB enhanced the stability of decameric eIF2B.

To study the interplay among ISRIB binding, eIF2B(α₂) incorporation into the decamer, and GEF activity, we mixed independently purified eIF2B(α₂) and eIF2B(βγδε) subcomplexes and assayed the combination for GDP unloading. When

assayed under these conditions, the specific activity was reduced by a factor of 4 relative to the fully assembled decamer (compare Fig. 1D and Fig. 1G, $k_{obs} = 0.17 \pm 0.006 \text{ min}^{-1}$ versus $0.04 \pm 0.009 \text{ min}^{-1}$). The addition of ISRIB restored GEF activity toward the level of fully assembled decamer by a factor of 3 ($k_{obs} = 0.11 \pm 0.002 \text{ min}^{-1}$) (Fig. 1G), which suggests that ISRIB's activity reflects enhanced decamer stability.

Using the GDP loading assay, we found that eIF2B activity was reduced profoundly ($k_{obs} = 0.01 \pm 0.007 \text{ min}^{-1}$) in the absence of eIF2B(α₂) (Fig. 1H), as previously reported (32, 33). Interestingly, ISRIB still activated eIF2B(βγδε) (Fig. 1I, $k_{obs} = 0.04 \pm 0.003 \text{ min}^{-1}$), indicating that ISRIB can enhance GEF activity independent of eIF2B(α₂) incorporation into the holoenzyme. To reconcile these unexpected findings, we next sought a structural understanding of the ISRIB-stabilized human eIF2B decameric complex.

ISRIB binds in a deep cleft, bridging the two-fold symmetric interface of the eIF2B decamer

We determined an atomic-resolution structure of eIF2B bound to ISRIB by cryo-electron microscopy (cryo-EM). We classified and refined a single consensus structure from 202,125 particles to an

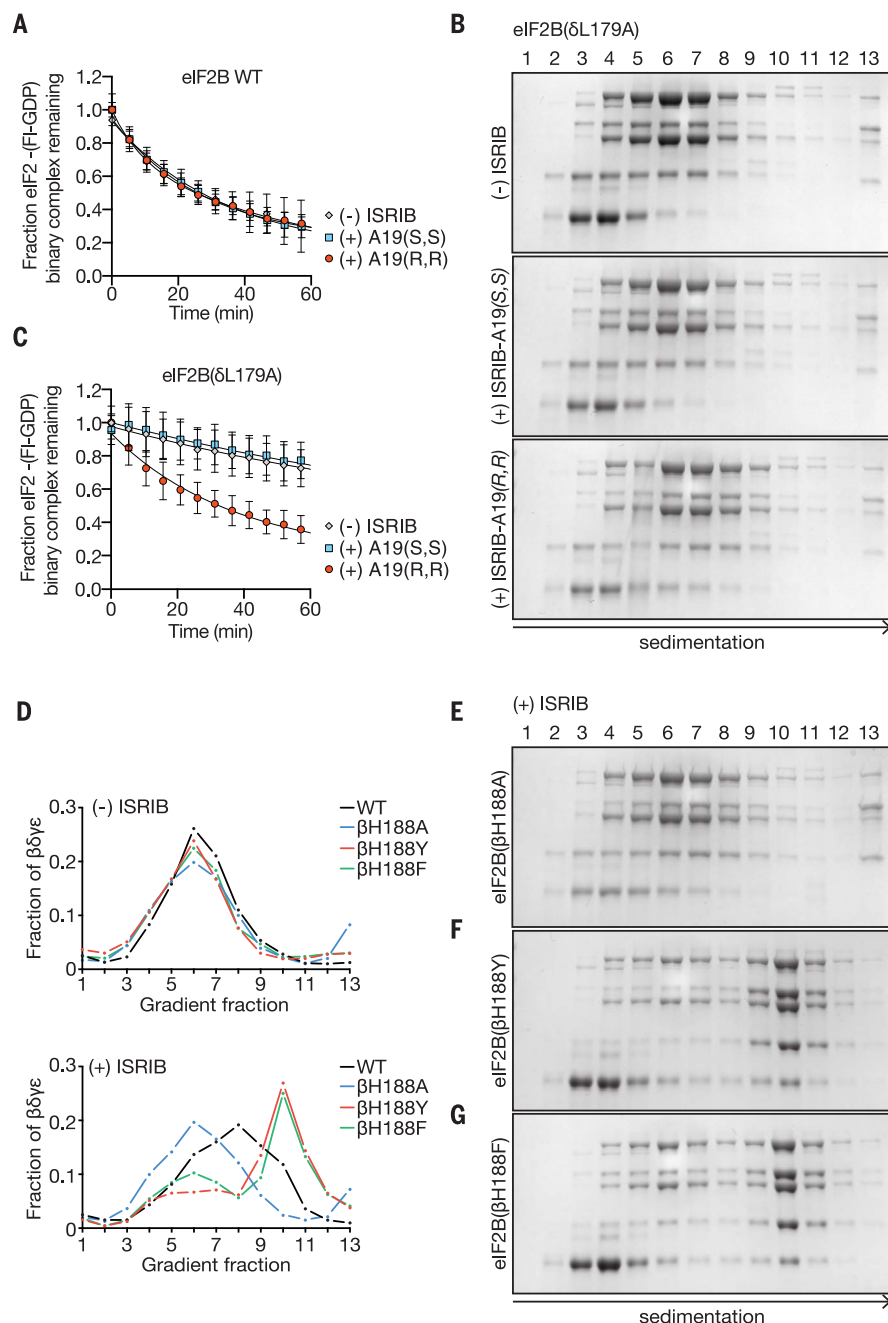


Fig. 3. eIF2B structure predicts activity of ISRIB analogs. (A) GEF activity of assembled eIF2B($\beta\gamma\delta\epsilon$) and eIF2B(α_2) in the presence and absence of ISRIB-A19(R,R) and ISRIB-A19(S,S) (mean \pm SD; $n = 3$). (B) Stability of decameric eIF2B(δ L179A) in the absence of ISRIB (top), presence of ISRIB-A19(S,S) (middle), or presence of ISRIB-A19(R,R) (bottom) as assessed by velocity sedimentation on sucrose gradients. (C) eIF2B GEF activity of assembled eIF2B($\beta\gamma\delta\epsilon$) and eIF2B(α_2) containing a δ L179A mutation in the presence and absence of ISRIB-A19(R,R) and ISRIB-A19(S,S) (mean \pm SD; $n = 3$). (D) Quantification of eIF2B decamer stability gradients plotted as fraction of eIF2B($\beta\gamma\delta\epsilon$) present in each of lanes 1 to 13 in (E) to (G). eIF2B (for comparison from data shown in Fig. 1F), eIF2B(β H188A), eIF2B(β H188Y), and eIF2B(β H188F) gradients are plotted in the presence (bottom) and absence (top) of 500 nM ISRIB. (E to G) Stability of decameric eIF2B(β H188A), eIF2B(β H188Y), and eIF2B(β H188F) in the presence of ISRIB, as assessed by velocity sedimentation on sucrose gradients.

average resolution of 2.8 Å, which varied from 2.7 Å in the stable core to 3.4 Å in the more flexible periphery (fig. S3). The overall structure bears clear resemblance to the *S. pombe* two-fold symmetric decameric structure determined by x-ray

crystallography (8). The symmetry interface comprises contacts between the α , β , and δ subunits, while the γ and ϵ subunits are attached at opposing ends (Fig. 2, A to C). As in the *S. pombe* crystal structure, the catalytic HEAT domains of the ϵ

subunits were not resolved, indicating their flexible attachment to the regulatory core. By contrast, densities for the “ear” domains of the γ subunits were resolved, but at a resolution that precluded atomic interpretation (Fig. 2B and figs. S3 and S4).

We observed a clearly defined density consistent with the dimensions of ISRIB and not attributable to protein bridging the symmetry interface of the decamer (Fig. 2, B, D, and E, and fig. S5). Modeling suggests that ISRIB binds with its central cyclohexane ring in the expected low-energy chair conformation, with the side chains projecting to the same face of the cyclohexane ring and inserting the distal 4-chlorophenyl rings into deep binding pockets (Fig. 2, D to F, and fig. S5). ISRIB’s “U-shaped” conformation may be stabilized by intramolecular N-H...O hydrogen-bonding interactions between its amide nitrogen N-H bond and the aryl ether oxygens, possibly explaining why non-ether-linked congeners of ISRIB are much less potent (fig. S6) (28, 34). The cryo-EM density most likely corresponds to an average of at least two energetically equivalent ISRIB conformations related by 180° rotations about both N-C bonds to the cyclohexane ring (both depicted in Fig. 2F and figs. S4 and S5). This superposition of two conformers accounts for the apparently symmetric density observed, even though in isolation each individual conformer is pseudo-symmetric (fig. S5). The multiple observed ISRIB binding modes may contribute to its free energy of binding by providing additional entropic wiggle room.

The N-terminal loop of the δ subunit contributes key residues to the binding pocket, and this loop differs from the ligand-free *S. pombe* structure (8). Residues in the δ loop are important for ISRIB activity (29), including Val¹⁷⁷ and Leu¹⁷⁹ (δ V177 and δ L179), which contribute directly to the hydrophobic surface of the binding pocket (Fig. 2F and fig. S6). In addition, the δ subunits contribute δ L485 to the hydrophobic wells that accommodate the halogenated benzene rings (Fig. 2F and fig. S6). The center of the binding site comprises residues from the β subunit, including Asn¹⁶² and His¹⁸⁸ (β N162 and β H188), which lie near ISRIB’s more polar functionality. In particular, one of the two C-H bonds at the glycolamide α -carbon is oriented perpendicular to the plane of the aromatic histidine ring (Fig. 2F and fig. S6), suggesting a C-H- π interaction with β H188. Residues on the β subunits, including Val¹⁶⁴ and Ile¹⁹⁰ (β V164 and β I190), also make key contributions to the hydrophobicity of the deep wells.

Thus, ISRIB enhances incorporation of the α subunit into the decamer despite not making direct contacts with this subunit. Rather, ISRIB stabilizes the symmetry interface of the β - δ core, which in turn favors stable eIF2B(α_2) binding. As such, ISRIB’s enhancement of GEF activity derives from its ability to promote higher-order holoenzyme assembly.

Structural model predicts the activity of modified compounds and mutations

To validate the structural model, we synthesized ISRIB analogs bearing a methyl group at the α

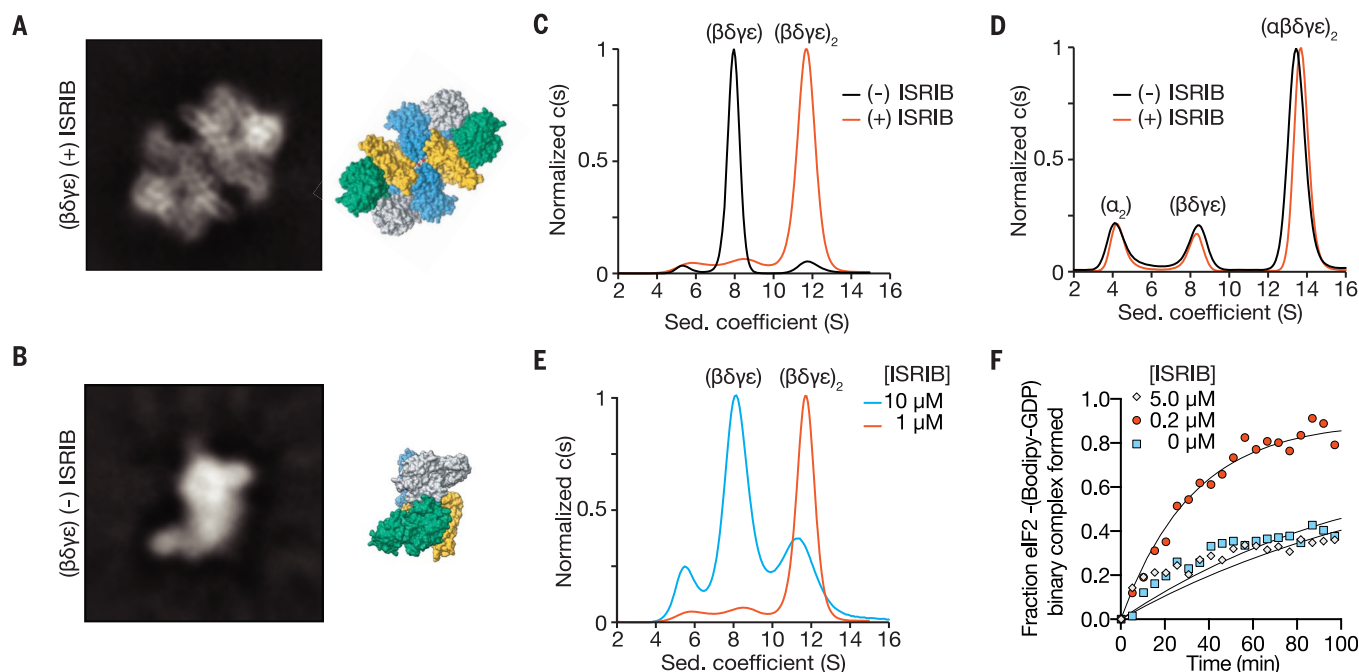


Fig. 4. ISIRIB induces dimerization of tetrameric eIF2B subcomplexes. (A and B) The most abundant 2D class averages from cryo-EM imaging of eIF2B($\beta\gamma\delta\epsilon$) in the presence (A) and absence (B) of ISIRIB. Subunit colors are as in Fig. 2. (C) Characterization of eIF2B($\beta\gamma\delta\epsilon$) by sedimentation velocity analytical ultracentrifugation. eIF2B($\beta\gamma\delta\epsilon$) (1 μ M) was analyzed in the presence and absence of 1 μ M ISIRIB. (D) Mixture

of 1 μ M eIF2B($\beta\gamma\delta\epsilon$) and 500 nM eIF2B(α_2) characterized by analytical ultracentrifugation in the presence and absence of 1 μ M ISIRIB. (E) eIF2B($\beta\gamma\delta\epsilon$) (1 μ M) characterized by analytical ultracentrifugation in the presence of 1 μ M or 10 μ M ISIRIB. (F) GEF activity of eIF2B($\beta\gamma\delta\epsilon$), here at a higher concentration (100 nM) to facilitate comparison of 0, 0.2, and 5 μ M ISIRIB.

position of the glycolamide side chains. Two enantiomers, ISIRIB-A19(*R,R*) and ISIRIB-A19(*S,S*), were prepared (fig. S7A) on the basis of predicted steric clashes with residue δ L179 for ISIRIB-A19(*R,R*) or β H188 for ISIRIB-A19(*S,S*) in the ISIRIB binding pocket (Fig. 2F and fig. S6). As expected, neither enantiomer enhanced GEF activity *in vitro* or in cells (Fig. 3A and fig. S7B), nor did they enhance the stability of purified decameric eIF2B (fig. S7C). We next engineered eIF2B to accommodate the additional methyl groups on ISIRIB-A19(*R,R*) by mutating δ L179 to alanine (δ L179A). We tested the effects of both compounds on eIF2B(δ L179A) by velocity sedimentation and GEF activity. As predicted, ISIRIB-A19(*R,R*) stabilized formation of mutant decamers (Fig. 3B) and stimulated nucleotide exchange (Fig. 3C). Treatment with ISIRIB-A19(*R,R*) activated eIF2B(δ L179A) by approximately a factor of 3 (Fig. 3C, $k_{\text{obs}} = 0.027 \pm 0.001 \text{ min}^{-1}$), similar to the activation of wild-type eIF2B by ISIRIB. By contrast, and as predicted, ISIRIB-A19(*S,S*) failed to activate eIF2B(δ L179A) (Fig. 3C, $k_{\text{obs}} = 0.007 \pm 0.001 \text{ min}^{-1}$). Notably, in the absence of ISIRIB analogs, eIF2B(δ L179A) was less active than eIF2B by a factor of 5 (compare Fig. 3A and Fig. 3C; eIF2B $k_{\text{obs}} = 0.04 \pm 0.009 \text{ min}^{-1}$, eIF2B(δ L179A) $k_{\text{obs}} = 0.008 \pm 0.002 \text{ min}^{-1}$). This result identifies δ L179A as a novel hypomorphic mutation and underscores the importance of this surface for holoenzyme assembly.

We next sought to verify the existence of a putative C-H- π interaction between β H188 and ISIRIB by mutating β H188 to alanine. As predicted,

ISIRIB did not stabilize eIF2B(β H188A) decamers (Fig. 3, D and E, and fig. S8). By contrast, although mutation of β H188 to an aromatic tyrosine (β H188Y) or phenylalanine (β H188F) was predicted to sustain and likely enhance C-H- π interactions, it did not impair ISIRIB's activity to stabilize decamers (Fig. 3, D, F, and G, and fig. S8). Rather, ISIRIB stabilized eIF2B(β H188Y) and eIF2B(β H188F) decamers to an even greater extent than wild-type eIF2B decamers (Fig. 3D). Whereas ISIRIB-stabilized wild-type eIF2B sedimented with a broad profile, indicating dissociation of the decamer through the course of sedimentation (Figs. 1F and 3D), ISIRIB-stabilized eIF2B(β H188Y) and eIF2B(β H188F) formed a sharp symmetric peak in fraction 10, indicative of enhanced complex integrity through sedimentation, presumably owing to enhanced C-H- π bonding interaction with ISIRIB (Fig. 3, D, F, and G, and fig. S8).

ISIRIB induces dimerization of tetrameric eIF2B subcomplexes

Because ISIRIB bridges the symmetry interface of the decamer without making direct contacts with eIF2B(α_2), we sought to understand how the small molecule promotes eIF2B(α_2) incorporation into the decamer. We imaged purified eIF2B($\beta\gamma\delta\epsilon$) tetramers in the presence and absence of ISIRIB by cryo-EM. In the presence of ISIRIB, the images revealed a predominant species consistent with an octameric complex of eIF2B lacking the α subunits (Fig. 4A). By contrast, in the absence of ISIRIB, the predominant

species was consistent with a tetrameric complex divided along the symmetry axis of the octamer (Fig. 4B). In accordance with the ISIRIB-dependent stabilization of the decamer by mutations in β H188 to other aromatic residues, β H188F and β H188Y mutants also stabilized the octamer in high-salt conditions (fig. S9). These images suggest a model in which ISIRIB dimerizes eIF2B($\beta\gamma\delta\epsilon$) by “stapling” the tetramers together to form the octameric binding platform for α subunit binding, consistent with the architecture of the ISIRIB-bound decamer.

We next substantiated eIF2B($\beta\gamma\delta\epsilon$) dimerization by analytical ultracentrifugation under physiological salt conditions. In the absence of ISIRIB, eIF2B($\beta\gamma\delta\epsilon$) sedimented as a predominant 8.0S peak and a minor 11.7S peak, corresponding to eIF2B($\beta\gamma\delta\epsilon$) and eIF2B($\beta\gamma\delta\epsilon$)₂, respectively (Fig. 4C). By contrast, in the presence of ISIRIB, we observed a marked increase in the 11.7S peak, demonstrating ISIRIB's role in stabilizing the eIF2B($\beta\gamma\delta\epsilon$)₂ octamer. Together with the observation that eIF2B($\beta\gamma\delta\epsilon$) has greater activity in the presence of ISIRIB (Fig. 1I), these data show the importance of octamer assembly in activating GEF activity.

Dimerization of eIF2B($\beta\gamma\delta\epsilon$) effectively doubles the surface area for eIF2B(α_2) binding, which suggests that the ISIRIB-enhanced incorporation of eIF2B(α_2) into the decamer originates from ISIRIB's ability to shift the tetramer/octamer equilibrium. To test this prediction, we combined eIF2B(α_2) and eIF2B($\beta\gamma\delta\epsilon$) in the presence and absence of ISIRIB and assessed decamer assembly

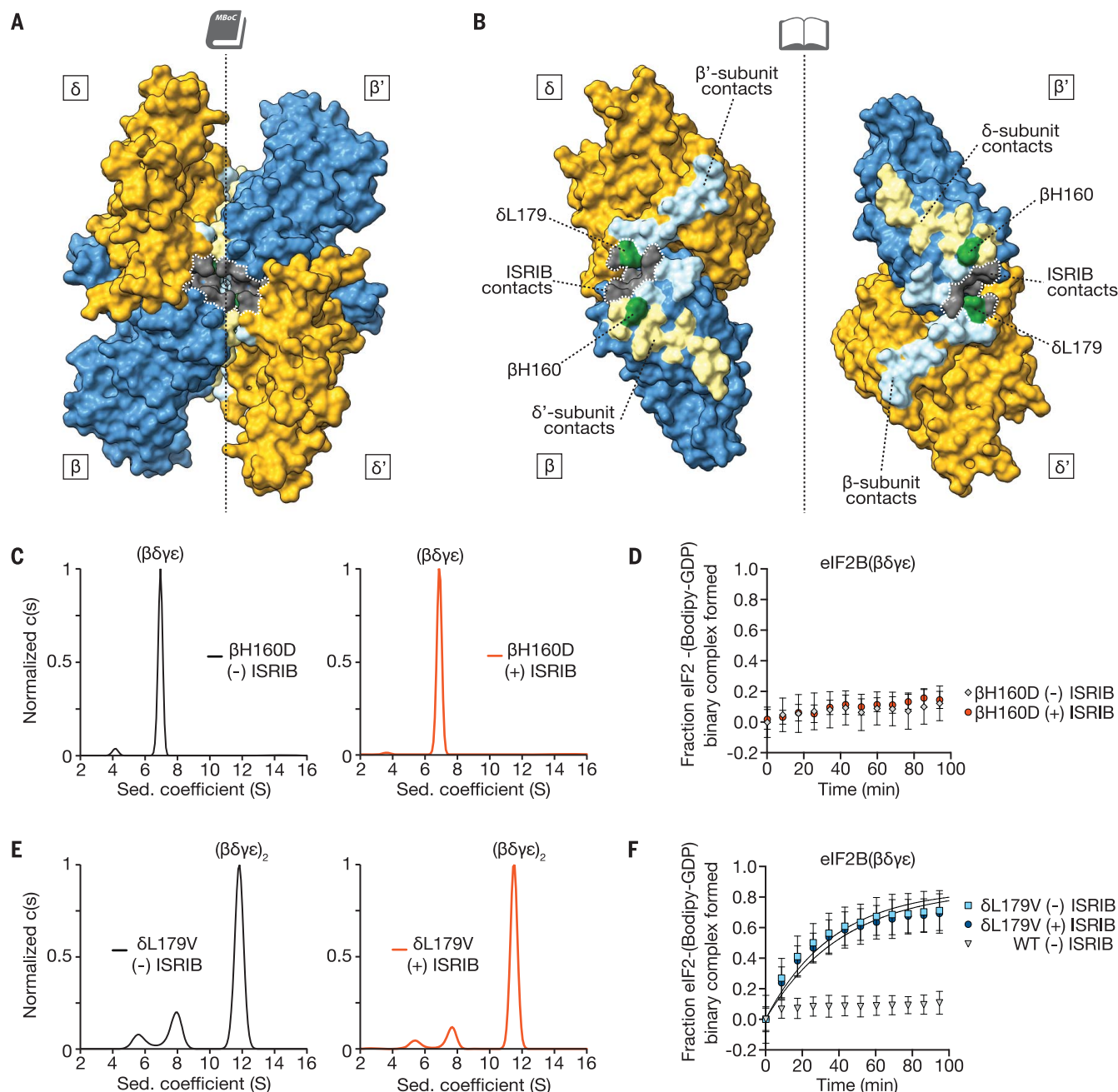


Fig. 5. Loss- and gain-of-function dimerization mutants resist or bypass the effects of ISRIB. (A) Surface rendering of core eIF2B β (blue) and eIF2B δ (gold) subunits; residues contacting ISRIB are highlighted in gray, and the dimer interface is indicated by a dashed line. Interface residues are highlighted in a lighter hue of the colors of the contacting subunits. (B) Open-book view of the dimer-dimer interface, such that each β and δ subunit is rotated by 90°. β H160, in green, contacts both β' and δ' ; δ L179, also in green, contacts both β' and ISRIB. (C) Characterization of

1 μ M eIF2B($\beta\gamma\delta\epsilon$) containing a β H160D mutation in the presence (right) and absence (left) of 1 μ M ISRIB by analytical ultracentrifugation. (D) GEF activity of eIF2B($\beta\gamma\delta\epsilon$) containing a β H160D mutation in the presence and absence of ISRIB (mean \pm SD; $n = 3$). (E) Characterization of 1 μ M eIF2B($\beta\gamma\delta\epsilon$) containing a δ L179V mutation in the presence (right) and absence (left) of 1 μ M ISRIB by analytical ultracentrifugation. (F) GEF activity of eIF2B($\beta\gamma\delta\epsilon$) containing a δ L179V mutation in the presence and absence of ISRIB (mean \pm SD; $n = 3$).

by analytical ultracentrifugation. Under the high protein concentrations used in these assays, we observed a predominant peak corresponding to the assembled eIF2B decamer at 13.6S both in the presence and absence of ISRIB, together with minor peaks corresponding to unincorporated eIF2B($\beta\gamma\delta\epsilon$) at 8.0S and eIF2B(α_2) at 4.1S (Fig.

4D). We did not observe an octamer peak, which suggests that the octamer has a high affinity for eIF2B(α_2) and assembles the full decamer under these conditions. Together with the cryo-EM images, these data demonstrate that eIF2B(α_2) and ISRIB synergistically promote dimerization of eIF2B($\beta\gamma\delta\epsilon$).

Given that ISRIB binds across the eIF2B($\beta\gamma\delta\epsilon$)₂ interface such that each tetramer contributes half of the ISRIB binding site, we reasoned that high ISRIB concentrations may occupy half-sites within the tetramers and interfere with octamer formation. Indeed, ISRIB promoted eIF2B($\beta\gamma\delta\epsilon$)₂ assembly at 1 μ M but failed to do so at 10 μ M

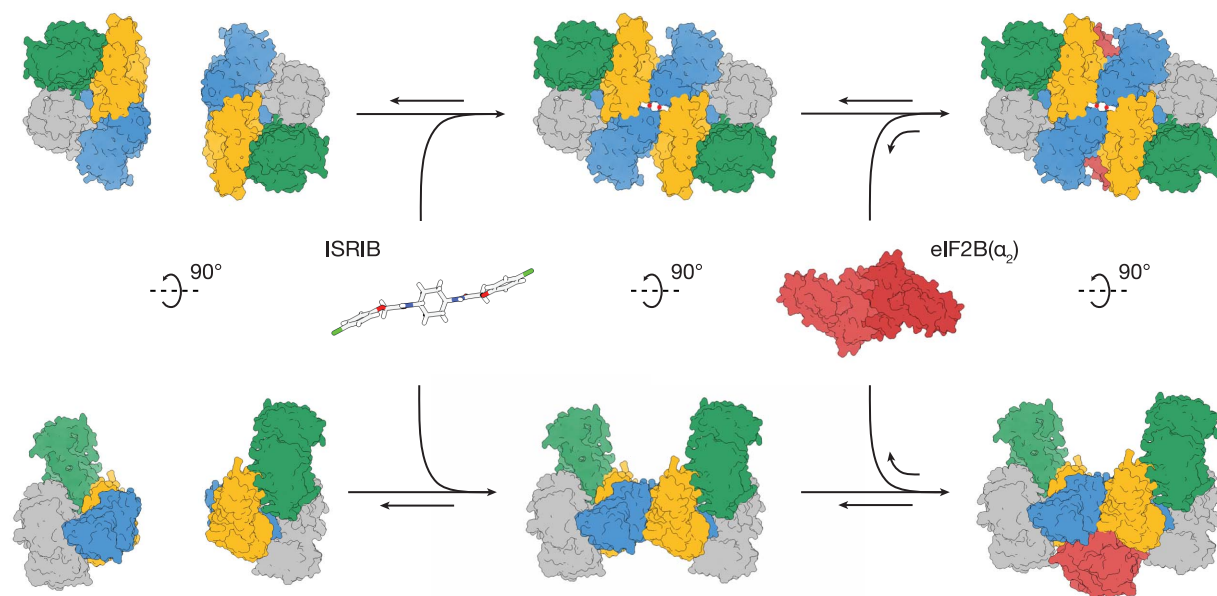


Fig. 6. Model for ISRIB's mechanism of action. ISRIB staples together tetrameric eIF2B($\beta\gamma\delta\epsilon$) subcomplexes, building a more active eIF2B($\beta\gamma\delta\epsilon$)₂ octamer. In turn, the ISRIB-stabilized octamer binds eIF2B(α_2) with greater affinity, enhancing the formation of a fully active, decameric holoenzyme.

(Fig. 4E). Similarly, ISRIB stimulated GEF activity of eIF2B($\beta\gamma\delta\epsilon$) at 0.2 μM but failed to do so at 5 μM (Fig. 4F). Note that the high ISRIB concentrations used in this assay did not reduce GEF activity below that of eIF2B($\beta\gamma\delta\epsilon$); this shows that the effect did not result from nonspecific enzymatic inhibition.

Loss- and gain-of-function dimerization mutants resist or bypass the effects of ISRIB

To visualize the determinants of octamerization, we highlighted the solvent-excluded surface area along the symmetry interface of the β and δ subunits in adjacent tetramers (Fig. 5, A and B, light yellow, light blue, green) and labeled the residues of the ISRIB binding pocket on this surface (Fig. 5, A and B, gray). The tetramer-tetramer contact residues form a thin strip along each neighboring β and δ subunit. Most of the β subunit residues contact the δ subunit across the symmetry interface, while a small number of residues also cement β - β' contacts. Of these, His¹⁶⁰ (β H160) and Arg²²⁸ (β R228) reside at the junction of β - β' and β - δ' subunits, which suggests that they play key roles in stabilizing the octamer. Accordingly, we observed that mutation of β H160 to aspartic acid, which we predicted would be repulsed by δ D450, completely precluded octamer assembly. Analytical ultracentrifugation of eIF2B($\beta\gamma\delta\epsilon$) containing the β H160D mutation revealed a sharp tetramer peak at 7S both in the absence and presence of ISRIB (Fig. 5C), and ISRIB was unable to enhance GEF activity for this mutant (Fig. 5D). Thus, the effect of this mutation on octamerization cannot be overcome by ISRIB binding, even though ISRIB binding buries an additional $\sim 11\%$ of solvent-exposed surface area—an increase from 3420 \AA^2 to 3790 \AA^2 —upon stapling of tetramers (Fig. 5, A and B).

Serendipitously, we also identified a gain-of-function mutation in eIF2B. We initially engineered a δ L179V mutation alongside the δ L179A mutation used above to accommodate the methylated analog ISRIB-A19(*R,R*) (Fig. 2F and fig. S6). To our surprise, we discovered that the predominant species of δ L179V-eIF2B($\beta\gamma\delta\epsilon$) sedimented as a remarkably stable octamer in the absence of ISRIB (Fig. 5E). GEF activity assays revealed that δ L179V-eIF2B($\beta\gamma\delta\epsilon$)₂ was 5 times as active as the wild-type octamers formed in the presence of ISRIB, and was not further activated by ISRIB (compare Fig. 5F and Fig. 1I; eIF2B(δ L179V) $k_{\text{obs}} = 0.027 \pm 0.001 \text{ min}^{-1}$, eIF2B(δ L179V) + ISRIB $k_{\text{obs}} = 0.024 \pm 0.001 \text{ min}^{-1}$, wild-type + ISRIB $k_{\text{obs}} = 0.005 \pm 0.001 \text{ min}^{-1}$). Together with the ISRIB-bound structure, these mutants indicate that the major contribution of ISRIB to increased GEF activity lies at the step of tetramer dimerization and assembly of the bipartite surface for α subunit homodimer binding (Fig. 6).

Discussion

We determined the structure of human eIF2B at sufficiently high resolution to characterize the binding site and coordination of a small molecule with therapeutic potential. In concomitant work, Zyryanova *et al.* report similar findings (35). The atomic model of ISRIB-bound eIF2B reconciles structure-activity relationships described previously (28, 34), predicted both loss- and gain-of-function mutations, and facilitates the rational design of small-molecule modulators of eIF2B activity. The structure provides an intuitive view of how ISRIB activates nucleotide exchange: ISRIB stabilizes the active decameric form of the eIF2B holoenzyme by stapling the constituents together across a two-fold symmetry axis.

Given that a catalytic residue essential for nucleotide exchange resides in the still-unresolved HEAT repeat of the ϵ subunit, how does assembly of the decameric holoenzyme enhance activity? Cross-linking studies suggest that eIF2 binds across the decameric interface, engaging the eIF2B α subunit along with β and δ subunits from opposing tetramers (8). We surmise that decamer assembly creates a composite surface for eIF2 binding that allows the flexibly attached HEAT domain to reach and engage its target. Although we consider it likely that the effects of ISRIB binding can be explained by the degree of holoenzyme assembly, additional ligand-induced allosteric changes may also contribute to its activity.

These observations provide a plausible model for ISRIB's ability to ameliorate the inhibitory effects of eIF2 α phosphorylation on ternary complex formation. ISRIB staples tetrameric building blocks together into an octamer, which enhances activity by a factor of 3 and forms a platform for association of the dimeric α subunits. The integrated effect of these sequential steps is an enhancement of activity by an order of magnitude. The inhibition resulting from a limiting amount of phosphorylated eIF2 would be reduced by the surplus of GEF activity provided by ISRIB. By contrast, an excess of ISRIB poisons the assembly reaction by saturating half-binding sites on unassembled tetramers. Thus, within its effective concentration range, ISRIB will enhance ternary complex formation even in unstressed conditions, opening an untapped reservoir of additional enzymatic capacity. We surmise that in vivo these activities are likely to be realized near the equilibrium points of the assembly reactions for the holoenzyme, allowing for ISRIB's observed phenotypic effects. Thus, eIF2B is poised to integrate diverse signals that affect translation initiation.

Phosphorylation of eIF2 may be just one of many mechanisms for modulating its activity. Posttranslational modifications, expression of other modulatory components, or binding of unidentified endogenous ligands (to the ISRIB binding pocket or elsewhere) are likely to modulate eIF2B activity under varying physiological conditions. Understanding the different modes of regulation of this vital translational control point will be of particular importance in the nervous system, where ISRIB has been shown to have a range of effects.

Materials and methods

Cloning of eIF2B expression plasmids

The five human eIF2B subunits were *E. coli* codon-optimized and synthesized on the BioXp 3200 System (SGI-DNA) in six blunt-end dsDNA fragments; see supplementary materials for synthesized sequences. Fragments were cloned into pCR-BluntII-TOPO vector with the Zero Blunt TOPO PCR Cloning Kit (Invitrogen) and verified by sequencing. In brief, subunits of eIF2B were PCR-amplified from TOPO cloned vectors and Infusion (Clontech) cloned into multigene expression plasmids with compatible drug resistances and origins of replication: pETDuet-1 (Novagen 7146-3), pACYCDuet-1 (Novagen 7147-3), or pCOLADuet-1 (Novagen 71406-3) vectors. Each expression plasmid contains two cloning sites (site 1 and site 2), enabling simultaneous expression of up to two genes per plasmid. eIF2B1 (encoding the α subunit) was inserted into site 1 of pETDuet-1 (pJT066). eIF2B2 (encoding the β subunit) and eIF2B4 (encoding the δ subunit) were inserted into sites 1 and 2 of pACYCDuet-1, respectively (pJT073). eIF2B3 (encoding the γ subunit) and eIF2B5 (encoding the ϵ subunit) were inserted into sites 1 and 2 of pCOLADuet-1, respectively (pJT074). eIF2B5 was synthesized in two fragments eIF2B5_1 and eIF2B5_2 that were simultaneously inserted into site 2 by Infusion.

Purification of decameric eIF2B($\alpha\beta\delta\gamma\epsilon$)₂

pJT066, pJT073, and pJT074 were cotransformed into One Shot BL21 Star (DE3) chemically competent *E. coli* cells (Invitrogen) and grown in Luria broth containing ampicillin, kanamycin, and chloramphenicol at 37°C on an orbital shaker. When the culture reached an OD₆₀₀ of 0.6, the temperature was reduced to 16°C, and the culture was induced with 0.8 mM IPTG (Gold Bio-technology) and grown for 16 hours. Cells were harvested and lysed with EmulsiFlex-C3 (Avestin) in a buffer containing 20 mM HEPES-KOH, pH 7.5, 250 mM KCl, 1 mM tris(2-carboxyethyl)phosphine (TCEP), 5 mM MgCl₂, 15 mM imidazole, and complete EDTA-free protease inhibitor cocktail (Roche). The lysate was clarified at 30,000g for 20 min at 4°C. Subsequent purification steps were conducted on the ÄKTA Pure (GE Healthcare) system at 4°C.

The clarified lysate was loaded onto a HisTrap HP 5 ml, washed in binding buffer (20 mM HEPES-KOH, pH 7.5, 200 mM KCl, 1 mM TCEP, 5 mM MgCl₂, and 15 mM imidazole), and eluted with a linear gradient (75 ml) of 15 mM to 300 mM imidazole in the same buffer. The eIF2B fraction eluted from the HisTrap column at 80 mM

imidazole. The eIF2B fraction was collected and loaded onto a 20 ml Mono Q HR16/10 column (GE Healthcare), washed in Buffer A (20 mM HEPES-KOH, pH 7.5, 200 mM KCl, 1 mM TCEP, and 5 mM MgCl₂) and eluted with a linear gradient (200 ml) of 200 mM to 500 mM KCl in the same buffer. The eIF2B fraction eluted off the Mono Q column at a conductivity of 46 mS/cm (corresponding to 390 mM KCl). Fractions were collected, concentrated with an Amicon Ultra-15 concentrator (EMD Millipore) with a 100,000-dalton molecular weight cutoff, and loaded onto a Superdex 200 10/300 GL column (GE Healthcare) equilibrated with Buffer A. A typical preparation yielded approximately 0.5 mg of eIF2B($\alpha\beta\delta\gamma\epsilon$)₂ from a 1-liter culture.

EM sample preparation and data collection

Decameric eIF2B($\alpha\beta\delta\gamma\epsilon$)₂ + ISRIB: After size exclusion chromatography, eIF2B($\alpha\beta\delta\gamma\epsilon$)₂ was diluted to 500 nM and a stock solution of 200 μ M ISRIB in *N*-methyl-2-pyrrolidone (NMP) was added to a final ISRIB concentration of 2 μ M in a final solution containing 20 mM HEPES-KOH, pH 7.5, 200 mM KCl, 1 mM TCEP, 5 mM MgCl₂, 0.5% NMP, and incubated on ice for 10 min. This sample was applied to either C-Flat 1.2/1.3-2C grids (EMS, USA) or Quantifoil R 1.2/1.3 200 Au mesh grids (Quantifoil, Germany). C-flat grids were used without additional cleaning or glow discharging. Quantifoil grids were soaked in chloroform for 30 min and desiccated overnight in a fume hood before use without glow discharging. Using a Vitrobot Mark IV at 4°C and 100% humidity, 3.5 μ l of sample was applied to the grid, incubated for an additional 10 s, then blotted with -0.5 mm offset for ~6 s and plunge-frozen in liquid ethane. Two data sets were collected on different microscopes. The first data set was collected with the 300-kV Titan Krios 2 at the HHMI Janelia Research Campus using a K2 Summit detector operated in super-resolution mode; 1780 images were collected at a magnification of 29,000 \times (0.51 Å per pixel) as dose-fractionated stacks of 67 \times 0.15-s exposures (1.19 e⁻/Å²) for a total dose of ~80 e⁻/Å² (table S1). The second data set was collected with the 300-kV Titan Krios at UC Berkeley using a K2 Summit detector operated in super-resolution mode; 1515 images were collected at a magnification of 29,000 \times (0.42 Å per pixel) as dose-fractionated stacks of 27 \times 0.18-s exposures (1.83 e⁻/Å²) for a total dose of ~44 e⁻/Å² (table S1).

Tetrameric eIF2B($\alpha\beta\gamma\delta$) + ISRIB: After size exclusion chromatography, tetrameric eIF2B($\alpha\beta\gamma\delta$) was diluted to 800 nM and vitrified in the absence of ISRIB and in the presence of 2 μ M ISRIB, as described above, but with ~4 s blot time; 129 micrographs of ligand-free and 67 micrographs of ISRIB-bound sample were collected on the 200 kV Talos Arctica at UCSF at 36,000 \times using a K2 Summit detector operated in super-resolution mode (1.15 Å/pixel).

Image analysis and 3D reconstruction

All dose-fractionated image stacks were corrected for motion artefacts, 2 \times binned in the Fourier

domain, and dose-weighted using MotionCor2 (36), resulting in one dose-weighted and one unweighted integrated image per stack with pixel sizes of 1.02 Å (Janelia) or 0.838 Å (UC Berkeley). The parameters of the contrast transfer function (CTF) were estimated using GCTF-v1.06 (37) and the motion-corrected but unweighted images; ~1000 particles per data set were manually selected and averaged in 2D using RELION 2.0 (38). The resulting class sums were then used as templates for automated particle picking using Gautamatch-v0.55 (37), followed by extraction and rescaling to a common pixel size of 0.838 Å and four rounds of 2D classification (table S2).

For the 3D reconstruction of decameric eIF2B($\alpha\beta\delta\gamma\epsilon$)₂ + ISRIB, the resulting subset of particles were input into cryoSPARC (39) to compute an ab initio reconstruction without symmetry, followed by homogeneous refinement in both cryoSPARC (dynamic masking) and in RELION 2.0 (unmasked) with no symmetry. Subsequent heterogeneous refinement (cryoSPARC) or multiclass 3D classification (RELION 2.0) removed less than 1% of the remaining particles (table S1).

High-resolution homogeneous refinement was then performed in parallel in cryoSPARC, RELION 2.1, and FREALIGN (40) using soft-edged masks and imposed C2 symmetry (figs. S3 and S4). All three approaches yielded maps of similar visual quality that differed in numerical resolution by ~0.1 Å, as measured by Fourier shell correlation. All three maps were low-pass filtered and sharpened using automated procedures and used comparatively during model building in COOT and PHENIX (see below). Molecular graphics and analyses were performed with the UCSF Chimera package and the FREALIGN map. Chimera is developed by the Resource for Biocomputing, Visualization, and Informatics at UCSF [supported by NIGMS P41-GM103311 (41)]. The map-versus-model FSC plots were generated using the FREALIGN map (see below and fig. S4). Accession numbers for the human eIF2B structures determined with FREALIGN, cryoSPARC, and RELION, respectively, are as follows: EMD-7442, EMD-7443, EMD-7444 (density maps; Electron Microscopy Data Bank) and 6CAJ (coordinates of atomic models; Protein Data Bank).

Atomic modeling and validation

An initial model of the human complex was generated using one-to-one threading as implemented in Phyre2 (42) using from the *S. pombe* crystal structure [PDB: 5B04 (8)] structure for the β , γ , δ , and ϵ subunits and the *H. sapiens* crystal structure [PDB: 3ECS (43)] for the α subunit. The initial ISRIB ligand model was generated in PHENIX eLBOW (44) using the SMILES, manually adjusted in COOT (45), and then refined with phenix.real_space_refine (46) using global minimization and simulated annealing. This initial model was manually adjusted in COOT a second time and further refined in phenix.real_space_refine using global minimization, secondary structure restraints, and local grid search. This model was manually adjusted a third and final time in COOT,

minimized in phenix.real_space_refine with per-residue B-factors, and the final model statistics were tabulated using Molprobity (47) (table S3). Map versus atomic model FSC plots for the entire decamer and the isolated $\beta\delta\beta'\delta'$ chains were computed using EMAN 2 (48) using calculated density maps from e2pdb2mrc.py with heteroatoms (ISIRIB) and per-residue B-factor weighting. Solvent accessible surfaces and buried surface areas were calculated from the atomic models using UCSF ChimeraX. Final atomic models have been deposited at the PDB with accession code 6CAJ.

Cloning of mutant eIF2B expression plasmids

Mutant eIF2B constructs were generated by site-directed mutagenesis on pJT073 using the primer indicated and its reverse complement.

δ L179A (pJT091): 5'-tagcttctaaagtttctgcttctcaccctgccgcag-3'

β H188A (pJT089): 5'-gctgctcgtaaacgtaaattcgctgtatcggtgctgaatgcgt-3'

β H188F (pJT094): 5'-gctcgttaaacgtaaattctggtatcggtgctgaatg-3'

β H188Y (pJT095): 5'-gctgctcgtaaacgtaaattctacgtatcggtgctgaatg-3'

δ L179V (pJT090): 5'-tacgggtctaaagtttctggtttctcaccgcgcag-3'

β H160D (pJT102): 5'-caggctctggaacacatcgactcaacgaagtatcatcg-3'

Purification of tetrameric eIF2B($\beta\delta\gamma\epsilon$)

Tetrameric eIF2B($\beta\delta\gamma\epsilon$) and tetrameric eIF2B($\beta\delta\gamma\epsilon$) mutant proteins were purified using the same protocol as described for the decamer with the exception that expression strains were cotransformed without the eIF2B α subunit expressing plasmid. A typical preparation yielded approximately 0.75 mg of eIF2B($\beta\delta\gamma\epsilon$) from a 1 liter culture.

eIF2B($\beta\delta\gamma\epsilon$) tetramer with co-transformed plasmids: pJT073, pJT074

δ L179A eIF2B($\beta\delta\gamma\epsilon$) tetramer with co-transformed plasmids: pJT091, pJT074

β H188A eIF2B($\beta\delta\gamma\epsilon$) tetramer with co-transformed plasmids: pJT089, pJT074

β H188F eIF2B($\beta\delta\gamma\epsilon$) tetramer with co-transformed plasmids: pJT094, pJT074

β H188Y eIF2B($\beta\delta\gamma\epsilon$) tetramer with co-transformed plasmids: pJT095, pJT074

δ L179V eIF2B($\beta\delta\gamma\epsilon$) tetramer with co-transformed plasmids: pJT090, pJT074

β H160D eIF2B($\beta\delta\gamma\epsilon$) tetramer with co-transformed plasmids: pJT102, pJT074

Purification of eIF2B(α_2)

Purification of the eIF2B(α_2) was adapted from previously published purifications (6, 43). The α subunit was N-terminally tagged with a 6×His tag followed by a TEV cleavage site (pJT075). pJT075 was transformed into BL21 (DE3) *E. coli* cells and grown in Luria broth containing ampicillin at 37°C on an orbital shaker. When the culture reached an OD₆₀₀ of 0.8, the temperature was reduced to 20°C, induced with 0.8 mM IPTG, and grown for 16 hours. Cells were harvested and lysed in a buffer containing 20 mM HEPES-

KOH, pH 7.5, 250 mM KCl, 1 mM TCEP, 5 mM MgCl₂, 20 mM imidazole, and 1× protease inhibitor cocktail, and clarified at 30,000g for 20 min at 4°C.

The clarified lysate was loaded onto a 5-ml HisTrap HP column, washed in a buffer containing 20 mM HEPES-KOH, pH 7.5, 30 mM KCl, 1 mM TCEP, 5 mM MgCl₂, and 20 mM imidazole, and eluted with 75-ml linear gradient of 20 to 300 mM imidazole. The HisTrap elution was then passed through a MonoQ HR 16/10 and subsequently a MonoS HR 10/10 (GE Healthcare), both equilibrated in a buffer containing 20 mM HEPES-KOH, pH 7.5, 30 mM KCl, 1 mM TCEP, and 5 mM MgCl₂. eIF2B(α_2) was collected in the flow-through fractions of both MonoQ and MonoS columns. The eIF2B(α_2) containing fraction was incubated for 16 hours at 4°C with TEV protease (50 µg of TEV per liter of culture) and passed through on a 5-ml HisTrap HP. Cleaved eIF2B(α_2) was recovered in the flow-through fraction, concentrated with an Amicon Ultra-15 concentrator (EMD Millipore) with a 30,000-dalton molecular mass cutoff and chromatographed on a Superdex 75 10/300 GL (GE Healthcare) column equilibrated in a buffer containing 20 mM HEPES-KOH, pH 7.5, 200 mM KCl, 1 mM TCEP, 5 mM MgCl₂, and 5% glycerol. A typical preparation yielded approximately 0.3 mg of eIF2B(α_2) from a 1-liter culture.

Preparation of human eIF2

Human eIF2 was prepared from an established recombinant *S. cerevisiae* expression protocol (30). In brief, the yeast strain GP6452 (gift from the Pavitt lab, University of Manchester) containing yeast expression plasmids for human eIF2 subunits and a deletion of GNC2 encoding the only eIF2 kinase in yeast, was grown to saturation in synthetic complete media (Sunrise Science Products) with auxotrophic markers (-Trp, -Leu, -Ura) in 2% dextrose. The β and α subunits of eIF2 were tagged with His6 and FLAG epitopes, respectively. A 12-liter yeast culture was grown in rich expression media containing yeast extract, peptone, 2% galactose, and 0.2% dextrose. Cells were harvested and resuspended in lysis buffer [100 mM Tris, pH 8.5, 300 mM KCl, 5 mM MgCl₂, 0.1% NP-40, 5 mM imidazole, 10% glycerol (Thermo Fisher Scientific), 2 mM DTT, 1× protease inhibitor cocktail (Sigma Aldrich #11836170001), 1 µg/ml each aprotinin (Sigma Aldrich), leupeptin (Sigma Aldrich), pepstatin A (Sigma Aldrich). Cells were lysed in liquid nitrogen using a steel blender. The lysate was centrifuged at 10,000g for 1 hour at 4°C. Subsequent purification steps were conducted on the ÄKTA Pure (GE Healthcare) system at 4°C. Lysate was applied to a 5-ml HisTrap Crude column (Thermo Fisher Scientific) equilibrated in buffer (100 mM HEPES, pH 7.5, 100 mM KCl, 5 mM MgCl₂, 0.1% NP-40, 5% glycerol, 1 mM dithiothreitol, 0.5× protease inhibitor cocktail, 1 µg/ml each aprotinin, leupeptin, pepstatin A). eIF2 bound to the column, was washed with equilibration buffer and eluted using a 50 ml linear gradient of 5 mM to 500 mM imidazole. Eluted eIF2 was incubated with FLAG M2 magnetic

affinity beads, washed with FLAG wash buffer (100 mM HEPES, pH 7.5, 100 mM KCl, 5 mM MgCl₂, 0.1% NP-40, 5% glycerol, 1 mM TCEP, 1× protease inhibitor cocktail, 1 µg/ml each aprotinin, leupeptin, pepstatin A) and eluted with FLAG elution buffer [identical to FLAG wash buffer but also containing 3× FLAG peptide (100 µg/ml, Sigma Aldrich)]. Concentration of purified protein was measured by BCA assay (Thermo Fisher Scientific #PI23225); protein was flash-frozen in liquid nitrogen and stored in elution buffer at -80°C. A typical preparation yielded 1 mg of eIF2 from a 12-liter culture.

GDP exchange assay

In vitro detection of GDP binding to eIF2 was adapted from a published protocol for a fluorescence intensity-based assay describing dissociation of eIF2 and nucleotide (29). We modified the procedure to establish both loading and unloading assays for fluorescent GDP.

For the “GDP loading assay,” purified eIF2 (200 pmol) was incubated with a molar equivalent Bodipy-FL-GDP (Thermo Fisher Scientific) in assay buffer (20 mM HEPES, pH 7.5, 100 mM KCl, 5 mM MgCl₂, 1 mM TCEP, and 1 mg/ml bovine serum albumin) to a volume of 18 µl in 384 square-well black-walled, clear-bottom polystyrene assay plates (Corning). The reaction was initiated by addition of 2 µl of buffer or purified eIF2B under various conditions to compare nucleotide exchange rates. For comparison of “purified decamer” rates, eIF2B($\alpha\beta\gamma\delta\epsilon$)₂ (2 pmol) was preincubated in 0.1% NMP or 0.1% NMP and 2 µM ISIRIB for 15 min. These concentrations of vehicle and ISIRIB were used throughout, unless otherwise specified. To ensure equal concentrations of GEF catalytic sites in all experiments, comparisons with tetramer used eIF2B($\beta\gamma\delta\epsilon$) (4 pmol). “Assembled decamer” was formed by incubating eIF2B($\beta\gamma\delta\epsilon$) (4 pmol) and eIF2B(α_2) (2 pmol) for 15 min in the presence or absence of ISIRIB prior to mixing with substrate eIF2. For the “GDP unloading assay,” each reaction was initiated by addition of excess unlabeled GDP (200 nmol). Fluorescence intensity for both loading and unloading assays was recorded every 10 s for 60 or 100 min using a TECAN Infinite M200 Pro plate reader (excitation wavelength: 495 nm, bandwidth 5 nm, emission wavelength: 512 nm, bandwidth: 5 nm). Data collected were fit to a first-order exponential.

Analytical ultracentrifugation

Analytical ultracentrifugation sedimentation velocity experiments were conducted using the ProteomeLab XL-I system (Beckman Coulter) with a Ti60 rotor. Protein samples were loaded into cells in a buffer containing 20 mM HEPES-KOH, pH 7.5, 150 mM KCl, 1 mM TCEP, and 5 mM MgCl₂. All runs were conducted at 20°C with a rotor speed of 40,000 rpm. Sedimentation was monitored at an absorbance of 280 nm. Subsequent data analysis was conducted with Sedfit (49) using a non-model-based continuous c(s) distribution corrected for time-invariant (TI) and radial-invariant (RI) noise.

Sucrose gradients

Protocol was adapted from a previous study (28). Sucrose gradients (5 to 20%, w/v) were prepared by tilted-tube rotation on the Gradient Master 107ip (Biocomp) in a high-salt buffer (20 mM HEPES-KOH, pH 7.5, 400 mM KCl, 1 mM TCEP, and 5 mM MgCl₂). Protein samples contained 1 μM eIF2B(βδγϵ), 500 nM eIF2B(α₂), and 500 nM ISRIB/analog (added from a 500 μM stock solution in NMP to yield a final NMP concentration of 0.1%). For each gradient, 200 μl of sample was loaded and centrifuges in a SW55 rotor (Beckman) for 14 hours at 40,000 rpm, 4°C. Thirteen fractions of 400 μl were collected by aspirating from the top of the gradient, and protein was precipitated by addition of trichloroacetic acid to 15%. After incubation for 90 min on ice, the protein precipitate was collected by centrifugation, and the pellet was resuspended in SDS loading buffer, loaded on a 10% SDS-polyacrylamide gel (Bio-Rad), and after electrophoresis stained with Coomassie Blue. Stained gels were then imaged on a ChemiDoc XRS+ imaging system (Bio-Rad). Quantification of gels was conducted in ImageJ. Fraction of total eIF2B(βγδϵ) in each of 13 lanes were quantified using a built-in gel-analyzer function. Area under each densitometry plot was calculated and divided by the sum of all areas measured from lanes 1 to 13 to obtain “fraction of eIF2B(βγδϵ).”

In-cell luciferase assays

Luciferase assays were conducted using a HEK293T cell line carrying an ATF4 luciferase reporter (18, 28). Cells were plated at a density of 30,000 cells per well in a 96-well polylysine-coated plate (Greiner Bio-One). Cells were treated the next day with tunicamycin (1 μg/ml) and varying ISRIB concentrations for 7 hours. Luciferase activity was then assayed using One Glo (Promega) and luminescence quantified in a SpectraMax M5 (Molecular Devices).

REFERENCES AND NOTES

- R. P. Dalton, D. B. Lyons, S. Lomvardas, Co-opting the unfolded protein response to elicit olfactory receptor feedback. *Cell* **155**, 321–332 (2013). doi: [10.1016/j.cell.2013.09.033](https://doi.org/10.1016/j.cell.2013.09.033); pmid: [24120133](https://pubmed.ncbi.nlm.nih.gov/24120133/)
- M. Costa-Mattoli et al., Translational control of hippocampal synaptic plasticity and memory by the eIF2α kinase GCN2. *Nature* **436**, 1166–1173 (2005). doi: [10.1038/nature03897](https://doi.org/10.1038/nature03897); pmid: [16121183](https://pubmed.ncbi.nlm.nih.gov/16121183/)
- D. H. Munn et al., GCN2 kinase in T cells mediates proliferative arrest and anergy induction in response to indoleamine 2,3-dioxygenase. *Immunity* **22**, 633–642 (2005). doi: [10.1016/j.immuni.2005.03.013](https://doi.org/10.1016/j.immuni.2005.03.013); pmid: [15894280](https://pubmed.ncbi.nlm.nih.gov/15894280/)
- N. C. Wortham, M. Martinez, Y. Gordiyenko, C. V. Robinson, C. G. Proud, Analysis of the subunit organization of the eIF2B complex reveals new insights into its structure and regulation. *FASEB J.* **28**, 2225–2237 (2014). doi: [10.1096/fj.13-243329](https://doi.org/10.1096/fj.13-243329); pmid: [24532666](https://pubmed.ncbi.nlm.nih.gov/24532666/)
- Y. Gordiyenko et al., eIF2B is a decameric guanine nucleotide exchange factor with a γ2ε2 tetrameric core. *Nat. Commun.* **5**, 3902 (2014). doi: [10.1038/ncomms4902](https://doi.org/10.1038/ncomms4902); pmid: [24852487](https://pubmed.ncbi.nlm.nih.gov/24852487/)
- A. M. Bogorad et al., Insights into the architecture of the eIF2Bα/β/δ regulatory subcomplex. *Biochemistry* **53**, 3432–3445 (2014). doi: [10.1021/ja121173](https://doi.org/10.1021/ja121173); pmid: [24811713](https://pubmed.ncbi.nlm.nih.gov/24811713/)
- B. Kuhle, N. K. Eulig, R. Ficner, Architecture of the eIF2B regulatory subcomplex and its implications for the regulation of guanine nucleotide exchange on eIF2. *Nucleic Acids Res.* **43**, 9994–10014 (2015). pmid: [26384431](https://pubmed.ncbi.nlm.nih.gov/26384431/)
- K. Kashiwagi et al., Crystal structure of eukaryotic translation initiation factor 2B. *Nature* **531**, 122–125 (2016). doi: [10.1038/nature16991](https://doi.org/10.1038/nature16991); pmid: [26901872](https://pubmed.ncbi.nlm.nih.gov/26901872/)
- E. Gomez, S. S. Mohammad, G. D. Pavitt, Characterization of the minimal catalytic domain within eIF2B: The guanine-nucleotide exchange factor for translation initiation. *EMBO J.* **21**, 5292–5301 (2002). doi: [10.1093/emboj/cdf515](https://doi.org/10.1093/emboj/cdf515); pmid: [12356745](https://pubmed.ncbi.nlm.nih.gov/12356745/)
- W. Yang, A. G. Hinnebusch, Identification of a regulatory subcomplex in the guanine nucleotide exchange factor eIF2B that mediates inhibition by phosphorylated eIF2. *Mol. Cell. Biol.* **16**, 6603–6616 (1996). doi: [10.1128/MCB.16.11.6603](https://doi.org/10.1128/MCB.16.11.6603); pmid: [8887689](https://pubmed.ncbi.nlm.nih.gov/8887689/)
- G. D. Pavitt, K. V. Ramaiah, S. R. Kimball, A. G. Hinnebusch, eIF2 independently binds two distinct eIF2B subcomplexes that catalyze and regulate guanine-nucleotide exchange. *Genes Dev.* **12**, 514–526 (1998). doi: [10.1101/gad.12.4.514](https://doi.org/10.1101/gad.12.4.514); pmid: [9472020](https://pubmed.ncbi.nlm.nih.gov/9472020/)
- T. Krishnamoorthy, G. D. Pavitt, F. Zhang, T. E. Dever, A. G. Hinnebusch, Tight binding of the phosphorylated α subunit of initiation factor 2 (eIF2α) to the regulatory subunits of guanine nucleotide exchange factor eIF2B is required for inhibition of translation initiation. *Mol. Cell. Biol.* **21**, 5018–5030 (2001). doi: [10.1128/MCB.21.15.5018-5030.2001](https://doi.org/10.1128/MCB.21.15.5018-5030.2001); pmid: [11438658](https://pubmed.ncbi.nlm.nih.gov/11438658/)
- A. G. Hinnebusch, J. R. Lorsch, The mechanism of eukaryotic translation initiation: New insights and challenges. *Cold Spring Harb. Perspect. Biol.* **4**, a011544 (2012). doi: [10.1101/cshperspect.a011544](https://doi.org/10.1101/cshperspect.a011544); pmid: [22815232](https://pubmed.ncbi.nlm.nih.gov/22815232/)
- A. G. Hinnebusch, The scanning mechanism of eukaryotic translation initiation. *Annu. Rev. Biochem.* **83**, 779–812 (2014). doi: [10.1146/annurev-biochem-060713-035802](https://doi.org/10.1146/annurev-biochem-060713-035802); pmid: [24499181](https://pubmed.ncbi.nlm.nih.gov/24499181/)
- H. P. Harding et al., Regulated translation initiation controls stress-induced gene expression in mammalian cells. *Mol. Cell* **6**, 1099–1108 (2000). doi: [10.1016/S1097-2765\(00\)00108-8](https://doi.org/10.1016/S1097-2765(00)00108-8); pmid: [11106749](https://pubmed.ncbi.nlm.nih.gov/11106749/)
- K. M. Vatter, R. C. Wek, Reinitiation involving upstream ORFs regulates ATF4 mRNA translation in mammalian cells. *Proc. Natl. Acad. Sci. U.S.A.* **101**, 11269–11274 (2004). doi: [10.1073/pnas.0400541101](https://doi.org/10.1073/pnas.0400541101); pmid: [15277680](https://pubmed.ncbi.nlm.nih.gov/15277680/)
- H. P. Harding et al., An integrated stress response regulates amino acid metabolism and resistance to oxidative stress. *Mol. Cell* **11**, 619–633 (2003). doi: [10.1016/S1097-2765\(03\)00105-9](https://doi.org/10.1016/S1097-2765(03)00105-9); pmid: [12667446](https://pubmed.ncbi.nlm.nih.gov/12667446/)
- C. Sidrauski et al., Pharmacological brake-release of mRNA translation enhances cognitive memory. *eLife* **2**, e00498 (2013). doi: [10.7554/eLife.00498](https://doi.org/10.7554/eLife.00498); pmid: [23741617](https://pubmed.ncbi.nlm.nih.gov/23741617/)
- C. Sidrauski, A. M. McGeachy, N. T. Ingolia, P. Walter, The small molecule ISRIB reverses the effects of eIF2α phosphorylation on translation and stress granule assembly. *eLife* **4**, (2015). doi: [10.7554/eLife.05033](https://doi.org/10.7554/eLife.05033)
- G. V. Di Prisco et al., Translational control of mGluR-dependent long-term depression and object-place learning by eIF2α. *Nat. Neurosci.* **17**, 1073–1082 (2014). doi: [10.1038/nn.3754](https://doi.org/10.1038/nn.3754); pmid: [24974795](https://pubmed.ncbi.nlm.nih.gov/24974795/)
- H. P. Harding, D. Ron, in *Translational Control in Biology and Medicine*, M. B. Mathews, N. Sonenberg, J. W. B. Hershey, Eds. (Cold Spring Harbor Laboratory Press, 2007), pp. 345–368.
- P. Remondelli, M. Renna, The endoplasmic reticulum unfolded protein response in neurodegenerative disorders and its potential therapeutic significance. *Front. Mol. Neurosci.* **10**, 187 (2017). doi: [10.3389/fnmol.2017.00187](https://doi.org/10.3389/fnmol.2017.00187); pmid: [28670265](https://pubmed.ncbi.nlm.nih.gov/28670265/)
- J. Obacz et al., Endoplasmic reticulum proteostasis in glioblastoma—From molecular mechanisms to therapeutic perspectives. *Sci. Signal.* **10**, eal2323 (2017). doi: [10.7554/eLife.05033](https://doi.org/10.7554/eLife.05033)
- G. Martinez, C. Duran-Aniotz, F. Cabral-Miranda, J. P. Vivar, C. Hetz, Endoplasmic reticulum proteostasis impairment in aging. *Aging Cell* **16**, 615–623 (2017). doi: [10.1111/acer.12599](https://doi.org/10.1111/acer.12599); pmid: [28436203](https://pubmed.ncbi.nlm.nih.gov/28436203/)
- P. A. J. Leegwater et al., Subunits of the translation initiation factor eIF2B are mutant in leukoencephalopathy with vanishing white matter. *Nat. Genet.* **29**, 383–388 (2001). doi: [10.1038/ng764](https://doi.org/10.1038/ng764); pmid: [11704758](https://pubmed.ncbi.nlm.nih.gov/11704758/)
- M. Halliday et al., Partial restoration of protein synthesis rates by the small molecule ISRIB prevents neurodegeneration without pancreatic toxicity. *Cell Death Dis.* **6**, e1672–e1679 (2015). doi: [10.1038/cddis.2015.49](https://doi.org/10.1038/cddis.2015.49); pmid: [25741597](https://pubmed.ncbi.nlm.nih.gov/25741597/)
- A. Chou et al., Inhibition of the integrated stress response reverses cognitive deficits after traumatic brain injury. *Proc. Natl. Acad. Sci. U.S.A.* **114**, E6420–E6426 (2017). doi: [10.1073/pnas.1707661114](https://doi.org/10.1073/pnas.1707661114); pmid: [28696288](https://pubmed.ncbi.nlm.nih.gov/28696288/)
- C. Sidrauski et al., Pharmacological dimerization and activation of the exchange factor eIF2B antagonizes the integrated stress

- response. *eLife* **4**, e07314 (2015). doi: [10.7554/eLife.07314](https://doi.org/10.7554/eLife.07314); pmid: [25875391](https://pubmed.ncbi.nlm.nih.gov/25875391/)
- Y. Sekine et al., Mutations in a translation initiation factor identify the target of a memory-enhancing compound. *Science* **348**, 1027–1030 (2015). doi: [10.1126/science.aaa6986](https://doi.org/10.1126/science.aaa6986); pmid: [25858979](https://pubmed.ncbi.nlm.nih.gov/25858979/)
 - R. A. de Almeida et al., A yeast purification system for human translation initiation factors eIF2 and eIF2B: and their use in the diagnosis of CACH/VWM disease. *PLOS ONE* **8**, e53958 (2013). doi: [10.1371/journal.pone.0053958](https://doi.org/10.1371/journal.pone.0053958); pmid: [23335982](https://pubmed.ncbi.nlm.nih.gov/23335982/)
 - A. G. Rowlands, R. Panniers, E. C. Henshaw, The catalytic mechanism of guanine nucleotide exchange factor action and competitive inhibition by phosphorylated eukaryotic initiation factor 2. *J. Biol. Chem.* **263**, 5526–5533 (1988). pmid: [3356695](https://pubmed.ncbi.nlm.nih.gov/3356695/)
 - D. D. Williams, N. T. Price, A. J. Loughlin, C. G. Proud, Characterization of the mammalian initiation factor eIF2B complex as a GDP dissociation stimulator protein. *J. Biol. Chem.* **276**, 24697–24703 (2001). doi: [10.1074/jbc.M011788200](https://doi.org/10.1074/jbc.M011788200); pmid: [11323413](https://pubmed.ncbi.nlm.nih.gov/11323413/)
 - B. L. Craddock, C. G. Proud, The α-subunit of the mammalian guanine nucleotide-exchange factor eIF-2B is essential for catalytic activity in vitro. *Biochem. Biophys. Res. Commun.* **220**, 843–847 (1996). doi: [10.1006/bbrc.1996.0495](https://doi.org/10.1006/bbrc.1996.0495); pmid: [8607853](https://pubmed.ncbi.nlm.nih.gov/8607853/)
 - B. R. Hearn et al., Structure-activity studies of Bis-O-aryl glycolamides: Inhibitors of the integrated stress response. *ChemMedChem* **11**, 870–880 (2016). doi: [10.1002/cmdc.201500483](https://doi.org/10.1002/cmdc.201500483); pmid: [26789650](https://pubmed.ncbi.nlm.nih.gov/26789650/)
 - A. F. Zyryanova et al., Binding of the integrated stress response inhibitor ISRIB reveals a regulatory site in the nucleotide exchange factor, eIF2B. *Science* **359**, 1533–1536 (2018).
 - S. Q. Zheng et al., MotionCor2: Anisotropic correction of beam-induced motion for improved cryo-electron microscopy. *Nat. Methods* **14**, 331–332 (2017). doi: [10.1038/nmeth.4193](https://doi.org/10.1038/nmeth.4193); pmid: [28250466](https://pubmed.ncbi.nlm.nih.gov/28250466/)
 - K. Zhang, Gctf: Real-time CTF determination and correction. *J. Struct. Biol.* **193**, 1–12 (2016). doi: [10.1016/j.jsb.2015.11.003](https://doi.org/10.1016/j.jsb.2015.11.003); pmid: [26592709](https://pubmed.ncbi.nlm.nih.gov/26592709/)
 - D. Kimanius, B. O. Forsberg, S. H. Scheres, E. Lindahl, Accelerated cryo-EM structure determination with parallelisation using GPUs in RELION-2. *eLife* **5**, e18722 (2016). doi: [10.7554/eLife.18722](https://doi.org/10.7554/eLife.18722); pmid: [27845625](https://pubmed.ncbi.nlm.nih.gov/27845625/)
 - A. Punjani, J. L. Rubinstein, D. J. Fleet, M. A. Brubaker, cryoSPARC: Algorithms for rapid unsupervised cryo-EM structure determination. *Nat. Methods* **14**, 290–296 (2017). doi: [10.1038/nmeth.4169](https://doi.org/10.1038/nmeth.4169); pmid: [28165473](https://pubmed.ncbi.nlm.nih.gov/28165473/)
 - N. Grigorieff, Frealign: An exploratory tool for single-particle cryo-EM. *Methods Enzymol.* **579**, 191–226 (2016). doi: [10.1016/bs.mie.2016.04.013](https://doi.org/10.1016/bs.mie.2016.04.013); pmid: [27572728](https://pubmed.ncbi.nlm.nih.gov/27572728/)
 - E. F. Pettersen et al., UCSF Chimera—a visualization system for exploratory research and analysis. *J. Comput. Chem.* **25**, 1605–1612 (2004). doi: [10.1002/jcc.20084](https://doi.org/10.1002/jcc.20084); pmid: [15264254](https://pubmed.ncbi.nlm.nih.gov/15264254/)
 - L. A. Kelley, S. Mezulis, C. M. Yates, M. N. Wass, M. J. E. Sternberg, The PyMol web portal for protein modeling, prediction and analysis. *Nat. Protoc.* **10**, 845–858 (2015). doi: [10.1038/nprot.2015.053](https://doi.org/10.1038/nprot.2015.053); pmid: [25950237](https://pubmed.ncbi.nlm.nih.gov/25950237/)
 - T. B. Hiyyama, T. Ito, H. Imataka, S. Yokoyama, Crystal structure of the α subunit of human translation initiation factor 2B. *J. Mol. Biol.* **392**, 937–951 (2009). doi: [10.1016/j.jmb.2009.07.054](https://doi.org/10.1016/j.jmb.2009.07.054); pmid: [19631657](https://pubmed.ncbi.nlm.nih.gov/19631657/)
 - N. W. Moriarty, R. W. Grosse-Kunstleve, P. D. Adams, Electronic Ligand Builder and Optimization Workbench (eLBOW): A tool for ligand coordinate and restraint generation. *Acta Crystallogr. D* **65**, 1074–1080 (2009). doi: [10.1107/S0907444909029436](https://doi.org/10.1107/S0907444909029436); pmid: [19770504](https://pubmed.ncbi.nlm.nih.gov/19770504/)
 - P. Emsley, B. Lohkamp, W. G. Scott, K. Cowtan, Features and development of Coot. *Acta Crystallogr. D* **66**, 486–501 (2010). doi: [10.1107/S0907444910007493](https://doi.org/10.1107/S0907444910007493); pmid: [20383002](https://pubmed.ncbi.nlm.nih.gov/20383002/)
 - P. D. Adams et al., PHENIX: A comprehensive Python-based system for macromolecular structure solution. *Acta Crystallogr. D* **66**, 213–221 (2010). doi: [10.1107/S0907444909052925](https://doi.org/10.1107/S0907444909052925); pmid: [20124702](https://pubmed.ncbi.nlm.nih.gov/20124702/)
 - V. B. Chen et al., MolProbity: All-atom structure validation for macromolecular crystallography. *Acta Crystallogr. D* **66**, 12–21 (2010). doi: [10.1107/S0907444909042073](https://doi.org/10.1107/S0907444909042073); pmid: [20057044](https://pubmed.ncbi.nlm.nih.gov/20057044/)
 - S. J. Ludtke, Single-particle refinement and variability analysis in EMAN2.1. *Methods Enzymol.* **579**, 159–189 (2016). doi: [10.1016/bs.mie.2016.05.001](https://doi.org/10.1016/bs.mie.2016.05.001); pmid: [27572727](https://pubmed.ncbi.nlm.nih.gov/27572727/)
 - P. Schuck, Size-distribution analysis of macromolecules by sedimentation velocity ultracentrifugation and lamm equation modeling. *Biophys. J.* **78**, 1606–1619 (2000). doi: [10.1016/S0006-3495\(00\)76713-0](https://doi.org/10.1016/S0006-3495(00)76713-0); pmid: [10692345](https://pubmed.ncbi.nlm.nih.gov/10692345/)

ACKNOWLEDGMENTS

We dedicate this work to the memory of Günter Blobel (1936–2018) and his foundational contributions to cell biology. We thank J. Peschek, E. Karagöz, R. Stroud, J. Fraser, G. Narlikar, R. Vale, A. Briot, N. Schirle Oakdale, N. Talledge, P. Tsai, Ni Mu, J. Choe, C. Upjohn, M. Jacobson, C. Kalyanaraman, and the Walter and Frost labs for reagents, technical advice, and helpful discussions; M. Braunfeld, D. Bulkley, and A. Myasnikov of the UCSF Center for Advanced CryoEM and D. Toso and P. Tobias of the Berkeley Bay Area CryoEM Facility, which are supported by NIH grants S10OD020054 and S10OD021741 and the Howard Hughes Medical Institute (HHMI); Z. Yu, R. Huang, and C. Hong of the CryoEM Facility at the HHMI Janelia Research Campus; the QB3 shared cluster and NIH grant S10OD021596-01 for computational support; and G. Pavitt for the GP6452 yeast strain used in the purification of eIF2. The Titan X Pascal used for this research was donated by the NVIDIA Corporation.

Funding: Supported by a HHMI Faculty Scholar grant, the Searle Scholars Program, and NIH grant 1DP2GM110772-01 (A.F.) and by Calico Life Sciences LLC, the Rogers Family Foundation, the Weill Foundation, and HHMI (P.W.). A.F. is a Chan Zuckerberg Biohub Investigator, and P.W. is an Investigator of HHMI. **Author contributions:** Conception and design, analysis and interpretation of data: J.C.T., L.M.V., A.A.A., A.R.R., A.F., and P.W.; acquisition of data: J.C.T., L.M.V., A.A.A., P.J., and H.C.N.; writing (original draft): J.C.T., L.M.V., A.A.A., A.F., and P.W.; Writing (review and editing): J.C.T., L.M.V., A.A.A., P.J., H.C.N., A.R.R., A.F., and P.W. **Competing interests:** P.W. and A.R.R. are inventors on U.S. Patent 9708247 held by the Regents of the University of California that describes ISRIB and its analogs. Rights to the invention have been licensed by UCSF to Calico. **Accession numbers:** Accession numbers for the human eIF2B structures determined with FREALIGN, cryoSPARC, and RELION, respectively, are as follows: EMD-7442, EMD-7443, EMD-7444 (density maps; Electron

Microscopy Data Bank) and 6CAJ (coordinates of atomic models; Protein Data Bank). **Data availability:** All data needed to evaluate the conclusions in the paper are present in the paper and/or the supplementary materials, and the structural data is available in public databases. All of the raw cryo-EM particle images are available upon request. The GP6452 yeast strain is available under a material transfer agreement with the University of Manchester.

SUPPLEMENTARY MATERIALS

www.sciencemag.org/content/359/6383/aaq0939/suppl/DC1

Supplementary Methods

Figs. S1 to S9

Tables S1 to S3

14 November 2017; accepted 9 February 2018
10.1126/science.aaq0939

RESEARCH ARTICLE

NITROGEN FIXATION

A bound reaction intermediate sheds light on the mechanism of nitrogenase

Daniel Sippel,¹ Michael Rohde,¹ Julia Netzer,¹ Christian Trncik,¹ Jakob Gies,¹ Katharina Grunau,¹ Ivana Djurdjevic,¹ Laure Decamps,¹ Susana L. A. Andrade,^{1,2} Oliver Einsle^{1,2,3*}

Reduction of N₂ by nitrogenases occurs at an organometallic iron cofactor that commonly also contains either molybdenum or vanadium. The well-characterized resting state of the cofactor does not bind substrate, so its mode of action remains enigmatic. Carbon monoxide was recently found to replace a bridging sulfide, but the mechanistic relevance was unclear. Here we report the structural analysis of vanadium nitrogenase with a bound intermediate, interpreted as a μ^2 -bridging, protonated nitrogen that implies the site and mode of substrate binding to the cofactor. Binding results in a flip of amino acid glutamine 176, which hydrogen-bonds the ligand and creates a holding position for the displaced sulfide. The intermediate likely represents state E₆ or E₇ of the Thorneley-Lowe model and provides clues to the remainder of the catalytic cycle.

Nitrogen bioavailability is limited by the chemical stability of N₂ gas, making modern agriculture dependent on inorganic nitrogen fertilizers that have boosted crop yields during the 20th century to enable unprecedented population growth (1). Today, excessive fertilization is leading to increasing environmental release of reactive nitrogen species that affect water quality and human health (2). Alternative strategies for sustained crop production are sought, and among these, the enzyme nitrogenase—the sole biological solution for reducing atmospheric N₂—is of outstanding importance. It provides fixed nitrogen in the exact quantities required and operates at ambient conditions, fueled by adenosine triphosphate (ATP) (3, 4). Nitrogenase is an oxygen-sensitive metalloenzyme consisting of a reductase, Fe protein, and a catalytic dinitrogenase that dynamically form a complex for every single-electron transfer event, triggered by ATP hydrolysis in Fe protein (4–6). All nitrogenases share a single evolutionary origin, but they group into three different classes according to the metal ions used at the catalytic site (7). In the most widespread molybdenum nitrogenases, this site is FeMo cofactor, a [Mo:7Fe:9S:C]:homocitrate cluster with a central carbide for structural rigidity (6, 8), an apical Mo³⁺ (9), and three characteristic “belt” sulfides termed S2B, S3A, and S5A (fig. S1A) (10). Alternative nitrogenases are produced from distinct gene

clusters under molybdenum limitation and replace molybdenum with vanadium (FeV cofactor) or iron (FeFe cofactor). FeV cofactor, a [V:7Fe:8S:C]:CO₃:homocitrate moiety in VFe protein, resembles FeMo cofactor but features a carbonate replacing S3A (fig. S1B) (11). Mo and V nitrogenases differ in potential and reactivity (12), most notably in that the MoFe protein inhibitor carbon monoxide (CO) is reduced by VFe protein to various hydrocarbons, in analogy to Fischer-Tropsch chemistry (13).

Before this work, all nitrogenases were isolated in a stable resting state, and because reduction requires the dynamic action of Fe protein, structural analysis to date was largely limited to this form. Mechanistic studies pioneered by Bulen and Lecomte showed H₂ to be a by-product of N₂ reduction (14), and Simpson and Burris found that it occurs at least stoichiometrically (15), leading Thorneley and Lowe (16) to outline an eight-electron catalytic cycle (states E₀ to E₇) for the six-electron reduction of N₂ and the concomitant generation of H₂. In the Thorneley-Lowe model, reduction of the enzyme by three or four electrons is required before N₂ binds in exchange for H₂ (fig. S2) (16, 17), whereby N₂ is the only substrate whose reduction is inhibited by H₂ (18). The question of how an already highly reduced cofactor accumulates three or four more electrons at isopotential was addressed by studying ligand binding to variants of MoFe protein, which suggested that electrons are stored as hydrides (H[−]) on the cluster surface (19, 20), in line with earlier findings that at no point would the cluster itself take up more than a single electron (21). In the critical E₄ state, two adjacent hydrides would undergo reductive elimination of H₂, leaving the metal

site reduced by two low-potential electrons that render it capable of binding and activating N₂ (22, 23). Based on a V70^{NifD} variant, Fe6 and the cluster face located beneath V70 and framed by Fe2, Fe3, Fe6, and Fe7 were indirectly implied as the site of N₂ binding (24). From this point, a deeper mechanistic understanding of nitrogenase catalysis thus awaits the assignment of actual molecular structures to reaction intermediates E₁ through E₇. When CO inhibition of Mo dinitrogenase was recently exploited to obtain the first ligand-bound structure of FeMo cofactor (25), CO replaced belt sulfide S2B, yielding a μ^2 -bridging metal carbonyl (fig. S1C). However, CO is a non-competitive inhibitor that binds to a less reduced form of the enzyme than N₂ does, presumably E₂ (26), and it was unclear how the observed binding mode related to N₂ catalysis. Importantly, although sulfide S2B was quantitatively replaced and was not detected in the immediate vicinity of the cofactor in the inhibited state, the subsequent removal of CO under turnover was sufficient to reinstate S2B and return the enzyme to the known resting state (25). The structure of VFe protein showed the E₀ state, with carbonate replacing sulfide S3A, whereas S2B remained unchanged (11). All of the different nitrogenases presumably share a common mechanism of dinitrogen activation and reduction. For further mechanistic insight, we thus set out to elucidate a nonresting state of the enzyme by x-ray crystallography.

Generation of a ligand-binding site on the cofactor

Previously, induction of VFe protein by Mo depletion and isolation in the presence of 2 to 5 mM Na₂S₂O₄ (11), serving as a reductant and O₂ scavenger, yielded pure enzyme and led to a structure at 1.35 Å of the resting state of FeV cofactor (11). We subsequently noted that if the isolation process was carried out swiftly and with a decreased amount of reductant, the intensity of electron paramagnetic resonance (EPR) signals—but not their position—changed characteristically (Fig. 1B). This gradual transition varied between preparations, but prolonged reduction with 20 mM dithionite consistently resulted in resting state spectra. Notably, both forms of the enzyme retained the same catalytic activity and reduced both acetylene and N₂ (fig. S3). Accordingly, decreasing the amount of reductant during protein isolation led to well-diffracting crystals of an uncharacterized state of V nitrogenase that we designate the “turnover” state. Several data sets were obtained to investigate the anomalous contributions of Fe and S, and diffraction data were collected at 1.2-Å resolution (fig. S4). VFe protein remained largely unchanged, including in particular the carbonate ligand bridging Fe4 and Fe5 of FeV cofactor, but the cluster contained a light atom replacing sulfide S2B.

The lability of the belt sulfides was established by the CO-inhibited structure of MoFe protein, but the fate of the released S2B remained unclear, and an anomalous difference density peak found at a distance of 21 Å from the cofactor was difficult to reconcile with an integral mechanistic

¹Institut für Biochemie, Albert-Ludwigs-Universität Freiburg, Albertstraße 21, 79104 Freiburg, Germany. ²BIOSS Centre for Biological Signalling Studies, Schänzlestraße 1, 79104 Freiburg, Germany. ³Freiburg Institute for Advanced Studies, 79104 Freiburg, Germany.

*Corresponding author. Email: einsle@biochemie.uni-freiburg.de

role of the sulfide exchange (25). Unfortunately, no structural data are available for the variants of Mo nitrogenase used for the cryo-annealing pulsed EPR studies that defined activated states (27). The ligand-bound form of VFe protein reported here provides a picture of a nitrogenase in a nonresting state obtained during N_2 turnover, with a previously uncharacterized μ^2 -bridging ligand to Fe2 and Fe6 displacing S2B (Figs. 1A and 2A). In contrast to the CO complex of FeMo cofactor (25), the displacement in VFe protein rearranged a nearby amino acid, glutamine 176 (Q176), which is conserved in all known structures of nitrogenases (Q191 in *Azotobacter vinelandii* MoFe protein; fig. S5). Its replacement by lysine abolished N_2 reduction and strongly diverted electron flux away from C_2H_2 toward H_2 (28, 29), but given that it pointed away from the cofactor, a role in catalysis remained unclear (fig. S5, C to H). In the turnover state, the side chain of Q176 rotated toward the FeV cofactor, placing the amide oxygen atom Oe1 at a distance of only 2.55 Å from the bridging light atom and 2.84 Å from imidazole Ne2 of residue histidine 180 (H180) (Fig. 2A), while retaining an H-bonding interaction with the α -carboxylate of homocitrate. The tight fixation of Oe1 of Q176 by three short hydrogen bonds would not be possible with a diatomic ligand at the cofactor, and glutamine rotation did not occur in the CO complex structure, where the carbonyl oxygen of the ligand is an exclusive H-bond acceptor (fig. S6) (25). It could also not be accommodated with S2B bridging Fe2 and Fe6

in the resting state of the enzyme, because the longer Fe–S distances of 2.3 Å compared with the distance to the light atom bound at 2.0 Å would leave no room for an inward-facing Q176 to form a direct hydrogen bond to H180 (Fig. 2B and fig. S7, A and B). Furthermore, the glutamine reorientation created a binding pocket within the protein cavity containing the cofactor, where we observed a new electron density maximum that was well modeled as a hydrosulfide anion (HS^-) (Fig. 1A). This makes the site a strong candidate for the long-sought temporary holding position for sulfide S2B close to the cofactor, which the CO complex did not reveal. To confirm the presence of HS^- , we collected diffraction data on the resting and ligand-bound states of VFe protein at 7000 eV (wavelength, 1.7711 Å) to maximize the anomalous scattering contribution of sulfur with respect to that of iron (Fig. 2, C and D). The resulting electron density maps show the disappearance of the anomalous signal at the bridging position in the cofactor and its reappearance 7.0 Å away, in the pocket created by the rotation of Q176 (Fig. 2C), whereas in the resting state, S2B was in place at the cofactor (Fig. 2D). In its holding position, S2B is H-bonded to the backbone amides of glycine 48 (3.13 Å) and Q176 (3.13 Å) that transiently stabilize its negative charge (Fig. 2A), reminiscent of an oxyanion hole in protease active sites (30).

We conclude that replacement of S2B at the cofactor is reversible and can occur during catalysis, with intermediate storage in a pocket pro-

vided by the side-chain swing of Q176, whose amide Oe1 interacts with the same residues in the resting state as HS^- does in the turnover state (Fig. 2, A and B). This defines an open active site at nitrogenase cofactor with free coordination sites for ligands at Fe2 and Fe6, residue H180 as a proton donor, and the inward-facing Oe1 of Q176 as an exclusive H-bond acceptor, marking its specific role in stabilizing protonated species. We assign the released sulfide as HS^- , given that rebinding at the conclusion of the reaction will be favored for a nucleophile.

Ligand binding to the active site

For our structure, cultures were harvested during diazotrophic growth, and neither cells nor isolated protein were exposed to CO, O_2 , or further substrates other than N_2 . At 1.2-Å resolution, we refrain from an assignment of the nature of the bridging ligand based solely on its electron density, but instead restrict our discussion to oxygen and nitrogen as chemically reasonable candidates. Bond distances at the cofactor were 2.01 ± 0.04 Å for the two Fe–X bonds and 2.55 Å for a short hydrogen bond to amide Oe1 of Q176. This implies a protonated ligand—either a μ -hydroxo (OH^-) or a μ -nitrido (HN^{2-}) species—in line with our electron density analysis (fig. S8 and supplementary materials) and as expected from diiron model compounds (31). These π -basic ligands would have a stabilizing effect, in particular with a more oxidized cluster, but are themselves fully reduced. μ -hydroxo represents the oxidation

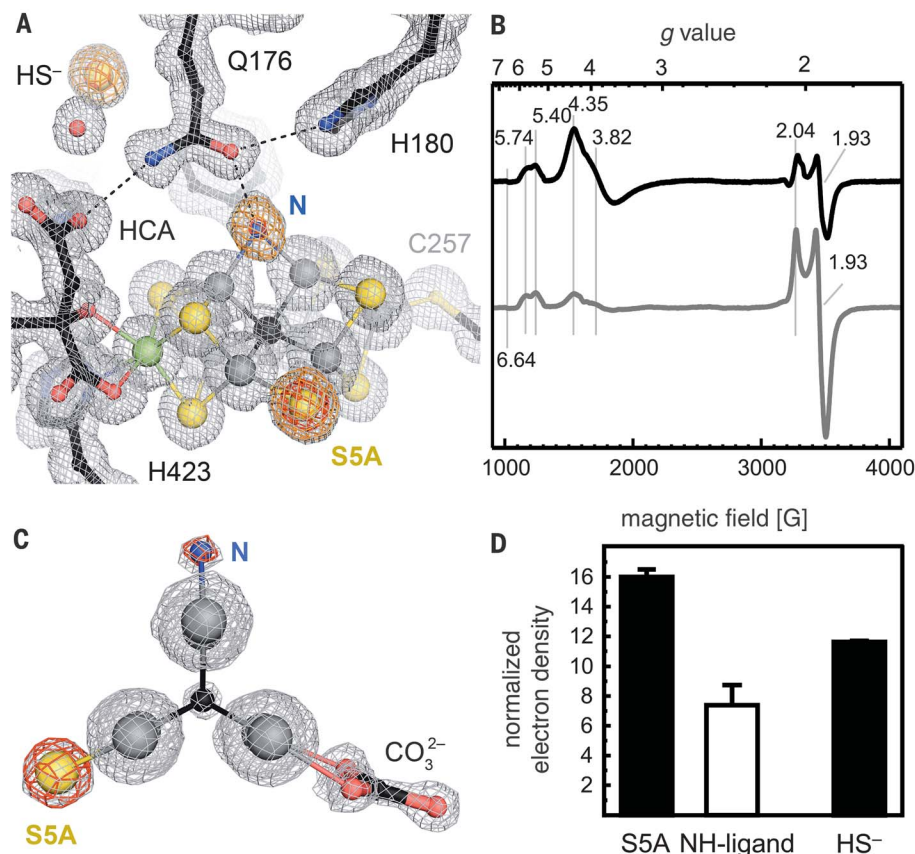


Fig. 1. Identification of a light atom ligand at FeV cofactor. (A) FeV cofactor and its immediate surroundings with residue Q176 in a flipped conformation, opening a binding site for sulfide S2B as HS^- . The bridging position of S2B at Fe2 and Fe6 is occupied by a light atom. A $2F_o - F_c$ omit electron density map calculated without the contribution of S2B, S5A, and the light atom is contoured at the 1σ level (gray) and is overlaid with $F_o - F_c$ omit maps contoured at 15σ (orange) and 25σ (red). C, cysteine. Here and throughout, spheres are color-coded as follows: gray, iron; black, carbon; green, vanadium; blue, nitrogen; yellow, sulfur. (B) X-band EPR spectra of *A. vinelandii* VFe protein as isolated in the turnover state (black) and the resting state (gray).

The known features of the spectrum change their relative intensities, but not their resonance energies. (C) View along the threefold pseudo-symmetry axis of FeV cofactor, highlighting the differences at the three belt positions. The omit maps [as shown in (A)] highlight the differences between the light N ligand and sulfide S5A. The $2F_o - F_c$ map (gray) is contoured at the 1σ level. (D) Integrated electron density at the three omitted positions (1-Å integration radius, normalized to the electron number of the fully occupied S5A). The maximum at Fe2 and Fe6 is very well defined and matches an N or NH ligand.

state of water and should be the more stable species. Although H_2O binding may be envisioned after the removal of S2B upon reduction to E_2 (discussed below), this would make water a competitive inhibitor of an enzymatic reaction, which would be biochemically peculiar, to say the least. O_2 , as an alternative source of oxygen, can be ruled out owing to strictly anoxic handling of the enzyme and the proven activity of turnover state preparations. Similarly, a μ -nitrido ligand represents nitrogen at the oxidation level of ammonia ($-\text{III}$), the product after the completed eight-electron reaction cycle. This would be an E_0 state of the reaction scheme, albeit with bound product rather than with the μ -sulfide S2B re-instated, and may correspond to an “ E_8 ” state previously reported as an interpretation of a spectroscopic intermediate “I” (32). In the case of our active preparations of VFe protein, this

would imply that the reinsertion of sulfide was not an integral part of the reaction cycle under high electron flux. However, an HN^{2-} complex is only two protonation events removed from releasing NH_3 , which should readily occur from H180, but we nevertheless find this state to be stable and persistent even on the time scale of protein crystallization. Together with the finding from EPR spectroscopy that turnover state preparations of VFe protein can be returned to the resting state by extended reduction (fig. S3B), this suggests that the observed structure is an earlier catalytic intermediate. Given that the state is paramagnetic (Fig. 2B), this should be E_6 , at a formal oxidation state of $-I$ for the bound nitrogen atom (Fig. 3, A and C), making the ligand formally a bridging nitrene. With its slightly distorted trigonal planar geometry (Fig. 3, A and B), this modification features an empty p_z -like orbital at

the nitrogen atom that also stabilizes the intermediate, this time through π -backdonation from both iron sites and with strong preference for a more reduced form of the cofactor. Nitrenes are unstable compounds, but the proximity of Fe2 and Fe6 to the central carbon in the cofactor—formally a C^{4-} —may imply that the iron ions are effectively more reduced, or even that the cluster is able to transiently transfer two electrons to the ligand. Such a redox shift would result in a two-electron oxidized cluster (still with spin $S = 3/2$) and a stable HN^{2-} ligand as described above that nevertheless would represent state E_6 rather than the resting state E_0 . Although speculative, this interpretation generates testable hypotheses for spectroscopic and theoretical studies that should unequivocally clarify the nature of the bound ligand.

From E_6 , two single-electron reduction steps return the enzyme to the known resting state E_0 , with S2B rebound and product NH_3 released. Assuming that the cluster itself is oxidized by two electrons at this stage, these reductions will take place on the cofactor, with each step successively decreasing the stabilizing effect of π -donation by the HN^{2-} ligand, rendering it prone to further protonation that will break the stabilizing, short hydrogen bond to Q176 to eventually release the bridging nitrogen in favor of end-on binding to either Fe2 or Fe6. We hypothesize that NH_2 will be bound at Fe2, as only there it can form a new short hydrogen bond to H180, with the imidazole N ϵ 2 of this histidine as a possible proton donor (Fig. 3D). Q176 then loses both the ligand atom and H180 as H-bonding partners, whereas Fe6 gains a free coordination site for a nucleophilic attack by HS^- . This causes the glutamine to return to its resting position, concomitant with rebinding of the hydrogen sulfide ligand at Fe6. The final electron transfer to E_0 then enables the dissociation of NH_3 , with the Fe6-SH group able to provide a proton to reform the μ^2 belt sulfide of the resting state E_0 (Fig. 3E). In this model, S2B is instrumental for product dissociation, in line with suggestions from theory (33).

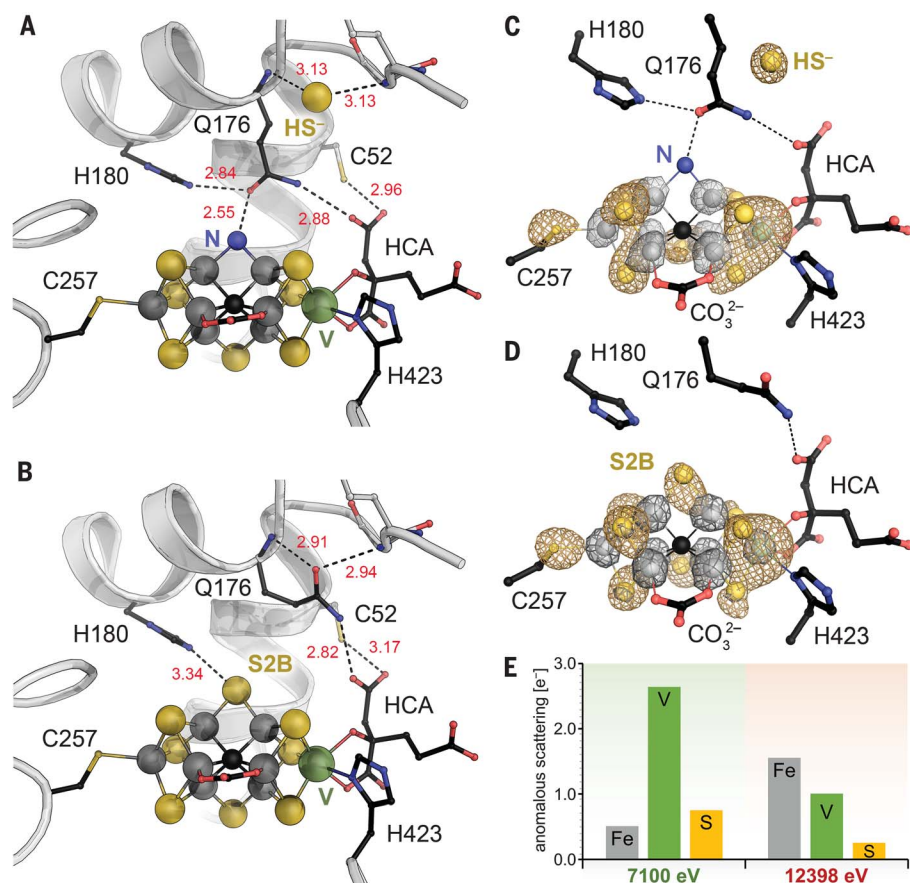


Fig. 2. Ligand-bound V nitrogenase in a turnover state. (A) FeV cofactor in the turnover state. Sulfide S2B is exchanged for a nitrogen ligand, and residue Q176 has rearranged, revealing a holding site for sulfide. (B) FeV cofactor in the resting state (Protein Data Bank ID, 5N6Y). S2B is in place, and Q176 occupies the holding site. Bond distances are in angstroms. (C) Turnover-state FeV cofactor, with anomalous difference electron density maps contoured at the 5σ level and collected at x-ray energies of 7000 eV (tan) for sulfur and 12398 eV (gray) for iron. The holding site shows a prominent peak for sulfur, whereas the bridging position at Fe2 and Fe6 does not. (D) In an analogous map for the resting-state enzyme, no electron density peak is observed in the holding site, but the bridging sulfide S2B is found at the cluster. (E) Relative anomalous scattering contributions of Fe, V, and S at the two energies used in (C) and (D). At 7100 eV, S shows a stronger signal than Fe, whereas at 12398 eV, the situation is the reverse. V is a strong contributor at both energies and the most dominant at 7100 eV.

Mechanistic axioms for nitrogenase catalysis

The structure of a nitrogenase turnover state establishes sulfide exchange in a bridging manner at Fe2 and Fe6 as part of the reaction mechanism and reveals the role of Q176 as an H-bond acceptor and a stabilizing structural element for intermediates of N_2 reduction. Although the power of x-ray diffraction to identify electronic states of individual atoms is limited, our structure has implications for earlier stages of the reaction cycle. Importantly, in spite of differences in activity and substrate range, all classes of nitrogenases are presumed to follow the same mechanistic pathway for N_2 reduction, and we therefore carefully extend data gained on MoFe protein to VFe protein. Also, the catalytic turnover of nitrogenase is rate-limited by electron delivery from Fe protein, which in turn is limited by the dissociation of phosphate (34). This implies that each E state must be sufficiently stable to persist until the

next electron transfer occurs. We thus avoid unfavorable geometries or unusual coordination numbers. Furthermore, bridging hydrides are thermodynamically more stable than terminal hydrides (35). Together with the demonstrated ability of nitrogenase cofactors to take up one electron only (21), the delivery of every second electron from Fe protein can give rise to a bridging hydride, and the reduction of substrate thus can be conceptually discussed in two-electron steps (24, 36). At the same time, proton supply from the protein surface to the cluster is straightforward once H180 is recognized as the prime proton donor in catalysis (fig. S9), as much as Q176 is a stabilizing H-bond acceptor whose inward movement is reversibly linked to S2B displacement.

Implications for N_2 reduction by nitrogenase

During the entire catalytic cycle, the cofactor oscillates between only two redox states, paramagnetic M^N (as isolated) and diamagnetic M^{-1} (one-electron-reduced). According to the current model of the electronic structure of the cofactor (fig. S10) (37), Fe2 and Fe6 are the most oxidized sites and are antiferromagnetically coupled to their respective neighbors (except for the apical Fe1 and Mo or V). Initially, electron transfer from Fe protein reduces Fe2 or Fe6, defining state E_1 . Further reduction to E_2 leads to the formation of a first hydride together with a proton. Bridging Fe2 and Fe6, this hydride should shift sulfide S2B out of the plane defined by Fe1, Fe2, Fe6, and Mo or V, as suggested previously (33). Alternatively, one or both Fe-S bonds to S2B may already be broken (Fig. 4A), in line with the presumed binding of CO at E_2 (26). An inward-facing Q176 might also stabilize a bridging hydride, but only after S2B moves to its holding site. If at this point the hydride is lost as H_2 owing to accidental protonation, an open, diferric binding site becomes available for CO but would not be sufficiently reduced for N_2 . States E_2 through E_4 can lose H^- by protonation to yield H_2 , rationalizing the observed nonproductive electron flux to this shunt product (fig. S2).

N_2 binding to cofactor occurs no earlier than at E_3 , where the association is reversible until further reduction, or at E_4 , from which the reaction is committed to proceed to ammonia release (38). We propose that E_3 retains the structural features of E_2 , but with one Fe site reduced to formal Fe^{2+} , rendering the state diamagnetic. From this, H_2 release would leave the cluster in a one-electron-reduced state with S2B removed and able to bind N_2 , but without constituting a reductive elimination and lacking a further electron for a bridging binding mode (Fig. 4A). This binding is reversible, with N_2 as a leaving group and the S2B sulfhydryl ready to reseal the binding site, returning the enzyme to the E_1 state. Alternatively, further productive reduction and protonation leads to the crucial E_4 state, where a second bridging hydride is formed. Guided by reasonable coordination geometries, we suggest that this occurs again between Fe2 and Fe6, ideally orienting both hydrides for subsequent

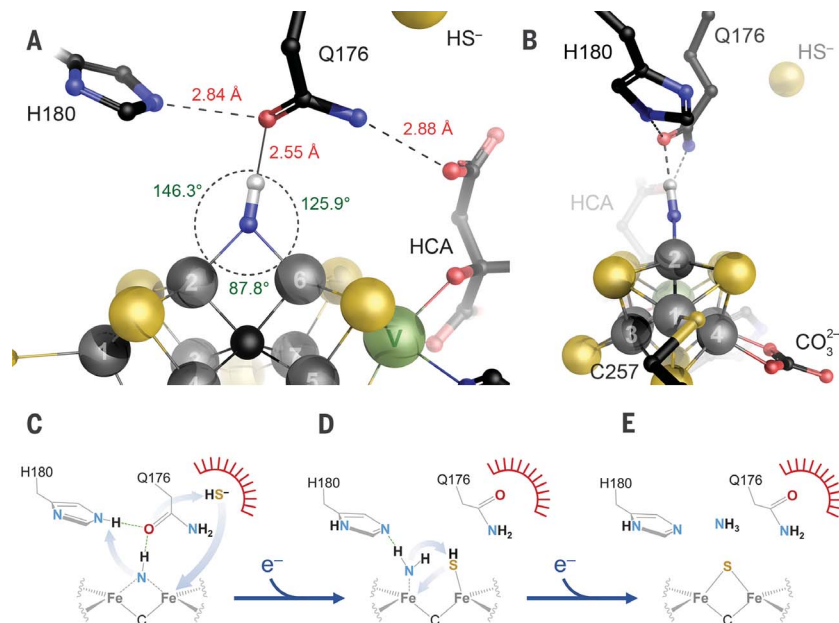


Fig. 3. Intermediate E_6 and the concluding steps of the nitrogenase reaction cycle. (A) Bond distances and angles in the structure of the E_6 intermediate, with implicit protonation of the ligand. (B) Side view of (A), highlighting the trigonal planar geometry of the nitrogen ligand. (C) Schematic representation of the E_6 state with the holding site for HS^- and implicit protonation. Blue arrows indicate rearrangements upon reduction. The red arc indicates the holding pocket for S2B. (D) Upon reduction of one Fe site in E_7 , the electron can be transferred to the bound ligand, leading to a second protonation, possibly from H180. The NH_2 ligand becomes monodentate, and nucleophilic HS^- rebinds to Fe6, causing Q176 to reorient to its resting-state position. (E) After the final reduction, N obtains a further proton, possibly from S2B, and dissociates as product ammonia, and S2B regains the μ -bridging position of the resting state E_0 . Alternatively, steps (D) and (E) may occur in a concerted fashion only after the second electron is transferred.

reductive elimination of H_2 , which leaves the cofactor in an activated, two-electron-reduced state able to bind N_2 (Fig. 4A). The antiferromagnetic coupling of Fe2 and Fe6 hereby determines that the residual electrons reside on different Fe centers rather than on a single, superreduced site (fig. S11). In its inward-facing conformation, the amide Oe1 atom of Q176 may stabilize the bridging hydrides, but upon elimination of H_2 , it readily makes room for an incoming N_2 molecule that undergoes a rapid two-electron reduction from both iron sites, leading to a bridging ligation, similar to the CO complex observed for MoFe protein (25). A fundamental difference between the ligands is that the oxygen atom of CO can exclusively serve as an H-bond acceptor, as it does for histidine (fig. S6), but cannot interact with Oe1 of the glutamine, preventing the conformational flip and keeping the holding site inaccessible for S2B. An N_2 molecule reduced by two electrons, however, would be twofold-protonated on the distal nitrogen (Fig. 4B), allowing it to donate hydrogen bonds to both active site residues to drive the reaction forward. In this state, the proximal nitrogen is once more found in an electron-deficient nitrene-like configuration that may be stabilized by electron transfer from the cluster, as described for E_6 . All three conformations of the E_4 state (E_4 -H2, diferrous E_4^* , and E_4 -N2H2; Fig. 4C) should readily inter-

convert, in line with the observed reversibility of N_2 binding and the known ability of nitrogenase to generate HD from D_2 (29, 39).

Further along the reaction pathway, the enzyme is now committed to the complete reduction of the bound intermediate. The reduction step that follows creates the odd-electron, diamagnetic E_5 intermediate, with reduction occurring on the cluster. N-N bond cleavage only occurs upon the transition from E_5 to E_6 , when the next electron cannot be accommodated in the cluster itself. Possibly via transient formation of a surface hydride, a two-electron transfer to both nitrogen atoms releases the distal N as NH_3 but retains the proximal one as NH , as observed in the crystal structure. Our proposed reaction scheme thus starts after the distal pathway of N_2 reduction (40), but it no longer fits this model at the important transition of E_5 to E_6 , where the N-N bond is eventually cleaved. An alternative pathway of N_2 reduction may be straightforwardly envisioned by starting from the open and reduced E_4^* state and binding N_2 in a side-on ($\mu-\eta^2:\eta^2$) mode at Fe2 and Fe6. This would directly lead to the intermediate diazene, but subsequently to hydrazine bound at E_6 , which is not congruent with our structural data (fig. S7D). On the other hand, this binding mode might apply to another important substrate, acetylene (C_2H_2). In contrast to N_2 and CO, this compound

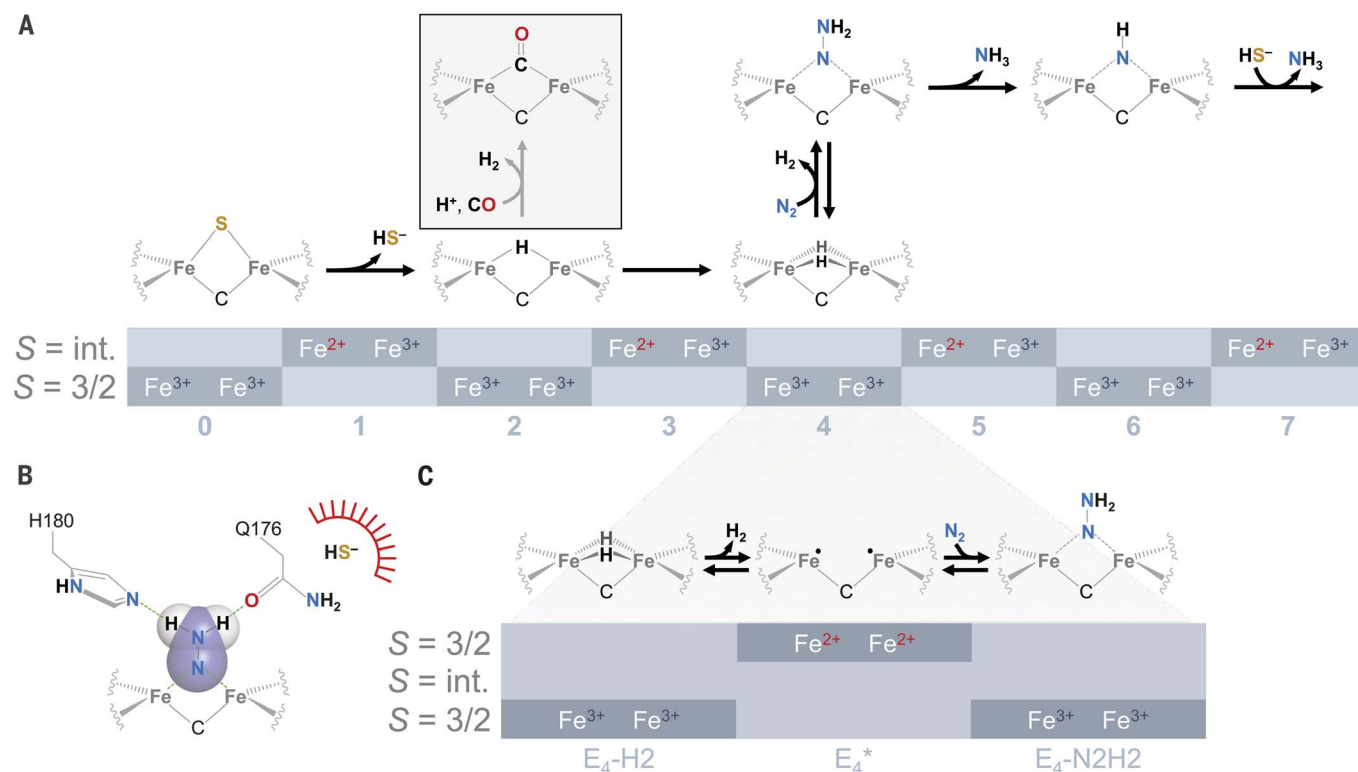


Fig. 4. Stepwise reduction of N_2 on nitrogenase cofactor and CO inhibition. (A) Nitrogenase cofactors alternate between an oxidized (M^N , $S = 3/2$) and a one-electron-reduced (M^{1-} , integer spin) state, so that the reduction of N_2 may be described in two-electron steps. From the resting state E_0 , reduction to E_2 leads to the formation of the first hydride. If this is lost owing to protonation, the state is susceptible to CO inhibition and consequently may have already eliminated HS^- . The critical E_4 state holds two hydrides and binds N_2 upon reductive elimination of H_2 . After two further reduction steps to E_6 , the first NH_3 is released, and the proximal nitrogen undergoes the first change of

oxidation state. Horizontal arrows represent two-electron transfer events. (B) An analogous arrangement of H180 and Q176 can also accommodate bound N_2 after double protonation in the E_4 state, but without forming a hydrogen bond between the amino acid residues, requiring a hypothetical rearrangement of Q176. (C) As the key intermediate, the E_4 state is generated by formation of two bridging hydrides (E_4-H_2). Reductive elimination of H_2 leaves Fe2 and Fe6 in a highly reactive, doubly reduced state (E_4^*) that can bind N_2 and immediately transfer two electrons ($E_4-N_2H_2$). These steps are reversible, explaining HD formation in the presence of D_2 .

is reduced by two electrons to ethylene (C_2H_4) and to a lesser degree to ethane (C_2H_6) by V nitrogenase (41). Cleavage of the C–C bond does not occur, and although we take this as an indication that the $\mu-\eta^2:\eta^2$ binding of N_2 is not part of the productive ammonium production reaction, it may well play a role in the reported formation of hydrazine by V nitrogenase (42), as well as in the trapping of hydrazine in a variant of MoFe protein (43).

Although this outline of a step-by-step mechanism for nitrogenase remains hypothetical, it reconciles existing biochemical data with new structural information, based on the direct observation of an accessible binding site with a bound catalytic intermediate of N_2 reduction by nitrogenase. Our findings are consistent with a bridging hydride replacing sulfide S2B at E_2 . Possibly only after H_2 loss through protonation, the open binding site at Fe2 and Fe6 of the cofactor becomes the binding site for less critical substrates such as C_2H_2 and CO , whereas N_2 binding requires E_3 or E_4 . These concepts open new avenues for biochemical and theoretical inves-

tigations and can be used for a reassessment of the large amount of available spectroscopic and functional data. They furthermore provide a sound basis for the generation and characterization of other reaction intermediates, in particular the mechanistically crucial N_2 -bound E_4 state, to complement the kinetic scheme with a detailed structural and electronic analysis.

REFERENCES AND NOTES

- V. Smil, *Sci. Am.* **277**, 76–81 (1997).
- D. Fowler, J. A. Pyle, J. A. Raven, M. A. Sutton, *Philos. Trans. R. Soc. London B Biol. Sci.* **368**, 20130165 (2013).
- Y. L. Hu, M. W. Ribbe, in *Nitrogen Fixation: Methods and Protocols*, M. W. Ribbe, Ed. (Springer, 2011), pp. 3–7.
- D. C. Rees et al., *Philos. Trans. A Math. Phys. Eng. Sci.* **363**, 971–984, discussion 1035–1040 (2005).
- O. Einsle et al., *Science* **297**, 1696–1700 (2002).
- T. Spatzal et al., *Science* **334**, 940 (2011).
- R. R. Eady, *Chem. Rev.* **96**, 3013–3030 (1996).
- K. M. Lancaster et al., *Science* **334**, 974–977 (2011).
- R. Björnsson et al., *Chem. Sci. (Camb.)* **5**, 3096–3103 (2014).
- O. Einsle, *J. Biol. Inorg. Chem.* **19**, 737–745 (2014).
- D. Sippel, O. Einsle, *Nat. Chem. Biol.* **13**, 956–960 (2017).
- J. L. Crossland, D. R. Tyler, *Coord. Chem. Rev.* **254**, 1883–1894 (2010).
- C. C. Lee, Y. Hu, M. W. Ribbe, *Science* **329**, 642 (2010).
- W. A. Bulen, J. R. LeCompte, *Proc. Natl. Acad. Sci. U.S.A.* **56**, 979–986 (1966).
- F. B. Simpson, R. H. Burris, *Science* **224**, 1095–1097 (1984).
- R. N. F. Thorneley, D. J. Lowe, in *Molybdenum Enzymes*, T. G. Spiro, Ed. (Wiley-Interscience, 1985), vol. 1, pp. 221–284.
- J. Liang, R. H. Burris, *Proc. Natl. Acad. Sci. U.S.A.* **85**, 9446–9450 (1988).
- B. K. Burgess, S. Werhland, W. E. Newton, E. I. Stiefel, *Biochemistry* **20**, 5140–5146 (1981).
- R. Y. Igarashi et al., *J. Am. Chem. Soc.* **127**, 6231–6241 (2005).
- L. C. Seefeldt, B. M. Hoffman, D. R. Dean, *Annu. Rev. Biochem.* **78**, 701–722 (2009).
- P. E. Doan et al., *J. Am. Chem. Soc.* **133**, 17329–17340 (2011).
- D. Lukoyanov, B. M. Barney, D. R. Dean, L. C. Seefeldt, B. M. Hoffman, *Proc. Natl. Acad. Sci. U.S.A.* **104**, 1451–1455 (2007).
- D. Lukoyanov et al., *J. Am. Chem. Soc.* **133**, 11655–11664 (2011).
- B. M. Hoffman, D. Lukoyanov, Z. Y. Yang, D. R. Dean, L. C. Seefeldt, *Chem. Rev.* **114**, 4041–4062 (2014).
- T. Spatzal, K. A. Perez, O. Einsle, J. B. Howard, D. C. Rees, *Science* **345**, 1620–1623 (2014).
- D. J. Lowe, K. Fisher, R. N. F. Thorneley, *Biochem. J.* **272**, 621–625 (1990).
- R. Y. Igarashi et al., *J. Biol. Chem.* **279**, 34770–34775 (2004).
- K. Fisher, M. J. Dilworth, C. H. Kim, W. E. Newton, *Biochemistry* **39**, 2970–2979 (2000).

29. K. Fisher, M. J. Dilworth, W. E. Newton, *Biochemistry* **39**, 15570–15577 (2000).
30. R. Ménard, A. C. Storer, *Biol. Chem. Hoppe Seyler* **373**, 393–400 (1992).
31. S. D. Brown, M. P. Mehn, J. C. Peters, *J. Am. Chem. Soc.* **127**, 13146–13147 (2005).
32. D. Lukoyanov *et al.*, *Proc. Natl. Acad. Sci. U.S.A.* **109**, 5583–5587 (2012).
33. J. B. Varley, Y. Wang, K. Chan, F. Studt, J. K. Nørskov, *Phys. Chem. Chem. Phys.* **17**, 29541–29547 (2015).
34. Z. Y. Yang *et al.*, *Biochemistry* **55**, 3625–3635 (2016).
35. D. Lukoyanov *et al.*, *J. Am. Chem. Soc.* **138**, 1320–1327 (2016).
36. B. M. Hoffman, D. Lukoyanov, D. R. Dean, L. C. Seefeldt, *Acc. Chem. Res.* **46**, 587–595 (2013).
37. T. Spatzal *et al.*, *Nat. Commun.* **7**, 10902 (2016).
38. D. J. Lowe, R. N. F. Thorneley, *Biochem. J.* **224**, 895–901 (1984).
39. B. K. Burgess, D. J. Lowe, *Chem. Rev.* **96**, 2983–3012 (1996).
40. I. Djurdjevic, O. Einsle, L. Decamps, *Chem. Asian J.* **12**, 1447–1455 (2017).
41. P. M. C. Benton, J. Christiansen, D. R. Dean, L. C. Seefeldt, *J. Am. Chem. Soc.* **123**, 1822–1827 (2001).
42. M. J. Dilworth, R. R. Eady, *Biochem. J.* **277**, 465–468 (1991).
43. B. M. Barney *et al.*, *Biochemistry* **44**, 8030–8037 (2005).

ACKNOWLEDGMENTS

We thank F. Meyer and R. Björnsson for helpful discussions; the beamline staff at the Swiss Light Source, Villigen, Switzerland, for excellent assistance with data collection; and B. Prasser for EPR measurements. **Funding:** This work was supported by the European Research Council (grant no. 310656), the Deutsche Forschungsgemeinschaft (RTG 1976 and PP 1927), and the BIOS Centre for Biological Signalling Studies at Albert-Ludwigs-Universität Freiburg. **Author contributions:** D.S., M.R., J.N., C.T., J.G., K.G., I.D., and L.D. performed the experiments; D.S., S.L.A.A., and O.E.

designed the experiments and processed data; D.S. and O.E. built and refined the structural model; and O.E. wrote the manuscript.

Competing interests: The authors declare no conflicts of interest.

Data and materials availability: Raw data and additional material are available from the corresponding author upon request. The structural model and structure factors have been deposited in the Protein Data Bank with accession code 6FEA.

SUPPLEMENTARY MATERIALS

www.sciencemag.org/content/359/6383/1484/suppl/DC1
Materials and Methods

Figs. S1 to S11

Table S1

References (44–57)

20 October 2017; accepted 31 January 2018
10.1126/science.aar2765

NANOMATERIALS

Carbothermal shock synthesis of high-entropy-alloy nanoparticles

Yonggang Yao,^{1*} Zhennan Huang,^{2*} Pengfei Xie,^{3*} Steven D. Lacey,^{1*} Rohit Jiji Jacob,⁴ Hua Xie,¹ Fengjuan Chen,¹ Anmin Nie,² Tiancheng Pu,³ Miles Rehwoldt,⁴ Daiwei Yu,⁵ Michael R. Zachariah,⁴ Chao Wang,^{3,†} Reza Shahbazian-Yassar,^{2,†} Ju Li,^{5,†} Liangbing Hu^{1,†}

The controllable incorporation of multiple immiscible elements into a single nanoparticle merits untold scientific and technological potential, yet remains a challenge using conventional synthetic techniques. We present a general route for alloying up to eight dissimilar elements into single-phase solid-solution nanoparticles, referred to as high-entropy-alloy nanoparticles (HEA-NPs), by thermally shocking precursor metal salt mixtures loaded onto carbon supports [temperature ~ 2000 kelvin (K), 55-millisecond duration, rate of $\sim 10^5$ K per second]. We synthesized a wide range of multicomponent nanoparticles with a desired chemistry (composition), size, and phase (solid solution, phase-separated) by controlling the carbothermal shock (CTS) parameters (substrate, temperature, shock duration, and heating/cooling rate). To prove utility, we synthesized quinary HEA-NPs as ammonia oxidation catalysts with $\sim 100\%$ conversion and $>99\%$ nitrogen oxide selectivity over prolonged operations.

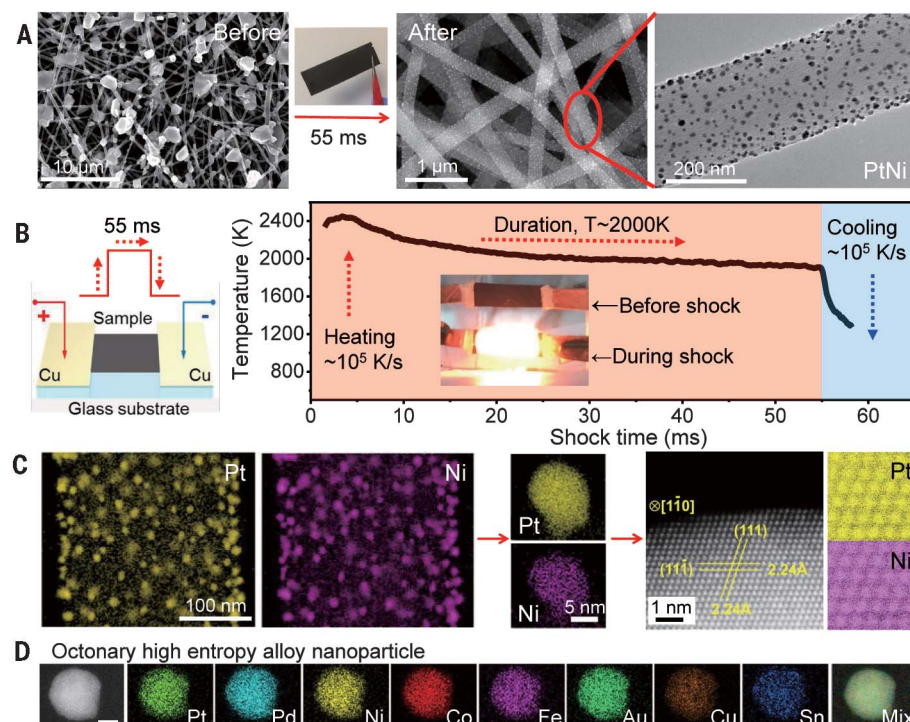
Multimetallic nanoparticles (MMNPs) are of interest in a wide range of applications, including catalysis (1–7), energy storage (8), and bio/plasmonic imaging (8, 9). Alloying multiple metallic elements into individual nanoscale products offers the promise of material properties that could exceed single-element (or unary) nanoparticles (2, 5, 6). The current and primary approaches toward the preparation of MMNPs arise from wet-chemistry synthesis, where a variety of particle sizes, shapes,

and phases can be attained (3, 4, 7, 10). However, most studies via wet-chemical methods report alloy compositions not exceeding three elements, which limits the compositional space. Additionally, more site-specific synthesis techniques, including printing- and lithography-based methods (1, 11, 12), have shifted the compositional space toward quaternary and even quinary nanostructures; however, the subsequent reduction procedures tend to limit the structural complexity to phase-separated MMNPs, especially for immiscible

elemental combinations (1, 12, 13). In terms of bulk material synthesis, melt processing is a scalable method that has led to the creation of high-entropy alloys (HEAs) consisting of five or more elements in a solid solution (uniform mixing), which have shown great potential as structural materials (14–18). To date, only a limited family of HEAs have been achieved, due to the difficulty of mixing elements with vastly different chemical and physical properties, as well as cooling rate constraints. Moreover, downsizing HEAs to the nanoscale is a daunting task, especially by conventional alloying methods. Therefore, the development of a synthesis method where elemental composition, particle size, and phase can be precisely controlled could bring about a new repertoire of alloys and nanostructures with unprecedented functionalities.

We developed a facile, two-step carbothermal shock (CTS) method that employs flash heating and cooling (temperature of ~ 2000 K, shock duration of ~ 55 ms, and ramp rates on the order of 10^5 K/s) of metal precursors on oxygenated carbon support to produce high-entropy-alloy nanoparticles (HEA-NPs) with up to eight dissimilar metallic elements (table S1). MMNPs synthesized by CTS have a narrow size distribution and are uniformly dispersed across the carbon support, despite being exposed to high temperatures that conventionally cause particle coarsening. The high temperature, in conjunction with the catalytic activities of the liquid metals, drives rapid particle “fission” and “fusion” events that result in uniform mixtures of multiple elements. Subsequently, the rapid cooling rate facilitates kinetic control over the thermodynamic mixing regimes and enables the formation of crystal-line solid-solution nanoparticles, analogous to

Fig. 1. CTS synthesis of HEA-NPs on carbon supports. (A) Microscopy images of micro-sized precursor salt particles on the carbon nanofiber (CNF) support before thermal shock, as well as the synthesized, well-dispersed (PtNi) nanoparticles after CTS. (B) Sample preparation and the temporal evolution of temperature during the 55-ms thermal shock. (C) Low-magnification and single-particle elemental maps, an HAADF image, and corresponding atomic maps for a binary PtNi alloy. (D) Elemental maps of an HEA-NP composed of eight dissimilar elements (Pt, Pd, Ni, Co, Fe, Au, Cu, and Sn). Scale bar, 10 nm.



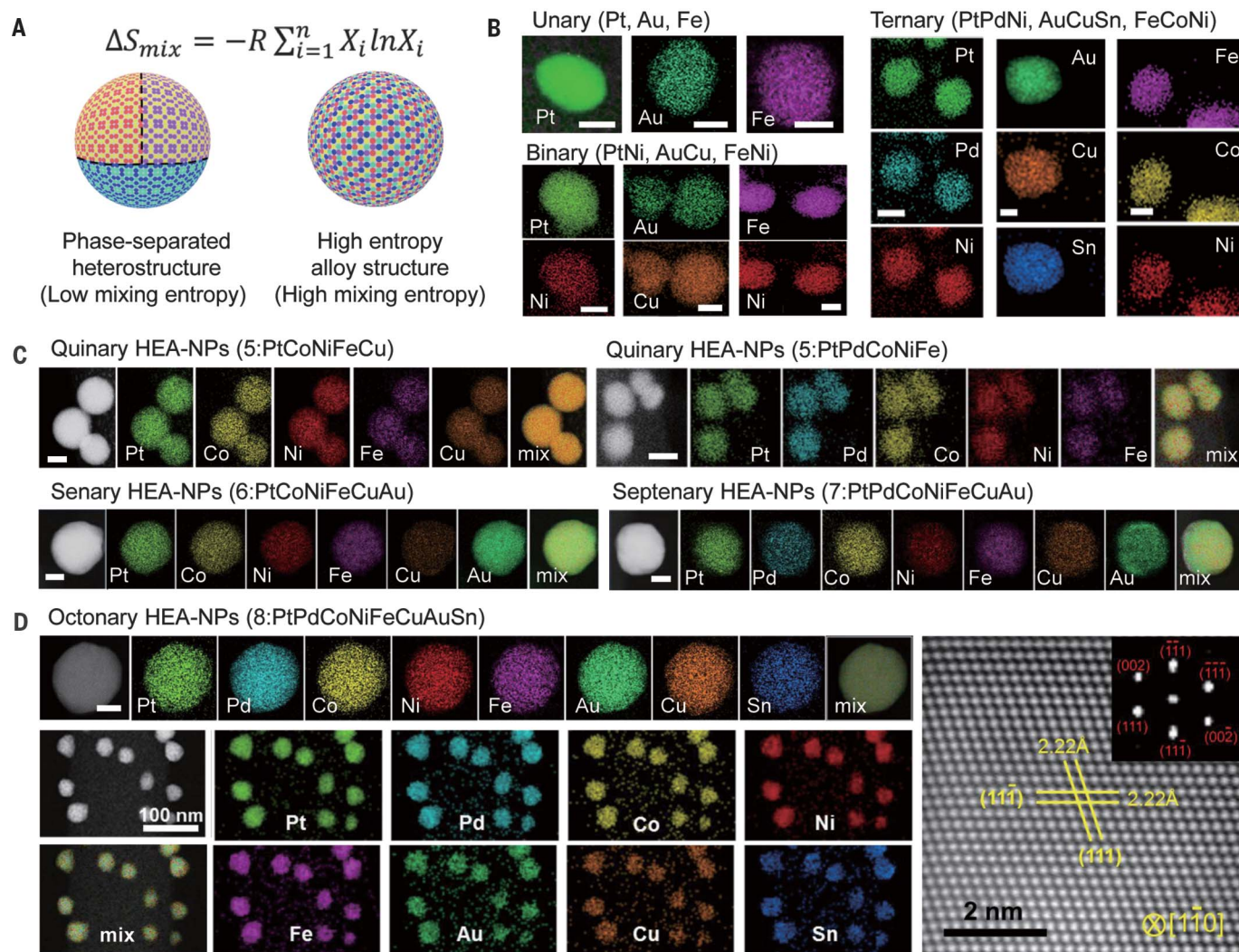


Fig. 2. Elemental characterization of HEA-NPs. (A) Schematic comparison of phase-separated heterostructures synthesized by a conventional slow reduction procedure (slow kinetics) versus solid-solution HEA-NPs synthesized by the CTS method (fast kinetics). (B) STEM elemental maps of unary (Pt, Au, and Fe), binary (PtNi, AuCu, and FeNi), and ternary (PtPdNi, AuCuSn, and FeCoNi) nanoalloys. Scale bar, 5 nm. (C) HAADF images and STEM elemental maps of HEA-NPs: quinary (PtFeCoNiCu and

PtPdCoNiFe), senary (PtCoNiFeCuAu), and septenary (PtPdCoNiFeCuAu). Scale bar, 10 nm. (D) Individual and low-magnification elemental maps (left) and a high-resolution HAADF-STEM image with fast Fourier transform analysis (right) of octonary (PtPdCoNiFeCuAuSn) HEA-NPs, showing solid solutions with an fcc structure. The low-magnification elemental maps verify the structural and compositional uniformity of the HEA-NPs. Scale bar, 10 nm.

martensitic steels and metallic glasses that are also kinetically trapped (19, 20). By adjusting the input electrical pulse parameters, we can also produce phase-separated nanoparticles by decreasing the cooling rate. This CTS technique opens a

vast space for synthesizing alloys and nanocrystals, which has potential for a wide range of applications.

Results

The CTS method we used to synthesize uniformly dispersed, solid-solution nanoparticles (up to eight elements) requires two steps (21). First, we mixed metal salt precursors $MCl_x \cdot H_y$ (M is Pt, Pd, Ni, Fe, Co, Au, Cu, or Sn, among others) into a solution and loaded onto a conductive carbon support, such as carbon nanofibers (CNFs). CNFs carbonized at 1073 K (CNF-1073K, denoted as CNF hereafter) are the substrates used in this work unless stated otherwise. After drying, we exposed the precursor-loaded sample to a rapid thermal shock (55 ms) in an Ar-filled glovebox, which leads to a high concentration of nanoparticles

(e.g., PtNi) that form across the carbon surface (Fig. 1A and figs. S1 to S4). The electrical pulse that we applied controls the thermal exposure conditions (Fig. 1B), with a common temperature of ~ 2000 K and heating/cooling rates up to $\sim 10^5$ K/s as measured with a pyrometer (figs. S5 to S7). We found no apparent elemental segregation or phase separation for the PtNi nanoparticles (Fig. 1C and fig. S4) using scanning transmission electron microscopy (STEM) elemental maps. The high-angle annular dark-field (HAADF) images and atomic maps also demonstrated both uniform atomic scale mixing and the formation of a face-centered cubic (fcc) crystalline structure (Fig. 1C). Our general method extends to more complex HEA-NPs. For example, we readily fabricated HEA-NPs composed of eight dissimilar elements (Pt, Pd, Ni, Co, Fe, Au, Cu, and Sn). These elements

¹Department of Materials Science and Engineering, University of Maryland, College Park, MD 20742, USA. ²Department of Mechanical and Industrial Engineering, University of Illinois at Chicago (UIC), Chicago, IL 60607, USA. ³Department of Chemical and Biomolecular Engineering, Johns Hopkins University, Baltimore, MD 21218, USA. ⁴Department of Chemical and Biomolecular Engineering and Chemistry and Biochemistry, University of Maryland, College Park, MD 20742, USA. ⁵Department of Nuclear Science and Engineering, Department of Materials Science and Engineering, and Department of Electrical Engineering and Computer Science, Massachusetts Institute of Technology, Cambridge, MA 02139, USA.

*These authors contributed equally to this work.

†Corresponding author. Email: binghu@umd.edu (L.H.); rsyassar@uic.edu (R.S.-Y.); liju@mit.edu (J.L.); chaowang@jhu.edu (C.W.)

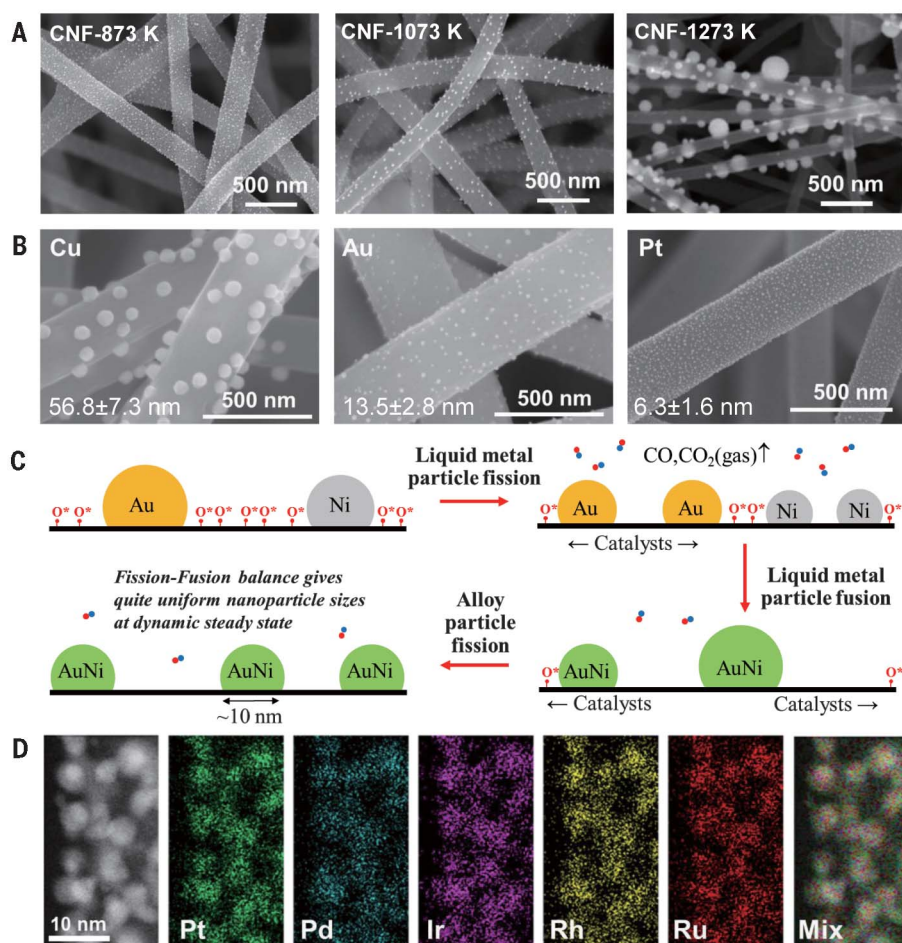


Fig. 3. Particle dispersion mechanism for the CTS process. (A) SEM images of synthesized AuNi nanoparticles on CNFs carbonized at different temperatures: 873, 1073, and 1273 K. A higher carbonization temperature leads to higher crystallinity and lower defect concentrations within the carbon support, which affects particle size and dispersion. (B) SEM images of Cu, Au, and Pt particle distributions synthesized on identical CNF supports via the same CTS process. The higher catalytic activities of the metal species (Au and Pt) lead to smaller nanoparticles and more uniform distributions. (C) An illustration of the catalysis-driven particle fission/fusion mechanism to synthesize uniformly dispersed HEA-NPs. (D) HAADF image and elemental maps of ultrafine and well-dispersed quinary HEA-NPs (PtPdIrRhRu) on CO₂-activated CNFs. A narrow size distribution is achieved by increasing the support's surface defect concentration through CO₂ activation, as well as employing metal species with high catalytic activities.

have a range of atomic radii (1.24 to 1.44 Å), reduction potentials (−0.25 to 1.5 V versus the standard hydrogen electrode), preferred crystal structures (fcc, body-centered cubic, hexagonal close-packed, or tetragonal), and melting temperatures (500 to 2000 K) that typically prevents solid-solution formation (Fig. 1D and table S2).

MMNPs have been previously synthesized using conventional reduction procedures (1, 3). However, these synthetic methods tend to create phase-separated heterostructures among immiscible elements, which greatly reduces the configurational entropy of mixing (fig. S8). The CTS process leads to solid solution MMNPs (i.e., HEA-NPs), where arbitrary metallic elements are completely mixed to maximize the mixing entropy (ΔS_{mix}) (Fig. 2A). We demonstrated the

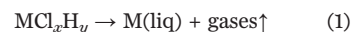
versatility by synthesizing a series of multi-element nanoparticles and characterized them by STEM, transmission EM (TEM), scanning EM (SEM), and energy-dispersive x-ray spectroscopy (EDS). We synthesized unary (Pt, Au, and Fe), binary (PtNi, AuCu, and FeNi), and ternary (PtPdNi, AuCuSn, and FeCoNi) nanoparticles that exhibit compositional uniformity (Fig. 2B). The nanoparticles also possess size uniformity, with diameters of ≥ 5 nm (fig. S9), regardless of the elemental compositions. By adding additional metal salts to the precursor solutions, we synthesized quinary (PtCoNiFeCu and PtPdCoNiFe), senary (PtCoNiFeCuAu), septenary (PtPdCoNiFeCuAu) and octonary (PtPdCoNiFeCuAuSn) HEA-NPs, which are solid solutions and evenly dispersed across the

carbon support (Fig. 2, C and D, and figs. S10 to S16). Moreover, the HEA-NPs are of nanoscale dimensions in fcc crystal structures (Fig. 2D and figs. S17 and S18).

The HEA-NPs exhibited solid solution mixing via the same 55-ms thermal shock protocol (figs. S19 and S21). We confirmed the structural uniformity (no phase separation) and negligible chlorine content with STEM (figs. S22 to S26), x-ray diffraction (XRD) (figs. S27 to S29), and x-ray photoelectron spectroscopy (XPS) (figs. S30 to S36). A statistical study conducted over different sample regions confirms the compositional uniformity among the synthesized nanoparticles (figs. S37 to S43). For example, the compositional variation for each element in our quinary HEA-NPs (PtPdCoNiFe) is $\sim 10\%$, which is smaller than the $>50\%$ variation reported for lithography-based techniques (fig. S42) (1). Additionally, the macroscopic compositions that we determined by inductively coupled plasma mass spectroscopy (ICP-MS) agree well with the STEM-derived statistics. The HEA-NP composition has a small deviation from the ideal composition based on the initial precursor salt molar ratios, due to vapor loss at high temperature (figs. S44 to S46 and table S3). To demonstrate compositional control, we employed the (precursor) compensation approach, which is a common strategy in high-temperature synthesis when volatile elements are involved (figs. S47 to S52).

The HEA-NPs deviate from the phase-separated thermodynamic equilibrium structures reported in literature (1, 3, 12) due to the rapid quench-induced nucleation/growth process of the CTS method, which “freezes” the liquid alloy state to create solid-solution nanoparticles. The synthesized HEA-NPs are stable at room temperature and remained unchanged in terms of size, structure, and composition after 11 months of storage under standard conditions.

In addition to the rich chemistries, the morphologies of the synthesized nanoparticles indicate a formation mechanism for CTS that differs from other alloying approaches. Because ~ 2000 K far exceeds the thermal decomposition temperature of metal precursors (table S1), the salts easily decompose:



However, ~ 2000 K is below the boiling points of the metallic elements. In this case, the metallic elements are likely in the liquid phase and should be on a similar length scale as the initial (microsized) salt precursors. Since metals are nonwetting with carbon, the liquid metals should coarsen to minimize their surface energy at high temperature (22). Our observation departs from this behavior, requiring a mechanism to explain how initially single-element, micron-sized liquid metal droplets form uniformly dispersed alloy nanoparticles.

We performed two control experiments to explore HEA-NP formation. We found distinct particle morphology differences using the same CTS protocol (Fig. 3A and figs. S53 and S54), but with

supports differing in carbonization temperature. Specifically, electrospun polyacrylonitrile fibers carbonized in argon at a range of temperatures (873, 1073, and 1273 K) generated CNF supports with various defect concentrations. Lower carbonization temperatures resulted in smaller, more uniform particle dispersions. Each pyrolysis temperature was insufficient to drive away all surface-bound oxygen (O^*) and thus resulted in an increasing amount of O^* residuals remaining on CNFs carbonized at lower temperatures (fig. S2). Therefore, we surmised that the surface defect concentration of the carbon support is an important parameter for particle dispersion. Our second control experiment used identical CNF supports (CNF-1073K) and synthesis conditions (55 ms, ~ 2000 K), but with a variety of single-metal salt precursors (Fig. 3B and figs. S55 to S57). Nanoparticle size distribution changes in this case with Cu having a much larger particle size (~ 56.8 nm) than Au (~ 13.5 nm) and Pt (~ 6.3 nm). This trend resembles the catalytic activities of the corresponding elements, with Pt and Cu being the most and least active, respectively. Because Au and Cu possess similar physical properties (table S4), the discrepancy requires a different particle dispersion mechanism than a simple, physical melting-and-nucleation process.

Since defects and metal catalysts play a key role during the CTS process, we considered a catalytically driven particle dispersion mechanism for the defective carbon supports. To verify this, we used in situ mass spectrometry to analyze the gases created during CTS for defective CNF supports with and without precursor salts. Compared with bare CNF, the precursor-loaded CNF exhibited a larger and much sharper release of CO gas during the CTS process (fig. S58). Thus, the release of CO gas upon thermal shock arises from a catalytically driven carbon metabolism reaction:



where O^* denotes surface-bound residual oxygen. The carbon metabolism reaction involves C (fuel), O^* (oxidizer), and metal (catalyst), which correlates the surface defect concentration (e.g., carbonization temperature) and the metal's catalytic activity to the final nanoparticle size and level of dispersity. We hypothesize that during the 55-ms high-temperature exposure, the liquid metal droplets actively travel around and split ("fission") to harvest the dispersed O^* on the carbon surface based on the catalytically driven reaction, $C + O^* = CO$ (gas) ($\Delta H = -110.5$ kJ/mol). Previously published works (23–26) and an in situ TEM study (27) also showed that metallic particles can move and split under a catalytic driving force, which is similar to our proposed carbon metabolism reaction.

Mechanistically (Fig. 3C), a larger O^* concentration and the use of catalytically active metals can drive vigorous metabolism with more frequent catalyst motion and fission events. This opposes equilibrium thermodynamic directive for the metal droplets to coarsen. Conversely,

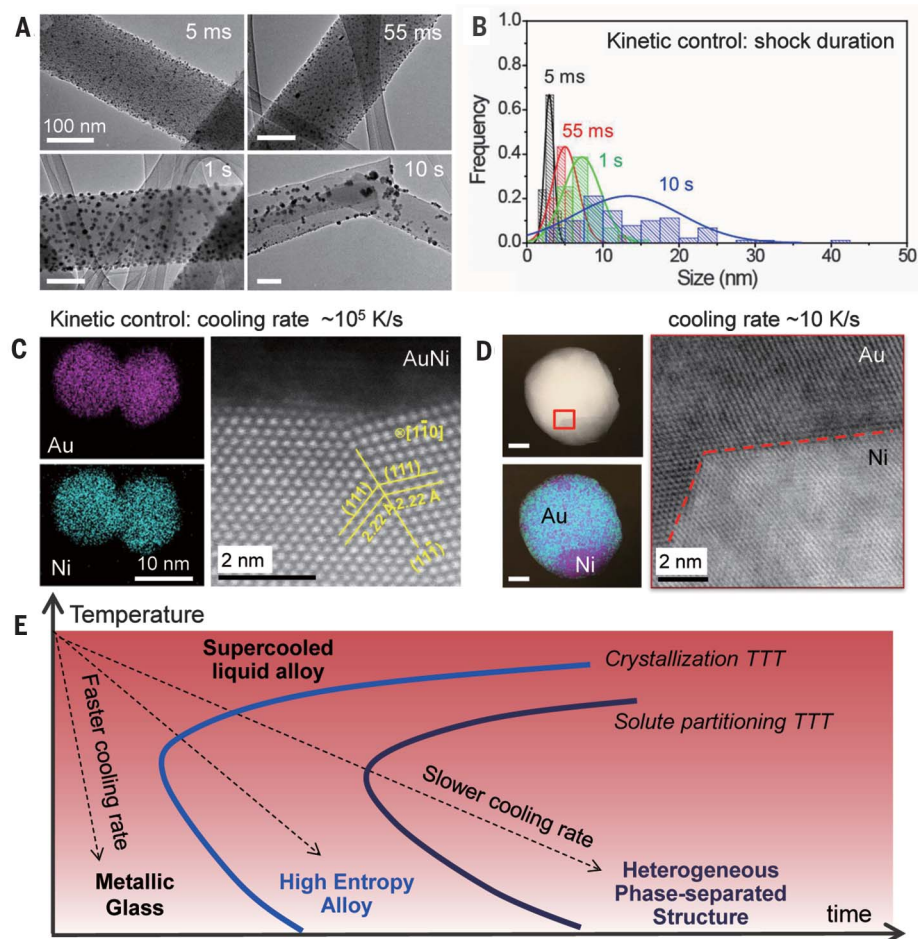


Fig. 4. Kinetic control over nanoparticle formation. (A) TEM images displaying the particle size and dispersity at various thermal shock durations (5 ms, 55 ms, 1 s, and 10 s). Scale bars, 100 nm. (B) Particle size distribution of PtNi nanoparticles on CNFs. (C and D) Cooling rate-dependent AuNi nanostructures determined by elemental maps, HAADF, and ADF images. Ultrafast cooling rates ($\sim 10^5$ K/s) enable the formation of solid-solution nanoparticles, whereas slower rates (~ 10 K/s) tend to induce phase separation. Scale bar, 10 nm. (E) Time-temperature-transformation (TTT) diagram showing the kinetic formation of metallic glass, HEA, and phase-separated structures, respectively, as a function of cooling rate.

depleted O^* concentrations should lead to decreased mobility and the localization of liquid droplets that coarsen slowly to reduce their total surface energy. The liquid alloys have a wide solubility range at ~ 2000 K. Therefore, the liquid metal movement driven by O^* harvesting allows different droplet compositions to continually meet and fuse into single-phase alloys during the CTS process. Numerous particle fusion and fission events, which we estimated to be $>10^6$ times based on time-scale analysis (fig. S59) (28–30), yield a dynamic steady state during the 55-ms high-temperature shock. This enables uniform nanoscale dispersions and homogeneous high-entropy mixing. To verify the effects of supports with more surface-bound defects, we synthesized quinary HEA-NPs (PtFeCoNiCu) on CNFs with and without CO_2 activation, resulting in 5.30 ± 1.31 -nm particles on CO_2 -activated CNFs and 11.3 ± 2.2 -nm particles on CNFs (fig. S60). We achieved further improvements in

ultrafine particle sizes and narrow distributions when more catalytically active metal combinations (PtPdIrRhRu HEA-NPs, 3.28 ± 0.81 nm) are employed on identical CO_2 -activated CNF supports (Fig. 3D and figs. S61 and S62). Therefore, the catalytic metabolism-induced particle fission/fusion mechanism for metal alloying at the nanoscale is distinct compared with previously reported alloying methods (1, 3, 7, 16).

By tuning the shock duration and heating/cooling rates, we can adjust the MMNP size, distribution, and structure. We loaded multiple CNF samples using an identical PtNi precursor solution and exposed the support to a temperature of ~ 2000 K for 5-ms, 55-ms, 1-s, and 10-s durations. The faster exposure times yield smaller particle sizes (3.51 ± 0.62 nm for 5 ms and 5.01 ± 1.69 nm for 55 ms) compared with prolonged shock durations (8.57 ± 1.98 nm for 1 s and 13.30 ± 6.98 nm for 10 s) (Fig. 4, A and B). We observed similar behavior with AuNi (fig. S63). As the thermal shock

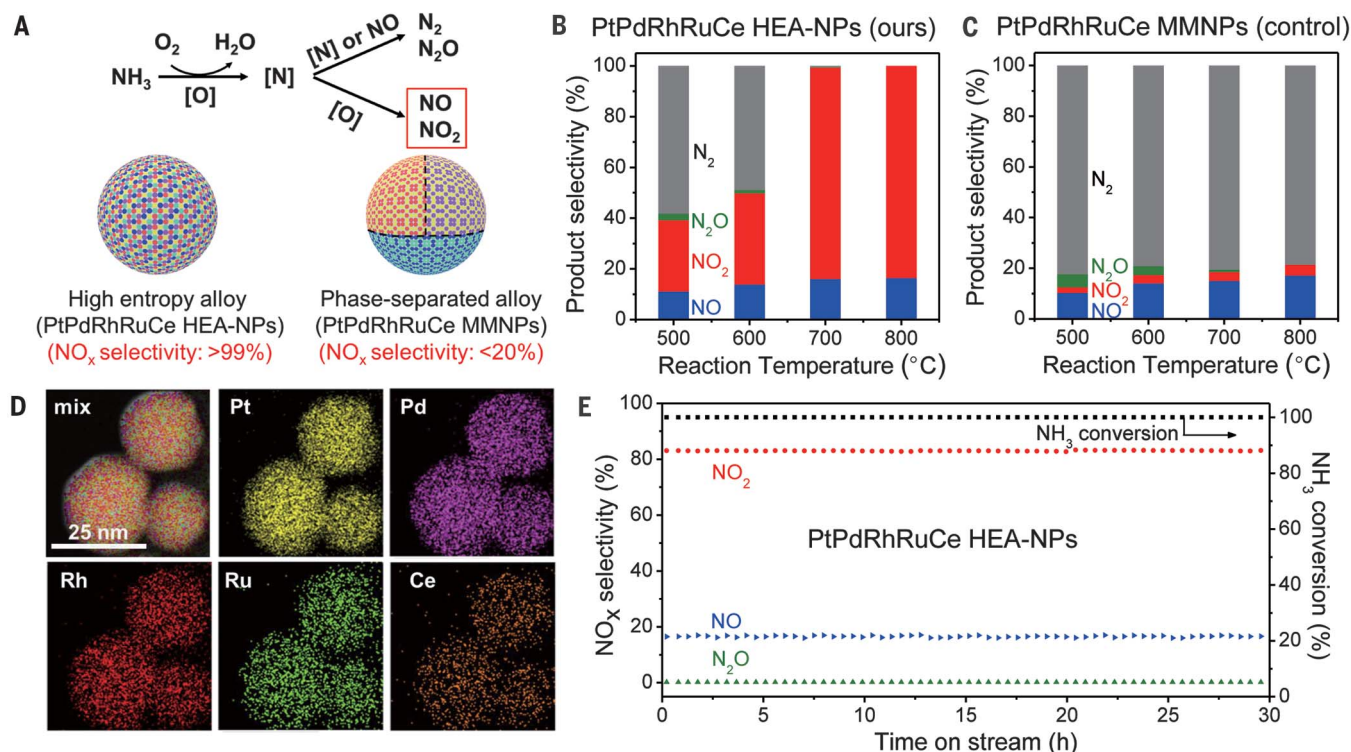


Fig. 5. Catalytic performance of quinary HEA-NPs (PtPdRhRuCe) for ammonia oxidation. (A) Reaction scheme for the ammonia oxidation process as well as the structural and performance differences between the PtPdRhRuCe HEA-NPs synthesized by CTS and the control sample (PtPdRhRuCe MMNPs) by wet impregnation.

(B and C) Temperature-dependent product distribution and conversion of NH₃ for PtPdRhRuCe HEA-NPs and PtPdRhRuCe MMNPs, respectively. (D) STEM elemental maps for PtPdRhRuCe HEA-NPs. (E) The time-dependent catalytic performance of PtPdRhRuCe HEA-NPs at 700°C.

duration increases to 10 s, the size of the HEA-NPs increases and the synthesized particles become less uniform; the high-temperature exposure depletes the number of O* present on the CNF support, which inhibits particle fission and corresponding dispersity (fig. S64).

We investigated the effect of cooling rate by tuning the electrical input parameters (Fig. 1B) with Au/Ni and Cu/Co, which are immiscible binary elemental compositions (Fig. 4, C and D, and figs. S65 to S67). Due to differences in lattice parameters and surface energies, these metallic combinations tend to phase-separate according to equilibrium phase diagrams (3, 20, 31). However, through rapid quenching, the high-entropy mixing state of the liquid metals is retained and yields single-phase solid-solution nanoparticles (i.e., HEA-NPs) by avoiding the time-temperature-transformation (TTT) nose (Fig. 4E). The AuNi binary alloy formed a solid solution when quenched at both $\sim 10^5$ and $\sim 10^3$ K/s (Fig. 4C and fig. S66). However, nanoscale phase separation occurred when cooled slowly (~ 10 K/s), with a clear phase boundary between Au and Ni shown in the annular bright-field (ABF) image (Fig. 4D) and HAADF image (fig. S66). For the CuCo binary system, the 10^5 K/s produced a solid solution, but phase separation began at a cooling rate of $\sim 10^3$ K/s (fig. S65). Very slow cooling and heating rates (~ 10 K/s) also alter the dispersion and size distribution of the synthesized nanoparticles, which leads to

aggregates and a nonuniform particle dispersion across the CNFs (figs. S67 and S68).

Our experimental results reveal valuable information about the nucleation and diffusion kinetics of the CTS method. The transformation of a liquid alloy into a single-phase solid solution with a specific elemental composition requires local structural rearrangements but no long-range solute partitioning. The cooling rate ($\sim 10^5$ K/s) that we achieved by CTS is still slow enough to form crystalline structures. If higher cooling rates are attained with the CTS method, it may be possible to use this route to synthesize metallic glasses. The $\sim 10^5$ K/s cooling rate is fast enough to prevent solute partitioning across a distance of ~ 10 nm, enabling the formation of high-entropy-alloy structures. On the other hand, slower cooling rates (e.g., ~ 10 K/s) enable solute partitioning to occur through (slow) kinetics, which caused the MMNPs to phase separate into a Janus particle. Both single-phase and phase-separated nanoparticles are useful for applications such as catalysis and plasmonic imaging (2, 3, 9, 10). The CTS method has the ability to control phase formation through ramp rates and may be useful for targeted nanoparticle synthesis.

The CTS method enables diverse compositions of uniformly mixed HEA-NPs that have potential for a wide range of applications. As a proof of concept, we demonstrated quinary HEA-NPs as advanced catalysts for ammonia oxidation, which

is the key processing step in the industrial synthesis of nitric acid (Fig. 5A) (32). Despite extensive efforts on the exploration of new catalysts, PtPdRh-based multimetallic catalysts are still widely employed in industry to this day (33). Beyond the high content of precious metals, these catalysts also require very high temperatures ($>800^\circ\text{C}$) to achieve high yields of NO_x (NO + NO₂) versus N₂/N₂O and tend to degrade under continuous operation (34). Using the CTS method, quinary PtPdRhRuCe HEA-NPs (figs. S69 and S70 and table S5 for the compositions) were prepared and employed as ammonia oxidation catalysts (27). We introduced Ru and Ce to improve the overall catalytic activity and reduce the Pt content (35, 36).

We achieved $\sim 100\%$ conversion of ammonia (NH₃) and $>99\%$ selectivity toward NO_x (NO + NO₂) at a relatively low operation temperature of 700°C with the PtPdRhRuCe HEA-NP catalyst (Fig. 5B). For comparison, we prepared similar catalysts (in terms of composition) by the wet impregnation method (denoted as PtPdRhRuCe MMNPs), which produced a 18.7% yield of NO_x at the same operation temperature, whereas most of the output was N₂ (Fig. 5C). An elemental map comparison between the two catalysts suggests that the enhanced catalytic selectivity of the HEA-NPs is likely due to the highly homogeneous nature of the solid-solution nanoparticles compared with the phase-separated heterostructures derived from the wet impregnation method

(Fig. 5D and fig. S70). Note that synthesizing solid-solution PtPdRh multimetallic systems by conventional synthetic methods is challenging due to immiscibility (2, 34). We also performed degradation testing to study catalytic performance under prolonged operation conditions, and we observe no degradation in terms of catalytic activity or selectivity over ~30 hours of continuous operation at 700°C (Fig. 5E and fig. S71). We attributed this durability to the high-entropy nature of the catalysts prepared by the CTS method, which helps stabilize the MMNPs in solid solutions (i.e., HEA-NPs) and prevents phase separation or elemental segregation under the reaction conditions (16, 18). Moreover, the precious metal content of the HEA-NPs can be reduced further without compromising catalytic performance or stability by replacing ~37.5% of Pt with Co and eliminating Ru (e.g., PtPdRhCoCe HEA-NPs) (fig. S72). Thus, HEA-NPs fabricated by the CTS method may be a general route toward highly active, durable, and cost-effective catalysts (see table S6 for a detailed literature comparison).

Discussion and conclusion

The CTS method provides an excellent platform for nanometallurgical studies. Immiscible elements are alloyed into single-phase nanoparticles on carbon supports with the following features: (i) high-entropy mixing, where multimetallic mixing leads to the creation of solid-solution nanoparticles with maximized configurational mixing entropy; (ii) nonequilibrium processing, where the shock process takes milliseconds to create HEA-NPs by rapid quenching and thus prevents phase separation among immiscible elements by avoiding the nose of the TTT curve (Fig. 4E); and (iii) uniform dispersion, where the catalytically driven carbon metabolism at high temperature enables uniform, well-dispersed, and controllably sized nanoparticles (as opposed to particle coarsening).

This synthetic technique also provides (i) generality, (ii) tunability, and (iii) potential scalability. The maximum temperature of the CTS method (2000 to 3000 K) is higher than the decomposition temperature of any metal salt, which promotes uniform mixing of nearly any metallic combination (i.e., generality). Precise control over the shock parameters (temperature, duration, and

ramp rates) effectively tunes the particle size, dispersity, as well as final structure. The synthesis of a diverse array of nanoparticles with easily tunable processing parameters is ideal for large-scale nanomanufacturing, where a rapid (synthesis in milliseconds) and energy-efficient (immediate heating through an electrical pulse) synthetic procedure could enable high-rate and high-volume production of quality nanoparticles. Moreover, a scalability evaluation exhibited a 100-fold increase in HEA-NP production without sacrificing nanoparticle quality or dispersion by employing a three-dimensional carbon support (figs. S73 to S75). These CTS capabilities facilitate a new research area for materials discovery and optimization, where the elemental composition and mixing entropy of nanoparticles can be carefully designed and controlled. Further compositional exploration has the potential to transcend research efforts to broad technological applications.

REFERENCES AND NOTES

- P.-C. Chen *et al.*, *Science* **352**, 1565–1569 (2016).
- L. Bu *et al.*, *Science* **354**, 1410–1414 (2016).
- S. G. Kwon *et al.*, *Nat. Mater.* **14**, 215–223 (2015).
- M. Takahashi *et al.*, *Sci. Adv.* **3**, e1700101 (2017).
- X. Huang *et al.*, *Science* **348**, 1230–1234 (2015).
- G. Chen *et al.*, *Science* **344**, 495–499 (2014).
- M. R. Buck, J. F. Bondi, R. E. Schaak, *Nat. Chem.* **4**, 37–44 (2011).
- N. A. Frey, S. Peng, K. Cheng, S. Sun, *Chem. Soc. Rev.* **38**, 2532–2542 (2009).
- M. B. Cortie, A. M. McDonagh, *Chem. Rev.* **111**, 3713–3735 (2011).
- K. D. Gilroy, A. Ruditskiy, H.-C. Peng, D. Qin, Y. Xia, *Chem. Rev.* **116**, 10414–10472 (2016).
- E. Reddington *et al.*, *Science* **280**, 1735–1737 (1998).
- P. C. Chen *et al.*, *J. Am. Chem. Soc.* **137**, 9167–9173 (2015).
- P.-C. Chen *et al.*, *J. Am. Chem. Soc.* **139**, 9876–9884 (2017).
- S. Ranganathan, *Curr. Sci.* **85**, 1404–1406 (2003).
- J.-W. Yeh *et al.*, *Adv. Eng. Mater.* **6**, 299–303 (2004).
- B. S. Murty, J.-W. Yeh, S. Ranganathan, *High-Entropy Alloys* (Butterworth-Heinemann, 2014).
- Z. Li, K. G. Pradeep, Y. Deng, D. Raabe, C. C. Tasan, *Nature* **534**, 227–230 (2016).
- Y. F. Ye, Q. Wang, J. Lu, C. T. Liu, Y. Yang, *Mater. Today* **19**, 349–362 (2016).
- D. C. Hofmann *et al.*, *Nature* **451**, 1085–1089 (2008).
- D. A. Porter, K. E. Easterling, M. Y. Sherif, *Phase Transformations in Metals and Alloys* (CRC Press, ed. 3, 2009).
- Materials and methods are available as supplementary materials.
- N. Eustathopoulos, M. G. Nicholas, B. B. Drevet, *Wettability at High Temperatures* (Elsevier, 1999), vol. 3.
- M. Lukas *et al.*, *Nat. Commun.* **4**, 1379 (2013).
- F. Tao *et al.*, *Science* **322**, 932–934 (2008).
- M. A. Newton, C. Belver-Coldeira, A. Martínez-Arias, M. Fernández-García, *Nat. Mater.* **6**, 528–532 (2007).
- F. Tao *et al.*, *Science* **327**, 850–853 (2010).
- P.-H. Lu *et al.*, arXiv:1802.00207 [physics.app-ph] (1 Feb 2018).
- N. Combe, P. Jensen, A. Pimpinelli, *Phys. Rev. Lett.* **85**, 110–113 (2000).
- C. C. Wang *et al.*, *Nano Res.* **8**, 2143–2151 (2015).
- D.-G. Xie *et al.*, *Nat. Mater.* **14**, 899–903 (2015).
- D. Wang, Y. Li, *J. Am. Chem. Soc.* **132**, 6280–6281 (2010).
- D. M. Considine, *Chemical and Process Technology Encyclopedia* (CRC Press, 1974).
- L. Xin, H. Yongqiang, J. Husheng, *Rare Met. Mater. Eng.* **46**, 339–343 (2017).
- P. A. J. Bagot *et al.*, *J. Phys. Chem. C* **118**, 26130–26138 (2014).
- B. V. I. Chernyshev, I. M. Kisil, *Platin. Met. Rev.* **37**, 136–143 (1993).
- X. Hu, Y. Ning, L. Chen, Q. Shi, C. Jia, *Platin. Met. Rev.* **56**, 40–46 (2012).

ACKNOWLEDGMENTS

The authors thank K. Gaskell and S. Xu, as well as B. Liu, for their help with XPS and XRD measurements/analysis, respectively. The authors acknowledge the use and support of the Maryland NanoCenter and its AIMLab. This work made use of the JEOL JEM-ARM200CF in the Electron Microscopy Service (Research Resources Center, UIC). **Funding:** This work has no direct funding support. The acquisition of the UIC JEOL JEM-ARM200CF was supported by a MRI-R2 grant from the National Science Foundation (NSF) (DMR-0959470). R.S.Y. and J.L. acknowledge financial support from NSF DMR-1620901 and NSF DMR-1410636, respectively. S.D.L. acknowledges support by the Department of Defense through the National Defense Science and Engineering Graduate Fellowship. M.R.Z. and R.J.J. were partially supported by an Office of Naval Research Multidisciplinary University Research Initiative grant. P.X. and C.W. acknowledge the Catalyst and Discovery Awards of Johns Hopkins University. **Author contributions:** L.H. and Y.Y. conceived the idea and designed the present work. Y.Y., S.D.L., H.X., and F.C. carried out the experiments. Z.H., A.N., and R.S.Y. performed detailed microscopic characterizations. P.X., T.P., and C.W. performed high-temperature characterization and in situ molecular beam measurements. D.Y. and J.L. developed the mechanism analysis. All authors discussed the results and contributed to the final manuscript. **Competing interests:** The authors declare no competing interests. Provisional patent applications have been applied for through the University of Maryland (62523646 and 62591638). **Data and materials availability:** All data are available in the manuscript and the supplementary materials.

SUPPLEMENTARY MATERIALS

www.sciencemag.org/content/359/6383/1489/suppl/DC1
Materials and Methods
Supplementary Text
Figs. S1 to S75
Tables S1 to S6
References (37–47)

28 April 2017; resubmitted 14 December 2017
Accepted 2 February 2018
10.1126/science.aan5412

MATERIALS SCIENCE

Adaptive infrared-reflecting systems inspired by cephalopods

Chengyi Xu,¹ George T. Stiubianu,¹ Alon A. Gorodetsky^{1,2*}

Materials and systems that statically reflect radiation in the infrared region of the electromagnetic spectrum underpin the performance of many entrenched technologies, including building insulation, energy-conserving windows, spacecraft components, electronics shielding, container packaging, protective clothing, and camouflage platforms. The development of their adaptive variants, in which the infrared-reflecting properties dynamically change in response to external stimuli, has emerged as an important unmet scientific challenge. By drawing inspiration from cephalopod skin, we developed adaptive infrared-reflecting platforms that feature a simple actuation mechanism, low working temperature, tunable spectral range, weak angular dependence, fast response, stability to repeated cycling, amenability to patterning and multiplexing, autonomous operation, robust mechanical properties, and straightforward manufacturability. Our findings may open opportunities for infrared camouflage and other technologies that regulate infrared radiation.

Materials and systems that statically reflect radiation in the short- to long-wavelength infrared region of the electromagnetic spectrum have been studied for decades and critically underpin the performance of many entrenched technologies, including building insulation (1), energy-conserving windows (2), spacecraft components (3), electronics shielding (4), container packaging (5), protective clothing (6), and camouflage platforms (7). One highly desirable but not easily attainable property for infrared-reflecting materials (and related technologies) is on-demand adaptability: precise and sensitive real-time dynamic responsiveness to changes in the surrounding environment. To date, only a limited number of adaptive infrared systems, such as infrared camouflage platforms, have been reported because they must satisfy stringent and demanding technical performance criteria, making the development of these technologies extremely challenging (a comparative overview for adaptive camouflage is provided in table S1). For example, thermochromic materials can display substantial infrared emissivity changes because of thermally induced phase transitions but feature high operating temperatures, hysteresis during cycling, and structural characteristics that are difficult to control (8–12). In addition, infrared electrochromic devices have optical properties that can be altered with electrochemical redox reactions but struggle with precise spectral tunability and necessitate the use of inert noble metals in order to achieve functionality and stability (13–16). Moreover, certain metamaterial-based systems can spatiotemporally modulate their emissivity through photo-generated carrier doping but use ultraviolet light for actuation, need elevated working tempera-

tures for adequate contrast, and display long recovery times (17). Furthermore, thermal cloaking platforms modify the infrared signatures of other objects by manipulating the heat flow in the surroundings but require large temperature gradients and demand complete object immersion, restricting implementation (18, 19). Last, soft robots with integrated microfluidics can alter their thermal appearance and infrared patterning via the pneumatic injection of heated or cooled liquids but rely on the continuous flow of multiple liquids maintained at different temperatures and have slow response times dictated by their thermal conductivities (20). Consequently, in order to enable a broad range of practical applications (such as camouflage), the “ideal” adaptive infrared-reflecting system would simultaneously possess a simple actuation mechanism, low working temperature, tunable spectral range, weak angular dependence, fast response, stability to repeated cycling, amenability to patterning and multiplexing, autonomous operation, robust mechanical properties, and straightforward manufacturability (table S1).

Biomimetic system design

As an active color-changing system, the skin of coleoid cephalopods (such as squid, octopuses, and cuttlefish) represents an exciting source of inspiration (21–23). The patterning and coloration of cephalopod skin can be altered autonomously and repeatedly for the purposes of concealment or signaling, as illustrated for the squid in Fig. 1A. Such remarkable feats of camouflage are enabled by the sophisticated architecture of the squid’s soft and flexible skin, in which innervated dermal layers contain chromatophore pigment cells (as part of larger chromatophore organs) and reflective cells called iridocytes (Fig. 1B) (21, 24, 25). The two cell types operate in tandem but perform distinct optical functions (adaptive chromatophores are present in many cephalopods, but adaptive iridocytes have only

been identified in a few squid species to date) (21, 24–27). The adaptive chromatophore pigment cells contain pigment granule-packed internal sacculi, which are expanded and contracted through the mechanical action of radial muscle cells (Fig. 1C). These yellow, red, and brown cells feature response times of hundreds of milliseconds and function as size-variable biological spectral filters that absorb and reflect visible light of specific wavelengths (21, 26). The adaptive iridocytes contain alternating arrangements of membrane-enclosed nanostructured protein layers and extracellular space, for which the geometries and refractive index differences are altered via a biochemical signaling cascade (Fig. 1D). These iridescent cells feature response times of tens of seconds and function like reconfigurable biological Bragg stacks that reflect visible light of variable wavelengths (21, 27). In part because of the properties of these cells, the skin of squid (and by extension, other cephalopods) behaves as a dynamic bioelectronic display, with the functionality summarized in table S1.

The remarkable capabilities of cephalopod skin and its components have inspired the engineering of various adaptive artificial optoelectronic devices (28–32). For example, dielectric elastomer actuators have been leveraged for cephalopod-inspired color-changing systems that function within the visible region of the electromagnetic spectrum (30–32). In the most basic incarnation, such devices consist of an elastomer membrane sandwiched between two electrodes, where the application of a voltage between the electrodes induces electrostatic pressure, leading to a decrease in the membrane’s thickness and an increase in the overall electrodes’ areas (33–35). More generally, such actuators, which essentially translate electrical stimuli into mechanical outputs, have been explored for a variety of applications, including artificial muscles, pneumatic automation, energy generation, tactile displays, and adaptive optics (33–35). However, the technological viability of dielectric elastomer actuators has been limited by challenges associated with a requirement for both high operating voltages and electrodes with a demanding combination of properties (33–37). For infrared camouflage applications, the latter requirement is particularly daunting because the electrode materials must simultaneously demonstrate straightforward processability into thin freestanding films, amenability to surface modification and patterning, excellent flexibility and compliance, high conductivity that does not drop upon deformation, transparency over a broad spectral range, lack of degradation under variable humidity, and stability to repeated cycling.

We designed a platform inspired by squid skin’s highly evolved bio-optical components while leveraging the technical foundation established for dielectric elastomer actuators. We conceptualized a device in a parallel plate capacitor-type configuration, which consists of a proton-conducting bottom electrode, a dielectric elastomer membrane, a proton-conducting top electrode, and an infrared-reflecting coating (Fig. 1, E and F). Before actuation, the devices

¹Department of Chemical Engineering and Materials Science, University of California, Irvine, Irvine, CA 92697, USA.

²Department of Chemistry, University of California, Irvine, Irvine, CA 92697, USA.

*Corresponding author. Email: alon.gorodetsky@uci.edu

feature relatively small but size-variable active areas (Fig. 1E, left), analogous to cephalopod chromatophores (Fig. 1C, left) (26), with the surfaces covered by a dense but geometrically reconfigurable arrangement of reflective microstructures (Fig. 1F, left), analogous to squid iridocytes (Fig. 1D, left) (27). After actuation, the devices expand their active areas to modulate the amount of absorbed incident infrared light (Fig. 1E, right)—again, analogous to cephalopod chromatophores (Fig. 1C, right) (26)—as well as alter the geometry of their active areas' microstructured surfaces to modulate the relative

intensity of the reflected incident infrared light (Fig. 1F, right)—again, analogous to squid iridocytes (Fig. 1D, right) (27).

System fabrication, characterization, and testing

We fabricated the cephalopod-inspired adaptive infrared-reflecting systems as detailed in the supplementary materials. We adapted protocols used for the lithographic fabrication of various dielectric elastomer actuators (33–35) and chose to manufacture devices with centimeter-scale active areas, allowing for benchtop assembly

and simplifying spectroscopic characterization. For the compliant electrodes, we prepared films from a sulfonated pentablock copolymer that features exceptional protonic conductivity, with the size and shape of the films defining the device's active area (38, 39). For the electroactive layer, we mounted an acrylate dielectric elastomer membrane within a size-adjustable holder and equiaxially stretched the membrane. Subsequently, to facilitate experiments within different infrared wavelength regimes, we produced two types of devices featuring chemically and structurally distinct infrared-reflecting coatings. In

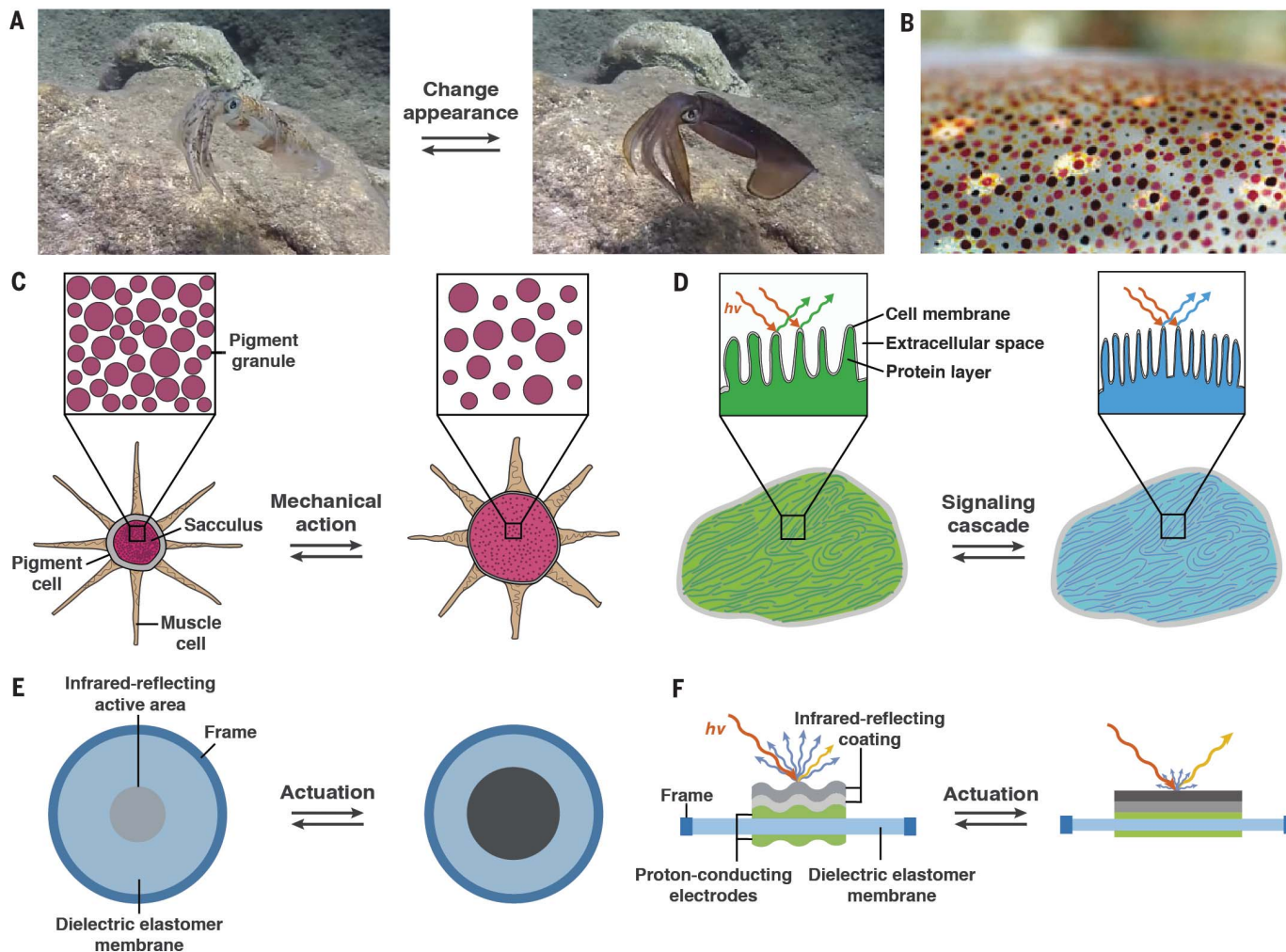


Fig. 1. Biological inspiration and system design. (A) Camera images of a squid changing its appearance in front of a rocky background. (B) An image of squid skin. The yellow, red, and brown circular regions are chromatophores, and the underlying bright iridescent regions are iridocytes. (C) A schematic of a cephalopod chromatophore organ, in which a central chromatophore pigment cell is ringed by muscle cells. The adaptive chromatophore pigment cells contain internal sacculi packed with pigment granules (inset), and they are expanded and contracted through the mechanical action of the muscle cells. The chromatophore pigment cells function as size-variable biological spectral filters that absorb and reflect visible light of specific wavelengths. (D) A schematic of a squid iridocyte. The adaptive iridocytes contain alternating arrangements of membrane-enclosed protein layers and extracellular

space (inset), for which the geometries and refractive index differences are altered via a biochemical signaling cascade. The iridocytes function like reconfigurable biological Bragg stacks that reflect visible light of variable wavelengths. (E) A generic schematic of the top view of our infrared-reflecting platform (left) before and (right) after actuation. Described is the areal change for the active region upon actuation. (F) A generic schematic of the side view of our infrared-reflecting platform (left) before and (right) after actuation. Described is the surface morphology change for the active region upon actuation. [The images in (A) are reproduced from a video by H. Steinfeldt under the YouTube Creative Commons Attribution license, and the image in (B) was obtained by G. Hanlon and reproduced with permission of R. Hanlon.]

order to fabricate broadband infrared-reflecting devices, we used electron-beam evaporation to deposit a thin film of aluminum (Al) metal onto a proton-conducting top electrode, which was then laminated onto a mounted acrylate membrane already outfitted with an unmodified bottom electrode (fig. S1A). In order to fabricate

narrowband infrared-reflecting devices, we used electron-beam evaporation to deposit alternating layers of titanium dioxide (TiO_2) and silicon dioxide (SiO_2) directly onto the top electrode of a mounted acrylate membrane, which was already outfitted with both the top and bottom electrodes (fig. S1B). For both device types, we mechanically

contracted the holder to release some of the tension introduced during the initial mounting of the membrane and thus introduced micro-structuring (wrinkles) to the surfaces of the devices' active areas. Last, when necessary for characterization, we transferred electrical lead-modified devices to rigid support frames. The

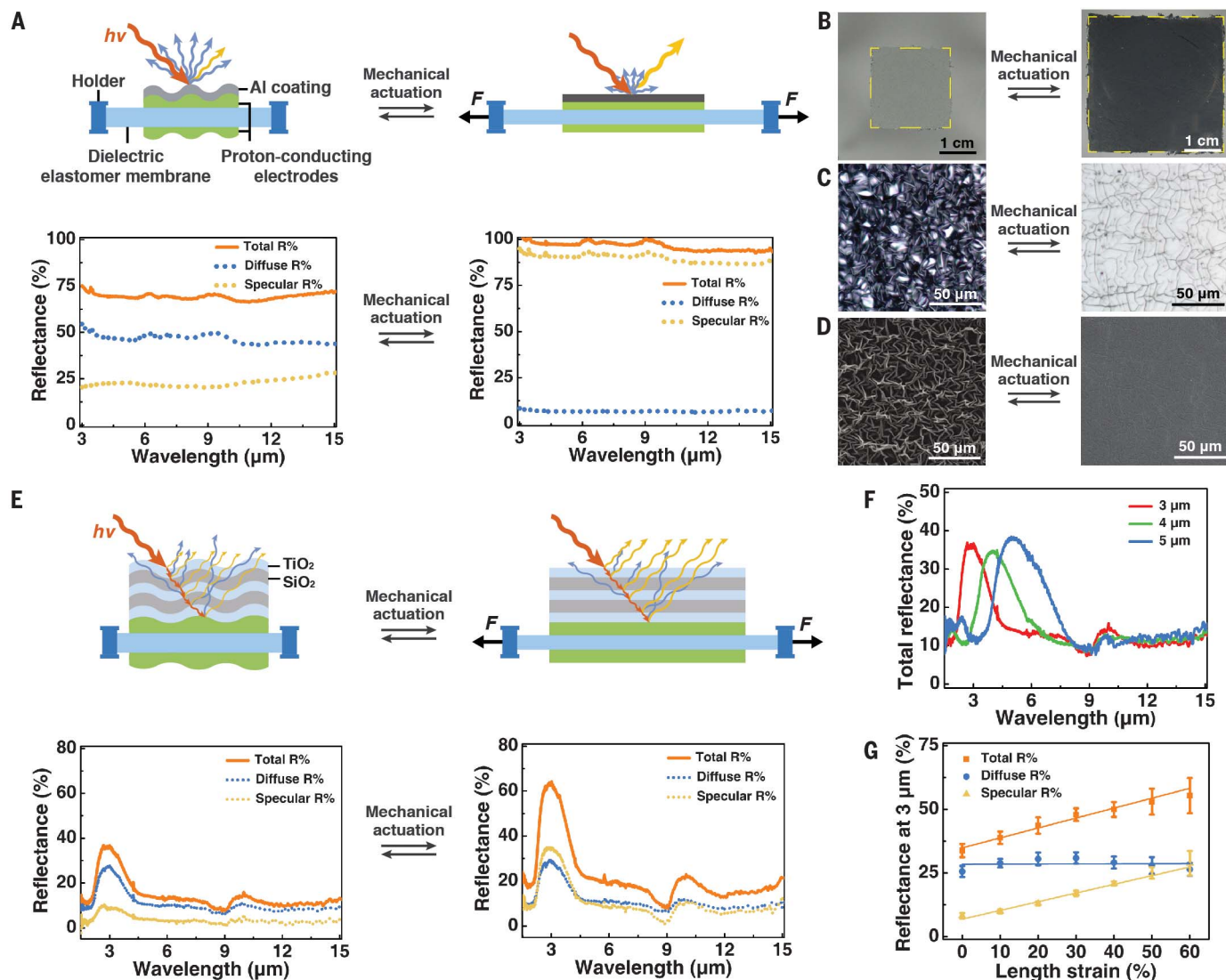


Fig. 2. Mechanical modulation of the broadband and narrowband reflectance. (A) (Top) Schematics of an aluminum-modified device (left) before and (right) after mechanical actuation in an adjustable holder, illustrating the change in the surface morphology and the reflection of infrared light. (Bottom) The infrared reflectance spectra of an aluminum-modified device (left) before and (right) after mechanical actuation. The total reflectances (solid orange traces) are shown along with their specular (dotted yellow traces) and diffuse (dotted blue traces) components. (B) Digital camera images of an aluminum-modified device's active area (left) before and (right) after mechanical actuation. The yellow dashed square indicates the active area. (C) Optical microscope images of the surface morphology of an aluminum-modified device's active region (left) before and (right) after mechanical actuation. (D) Scanning electron microscopy images of the surface morphology of an aluminum-modified device's active region (left) before and (right) after mechanical

actuation. (E) (Top) Schematics of a $\text{TiO}_2/\text{SiO}_2$ Bragg stack-modified device (left) before and (right) after mechanical actuation in an adjustable holder, illustrating the change in the surface morphology and the reflection of infrared light. (Bottom) The infrared reflectance spectra of a $\text{TiO}_2/\text{SiO}_2$ Bragg stack-modified device, with a peak reflectance intensity at 3 μm , (left) before and (right) after mechanical actuation. The total reflectances (solid orange traces) are shown along with their specular (dotted yellow traces) and diffuse (dotted blue traces) components. (F) The infrared spectra of three unactuated devices that have been designed to feature peak reflectance wavelengths of 3 μm (red trace), 4 μm (green trace), and 5 μm (blue trace). (G) Plots of the total (orange squares), specular (yellow triangles), and diffuse (blue circles) peak reflectances of the $\text{TiO}_2/\text{SiO}_2$ Bragg stack-modified devices as functions of the applied length strain. The lines represent linear fits of the data.

overall scalable procedure furnished infrared-reflecting systems with the general architecture depicted in Fig. 1, E and F.

We investigated the effect of mechanical actuation (equiaxial strain) on the properties of devices with a broadband infrared reflectance (Fig. 2A). Before mechanical actuation, our devices possessed relatively small active areas (Fig. 2B) and relatively large thicknesses, with their surfaces covered by a dense three-dimensional network of micrometer-sized wrinkles, as revealed with optical microscopy (Fig. 2C) and scanning electron microscopy (Fig. 2D). The corresponding infrared spectra showed that the unactuated devices featured a high average total reflectance of $71 \pm 3\%$ (Fig. 2A, bottom left), a low average total transmittance of $<1\%$ (fig. S2), and a moderate average total absorptance of $28 \pm 2\%$ (fig. S2). For the wrinkled surfaces, the total reflectance featured a weak average specular component of $23 \pm 1\%$ and a dominant average diffuse component of $48 \pm 2\%$, in a ratio of ~ 0.5 (Fig. 2A, bottom left). By contrast, upon mechanical actuation, our devices possessed larger active areas (Fig. 2B) and smaller thicknesses, with the wrinkles flattened into a quasi two-dimensional network of irregular domains, as revealed with optical microscopy (Fig. 2C) and scanning electron microscopy (Fig. 2D). The corresponding infrared spectra showed that the actuated devices featured an increased average total reflectance of $96 \pm 1\%$ (Fig. 2A, bottom right), a low average total transmittance of $<1\%$ (fig. S2), and a low average total absorptance of $3 \pm 1\%$ (fig. S2). For the flattened surfaces, the total reflectance featured a much larger average specular component

of $88 \pm 3\%$ and a smaller average diffuse component of $8 \pm 2\%$, in a ratio of ~ 11 (Fig. 2A, bottom right). For our devices, mechanical actuation dynamically modulated both the specular-to-diffuse reflectance ratios (owing to the change in the morphology) and the total absorptance (owing to the change in the thickness) by approximately an order of magnitude. Moreover, the specular component of the reflectance exhibited a weak angular dependence in the devices' unactuated and actuated states (fig. S3). The changes in the devices' infrared-reflecting properties were consistent and fully reversible upon repeated actuation, with no physical delamination and only minor performance degradation observed after 75 and 750 cycles (fig. S4). Thus, actuation of our devices induced a change in the microstructure of their active areas and enabled concomitant reversible, angle-independent, and stable modulation of the broadband reflectance (and absorptance) within the short- to long-wavelength infrared region.

We investigated the effect of mechanical actuation (equiaxial strain) on the properties of devices with a narrowband infrared reflectance (Fig. 2E). To obtain reflectances that featured peak wavelengths (λ_{peak}) in the mid-wavelength infrared region of the electromagnetic spectrum, we used infrared-reflecting coatings composed of Bragg stacks, alternating TiO_2 and SiO_2 layers with thicknesses of $\lambda_{\text{peak}}/(4 \cdot n_{\text{TiO}_2})$ and $\lambda_{\text{peak}}/(4 \cdot n_{\text{SiO}_2})$ (where n_{TiO_2} and n_{SiO_2} are the refractive indices). This straightforward approach furnished devices with peak reflectance intensities at wavelengths of 3, 4, and 5 μm (Fig. 2F). For such narrowband-reflecting devices, the optical prop-

erties were responsive to the applied strain, analogous to their broadband-reflecting counterparts. As a specific example, before mechanical actuation, the infrared spectra obtained for representative microstructured (wrinkled) and relatively thicker devices featured peak total reflectance intensities of $34 \pm 3\%$ at a wavelength of 3 μm , with a weak specular component of $8 \pm 1\%$ and a dominant diffuse component of $26 \pm 2\%$ in a ratio of ~ 0.3 (Fig. 2E, bottom left). However, after mechanical actuation, the infrared spectra of the now flattened and relatively thinner devices featured increased peak total reflectance intensities of $55 \pm 7\%$ at a wavelength of 3 μm , with a much larger specular component of $29 \pm 5\%$ and a nearly unchanged diffuse component of $26 \pm 2\%$ in a ratio of ~ 1.1 (Fig. 2E, bottom right). In general, the devices' total reflectances at this specific wavelength increased as a function of the strain (whereas the corresponding total absorptances presumably decreased) (Fig. 2G). The reflectances' specular components likewise increased with the strain, but the diffuse components remained relatively unaffected (Fig. 2G). Moreover, the changes in the devices' infrared-reflecting properties were fully reversible, with only minor performance degradation observed after 100 actuation cycles (fig. S5). Therefore, actuation of our devices directly induced dynamic modulation of their reflectance within a specific narrow wavelength range of the infrared region.

We studied electrical actuation of our devices in a standard dielectric elastomer actuator configuration (Fig. 3A). In agreement with the mechanical actuation experiments, the devices possessed a relatively small active area with a wrinkled surface before electrical actuation, but a larger active area with a flattened surface after electrical actuation (Fig. 3A and movie S1). We found that the areal strain demonstrated an exponential dependence on the applied voltage, with a voltage of ~ 3.5 kV, resulting in a maximum strain of $\sim 230\%$ (Fig. 3B). In addition, the areal strain exhibited a distinct dependence on the frequency of the applied voltage; for example, a variable-frequency square waveform (minima of 0 kV and maxima of 3.2 kV) induced a drop in the maximum areal strain from $181 \pm 11\%$ to $85 \pm 5\%$ between the frequencies of 0.05 and 2 Hz, followed by an increase in the maximum areal strain to $110 \pm 5\%$ at a frequency of 16 Hz (Fig. 3C). Moreover, for the aforementioned square waveform at a frequency of 0.5 Hz, the devices' response time (defined as the rise time from 10 to 90% of the strain change) was 720 ± 50 ms because of the rapid areal expansion and shrinkage rates of 55.8 ± 1.6 and $56.8 \pm 0.8\%$ per second, respectively (Fig. 3D), and the energy associated with device actuation during one typical cycle was estimated to be >8 J/m² (supplementary materials). These systems' figures of merit were comparable with or even exceeded those reported for analogous acrylate dielectric elastomer-based devices with conventional ionic hydrogel, carbon grease, or conductive nanowire composite electrodes (36, 37).

We showed electrical modulation of our systems' infrared-reflecting properties in multiple

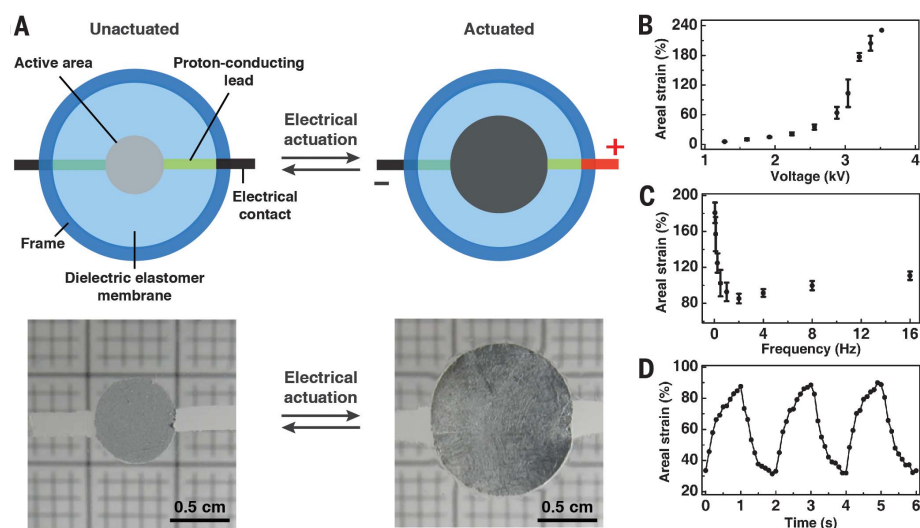


Fig. 3. Electrical characteristics of single devices. (A) (Top) Schematics of an aluminum-modified device (left) before and (right) after electrical actuation in a rigid frame, illustrating the areal change for the active region. (Bottom) Digital camera images of an aluminum-modified device's active region (left) before and (right) after electrical actuation. (B) A plot of the areal strain as a function of the applied voltage for aluminum-modified devices. (C) A plot of the maximum areal strain as a function of the frequency for square waveforms with identical minima of 0 kV and maxima of 3.2 kV. (D) A plot of the areal strain as a function of time for three consecutive cycles of a square waveform with a frequency of 0.5 Hz, as well as minima of 0 kV and maxima of 3.2 kV.

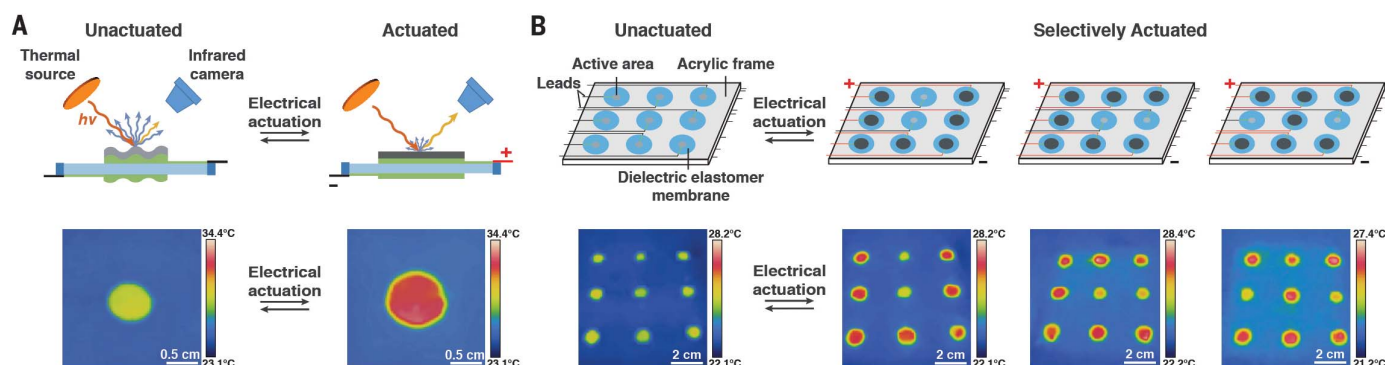


Fig. 4. Electrical modulation of the infrared appearance for single and multiplexed devices. (A) (Top) Schematics of an aluminum-modified device under a constant thermal flux (left) before and (right) after electrical actuation in a rigid frame, illustrating the change in the surface morphology and the reflection of infrared light. (Bottom) Infrared camera images of a representative aluminum-modified device's active region (left) before and (right) after electrical actuation. The change in apparent temperature and thermal appearance is represented by a change in color.

(B) (Top) Schematics of three-by-three arrays of multiplexed devices (left) before electrical actuation and (right) after selective electrical actuation of different device (pixel) combinations as the letters "U," "C," and "I." (Bottom) Infrared camera images of representative three-by-three arrays of multiplexed devices (left) before electrical actuation and (right) after selective electrical actuation of different device (pixel) combinations as the letters "U," "C," and "I." The changes in apparent temperature and thermal appearance are represented by changes in color.

configurations (Fig. 4). To this end, we prepared not only single devices but also three-by-three arrays in which such devices served as independently addressable "pixels" and then visualized both platforms with a thermal infrared camera under an incident heat flux (supplementary materials). We focused our experiments on aluminum-coated devices because of most commercial infrared cameras' spectral range of 7.5 to 14 μm . As an example, a representative single device featured an apparent temperature difference of $\sim 3.6^\circ\text{C}$ between its aluminum-coated active area and the surrounding membrane before electrical actuation (Fig. 4A), presumably because of the dominance of the reflectance's diffuse component in the unactuated state. By contrast, the same device featured an increased apparent temperature difference of $\sim 6.8^\circ\text{C}$ between its aluminum-coated active area and the surrounding membrane after electrical actuation (Fig. 4A), presumably because of the dominance of the reflectance's specular component in the actuated state. The observed changes in the apparent temperature were rapid, stable, and fully reversible over numerous distinct on/off cycles for such devices (movie S2). As another example, the devices in a representative array featured analogous modulation of the apparent temperature differences between their active areas and the surrounding membranes upon device-specific, independent electrical actuation (fig. S6). Multiple devices in the arrays also readily exhibited tandem changes in their active areas' local apparent temperatures (Fig. 4B). Indeed, electrical actuation of different combinations of seven multiplexed devices enabled distinct representative arrays to "spell out" the letters "U," "C," and "I" (Fig. 4B). In principle, the general fabrication approach is amenable to the fabrication of advanced displays with higher pixel densities and/or submillimeter pixel sizes (35, 40).

We demonstrated that our systems could operate without input from an external operator

(Fig. 5A). We connected electrically controlled devices (with aluminum-coated active areas) to a remotely positioned, independently heated temperature sensor, which transduced thermal information from a distal environment while avoiding undesired cross-talk. At a sensor temperature of $\sim 26^\circ\text{C}$, a representative autonomous system possessed a wrinkled active area and an apparent temperature difference between the active area and surrounding unmodified membrane of $\sim 3.4^\circ\text{C}$, as revealed with digital and infrared camera imaging, respectively (Fig. 5A). Upon a change in the temperature of the sensor to $\sim 34^\circ\text{C}$, the system's active area flattened and expanded by $18 \pm 5\%$ (relative to the initial value), and its apparent temperature difference increased to $\sim 3.7^\circ\text{C}$ with respect to the unmodified membrane (Fig. 5A). After a further rise in the sensor's temperature to $\sim 42^\circ\text{C}$, the active area flattened and expanded further by $35 \pm 6\%$ (relative to the initial value), and its apparent temperature difference increased to $\sim 4.0^\circ\text{C}$ with respect to the unmodified membrane (Fig. 5A). With an additional rise in the sensor's temperature to $\sim 48^\circ\text{C}$, the active area flattened and expanded even more by $74 \pm 3\%$ (relative to the initial value), and its apparent temperature difference increased to $\sim 4.4^\circ\text{C}$ with respect to the unmodified membrane (Fig. 5A). Over a temperature window of $>20^\circ\text{C}$ for the sensor, our autonomous system exhibited reproducible and stable changes in the size of its active area (and apparent temperature), albeit in nonlinear fashion (fig. S7).

Last, we evaluated the ability of our infrared camouflage systems to conceal themselves under infrared visualization (Fig. 5B). We prepared devices with aluminum-coated active areas in the shape of a swimming squid's silhouette and then imaged them with a thermal infrared camera under an incident heat flux above a surface with a locally elevated temperature (Fig. 5B and supplementary materials). Before electrical ac-

tuation, a representative squid silhouette-shaped device featured a relatively small microstructured (wrinkled) active area (Fig. 5B) and a negligible apparent temperature difference with the immediate surroundings that effectively made it invisible above a warm surface with a temperature of $\sim 35^\circ\text{C}$, as revealed with infrared camera imaging (Fig. 5B). By contrast, after electrical actuation, the squid silhouette-shaped device featured a larger flattened active area (Fig. 5B) and an apparent temperature difference of $\sim 2^\circ\text{C}$ with the immediate surroundings that made it stand out as a specific shape, as revealed with infrared camera imaging (Fig. 5B). In general, the observed changes in appearance under infrared visualization were again rapid, stable, and fully reversible over numerous distinct on/off cycles (movie S3).

Conclusion

By drawing inspiration from cephalopods, we have developed and validated a new class of adaptive infrared-reflecting materials and devices with an unprecedented combination of properties. First, our artificial platforms translate many of the key natural capabilities of cephalopods from the visible to the infrared regions of the electromagnetic spectrum (although in principle they could be adapted for functionality within the visible). Second, our presented systems feature capabilities and figures of merit that exceed or match the state of the art for adaptive infrared camouflage technologies (table S1). Third, the systems have been intrinsically designed for ready manufacturability and straightforward integration, potentially facilitating applications in dielectric elastomer-based artificial muscles, pneumatic automation, energy generation, and adaptive optics (as well as in other areas). Last, the systems may enable new autonomous portable or wearable thermoregulatory technologies, although such applications will likely require optimization of mechanical actuation strategies or the reduction of

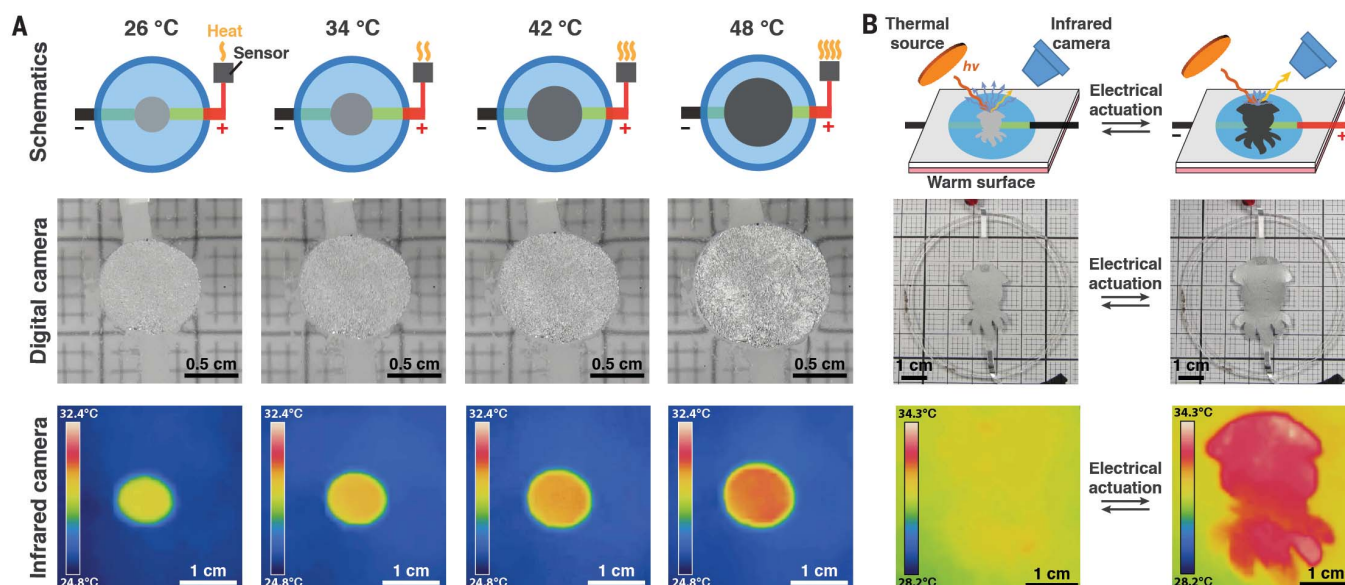


Fig. 5. Autonomous operation and reversible concealment of devices in the infrared. (A) (Top) Schematics of a sensor-connected, aluminum-modified device. The remote sensor is positioned in a different local thermal environment, with increasing temperatures of ~26, ~34, ~42, and ~48°C (from left to right). (Middle) Digital camera images of a representative device's active region at the different sensor temperatures. (Bottom) Infrared camera images of the same device's active region at the different sensor temperatures. Shown are the expansion and change in thermal appearance for the autonomous device's active region, with increasing local temperature for the sensor. (B) (Top) Schematics of a

squid silhouette-shaped, aluminum-modified device maintained under a constant thermal flux and positioned above a warm surface (left) before and (right) after electrical actuation. (Middle) Digital camera images of a representative squid silhouette-shaped, aluminum-modified device's active region (left) before and (right) after electrical actuation. (Bottom) Infrared camera images of the same squid silhouette-shaped, aluminum-modified device's active region (left) before and (right) after electrical actuation. The device alters its thermal appearance and becomes distinguishable from the background only after actuation.

the associated operating voltages. Ultimately, the described materials and devices may afford new possibilities for the many modern technologies that rely on controlling the transfer of thermal radiation and thus may help transform many aspects of daily life.

REFERENCES AND NOTES

- Hernández-Pérez et al., *Energy Build.* **80**, 81–105 (2014).
- U.S. Department of Energy, "Energy-efficient windows"; <https://energy.gov/energysaver/energy-efficient-windows>.
- NASA, A shining example of space benefits (2007); www.nasa.gov/vision/earth/technologies/silver_insulation.html.
- S. Geetha, K. K. Satheesh Kumar, C. R. K. Rao, M. Vijayan, D. C. Trivedi, *J. Appl. Polym. Sci.* **112**, 2073–2086 (2009).
- S. P. Singh, G. Burgess, J. Singh, *Packag. Technol. Sci.* **21**, 25–35 (2008).
- J. F. Sacadura, *J. Quant. Spectrosc. Radiat. Transf.* **93**, 5–24 (2005).
- L. V. Wake, R. F. Brady, *Formulating Infrared Coatings for Defence Applications* (U.S. Defense Technical Information Center, 1993).
- H. Ji et al., *RSC Advances* **7**, 5189–5194 (2017).
- D. Liu, H. Cheng, X. Xing, C. Zhang, W. Zheng, *Infrared Phys. Technol.* **77**, 339–343 (2016).
- L. Xiao et al., *Nano Lett.* **15**, 8365–8370 (2015).
- Z. Mao et al., *Thin Solid Films* **558**, 208–214 (2014).
- M. A. Kats et al., *Phys. Rev. X* **3**, 041004 (2013).
- Y. Tian et al., *Sol. Energy Mater. Sol. Cells* **170**, 120–126 (2017).
- B. Kim et al., *Nano Converg.* **2**, 19 (2015).
- P. Chandrasekhar et al., *Adv. Funct. Mater.* **12**, 95–103 (2002).
- P. Chandrasekhar et al., *Synth. Met.* **135–136**, 23–24 (2003).
- Z. J. Coppens, J. G. Valentine, *Adv. Mater.* **29**, 1701275 (2017).
- R. Schittny, M. Kadic, S. Guenneau, M. Wegener, *Phys. Rev. Lett.* **110**, 195901 (2013).
- T. Han, X. Bai, J. T. L. Thong, B. Li, C.-W. Qiu, *Adv. Mater.* **26**, 1731–1734 (2014).
- S. A. Morin et al., *Science* **337**, 828–832 (2012).
- L. M. Mäthger, E. J. Denton, N. J. Marshall, R. T. Hanlon, *J. R. Soc. Interface* **6** (suppl. 2), S149–S163 (2009).
- R. Hanlon, *Curr. Biol.* **17**, R400–R404 (2007).
- L. Phan et al., *Chem. Mater.* **28**, 6804–6816 (2016).
- L. M. Mäthger, R. T. Hanlon, *Cell Tissue Res.* **329**, 179–186 (2007).
- T. J. Wardill, P. T. Gonzalez-Bellido, R. J. Crook, R. T. Hanlon, *Proc. Biol. Sci.* **279**, 4243–4252 (2012).
- L. F. Deravi et al., *J. R. Soc. Interface* **11**, 20130942 (2014).
- D. G. DeMartini, D. V. Krogstad, D. E. Morse, *Proc. Natl. Acad. Sci. U.S.A.* **110**, 2552–2556 (2013).
- C. Yu et al., *Proc. Natl. Acad. Sci. U.S.A.* **111**, 12998–13003 (2014).
- C. Larson et al., *Science* **351**, 1071–1074 (2016).
- Q. Wang, G. R. Gossweiler, S. L. Craig, X. Zhao, *Nat. Commun.* **5**, 4899 (2014).
- J. Rossiter, B. Yap, A. Conn, *Bioinspir. Biomim.* **7**, 036009 (2012).
- J. Rossiter, A. Conn, A. Cerruto, A. Winters, C. Roke, *Proc. SPIE* **9056**, 905620 (2014).
- F. Carpi, D. De Rossi, R. Kornbluh, R. Pelrine, P. Sommer-Larsen, *Dielectric Elastomers as Electromechanical Transducers* (Elsevier, 2008).
- J. Biggs et al., *Angew. Chem. Int. Ed.* **52**, 9409–9421 (2013).
- F. Carpi, *Electromechanically Active Polymers* (Springer, 2016).
- S. Rosset, H. R. Shea, *Appl. Phys., A Mater. Sci. Process.* **110**, 281–307 (2013).
- D. McCoul, W. Hu, M. Gao, V. Mehta, Q. Pei, *Adv. Electron. Mater.* **2**, 1500407 (2016).
- J. H. Choi, C. L. Willis, K. I. Winey, *J. Membr. Sci.* **394–395**, 169–174 (2012).
- Y. Fan, M. Zhang, R. B. Moore, C. J. Cornelius, *J. Membr. Sci.* **464**, 179–187 (2014).
- S. Akbari, H. R. Shea, *J. Micromech. Microeng.* **22**, 045020 (2012).

ACKNOWLEDGMENTS

The authors thank I. Gorodetskaya and L. Bagge for invaluable discussions and A. Yee's laboratory for the use of an optical microscope. The authors thank G. Hanlon and R. Hanlon for the use of the image in Fig. 1B. The authors thank Kraton Polymers for their support and assistance, by providing samples of NEXARpolymers for use in the project, and for their appreciation of the benefits from university research. **Funding:** The authors are grateful to the Advanced Research Projects Agency–Energy (cooperative agreement DE-AR0000534), the Defense Advanced Research Projects Agency (cooperative agreement HR0011621411), and the Air Force Office of Scientific Research (grant FA2386-14-1-3026) for their financial support. **Author contributions:** C.X. and A.A.G. conceived, designed, and interpreted the experiments. C.X. carried out the experiments. G.T.S. aided with the interpretation of the spectroscopic measurements. C.X. and A.A.G. wrote the manuscript. **Competing interests:** C.X., G.T.S., and A.A.G. are listed as inventors on a provisional U.S. patent application (no. 62/643403) from the University of California, Irvine, which describes the design and working principle of the reported adaptive infrared-reflecting platforms. **Data and materials availability:** All data needed to evaluate the conclusions in the paper are present in the paper and/or the supplementary materials.

SUPPLEMENTARY MATERIALS

www.sciencemag.org/content/359/6383/1495/suppl/DC1
Materials and Methods
Figs. S1 to S7
Table S1
References (41–49)
Movies S1 to S3

17 November 2017; accepted 16 February 2018
10.1126/science.aar5191

REPORT

ORGANIC CHEMISTRY

Activation of olefins via asymmetric Brønsted acid catalysis

Nobuya Tsuji,¹ Jennifer L. Kennemur,¹ Thomas Buyck,¹ Sunggi Lee,¹ Sébastien Prévost,¹ Philip S. J. Kaib,¹ Dmytro Bykov,^{2,3} Christophe Farès,¹ Benjamin List^{1*}

The activation of olefins for asymmetric chemical synthesis traditionally relies on transition metal catalysts. In contrast, biological enzymes with Brønsted acidic sites of appropriate strength can protonate olefins and thereby generate carbocations that ultimately react to form natural products. Although chemists have recently designed chiral Brønsted acid catalysts to activate imines and carbonyl compounds, mimicking these enzymes to protonate simple olefins that then engage in asymmetric catalytic reactions has remained a substantial synthetic challenge. Here, we show that a class of confined and strong chiral Brønsted acids enables the catalytic asymmetric intramolecular hydroalkoxylation of unbiased olefins. The methodology gives rapid access to biologically active 1,1-disubstituted tetrahydrofurans, including (–)-Boivinianin A.

Alkenes are a fundamental and ubiquitous class of organic compounds, often obtained in a single step from crude oil. Among the diverse synthetic applications of olefins, hydrofunctionalization reactions are prized due to their conceptual simplicity, perfect atom economy, and the increased value of the resulting products (1, 2). Although such transformations have been extensively studied for decades using

either Brønsted acid or transition metal catalysts, enantioselective variations remain challenging. For example, in contrast to catalytic asymmetric hydroaminations (3–5) or hydrofunctionalizations of dienes and allenes (6, 7), which are relatively well developed, the enantioselective hydroalkoxylation of electronically neutral olefins is extremely rare, despite its great potential value. Whereas asymmetric photocatalysis can provide

anti-Markovnikov adducts in moderate enantioselectivities (8–10), asymmetric Markovnikov hydroalkoxylation are mainly studied using chiral metal catalysts. However, a highly enantioselective variant with sterically and electronically unbiased olefins has so far not been described, despite major advances in asymmetric metal catalysis (11–14). The lack of progress in this field is presumably due to so-called “hidden acid catalysis,” referring to the in situ release of an achiral Brønsted acid that promotes the nonasymmetric background transformation (15, 16). In contrast, enzymes can activate olefins by protonation and achieve excellent stereoselectivities (17). Recently, an enzyme-catalyzed hydroalkoxylation involving an olefin protonation was reported, albeit with a limited substrate scope (18).

Inspired by the extraordinary capacity of such enzymes to catalyze asymmetric functionalizations of simple olefins, we hypothesized that a well-designed chiral Brønsted acid could induce asymmetric chemical functionalizations of olefins with a more general scope. Such acids should, on the one hand, display very high acidity to enable olefin protonation and, on the other hand, provide a confined, enzyme-like microenvironment to favor the desired transformation with high selectivity, avoiding potential side reactions (Fig. 1A). Although chiral Brønsted acids are now widely used catalytic motifs, enabling numerous asymmetric transformations, their use is still largely limited to the activation of imines and carbonyls. In stark contrast, unactivated alkenes, because of their weak basicity, have remained out of reach for current chiral Brønsted acid catalysts (19–23).

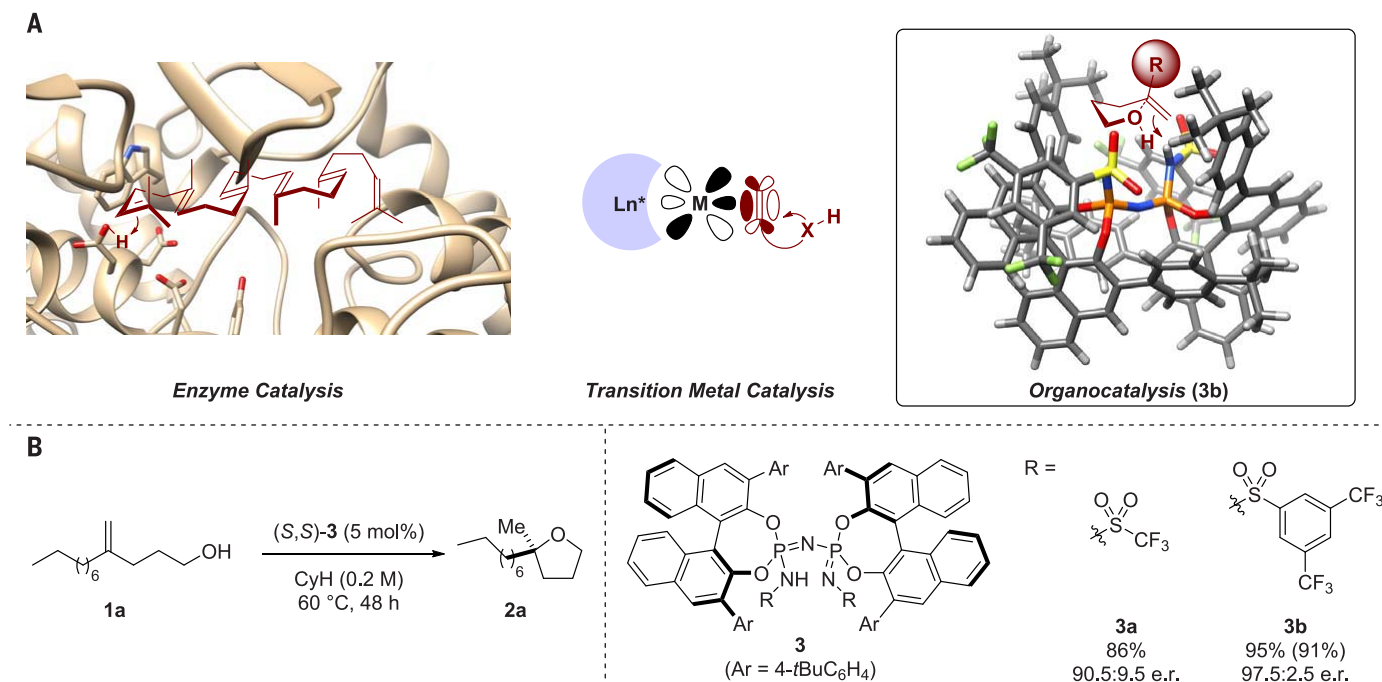


Fig. 1. Olefin activation in biology and chemistry. (A) Three approaches for the activation of olefins. Shown from left to right are the enzyme squalene-hopene cyclase [PDB: 1SQC (17)], a general depiction of the well-defined activation of an olefin with a transition metal complex, and

the posited binding mode of a strong and confined Brønsted acid organocatalyst. (B) Catalyst optimization. Yields were determined by proton nuclear magnetic resonance (¹H NMR) using mesitylene as an internal standard. Isolated yield in parentheses. CyH, cyclohexane.

We have previously introduced the chiral, confined imidodiphosphate (IDP) motif as a highly selective Brønsted acid catalyst that can handle small and unfunctionalized aliphatic substrates (24). Recently, we have accomplished a substantial increase in the acidity of our IDPs by replacing the phosphoryl oxygen atoms with *N*-triflyl groups. The resulting imidodiphosphorimidate (IDPi) catalysts have proven to be highly acidic Lewis acid precatalysts of great utility in silylium-based Lewis acid organocatalysis (25). We became interested in further exploring their utility in Brønsted acid catalysis (26), envisioning that IDPi catalysts could potentially be used in the asymmetric activation of simple olefins.

Multisubstituted oxygen heterocycles are common motifs in natural products and pharmaceuticals such as polyketides (27). The stereoselective

synthesis of substituted tetrahydrofurans typically relies on the use of enantiomerically pure alcohols. We envisioned the direct asymmetric hydroalkoxylation of alkenols as a more straightforward and atom-economical approach. Indeed, the electronically and sterically unbiased alkenol **1a** was used as a model substrate to test the validity of our hypothesis (Fig. 1B). Although most of the conventional Brønsted acid catalysts were inefficient (see the supplementary materials), IDPi **3a** turned out to be promising in terms of both reactivity and enantioselectivity. We realized an additional benefit of our IDPi design toward identifying an optimal catalyst for our desired transformations. Beyond the 3,3'-positions of the IDP catalysts, the two alkylsulfonyl substituents of the IDPi motif offer an additional dimension for diversification and fine-tuning. Excellent yield and enantioselectivity were obtained using IDPi **3b**, bearing sterically more demanding arylsulfonyl groups at nitrogen, instead of triflyl groups. The most stable conformation of **3b** was calculated based on the x-ray structure of an *N*-triflyl IDPi catalyst (25). Because the larger substituent on the sulfonamide (R) is located in the confined environment, steric repulsions between R and the

BINOL backbones presumably make the conformation more rigid and the cavity narrower in the transition states (see the supplementary materials for a detailed discussion).

With an optimal catalyst and conditions in hand, we started investigating the scope and limitation of this hydroalkoxylation reaction (Fig. 2). In addition to different aliphatic substituents (**2b** and **2c**), other functional groups, such as an ether (**2d**) and even an unprotected hydroxyl group (**2e**), were compatible under the reaction conditions. Sulfonamide-containing tetrahydrofuran **2f** which possesses the core skeleton of the marketed pharmaceutical Mefruside (**28**), was also obtained in excellent enantioselectivity. Substrates with tertiary (**2g** and **2h**) and even quaternary (**2i**) centers next to the alkene were compatible with this transformation. Dienes, which generate synthetically useful allylic ethers, were also readily converted (**2j** and **2k**). To our delight, styrene derivatives also reacted to form the desired tetrahydrofurans in excellent yields and enantioselectivities. In addition to the phenyl (**2l**) and naphthyl (**2m**) groups, a variety of functional groups, such as aryl halides (**2n**, **2o**, and **S2a**), an alkyl group (**S2b**), an isolated olefin (**2p**), and an ether (**2q**), were compatible.

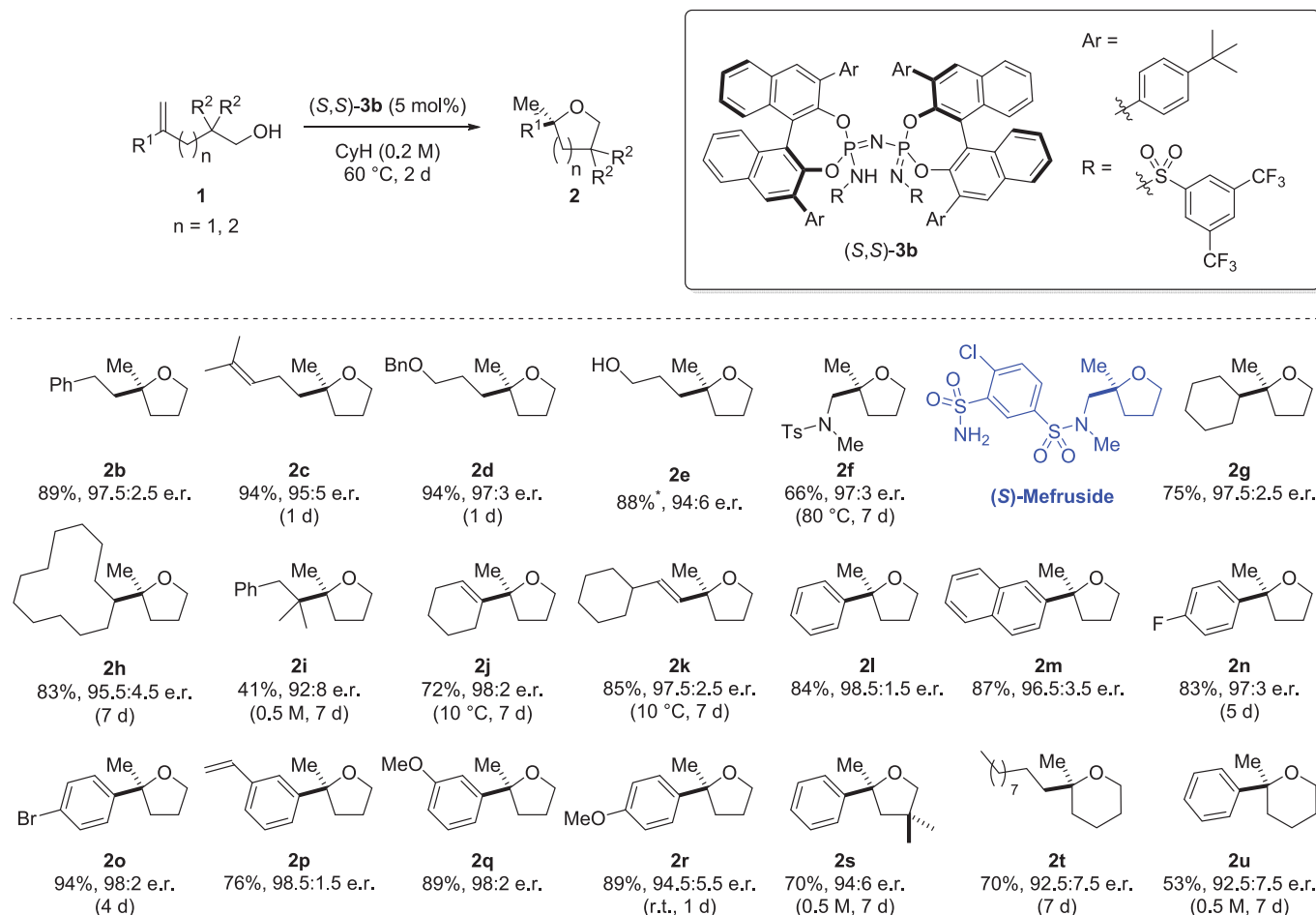
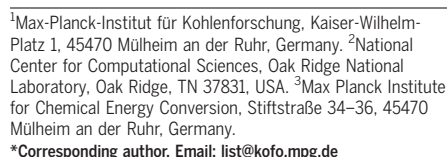


Fig. 2. Scope of the hydroalkoxylation. Isolated yields are presented. Enantiomeric ratio (e.r.) determined either via high-performance liquid chromatography (HPLC) or gas chromatography (GC). *The reaction was performed in 1,2-dichloroethane–cyclohexane (1:1). Ts, *p*-toluenesulfonyl.

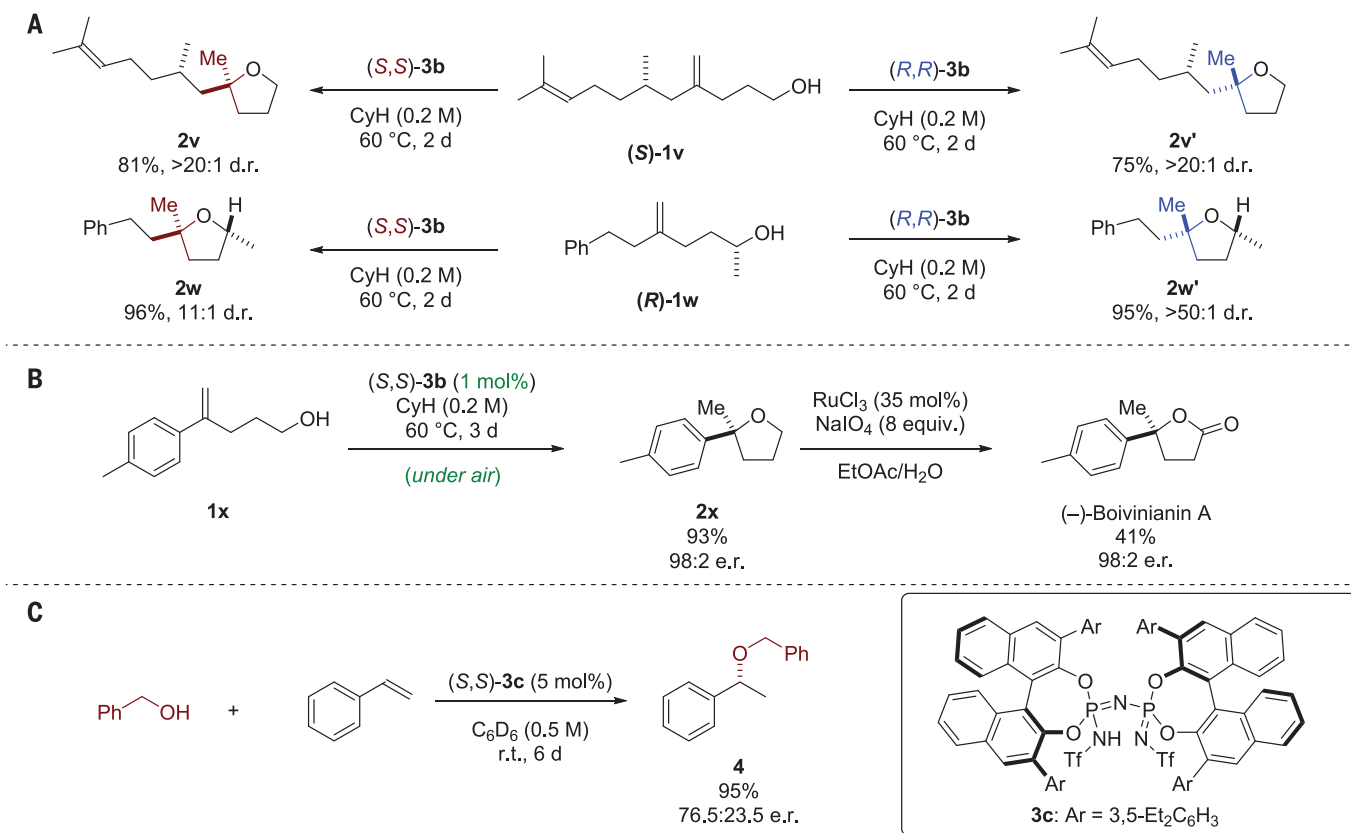


Fig. 3. Further application of the methodology. (A) Catalyst-controlled diastereoselective hydroalkoxylations. Diastereomeric ratios (d.r.) were determined by ¹H-NMR and GC or HPLC. (B) Concise synthesis of (-)-Boivinianin A. (C) A preliminary intermolecular hydroalkoxylation.

A methoxy-substituted styrene (**1r**) was also a good substrate. Although this electron-rich styrene might be considered activated for the cyclization, it could also have led to product racemization under the acidic conditions. Interestingly, a higher concentration and longer reaction time were required in the case of dimethyl-substituted styrene **1s** to achieve reasonable conversion, despite a possible Thorpe-Ingold effect. The bulky *gem*-dimethyl group presumably hinders access of this substrate into the sterically demanding catalyst active site. We also envisioned the same strategy for the synthesis of substituted tetrahydropyrans. Like tetrahydrofurans, the tetrahydropyran skeleton is ubiquitous in natural products and pharmaceuticals, such that enantioselective syntheses of this motif are of great value. Indeed, 2,2-disubstituted tetrahydropyrans were obtained in good yields and slightly reduced enantioselectivities (**2t** and **2u**).

In addition to enantioselective hydroalkoxylations, diastereoselective versions may provide a valuable approach to natural products or pharmaceuticals with multiple stereogenic centers (27). In contrast to six-membered ring-forming cyclizations, which are often highly diastereoselective due to well-defined chair- or boatlike transition states, the diastereocontrolled synthesis of multi-substituted tetrahydrofurans is typically more difficult because the energetic difference between

isomeric transition states is often smaller. We envisioned that a catalyst-controlled diastereoselective transformation that is independent of existing stereocenters would be powerful. In this vein, the two diastereoisomeric products **2v** and **2v'** could be selectively obtained from alcohol (**S**)-**1v**, fully controlled by using either the (*S*, *S*) or the (*R*, *R*) enantiomer of the catalyst (Fig. 3A). Moreover, optically pure secondary alcohol (*R*)-**1w** selectively furnished 2,2,5-trisubstituted tetrahydrofurans **2w** or **2w'** in excellent yields and diastereoselectivities, which were mainly controlled by the catalyst.

Encouraged by the wide scope of our method, we designed a concise synthesis of (-)-Boivinianin A (29) to demonstrate the utility, simplicity, and efficiency of the developed transformation (Fig. 3B). Accordingly, alkenol **1x** was subjected to the reaction conditions, using a lower loading of catalyst (1 mole %) under air, to provide the corresponding tetrahydrofuran in excellent yield and enantioselectivity. The obtained product was oxidized without erosion of enantiopurity to furnish the corresponding lactone, which was confirmed to be (-)-Boivinianin A by comparison to analytical data (30).

To demonstrate the generality of this approach, we also investigated an intermolecular hydroalkoxylation, which is considered another major synthetic challenge with respect to both reac-

tivity and enantioselectivity (Fig. 1C) (13). Gratifyingly, IDPi **3c** catalyzed the reaction of styrene with benzyl alcohol to furnish product **4** in 95% yield and with very promising enantioselectivity [enantiomeric ratio (e.r.) = 76.5:23.5]. Further optimizations are currently ongoing.

Mechanistically, we initially envisioned the reaction to proceed via a stepwise protonation, cyclization pathway. However, a concerted mechanism in which protonation and C–O bond formation occur more synchronously is also plausible (18, 31). Toward gaining more insight into the reaction mechanism and the origin of enantioselectivity, we performed density functional theory (DFT) studies (see the supplementary materials for a description of the methods and a detailed discussion). The energies were obtained under B3LYP/def2-TZVP/D3(BJ)/CPCM level of theory. The lowest energy transition state **TS1** suggests a concerted though asynchronous mechanism in which the reaction is triggered by the protonation of the olefin followed by C–O bond formation (Fig. 4A). The proposed transition state also describes the origin of enantioselectivities (Fig. 4B). Whereas the major enantiomer is generated via **TS1** with 13.8 kcal/mol of activation barrier, the minor enantiomer requires 15.4 kcal/mol to reach **TS1'**. In addition, in **TS1**, the substituent of the substrate points toward the outside of the pocket due to the sterically demanding 3,3'-position of

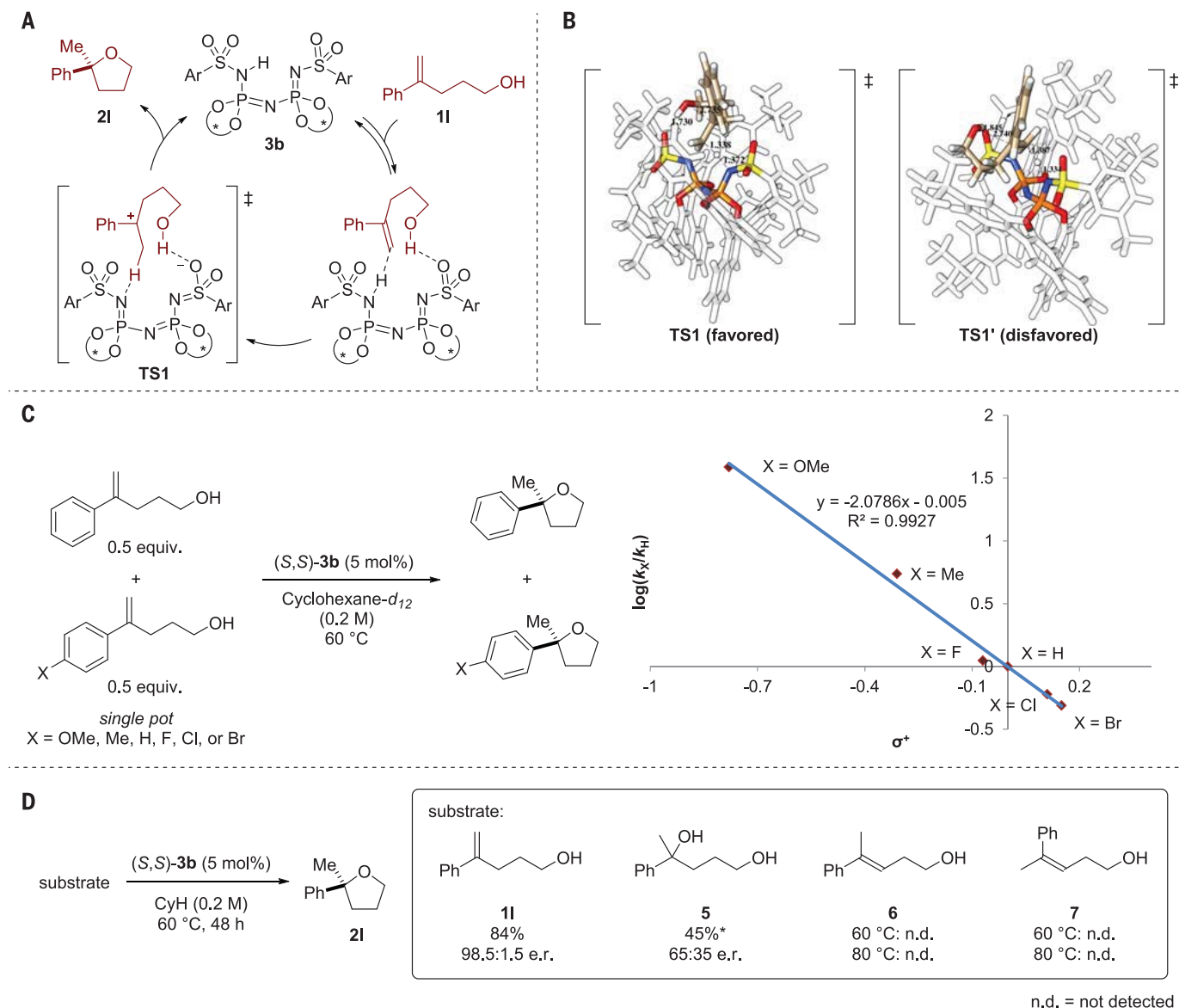


Fig. 4. Mechanistic studies. (A) A plausible catalytic cycle. (B) DFT-calculated enantiodetermining transition states of the hydroalkoxylation of **1I**. To increase visibility, the bulky substituents in the catalyst are whitened in this picture. All distances are in angstroms. For more details, see the supplementary materials. (C) Intramolecular Hammett

analysis (σ^+) is consistent with asynchronous concerted mechanism. For more details, see the supplementary materials. (D) Hydroalkoxylation with olefin isomers and etherification of the corresponding alcohol. *Yield was determined by ^1H NMR using mesitylene as an internal standard.

the BINOL backbones, which presumably allowed for the broad substrate scope.

To further evaluate the mechanism experimentally, a Hammett analysis with a series of styrene derivatives was performed (Fig. 4C). Plotting $\log(k_X/k_H)$ against substituent parameter σ^+ gave a linear correlation with a negative slope ($\rho = -2.08 \pm 0.04$), which is consistent with the proposed carbocationic intermediate in the transition state. To gain further insight into the reaction mechanism, the corresponding alcohol **5** and olefin isomers **6** and **7** were subjected to the reaction conditions (Fig. 4D). If the reaction indeed proceeds via a carbocation, either within an ion pair or covalently bound to the catalyst, substrates **5**

to **7** should provide essentially identical enantioselectivities. Whereas substrate **1I** afforded the desired tetrahydrofuran **2I** in excellent yield and enantioselectivity, **5** provided product **2I** in only moderate yield and with poor enantioselectivity. Neither **6** nor **7** gave any of the desired products under these conditions or at higher temperatures. These results are consistent with the proposed asynchronous concerted mechanism.

The approach delineated here enables the asymmetric activation of electronically and sterically unbiased alkenes by highly confined and highly acidic organocatalysts. The methodology is operationally simple, and a variety of alkenols could be converted in high yields and enantioselectivities.

We believe that the presented approach bears great potential for various other hydrofunctionalizations and related reactions of olefins.

REFERENCES AND NOTES

- M. Beller, J. Seayad, A. Tillack, H. Jiao, *Angew. Chem. Int. Ed.* **43**, 3368–3398 (2004).
- V. Rodriguez-Ruiz et al., *Dalton Trans.* **44**, 12029–12059 (2015).
- E. Bernoud, C. Lepori, M. Mellah, E. Schulz, J. Hannedouche, *Catal. Sci. Technol.* **5**, 2017–2037 (2015).
- J.-S. Lin et al., *Angew. Chem. Int. Ed.* **54**, 7847–7851 (2015).
- L. Ackermann, A. Althammer, *Synlett* **2008**, 995–998 (2008).
- N. D. Shapiro, V. Raniyar, G. L. Hamilton, J. Wu, F. D. Toste, *Nature* **470**, 245–249 (2011).
- G. L. Hamilton, E. J. Kang, M. Mba, F. D. Toste, *Science* **317**, 496–499 (2007).
- D. S. Hamilton, D. A. Nicewicz, *J. Am. Chem. Soc.* **134**, 18577–18580 (2012).

9. Y. Nishiyama *et al.*, *J. Am. Chem. Soc.* **130**, 7526–7527 (2008).
10. Z. Yang, H. Li, S. Li, M.-T. Zhang, S. Luo, *Org. Chem. Front.* **4**, 1037–1041 (2017).
11. H. Murayama, K. Nagao, H. Ohmiya, M. Sawamura, *Org. Lett.* **17**, 2039–2041 (2015).
12. J. Schlüter, M. Blazejak, F. Boeck, L. Hintermann, *Angew. Chem. Int. Ed.* **54**, 4014–4017 (2015).
13. C. S. Sevov, J. F. Hartwig, *J. Am. Chem. Soc.* **135**, 9303–9306 (2013).
14. H. Shigehisa *et al.*, *J. Am. Chem. Soc.* **138**, 10597–10604 (2016).
15. T. T. Dang, F. Boeck, L. Hintermann, *J. Org. Chem.* **76**, 9353–9361 (2011).
16. D. C. Rosenfeld, S. Shekhar, A. Takemiya, M. Utsunomiya, J. F. Hartwig, *Org. Lett.* **8**, 4179–4182 (2006).
17. K. U. Wendt, K. Poralla, G. E. Schulz, *Science* **277**, 1811–1815 (1997).
18. S.-S. Gao *et al.*, *J. Am. Chem. Soc.* **139**, 3639–3642 (2017).
19. M. Terada, *Synthesis* **2010**, 1929–1982 (2010).
20. G. Adair, S. Mukherjee, B. List, *Aldrichim Acta* **41**, 31–39 (2008).
21. D. Parmar, E. Sugiono, S. Raja, M. Rueping, *Chem. Rev.* **114**, 9047–9153 (2014).
22. T. Akiyama, K. Mori, *Chem. Rev.* **115**, 9277–9306 (2015).
23. A. Sakakura, M. Sakuma, K. Ishihara, *Org. Lett.* **13**, 3130–3133 (2011).
24. I. Čorić, B. List, *Nature* **483**, 315–319 (2012).
25. P. S. J. Kaib, L. Schreyer, S. Lee, R. Properzi, B. List, *Angew. Chem. Int. Ed.* **55**, 13200–13203 (2016).
26. L. Liu *et al.*, *J. Am. Chem. Soc.* **139**, 13656–13659 (2017).
27. A. Lorente, J. Lamiariano-Merketegi, F. Albericio, M. Álvarez, *Chem. Rev.* **113**, 4567–4610 (2013).
28. H. B. Allen, D. A. Lee, *Curr. Med. Res. Opin.* **1**, 547–553 (1973).
29. D. A. Mulholland, K. McFarland, M. Randrianarivelosia, *Biochem. Syst. Ecol.* **34**, 365–369 (2006).
30. I. Čorić, S. Müller, B. List, *J. Am. Chem. Soc.* **132**, 17370–17373 (2010).
31. Y. Y. Khomutnyk *et al.*, *J. Am. Chem. Soc.* **138**, 444–456 (2016).

ACKNOWLEDGMENTS

We thank the gas chromatography, mass spectrometry, and nuclear magnetic resonance departments, especially C. Hartding, of the Max-Planck-Institut (MPI) für Kohlenforschung for analytics. We thank M. Klußmann for discussions about Hammett analysis and C. K. De for general discussions. **Funding:** Generous support from the Max Planck Society, the Deutsche Forschungsgemeinschaft (Leibniz Award to B.L. and Cluster of Excellence Ruhr Explores Solvation (RESOLV, EXC 1069), the Swiss National Science Foundation (Fellowship to T.B.), and the European Research Council (Advanced Grant “C–H Acids for Organic Synthesis, CHAOS”) is gratefully acknowledged. This research used resources of the Oak Ridge Leadership Computing Facility, which is a Department of Energy Office of Science User Facility supported

under contract DE-AC05-00OR22725. **Author contributions:** B.L. conceived and directed the project. N.T., S.L., and J.L.K. performed experiments and analysis. N.T. found the optimized catalyst and conditions. N.T. and S.L. jointly designed and prepared the catalyst. J.L.K. developed the intermolecular hydroalkoxylation. T.B., S.P., and P.S.J.K. contributed to initial studies. D.B. performed the computational studies. C.F. contributed to the NMR studies. N.T. and B.L. prepared the manuscript. **Competing interests:** B.L., P.S.J.K., and S.L. are inventors on patent WO2017037141 (A1) filed by the MPI für Kohlenforschung covering the IDPi catalyst class and their applications in asymmetric synthesis. **Data and materials availability:** Data are available in the supplementary materials.

SUPPLEMENTARY MATERIALS

www.sciencemag.org/content/359/6383/1501/suppl/DC1

Materials and Methods

Figs. S1 to S15

Tables S1 to S3

References (32–70)

25 September 2017; resubmitted 7 December 2017

Accepted 2 February 2018

10.1126/science.aag0445

APPLIED PHYSICS

Nanofluidic rocking Brownian motors

Michael J. Skaug,* Christian Schwemmer,* Stefan Fringes,*
Colin D. Rawlings, Armin W. Knoll†

Control and transport of nanoscale objects in fluids is challenging because of the unfavorable scaling of most interaction mechanisms to small length scales. We designed energy landscapes for nanoparticles by accurately shaping the geometry of a nanofluidic slit and exploiting the electrostatic interaction between like-charged particles and walls. Directed transport was performed by combining asymmetric potentials with an oscillating electric field to achieve a rocking Brownian motor. Using gold spheres 60 nanometers in diameter, we investigated the physics of the motor with high spatiotemporal resolution, enabling a parameter-free comparison with theory. We fabricated a sorting device that separates 60- and 100-nanometer particles in opposing directions within seconds. Modeling suggests that the device separates particles with a radial difference of 1 nanometer.

Lab-on-chip devices that can size-selectively transport and collect nanoscale particles are expected to find applications in materials and environmental sciences [e.g., size analysis, filtration, and monodisperse production (1, 2)] as well as in point-of-care diagnostics and biochemistry [e.g., molecular separation and preconcentration (1, 3–5)]. For example, directed transport may overcome fundamental limits in the detection of dilute species in fluidics (6) by actively transporting and accumulating them at the sensor area. Inspired by molecular motors in biology, Magnasco (7) and Prost *et al.* (8) proposed that such particle transport could be achieved with artificial Brownian motors (BMs) based on an asymmetric energy landscape and non-equilibrium fluctuations. Previous experiments (9–14) focused primarily on “flashing ratchet”-type BMs that exploit a periodically generated asymmetric trapping potential and isotropic diffusion to transport micrometer-scale particles. The required potentials were obtained using optical (9, 10) or dielectrophoretic (11–13) forces, which scale with the particle volume and therefore are not efficient at the nanoscale. Accordingly, direct charge-charge interactions were required to transport DNA molecules by means of intercalated electrodes (14).

Such flashing BMs were also explored for particle sorting by exploiting the dependence of diffusion on particle size. However, similar to the case of continuous-flow devices (4, 15), it is expected that using external forcing instead of diffusion will result in greater separation precision. Rocking BMs (7, 12, 16) use a zero-mean external force and a static potential landscape to generate directed particle motion. Their transport exhibits a strong nonlinear dependence on particle diffusivity, which is promising for nanoparticle separation (17). However, for nanoscale particles, creating a sufficiently strong static energy landscape remains a challenge.

Electrostatic trapping (18) addresses this challenge by confining like-charged particles between

uniformly charged surfaces. A geometrical recess in one of the surfaces lowers the particle-surface interaction energy locally and thus defines a lateral trapping potential. Confinement energies of several multiples of $k_B T$ (where k_B is the Boltzmann constant and T is absolute temperature) were achieved, resulting in the stable trapping of various types of charged nanoparticles, such as 10- to 100-nm-diameter Au nanospheres (18–20), Au nanorods (21), 50-nm-diameter vesicles (18), and even 10- to 60-base DNA oligonucleotides and 10-kDa proteins (22). External forcing by optical and electrical fields was also explored as a means of driving the particles from one stable minimum to another (23).

We expanded the concept of geometry-induced electrostatic trapping to create complex two-dimensional (2D) energy landscapes for nanoparticles by replacing the simple recess geometries with lithographically patterned 3D topographies. The patterns were fabricated using thermal scanning probe lithography (t-SPL) (24), which has a depth accuracy in the nanometer range (25). We implemented nanofluidic rocking BMs for our model particle system of 60-nm Au nanospheres. We created energy landscapes of up to $\sim 10 k_B T$ in scale at a lateral resolution of less than 100 nm. Using high spatiotemporal resolution optical microscopy, we determined all relevant physical system parameters in situ, such as the ~ 10 -nm spatially resolved particle interaction potential and the millisecond-resolved particle motion. We find excellent agreement with theory and demonstrate a sorting device.

Gold nanoparticles in electrolyte were confined in a nanofluidic slit of controllable gap distance d (Fig. 1A and fig. S1) (26) using the nanofluidic confinement apparatus described in (27). We used closed-loop t-SPL (25) to pattern the thermally sensitive polymer polyphthalaldehyde with a sawtooth profile along complex-shaped transport tracks having a depth of 30 to 50 nm and a period of $L \approx 550$ nm (Fig. 1, B to D). The modulated gap height (Fig. 1A) in the slit results in a static lateral particle energy landscape, which confines the particles to the tracks (Fig. 1E) and provides the static asymmetric potential required for the rocking BM.

To elucidate the effect of the topography on the particle's interaction energy and to demonstrate the operation of the BMs, we resorted to simple linear ratchets (Fig. 2A). We define the direction of the BMs as the direction of the shallow slope profile (Fig. 2B), indicated by the arrows in Fig. 2A. In addition, three control fields, C1, C2, and C3, were written with depths of the maximum, mean, and minimum depth of the ratchets, respectively. The control fields are used for in situ measurement of the mean particle diffusivity and the mean particle speed in the non-driven and driven case, respectively.

We recorded the position of the particles with an effective particle illumination time of ~ 40 μ s and a frame rate of 1000 fps (27) using interferometric scattering detection microscopy (27, 28) (movie S1). The overlaid heat map (2D histogram) in Fig. 2A indicates the density of all recorded particle positions. Owing to the brief illumination time, the particle positions obtained from each frame can be used directly to obtain particle occupation histograms (26) (fig. S2). We collapsed the observed 2D particle positions onto the x axis and calculated an average 1D histogram for a single ratchet cell by cross-correlation averaging. The normalized histograms of the single cells are shown in the inset of Fig. 2C. Identifying the histograms with the average 1D occupation probabilities $p(x)$, we calculated the effective 1D interaction energy $V_0(x)$ of the particles using Boltzmann's principle $p(x) \propto \exp[-V_0(x)/k_B T]$ (Fig. 2C).

In the nanofluidic confinement apparatus, the gap distance is controlled and measured (27) with nanometer accuracy, which provides a convenient handle to tune the energy scale. Figure 2D shows nine recorded energy profiles for $127 \text{ nm} < d < 148 \text{ nm}$. Within this range the curves are self-similar, and they collapse on a master curve obtained by linear scaling (Fig. 2E). The scaling coefficient α decreases exponentially: $\alpha \propto \exp(-d/2l)$, where $l = 18 \pm 3 \text{ nm}$. Finite element modeling simulations (26) (figs. S3 and S4) yield similar potential shapes (Fig. 2C) and indicate that l is slightly greater than the Debye length $\kappa^{-1} \approx 12 \text{ nm}$ (26) (table S1).

The patterned nanofluidic slit thus defines an asymmetric static potential landscape for the particles—one of the two required ingredients for a rocking BM. The other necessary ingredient is non-equilibrium fluctuations, which we created by applying a 10-Hz electric square-wave potential to gold electrodes (Fig. 1A and fig. S1). The electric field induces both an electrophoretic force on the nanoparticles and an electro-osmotic plug flow of the electrolyte, acting on the particles in opposite directions. Our experiments showed that electro-osmotic effects dominate because the particles are dragged toward the negative electrode. Figure 3A depicts the particle drift velocities measured at time intervals of 1 ms, $d = 127 \text{ nm}$, and applied voltage $U = 3.5 \text{ V}$ @ 10 Hz, resolving each half-cycle of the electric field.

We used the average drift velocity (fig. S5) in the control fields, $\langle v_c \rangle$, to quantify the total force as a function of the gap distance (Fig. 3B). Combining Einstein's relation $D_0 = k_B T / 6\pi\eta a$ and Stokes' equation for particle drag $F = 6\pi\eta a \langle v_c \rangle$

IBM Research–Zurich, 8803 Rüschlikon, Switzerland.

*These authors contributed equally to this work.

†Corresponding author. Email: ark@zurich.ibm.com

(where η is dynamic viscosity and a is particle radius) yields $F/k_B T = \langle v \rangle / D_0$. At $U = 5$ V and $d = 127$ nm, we observed $F = 39 \pm 2$ $k_B T / \mu\text{m}$ for the measured average diffusion coefficient $D_0 = 4.6 \pm 0.2$ $\mu\text{m}^2 \text{s}^{-1}$ (SD of 18 measurements). Maximum voltages were restricted to 5 V at $d = 127$ nm and 3 V at $d = 147$ nm (movies S2 and S3) to prevent particles escaping from the reservoirs.

In each half-cycle of the electric field, the force is approximately constant, which corresponds to a linear potential being added to the static potential V_0 : $V(x) = V_0(x) \pm xF$. Figure 3C shows the tilted potentials for the most- and least-confined experiments ($d = 127$ nm and $d = 147$ nm) and the maximally applied voltages of 5 and 3 V, respectively. In the forward direction, all energy barriers disappear and the particles begin to drift. In the backward direction, however, finite energy

barriers ΔV_B remain, thus hindering drift. Oscillating the force leads to a “rocking” of the asymmetric particle potential, resulting in directed transport due to the rectification of particle drift.

According to Reimann *et al.*, the average drift velocity can be computed for the tilted potentials shown in Fig. 3C using the first passage time model (29):

$$\langle v \rangle = \frac{1 - \exp\left(\frac{-LF}{k_B T}\right)}{\int_0^L L^{-1} I_{\pm}(x) dx} \quad (1)$$

$$I_{\pm}(x) = \frac{1}{D_0} \int_0^L \exp\left\{\frac{\pm[V_0(x) - V_0(x \mp z)]}{k_B T}\right\} dz \quad (2)$$

All relevant, nontrivial quantities $V_0(x)$, D_0 , and F in this theoretical description were measured in situ, and a parameter-free comparison with theory is possible. Equation 1 was evaluated numerically and the total drift was calculated as one-half of the drift difference in forward and backward directions (lines in Fig. 3, D and E). The theoretical description assumes slow rocking; that is, the actuation time of each half-cycle is long relative to the particle-drift time across a single ratchet element. Our experiments show excellent agreement with the model at 10 Hz (fig. S6). Moreover, we found a frequency dependence of the ratchet performance (Fig. 3F). Best performance is observed when the actuation time at 30 to 50 Hz is about twice the particle-drift time $L/\langle v \rangle \approx 6$ ms in the forward direction (movies S4 to S6).

Fig. 1. Nanofluidic Brownian motor setup and ratchet topography defined by thermal scanning probe lithography (t-SPL).

(A) Schematic cross section and top view of the nanofluidic slit. Top left: A pillar (height 30 to 50 μm) etched into the cover glass provides close proximity, optical access, and space for electrodes. Top right: The top view (not to scale) depicts the electrodes (yellow, spaced by ~ 1.2 mm) and the pillar in the center (width ~ 100 μm). Two voltage signals $U_{x,y}(t)$, zero mean square-shaped with a phase shift of 90° , are applied in the x and y directions to the electrodes, thus creating a rotating electric field that drives the motor. Bottom: The ratchet topography in polyphthalaldehyde and the 60-nm gold nanoparticle, drawn to scale. The particle experiences a ratchet-shaped energy landscape due to the ion-cloud interactions (orange) between like-charged surfaces. The gap distance is $d = 150 \pm 1$ nm. (B) Topography image of the patterned geometry. (C) Close-up of the small circular ratchet shape of (B). (D) Cross section of the track's sawtooth geometry measured along the white dashed line in (B). (E) Optical image of particles trapped in the ratchet. The color overlay indicates the average speed measured along the ratchet path in the counterclockwise direction at an applied rotating voltage of 3 V @ 30 Hz.

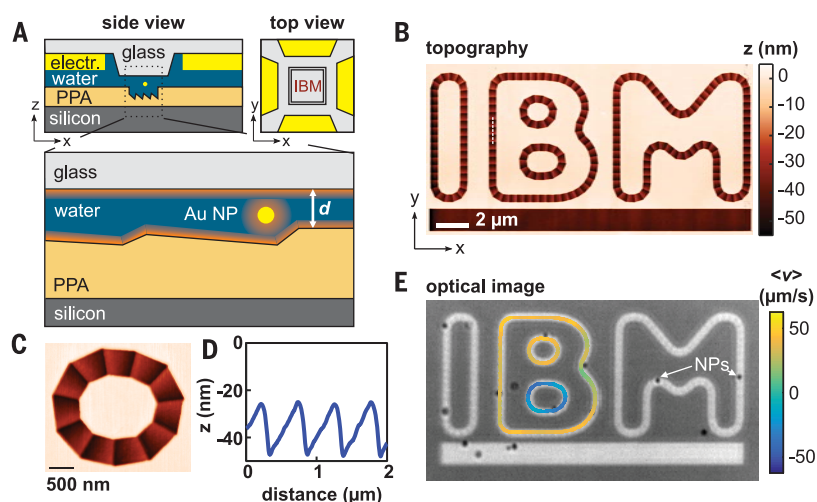
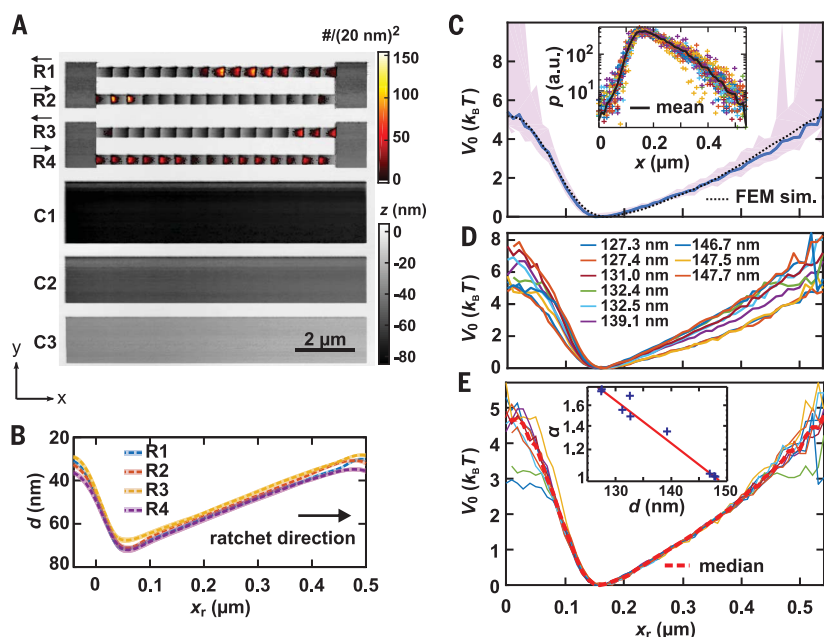


Fig. 2. Experimental determination of the average energy landscape.

(A) Topography image of the patterned ratchets R1 to R4 and three control fields, C1 to C3. Arrows indicate the ratchets' direction. The observed particle positions are overlaid as a heat map. (B) Single-cell averaged cross sections (dashed lines) of the four ratchets including standard deviations (areas, 15 cells per ratchet) along the ratchet direction x_r . (C) Average experimental 1D energy profiles $V_0(x_r)$ of the particles in the ratchet compared to a profile obtained from finite element modeling (FEM; dotted line). The blue line denotes the average interaction energy as estimated from the average occupation probability (inset, 24 profiles) using Boltzmann's principle. The shaded region marks the standard deviation. (D) $V_0(x_r)$ for nine gap distances of $127 \text{ nm} < d < 148 \text{ nm}$ (standard deviation of d , ~ 1 nm). (E) Master curve obtained by linear scaling of the potentials by a factor of α . The inset depicts the exponential dependence of α on d .



For the curved paths shown in Fig. 1C, a rotating electric field was applied to achieve efficient operation (fig. S7 and movie S7). The electric field direction can also be used to selectively power ratchets written in orthogonal directions—for ex-

ample, to shuttle particles between several reservoirs (fig. S8 and movie S8).

Finally, we exploited the strong nonlinear gap distance dependence of the energy landscape to separate 60- and 100-nm particles into oppo-

site compartments, LC and RC, of a sorting device (Fig. 4, A and B). The middle area between the compartments contains three deep (local $d = 185$ to 210 nm) and narrow (width ≈ 140 nm) ratchets pointing to the left and embedded in a wide ($8\ \mu\text{m}$) and shallow (local $d = 160$ to 190 nm) ratchet pointing to the right. Our experiments show that at a gap distance of $d = 150$ nm, the large particles are well confined to the deep ratchets (movie S9). Although the small particles experience an energy barrier of $\Delta V_0 \geq 1.3k_B T$ (Fig. 4C and fig. S9) to move from the deep ratchet into the shallow ratchet, its wide area ($4\ \mu\text{m} \times 2\ \mu\text{m}$ versus $3\ \text{nm} \times 140\ \text{nm}$) leads to a measured occupation probability of 76% in the shallow ratchet. Combined with the measured ratchet potential of $\sim 4.5k_B T$ (red line in Fig. 4C), this leads to a transport of 60-nm particles toward RC.

The optical images in Fig. 4D demonstrate the efficient sorting of the particle populations in opposite directions. Initially, the particles were distributed randomly across the ratchet field. Applying a square-wave voltage of $4\ \text{V}$ @ $30\ \text{Hz}$, we found that the populations were fully separated into the respective compartments after 2 s, except for a single 100-nm particle stuck in the shallow ratchet. After 6.3 s, this particle diffused into the deep channel and was transported into the LC. Figure 4E depicts the median brightness of measured particle trajectories in the left and right halves of the field. The histograms at the right in Fig. 4E indicate that next to the majority particle types of 60-nm (red) and 100-nm (blue) spheres, there is a small population of a third particle type (light blue) in the sample. Inspection by scanning electron microscopy (SEM)

Fig. 3. Brownian motor operation.

(A) Time-resolved average velocities measured in the control fields C1 and C2 and ratchets R1 to R4. (B) Average particle speed in the control fields as a function of applied voltage U and for two gap distances, $d = 147$ nm and 127 nm. (C) Estimated forward (solid lines) and backward (dashed lines) 1D potential energy $V(x)$ for the two gap distances and applied voltages of 3 and 5 V. Arrows indicate the magnitude of ΔV_B . (D) Average measured particle drift velocity in ratchets R1 to R4. (E) Average particle drift velocities shown separately in the forward (blue and light blue) and backward directions (black and gray) of the ratchets. Lines in (D) and (E) indicate a fit parameter-free comparison with theory. (F) Average overall drift velocity ($\langle v \rangle$) observed in ratchets R1 to R4 as a function of the driving frequency for three gap distances and their respective maximum voltages. Error bars in (B), (D), (E), and (F) denote SD of measurements obtained for each (ratchet) field.

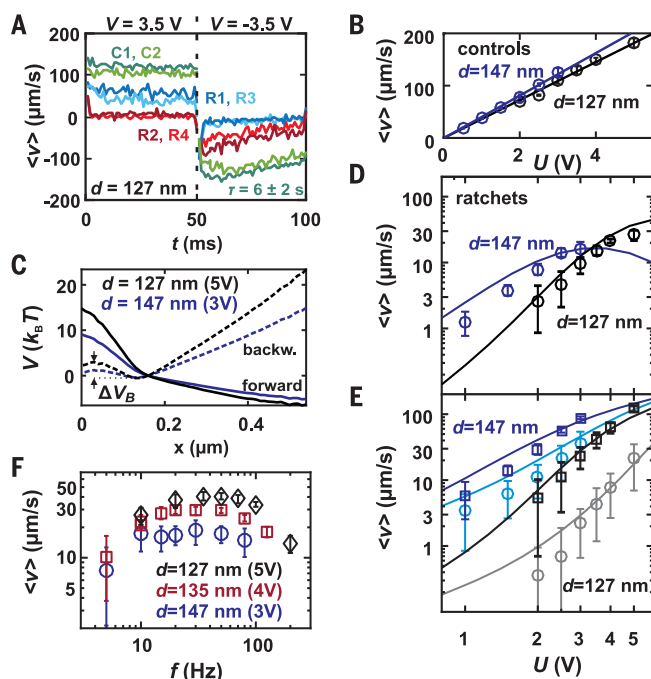
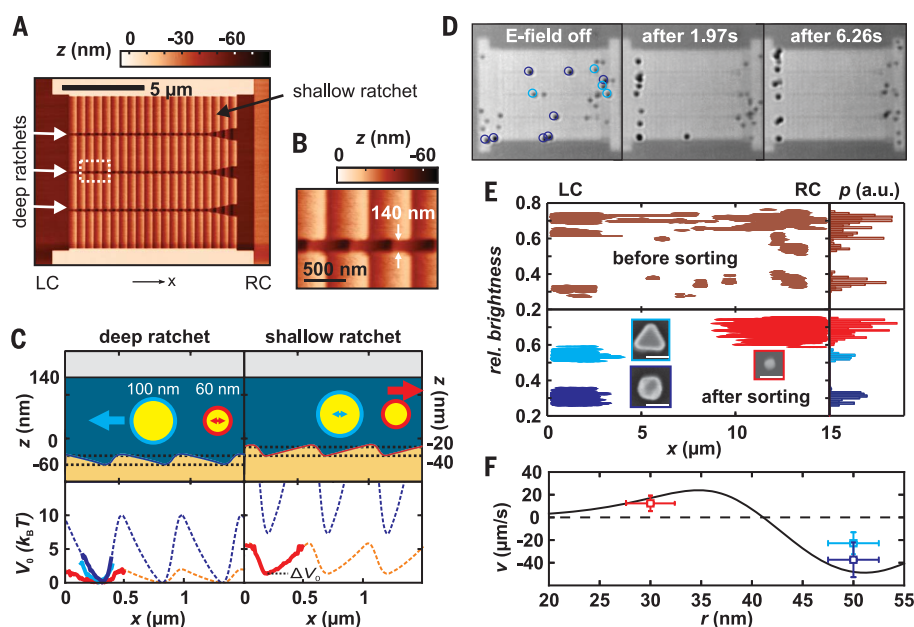


Fig. 4. Sorting of 60- and 100-nm Au particles.

(A) Topography of the sorting device as determined by t-SPL. Three deep ratchets (white arrows) are embedded in a wide shallow ratchet for transporting the 100- and 60-nm particles into compartments LC and RC, respectively. The deep ratchets comprise wide ends for better entrance of nanoparticles from RC. (B) Close-up of the dotted white box in (A) depicting the central deep ratchet (width $140\ \text{nm}$). (C) Top: Schematics of the sorting device, roughly to scale with experimental conditions. The 60-nm particles (red) in the shallow ratchet and the 100-nm particles (blue) in the deep ratchet are transported in opposite directions (arrows). Bottom: The corresponding measured (solid) and modeled (dashed) static energies. The 60-nm particles experience an energy barrier of $\Delta V_0 \approx 1.3k_B T$ as they move into the shallow ratchet. (D) Optical microscopy images before sorting, and after 2 s and 6.3 s of applied voltage of $4\ \text{V}$ @ $30\ \text{Hz}$ AC. Colored circles indicate the 100-nm particle types depicted in (E). (E) Spatial particle distribution (left) and histograms (right) of the median relative brightness of the particle trajectories measured before and after sorting. We observed a third particle population (light blue), which we attribute to platelets according to their relative abundance. Insets: SEM images of the corresponding particles (scale bars, $100\ \text{nm}$). (F) Modeled average particle drift v as a function of particle radius r . The data points indicate the measured speed (mean \pm SD) of 15 particles. The radial error corresponds to the measured SD (60 nm, 8%; 100 nm, 5%) of the particle size determined by SEM (26).



revealed that, apart from the spheres, the 100-nm dispersion contained a small fraction of “platelets,” which we assign to the intermediate particle type (26) (figs. S10 and S11). Using the median trajectory contrast for differentiation, we measured a particle potential for this population of $\sim 6k_B T$ in the deep ratchet (Fig. 4A). Note that although the brightness histograms of 60-nm spheres and 100-nm platelets almost overlap, all platelets were actively driven toward LC (movie S9).

The operation and separation potential of the device can be understood using a simple electrostatic model (26, 30) to calculate the particle energy (dashed lines in Fig. 4C), assuming a linear scaling of the applied force with particle radius, and using equation 1 to calculate the particle speed as a function of radius (26). The model yields an average drift speed, which is compared to the measured speeds in Fig. 4F. With increasing particle size, the deep ratchets produce an increasingly dominating bias of a negative drift speed. This is due to a stronger confinement to the deep ratchets and an increasing ratchet potential experienced by the particles in the deep ratchets (from $\sim 2k_B T$ for the 60-nm particles to $\sim 10k_B T$ for the 100-nm particles; Fig. 4C). This leads to a zero crossing of the net drift at a particle diameter of ~ 82 nm ($r = 41$ nm). The strong nonlinear character of the curve originates from the intrinsically nonlinear BM transport and the exponentially increasing interaction energy, resulting in a slope of $\sim 7 \mu\text{m s}^{-1} \text{nm}^{-1}$ at the zero crossing. Thus, two particle species with a radial difference of 1 nm would drift at $>3 \mu\text{m s}^{-1}$ in opposite directions, which is sufficient to overcome the diffusion current that drives the particles back into the device (26) (figs. S12 and S13).

Our results show that confining nanoparticles in electrolyte between a flat surface and a topographically patterned surface creates an energy landscape defined by the topography. By tuning the gap distance, the potential landscape to first order is simply scaled in magnitude, providing a convenient handle to optimize the system. All relevant physical quantities necessary to model the system are accessible in situ. Agreement be-

tween theory and experiment proves the validity of the interpretation and the predictability of the system. The nonlinear character of rocked BM transport (17) and of the electrostatic interaction leads to efficient separation (26) by our device, similar to the case of other concepts based on geometrical constrictions (3, 31).

Moreover, our modeling (26) and the trapping results of Ruggeri *et al.* (22) indicate that the method should scale to relatively small biomolecules. In contrast to flow-based separation (15), the rocked Brownian motor implementation provides selective transport, precise separation, and accumulation of nanoparticles without a net flow of the electrolyte or sustained thermodynamic gradients. Combined with the small footprint and the low applied voltage, such devices are ideally suited for the precise analysis of small liquid volumes in lab-on-chip technology.

REFERENCES AND NOTES

1. T. Salafi, K. K. Zeming, Y. Zhang, *Lab Chip* **17**, 11–33 (2016).
2. O. M. Maragò, P. H. Jones, P. G. Gucciardi, G. Volpe, A. C. Ferrari, *Nat. Nanotechnol.* **8**, 807–819 (2013).
3. J. Fu, R. B. Schoch, A. L. Stevens, S. R. Tannenbaum, J. Han, *Nat. Nanotechnol.* **2**, 121–128 (2007).
4. B. H. Wunsch *et al.*, *Nat. Nanotechnol.* **11**, 936–940 (2016).
5. M. Napoli, J. C. Eijkel, S. Pennathur, *Lab Chip* **10**, 957–985 (2010).
6. T. M. Squires, R. J. Messinger, S. R. Manalis, *Nat. Biotechnol.* **26**, 417–426 (2008).
7. M. O. Magnasco, *Phys. Rev. Lett.* **71**, 1477–1481 (1993).
8. J. Prost, J.-F. Chauwin, L. Peliti, A. Ajdari, *Phys. Rev. Lett.* **72**, 2652–2655 (1994).
9. L. P. Faucheux, L. S. Bourdieu, P. D. Kaplan, A. J. Libchaber, *Phys. Rev. Lett.* **74**, 1504–1507 (1995).
10. S.-H. Lee, K. Ladavac, M. Polin, D. G. Grier, *Phys. Rev. Lett.* **94**, 110601 (2005).
11. J. Rousselet, L. Salome, A. Ajdari, J. Prost, *Nature* **370**, 446–448 (1994).
12. C. Marquet, A. Buguin, L. Talini, P. Silberzan, *Phys. Rev. Lett.* **88**, 168301 (2002).
13. L. Bogunovic, R. Eichhorn, J. Regtmeier, D. Anselmetti, P. Reimann, *Soft Matter* **8**, 3900 (2012).
14. J. S. Bader *et al.*, *Proc. Natl. Acad. Sci. U.S.A.* **96**, 13165–13169 (1999).
15. L. R. Huang, E. C. Cox, R. H. Austin, J. C. Sturm, *Science* **304**, 987–990 (2004).
16. R. D. Astumian, *Science* **276**, 917–922 (1997).
17. R. Bartussek, P. Hänggi, J. G. Kissner, *Europhys. Lett.* **28**, 459–464 (1994).
18. M. Krishnan, N. Mojarad, P. Kukura, V. Sandoghdar, *Nature* **467**, 692–695 (2010).

19. J. Tae Kim, S. Spindler, V. Sandoghdar, *Nat. Commun.* **5**, 3380 (2014).
20. M. A. Gerspach, N. Mojarad, T. Pfohl, Y. Ekinici, *Microelectron. Eng.* **145**, 43–48 (2015).
21. M. Celebrano, C. Rosman, C. Sönnichsen, M. Krishnan, *Nano Lett.* **12**, 5791–5796 (2012).
22. F. Ruggeri *et al.*, *Nat. Nanotechnol.* **12**, 488–495 (2017).
23. C. J. Myers, M. Celebrano, M. Krishnan, *Nat. Nanotechnol.* **10**, 886–891 (2015).
24. D. Pires *et al.*, *Science* **328**, 732–735 (2010).
25. C. D. Rawlings *et al.*, *Sci. Rep.* **7**, 16502 (2017).
26. See supplementary materials.
27. S. Fringes, F. Holzner, A. W. Knoll, *Beilstein J. Nanotechnol.* **9**, 301–310 (2018).
28. K. Lindfors, T. Kalkbrenner, P. Stoller, V. Sandoghdar, *Phys. Rev. Lett.* **93**, 037401 (2004).
29. P. Reimann *et al.*, *Phys. Rev. E* **65**, 031104 (2002).
30. S. H. Behrens, D. G. Grier, *J. Chem. Phys.* **115**, 6716–6721 (2001).
31. I. Derényi, R. D. Astumian, *Phys. Rev. E* **58**, 7781–7784 (1998).

ACKNOWLEDGMENTS

We thank U. Drechsler for assistance in fabricating of the glass pillars, U. Duerig and H. Wolf for stimulating discussions, R. Allenspach and W. Riess for support, and C. Bolliger and L.-M. Pavka for proofreading the manuscript. **Funding:** Supported by European Research Council Starting Grant 307079, European Commission FP7-ICT-2011-8 no. 318804, and Swiss National Science Foundation grant 200020-144464. **Author contributions:** M.J.S. and A.W.K. jointly conceived the idea and the experimental concept; M.J.S. implemented first working devices and started theoretical analysis; C.S. and S.F. performed the sorting experiment; C.S. performed the analysis of the sorting experiment and the numerical modeling for the BMs and the sorting experiment; S.F. performed the BM experiments and contributed to their analysis; C.D.R. performed the finite element modeling and analysis; A.W.K. performed t-SPL, analyzed the BM function, supervised the work, and wrote the manuscript; C.S., C.D.R., S.F., and A.W.K. wrote the supplementary materials. **Competing interests:** The authors declare no competing interest. **Data and materials availability:** All data needed to evaluate our conclusions are present in the paper and/or the supplementary materials. All authors are inventors on U.S. patent application 15/469995 submitted by IBM that covers transport and separation of nanoparticles.

SUPPLEMENTARY MATERIALS

www.sciencemag.org/content/359/6383/1505/suppl/DC1
Materials and Methods
Supplementary Text
Figs. S1 to S13
Table S1
Movies S1 to S9
References (32–37)

31 January 2017; accepted 1 February 2018
10.1126/science.aal3271

MATERIALS SCIENCE

Chameleon-like elastomers with molecularly encoded strain-adaptive stiffening and coloration

Mohammad Vatanikhah-Varnosfaderani,¹ Andrew N. Keith,^{1*} Yidan Cong,^{1*} Heyi Liang,^{2*} Martin Rosenthal,³ Michael Sztucki,³ Charles Clair,⁴ Sergei Magonov,⁵ Dimitri A. Ivanov,^{6,7} Andrey V. Dobrynin,^{2†} Sergei S. Sheiko^{1†}

Active camouflage is widely recognized as a soft-tissue feature, and yet the ability to integrate adaptive coloration and tissue-like mechanical properties into synthetic materials remains elusive. We provide a solution to this problem by uniting these functions in moldable elastomers through the self-assembly of linear-bottlebrush-linear triblock copolymers. Microphase separation of the architecturally distinct blocks results in physically cross-linked networks that display vibrant color, extreme softness, and intense strain stiffening on par with that of skin tissue. Each of these functional properties is regulated by the structure of one macromolecule, without the need for chemical cross-linking or additives. These materials remain stable under conditions characteristic of internal bodily environments and under ambient conditions, neither swelling in bodily fluids nor drying when exposed to air.

The mechanical and optical properties of biological tissues emerge from distinct physical origins but act in concert to serve living organisms such as chameleons, cephalopods, and amphibians (1–3). For example, initially soft and compliant tissues such as skin stiffen rapidly during deformation to prevent injury. Within narrow intervals of strain, their elastic

moduli increase by several orders of magnitude at rates far beyond those observed for conventional elastomers, gels, and thermoplastics (Fig. 1, A to C). These tissues may also simultaneously convert white light into colorful patterns through constructive interference with light waves coherently scattered by periodic or quasi-periodic structures (Fig. 1D) (4). Collectively, these func-

tions constitute defense and signaling mechanisms that have inspired the design of various biomimetic materials that either have tissue-like mechanics (5–11) or display structural colors (12–14). However, integrating both attributes into the molecular structure of a single material proves to be extremely challenging.

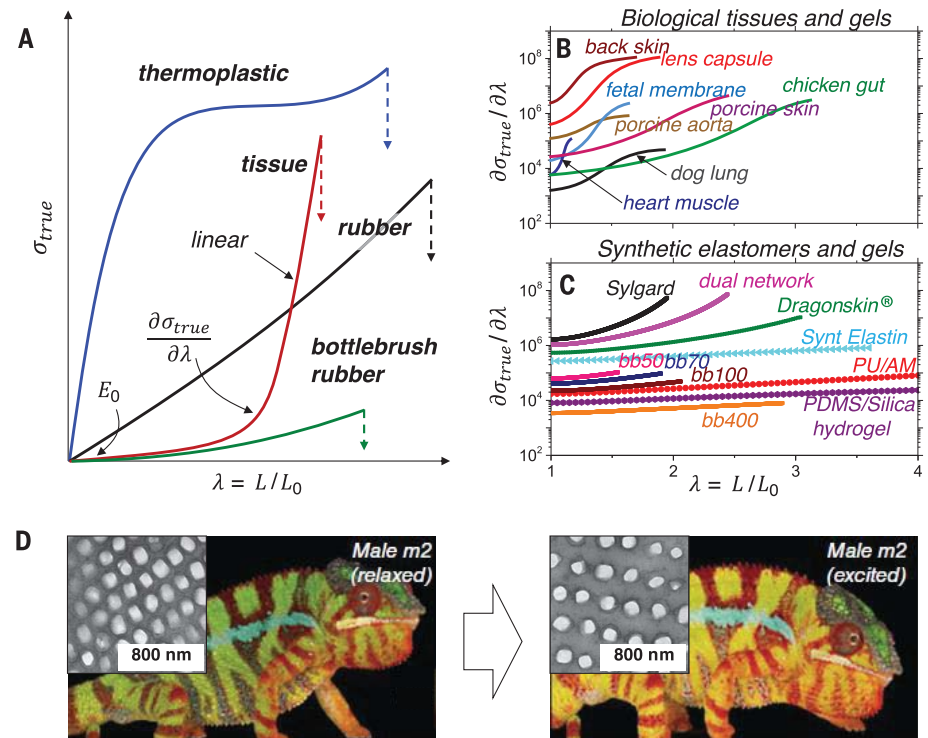
The mechanics of biological tissues arise from their composite nature, defined by the distinct mechanical response of two proteins, collagen and elastin (15). A scaffold of stiff collagen fibers resists deformation, and an interwoven elastin network ensures elastic recoil. This structural duet produces a characteristic, two-phase mechanical response (16), beginning with exponential stiffening and switching to a linear response ($\sigma_{\text{true}} \sim \lambda$, where σ_{true} is the true stress and λ is the elongation ratio) halfway before the point of rupture, as exhibited by plotting differential modulus $\partial\sigma_{\text{true}}/\partial\lambda$ as a function of λ (Fig. 1B). The

¹Department of Chemistry, University of North Carolina at Chapel Hill, Chapel Hill, NC 27599, USA. ²Department of Polymer Science, University of Akron, Akron, OH, 44325-3909, USA. ³European Synchrotron Radiation Facility, F-38043 Grenoble, France. ⁴Université de Haute Alsace, Laboratoire de Physique et Mécanique Textiles, F-68093 Mulhouse Cedex, France. ⁵Scanning Probe Microscopy (SPM) Labs, Tempe, AZ 85283, USA. ⁶Institut de Sciences des Matériaux de Mulhouse-IS2M, CNRS UMR 7361, F-68057 Mulhouse, France. ⁷Lomonosov Moscow State University, Faculty of Fundamental Physical and Chemical Engineering, Leninskie Gory 1/51, 119991 Moscow, Russian Federation.

*These authors contributed equally to this work.

†Corresponding author. Email: adobrynin@uakron.edu (A.V.D.); sergei@mail.unc.edu (S.S.S.)

Fig. 1. Distinct mechanics and coloration of biological tissue. (A) A schematic of materials' true stress–elongation curves demonstrates the diversity of possible mechanical responses and the intense strain stiffening of initially soft tissue. Apparent Young's modulus E_0 is determined as the tangent of a stress-strain curve at $\lambda = 1$. L , length of the sample at a given instant; L_0 , initial length of the sample. (B and C) Differential modulus of biological tissues and synthetic materials (tables S6 and S7). bb, bottlebrush; Synt., synthetic; PU/AM, polyurethane/acrylamide hydrogel. (D) Color variation in the skin of a male panther chameleon changing from a relaxed to an excited state. [Adapted from (1)] (Insets) Transmission electron microscopy images of the guanine nanocrystal lattice from the same individual in the corresponding states.



resulting sigmoid shape of the $\partial\sigma_{\text{true}}/\partial\lambda$ curves contrasts with the steady increase in stiffness displayed by synthetic elastomers and gels (Fig. 1C). Although various molecular and macroscopic constructs implement the basic principles of strain stiffening (6–11), none replicate tissue's deformation response completely and precisely. For example, various silicone rubbers, such as Ecoflex and Dragon Skin, which are widely used in orthotics and cinematography (17), have skinlike softness but lack the strain-stiffening characteristics of skin (Fig. 1C). Polymeric gels are similarly incapable of replicating tissue mechanics (Fig. 1C) and further suffer from solvent leakage upon deformation (18).

We simultaneously enhanced softness and strain stiffening in recent work by employing brushlike architecture in solvent-free elastomers (Fig. 1C) (19). The attachment of side chains to network strands yielded a dual mechanical effect: Moduli were reduced to 100 Pa via chain disentanglement, and strain stiffening increased by an order of magnitude via strand extension due to side-chain steric repulsion (20). Although this effect enables mechanical replicas of gel-like tissues such as lung and jellyfish (5), the strain stiffening of these systems pales when compared with that of soft connective tissues like skin. In parallel, various chromogenic polymers have been created (21–23), but they fail to incorporate

tissuelike mechanical properties. This conventional divide presents a material design challenge aimed at mimicking skin tissue—soft on touch, stiff upon deformation, and colored for appeal or camouflage.

We report the design of chromogenic elastomers, formed by microphase separation of linear-bottlebrush-linear ABA triblock copolymers (Fig. 2A), that are solvent free, supersoft (apparent Young's modulus $E_0 \sim 10^3$ to 10^5 Pa), and strongly strain stiffening ($E_0^{-1}\partial\sigma_{\text{true}}/\partial\lambda \sim 1$ to 10^2). We explored the symbiosis of two blocks that are both chemically and physically distinct: (i) flexible linear chains that aggregate into rigid domains and (ii) stiff bottlebrush strands that form a supersoft matrix. This interplay of the attributes of rigid-while-flexible and soft-while-stiff, which are oxymoronic upon first glance, is actually representative of the distinctive potential of architectural control over materials' mechanical and optical properties. Elucidating how both building blocks not only play individual roles in this control but also synergize with each other to enhance biomimetic performance is a central feature of this study. Specifically, we show that aggregation of linear blocks yields physical networks, and bottlebrush strands provide these networks with a low modulus. Further, the strong segregation of the chemically dissimilar blocks (24) augments the architectural prestrain of the bottlebrush blocks

(20) and thereby markedly improves the networks' strain-stiffening characteristics (fig. S15). These effects enable replication of the mechanical response of porcine skin and achieve substantial progress toward replicating that of human skin, as discussed below.

To validate this concept, we have synthesized several series of linear-bottlebrush-linear ABA triblock copolymers with different degrees of polymerization (DPs; represented as n) of the bottlebrush backbone ($n_{\text{bb}} \approx 300$ to 1800) and identical DPs of the polydimethylsiloxane (PDMS) side chains ($n_{\text{sc}} = 14$) (Fig. 2A, fig. S1 to S3, and table S1). Each series contains molecules with different DPs of the linear A block ($n_{\text{A}} \approx 80$ to 1200) corresponding to A-block volume fractions (ϕ_{A}) of 0.03 to 0.3, where the A block may be poly(methyl methacrylate) (PMMA), poly(benzyl methacrylate) (PBzMA), or poly(oligo(ethylene glycol) monomethyl ether methacrylate) [P(OEOMA)]. For physical tests, thin films were prepared by solution casting. During solvent evaporation, microphase separation results in thermoplastic elastomers (plastomers) with characteristic coloration produced by constructive interference with light waves reflected by domain interfaces (Fig. 2B and movie S1). Both color and mechanical properties depend on plastomer morphology, which was characterized by differential scanning calorimetry (DSC) and atomic force microscopy (AFM)

Fig. 2. Structural coloration of plastomers.

(A) Self-assembly of linear-bottlebrush-linear ABA triblock copolymers yields physical networks—A domains of linear blocks embedded in a B matrix of bottlebrush strands, where n_{A} , n_{bb} , and n_{sc} are degrees of polymerization (DPs) of the linear block, the bottlebrush backbone, and the bottlebrush side chains, respectively. The microphase-separated structure is described in terms of the interbrush distance (d_1), the diameter of the spherically shaped PMMA domains (d_2), and the interdomain distance (d_3). Q , aggregation number. (B) Structural coloration in a broad spectral range is typically observed during solvent evaporation and is indicative of decreasing distance between A domains (movie S1). (C) AFM height micrographs corroborate microphase separation of PMMA–bottlebrush backbone PDMS (bbPDMS)–PMMA plastomers with identical n_{bb} values of 938, varied linear PMMA DPs, and a designated PMMA volume fraction (ϕ_{A}) (series M900- x , where x is any number, in table S1). (D) USAXS patterns of the plastomers represented above display characteristic length scales as depicted in (A) and summarized in table S4. a.u., arbitrary units; q , magnitude of the scattering wave vector. (E) Concentrated solutions (25 weight %) of the corresponding plastomers. Evaporation of turquoise solution 4 (M900-4) yields a blue film. v%, volume %; NA, not applicable.

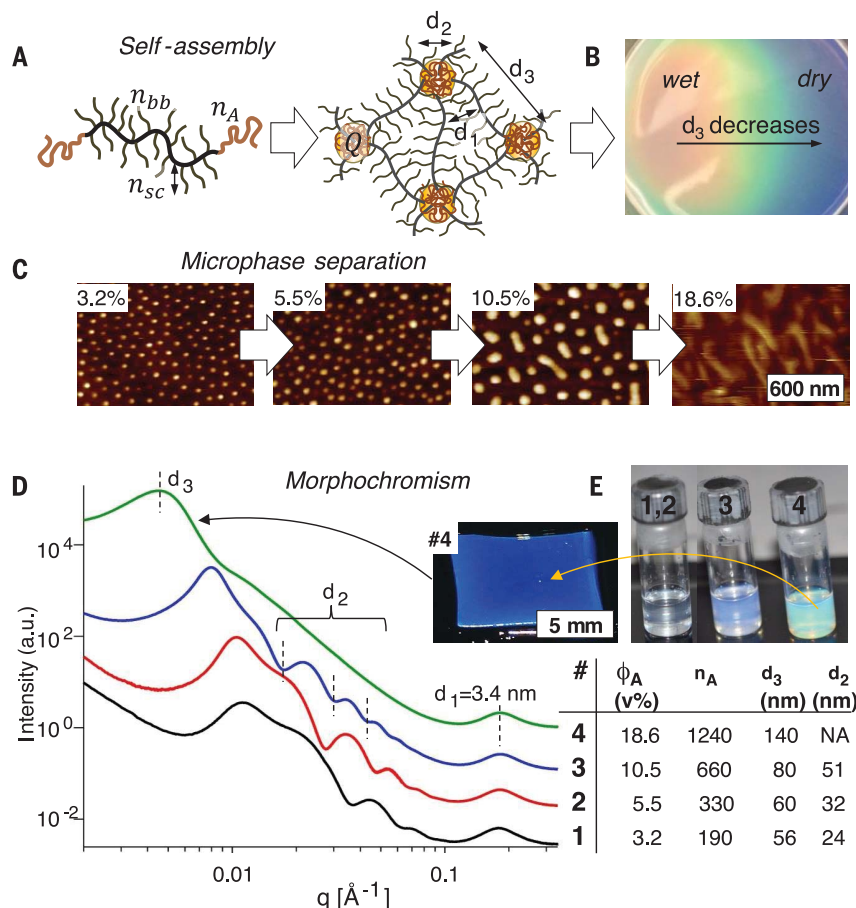


(Fig. 2C, figs. S5 to S7, and table S2) and ultra-small-angle x-ray scattering (USAXS) (Fig. 2D and fig. S17). This combination of techniques provided the interbrush distance ($d_1 = 3.4$ nm), the domain diameter ($d_2 = 20$ to 40 nm), the aggregation number ($Q \cong 300$ to 1000), and the interdomain distance ($d_3 = 40$ to 150 nm) as summarized in table S4 for different copolymer compositions.

Corresponding analysis revealed that plastoformers' block dimensions (n_{bb} , n_A , and ϕ_A) strongly affect their mechanical properties (Fig. 3, A and B, and figs. S8 to S11), which include a low initial modulus ($E_0 = 4$ to 50 kPa) (table S1); intense strain stiffening, depicted as a 10- to 100-fold increase of the differential modulus within a short

strain interval (Fig. 3, C and D); and the characteristic sigmoid shape of the $\partial\sigma/\partial\lambda$ curves, which is markedly similar to that for biological tissues (Fig. 1B). All of these features are a manifestation of a two-phase deformation process, which starts with the extension of architecturally prestrained bottlebrush network strands (the elastic regime) and proceeds with the uncoiling of linear chains in A domains (the yielding regime) (figs. S20 and S23). Unlike that in the elastic phase of deformation, yielding-phase stress depends on strain rate (fig. S13) and develops small (<10%) hysteresis in loading-unloading cycles (fig. S14). All three features (reversibility, strain-rate dependence, and hysteresis) are also observed via yielding of

collagen assemblies in biological tissues, which provides energy dissipation and additional extensibility (9, 25). Even though plastoformers have a completely different structure and distinct deformation mechanisms from biological tissues, they display a tissuelike mechanical response. Although one may intuitively presume that the prestrain of the B blocks would impair network extensibility, uncoiling of the flexible A blocks compensates for this inherent characteristic. In other words, the A domains serve as reservoirs of untapped network extension and yield synergy that is muted in all-linear ABAs, where in the absence of prestrain diminishes the phase-separation enhancement of strain stiffening (fig.

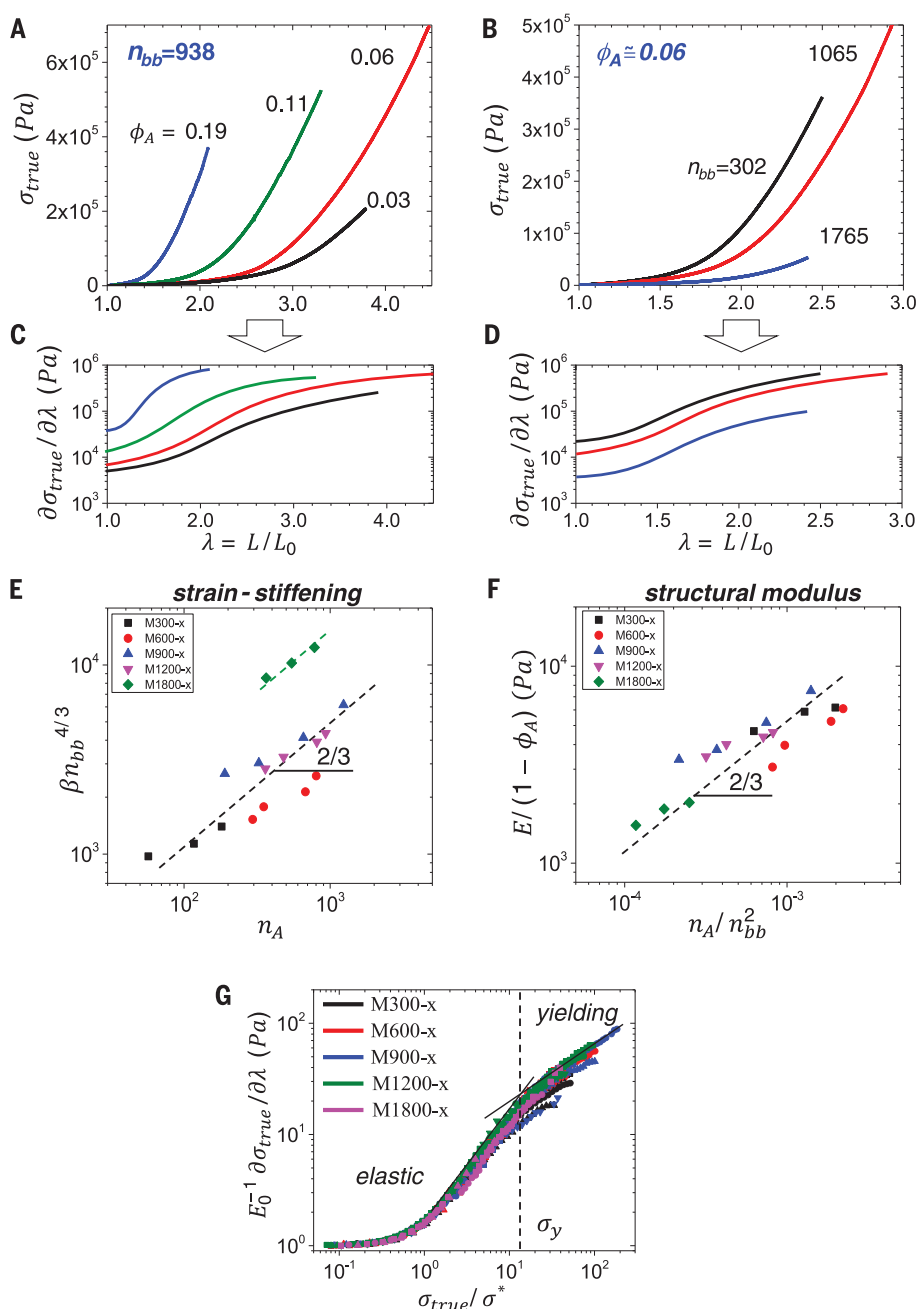


Fig. 3. Mechanical properties of plastoformers as a function of block copolymer composition.

(A) Stress-strain curves of PMMA-bbPDMS-PMMA plastoformers with identical n_{bb} values of 938 and varied A-block volume fractions (ϕ_A) (series M900-x in table S1) measured upon uniaxial extension in the elastic regime (constant strain rate, 0.005 s $^{-1}$; temperature, 25°C) (fig. S4). (B) Stress-strain curves of PMMA-bbPDMS-PMMA plastoformers with different n_{bb} values but similar ϕ_A values of ~ 0.06 . (C and D) Differential moduli for plots in (A) and (B), respectively. (E) Normalized strain-stiffening parameter β increases with the DP of linear PMMA blocks as $\beta n_{bb}^{4/3} \sim n_A^{2/3}$. E and β values are obtained by fitting stress-strain curves using eq. S6.18 in the elastic phase of network deformation (fig. S12). (F) Structural Young's modulus decreases with n_{bb} and increases with n_A as $E \sim n_A^{2/3} n_{bb}^{-4/3}$. The data in (E) and (F) are means with SDs of 5 to 15% (table S1). (G) Universal plot of normalized differential modulus $E_0^{-1} \partial\sigma_{true}/\partial\lambda$ versus σ_{true}/σ^* , where $\sigma^* = E^{1/3} E_0^{2/3} / 3\beta^{2/3}$ is the crossover stress between the linear and strain-stiffening regimes (eq. S6.27 and table S3).

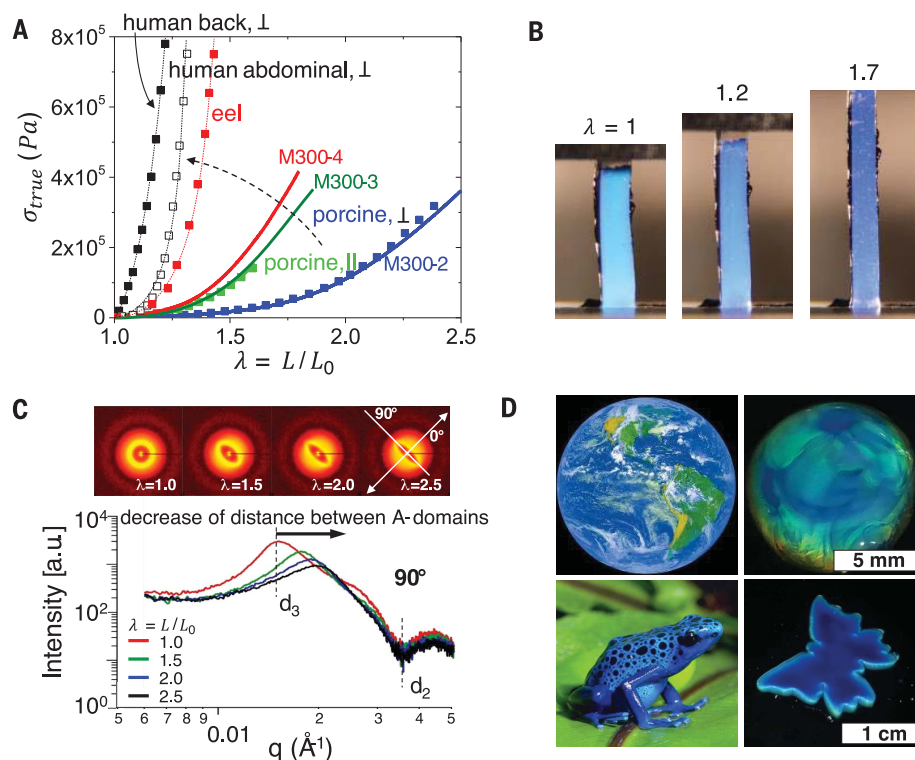


Fig. 4. Mimicking skin tissue. (A) True stress–elongation curves for assorted skin tissues (human back, human abdominal, eel, and porcine in table S7 and fig. S24) (squares) and M300-*x* plastomers cast from tetrahydrofuran with identical n_{bb} values of 302 and varied DPs of the linear PMMA block (lines). Current progress toward mimicking human skin is highlighted by the dashed arrow. \perp , tissue was measured perpendicularly to the spine; \parallel , tissue was measured parallel to the spine. (B) An observed color alteration from turquoise to dark blue during uniaxial stretching of a 2-mm-thick (G900-1) P(OEOMA)-bbPDMS-P(OEOMA) film (movie S2). (C) Two-dimensional USAXS patterns corresponding to different extension ratios exemplified for M300-2. Sections of the USAXS patterns are measured perpendicularly (at a 90° angle) to the stretching direction at different elongation ratios. Elongation shifts the main interference maximum, which suggests a shortening between a PMMA domain's nearest neighbors (d_3 in Fig. 2A). Deformation has no effect on the A-domain form factor (d_2). (D) (Top) Satellite image of Earth (left) and a drop of P(OEOMA)-bbPDMS-P(OEOMA) solution in toluene during drying (right). (Bottom) Blue poison dart frog (left) and a thin butterfly cutout of PBzMA-bbPDMS-PBzMA plastomer B1000-2 (table S1) with edges swollen with linear PDMS for contrast on a glass substrate (right). The back side of the glass substrate was painted black to enhance reflectance.

S16), and all-brush ABAs, wherein added architectural prestrain impedes the overall extensibility of the material (26–29).

For the elastic phase of deformation, we analyzed the stress-strain curves using a constitutive network deformation model (eq. S6.18), which has been validated for various polymer networks, including biological gels (5, 19, 30). This model is described by two parameters: (i) structural Young's modulus, a measure of cross-link density (eq. S6.22), and (ii) the strain-stiffening parameter (β), a measure of strand extension defined as $\beta \equiv \langle R_{in}^2 \rangle / R_{max}^2$, where R_{max} is the contour length of a fully extended strand and $\langle R_{in}^2 \rangle$ is the mean square end-to-end distance of strands in as-prepared elastomers (eq. S6.19). Parameter β is controlled by finite extensibility of network strands, with the lower and upper bounds cor-

responding to networks with coiled ($R_{in} \ll R_{max}$, $\beta \rightarrow 0$) and extended ($R_{in} \cong R_{max}$, $\beta \rightarrow 1$) strands, respectively. For comparison, typical linear-chain elastomers, including linear ABAs (26), are characterized by $\beta \cong 0.01$ (fig. S16). Although bottle-brush covalent networks allow for a substantial increase, up to $\beta \cong 0.3$ (table S6) (19), this value is nonetheless notably lower than those in the range for tissue, where $\beta \cong 0.5$ to 0.9 (table S7). Microphase separation in our plastomers results in additional strand extension, with $\beta \cong 0.3$ to 0.8 (table S1), a range that favorably overlaps with values for tissues, such as $\beta = 0.69$ (lung), $\beta = 0.75$ (brain), $\beta = 0.78$ (skin), and $\beta = 0.75$ (blood vessel) (table S7).

To highlight the corresponding capacity for predictably controlling strain stiffening, table S1 summarizes the molecular and mechanical pa-

rameters of the studied plastomers. The strain-stiffening parameter (β) follows the theoretically predicted scaling relation $\beta \sim n_A^{2/3} n_{bb}^{-4/3}$ (Fig. 3E), which originates from chain extension ($\langle R_{in}^2 \rangle \sim n_A^{2/3} n_{bb}^{2/3}$ (eqs. S6.12 and S6.17), as is well documented for block copolymer systems in the strong segregation limit (24). Similarly, the structural modulus follows $E \sim (1 - \phi_A) n_A^{2/3} n_{bb}^{-4/3} \sim (1 - \phi_A) \beta$ (Fig. 3F and fig. S21), which originates from prestretching of the bottlebrush strands upon microphase separation (eq. S6.22). The established structure-property correlations therefore allow for universal presentation of the differential modulus as a function of stress (Fig. 3G). The observed deviation of $\partial \sigma_{true} / \partial \lambda$ curves in the yielding regime occurs at different elongations because of the difference in finite extensibility of the various ABA network strand lengths (Fig. 3, C and D). Because chain withdrawal proceeds at constant force ($f \sim \sigma_{eng}$, where σ_{eng} is engineering stress), the true stress in the yielding regime scales linearly with λ as $\sigma_{true} \sim \lambda$ (fig. S23). In other words, the stress-strain behavior of different plastomers follows a universal trend that is architecturally controlled.

Tensile stress-strain curves for assorted skin tissues, like those for plastomers, exhibit broad variation of mechanical properties defined by low modulus E (0.4 to 12 kPa) and substantial strain stiffening, with $\beta \cong 0.5$ to 0.9 (Fig. 4A and table S7). This parallel is exemplified by comparing the stress-strain curves of samples M300-2 and M300-3 with those of porcine skin measured perpendicularly and parallel to the spine, respectively. The precise overlap thereof demonstrates that plastomers can replicate the deformation response of certain strain-stiffening tissues completely and precisely. Furthermore, elongation results in a blue shift of sample color (Fig. 4B and movie S2) because of the corresponding decrease in interdomain distance (d_3) (Fig. 4C). This deformation does not affect domain size (d_2) and underlines the robust nature of the physical network. Similarly, solvent swelling results in omnidirectional expansion between domains, with an observed shift in color (Fig. 2B and movie S1), which is consistent with USAXS (fig. S18A) and reflectance (fig. S18B) measurements of plastomers in selective solvents. Inhomogeneous swelling (or drying) thus demonstrates spectacular visuals that resemble the optical complexity of natural systems such as Earth and blue poison dart frogs (Fig. 4D). This color shift also highlights how the same network structure that lends plastomers their mechanical characteristics also imbues them with adaptive structural coloration.

In conclusion, we have established that the self-assembly of linear-bottlebrush-linear triblock copolymers (plastomers) empowers the integration of strain-adaptive stiffening and strain-induced coloration. We have further demonstrated that this class of materials enables replication of the mechanical response of strongly strain-stiffening tissues, with porcine skin as an example, and we have shown that replication of the response of human skin is within reach. We hope to expand

this materials design platform by achieving independent control over mechanical and coloration responses.

REFERENCES AND NOTES

- J. Teyssier, S. V. Saenko, D. van der Marel, M. C. Milinkovitch, *Nat. Commun.* **6**, 6368 (2015).
- L. M. Mäthger, E. J. Denton, N. J. Marshall, R. T. Hanlon, *J. R. Soc. Interface* **6** (suppl. 2), S149–S163 (2009).
- I. C. Cuthill *et al.*, *Science* **357**, eaan0221 (2017).
- J. P. Vigneron, P. Simonis, *Physica B* **407**, 4032–4036 (2012).
- M. Vatanikhah-Varnosfaderani *et al.*, *Nature* **549**, 497–501 (2017).
- S. C. Grindy *et al.*, *Nat. Mater.* **14**, 1210–1216 (2015).
- B. Yu *et al.*, *Nat. Mater.* **15**, 911–918 (2016).
- A. S. So, Tayi, F. Güder, G. M. Whitesides, *Adv. Funct. Mater.* **24**, 7197–7204 (2014).
- W. Yang *et al.*, *Nat. Commun.* **6**, 6649 (2015).
- M. Jaspers *et al.*, *Nat. Commun.* **8**, 15478 (2017).
- E. Ducrot, Y. Chen, M. Bulters, R. P. Sijbesma, C. Creton, *Science* **344**, 186–189 (2014).
- K. Yu, T. Fan, S. Lou, D. Zhang, *Prog. Mater. Sci.* **58**, 825–873 (2013).
- S. A. Morin *et al.*, *Science* **337**, 828–832 (2012).
- Y. Zhao, Z. Xie, H. Gu, C. Zhu, Z. Gu, *Chem. Soc. Rev.* **41**, 3297–3317 (2012).
- G. A. Holzapfel, in *Handbook of Material Behavior Models*, J. Lemaitre, Ed. (Academic Press, 2001), pp. 1057–1071.
- C. Storm, J. J. Pastore, F. C. MacKintosh, T. C. Lubensky, P. A. Janmey, *Nature* **435**, 191–194 (2005).
- T. Ranzani, G. Gerboni, M. Cianchetti, A. Menciassi, *Bioinspir. Biomim.* **10**, 035008 (2015).
- Y. Li *et al.*, *Sci. Rep.* **5**, 17017 (2015).
- M. Vatanikhah-Varnosfaderani *et al.*, *Adv. Mater.* **29**, 1604209 (2017).
- S. S. Sheiko *et al.*, *Nature* **440**, 191–194 (2006).
- J. H. Lee *et al.*, *Adv. Mater.* **26**, 532–569 (2014).
- A. L. Liberman-Martin, C. K. Chu, R. H. Grubbs, *Macromol. Rapid Commun.* **38**, 1700058 (2017).
- Y. Fu, C. A. Tippets, E. U. Donev, R. Lopez, *Wiley Interdiscip. Rev. Nanomed. Nanobiotechnol.* **8**, 758–775 (2016).
- F. S. Bates, G. H. Fredrickson, *Annu. Rev. Phys. Chem.* **41**, 525–557 (1990).
- B. Depalle, Z. Qin, S. J. Shefelbine, M. J. Buehler, *J. Mech. Behav. Biomed. Mater.* **52**, 1–13 (2015).
- J. M. Yu, Ph. Dubois, Ph. Teyssie, R. Jerome, *Macromolecules* **29**, 6090–6099 (1996).
- K. A. Erk, K. J. Henderson, K. R. Shull, *Biomacromolecules* **11**, 1358–1363 (2010).
- R. Verduzco, X. Li, S. L. Pesek, G. E. Stein, *Chem. Soc. Rev.* **44**, 2405–2420 (2015).
- C. M. Bates, A. B. Chang, N. Momčilović, S. C. Jones, R. H. Grubbs, *Macromolecules* **48**, 4967–4973 (2015).
- J.-M. Y. Carrillo, F. C. MacKintosh, A. V. Dobrynin, *Macromolecules* **46**, 3679–3692 (2013).

ACKNOWLEDGMENTS

We thank K. Matyjaszewski for illuminating discussions; Q. Li, W. Daniel, and B. Morgan for their assistance in mechanical tests; and M. Everhart for reviewing the manuscript. **Funding:** This work made use of the Cary 5000 ultraviolet–visible–near-infrared (UV-Vis-NIR) with Agilent diffuse reflectance accessory instrument in the University of North Carolina (UNC) Energy Frontier Research Center (EFRC) instrumentation facility established by the UNC EFRC Center for Solar Fuels, an EFRC funded by the U.S. Department of Energy, Office of Science, Office of Basic Energy Sciences, under award number DE-SC0001011. USAXS measurements were performed at the ID02 beamline, European

Synchrotron Radiation Facility. We gratefully acknowledge funding from the NSF (DMR 1407645, DMR 1436201, and DMR 1624569) and from the Russian Science Foundation (project no. 16-13-10369).

Author contributions: M.V.-V. designed, synthesized, and characterized the monomers, block copolymers, and polymer networks; A.N.K. performed synthesis of block copolymers, mechanical tests, and AFM experiments; Y.C. synthesized PBzMA–bottlebrush backbone PDMS–PBzMA elastomers and studied structural coloration; H.L. and A.V.D. provided theoretical analysis of mechanical properties and performed computer simulations; M.R., M.S., C.C., and D.A.I. conducted x-ray studies and data analysis; S.M. oversaw AFM studies; S.S.S. and A.V.D. were primary writers of the manuscript; and S.S.S. was the principal investigator. All authors discussed the results and provided feedback on the manuscript. **Competing interests:** M.V.-V. and S.S.S. are inventors on patent application US 62/585,124, submitted by the University of North Carolina at Chapel Hill, which covers synthesis of elastomers. **Data and materials availability:** All data needed to evaluate the conclusions in the paper are present in the paper and/or the supplementary materials. Data in the supplementary materials are presented in the form of tables and graphs. These include data on chemical composition and corresponding mechanical properties for each specific material studied in the paper.

SUPPLEMENTARY MATERIALS

www.sciencemag.org/content/359/6383/1509/suppl/DC1
Materials and Methods
Figs. S1 to S24
Tables S1 to S7
References (31–54)
Movies S1 and S2

18 November 2017; accepted 30 January 2018
10.1126/science.aar5308

BATTERIES

Self-heating-induced healing of lithium dendrites

Lu Li,¹ Swastik Basu,¹ Yiping Wang,² Zhizhong Chen,² Prateek Hundekar,^{1,2} Baiwei Wang,² Jian Shi,² Yunfeng Shi,² Shankar Narayanan,¹ Nikhil Koratkar^{1,2*}

Lithium (Li) metal electrodes are not deployable in rechargeable batteries because electrochemical plating and stripping invariably leads to growth of dendrites that reduce coulombic efficiency and eventually short the battery. It is generally accepted that the dendrite problem is exacerbated at high current densities. Here, we report a regime for dendrite evolution in which the reverse is true. In our experiments, we found that when the plating and stripping current density is raised above ~9 milliamperes per square centimeter, there is substantial self-heating of the dendrites, which triggers extensive surface migration of Li. This surface diffusion heals the dendrites and smoothens the Li metal surface. We show that repeated doses of high-current-density healing treatment enables the safe cycling of Li-sulfur batteries with high coulombic efficiency.

The demand for higher-energy-density battery systems (1, 2) has created a renewed interest in the exploration of metallic lithium (Li) as an anode material. This is because the packing density of Li atoms is the highest in its metallic form, resulting in an ultra-high (3) theoretical specific capacity of 3861 mAh g⁻¹. However, the main stumbling block to deployment of Li metal anodes is the nucleation and growth of “dendritic” projections (4, 5) during the electrochemical plating-stripping process that occurs when the battery is being charged or discharged. These Li dendrites are problematic in many respects. They increase irreversible capacity loss, reduce the coulombic efficiency (CE), and promote the degradation and drying of the electrolyte (6, 7). However, the most pressing issue is that the sharp dendritic projections can pierce through the battery separator and electrically short the battery (8–10). This results in a severe thermal runaway situation, which could result in the battery catching fire.

Researchers have over the years devised various innovative approaches (11–17) to control and suppress the growth of Li dendrites, but 100% suppression is challenging. This is because kinetically, the nucleation and growth of Li dendrites is highly favorable during electrochemical plating and stripping reactions. In general, it is taken for granted that higher current densities in a Li metal battery will yield accelerated growth of dendrites. In this Report, we demonstrate a distinct regime for Li dendrite evolution in which the opposite holds true. For our battery system, we found that when the plating-stripping current density is raised above ~9 mA cm⁻², there is substantial self-heating of the dendrites. The local heating

gives flux and flow to Li, triggering extensive surface diffusion, which smoothens the dendrites and enables the equilibrium flat configuration to be established quicker. The self-heating is at safe levels, below any danger of electrolyte breakdown or thermal damage to the separator.

To elucidate the underlying science behind the dendrite healing, we tested Li-Li symmetric cells (fig. S1A). The tests were performed over a wide range of operating current densities, ranging from low (~0.75 mA cm⁻²) to very high values (~15 mA cm⁻²). The potential-time and current-time profiles during galvanostatic charge-discharge cycling in Li-Li symmetric cells under different current densities are shown in fig. S1, D and E. In the ideal thermodynamic condition, the voltage of Li stripping and plating should be at 0 V (versus Li-Li⁺). However, in practice an overpotential exists, which increases substantially with the operating current density (figs. S1, D and E, and S2). Electrochemical impedance spectra (EIS) of the Li-Li symmetric cells were recorded before and after 50 charge-discharge cycles at different current densities, and the results are summarized in fig. S1, B and C. A striking observation is that the electrolyte resistance of the Li-Li symmetrical cell cycled at ~15 mA cm⁻² remains ~8 ohms both before and after 50 cycles, whereas the corresponding resistance of the cell cycled at ~0.75 mA cm⁻² increases by ~75% from ~10 ohms before cycling to ~17.5 ohms after only 50 charge-discharge steps. The rapid increase in electrolyte resistance observed in fig. S1, B and C, is a signature of dendritic growth. The continuous formation of solid electrolyte interface (SEI) on the proliferating dendrites will cause electrolyte drying, which increases the resistance to Li⁺ transport. The electrochemical evidence in fig. S1, B and C, therefore suggests that Li dendrite nucleation and growth appears to flourish at current densities of ~0.75 mA cm⁻², whereas it seems to be suppressed when the cell is operated at

current densities of ~15 mA cm⁻², an order of magnitude higher.

To corroborate the electrochemical evidence, we carried out ex situ scanning electron microscopy (SEM) imaging of the surfaces of the Li metal foils used in the experiments. Before cycling, the Li foils displayed a relatively smooth appearance and were completely free of dendrites (fig. S3). Shown in Fig. 1, A to D, are SEM images of the Li metal electrode surface after 50 cycles of charge and discharge at current densities of ~0.75, ~4.5, ~9.0, and ~15 mA cm⁻². Under low current density (~0.75 mA cm⁻²) (Fig. 1A), a few isolated but large-diameter dendritic particles can be observed. With the increase of current density (Fig. 1B), the diameter of Li dendrites decreases, but the packing density of the protrusions has increased substantially. However, when the current density was increased all the way up to ~15 mA cm⁻² (Fig. 1D), the dendrites tend to fuse (merge) together. As a consequence, the surface of the Li electrode becomes much smoother, which substantially lowers the risk of dendrite penetration through the separator. At an intermediate current density of ~9 mA cm⁻², there is partial healing (Fig. 1C) of dendrites. This was also corroborated with cross-sectional SEM imaging of the Li metal foils (Fig. 1, E to H). As the current density is raised from ~0.75 to ~9 mA cm⁻², the dendritic layer becomes more prominent, increasing in thickness from ~14 to ~37% of the Li foil thickness. However, at ~15 mA cm⁻² current density the dendritic layer undergoes a striking transformation. The dendrites fuse through the entire thickness of the dendritic layer (~48% of the Li foil thickness), transforming into a relatively smooth and compact (dense) layer.

High-magnification SEM images of the dendrite particles in Fig. 1 are provided in fig. S4. Direct microscopy evidence for fusing of the dendrites is provided in fig. S5. X-ray diffraction (XRD) and Raman spectroscopy confirms that these particles are Li dendrites and not surface contaminants (figs. S6 and S7). SEI compositional analysis indicates that the material composition of the SEI is similar over a wide range of current densities (fig. S8). To verify that electrical shorting is suppressed in cells with the healed Li surface, we performed extended cycling of the Li-Li symmetrical cells (fig. S9). We found that at the lower current densities (such as ~4.5 mA cm⁻²), the Li-Li cell shorts in ~500 hours because of the dendritic projections that develop on the surfaces of the Li electrodes. By contrast, cells that were cycled at ~15 mA cm⁻² showed no indication of electrical shorting even after 2000 hours (fig. S9).

To obtain a better understanding of the dendrite nucleation and growth process, in situ observation was carried out by using an optical microscope (figs. S10 and S11). As shown in fig. S11, when different current densities are applied, distinct nucleation patterns emerge. When low current density (fig. S11, A to D) is applied, there are almost no dendrite nuclei observed on the Li electrode in the initial 20 min. At further times, several large Li nuclei gradually arise

¹Department of Mechanical, Aerospace and Nuclear Engineering, Rensselaer Polytechnic Institute, Troy, NY 12180, USA. ²Department of Material Science and Engineering, Rensselaer Polytechnic Institute, Troy, NY 12180, USA.

*Corresponding author. Email: koratn@rpi.edu

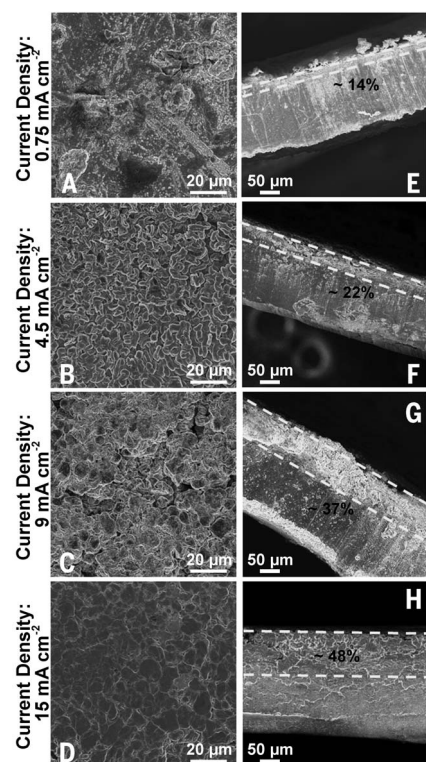


Fig. 1. Morphology evolution of Li dendrites in Li-Li symmetrical cells under different current densities. (A and E) $\sim 0.75 \text{ mA cm}^{-2}$. (B and F) $\sim 4.5 \text{ mA cm}^{-2}$. (C and G) $\sim 9 \text{ mA cm}^{-2}$. (D and H) $\sim 15 \text{ mA cm}^{-2}$.

but are well spaced apart. In contrast to this, at high current density (fig. S11, E to H), densely packed dendritic nuclei (dark spots) spring out over the entire Li electrode surface within just a few minutes. Additional microscopy evidence of finer and densely populated dendrites at higher current densities is provided in fig. S12. We used classical nucleation and growth theory to model this phenomenon (supplementary text). The predictions (fig. S11K) indicate that the electrochemical over-potential increases with increase in the current density. This higher over-potential reduces the nucleation radius and increases the nucleation rate and the nucleation site density of the dendrites (fig. S11, J and L). The dense-packing of dendrites implies that the majority of the current must collectively flow through the dendrites to reach the Li electrode. The resulting Joule heating of the dendrites could trigger extensive surface diffusion of Li, enabling the closely packed dendritic particles to be fused together. In addition to high packing density, the large over-potentials also generate finer dendrites, which in conjunction with the high current density should generate substantial self (Joule) heating.

To evaluate the temperature rise in the dendrites, we carried out detailed heat transfer simulations (Fig. 2A and supplementary text). We found that the predicted temperature rise (Fig. 2B) in the dendrites at current densities of $\sim 15 \text{ mA cm}^{-2}$ are on the order of 40 to 60°C .

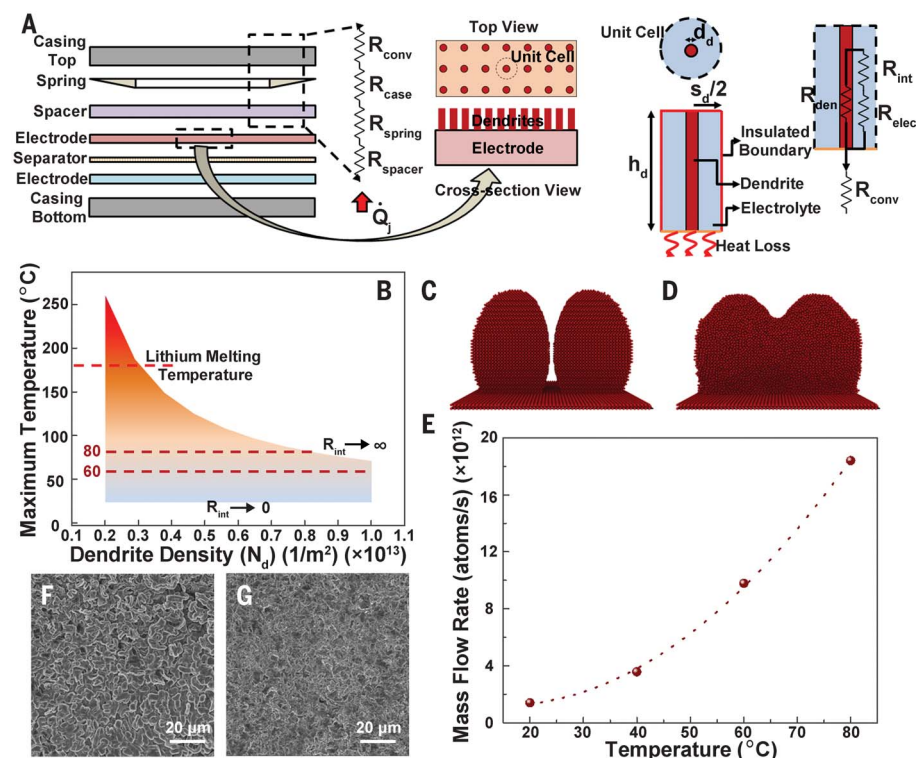


Fig. 2. Dendrite healing mechanism. (A) Cross-section diagram of the coin cell. Because of a repetitive geometry, a unit cell is used for thermal modeling of a single dendrite with characteristic diameter (d_d), height (h_d), and spacing (s_d). As shown in the resistance diagram, heat generated in the dendrite can either be conducted to the substrate directly or via the surrounding electrolyte. R_{conv} , R_{case} , R_{spring} , and R_{spacer} denote thermal resistances to heat transfer, corresponding to natural convection, casing, spring and spacer, respectively. R_{den} , R_{elec} , and R_{int} denote thermal resistances to heat transfer, corresponding to the dendrite, electrolyte and their interface, respectively. (B) Maximum dendrite temperatures at a current density of $\sim 15 \text{ mA cm}^{-2}$. For the typical range of interfacial thermal resistances, dendrite temperatures in the range of 60 to 80°C are predicted. (C and D) Screenshots of molecular models used in MD simulation, (C) initial state and (D) after $\sim 50 \text{ ps}$ at $\sim 80^\circ\text{C}$. (E) Migration mass flow rate of Li atoms at different temperatures as predicted with MD. (F) SEM image of Li dendrites in Li-Li symmetrical cells operated at a current density of $\sim 4.5 \text{ mA cm}^{-2}$ for 50 charge-discharge cycles. (G) Healing of the dendrites in (F) by means of thermal annealing in an inert Ar environment at $\sim 70^\circ\text{C}$ for 3 days.

The electrolyte and membrane separator (18) used in our experiments did not degrade at these temperatures. Our thermal model indicates that even such moderate temperature increases are not feasible at low current densities (such as $\sim 0.75 \text{ mA cm}^{-2}$) (fig. S13). Although temperature increases on the order of 40 to 60°C are clearly not large enough to melt dendrites (the melting temperature of Li is $\sim 180.5^\circ\text{C}$, and the dendrites are large enough to rule out any size effect on the melting temperature), they may be sufficiently high to promote diffusion of Li atoms on the dendritic surfaces. To investigate this, we carried out molecular dynamics (MD) simulations of the Li diffusion process at various temperatures from room temperature (20°C) to 80°C (temperature rise of $\sim 60^\circ\text{C}$). The molecular model and arrangement of the Li dendrite particles used in our simulation is shown in Fig. 2C. To quantitatively assess the mass transport as a function of temperature, we focused on the atom migration from the dendrite surface to the valley formed between

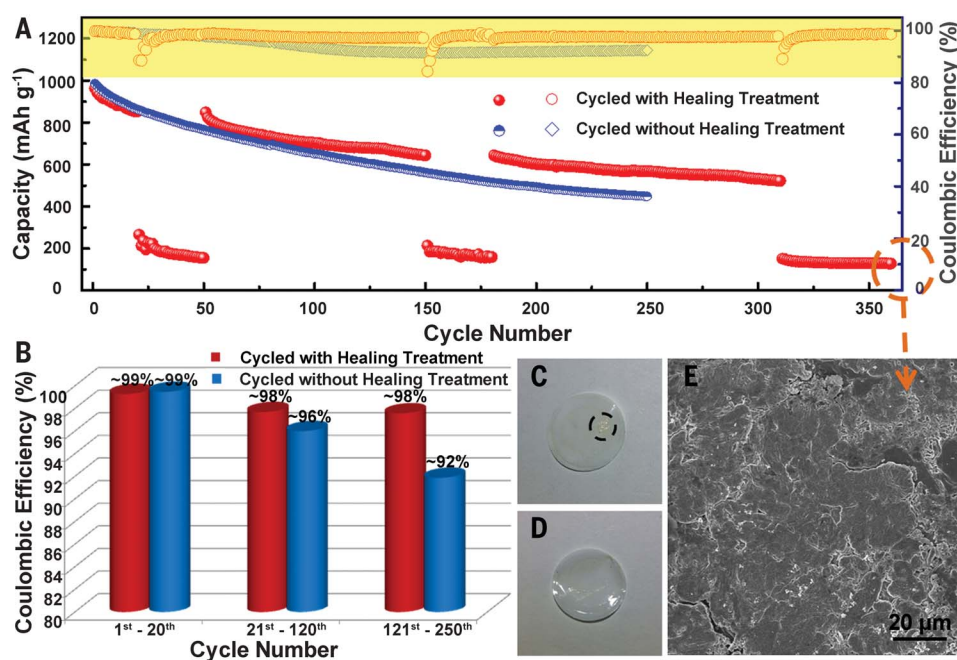
two neighboring dendrite particles. The results for the migration mass flow rate (atoms per second) of Li atoms as a function of temperature is shown in Fig. 2E. Because the driving force for surface migration is essentially the difference in chemical potential because of curvature (very similar to Ostwald ripening), a nonzero flux was observed even at room temperature. However, the surface diffusion of Li is strongly temperature-dependent, with a sharp increase in the migration mass flow rate above 40°C . Shown in Fig. 2D is the MD prediction for the morphology of the dendritic particles after annealing at $\sim 80^\circ\text{C}$ for $\sim 50 \text{ ps}$. We clearly observed merging and fusing of the dendrite particles, which is consistent with our experimental observations. Although the time scales in the MD simulations are very different from the experiments, the essential physics remain the same.

To confirm that the healing is a thermal effect, we carried out a dendrite annealing control experiment. In this test, a Li-Li symmetrical cell

Fig. 3. Dendrite healing in a Li-S battery.

(A) Cycle stability and CE (highlighted in yellow) of Li-S batteries with and without periodic doses of healing treatment. Blue data points indicate performance of the baseline Li-S cell cycled at $\sim 0.75 \text{ mA cm}^{-2}$ without healing treatment. The red data points are for intermittent healing treatment (at current density of $\sim 9 \text{ mA cm}^{-2}$) applied between the 21st and 50th, 151st and 180th, and 311th and 360th cycles. For the remaining cycles, a current density of $\sim 0.75 \text{ mA cm}^{-2}$ was applied, which is identical to the baseline cell without healing. **(B)** Comparison of average CE of the Li-S battery when operated at a current density of $\sim 0.75 \text{ mA cm}^{-2}$ with and without the healing treatment. **(C)** Digital photo of membrane separator in the cycled Li-S batteries after 250 cycles of charge-discharge at a current density of $\sim 0.75 \text{ mA cm}^{-2}$ without the healing treatment. The dashed circle indicates the presence of dendritic Li particles that are impregnated in the separator.

(D) Corresponding photo of the membrane separator taken after 360 cycles of charge-discharge with the healing treatment. **(E)** Morphology of the Li metal electrode surface after the third healing stage [after the 360th charge-discharge cycle indicated in (A) by the dashed circle].



was cycled at a current density of $\sim 4.5 \text{ mA/cm}^2$ for 50 charge-discharge cycles (~ 200 hours). Then, the cell was thermally annealed at a temperature of $\sim 70^\circ\text{C}$ for ~ 3 days. SEM images of the Li metal electrode before and after annealing are shown in Fig. 2, F and G, respectively. The annealed Li foil displays a relatively smooth film-like morphology, similar to the electrochemically tested Li foils that were cycled at high current densities (Fig. 1D). To eliminate the possibility that pressure buildup in a closed coin cell contributes to the healing, we also performed an annealing experiment in an open-cell configuration. For this test, a Li-Li cell was cycled at $\sim 4.5 \text{ mA/cm}^2$ for 50 charge-discharge steps in order to form the dendrites. Then the cell was opened in an inert argon (Ar) environment, inside a glove box. The Li foil was removed from the cell and placed on a hot plate (within the glove box) and thermally annealed at $\sim 70^\circ\text{C}$ for ~ 3 days. Similar to the closed-cell case, SEM imaging (after annealing) of the Li foil in the open-cell configuration also revealed a relatively smooth surface (fig. S14), indicating healing of the dendrites.

We investigated the grain size distribution of the Li dendrites based on image analysis of Fig. 1, B and D. At moderately large current densities ($\sim 4.5 \text{ mA cm}^{-2}$), the average grain sizes are $\sim 5.7 \pm 2 \mu\text{m}$ along the longest dimensions and $\sim 2.7 \pm 0.7 \mu\text{m}$ along the shortest dimensions (fig. S15). However, at ultrahigh current densities ($\sim 15 \text{ mA cm}^{-2}$), it is evident that the dendrite morphology has changed because the grains get much larger— $\sim 8.8 \pm 3 \mu\text{m}$ along the longest dimensions and $\sim 5.2 \pm 2 \mu\text{m}$ along the shortest dimensions—and are more broadly distributed (fig. S15). These results are consistent with the picture of surface

diffusion-driven dissolution and merging (coarsening) of the dendrites. Because the high current density is applied during both plating and stripping, we expected the healing to occur during both the plating and stripping step. This was corroborated by a comparison of the Li foils after plating and stripping at a current density of $\sim 15 \text{ mA cm}^{-2}$ (fig. S16), indicating a similar (flat) morphology with comparable grain sizes.

So far, we have reported dendrite healing in Li-Li symmetrical cells. The question remained whether such effects can be reproduced in practical situations. To study this, we tested a Li-sulfur (Li-S) full cell (fig. S17A) (19). For this configuration, the anode is a Li metal foil, whereas the cathode is a S-carbon composite (18). Unlike Li-Li symmetrical cells, for Li-S batteries, even under a low current density ($\sim 0.75 \text{ mA cm}^{-2}$), the Li dendrites are densely packed (fig. S17D). This can be understood from the voltage profile for the Li-S battery (fig. S17B). On the basis of the thermodynamics of the Li anode and sulfur cathode, the electrochemical reaction (20) takes place at $\sim 2 \text{ V}$. Because of this large over-potential (related to Li plating and stripping), the dendrites are densely packed irrespective of the current density at which the cell is operated. Of course, current densities of $\sim 0.75 \text{ mA cm}^{-2}$ are insufficient to heal the dendrites through Joule heating; however, when we increased the current density to $\sim 9.0 \text{ mA cm}^{-2}$, we clearly observed healing of the dendrites into a relatively smooth (film-like) morphology (fig. S17E). The galvanostatic charge-discharge cycling and CE results for the Li-S battery are provided in fig. S17C. A key indicator of the severity of dendrites is low CE; as indicated in fig. S17C, the CE of the cell cycled under

high current density is close to 100%, whereas the CE is continuously decreasing when the cell is cycled at low current density. To demonstrate that the healing mechanism in this case is identical to the previously studied Li-Li symmetrical cells, we also annealed the Li anode cycled at $\sim 0.75 \text{ mA cm}^{-2}$ in the Li-S battery at a temperature of $\sim 70^\circ\text{C}$ for ~ 3 days in an Ar environment. The relatively smooth morphology of the thermally annealed Li foil (fig. S17F) closely matches the foil (fig. S17E) that was tested at a current density of $\sim 9.0 \text{ mA cm}^{-2}$ in the Li-S cell. EIS analysis (fig. S18 and tables S1 and S2) indicated that even after only 50 cycles, the electrolyte and interface resistance increased greatly when the Li-S cell was cycled at $\sim 0.75 \text{ mA cm}^{-2}$ as compared with $\sim 9.0 \text{ mA cm}^{-2}$, which is consistent with dendrite healing at the high current density. The dendrite healing was also verified by means of cross-section SEM of the Li electrode (fig. S19).

We further investigated whether the Li-S battery could operate in short bursts at high current densities (with the purpose of healing the dendritic projections) and then revert back to operation at normal (low) current densities. This is demonstrated in Fig. 3A, indicating that periodic operation at high current densities ($\sim 9 \text{ mA cm}^{-2}$) for a limited duration is sufficient to heal the dendrites and substantially improve the CE (Fig. 3B) and to a lesser degree the capacity retention (fig. S20) performance of the battery under regular ($\sim 0.75 \text{ mA cm}^{-2}$ current density) operating conditions. The gradual capacity fade over extended cycling (300 charge-discharge steps) observed in Fig. 3A was caused by dissolution of intermediate Li polysulfides into the electrolyte on the cathode (S) side. Such

capacity fade is typical of Li-S batteries without polysulfide immobilizers (19) or specialized barrier coatings (20) to prevent polysulfide dissolution.

We performed post-cycling characterization of the Li metal electrodes and the membrane separators used in these tests. SEM imaging of the Li anode surface at the end of the third healing step in Fig. 3A (after the 360th charge-discharge cycle) is shown in Fig. 3E. The results indicate a healed (relatively smooth) surface morphology without any sharp dendritic features. It is improbable that such a relatively flat surface could penetrate and punch through the separator membrane. This was confirmed with the optical microscopy images (Fig. 3, C and D) of the separator membrane in the post-cycled state. The membrane from the cell that was cycled at $\sim 0.75 \text{ mA cm}^{-2}$ for 250 charge-discharge steps without any healing treatment showed the presence of prominent dendritic Li deposits that were impregnated into the separator (Fig. 3C). Such Li metal deposits will eventually electrically short the Li-S battery (fig. S21). By contrast, the separator taken from the Li-S cell that was exposed to periodic doses of healing treatment (at $\sim 9 \text{ mA cm}^{-2}$) (Fig. 3A) showed no indication (Fig. 3D) of such Li metal deposits even after extended cycling for 360 charge-discharge steps.

An important practical consideration for the healing strategy presented here is the time taken for the healing to be complete. When high current density is applied, there is an initial drop

(fig. S22A) in the CE as the dendritic surface and SEI reconstructs. Subsequently, as the surface smoothen (fig. S22B) and stabilizes, the CE rises back up to a high value. The healing time can be inferred from the time (~ 2 to 3 hours in fig. S22A) that it takes for the CE to recover back to a high value after the initial dip. This healing time is expected to vary as a function of the applied current density. In addition to duration of healing, the frequency at which the healing treatment is repeated is also an important parameter, especially for minimizing the drying of the electrolyte. Our results showcase a promising path toward the effective deployment of Li metal electrodes in rechargeable batteries.

REFERENCES AND NOTES

1. P. Simon, Y. Gogotsi, B. Dunn, *Science* **343**, 1210–1211 (2014).
2. E. M. Lotfabad *et al.*, *ACS Nano* **8**, 7115–7129 (2014).
3. J. M. Tarascon, M. Armand, *Nature* **414**, 359–367 (2001).
4. W. Xu *et al.*, *Energy Environ. Sci.* **7**, 513–537 (2014).
5. H. Kim *et al.*, *Chem. Soc. Rev.* **42**, 9011–9034 (2013).
6. D. Aurbach, E. Zinigrad, Y. Cohen, H. Teller, *Solid State Ion.* **148**, 405–416 (2002).
7. Y. Lu, Z. Tu, L. A. Archer, *Nat. Mater.* **13**, 961–969 (2014).
8. A. Kushima *et al.*, *Nano Energy* **32**, 271–279 (2017).
9. A. Aryanfar *et al.*, *J. Phys. Chem. Lett.* **5**, 1721–1726 (2014).
10. A. Pei, G. Zheng, F. Shi, Y. Li, Y. Cui, *Nano Lett.* **17**, 1132–1139 (2017).
11. M. Ishikawa, H. Kawasaki, N. Yoshimoto, M. Morita, *J. Power Sources* **146**, 199–203 (2005).
12. T. J. Richardson, G. Chen, *J. Power Sources* **174**, 810–812 (2007).
13. L. Gireaud, S. Grugeon, S. Laruelle, B. Yrieix, J. M. Tarascon, *Electrochem. Commun.* **8**, 1639–1649 (2006).
14. G. Zheng *et al.*, *Nat. Nanotechnol.* **9**, 618–623 (2014).
15. C. P. Yang, Y. X. Yin, S. F. Zhang, N. W. Li, Y. G. Guo, *Nat. Commun.* **6**, 8058 (2015).
16. R. Mukherjee *et al.*, *Nat. Commun.* **5**, 3710 (2014).
17. Y. Liu *et al.*, *Nat. Energy* **2**, 17083 (2017).
18. Materials and methods are available as supplementary materials.
19. J. Gao *et al.*, *Nano Lett.* **16**, 3780–3787 (2016).
20. G. Zhou *et al.*, *Adv. Mater.* **27**, 641–647 (2015).

ACKNOWLEDGMENTS

Funding: N.K. acknowledges support from the U.S. National Science Foundation (awards 1234641, 1435783, 1510828, and 1608171) and the John A. Clark and Edward T. Crossan endowed Chair Professorship at the Rensselaer Polytechnic Institute. J.S. acknowledges the support from U.S. National Science Foundation under award CMMI 1635520. **Author contributions:** L.L. performed electrochemical testing and materials characterization; Y.W. contributed to interpreting the healing mechanism; L.L. and N.K. performed modeling of dendrite nucleation; S.B., N.K., and Y.S. carried out MD simulations; L.L., Y.W., Z.C., and J.S. carried out in situ optical imaging; L.L., P.H., and B.W. carried out x-ray photoelectron spectroscopy and XRD analysis; N.K. and S.N. carried out computational thermal modeling; and L.L., S.B., Y.S., S.N., and N.K. wrote the paper. The project was directed and supervised by N.K. **Competing interests:** Authors have no competing interests. **Data and materials availability:** All data are available in the manuscript or the supplementary materials.

SUPPLEMENTARY MATERIALS

www.sciencemag.org/content/359/6383/1513/suppl/DC1
Materials and Methods
Supplementary Text
Figs. S1 to S22
Tables S1 and S2
References (21–25)

5 September 2017; resubmitted 2 November 2017
Accepted 21 February 2018
10.1126/science.aap8787

AMPHIBIAN DISEASE

Shifts in disease dynamics in a tropical amphibian assemblage are not due to pathogen attenuation

Jamie Voyles,^{1*} Douglas C. Woodhams,^{2,3} Veronica Saenz,⁴ Allison Q. Byrne,⁵ Rachel Perez,⁶ Gabriela Rios-Sotelo,¹ Mason J. Ryan,^{1,7} Molly C. Bletz,² Florence Ann Sobell,⁸ Shawna McLetchie,⁸ Laura Reinert,⁸ Erica Bree Rosenblum,⁵ Louise A. Rollins-Smith,⁸ Roberto Ibáñez,^{3,9} Julie M. Ray,¹⁰ Edgardo J. Griffith,¹¹ Heidi Ross,³ Corinne L. Richards-Zawacki^{3,4}

Infectious diseases rarely end in extinction. Yet the mechanisms that explain how epidemics subside are difficult to pinpoint. We investigated host-pathogen interactions after the emergence of a lethal fungal pathogen in a tropical amphibian assemblage. Some amphibian host species are recovering, but the pathogen is still present and is as pathogenic today as it was almost a decade ago. In addition, some species have defenses that are more effective now than they were before the epidemic. These results suggest that host recoveries are not caused by pathogen attenuation and may be due to shifts in host responses. Our findings provide insights into the mechanisms underlying disease transitions, which are increasingly important to understand in an era of emerging infectious diseases and unprecedented global pandemics.

How do infectious disease outbreaks end? Especially in highly lethal diseases, there is often a shift from an outbreak (epidemic or epizootic phase) to a period when hosts and pathogens coexist (endemic or enzootic phase) (1). Resolving the mechanisms that underpin such disease transitions is challenging because their dynamics hinge on complex and interrelated factors, including the host, the pathogen, and their shared environment (1, 2).

The amphibian disease chytridiomycosis provides a model to investigate the mechanisms underlying epizootic-enzootic transitions. The fungal pathogen that causes chytridiomycosis, *Batrachochytrium dendrobatidis* (*Bd*), has been linked to population declines in amphibian species around the world (3–5). We investigated a chytridiomycosis epizootic-enzootic transition in a tropical amphibian assemblage by tracking shifts in species detection, community composition, and infection patterns, as well as host resistance and pathogen virulence over time.

More than a decade ago, a series of *Bd*-driven amphibian declines were documented at three sites in Panamá (5–10) (Fig. 1A). These epizootic

events were characterized by increases in *Bd* prevalence with concomitant declines in amphibian host densities (5–10). We conducted long-term field surveys at these three sites (Fig. 1A) (5–10). Within ~5 to 13 years after the epizootic events, populations of some species began to reappear, but *Bd* was still present (11), suggesting a shift to an enzootic phase of disease. We used samples collected before, during, and after the epizootic-enzootic transition and integrated common garden experiments and genomic sequencing to test for temporal shifts in *Bd* pathogenicity. We predicted that the mechanism(s) associated with host recoveries would be a decrease in *Bd* pathogenicity (pathogen attenuation) (table S1), an increase in host resistance, or both.

To test whether the detection of individual species changed over time, we used a binomial generalized linear model to evaluate the presence or absence of 12 riparian species that were driven to critically low levels, or putatively extirpated, by chytridiomycosis (10). We found that nine amphibian species are recovering after a period of no detection during the epizootic phase (Fig. 1B and table S2) (10). Two species, variable harlequin frogs (*Atelopus varius*) and common rocket frogs (*Colostethus panamansis*) (Fig. 1B), provide compelling examples of highly susceptible species that declined (8–10) and subsequently recovered in the same locations (Fig. 1B). We also used species community indices to evaluate changes in the community composition similarity over time. After the epizootic events, the number of detected species increased, and host community composition became more similar to that in the pre-disease reference year (Fig. 1, C to E).

To test for changes in *Bd* infection patterns, we collected 2035 diagnostic samples. We found that *Bd* prevalence has decreased since the epizootic events. Prevalence of *Bd* is now low among

amphibian host species at our three study sites (Fig. 2A), within individual species (such as *C. panamansis*) at a single site (Fig. 2, B and C), and across wet and dry seasons (fig. S1).

To test for changes in *Bd* pathogenicity, we conducted common garden experiments with *Bd* isolates that were collected and cryo-archived from two time points: one in 2004, during epizootic events, and one in 2012–2013, after amphibian communities exhibited signs of recovery (Fig. 1A). *Bd* isolates from these time points are hereafter referred to as “historic” and “contemporary” isolates (table S3). We used identical procedures to cryo-archive and revive all isolates (12). We predicted that *Bd* attenuation would be characterized by measurable changes in *Bd* phenotype, immune evasion, disease outcome in live hosts, and genomic structure (table S1).

To test whether historic and contemporary *Bd* isolates differed in reproductive rate and phenotype, we estimated growth rates, zoospore density, and densities of infectious zoospores. Growth rates did not differ among isolates [linear mixed model (LMM), $F_{4,379} = 1.856$, $P = 0.117$] (fig. S2A), nor did zoospore density (LMM, $F_{1,47} = 0.292$, $P = 0.591$). Moreover, all isolates reached their maximum zoospore densities by days 5 to 6 of growth and produced similar numbers of zoospores (LMM, $F_{1,120} = 1.968$, $P = 0.163$) (fig. S2B).

To test whether historic and contemporary *Bd* isolates differed in their capacities to evade host defense mechanisms, we estimated the differences in growth rates for isolates cultured in the presence of anti-*Bd* skin secretions and in the presence of supernatants from anti-*Bd* cutaneous bacteria (13, 14). The inhibitory effects of skin secretions on *Bd* growth did not differ among historic and contemporary isolates (LMM, $F_{1,80} = 0.029$, $P = 0.865$) (fig. S2C), indicating that all isolates had comparable growth when challenged with anti-*Bd* skin secretions. Similarly, there was no difference in *Bd* growth when isolates were exposed to any of 18 bacterial supernatants (LMM, $F_{1,72} = 0.725$, $P = 0.768$) (table S4).

Bd is known to produce factors that inhibit proliferation and induce apoptosis in B and T lymphocytes (15). We used a lymphocyte viability assay to test the immunotoxicity of supernatants collected from historic and contemporary *Bd* isolates. We used two supernatant concentrations that cause lymphocyte inhibition in other amphibian species (15). The percentages of lymphocyte inhibition did not differ among historic and contemporary isolates, regardless of concentration (2.5× concentration, $F_{1,6.3} = 0.838$, $P = 0.394$; 5× concentration, $F_{1,1.5} = 1.460$, $P = 0.282$) (Fig. 3A and fig. S2D). These results suggest that historic and contemporary *Bd* isolates have similar capacities to evade and inhibit amphibian immunity.

To test for differences in *Bd* pathogenicity in live hosts, we conducted common garden exposure experiments with two frog species, *A. varius* and *Litoria caerulea*. For *A. varius*, we exposed frogs to identical doses of three historic isolates, three contemporary isolates, or a sham inoculation (negative control) solution, for a total of seven

¹Department of Biology, University of Nevada, Reno, Reno, NV, USA. ²Department of Biology, University of Massachusetts–Boston, Boston, MA, USA. ³Smithsonian Tropical Research Institute, Panamá, Panamá. ⁴Department of Biological Sciences, University of Pittsburgh, Pittsburgh, PA, USA. ⁵Department of Environmental Science, Policy, and Management, University of California, Berkeley, Berkeley, CA, USA. ⁶Department of Biology, New Mexico Institute of Mining and Technology, Socorro, NM, USA. ⁷Arizona Game and Fish Department, Phoenix, AZ, USA. ⁸Department of Pathology, Microbiology, and Immunology, Vanderbilt University School of Medicine, Nashville, TN, USA. ⁹Sistema Nacional de Investigación, Panamá, Panamá. ¹⁰La Mica Biological Station, El Copé, Panamá. ¹¹Fundación Centro de Conservación de Anfibios, El Valle, Panamá.

*Corresponding author. Email: jvoyles@unr.edu

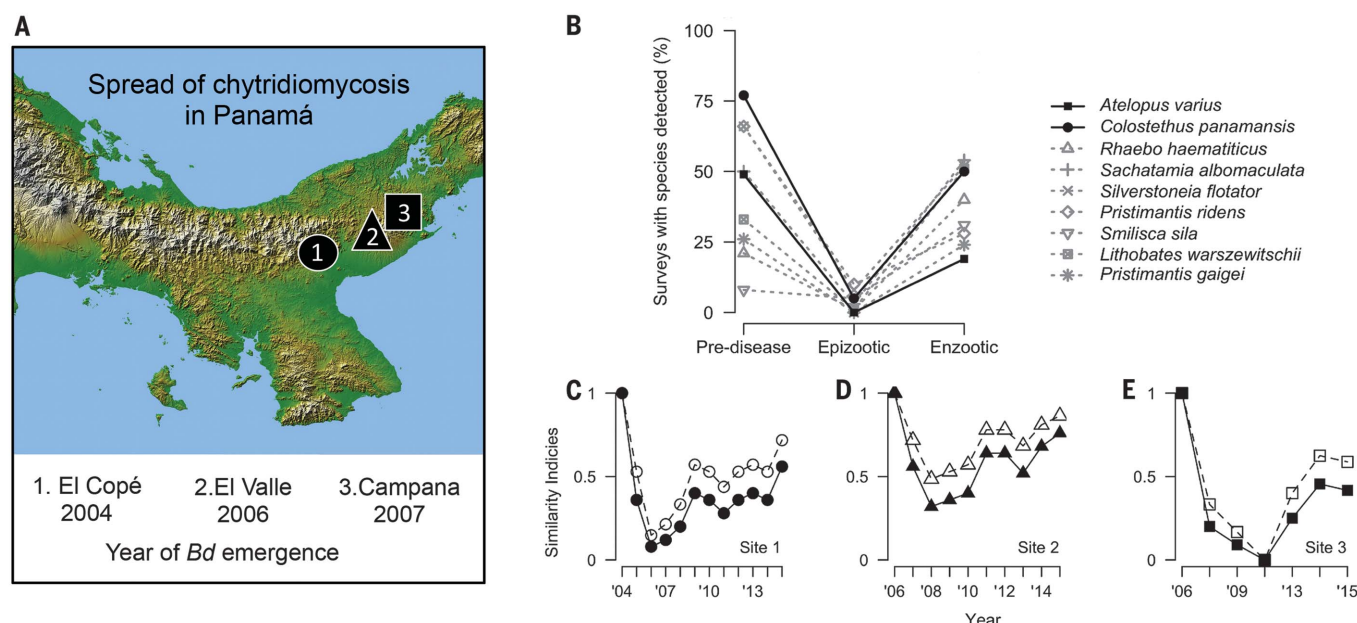


Fig. 1. Amphibian responses to chytridiomycosis outbreaks in Panamá. (A) Map of disease outbreaks in 2004 at El Copé (site 1), 2006 at El Valle (site 2), and 2007 at Altos de Campana (site 3). (B) Proportions of surveys in which amphibian species were detected across three

disease phases. (C to E) Changes in similarity of community composition over time, evaluated with two indices, the Jaccard classic index (closed shapes) and the Sorensen classic index (open shapes). Indices show community similarity relative to the pre-disease year.

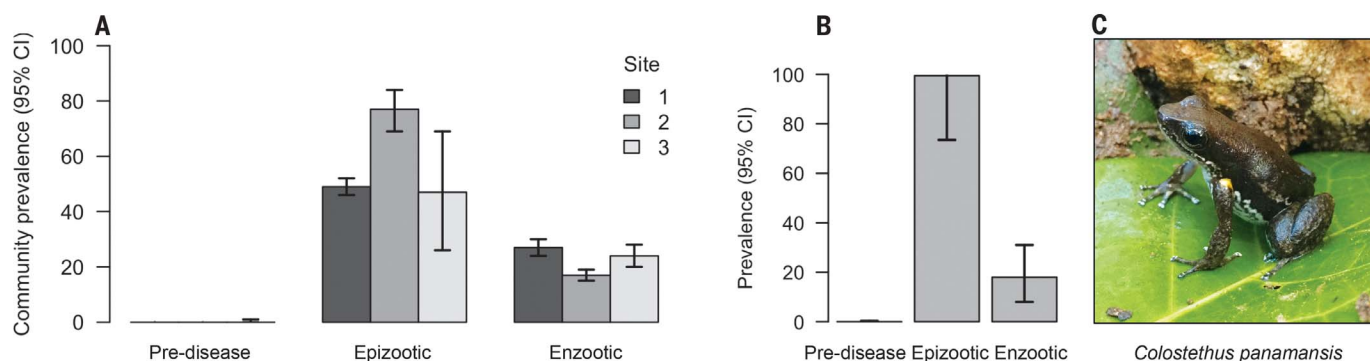


Fig. 2. Prevalence of *Bd* at three sites and within a single amphibian host species. (A) Community prevalence levels with 95% confidence intervals (CI) for the three study sites in Fig. 1A. Data for the pre-disease

and epizootic phases were obtained from published sources (5–10). (B and C) Prevalence in *C. panamansis* [pictured in (C)] with 95% confidence intervals over three disease phases at site 1.

treatment groups (16). We found no significant differences among the *Bd*-exposed treatment groups in prevalence (100% were infected), infection intensity (LMM, $F_{1,135} = 0.020$, $P = 0.887$) (Fig. 3B), body condition (LMM, $F_{1,207} = 2.625$, $P = 0.107$), or survival (100% mortality within 48 days; Cox regression, $P = 0.331$) (Fig. 3C). We conducted a similar experiment using *L. caerulea* and tested for differences in transmission rates between directly and indirectly exposed frogs (fig. S3). There were no significant differences in infection intensity (LMM, $F_{1,12} = 0.793$, $P = 0.391$) or survival (Mantel-Cox, $P = 0.87$). We also evaluated infection probability over time and found no interaction between exposure methods (direct and indirect) and isolate types (historic and contemporary), indicating that infection probabilities were similar regardless of exposure to

historic or contemporary isolates (LMM, $F_{1,76} = 1.733$, $P = 0.192$).

To investigate genetic diversity and relatedness among *Bd* isolates, we used whole-genome sequencing. All isolates were nested within the global pandemic lineage (17), and there was no phylogenetic substructure or signature of temporal divergence among historic and contemporary isolates (fig. S4). We also evaluated chromosomal copy number variation (CNV) among isolates because gain and loss of chromosomal segments is a proposed mechanism for shifts in *Bd* pathogenicity (17, 18). We found an overall signal of diploidy for all isolates (fig. S5) and no shared patterns of CNV among historic and contemporary *Bd* isolates. Thus, genomic data provided no evidence for differentiation, or shifts in *Bd* pathogenicity, among historic and contemporary *Bd* isolates.

Testing for shifts in host defensive capacities was more challenging because we could not use a common garden approach with live hosts. Instead, we used samples of skin secretions that are indicative of host resistance (13). We compared the *Bd*-inhibitory effects of skin secretions from pre-disease and enzootic populations at different geographic locations (13) and from captive *A. varius* frogs (frogs moved to captive breeding programs before *Bd* emergence and therefore *Bd* naïve) and wild, *Bd*-infected enzootic populations (11). The levels of inhibitory effectiveness differed among species (LMM, $F_{5,109} = 5.501$, $P < 0.001$) and between disease phases ($F_{1,109} = 5.131$, $P = 0.025$) (Fig. 4A). Also, inhibitory effectiveness was greater in samples from wild *A. varius* than in those from frogs in captivity (t test, $t_7 = 44.68$, $P < 0.001$) (Fig. 4B). Though

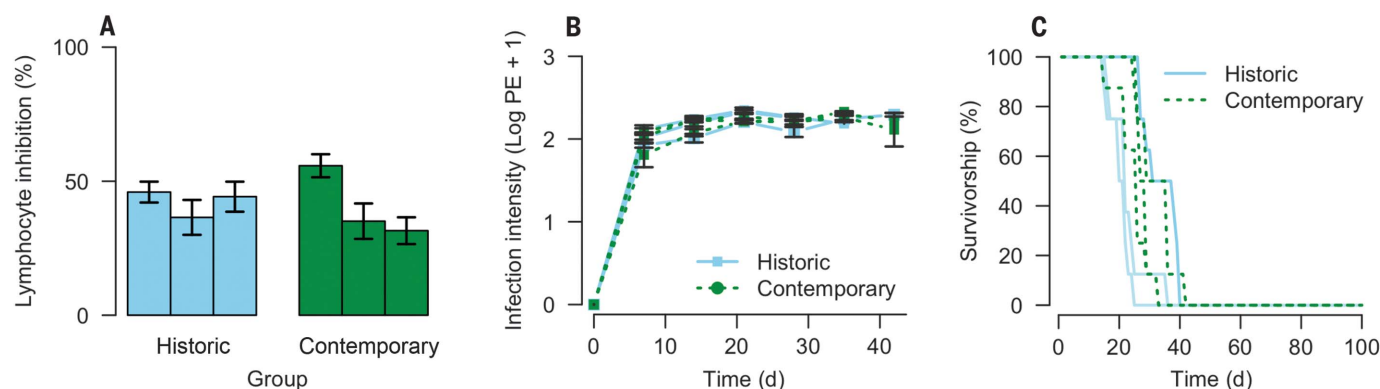


Fig. 3. Comparisons of three historic and three contemporary isolates of *Bd* for immunotoxicity, infection intensity, and survivorship in live hosts. (A) Percentages of lymphocyte inhibition (means \pm SEM) by

historic and contemporary *Bd* supernatants. (B and C) Infection intensity [mean plasmid equivalents (PE) \pm SEM] (B) and survivorship of *A. varius* (C) after exposure to historic and contemporary *Bd* isolates. d, day.

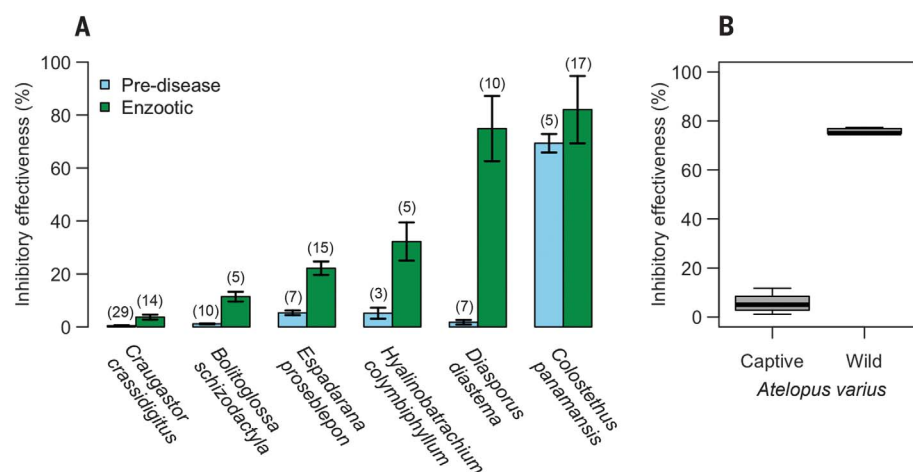


Fig. 4. Comparisons of the levels of effectiveness of skin secretions from amphibian hosts against *Bd*. Percentages of inhibitory effectiveness (means \pm SEM) for skin secretions from six species at the pre-disease and enzootic disease stages (A) and from wild (*Bd*-infected) and captive-bred (*Bd*-naïve) *A. varius* populations (B). Numbers in parentheses above the bars are sample sizes for each species.

many host factors warrant investigation, these results support the hypothesis that shifts in host resistance may be contributing to the recovery of some amphibian species.

Overall, our study reveals that some species have recovered in the 11 to 13 years since the initial chytridiomycosis epizootic events at three Panamanian study sites. Although these recoveries represent a subset (~20% at El Copé) of all the species that declined, they nonetheless provide key insights into the mechanisms driving the epizootic-enzootic transition. Specifically, host recoveries are associated with marked shifts in prevalence but no evidence of attenuated pathogenicity in *Bd*. Some recoveries could be explained by upslope dispersal and recolonization of frogs from lowland populations. However, there is currently no evidence that lowland populations are more resistant to *Bd* infection, and this explanation is unlikely for montane endemics that lack low-elevation source populations (such as *Agalychnis lemur*, *Hyalinobatrachium*

viverrivittatum, and *Hyloscirtus colymba*). An additional plausible mechanism is that some species persisted at low numbers and subsequently increased in abundance, possibly because of evolution in host defenses.

Our results, along with those from studies of other highly virulent disease systems (19, 20), suggest that some disease dynamics may be driven largely by host factors (e.g., standing genetic variation or the capacity to rapidly evolve effective pathogen resistance), particularly when infectious agents remain highly pathogenic. Such insights are increasingly important for understanding spatiotemporal shifts in host-pathogen interactions, especially in this extraordinary time of emerging infectious diseases that threaten plant, animal, and human health (1, 21).

REFERENCES AND NOTES

- K. E. Langwig et al., *Front. Ecol. Environ.* **13**, 195–202 (2015).
- R. S. Ostfeld, F. Keasing, V. T. Eviner, *Infectious Disease Ecology* (Princeton Univ. Press, 2010).

- L. Berger et al., *Proc. Natl. Acad. Sci. U.S.A.* **95**, 9031–9036 (1998).
- J. E. Longcore, A. P. Pessier, D. K. Nichols, *Mycologia* **91**, 219–227 (1999).
- K. R. Lips et al., *Proc. Natl. Acad. Sci. U.S.A.* **103**, 3165–3170 (2006).
- K. R. Lips, J. Diffendorfer, J. R. Mendelson, M. W. Sears, *PLOS Biol.* **6**, e72 (2008).
- V. L. Kilburn et al., *Ecohealth* **7**, 537–548 (2010).
- D. C. Woodhams et al., *Ecohealth* **5**, 268–274 (2008).
- F. M. Brem, K. R. Lips, *Dis. Aquat. Organ.* **81**, 189–202 (2008).
- A. J. Crawford, K. R. Lips, E. Bermingham, *Proc. Natl. Acad. Sci. U.S.A.* **107**, 13777–13782 (2010).
- R. Perez, C. L. Richards-Zawacki, A. R. Krohn, M. Robak, E. J. Griffith, H. Ross, B. Gratwicke, R. Ibáñez, J. Voyles, *Amphib. Reptile Conserv.* **8**, 30–35 (2014).
- D. G. Boyle et al., *Dis. Aquat. Organ.* **56**, 59–64 (2003).
- D. C. Woodhams, J. Voyles, K. R. Lips, C. Carey, L. A. Rollins-Smith, *J. Wildl. Dis.* **42**, 207–218 (2006).
- S. C. Bell, R. A. Alford, S. Garland, G. Padilla, A. D. Thomas, *Dis. Aquat. Organ.* **103**, 77–85 (2013).
- J. S. Fites et al., *Science* **342**, 366–369 (2013).
- J. Voyles et al., *Science* **326**, 582–585 (2009).
- E. B. Rosenblum, et al., *Proc. Natl. Acad. Sci. U.S.A.* **110**, 9385–9390 (2013).
- J. M. Refsnider, T. J. Poorten, P. F. Langhammer, P. A. Burrows, E. B. Rosenblum, *G3* **5**, 2291–2298 (2015).
- P. J. Kerr, *Antiviral Res.* **93**, 387–415 (2012).
- C. Bonneaud et al., *Proc. Natl. Acad. Sci. U.S.A.* **108**, 7866–7871 (2011).
- K. E. Jones et al., *Nature* **451**, 990–993 (2008).

ACKNOWLEDGMENTS

We thank A. Estrada, M. Forriester, B. Gratwicke, D. Medina, R. Puschendorf, M. Robak, A. Smilanch, the Cruz family, UNR (University of Nevada, Reno) Evol-Doers, the Maryland Zoo, and the Smithsonian Tropical Research Institute. **Funding:** This study was supported by Disney Worldwide Conservation Fund, the Association of Zoos and Aquariums, NSF (grants DEB-1551488, 1660311, IOS-1603808, 13542421, 1121758, and 1557634), and the NIH (grant P20GM03451). **Author contributions:** J.V., C.L.R.-Z., E.B.R., and L.A.R.-S. conceived of the project and designed the experiments. J.V., D.C.W., V.S., A.Q.B., R.P., G.R.-S., M.J.R., M.C.B., F.A.S., S.M., L.R., L.A.R.-S., R.I., J.M.R., E.J.G., H.R., and C.L.R.-Z. performed field and experimental work. J.V., D.C.W., M.J.R., E.B.R., L.A.R.-S., and C.L.R.-Z. analyzed the data and wrote the manuscript. **Competing interests:** None declared. **Data and materials availability:** Sequences are available from National Center for Biotechnology Information BioProject (accession no. PRJNA395742). All data needed to evaluate the conclusions in the paper are present in the paper or the supplementary materials.

SUPPLEMENTARY MATERIALS

www.sciencemag.org/content/359/6383/1517/suppl/DC1
Materials and Methods
Figs. S1 to S5
Tables S1 to S4
References (22–25)

30 July 2017; accepted 1 March 2018
10.1126/science.aao4806

IRON HOMEOSTASIS

Erythrocytic ferroportin reduces intracellular iron accumulation, hemolysis, and malaria risk

De-Liang Zhang,¹ Jian Wu,² Binal N. Shah,³ Katja C. Greutelaers,⁴ Manik C. Ghosh,¹ Hayden Ollivierre,¹ Xin-zhuan Su,² Philip E. Thuma,⁵ George Bedu-Addo,⁶ Frank P. Mockenhaupt,⁴ Victor R. Gordeuk,³ Tracey A. Rouault^{1*}

Malaria parasites invade red blood cells (RBCs), consume copious amounts of hemoglobin, and severely disrupt iron regulation in humans. Anemia often accompanies malaria disease; however, iron supplementation therapy inexplicably exacerbates malarial infections. Here we found that the iron exporter ferroportin (FPN) was highly abundant in RBCs, and iron supplementation suppressed its activity. Conditional deletion of the *Fpn* gene in erythroid cells resulted in accumulation of excess intracellular iron, cellular damage, hemolysis, and increased fatality in malaria-infected mice. In humans, a prevalent FPN mutation, Q248H (glutamine to histidine at position 248), prevented hepcidin-induced degradation of FPN and protected against severe malaria disease. FPN Q248H appears to have been positively selected in African populations in response to the impact of malaria disease. Thus, FPN protects RBCs against oxidative stress and malaria infection.

Humans have coevolved with malaria parasites of the genus *Plasmodium* for millennia (1). Plasmodia invade red blood cells (RBCs) and feed on hemoglobin, and thus, malaria infection profoundly disrupts iron homeostasis, as erythroblasts consume 90% of the daily available iron to produce RBCs. Paradoxically, malaria parasites cannot acquire iron from intact heme (2–5), leaving iron released by hemoglobin autoxidation as the most likely iron

source for plasmodia (6–8). Furthermore, for unknown reasons, iron supplementation exacerbates the severity of malarial infections (3, 9–11). However, mechanistic understanding of iron homeostasis in RBCs is surprisingly incomplete because most iron homeostasis proteins are absent in mature RBCs (12, 13).

Ferroportin (FPN) is the only known iron exporter in mammalian cells; it transports iron from enterocytes, hepatocytes, and splenic mac-

rophages into the blood to optimize systemic iron homeostasis (14, 15). FPN expression is regulated in nucleated cells at the translational level by iron regulatory proteins and also posttranslationally by hepcidin, a systemic iron regulatory hormone, to optimize plasma iron homeostasis (16, 17). Recently, we found that FPN was highly expressed in erythroblasts (18, 19). Thus, we hypothesized that FPN is probably present in mature RBCs to export iron generated by hemoglobin autoxidation and thereby protect against iron accumulation, as well as malaria infection.

Confirming our hypothesis, immunoblots with different FPN antibodies detected a strong signal in both mouse and human RBCs, indicating that FPN was present in mature RBCs (Fig. 1A). Next, we deleted the *Fpn* gene specifically in erythroblasts (fig. S1, A to D) (14, 20), which reduced FPN to a faint signal in RBCs of *Fpn* knockout (KO) (*Fpn^{fl/fl};ErCre^{+/+}*) mice (Fig. 1B). In purified cells, the intensity of the FPN signal from RBCs was about 40% of that from erythroblasts, whereas other iron-regulatory proteins, including transferrin receptor 1, divalent metal transporter 1, and iron regulatory protein 1, were

¹Section on Human Iron Metabolism, Eunice Kennedy Shriver National Institute of Child Health and Human Development, National Institutes of Health, Bethesda, MD 20892, USA.

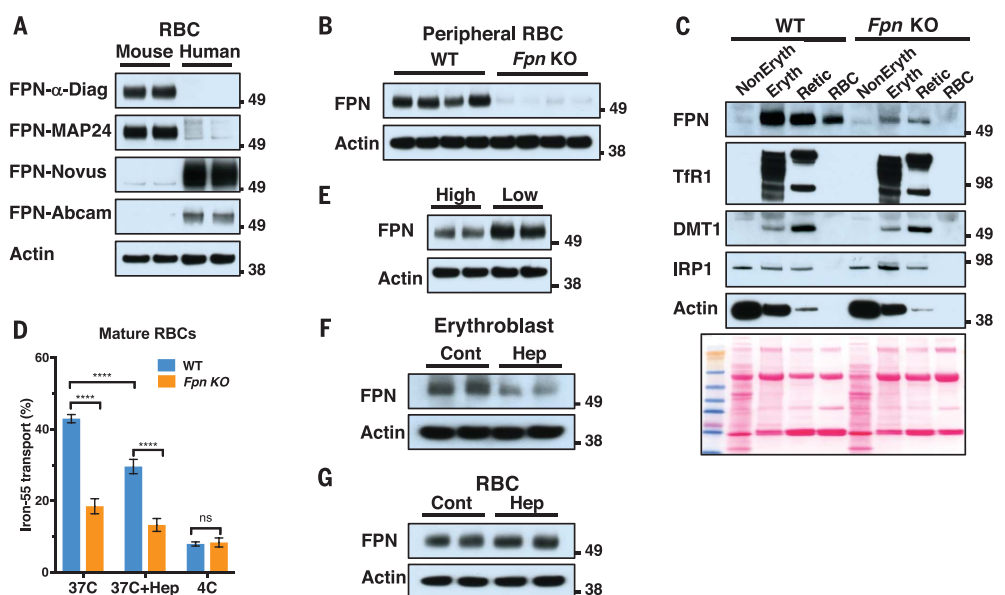
²Laboratory of Malaria and Vector Research, National Institute of Allergy and Infectious Diseases, National Institutes of Health, Bethesda, MD 20892, USA. ³Sickle Cell Center, University of Illinois at Chicago, Chicago, IL 60612, USA.

⁴Charité—Universitätsmedizin Berlin, Freie Universität Berlin, Humboldt-Universität zu Berlin, and Berlin Institute of Health, Institute of Tropical Medicine and International Health, Berlin 13353, Germany. ⁵Malaria Research Trust, Choma 630166, Zambia. ⁶Komfo Anokye Teaching Hospital, Kwame Nkrumah University of Science and Technology, Kumasi, Ghana.

*Corresponding author: Email: rouault@mail.nih.gov

Fig. 1. FPN is highly abundant on mature RBCs, and its activity is inhibited by iron supplementation and hepcidin. (A) Immunoblots

with four different FPN antibodies showed that FPN protein was present in membrane fractions of human and mouse RBCs. Actin is present as a loading control. **(B)** FPN protein levels were reduced in RBCs of erythroblast-specific *Fpn* KO mice. **(C)** FPN was about half as abundant in RBCs as in erythroblasts, but other iron metabolism proteins, including transferrin receptor 1 (TfR1), divalent metal transporter 1 (DMT1), and iron regulatory protein 1 (IRP1), were absent in RBCs (total lysate). Cells were purified by flow cytometry from bone marrow (fig. S2). Bottom image shows Ponceau S staining as a loading control. NonEryth, nonerythroblasts; Eryth, erythroblasts; Retic, reticulocytes. **(D)** Export of Fe⁵⁵ by WT and *Fpn* KO RBCs was measured after 1 hour at 37°C, at 37°C with 1 μg/ml hepcidin (hep), or at 4°C. Mean ± 95% confidence interval (CI); *n* = 12. The experiments were independently repeated three times. Significance was determined by two-way analysis of variance (ANOVA) and Sidak's multiple comparisons test. *****P* < 0.0001; ns, not significant. **(E)** FPN levels were lower in membranes of RBCs from mice treated on high-iron diets (high) versus low-iron diets (low). Each lane represents a sample from one individual mouse. **(F and G)** FPN levels in total lysates of (F) erythroblasts and (G) RBCs treated ex vivo without (cont) or with 1 μg/ml hepcidin (hep) for 24 hours. Two independent replicates are shown in adjacent lanes. Numbers to the right of immunoblots are in kDa.



not detected in RBCs (Fig. 1C and fig. S2). We further evaluated FPN abundance in a mass-spectrum database of human RBC membranes, which included healthy controls and Diamond-Blackfan anemia (DBA) patients (Table 1 and table S1) (27), and estimated that FPN occurred at 54,000 copies per cell, an amount greater than

that of the integral RBC membrane protein component glycophorin C. These results indicated that FPN was highly abundant in mature RBCs.

To evaluate whether FPN on RBC membranes was a functional iron exporter, we loaded RBCs with the radioisotope ^{55}Fe and measured its efflux to the medium (Fig. 1D). Within 60 min, wild-type

(WT) RBCs exported 43% of ^{55}Fe to the medium compared with 18% exported by *Fpn* KO RBCs, indicating that erythrocytic FPN exported iron. Surprisingly, exogenous hepcidin reduced ^{55}Fe export from 43 to 30% (Fig. 1D), indicating that hepcidin inhibited FPN activity in mature RBCs. In animals fed on a high-iron diet, FPN levels

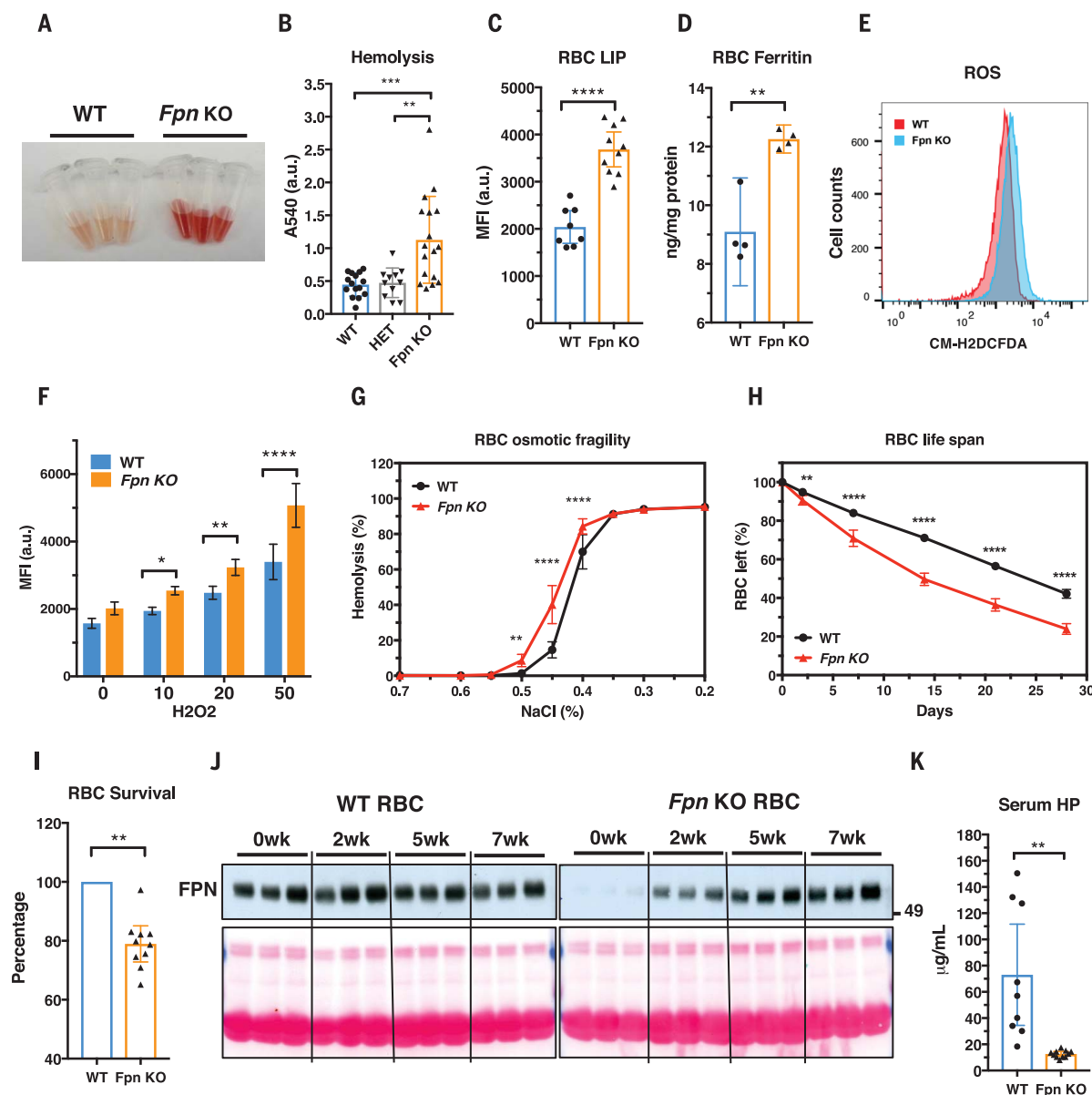


Fig. 2. *Fpn* knockout in erythroblasts leads to RBC iron overload and intravascular hemolysis. (A) Plasma of WT and *Fpn* KO mice after storing blood samples for 20 hours at 4°C showed increased hemolysis of *Fpn* KO RBCs. (B) Free-hemoglobin levels in plasma of WT, heterozygote (HET), and *Fpn* KO mice. Significance determined by one-way ANOVA and Tukey's multiple comparisons test. A540, absorption at 540 nm; a.u., arbitrary units. (C) Labile iron pool (LIP) and (D) ferritin levels were dramatically increased in RBCs of *Fpn* KO mice. MFI, median fluorescence intensity. (E) Representative flow cytometry of reactive oxygen species (ROS) in RBCs of WT and *Fpn* KO mice and (F) quantification of ROS levels in RBCs of WT and *Fpn* KO mice after stimulation by H_2O_2 at different micromolar concentrations. $n = 8$. CM-H2DCFDA is a ROS indicator. (G) Osmotic fragility of RBCs, $n = 9$. (H) RBC life span of *Fpn* KO mice, $n = 9$. (I) Survival of

ex vivo biotin-labeled WT and *Fpn* KO RBCs in the same WT mice (fig. S9). (J) Immunoblots showing FPN levels in the aging process of the RBCs of three WT and three *Fpn* KO mice in vivo. Sulfo-NHS-LC-Biotin was injected intravenously to label all RBCs, and after 0, 2, 5, and 7 weeks (wk), biotinylated RBCs were purified and FPN levels were then measured with immunoblots in total lysates. Ponceau S staining (bottom) is shown as a loading control. The increase of FPN levels in RBCs of *Fpn* conditional KO mice indicated that the few FPN-expressing RBCs survived longer than *Fpn*-null RBCs and were proportionally enriched over time (fig. S10). (K) Serum haptoglobin (HP) was depleted in *Fpn* KO mice. Data are presented as mean \pm 95% CI. Significances for (F) to (H) were determined by two-way ANOVA and Sidak's multiple comparisons test; significances for (I) and (K) were determined by Welch's t test. * $P < 0.05$; ** $P < 0.01$; *** $P < 0.001$; **** $P < 0.0001$.

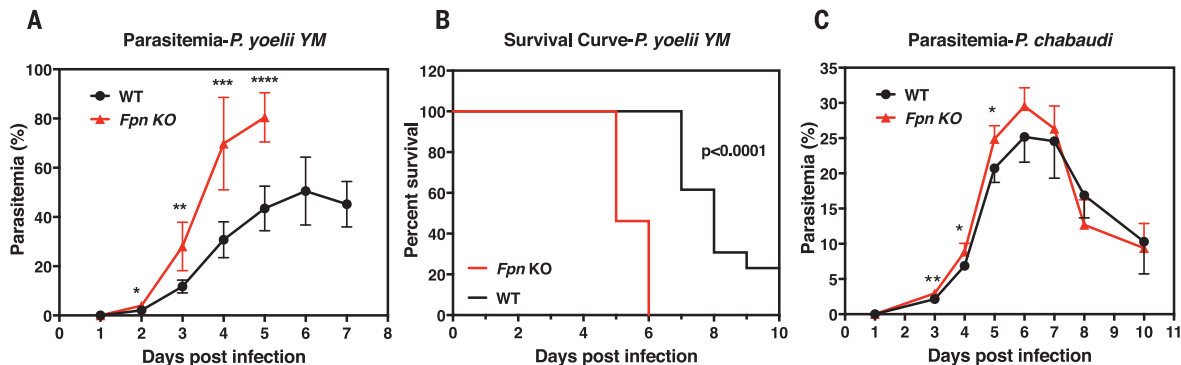


Fig. 3. FPN protects mice from severe malarial infection. (A) Parasitemia ($n = 5$ for each group) and (B) survival curve ($n = 13$ for each group) of WT and *Fpn* KO mice after *P. yoelii* YM infection. (C) Parasitemia of WT and *Fpn* KO mice after *P. chabaudi* infection; $n = 5$ for WT and $n = 7$ for *Fpn* KO mice.

Data are presented as mean \pm 95% CI. Statistical significances determined for (A) and (C) with the Holm-Sidak multiple comparisons test with $\alpha = 0.05$. Survival curves were analyzed with the log-rank test and Gehan-Breslow-Wilcoxon test. * $P < 0.05$; ** $P < 0.01$; *** $P < 0.001$; **** $P < 0.0001$.

decreased in RBCs, as hepcidin expression increased (Fig. 1E, fig. S3A). Exogenous hepcidin treatment decreased FPN levels in erythroblasts (Fig. 1F), in which the degradation apparatus is intact, but not in RBCs (Fig. 1G), which lack the proteasomal degradation pathway for hepcidin. Together with findings in DBA patients (22) (Table 1 and table S1) and sickle cell disease patients (23) (fig. S3, B and C), we observed that RBC FPN levels inversely correlated with hepcidin expression, likely owing to the regulation of FPN in erythroblasts (Fig. 1F). Hepcidin inhibited FPN iron-export activity (Fig. 1D) but did not change FPN abundance on RBCs (Fig. 1G), indicating that hepcidin binding sterically suppressed the iron-export activity of FPN (24, 25).

Fpn knockout increased non-heme iron content and intracellular ferritin levels of erythroblasts (fig. S1, E and F) and resulted in a mild compensated anemia and extramedullary erythropoiesis (figs. S4 to S6 and table S2). The anemia was not caused by a defect of erythroblast differentiation (fig. S7) but instead by the increased fragility and hemolysis of the mature RBCs, as evidenced by the 2.5-fold increase of free plasma hemoglobin after storage at 4°C for 20 hours (Fig. 2, A and B, and fig. S8A). Consistently, we found that the labile iron pool of *Fpn* KO RBCs increased by 80% (Fig. 2C), and non-heme iron and ferritin levels (Fig. 2D and fig. S8B) also significantly increased. Iron overload increased reactive oxygen species production by 30% (Fig. 2, E and F), which damaged RBC plasma membranes, as shown by increased annexin V staining (fig. S8C) and osmotic fragility (Fig. 2G). Consequently, the RBC half-life was reduced from 25 days in WT mice to 14 days in *Fpn* KO mice (Fig. 2H). The shorter life span was attributable to a cell-autonomous defect of *Fpn* KO RBCs, because only 80% of *Fpn* KO RBCs remained in the circulation relative to WT RBCs when their survival was compared in the same animal (Fig. 2I and fig. S9) and the few remaining WT RBCs in the conditional KO mice increased in proportion during the RBC aging process (Fig. 2J and fig. S10). Consistently, serum haptoglobin depletion (Fig. 2K and fig. S11A), in-

Table 1. Mass spectrum analysis shows high abundance of FPN in RBC membrane fractions.

Protein copy number in RBC membrane fractions of control and DBA patients, as reported in mean \pm SEM. Data are normalized to Band3, an abundant RBC membrane protein; thus, SEM is not applicable for Band3. Protein 4.1, a major erythrocyte membrane skeleton protein; GLUT1, glucose transporter 1; GYPC, glycophorin C; CYBRD1, cytochrome b reductase 1. See table S3 for details. NA, not applicable.

Protein	Control group ($n = 4$)	DBA group ($n = 8$)	P value	Rank*
Band3	1,000,000	1,000,000	NA	5
Protein 4.1	321,088 \pm 8,399	310,758 \pm 5,080	0.291	8
GLUT1	153,326 \pm 5,628	151,351 \pm 2,637	0.720	18
FPN	54,082 \pm 1,286	41,694 \pm 3,025	0.019	54
GYPC	50,554 \pm 2,919	49,348 \pm 1,483	0.687	64
CYBRD1	25,158 \pm 1977	22,212 \pm 1521	0.278	257

*Rank represents the order of the protein on the list when sorted by protein abundance.

creased CD163 and heme oxygenase 1 expression (figs. S11, B and C, and S5F), and iron overload observed in splenic macrophages, Kupffer cells, and renal proximal tubules (fig. S11D) indicated that *Fpn* KO mice were suffering from hemolytic anemia. These results showed that FPN was critical for exporting free iron to maintain the integrity of mature RBCs.

The high abundance of FPN on RBCs, its effects on RBC iron status, and its down-regulation by iron supplementation could therefore influence the growth of malaria parasites (3–5, 9, 10, 26). To test this hypothesis, we intravenously injected WT and *Fpn* KO mice with *Plasmodium yoelii* YM, a lethal murine malaria strain. *Fpn* KO mice had 60% more parasite-infected RBCs than WT mice on multiple successive days after infection (Fig. 3A), and they died more rapidly after infection (Fig. 3B). We next infected multiple mice with *P. chabaudi chabaudi* AS, a murine strain that almost exclusively infects mature RBCs (fig. S12). Consistently, the parasitemia of *Fpn* KO mice was higher than that of WT mice from days 3 to 6, before reticulocyte numbers increased and mature RBCs declined (Fig. 3C and fig. S12).

Because malaria has long driven the evolution of the human genome (1), we hypothesized that

mutations that increased FPN levels would protect humans from malaria infection and be evolutionarily enriched in malaria-endemic regions. The *FPN* Q248H (glutamine to histidine at position 248) mutation occurs in sub-Saharan African populations with a heterozygote prevalence of 2.2 to 20%, depending on location (27–29). The mutation renders FPN resistant to hepcidin-induced degradation (30), and carriers have lower hemoglobin concentrations than controls (29), consistent with our hypothesis that high FPN levels in erythroblasts export iron and diminish hemoglobin production (18, 19). After screening 27 African Americans, we found three Q248H heterozygotes. Immunoblot analyses confirmed that FPN levels were increased in the RBCs of Q248H heterozygotes relative to control donors (fig. S13), indicating that the mutation could have as yet unknown health consequences in carriers of African descent.

We then analyzed the parasitemia of 66 hospitalized Zambian children with uncomplicated *P. falciparum* malaria who were <6 years of age (Table 2 and table S3) (31, 32). The Q248H mutation was observed in 19.7% of the children (12 heterozygotes, 1 homozygote). Compared to patients with a WT allele, who had a median

Table 2. FPN Q248H mutation was associated with reduced parasitemia in Zambian children with uncomplicated malaria. Characteristics of Zambian children with uncomplicated malaria (hematocrit >18% and Blantyre coma score = 5) and either WT or Q248H FPN. Results are presented as median interquartile range. Significances analyzed with Fisher’s exact test and chi-square test.

Characteristic	WT (n = 53)	Q248H* (n = 13)	P value
Fever duration before presentation (hours)	37 (21 to 70)	69 (24 to 113)	0.1
Asexual parasites in peripheral blood (parasites/μl)	189,667 (37,108 to 256,129)	28,000 (11,813 to 107,034)	0.025
Hemoglobin (g/dl)	10.1 (8.2 to 11.1)	8.8 (6.6 to 10.3)	0.1

*12 heterozygotes, 1 homozygote.

Table 3. FPN Q248H mutation protected from malarial infection in primiparous Ghanaian women. Proportion of *P. falciparum* infection among primiparous Ghanaian women with live singleton delivery and either WT or Q248H FPN. Proportions were compared between groups by chi-square test. PCR, polymerase chain reaction.

Characteristic	All (n = 290)	WT (n = 265)	Q248H* (n = 25)	P value
Past or present placental infection [†]	197/290 (67.9%)	186/265 (70.2%)	11/25 (44%)	0.007
Placental blood <i>P. falciparum</i> PCR positivity	188/290 (64.8%)	177/265 (66.8%)	11/25 (44%)	0.03
Peripheral blood <i>P. falciparum</i> PCR positivity	171/290 (59%)	160/265 (60.4%)	11/25 (44%)	0.11

*24 heterozygotes, 1 homozygote. [†]Microscopic detection of placental parasitemia or malaria pigment, or a positive PCR result on placental blood samples.

of 189,667 parasites/μl, Q248H patients had 28,000 parasites/μl (two-sided Fisher’s test and chi-square test, $P = 0.025$). Q248H patients also experienced less fulminant malaria, as manifested by tolerance of longer fever times before presentation to the hospital (median of 69 versus 37 hours, Q248H versus WT, $P = 0.1$). Additionally, the hemoglobin concentrations of Q248H patients were lower than those of patients with a WT allele (median of 8.8 versus 10.1 g/dl, Q248H versus WT, $P = 0.1$), which was consistent with the possibility that increased FPN abundance in Q248H carriers reduced the amount of iron available for hemoglobin synthesis (29, 30).

We next investigated the effects of the Q248H mutation on malarial infection in 290 primiparous Ghanaian women (Table 3 and table S4). Primiparae are particularly prone to placental malaria, because acquired immunity against parasites adhering to the placental syncytiotrophoblast is insufficiently developed in the first pregnancy (33). Of 290 women, 8.6% were Q248H carriers (24 heterozygotes, 1 homozygote). Present or past placental *P. falciparum* infection occurred less frequently in Q248H carriers (44.0%) than in women with the respective WT allele

(70.2%, $P = 0.007$), even after adjusting by logistic regression for known predictors of placental malaria (34). The apparent protection that the Q248H mutation conferred against malaria infection was also seen in the analysis of peripheral blood samples (44.0 versus 60.4%, $P = 0.11$), even though analysis of peripheral blood is relatively insensitive for diagnosing malaria in pregnant women.

We found that the iron exporter FPN was highly abundant on mature RBCs. FPN prevents erythrocytic iron accumulation and concomitant oxidative stress and protects RBCs against malarial infection (fig. S14). FPN on mature RBCs was abundant under conditions of iron deficiency but diminished with iron supplementation. Its activity was inhibited by hepcidin, which would increase the labile iron pool within RBCs and promote the growth of plasmodial parasites. These findings help to explain why iron deficiency protects against malarial infection, why iron supplementation promotes malaria-related hospitalization and mortality, and why the Q248H mutation may have undergone positive selection in African populations of malaria-endemic regions, among other protective mutations (9, 10, 35).

REFERENCES AND NOTES

1. A. F. Cowman, J. Healer, D. Marapana, K. Marsh, *Cell* **167**, 610–624 (2016).
2. P. A. Sigala, J. R. Crowley, S. Hsieh, J. P. Henderson, D. E. Goldberg, *J. Biol. Chem.* **287**, 37793–37807 (2012).
3. M. A. Clark, M. M. Goheen, C. Cerami, *Front. Pharmacol.* **5**, 84 (2014).
4. P. F. Scholl, A. K. Tripathi, D. J. Sullivan, *Curr. Top. Microbiol. Immunol.* **295**, 293–324 (2005).
5. A. M. Prentice, *J. Nutr.* **138**, 2537–2541 (2008).
6. J. M. Rifkind, E. Nagababu, S. Ramasamy, L. B. Ravi, *Redox Rep.* **8**, 234–237 (2003).
7. J. Umbreit, *Am. J. Hematol.* **82**, 134–144 (2007).
8. T. Kanias, J. P. Acker, *FEBS J.* **277**, 343–356 (2010).
9. S. Sazawal et al., *Lancet* **367**, 133–143 (2006).
10. M. Gwamaka et al., *Clin. Infect. Dis.* **54**, 1137–1144 (2012).
11. N. Spottiswoode, P. E. Duffy, H. Drakesmith, *Front. Pharmacol.* **5**, 125 (2014).
12. D. L. Zhang, M. C. Ghosh, T. A. Rouault, *Front. Pharmacol.* **5**, 124 (2014).
13. N. Wilkinson, K. Pantopoulos, *Front. Pharmacol.* **5**, 176 (2014).
14. A. Donovan et al., *Cell Metab.* **1**, 191–200 (2005).
15. H. Drakesmith, E. Nemeth, T. Ganz, *Cell Metab.* **22**, 777–787 (2015).
16. S. Abboud, D. J. Haile, *J. Biol. Chem.* **275**, 19906–19912 (2000).
17. E. Nemeth et al., *Science* **306**, 2090–2093 (2004).
18. D. L. Zhang, R. M. Hughes, H. Ollivierre-Wilson, M. C. Ghosh, T. A. Rouault, *Cell Metab.* **9**, 461–473 (2009).
19. D. L. Zhang et al., *Blood* **118**, 2868–2877 (2011).
20. A. C. Heinrich, R. Pelanda, U. Klingmüller, *Blood* **104**, 659–666 (2004).
21. E. N. Pesciotta et al., *PLOS ONE* **9**, e85504 (2014).
22. D. Pospisilova et al., *Haematologica* **99**, e118–e121 (2014).
23. Z. A. Jenkins et al., *Pediatr. Hematol. Oncol.* **24**, 237–243 (2007).
24. R. Taniguchi et al., *Nat. Commun.* **6**, 8545 (2015).
25. S. Aschemeyer et al., *Blood* **131**, 899–910 (2018).
26. K. Schümann, N. W. Solomons, *Food Nutr. Bull.* **34**, 349–356 (2013).
27. I. Kasvosve et al., *Am. J. Clin. Nutr.* **82**, 1102–1106 (2005).
28. D. Albuquerque et al., *Ann. Hum. Biol.* **38**, 378–381 (2011).
29. V. R. Gordeuk et al., *Blood Cells Mol. Dis.* **31**, 299–304 (2003).
30. S. Nekhai et al., *Haematologica* **98**, 455–463 (2013).
31. M. E. Molyneux, T. E. Taylor, J. J. Wirima, A. Borgstein, *Q. J. Med.* **71**, 441–459 (1989).
32. P. E. Thuma et al., *J. Infect. Dis.* **203**, 211–219 (2011).
33. M. Fried, F. Nosten, A. Brockman, B. J. Brabin, P. E. Duffy, *Nature* **395**, 851–852 (1998).
34. M. A. Grundy, N. Gorman, P. R. Sinclair, M. J. Chorney, G. S. Gerhard, *J. Biochem. Biophys. Methods* **59**, 195–200 (2004).
35. M. J. Murray, A. B. Murray, M. B. Murray, C. J. Murray, *BMJ* **2**, 1113–1115 (1978).

ACKNOWLEDGMENTS

We thank N. Andrews for providing us the Fpn-flox mice, S. Orkin for providing us the ErCre mice, the Department of Transfusion Medicine of the NIH Clinical Center for providing Buffy Coats for the research, J. Tisdale for providing sickle cell disease samples, and J. Langhorne from The Francis Crick Institute, U.K., for providing *P. chabaudi*.

Funding: This work was supported by the intramural program of the Eunice Kennedy Shriver National Institute of Child Health and Human Development and by the Division of Intramural Research at the National Institute of Allergy and Infectious Diseases (NIAID), NIH. **Author contributions:** D.L.Z. designed the project, performed the experiments, analyzed the data, and wrote the paper; T.A.R. supervised the project and wrote the paper; M.C.G. supervised the mouse colonies and reviewed the paper; H.O. performed the mouse experiments and reviewed the paper; J.W. and X.S. performed and analyzed the mouse malarial study and reviewed the paper; B.N.S., V.R.G., and P.E.T. performed and analyzed the human malaria study for Zambian children and reviewed the paper; K.C.G., G.B.-A., and F.P.M. performed and analyzed the human malaria study for Ghanaian women and reviewed the paper. **Competing interests:** All authors declare no competing interests. **Data and materials availability:** All data to understand and assess the conclusions of this research are available in the main text and supplementary materials.

SUPPLEMENTARY MATERIALS

www.sciencemag.org/content/359/6383/1520/suppl/DC1
Materials and Methods
Figs. S1 to S14
Tables S1 to S5
References (36–47)

12 October 2016; resubmitted 15 August 2017
Accepted 25 January 2018
10.1126/science.aal2022

NEUROSCIENCE

Hippocampal ripples down-regulate synapses

Hiroaki Norimoto,^{1,2} Kenichi Makino,^{1*} Mengxuan Gao,^{1*} Yu Shikano,¹ Kazuki Okamoto,¹ Tomoe Ishikawa,¹ Takuya Sasaki,¹ Hiroyuki Hioki,^{3,4} Shigeyoshi Fujisawa,^{2†} Yuji Ikegaya^{1,5†}

The specific effects of sleep on synaptic plasticity remain unclear. We report that mouse hippocampal sharp-wave ripple oscillations serve as intrinsic events that trigger long-lasting synaptic depression. Silencing of sharp-wave ripples during slow-wave states prevented the spontaneous down-regulation of net synaptic weights and impaired the learning of new memories. The synaptic down-regulation was dependent on the *N*-methyl-D-aspartate receptor and selective for a specific input pathway. Thus, our findings are consistent with the role of slow-wave states in refining memory engrams by reducing recent memory-irrelevant neuronal activity and suggest a previously unrecognized function for sharp-wave ripples.

Hippocampal and neocortical plasticity during the awake state is dominated by net synaptic potentiation, whereas plasticity during sleep, especially during slow-wave (SW) sleep, is dominated by net synaptic depression (1, 2). These circadian alternations in synaptic weights manifest a homeostatic balancing function for sleep (3, 4); however, the mechanisms behind the synaptic downscaling during SW states remain to be identified. During SW states—which include SW sleep, awake immobility, and consummatory behavior—the hippocampus spontaneously emits transient high-frequency field oscillations called sharp-wave ripples (SWRs) (fig. S1). SWRs represent the reactivation of neurons involved in recently acquired memory (5) and contribute to memory consolidation (6–9). Although memory consolidation may rely on synaptic plasticity, no consensus has yet been reached on the relationship between SWRs and synaptic plasticity (10–12).

We first investigated whether suppression of SWRs affects the synaptic down-regulation that occurs during SW states. We allowed mice to explore novel environments for 30 min before sleep because SWRs are known to occur more frequently after spatial learning (13). Indeed, the 30-min exploration increased the SWR event frequencies from 0.48 ± 0.03 Hz under naïve conditions to 0.88 ± 0.07 Hz (mean \pm SEM of eight trials from three mice; $P = 3.1 \times 10^{-8}$, $t_7 = 6.56$, paired *t* test). The SWR increase may reflect the strengthening of synaptic weights in the learning process (14). We then perturbed the SWRs

during SW states for 7 hours by using optogenetic feedback stimulation triggered upon the online detection of ripples in local field potentials (LFPs) recorded from the hippocampal CA1 region (Fig. 1A) (15). Simultaneous LFP recordings and electromyograms revealed that $84.6 \pm 2.9\%$ of the SW periods over 7 hours coincided with SW sleep, whereas the remaining SW periods were detected during awake immobility or consummatory behavior. Feedback illumination but not time-mismatched control illumination with random delays ranging from 80 to 120 ms to the dorsal CA3 region of somatostatin (SOM)::channelrhodopsin2 (ChR2) transgenic mice (Fig. 1B) reduced both ripple power (Fig. 1C) and the firing rates of CA1 pyramidal cells during the SWRs (Fig. 1C). This closed-loop technique silenced $97.7 \pm 1.8\%$ of the total SWRs (mean \pm SEM of 10 trials from five mice). We measured field excitatory postsynaptic potentials (fEPSPs) from the CA1 stratum radiatum while single-pulse field stimulation was applied every 20 s to the Schaffer collaterals, which per se did not induce SWRs. Consistent with previous studies (1), the fEPSP slopes in no-light control and delayed control groups gradually decreased during the SW periods, but this spontaneous synaptic depression did not occur in the SWR-silenced mice (Fig. 1D). Neither the total sleep length nor the percentage occupied by each brain state differed between the groups (fig. S2), but the event incidence of SWRs remained higher in the SWR-silenced group (fig. S3).

After the SWRs were silenced for 7 hours, animals were tested in an object-place recognition task that consisted of two phases (Fig. 1E). During the first encoding phase, mice explored a familiar open arena with two identical novel objects, and none of the mouse groups exhibited a preference for one object over the other (fig. S4). The second recall phase, in which one of the objects was moved to a previously empty location, was conducted after a 2-hour resting period in the home cages. In this phase, the SWR-silenced group did not discriminate between the relocated and unmoved objects (Fig. 1F). Thus, object-place learning was disturbed after SWR silencing during SW states.

To more directly examine whether SWRs induce synaptic depression, we used obliquely sliced hippocampal preparations (16), which spontaneously emit SWRs (fig. S5). Slices prepared from animals that had explored a novel environment for 30 min exhibited higher SWR event frequencies than slices from naïve mice (fig. S5). Therefore, in the following experiments, we used slices from animals after exploration. Single-pulse field stimulation was applied to the Schaffer collaterals, and fEPSPs were recorded from the CA1 stratum radiatum. The fEPSP slopes were spontaneously reduced over time, and this reduction was inhibited by bath application of $50 \mu\text{M}$ D-AP5, an *N*-methyl-D-aspartate receptor (NMDAR) antagonist (fig. S6A). Thus, the spontaneous depression reflected actively occurring synaptic plasticity (17) rather than deterioration of the slice preparations or synaptic fatigue. We also prepared conventional horizontal hippocampal slices, which do not emit SWRs (16). Although these slices did not exhibit spontaneous synaptic depression (fig. S6B), even without SWRs, synaptic depression was inducible in a D-AP5-sensitive manner when the Schaffer collaterals were repetitively stimulated at event timings of the SWRs recorded in vivo after spatial exploration but not under naïve conditions without exploration (fig. S7).

We used slices prepared from SOM::ChR2 mice to conduct closed-loop SWR inhibition (Fig. 2A). Blue light pulsed upon SWR detection suppressed the firing rates of the neurons during SWRs (Fig. 2B). The SWR silencing prevented spontaneous synaptic depression, whereas control stimulation with a delay of 100 ms failed to replicate this effect (Fig. 2C).

We next attempted to confirm the spontaneous synaptic depression in SWR-emitting slices at the single-synapse level. The head sizes of dendritic spines are correlated with synaptic strength (18, 19) and are subject to shrinkage during NMDAR-dependent long-term depression (20). We therefore examined whether spine shrinkage accompanied the spontaneous synaptic depression. We prepared oblique hippocampal slices from Thy1-mGFP mice and performed two-photon imaging of spines on the apical dendrites of CA1 pyramidal cells for 180 min (fig. S8A). The mean head volume of the spines decreased spontaneously as a function of time, an effect that was blocked by $50 \mu\text{M}$ D-AP5 (fig. S8B). The mean density of the spines did not change, indicating that few spines disappeared during the recording time ($P = 0.686$, $U = 6.00$, Mann-Whitney *U* rank sum test). As spines are typically categorized into thin, stubby, and mushroom types, we separately analyzed spine shrinkage for these types (fig. S8C, left). Thin and stubby spines shrank in a D-AP5-sensitive manner, but mushroom spines maintained their volumes throughout our observation period (fig. S8C, right).

Given the heterogeneity and specificity in spine shrinkage, we reasoned that patterns of CA1 neuronal activity may also be modulated in an NMDAR-dependent manner, because individual synaptic weights collectively orchestrate patterns of neuronal activity (21). Arc-dVenus transgenic mice (22) were allowed to freely explore a

¹Laboratory of Chemical Pharmacology, Graduate School of Pharmaceutical Sciences, The University of Tokyo, Tokyo, Japan. ²Laboratory for Systems Neurophysiology, RIKEN Brain Science Institute, 2-1 Hirosawa, Wako City, Saitama, Japan. ³Department of Morphological Brain Science, Graduate School of Medicine, Kyoto University, Kyoto, Japan. ⁴Department of Cell Biology and Neuroscience, Juntendo University Graduate School of Medicine, Tokyo, Japan. ⁵Center for Information and Neural Networks, National Institute of Information and Communications Technology, Osaka, Japan.

*These authors contributed equally to this work.

†Corresponding author. Email: yuji@ikegaya.jp (Y.I.); fujisawa@brain.riken.jp (S.F.)

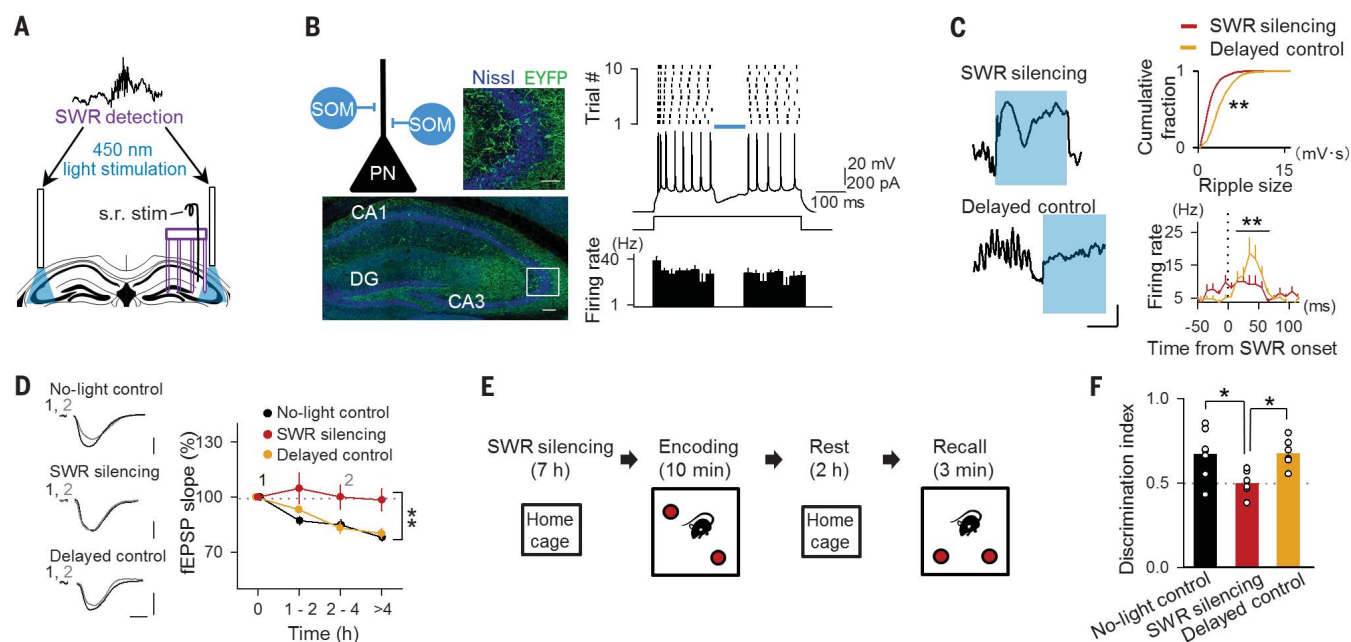


Fig. 1. SWR silencing prevents spontaneous synaptic depression during SW states and impairs subsequent spatial memory acquisition.

(A) Schematic illustration of closed-loop SWR silencing. CA1 ripples were detected in real time after the experimental onset, triggering blue-light illumination targeting the bilateral dorsal CA3 region. s.r. stim, stratum radiatum stimulation. (B) (Left) Representative confocal image showing SOM::Chr2-enhanced yellow fluorescent protein (EYFP) expression in a hippocampal section that was counterstained with fluorescent Nissl. The boxed region is magnified in the top right image. Scale bars, 100 μm (top right) and 50 μm (bottom). DG, dentate gyrus. The top left image illustrates inhibition of a pyramidal neuron (PN) by SOM-positive interneurons. (Right) Whole-cell patch clamp recording showing that blue-light illumination suppressed current injection-evoked spiking in pyramidal cells. $n = 5$ cells in five slices from three mice. (C) (Left) Examples of the online feedback illumination (top) and control illumination with a delay (bottom). Scale bars, 0.2 mV (vertical) and 50 ms (horizontal). (Right) SWR silencing via SOM activation suppressed the ripple size (top) and SWR-locked units (bottom) recorded from CA1 shanks. Delayed illumination was used as a control. Kolmogorov-Smirnov test: $**P = 2.7 \times 10^{-154}$.

$D_{3693} = 0.437$, $n = 1731$ (silencing) and 1962 (delayed) ripples from six mice each. Mann-Whitney U rank sum test: $P = 1.0 \times 10^{-3}$, $U = 3477.0$, $n = 18$ (silencing) and 21 (delayed) cells from six mice. (D) Time course of the fEPSP slopes normalized at 0 min. SWR silencing during SW states suppressed the spontaneous fEPSP attenuation that occurred in the control groups. The images at left show typical fEPSP traces at times 1 and 2. Scale bars, 2 mV (vertical) and 5 ms (horizontal). Two-way analysis of variance (ANOVA), $n = 6$ mice each: $**P = 5.5 \times 10^{-4}$, $F_{1,28} = 15.19$ versus no-light control; $**P = 1.2 \times 10^{-3}$, $F_{1,30} = 12.90$ versus delayed control. (E) Behavioral paradigm. After SWR silencing in a home cage for 7 hours, mice were exposed to two identical objects for 10 min (encoding phase). After a 2-hour rest in the home cage, the mice were allowed to explore the same arena for 3 min with one of the objects relocated to the opposite corner (recall phase). The preferential exploration of the relocated object was measured as memory recall. (F) Discrimination indices during the recall phase were computed during the first 3 min of exploration. The SWR-silenced mice did not discriminate between the objects. Tukey's test after one-way ANOVA, $n = 6$ or 7 mice: $*P = 0.031$, $Q_{3,16} = 4.00$ versus no-light control; $*P = 0.033$, $Q_{3,16} = 3.96$ versus delayed control.

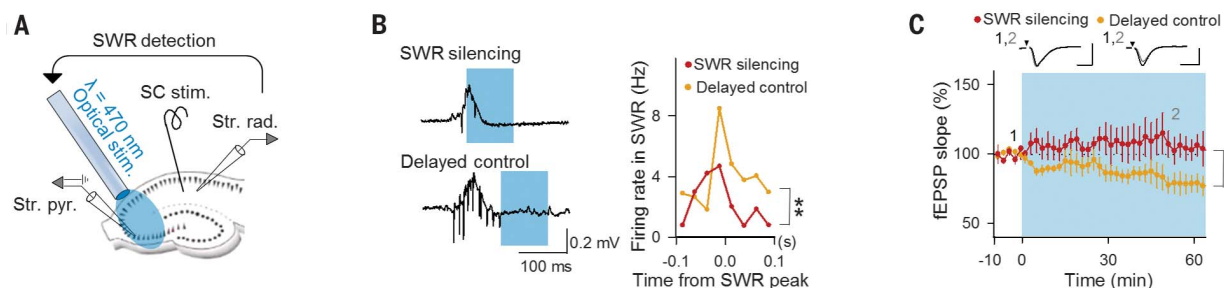


Fig. 2. Inhibiting hippocampal neurons during SWR impairs spontaneous synaptic depression in SWR-emitting slices. (A) Experimental procedures for recording fEPSPs at CA3 and CA1 synapses and silencing SWRs. SWRs and fEPSPs in the CA1 region were monitored in hippocampal slices prepared from SOM::Chr2-EYFP transgenic mice. A stimulating electrode was placed on the CA1 stratum radiatum to stimulate Schaffer collateral (SC) afferents. As SWRs were detected online, blue-light pulses were applied through an objective lens located over the CA3 region. Str. rad., stratum radiatum; Str. pyr., stratum pyramidale. (B) (Left) Examples of online feedback illumination (top) and delayed control (bottom). Scale bars, 0.2 mV (vertical) and 100 ms (horizontal). (Right) Firing rate in SWR (Hz) vs Time from SWR peak (s). **C** Time course of the fEPSP slopes after closed-loop illumination. SWR silencing but not delayed control impaired the spontaneous fEPSP depression. The slopes were normalized to the 10-min baseline values. The insets show typical fEPSP traces at times 1 and 2. Scale bars, 0.3 mV (vertical) and 20 ms (horizontal). Two-way ANOVA, $n = 5$ slices: $**P = 3.1 \times 10^{-15}$, $F_{1,237} = 71.3$.

control illumination with a delay of 100 ms (bottom). Cyan boxes indicate the periods of light illumination. (Right) SOM activation during SWRs, but not outside of SWRs, suppressed SWR-locked multiunits. Z test for comparing two counts, $n = 3197$ and 863 events: $**P = 4.0 \times 10^{-13}$. (C) Time course of the fEPSP slopes after closed-loop illumination. SWR silencing but not delayed control impaired the spontaneous fEPSP depression. The slopes were normalized to the 10-min baseline values. The insets show typical fEPSP traces at times 1 and 2. Scale bars, 0.3 mV (vertical) and 20 ms (horizontal). Two-way ANOVA, $n = 5$ slices: $**P = 3.1 \times 10^{-15}$, $F_{1,237} = 71.3$.

novel environment for 30 min (Fig. 3A) and were euthanized for hippocampal slice preparations. Cells positive for the modified yellow fluorescent protein dVenus (dVenus⁺) putatively corresponded to neurons that had been activated during the exploration of the novel environment (16). We monitored the activity of CA1 neurons by functional calcium imaging while recording CA1 LFPs

(Fig. 3B). Although dVenus⁺ and dVenus⁻ neurons were both activated during SWRs, dVenus⁺ neurons tended to be more likely to participate in SWRs than dVenus⁻ neurons (Fig. 3C). After 40 min, this difference increased further; that is, the SWR participation probability (the mean probability that a given cell exhibited a calcium transient during a given SWR event) became

significantly higher for dVenus⁺ cells than for dVenus⁻ cells, mainly through a decrease in the probability of the SWR participation probability in dVenus⁻ cells (Fig. 3D). The participation probability of neither dVenus⁺ nor dVenus⁻ cells was altered by treatment of slices with D-AP5 (Fig. 3E). Thus, the proportion of dVenus⁺ cells in the cells activated during SWRs increased over time.

Fig. 3. NMDAR regulates the refinement of in vitro engram reactivation. (A) Experimental procedures for the in vitro SWR assay using hippocampal slices prepared from Arc-dVenus mice that had explored a novel environment for 30 min. (B) (Top) Calcium imaging from dVenus⁺ and dVenus⁻ CA1 neurons loaded with Fura-2AM. (Bottom) Three representative traces of the Fura-2AM-loaded neurons. *F*, fluorescence. (C) Representative raster plot of 39 simultaneously recorded CA1 cells around 0 and 40 min. The first set of images was taken 5 min after the SWR event frequency reached 0.80 Hz (see materials and methods for details). (D) The participation probability of dVenus⁻ neurons during SWRs (participation rates) was smaller at 40 min than at 0 min, whereas the participation probability of dVenus⁺ neurons did not change over time. dVenus⁺ at 0 min versus dVenus⁻ at 40 min: $**P = 8.0 \times 10^{-5}$, $U = 15,991$; dVenus⁺ at 40 min versus dVenus⁻ at 40 min: $**P = 3.2 \times 10^{-5}$, $U = 1960$; Mann-Whitney U rank sum test with Bonferroni's correction. Error bars indicate SEM of 192 dVenus⁻ and 31 dVenus⁺ cells. (E) The participation probability of neither dVenus⁺ nor dVenus⁻ neurons in slices treated with 50 μ M D-AP5 differed between 0 and 40 min. dVenus⁺: $P = 0.47$, $U = 488.5$; dVenus⁻: $P = 0.34$, $U = 10,571$. Error bars indicate SEM of 39 dVenus⁻ and 145 dVenus⁺ cells.

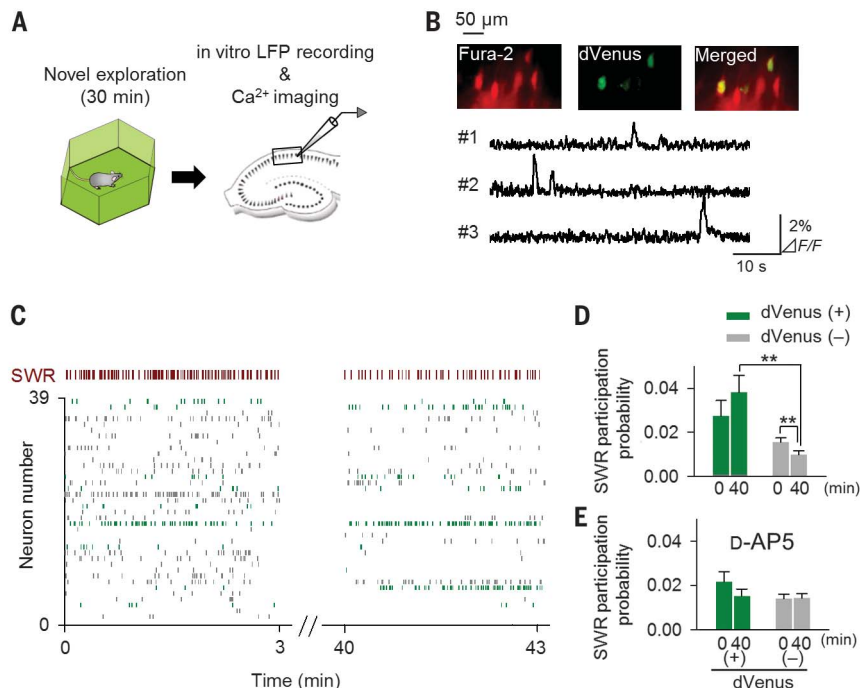
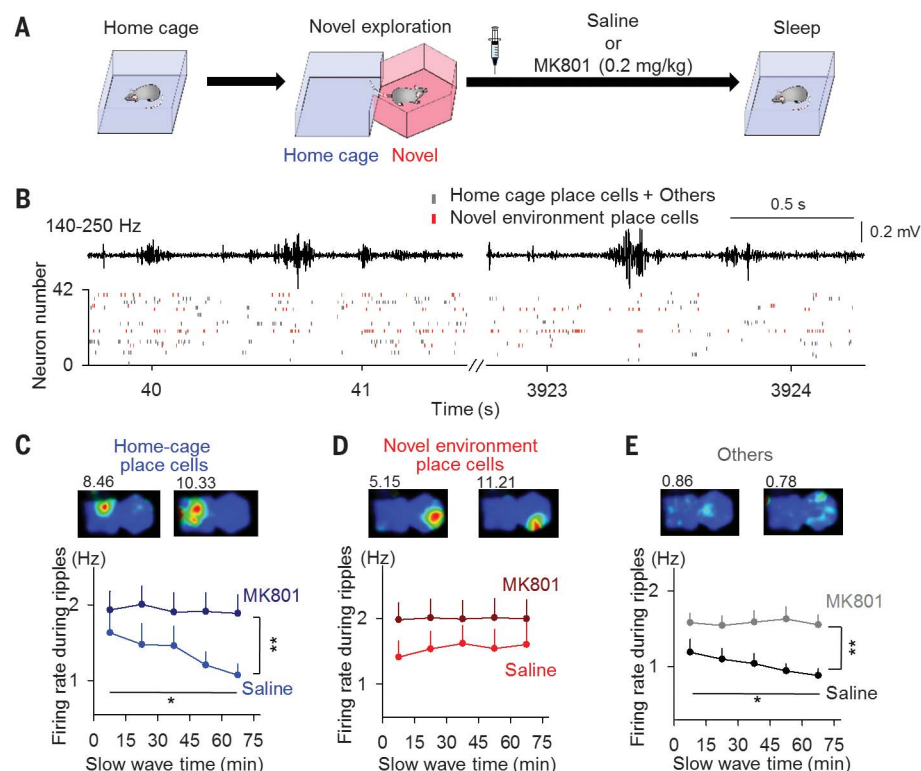


Fig. 4. NMDAR regulates the refinement of memory reactivation. (A) Time course of the experimental procedures. (B) Examples of representative spike events in a sleep session. The red rectangles indicate spikes of neurons that had place fields in the novel environment. The top traces represent ripple-band LFPs. (C to E) (Top) Color-coded rate maps for neurons with place fields in the home cage (C) and novel environment (D) and for other nonplace cells (E). The numbers above the maps represent the peak firing rates (hertz). (Bottom) Time courses of firing rates in SWRs during SW periods. SWR-relevant firing rates of home-cage place cells and other cells, but not novel-environment place cells, decreased with time, an effect that was abolished by the systemic injection of MK801. Home-cage place cells: $*P = 0.048$, $Z = -5.88$; others: $*P = 0.026$, $Z = -1.95$; Jonckheere-Terpstra trend test. Home-cage place cells: $P = 7.3 \times 10^{-4}$, $F_{1,368} = 11.6$; others: $P = 8.5 \times 10^{-4}$, $F_{1,1470} = 11.1$; two-way ANOVA. $n = 37$ to 145 cells from eight or nine trials from three mice (saline) and 28 to 195 cells from eight or nine trials from three mice (MK801).



Finally, we examined whether an NMDAR-dependent refinement of neuronal activity during SWRs also occurs in vivo. Mice were implanted with 32-site silicon probes in the CA1 region to monitor LFPs and unit spikes while the mice traversed their home cages. Each home cage was immediately joined to a novel environment that was not accessible to the mice unless an experiment was being conducted. During the 30-min exploration period in the novel environment, new place cells were detected in addition to the pre-established place cells in the home cage. Immediately after the exploration, the mice were treated intraperitoneally with either saline or 0.2 mg of MK801, an NMDAR blocker, per kilogram of body weight (Fig. 4A). Then, the mice were placed in the original home cage for 4 to 6 hours, and spikes during SW states were analyzed. The place cells were reactivated during SWRs (Fig. 4B). In the saline group, the novel-environment place cells did not change their firing rates during the SWRs throughout the entire recording session, whereas the home-cage place cells and the other cells that did not code either place in the environment (others) gradually decreased their SWR-related firing rates (Fig. 4, C to E). In the MK801-treated group, neither neuron type exhibited such delays in the firing rates (Fig. 4, C to E).

We discovered that hippocampal SWRs triggered persistent synaptic depression and that silencing SWRs impaired subsequent new learning, which appears to be consistent with the hypothesis that overstrengthened synapses impair neuronal responsiveness and saturate the ability to learn (23, 24). We consider three possible but not mutually exclusive mechanisms by which SWRs induce synaptic depression: (i) synaptic delay lines in activity propagation during SWRs decouple hippocampal network activity and weaken synaptic weights (10), (ii) uncorrelated presynaptic and postsynaptic activity during SWRs causes heterosynaptic depression because memory-irrelevant cells are rarely fired during SWRs (25), and (iii) the event frequency of SWRs reaches ~1 Hz after spatial exploration, which may induce homosynaptic depression (26, 27). Notably, field

stimulation with the event timing of SWRs after spatial exploration was sufficient to induce depression, suggesting the importance of the role of the timing, rather than the spike contents, of SWRs. On the other hand, mushroom spines did not shrink in SWR-emitting slices; that is, not all spines were equally subject to depression. This finding is in agreement with the hypothesis that sleep leads to net depression through the removal of unstable synapses [(28), but see also (29)]. A recent in vitro study demonstrated that the relative spike timings of CA3 and CA1 place cells during SWRs cause synaptic potentiation (9). Thus, synapses involved in memory engrams may escape depression through presynaptic and postsynaptic coactivation. Together with our findings, we propose dual roles of SWR-induced depression: (i) SWRs reset unnecessary synapses and avoid memory saturation (30), and (ii) SWRs purify recent memory engrams by shearing irrelevant neuronal activity and perhaps strengthening memory-relevant synapses, thereby contributing to memory consolidation.

REFERENCES AND NOTES

1. V. V. Vyazovskiy, C. Cirelli, M. Pfister-Genskow, U. Faraguna, G. Tononi, *Nat. Neurosci.* **11**, 200–208 (2008).
2. R. Huber *et al.*, *Cereb. Cortex* **23**, 332–338 (2013).
3. G. Tononi, C. Cirelli, *Brain Res. Bull.* **62**, 143–150 (2003).
4. G. Tononi, C. Cirelli, *Neuron* **81**, 12–34 (2014).
5. A. K. Lee, M. A. Wilson, *Neuron* **36**, 1183–1194 (2002).
6. V. Ego-Stengel, M. A. Wilson, *Hippocampus* **20**, 1–10 (2010).
7. G. Girardeau, K. Benchenane, S. I. Wiener, G. Buzsáki, M. B. Zugaro, *Nat. Neurosci.* **12**, 1222–1223 (2009).
8. G. M. van de Ven, S. Trouche, C. G. McNamara, K. Allen, D. Dupret, *Neuron* **92**, 968–974 (2016).
9. J. H. Sadowski, M. W. Jones, J. R. Mellor, *Cell Rep.* **14**, 1916–1929 (2016).
10. E. V. Lubenov, A. G. Siapas, *Neuron* **58**, 118–131 (2008).
11. L. L. Colgin, D. Kubota, Y. Jia, C. S. Rex, G. Lynch, *J. Physiol.* **558**, 953–961 (2004).
12. O. Bukalo, E. Campanac, D. A. Hoffman, R. D. Fields, *Proc. Natl. Acad. Sci. U.S.A.* **110**, 5175–5180 (2013).
13. O. Eschenko, W. Ramadan, M. Mölle, J. Born, S. J. Sara, *Learn. Mem.* **15**, 222–228 (2008).
14. C. J. Behrens, L. P. van den Boom, L. de Hoz, A. Friedman, U. Heinemann, *Nat. Neurosci.* **8**, 1560–1567 (2005).
15. E. Stark *et al.*, *Neuron* **83**, 467–480 (2014).
16. M. Mizunuma *et al.*, *Nat. Neurosci.* **17**, 503–505 (2014).
17. G. L. Collingridge, S. J. Kehl, H. McLennan, *J. Physiol.* **334**, 33–46 (1983).
18. M. Matsuzaki *et al.*, *Nat. Neurosci.* **4**, 1086–1092 (2001).
19. M. Masugi-Tokita *et al.*, *J. Neurosci.* **27**, 2135–2144 (2007).
20. Q. Zhou, K. J. Homma, M. M. Poo, *Neuron* **44**, 749–757 (2004).
21. O. Paulsen, T. J. Sejnowski, *Curr. Opin. Neurobiol.* **10**, 172–179 (2000).
22. M. Eguchi, S. Yamaguchi, *Neuroimage* **44**, 1274–1283 (2009).
23. D. Balduzzi, G. Tononi, *Theory Biosci.* **132**, 27–39 (2013).
24. S. S. Yoo *et al.*, *Nat. Neurosci.* **10**, 385–392 (2007).
25. G. S. Lynch, T. Dunwiddie, V. Gribkoff, *Nature* **266**, 737–739 (1977).
26. R. M. Mulkey, R. C. Malenka, *Neuron* **9**, 967–975 (1992).
27. S. M. Dudek, M. F. Bear, *Proc. Natl. Acad. Sci. U.S.A.* **89**, 4363–4367 (1992).
28. L. de Vivo *et al.*, *Science* **355**, 507–510 (2017).
29. G. H. Diering *et al.*, *Science* **355**, 511–515 (2017).
30. M. R. Mehta, *Nat. Neurosci.* **10**, 13–15 (2007).

ACKNOWLEDGMENTS

We thank C. Cirelli, L. Fenk, Y. Goda, G. Laurent, T. McHugh, S. Reiter, and G. Tononi for comments on early versions of the manuscript; T. Danjo and Y. K. Park for technical assistance; and S. Yamaguchi for providing Arc-dVenus mice. **Funding:** This work was supported by Ministry of Education, Culture, Sports, Science and Technology Grants-in-Aid for Scientific Research (25119004 and 26250003 to Y.I. and 16H01519 to S.F.); “Resonance Bio” (16H01426 to H.H.); Japan Society for the Promotion of Science Grant-in-Aid for Research Activity start-up (16H07453 to H.N.); RIKEN Special Postdoctoral Researchers Program research grant (201600059347 to H.N.); the Sasakawa Scientific Research Grant from the Japan Science Society (28-402 to H.N.); Brain/MINDS (Brain Mapping by Integrated Neurotechnologies for Disease Studies) from the Japan Agency for Medical Research and Development (AMED) (to H.H. and S.F.); the Strategic Research Program for Brain Sciences on “Development of BMI Technologies for Clinical Application” (to Y.I.); and a Human Frontier Science Program (RGP0019/2016 to Y.I.). This work was partly facilitated by a program in the International Research Center for Neurointelligence (WPI-IRCN) of The University of Tokyo Institutes for Advanced Study at The University of Tokyo. **Author contributions:** H.N., S.F., and Y.I. designed and implemented the study and wrote the manuscript. H.N., Y.S., and S.F. performed in vivo physiology. K.M. performed immunohistochemistry. H.N., M.G., and K.O. performed in vitro electrophysiology. H.N. and T.I. performed optical recording. T.S. and H.H. helped with analysis. All authors discussed the results and commented on the manuscript. **Competing interests:** The authors declare no competing interests. **Data and materials availability:** All data necessary to support this paper’s conclusions are available in the main paper or the supplementary materials. The full primary data are available at http://ikegaya.jp/data/norimoto_science2018/.

SUPPLEMENTARY MATERIALS

www.sciencemag.org/content/359/6383/1524/suppl/DC1
Materials and Methods
Figs. S1 to S8
References (31–42)

10 June 2017; accepted 26 January 2018
Published online 8 February 2018
10.1126/science.aao0702

BIOPHYSICS

Molecular mechanism of extreme mechanostability in a pathogen adhesin

Lukas F. Milles,¹ Klaus Schulten,^{2*} Hermann E. Gaub,^{1†} Rafael C. Bernardi^{2‡}

High resilience to mechanical stress is key when pathogens adhere to their target and initiate infection. Using atomic force microscopy–based single-molecule force spectroscopy, we explored the mechanical stability of the prototypical staphylococcal adhesin SdrG, which targets a short peptide from human fibrinogen β . Steered molecular dynamics simulations revealed, and single-molecule force spectroscopy experiments confirmed, the mechanism by which this complex withstands forces of over 2 nanonewtons, a regime previously associated with the strength of a covalent bond. The target peptide, confined in a screwlike manner in the binding pocket of SdrG, distributes forces mainly toward the peptide backbone through an intricate hydrogen bond network. Thus, these adhesins can attach to their target with exceptionally resilient mechanostability, virtually independent of peptide side chains.

Gram-positive pathogenic bacteria have developed an arsenal of virulence factors specifically targeting and adhering to their host's proteins. Termed microbial surface components recognizing adhesive matrix molecules (MSCRAMMs), they promote “adhesion, invasion, and immune evasion” (1) (Fig. 1A). The prototypical adhesin is SD-repeat protein G (SdrG) from *Staphylococcus epidermidis*, the leading cause of medical device- and implant-related nosocomial infections (2). SdrG uses a key motif found in pathogenic staphylococci—the “dock, lock, and latch” (DLL) mechanism—in which the host target, usually a peptide on the order of 15 residues, is first bound (dock), then buried (lock) between two immunoglobulin-like (Ig) fold domains N2 and N3 (3). Finally, the target is snugly locked in place with a strand connecting N3 to N2 by β -strand complementation (latch) (Fig. 1B) (4). The DLL mechanism has appeared in many homologous domains—for example, in *Staphylococcus aureus* with targets such as keratin (5), complement system proteins (6), other chains of fibrinogen (7) and collagen (8). SdrG uses the DLL to target the N terminus of the β chain of human fibrinogen (Fg). The Fg sequence bound by SdrG is also the substrate of thrombin (Fg β , NEEGFFSARGHRPLD, thrombin cleavage between R and G). However, once bound by SdrG, it can no longer be cut by thrombin, a step necessary for blood clotting and fibrin formation (9). Thrombin cleavage also releases fibrinopeptide B, which in turn recruits neutrophils. Additionally, the adhesin coats and thus camouflages the bacterium in host proteins. Combined, these MSCRAMM mechanisms allow staphylococci to evade immune response, making

them attractive targets for drug development, such as designing MSCRAMM inhibitors for antiadhesion therapy (10, 11).

Here, we use the interplay between atomic force microscopy (AFM)–based single-molecule force spectroscopy (SMFS) (12–14) and all-atom steered molecular dynamics (SMD) simulations to elucidate the mechanics of the SdrG:Fg β interaction with atomic resolution. Previous *in vivo* measurements using single-cell force spectroscopy of the SdrG fibrinogen interaction found adhesion forces on the order of 2 nN (15, 16); in addition, comparable *in vivo* forces appeared in closely related adhesins (17, 18). In agreement with these results, we measured rupture forces of more than 2 nN for a single SdrG:Fg β complex at force loading rates around 10^5 pN s^{−1}. This extreme stability is the highest among all non-covalent interactions by a large margin. SdrG:Fg β outperforms the current champion—the cohesin-dockerin type III interaction—by a factor of four (19) and Biotin-Streptavidin by more than an order of magnitude (20). It even rivals the strength of a covalent bond (21). Interestingly, the affinity between the peptide and SdrG is moderate, with a dissociation constant (K_d) ~400 nM (4). Accordingly, this system is adapted for strong mechanical attachment to its target, rather than high affinity. It was thus to be expected that these extreme SdrG:Fg β mechanics were governed by a special, currently unknown mechanism.

The Fg β wild-type (WT) peptide is located at the N terminus of the mature Fg β chain. Thus, it can only be mechanically loaded from the C terminus (Fig. 1B). The SdrG N2 and N3 domains, responsible for binding the peptide (SdrG), are covalently anchored to the *S. epidermidis* cell wall by a C-terminal sortase motif. Hence, in the native, physiological configuration of the SdrG:Fg β complex, force is applied from the C termini of both SdrG and Fg β . To mechanically probe this interaction, all surface anchoring onto AFM cantilever and surface was site-specific and covalent (Fig. 1C). To ensure unambiguous identification of single-molecule events in force-extension traces, a refolding molecular “fingerprint” (22) was cloned

adjacent to the peptide. Under physiologically relevant direction of force application from the C terminus, the complex withstood extremely high forces of up to 2500 pN *in vitro* (Fig. 1, D and E) and even higher forces in corresponding SMD simulations (Fig. 1, F and G), due to higher force loading rates *in silico* (23, 24) (see also figs. S1 to S3).

The force regime around 2 nN is typically associated with the stability of covalent bonds, raising the concern that our surface chemistry—not the complex—was breaking, most likely a Si-C bond in the aminosilane anchors used (21). Because the cantilevers' apexes have radii of ~10 nm, they can only present a few molecules. If the covalent attachment of SdrG to the tip was being mechanically cleaved, the SdrG coating on the apex of the tip would be left attached to the surface, resulting in a rapidly decreasing frequency of interactions over time. In contrast, a single cantilever remained active over thousands of interactions, indicating that covalent bonds in the surface functionalization largely sustained the high forces.

We were convinced that an alteration that lowered the unbinding force would be the key to deconstructing the mechanism of this exceptional mechanostability. The presence of the “bulky” hydrophobic amino acid side chains of two phenylalanines (F) in Fg β had been previously described as a “bulgy plug” (4). Buried behind the locking β strand, it seemed conceptually and intuitively plausible that wiggling them through the narrow constriction created by the locking strand caused the high forces (Fig. 2, A and B, and fig. S4).

The force dependence on the number of Fs was tested by addition of an F or by alanine replacement. Four constructs were investigated: a Fg β with three phenylalanines (Fg β F3), the WT Fg β having 2 Fs, and mutants with one (Fg β F1), or both (Fg β F0), Fs replaced by alanines. The F3 mutant had been shown to have higher affinity (K_d ~50 nM) for SdrG (4), whereas the affinity of the F1 mutant was lower compared to WT Fg β , because the F's hydrophobicity is important for initiating the DLL (25). All three mutants produced high forces around 2 nN (fig. S5, A and B). A negative correlation of the most-probable rupture force on the number of Fs was measurable but only marginal (Fig. 2C). With reference to the Fg β WT force, the most-probable rupture force of the F0 mutant was only about 10% weaker than the WT. Multiple all-atom SMD simulations of all four systems reproduced the miniscule correlation between the presence of bulky F side chains and the high forces (Fig. 2B). The F0 mutant was ~20% weaker than WT Fg β . Thus, the bulky residues only contributed marginally to the high forces, whereas they had been established as crucial for initial binding (4).

As the bulky phenylalanines in Fg β were largely irrelevant for reaching high forces, we investigated minimizing the peptide. We employed QwikMD (26) to sequentially remove amino acids from the N terminus of Fg β and tested their stability in SMD simulations. As expected, shortened peptides had lower unbinding forces. However,

¹Lehrstuhl für Angewandte Physik and Center for Nanoscience, Ludwig-Maximilians-University, Amalienstrasse 54, 80799 Munich, Germany. ²NIH Center for Macromolecular Modeling and Bioinformatics, Beckman Institute for Advanced Science and Technology, University of Illinois at Urbana-Champaign, Urbana, IL 61801, USA.

*Deceased.

†Corresponding author. Email: rcbernardi@ks.uiuc.edu (R.C.B.); gaub@lmu.de (H.E.G.)

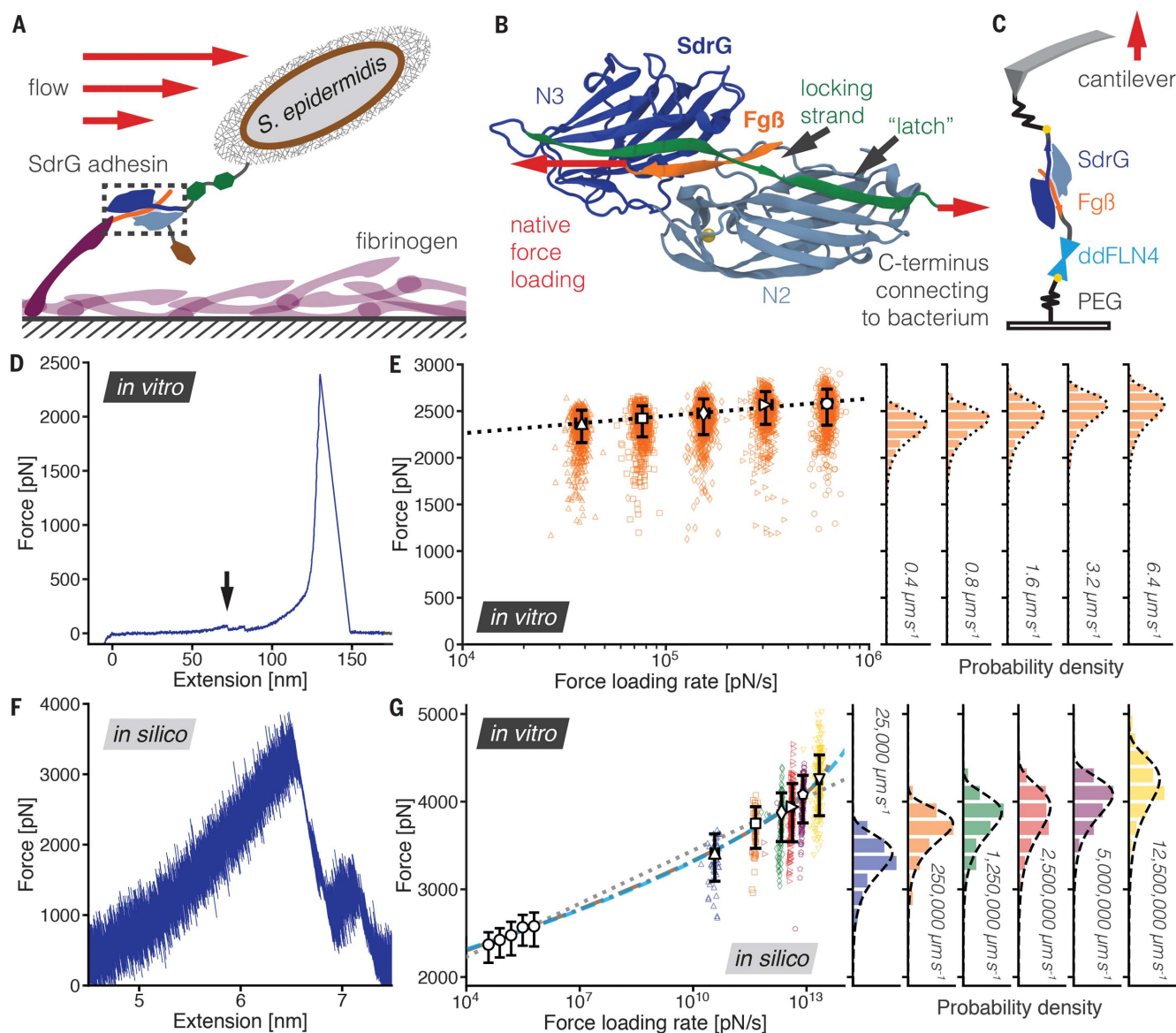


Fig. 1. The SdrG:Fg β complex withstands enormous forces in vitro and in silico. (A) SdrG function, attached to the N-terminal peptide of the fibrinogen (purple) β chain (orange) adsorbed on a surface. This interaction prevents detachment of the bacterium by hydrodynamic forces. (B) Structure of the SdrG (blue):Fg β (orange) complex. The locking strand (green) encloses the peptide in the binding pocket between the Ig-fold N2 (light blue) and N3 (dark blue) domain and a calcium (yellow) binding loop. The red arrows indicate the force applied to the molecular complex. (C) Experimental AFM setup, including the ddFLN4 fingerprint domain (cyan). All constructs are covalently bound to the surface via polyethyleneglycol (PEG) linkers and the ybbR-tag (yellow dots). In the native configuration, Fg β and SdrG are force-loaded from their respective C termini. The AFM cantilever is retracted at constant velocity until the complex breaks. (D) Resulting force-extension trace in the native force propagation (blue), as it would occur at sites of staphylococcal adhesion. The distinctive fingerprint unfolding around 90 pN ddFLN4 (black arrow) featuring a substep was used to find specific interactions. It is followed by SdrG:Fg β complex rupture, here at almost 2500 pN. (E) Dynamic force spectrum of the SdrG:Fg β native geometry at cantilever retraction velocities 0.4 $\mu\text{m s}^{-1}$ (triangles, $N = 749$), 0.8 $\mu\text{m s}^{-1}$ (squares, $N = 696$), 1.6 $\mu\text{m s}^{-1}$ (diamonds, $N = 758$), 3.2 $\mu\text{m s}^{-1}$ (forward triangles, $N = 749$), 6.4 $\mu\text{m s}^{-1}$ (circles, $N = 851$), with corresponding complex rupture-force histograms for each velocity projected onto individual axes on the right. A Bell-Evans (BE) model fit

(dotted line, $\Delta x = 0.051 \text{ nm}$, $k_{\text{off}}^0 = 9.2 \times 10^{-11} \text{ s}^{-1}$) through the most-probable rupture force and force loading rate of each velocity (large open markers, with errors given as full-width at half maximum for each distribution) shows the expected force loading-rate dependency of the rupture force. (F) SMD force-extension trace (blue) in the native force propagation of SdrG:Fg β , including experimental peptide linkers. The complex ruptured at almost 4000 pN; the extension is shorter than in the experimental trace because there are no PEG spacers. The peak following the highest force peak corresponds to another metastable geometry after slipping of the Fg β peptide that is below the resolution limit of our AFM. (G) The experimentally determined dynamic force spectrum from velocities of 0.4 to 6.4 $\mu\text{m s}^{-1}$ for the native propagation from (E) is shown condensed as open circles. The dynamic force spectrum of SMD simulations for velocities of 25,000 $\mu\text{m s}^{-1}$ to 12,500,000 $\mu\text{m s}^{-1}$, triangle $N = 49$, square $N = 50$, diamond $N = 100$, forward triangle $N = 200$, pentagon $N = 147$, inverted triangle $N = 200$, respectively. Fits through SMD and experimental data, for BE model (gray, dotted line, $\Delta x = 0.047 \text{ nm}$, $k_{\text{off}}^0 = 1.0 \times 10^{-9} \text{ s}^{-1}$) and fit of a model by Dudko *et al.* (DHS model, cusp potential $\Delta x = 0.12 \text{ nm}$, $k_{\text{off}}^0 = 6.1 \times 10^{-22} \text{ s}^{-1}$, $\Delta G^{++} = 78 \text{ k}_\text{B}T$, cyan dashed line and linear-cubic potential $\Delta x = 0.093 \text{ nm}$, $k_{\text{off}}^0 = 7.7 \times 10^{-18} \text{ s}^{-1}$, $\Delta G^{++} = 66 \text{ k}_\text{B}T$, brown dash-dotted line, both at $T = 300 \text{ K}$). In vitro and in silico data agree exceptionally well, although they are separated by six orders of magnitude in force loading rate and can be fit with a single model.

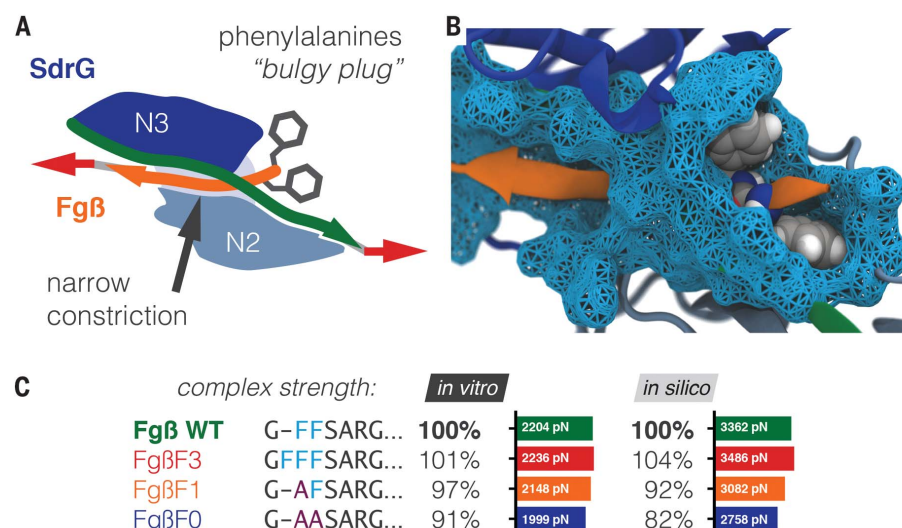


Fig. 2. Phenylalanine side chains only marginally influence SdrG:Fgβ mechanostability. (A) Sketch of the “bulgy plug” hypothesis. The bulky phenylalanine side chains (gray) of Fgβ (orange) are blocked by the locking strand (green). (B) Crystal structure showing the bulky phenylalanine side chains in van der Waals representation (gray spheres) of Fgβ (orange). They have to wiggle through a narrow constriction (cyan surface). (C) Dependence of complex rupture force on the presence of phenylalanines, if replaced by alanines. Most-probable rupture forces (absolute values in bar graphs) are compared relative to WT Fgβ. Either recorded experimentally with a single cantilever retracted at $1.6 \mu\text{m s}^{-1}$ or corresponding results for SMD simulations at $250,000 \mu\text{m s}^{-1}$. Adding one F (FgβF3 mutant) slightly increases forces. Yet, both results show a trend of weak dependence of rupture force on the presence of phenylalanines. Even when removing all bulky side chains (FgβF0 mutant), experimental rupture forces drop no more than 10% compared with WT Fgβ; in silico, no more than 20%. The “bulgy plug” only marginally contributes, hinting that another mechanism must be responsible for the high forces. Single-letter abbreviations for the amino acid residues are as follows: A, Ala; C, Cys; D, Asp; E, Glu; F, Phe; G, Gly; H, His; I, Ile; K, Lys; L, Leu; M, Met; N, Asn; P, Pro; Q, Gln; R, Arg; S, Ser; T, Thr; V, Val; W, Trp; and Y, Tyr.

provided that the peptide was long enough to directly interact with SdrG's locking strand, forces were still in the nN regime (Fig. 3A). Removing all residues contacting the locking strand up to Fgβ's A13 eliminated clear complex rupture forces in the nN regime. Consequently, the minimal six-residue peptide sequence in closest contact with the locking strand (FFSARG) was sufficient to both bind SdrG and withstand forces indistinguishable from WT Fgβ in vitro (Fig. 3B and fig. S5C).

Provided a mutant could still bind SdrG, modifying the Fgβ peptide had only minor effects on mechanostability. Thus, we investigated the mechanical properties of SdrG. Previously, the presence and flexibility of the locking strand was shown to be crucial for the DLL mechanism and thus SdrG:Fgβ affinity (25). Locking strand deletion inhibits binding of Fgβ (4). In accordance with these results, a mutant SdrG(274–580) devoid of the locking strand failed to bind Fgβ in vitro. Still, the contribution of the locking strand to the mechanics was unclear. If the interaction between the N2 domain and the locking strand propagated force away from the complex, its truncation should significantly weaken rupture forces. A truncated SdrG(274–590)—which removed the locking strand's C-terminal half of the “latch” region (fig. S6)—still bound SdrG, yet its mecha-

nostability was indistinguishable from the WT. Possible covalent isopeptide bonds (27, 28) between the locking strand and the N2 domain had been suggested to contribute to its stability. We could exclude this hypothesis as cause of the unusually high mechanostability because the SdrG truncation mutant removed D593, a key amino acid required for a potential isopeptide bond (29).

As simulations and experiments strongly agreed, we were confident to explore mutants and setups created in silico that could not be realized in vitro. SMD became a gedankenexperiment to deconstruct the mechanism. It is important to emphasize that the strong agreement was provided in part by our enhanced sampling strategy (30). Performing many (at least 50 per system, more than 2400 total; see overview in table S1) simulation replicas allowed the comparison of simulation and experiment within the same theoretical framework of the Bell-Evans (BE) and Dudko-Hummer-Szabo (DHS) models (24, 31, 32).

Simulations revealed the presence of strikingly frequent and persistent hydrogen bonds (H bonds) between the Fgβ peptide backbone and SdrG (Fig. 3, D and F, and figs. S7 and S8). We investigated the contribution of the backbone H bonds in SMD simulations by replacing Fgβ with a polyglycine peptide, which has no side chains.

In silico, the rupture forces were merely 27% weaker than the WT, comparable to the FgβF0 mutant (Fig. 3E). Thus, we updated our initial hypothesis: Reaching the regime of 2 nN was largely independent of Fgβ's side chains and mainly caused by SdrG interacting with the Fgβ peptide backbone (figs. S9 and S10). Breaking the SdrG:Fgβ complex in the native configuration requires all H bonds to be broken in parallel: a cooperative shear geometry (see movie S1).

Similar shear geometries appear in folds such as the muscle protein titin-Ig. However, this protein unfolds at lower forces around 200 pN (33), in stark contrast to SdrG's over 2000 pN. The shear geometry in titin breaks because its backbone H bonds have the freedom to move orthogonally to the force load, ultimately circumventing the shear geometry (34). In the SdrG:Fgβ complex, the peptide is snugly confined in the interface between N2 and N3 domain by the locking strand (figs. S10 and S11). The rigid and coiled (Fig. 3C and fig. S12) alignment of the two interacting backbones neither bends nor buckles. Peptide movement orthogonal to the pulling force vector is not possible, so all H bonds must be broken at once. The importance of this packed confinement was also demonstrated by analyzing the correlation-based dynamical network (35), which shows how force propagates through the system (fig. S13) and how atom motion is clustered in communities (fig. S14). These analyses revealed that force is propagated not directly by the latch strand, as demonstrated experimentally, but by neighboring strands, reducing the load over the H bonds. Notably, the movement of the Fgβ peptide and both the N2 and N3 domain were highly correlated. To demonstrate the importance of the correct H-bond alignment, Fgβ was tethered non-natively from its N terminus, effectively pulling orthogonally to the native force propagation. The non-native pulling of Fgβ peaked at forces around 60 pN (Fig. 4A), smaller than the native configuration by a factor of more than 40 (fig. S15). Simulations showed that this geometry is weaker, because the interactions between N2 and N3 are broken, resulting in a loss of peptide confinement (see figs. S16 and S17, and movie S2).

In a simplified model, the DLL mechanism creates a deep and rigid binding pocket for the peptide, which is confined in a coiled geometry similar to a corkscrew in a cork (figs. S12 and S18). If pulled upon, the load is dissipated cooperatively over all H bonds that are radially pointed outward of Fgβ (Fig. 3G), causing the high mechanostability.

The importance of these H bonds was confirmed in an exploratory SMD through removing coulomb interactions from parts of the peptide required for hydrogen bonding. Eliminating backbone H bonds resulted in a significant reduction in rupture force in silico (Fig. 3E). Additionally, eliminating hydrogen bonds formed by the side chains of Fgβ further reduced the forces, but only marginally, in agreement with the mechanism proposed (Fig. 3E). Still, the forces observed were only about 40% smaller than the WT. Furthermore, we tested turning off H bonds of the all-glycine peptide, which finally led to

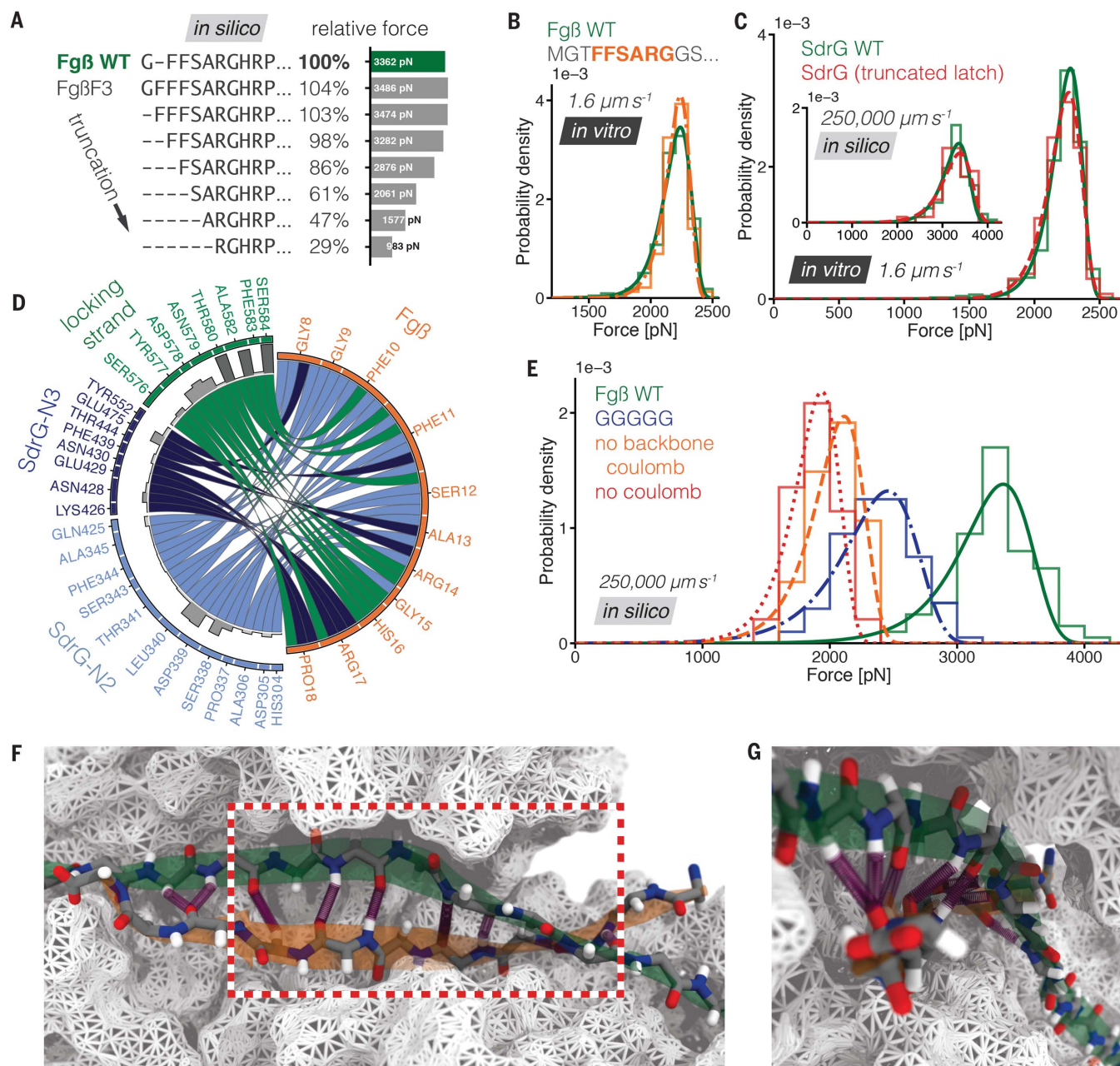


Fig. 3. Backbone H bonds are deciding factors in the high mechanostability of SdrG:Fgβ and a minimized peptide. (A) Fgβ peptide truncations from the N terminus *in silico*. Removing amino acids causes the forces to drop (relative to the WT), with the most significant drop when removing the sequence FSAR, leading to FFSARG as the minimum peptide. (B) Rupture forces for SdrG binding to WT Fgβ (green, continuous line, $N = 437$), and the six-residue minimized peptide FFSARG (orange, dash-dotted line, here shown with surrounding amino acids in gray, $N = 471$). Strikingly, there is hardly any difference between WT Fgβ and the minimized peptide. (C) Rupture-force histograms comparing the WT Fgβ:SdrG interaction (green, continuous line, $N = 463$) and the SdrG mutant with the truncated latch region (red, dashed line, $N = 131$). WT and mutant are virtually indistinguishable (no significant difference in Kolmogorov-Smirnov test, *in vitro* $P = 0.29$, *in silico* $P = 0.88$). Corresponding SMD results (WT $N = 100$, mutant $N = 50$) are shown as inset. (D) Relative prevalence (bar graphs;

precise values in fig. S7) of H bonds between SdrG domains, the locking strand, and the WT Fgβ peptide (also available for F3, F1, F0, and all-glycine mutants in fig. S8). The locking strand connects to nearly every Fgβ residue. (E) Rupture forces from exploratory simulations for SdrG and Fgβ WT (green, continuous line, $N = 100$), a replacement of each Fgβ residue with glycine (blue, dash-dotted line, $N = 100$), FgβF3 peptide without coulomb interactions, and subsequently H bonds, on its backbone (orange, dashed line, $N = 47$), FgβF3 devoid of all coulomb interactions (red, dotted line, $N = 48$). Backbone H bonds in the Fgβ confinement allow even a pure glycine sequence to withstand high force. (F) H-bond (purple) contacts respective to the backbone of Fgβ (orange) and locking strand (green) confined by SdrG (white surface) from simulations in a force-loaded state. The minimum peptide sequence is highlighted in the red box. (G) Radial distribution of backbone H bonds between locking strand (green) caused by the screwlike winding of the Fgβ sheet (orange). Peptide backbones are shown as sticks.

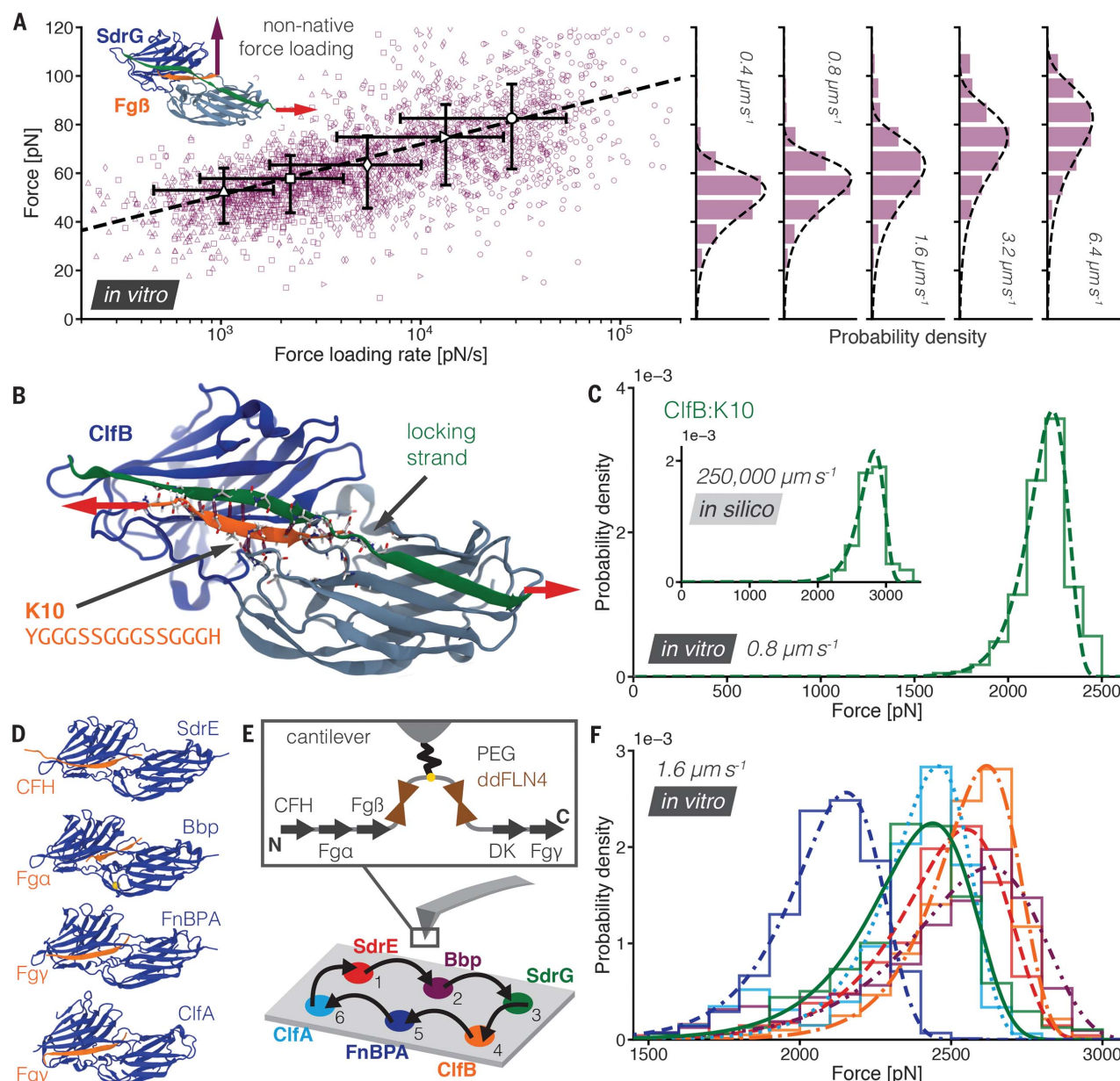


Fig. 4. A non-native SdrG:Fgβ force loading shows weak forces, a homologous domain ClfB reaches 2 nN stability binding a mainly glycine-serine peptide, and SdrG homologs consistently exceed 2 nN binding to their ligands. (A) Dynamic force spectrum of the SdrG:Fgβ non-native configuration (see inset with purple arrow), breaking around 60 pN as opposed to >2 nN for the native case (for SMD results, see figs. S15 to S17 and movie S2). Cantilever retraction velocities were varied: $0.4 \mu\text{m s}^{-1}$ (triangles, $N = 511$), $0.8 \mu\text{m s}^{-1}$ (squares, $N = 564$), $1.6 \mu\text{m s}^{-1}$ (diamonds, $N = 487$), $3.2 \mu\text{m s}^{-1}$ (forward triangles, $N = 395$), $6.4 \mu\text{m s}^{-1}$ (circles, $N = 471$), with corresponding complex rupture-force histograms projected on the right. A BE model fit (dashed line) through the most-probable rupture force and force loading rate of each velocity (large open markers) shows the expected force loading-rate dependency of the rupture force ($\Delta x = 0.46 \text{ nm}$, $k_{\text{off}}^0 = 0.39 \text{ s}^{-1}$). (B) ClfB (blue):K10 (orange) complex, including the locking strand (green) and H-bonding (purple) amino acids, shown as sticks. Notably, the latch region was not crystallized and needed to be modeled from a homolog. The native pulling configuration is indicated with an arrow; compared with Fgβ, the peptide is oriented inversely in the binding pocket. (C) Rupture-force histogram and fit for ClfB:K10 at a velocity of $0.8 \mu\text{m s}^{-1}$ (green, dashed line,

$N = 1035$), peaking around 2.3 nN. Simulation data ($N = 50$) confirming the force regime are shown as inset. (D) Homologous systems employing the DLL mechanism, all from *S. aureus* (N2 and N3 domains in blue, target peptides in orange) SdrE, Bbp, FnBPA, and ClfA. (E) Comparison of absolute mechanostability of all homologous systems, as well as SdrG and ClfB, with a single force probe. The cantilever is modified with five different peptides tethered in their native force loading geometry, respectively: from the C terminus of complement factor H (CFH), Fga chain (Fga), and Fgβ, tethered from the N terminus are sequences from dermokine (DK) and Fgy chain (Fgy). This selection is presented to all adhesins, which are known to bind at least one of them, spatially separated on a surface. One cannot exclude that one adhesin may bind more than one peptide target. (F) Resulting relative stabilities of the complexes for SdrE (red, dashed line, $N = 680$), ClfB (orange, dash-dotted line, $N = 605$), ClfA (cyan, dashed line, $N = 2292$), Bbp (purple, dot-dot-dashed line, $N = 319$), SdrG (green, continuous line, $N = 478$), FnBPA (blue, dash-dash-dotted line, $N = 2483$). SdrG is not the strongest system at a retraction velocity of $1.6 \mu\text{m s}^{-1}$. In accordance with the largely side-chain independent mechanics proposed for SdrG and ClfB, every DLL adhesin withstands forces exceeding 2 nN.

no detectable peak in the force profile. H bonds with the peptide backbone were key to the mechanostability.

A pure glycine sequence—i.e., no side chains—showed high forces when bound to SdrG *in silico*. An analogous experiment was not possible, because such a sequence did not bind SdrG. The side chains, such as the hydrophobic phenylalanine residues, were not essential for mechanostability but were crucial for affinity. A homologous DLL motif adhesin, clumping factor B (ClfB) from *S. aureus*, had been found to promiscuously bind short sequences of extracellular matrix proteins. Among its targets is a C-terminal cytoskeletal keratin peptide (K10, YGGGSSGGSSGGGH) (5). This unusually unremarkable target is essentially a flexible linker terminating in a charged residue. K10 contains no bulky, charged, or hydrophobic side chains, except for the C-terminal histidine, secured by the locking strand in the complex structure. ClfB:K10 interactions also exceed the 2 nN mark, both *in vitro* and *in silico* (see Fig. 4, B and C). More prominently than in SdrG, ClfB's mechanostability must be based on H bonds to the K10 backbone, simply because it has no notable side chains. In last consequence, even a shortened K10 and pure GS sequence (GGGSSGGSSGGG) binds ClfB and reaches more than 2nN in force (fig. S19). Moreover, the peptide β sheet is parallel to the locking strand, whereas the orientation is antiparallel in SdrG. Accordingly, it was natively tethered from its N terminus, showing that nN stability is also possible for an inversely oriented peptide configuration. Finally, to generalize the mechanics, we probed four additional homologs of SdrG and ClfB, all from *S. aureus*. SD repeat protein E (SdrE), clumping factor A (ClfA), bone sialoprotein binding protein (Bbp), and fibronectin binding protein A (FnBPA) had been crystallized with a known ligand bound (Fig. 4D) (36–39). Although most-probable rupture forces varied up to 20% depending on the adhesin, the overall forces were consistently in the 2 nN regime (Fig. 4, E and F).

Side-chain independent mechanics confer an invasive advantage to staphylococci. No matter which sequence is targeted by their adhesins, invading pathogens using the DLL mechanism can adhere to their hosts even under the most demanding mechanical stress. One could speculate that this mechanism provides a flat fitness landscape. Adaption to a target will automatically yield extremely resilient mechanics, even if the sequence is mainly glycines and serines. The moderate bulk affinity of SdrG:Fg β allows for flexible unbinding and rebinding when no mechanical stress is applied. One could further speculate that a high-complex lifetime under force, which seems probable given the overall extreme mechanostability, is indicative of a very different unbinding pathway

when compared with the moderate lifetimes of spontaneous unbinding in bulk experiments (4). Thus, these differing pathways would make a catch-bond behavior not surprising, considering that such bonds have been found in bacterial adhesins with similar functions, albeit much lower mechanical strength (40, 41).

In conclusion, SdrG:Fg β and its homologs are the mechanically strongest noncovalent protein-protein receptor-ligand interactions to date, rivaling a regime formerly exclusively associated with covalent bonds. The DLL mechanism creates a deep and rigid binding pocket confining the target in a stable geometry that mainly relies on backbone H bonds. Hence, the mechanostability of the complex only marginally depends on the target side chains and thus sequence, even if it is minimized to merely six amino acids. These adhesins are hyperstable protein handles suitable for mechanochemistry and able to unfold almost any protein. They may serve as templates to design even stronger ones—a noncovalent superglue (42, 43). The mechanism proposed provides an atomistic understanding of why these adhesins can adhere to their hosts so resiliently, from which possible routes to inhibit it and impede staphylococcal adhesion may be derived.

REFERENCES AND NOTES

1. T. J. Foster, J. A. Geoghegan, V. K. Ganesh, M. Höök, *Nat. Rev. Microbiol.* **12**, 49–62 (2014).
2. M. Otto, *Nat. Rev. Microbiol.* **7**, 555–567 (2009).
3. C. C. S. Deivanayagam *et al.*, *EMBO J.* **21**, 6660–6672 (2002).
4. K. Ponnuraj *et al.*, *Cell* **115**, 217–228 (2003).
5. V. K. Ganesh *et al.*, *J. Biol. Chem.* **286**, 25963–25972 (2011).
6. J. A. Sharp *et al.*, *PLOS ONE* **7**, e38407 (2012).
7. T. J. Foster, M. Höök, *Trends Microbiol.* **6**, 484–488 (1998).
8. Y. Zong *et al.*, *EMBO J.* **24**, 4224–4236 (2005).
9. S. L. Davis, S. Gurusiddappa, K. W. McCrea, S. Perkins, M. Höök, *J. Biol. Chem.* **276**, 27799–27805 (2001).
10. H. Breithaupt, *Nat. Biotechnol.* **17**, 1165–1169 (1999).
11. J. A. Geoghegan, T. J. Foster, P. Speziale, Y. F. Dufrene, *Trends Microbiol.* **25**, 512–514 (2017).
12. D. J. Müller, Y. F. Dufrene, *Nat. Nanotechnol.* **3**, 261–269 (2008).
13. V. Vogel, M. Sheetz, *Nat. Rev. Mol. Cell Biol.* **7**, 265–275 (2006).
14. H. Yu, M. G. W. Siewny, D. T. Edwards, A. W. Sanders, T. T. Perkins, *Science* **355**, 945–950 (2017).
15. P. Herman *et al.*, *Mol. Microbiol.* **93**, 356–368 (2014).
16. T. Vanzielegheem, P. Herman-Bausier, Y. F. Dufrene, J. Mahillon, *Langmuir* **31**, 4713–4721 (2015).
17. P. Vitry *et al.*, *mBio* **8**, e01748–e17 (2017).
18. P. Herman-Bausier *et al.*, *mBio* **7**, e01529–e16 (2016).
19. C. Schoeler *et al.*, *Nat. Commun.* **5**, 5635 (2014).
20. R. Merkel, P. Nassoy, A. Leung, K. Ritchie, E. Evans, *Nature* **397**, 50–53 (1999).
21. M. Grandbois, M. Beyer, M. Rief, H. Clausen-Schaumann, H. E. Gaub, *Science* **283**, 1727–1730 (1999).
22. I. Schwaiger, A. Kardinal, M. Schleicher, A. A. Noegel, M. Rief, *Nat. Struct. Mol. Biol.* **11**, 81–85 (2004).
23. F. Rico, L. Gonzalez, I. Casuso, M. Puig-Vidal, S. Scheuring, *Science* **342**, 741–743 (2013).
24. O. K. Dudko, G. Hummer, A. Szabo, *Phys. Rev. Lett.* **96**, 108101 (2006).
25. M. G. Bowden *et al.*, *J. Biol. Chem.* **283**, 638–647 (2008).
26. J. V. Ribeiro *et al.*, *Sci. Rep.* **6**, 26536 (2016).
27. M. Walden *et al.*, *eLife* **4**, 1–24 (2015).
28. J. Alegre-Cebollada, C. L. Badilla, J. M. Fernández, *J. Biol. Chem.* **285**, 11235–11242 (2010).
29. U. Sridharan, K. Ponnuraj, *Biophys. Rev.* **8**, 75–83 (2016).
30. R. C. Bernardi, M. C. R. Melo, K. Schulten, *Biochim. Biophys. Acta* **1850**, 872–877 (2015).
31. E. Evans, K. Ritchie, *Biophys. J.* **72**, 1541–1555 (1997).
32. S. Izraïlev, S. Stepaniants, M. Balsera, Y. Oono, K. Schulten, *Biophys. J.* **72**, 1568–1581 (1997).
33. M. Rief, M. Gautel, F. Oesterhelt, J. M. Fernandez, H. E. Gaub, *Science* **276**, 1109–1112 (1997).
34. H. Lu, K. Schulten, *Biophys. J.* **79**, 51–65 (2000).
35. C. Schoeler *et al.*, *Nano Lett.* **15**, 7370–7376 (2015).
36. X. Zhang *et al.*, *Protein Cell* **6**, 757–766 (2015).
37. Y. Zhang *et al.*, *Biochem. J.* **474**, 1619–1631 (2017).
38. V. Stemberk *et al.*, *J. Biol. Chem.* **289**, 12842–12851 (2014).
39. V. K. Ganesh *et al.*, *PLOS Pathog.* **4**, e1000226 (2008).
40. W. E. Thomas, V. Vogel, E. Sokurenko, *Annu. Rev. Biophys.* **37**, 399–416 (2008).
41. M. M. Sauer *et al.*, *Nat. Commun.* **7**, 10738 (2016).
42. G. Veggiani, B. Zakeri, M. Howarth, *Trends Biotechnol.* **32**, 506–512 (2014).
43. T. Verdorfer *et al.*, *J. Am. Chem. Soc.* **139**, 17841–17852 (2017).

ACKNOWLEDGMENTS

We thank T. Nicolaus and A. Kardinal for laboratory assistance; E. Durner, M. A. Jobst, W. Ott, and T. Verdorfer for work on instrumentation and surface chemistry; M. C. R. Melo for assistance with correlation-based network analysis; M. Scheurer for assistance with PyContact; and H. Clausen-Schaumann, Daniel Müller, and Z. Luthey-Schulten for helpful discussions. **Funding:** We gratefully acknowledge funding from an advanced grant of the European Research Council (ERC, Cellufuel Grant 294438) and from the Deutsche Forschungsgemeinschaft (DFG, Sonderforschungsbereich 1032). This work was supported by National Institutes of Health (NIH) grant P41-GM104601, “Center for Macromolecular Modeling and Bioinformatics.” R.C.B. is partially supported by National Science Foundation (NSF) grant MCB-1616590, “Molecular Modeling of Bioenergetic Systems.” Molecular dynamics simulations made use of GPU-accelerated nodes of Blue Waters supercomputer as part of the Petascale Computational Resource (PRAC) grant “The Computational Microscope,” which is supported by the National Science Foundation (award numbers ACI-1440026 and ACI-1713784). Blue Waters sustained-petascale computing project is supported by the National Science Foundation (awards OCI-0725070 and ACI-1238993) and the state of Illinois. **Author contributions:** R.C.B., H.E.G., K.S., and L.F.M. conceived the research and interpreted the results; L.F.M. performed all experiments; R.C.B. performed all simulations; R.C.B., H.E.G., and L.F.M. wrote and revised the manuscript. **Competing interests:** The authors declare no competing interests. **Data and materials availability:** Key plasmids are available on Addgene; see the supplementary materials for identifiers.

SUPPLEMENTARY MATERIALS

www.sciencemag.org/content/359/6383/1527/suppl/DC1
Materials and Methods
Figs. S1 to S19
Table S1
Movies S1 and S2
References (44–71)

13 October 2017; accepted 1 March 2018
10.1126/science.aar2094

BIOCHEMISTRY

Binding of ISRIB reveals a regulatory site in the nucleotide exchange factor eIF2B

Alisa F. Zyryanova,^{1*} Félix Weis,^{1,2,3,4†} Alexandre Faille,^{1,2,3†} Akeel Abo Alard,⁵ Ana Crespo-Casado,¹ Yusuke Sekine,¹ Heather P. Harding,¹ Felicity Allen,⁶ Leopold Parts,⁶ Christophe Fromont,⁵ Peter M. Fischer,⁵ Alan J. Warren,^{1,2,3,4*} David Ron^{1*}

The integrated stress response (ISR) is a conserved translational and transcriptional program affecting metabolism, memory, and immunity. The ISR is mediated by stress-induced phosphorylation of eukaryotic translation initiation factor 2 α (eIF2 α) that attenuates the guanine nucleotide exchange factor eIF2B. A chemical inhibitor of the ISR, ISRIB, reverses the attenuation of eIF2B by phosphorylated eIF2 α , protecting mice from neurodegeneration and traumatic brain injury. We describe a 4.1-angstrom-resolution cryo-electron microscopy structure of human eIF2B with an ISRIB molecule bound at the interface between the β and δ regulatory subunits. Mutagenesis of residues lining this pocket altered the hierarchical cellular response to ISRIB analogs in vivo and ISRIB binding in vitro. Our findings point to a site in eIF2B that can be exploited by ISRIB to regulate translation.

The integrated stress response (ISR) has homeostatic functions that increase fitness. However, in some pathological circumstances, benefit arises from attenuated signaling in the ISR (1). A search for ISR inhibitors led to the discovery of the integrated stress response inhibitor, ISRIB (2), a small molecule efficacious in mouse models of neurodegeneration (3) and traumatic brain injury (4).

ISRIB action converges on eukaryotic translation initiation factor 2B (eIF2B), a protein complex with guanine nucleotide exchange factor (GEF) activity toward eIF2 (5) that is inhibited by phosphorylated eIF2 (6, 7). Addition of ISRIB

accelerates eIF2B GEF activity in vitro, and targeting eIF2B's δ regulatory subunit can impart ISRIB resistance (8, 9). However, known ISRIB-resistant mutations in eIF2B cluster at a distance from both the regulatory site engaged by eIF2(α P) and the catalytic site engaged by eIF2 γ (10). Thus, although the bulk of the evidence suggests that ISRIB binds eIF2B to regulate its activity, indirect modes of action are not excluded.

ISRIB stabilized the eIF2B complex from HeLa cells (fig. S1), as expected (9). Thus, we added a fluorescently labeled derivative of ISRIB (AAA2-101) (fig. S2A) to purified eIF2B and observed increased fluorescence polarization (FP) (Fig. 1A, left panel).

Unlabeled ISRIB competed for eIF2B in the FP assay with a half-maximal effective concentration (EC₅₀) in the nanomolar range (Fig. 1A, right panel). As observed for ISRIB action in cells, less-active analogs competed less successfully (fig. S2, B and C).

We purified endogenous eIF2B from HeLa cell lysates in the presence of ISRIB and determined the structure of the complex by single-particle cryo-electron microscopy (cryo-EM) at an overall resolution of 4.1 Å (Fig. 1B, figs. S1A and S3, and table S6). Within the β and δ regulatory core, protein side chains were clearly resolved, resulting in a near-complete atomic model of this region (Fig. 1C and fig. S4, A and B). The resolution of the γ and ϵ human catalytic subcomplex was lower compared with that of the regulatory core (fig. S4A), and the catalytically important C-terminal HEAT domain of the ϵ subunit remained unresolved in the cryo-EM map.

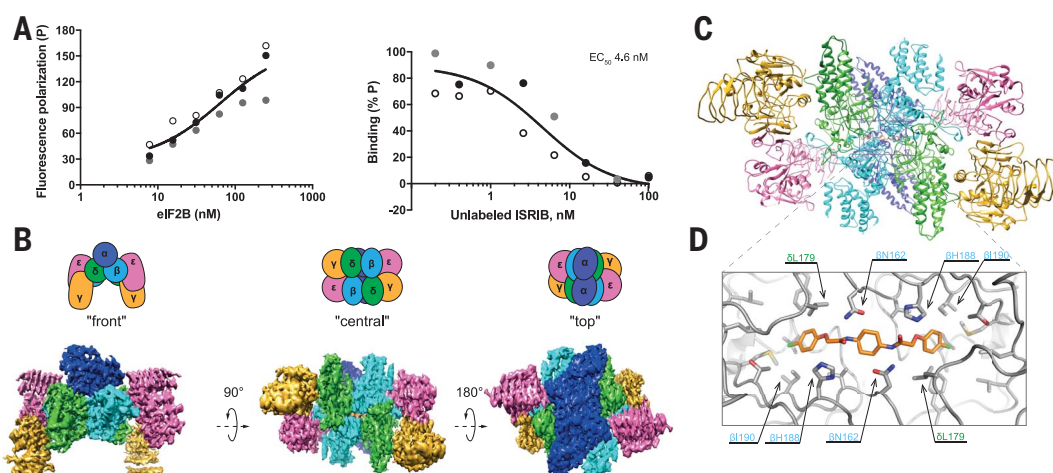
Owing to a lack of sufficient high-quality cryo-EM images of an apo-eIF2B complex, we were unable to calculate a difference map of eIF2B with and without ISRIB. However, a nearly continuous density with a shape and size of a single ISRIB molecule was conspicuously present at the interface of the β and δ regulatory subunits (Fig. 1B, “central view,” and fig. S4C). The ISRIB-binding

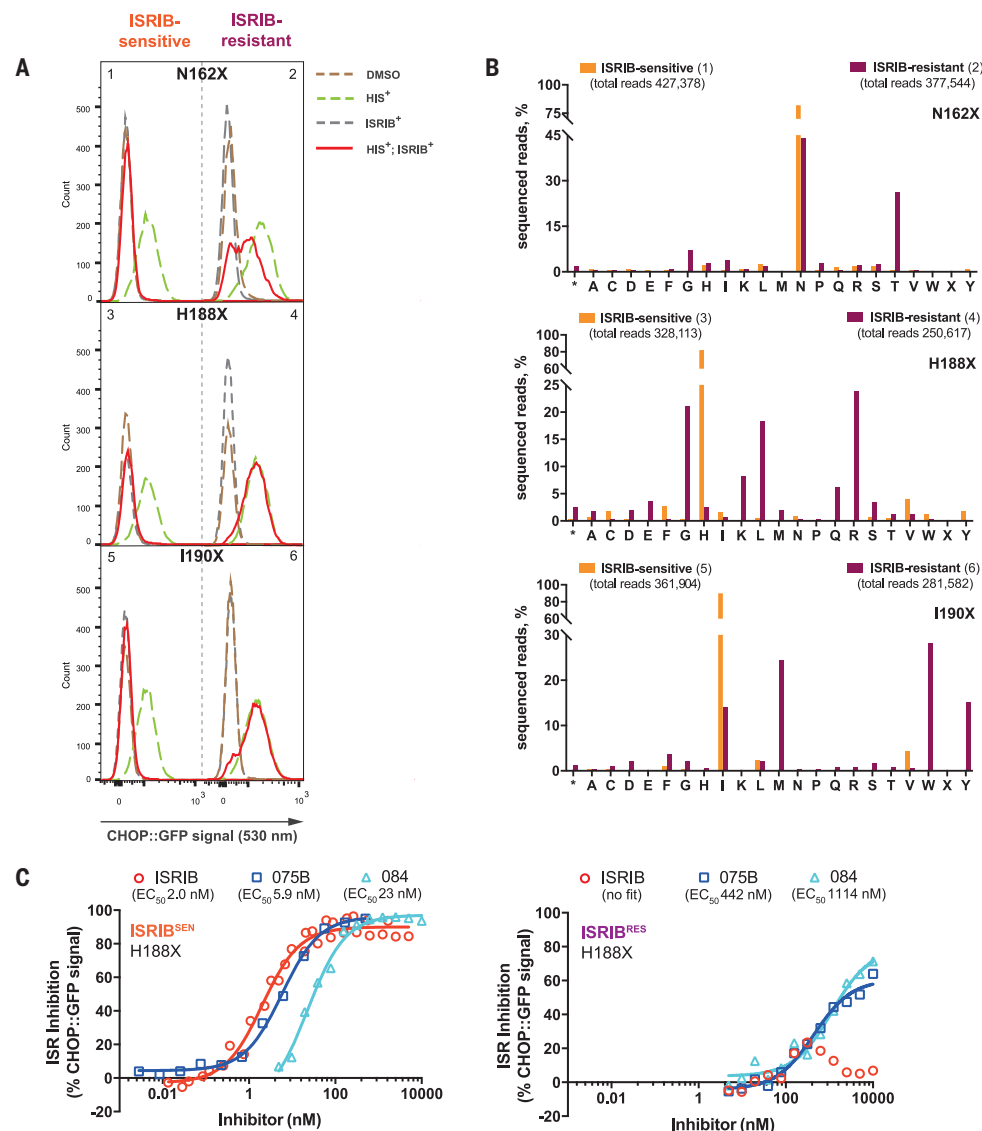
¹Cambridge Institute for Medical Research, University of Cambridge, Cambridge CB2 0XY, UK. ²Department of Haematology, University of Cambridge, Cambridge, UK.

³Wellcome Trust—Medical Research Council Stem Cell Institute, University of Cambridge, Cambridge, UK. ⁴MRC Laboratory of Molecular Biology, Francis Crick Avenue, Cambridge CB2 0QH, UK. ⁵Division of Biomolecular Science and Medicinal Chemistry, School of Pharmacy, University of Nottingham, Nottingham NG7 2RD, UK. ⁶Wellcome Trust Sanger Institute, Wellcome Genome Campus, Hinxton, Cambridgeshire CB10 1SA, UK.

*Corresponding author. Email: az310@cam.ac.uk (A.F.Z.); ajw1000@cam.ac.uk (A.J.W.); dr360@medschl.cam.ac.uk (D.R.)
†These authors contributed equally to this work.

Fig. 1. Biophysical and structural analysis of ISRIB binding to human eIF2B. (A) Fluorescence polarization (FP) assays showing binding of ISRIB to human eIF2B. (Left) A plot of the FP signal arising from fluorescein-labeled ISRIB analog (AAA2-101) (2.5 nM) as a function of the concentration of eIF2B in the sample. (Right) A plot of the relative FP signal arising from samples with fluorescein-labeled AAA2-101 (2.5 nM) bound to purified human eIF2B (30 nM) in the presence of the indicated concentration of unlabeled *trans*-ISRIB introduced as a competitor. Concentrations of eIF2B and ISRIB on respective plots are represented on a log₁₀ scale. Curve fitting and EC₅₀ were generated using agonist versus response function on GraphPad Prism; shown are values of three independently acquired measurements. (B) Representative views of the cryo-EM map of the ISRIB-bound decameric human eIF2B complex. Density is colored according to the subunit architecture indicated in the cartoons: α , blue; β , cyan; δ , green; γ , gold; ϵ , pink; ISRIB, orange. (C) Ribbon representation of ISRIB-bound human eIF2B “central” view of the ($\beta\delta$)₂ dimer interface with a single molecule of ISRIB. (D) Close-up of the “central” view showing the ISRIB-binding site. An ISRIB molecule is docked into the cavity at the ($\beta\delta$)₂ dimer interface. Residues contacting ISRIB in the central part of the pocket from the β (blue) and δ (green) subunits are indicated. ISRIB is represented in orange sticks.





pocket was located at the plane of symmetry between the β and δ subunits. In the central part of the pocket, the side chain of β H188 was positioned in the vicinity of the essential carbonyl moiety of ISRIB (1I), and β N162 was poised to stabilize the diaminocyclohexane moiety of ISRIB through hydrogen-bonding interactions (Fig. 1D). More distally, the side chains of δ L179, δ F452, δ L485, δ L487, β V164, β I190, β T215, and β M217 formed the hydrophobic end of the symmetrical pocket that accommodated the aryl groups of ISRIB, with β I190 and δ L179 located within van der Waals interaction distance to the aryl group (Fig. S4D). A hamster *Eif2b4*^{L180F} mutation (δ L179 in the human eIF2B) disrupts ISRIB action in cells (8), which is consistent with a potential loss of these interactions as well as a clash between the bulkier side chain of phenylalanine and the bound ISRIB molecule (Fig. 1D).

Overall, the human structure is highly similar to that of the published *Schizosaccharomyces pombe* eIF2B structure (10) (root mean square deviation of 2.57 Å over 3049 α carbons, Fig. S4E).

However, there is no density in the corresponding region in the *S. pombe* eIF2B map, indicating that the density found in the human structure was that of the bound ISRIB.

To test these features of ISRIB binding, we used CRISPR-Cas9 to randomize residues lining the ISRIB-binding pocket (*Eif2b2*^{N162}, *Eif2b2*^{H188}, or *Eif2b2*^{I190}) and correlated amino acid substitutions to ISRIB activity in the mutagenized cells. Histidinol, an agent that activates the eIF2 α kinase GCN2 and induces the ISR, normally activates a CHOP::GFP (green fluorescent protein) reporter gene, whereas ISRIB represses the reporter (8). Fluorescence-activated cell sorting (FACS) of histidinol-treated, mutagenized cells segregated them into ISRIB-sensitive [ISRIB^{SEN} (CHOP::GFP inhibited)] and ISRIB-resistant [ISRIB^{RES} (CHOP::GFP activated)] classes (Fig. 2A, left and right panels, respectively).

To determine if the phenotypically distinguished pools of mutagenized cells (Fig. 2A) were enriched in different mutations, we subjected genomic DNA derived from each population to deep-

sequencing analysis (Fig. 2B and table S4). The ISRIB^{RES} pool targeted at *Eif2b2*^{H188} diverged markedly from the parental sequence (Fig. 2B, middle panel). Of a total of 250,617 sequencing reads, histidine was present in only 6443 (2.6%), with arginine, glycine, leucine, lysine, and glutamine dominating (24, 21, 18, 8.2, and 6.2%, respectively). Histidine was preserved in the ISRIB^{SEN} pool (269,253 of 328,113 reads, 82%). The ISRIB^{RES} pool of cells targeted at *Eif2b2*^{I190} was dominated by tryptophan, methionine, and tyrosine (28, 24, and 15%, respectively), consistent with a role for these bulky side chains in occluding the ISRIB-binding pocket (Fig. 2B, bottom panel). Mutagenesis of *Eif2b2*^{N162} was less successful in generating a pool of strongly ISRIB-resistant cells; nonetheless, threonine was enriched in the ISRIB^{RES} pool (26%) (Fig. 2B, top panel). Thus, residues lining the ISRIB-binding pocket play a role in ISRIB action.

Despite considerable allele diversity, the *Eif2b2*^{H188X} ISRIB^{RES} pool exhibited selective loss of sensitivity to ISRIB, while retaining a measure of responsiveness to certain ISRIB analogs

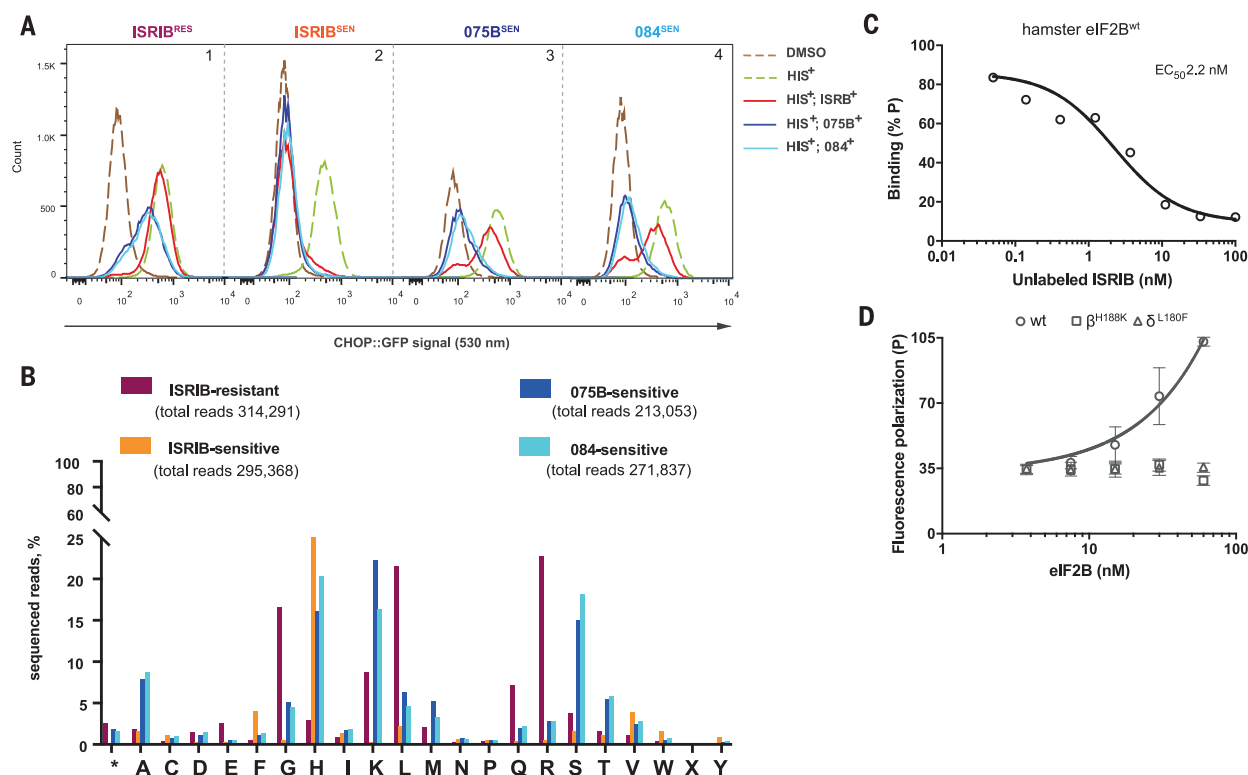


Fig. 3. Sensitivity to ISRIB analogs selects for a divergent palette

of mutations in codon 188 of *Eif2b2*. (A) Histograms of the ISR-responsive CHOP::GFP fluorescent reporter activity, induced by histidinol (*HIS⁺*, 0.5 mM) in *ISRIB^{RES}*, *ISRIB^{SEN}*, compound 075B^{SEN}, and compound 084^{SEN} subpools, selected for their responsiveness to ISRIB or its analogs (2.5 μ M) from a population of originally *ISRIB^{RES}* *Eif2b2^{H188X}* mutant cells. (B) Bar graph of the distribution of residues identified at *Eif2b2* codon 188 in phenotypically divergent pools of CHO-K1 cells. The number of sequenced reads in *ISRIB^{RES}* (purple), *ISRIB^{SEN}* (orange), compound 075B^{SEN} (blue), and compound 084^{SEN} (cyan) pools encoding each amino acid (*, stop codon; X, ambiguous)

is plotted. (C) Plot of the relative FP signal arising from samples with fluorescein-labeled AAA2-101 (2.5 nM) bound to purified hamster eIF2B (30 nM) in the presence of the indicated concentration of unlabeled ISRIB introduced as a competitor (represented on a log₁₀ scale). Shown is a representative of two independent experiments. The fitting curve and EC₅₀ were generated using “agonist versus response” function on GraphPad Prism. (D) A plot of the FP signal arising from fluorescein-labeled AAA2-101 (2.5 nM) as a function of the concentration of wild-type (wt) or mutant eIF2B (β^{H188K} or δ^{L180F}) in the sample. Shown are mean \pm SD ($n = 3$). Concentrations of eIF2B are represented on a log₁₀ scale.

(Fig. 2D). The residual response to analogs AAA1-075B (075B) and AAA1-084 (084) (albeit with much reduced affinity compared to the *ISRIB^{SEN}* population) (Fig. 2C), pointed to a shift in the binding properties of the ISRIB pocket, induced by the mutations at β 188.

Next, we exploited the diversity of *ISRIB^{RES}* mutations in the *Eif2b2^{H188X}* population to select for subpools that either acquired sensitivity to compounds AAA1-075B or AAA1-084, regained sensitivity to ISRIB, or retained ISRIB resistance (Fig. 3A) and sequenced their *Eif2b2* alleles (Fig. 3B and table S5). As expected, sorting for ISRIB sensitivity enriched, by >20-fold, rare wild-type H188 alleles that persisted in the *ISRIB^{RES}* *Eif2b2^{H188X}* pool (Fig. 3B, compare purple and orange bars). H188 was also somewhat enriched in the pools of 075B^{SEN} or 084^{SEN} cells, but unlike the *ISRIB^{SEN}*, these pools were also enriched for residues other than histidine (Fig. 3B and table S5). Notably, selecting for sensitivity to these ISRIB analogs enriched for different residues than those found in the original *ISRIB^{RES}* pool: Arginine, glycine, and leucine were depleted and replaced by lysine, serine, alanine, and threonine (Fig.

3B, compare purple to blue and cyan bars). The correlation between mutations in residues lining the ISRIB-binding pocket and selective responsiveness to ISRIB analogs, observed in the pools, was confirmed in individual mutant clones (fig. S5).

To directly address the effect of ISRIB-resistant mutations on ISRIB binding, we purified eIF2B from wild-type, *Eif2b4^{L180F}*, and *Eif2b2^{H188K}* Chinese hamster ovary (CHO) cells (fig. S6). The wild-type eIF2B gave rise to a concentration-dependent FP signal in the presence of a fluorescein-labeled AAA2-101 that was readily competed with unlabeled ISRIB (Fig. 3C). However, eIF2B purified from the mutant cells failed to give rise to an FP signal (Fig. 3D), thereby establishing a correlation between ISRIB resistance in cells and defective ISRIB binding in vitro.

The ISRIB-binding pocket, defined structurally and validated chemogenetically, straddles the twofold axis of symmetry of the core regulatory subcomplex, and a single molecule of ISRIB appears to engage the same residues from opposing protomers of the ($\beta\delta$)₂ dimer. These features fit with ISRIB's own symmetry and could

explain the ability of ISRIB to stabilize the eIF2B decamer, possibly increasing its abundance in *ISRIB*-treated cells. Our findings are also consistent with ISRIB's ability to stabilize a rate-limiting assembly intermediate of the active decamer, as demonstrated biochemically in an accompanying manuscript (12). Indeed, comparison of the *S. pombe* (10) and ISRIB-bound human eIF2B argues against large domain movements associated with ISRIB binding. However, an important allosteric effect of ISRIB binding might easily have been overlooked, as the critical catalytic domain of the ϵ subunit is resolved in neither structure. Similar considerations apply to the potential effect of ISRIB on the inhibitory interaction between eIF2B with eIF2(α P). These might arise from subtle ISRIB-induced conformational changes propagated through the regulatory core to the eIF2(α P) binding cavity formed by the convergence of the tips of the α , β , and δ subunits (10, 13–15). The lower resolution of the cryo-EM density in that region might have masked important allosteric changes. Although the relative contribution of accelerated assembly, enhanced stability, or allostery to ISRIB action remain to be

resolved, it is intriguing to consider that endogenous ligands might engage the ISRIB-binding site to regulate eIF2B in yet-to-be-determined physiological states.

REFERENCES AND NOTES

1. K. Pakos-Zebrucka *et al.*, *EMBO Rep.* **17**, 1374–1395 (2016).
2. C. Sidrauski *et al.*, *eLife* **2**, e00498 (2013).
3. M. Halliday *et al.*, *Cell Death Dis.* **6**, e1672 (2015).
4. A. Chou *et al.*, *Proc. Natl. Acad. Sci. U.S.A.* **114**, E6420–E6426 (2017).
5. R. Panniers, E. C. Henshaw, *J. Biol. Chem.* **258**, 7928–7934 (1983).
6. J. Siekierka, K. I. Mitsui, S. Ochoa, *Proc. Natl. Acad. Sci. U.S.A.* **78**, 220–223 (1981).
7. M. J. Clemens, V. M. Pain, S. T. Wong, E. C. Henshaw, *Nature* **296**, 93–95 (1982).
8. Y. Sekine *et al.*, *Science* **348**, 1027–1030 (2015).
9. C. Sidrauski *et al.*, *eLife* **4**, e07314 (2015).
10. K. Kashiwagi *et al.*, *Nature* **531**, 122–125 (2016).
11. B. R. Hearn *et al.*, *ChemMedChem* **11**, 870–880 (2016).
12. J. C. Tsai *et al.*, *Science* **359**, aaq0939 (2018).
13. C. R. Vazquez de Aldana, A. G. Hinnebusch, *Mol. Cell. Biol.* **14**, 3208–3222 (1994).
14. G. D. Pavitt, W. Yang, A. G. Hinnebusch, *Mol. Cell. Biol.* **17**, 1298–1313 (1997).
15. A. M. Bogorad, K. Y. Lin, A. Marintchev, *Nucleic Acids Res.* **45**, 11962–11979 (2017).

ACKNOWLEDGMENTS

We thank D. Barrett and C. Ortori (University of Nottingham) for measuring the ISRIB content of eIF2B; P. Sterk (University of Cambridge) for next-generation sequencing analysis; S. Chen, C. Savva, G. McMullan, T. Darling, and J. Grimmett (MRC Laboratory for Molecular Biology) for technical support with cryo-EM, movie data acquisition, and help with computing; S. Preissler (University of Cambridge) for editorial comments; and Diamond for access and support of A. Siebert and C. Hecksel from the cryo-EM facilities at the UK National Electron Bio-Imaging Centre (eBIC) (proposals EM-14606 and EM-17057), funded by the Wellcome Trust, MRC, and Biotechnology and Biological Sciences Research Council. **Funding:** We acknowledge funding by a Wellcome Trust Principal Research Fellowship (Wellcome 200848/Z/16/Z) to D.R.; a Specialist Programme from Bloodwise (12048), the UK Medical Research Council (MC_U105161083), and core support from the Wellcome Trust Medical Research Council Cambridge Stem Cell Institute to A.J.W.; and a Wellcome Trust Strategic Award to the Cambridge Institute for Medical Research (Wellcome 100140). Support from A Higher Committee for Education Development, Iraq, Scholarship (4241047) to A.A.A. and a Research Fellowship from Royal Commission for the Exhibition of 1851 to F.A. is greatly appreciated. **Author contributions:** A.F.Z. and D.R. designed

and implemented the study and wrote the manuscript. F.W., A.F., and A.J.W. obtained and interpreted the structural data and edited the manuscript. A.A.A., C.F., and P.M.F. designed and synthesized compounds, interpreted the chemogenetic data, and edited the manuscript. A.C.-C., Y.S., and H.P.H. designed and implemented the somatic cell genetics, cell phenotyping, and deep sequencing and edited the manuscript. F.A. and L.P. analyzed NGS sequencing data and edited the manuscript.

Competing interests: None declared. **Data and materials availability:** Cryo-EM density maps are deposited in the Electron Microscopy Data Bank (EMD-4162), atomic coordinates are deposited in the Protein Data Bank (6EZO), and raw sequencing reads are deposited in the BioProject database (PRJNA432684).

SUPPLEMENTARY MATERIALS

www.sciencemag.org/content/359/6383/1533/suppl/DC1
Materials and Methods
Supplementary Text
Schemes S1 to S4
Figs. S1 to S6
Tables S1 to S6
References (16–33)

16 November 2017; accepted 9 February 2018
10.1126/science.aar5129

CANCER IMMUNOLOGY

Antibody-mediated inhibition of MICA and MICB shedding promotes NK cell-driven tumor immunity

Lucas Ferrari de Andrade,^{1,2} Rong En Tay,^{1,2} Deng Pan,^{1,2} Adrienne M. Luoma,^{1,2} Yoshinaga Ito,^{1,2} Soumya Badrinath,^{1,2} Daphne Tsoucas,³ Bettina Franz,^{1,2} Kenneth F. May Jr.,⁴ Christopher J. Harvey,¹ Sebastian Kobold,¹ Jason W. Pyrdol,¹ Charles Yoon,^{4,5} Guo-Cheng Yuan,³ F. Stephen Hodi,⁴ Glenn Dranoff,^{4*} Kai W. Wucherpfennig^{1,2†}

MICA and MICB are expressed by many human cancers as a result of cellular stress, and can tag cells for elimination by cytotoxic lymphocytes through natural killer group 2D (NKG2D) receptor activation. However, tumors evade this immune recognition pathway through proteolytic shedding of MICA and MICB proteins. We rationally designed antibodies targeting the MICA $\alpha 3$ domain, the site of proteolytic shedding, and found that these antibodies prevented loss of cell surface MICA and MICB by human cancer cells. These antibodies inhibited tumor growth in multiple fully immunocompetent mouse models and reduced human melanoma metastases in a humanized mouse model. Antitumor immunity was mediated mainly by natural killer (NK) cells through activation of NKG2D and CD16 Fc receptors. This approach prevents the loss of important immunostimulatory ligands by human cancers and reactivates antitumor immunity.

The stress proteins MICA and MICB are expressed by many human cancers as a consequence of genomic damage, enabling elimination of cancer cells by cytotoxic lymphocytes expressing the natural killer group 2D (NKG2D) receptor (1–6). Engagement of NKG2D receptors triggers natural killer (NK) cell-mediated cytotoxicity and provides a costimulatory signal for CD8 T cells and $\gamma\delta$ T cells (7, 8). However, advanced cancers frequently escape this immune mechanism by proteolytic shedding of cell surface-bound MICA and MICB molecules through the coordinated action of a disulfide isomerase (ERp5) and several proteases belonging to the ADAM (a disintegrin and metalloproteinase) and MMP (matrix metalloproteinase) families (9–12). High serum concentrations of shed MICA are associated with disease progression in many human cancers, including melanoma, neuroblastoma, prostate cancer, kidney cancer, multiple myeloma, and chronic lymphocytic leukemia (13–20).

It is impossible to specifically block MICA and MICB shedding in vivo with small-molecule inhibitors because multiple proteases with broad substrate specificities contribute to this process

(10–12). The membrane-proximal MICA and MICB $\alpha 3$ domain is the site of proteolytic shedding, whereas the membrane-distal $\alpha 1$ and $\alpha 2$ domains bind to the NKG2D receptor (Fig. 1A) (9, 21, 22). We hypothesized that shedding could be inhibited in a highly specific manner, with antibodies binding to key epitopes on the MICA and MICB $\alpha 3$ domain required for initiation of shedding and that such antibodies would not interfere with NKG2D binding. We further reasoned that the Fc segment of such antibodies could contribute to therapeutic efficacy by engaging activating Fc receptors. We immunized mice with the recombinant MICA $\alpha 3$ domain and identified three monoclonal antibodies (mAbs) (7C6, 6F11, and 1C2) that bound to the $\alpha 3$ domain and the full-length MICA extracellular domain (Fig. 1B and fig. S1, A, B, and D). *MICA* and *MICB* genes are polymorphic, but the $\alpha 3$ domain is more conserved than the $\alpha 1$ and $\alpha 2$ domains, explaining why these antibodies bound to all tested MICA variants and also MICB (fig. S1, B and C).

Functional studies showed that MICA and MICB $\alpha 3$ domain-specific antibodies strongly inhibited MICA shedding by a diverse panel of human tumor cell lines, resulting in a substantial increase in the cell surface density of MICA (Fig. 1, C and D, and fig. S2, A and B). By contrast, the previously reported 6D4 mAb (23) bound outside the MICA $\alpha 3$ domain and did not inhibit MICA shedding (Fig. 1, B to D, and fig. S2B). The $\alpha 3$ domain-specific antibodies also reduced MICA and MICB shedding by murine tumor cell lines expressing cDNAs encoding full-length human MICA or MICB under the control of a lentiviral vector (figs. S2C; S3, A to C; and S4D) but did not affect amounts of secreted MICA by cells expressing only the MICA extracellular domain (fig. S4,

C and D). These antibodies minimally affected detection of recombinant soluble MICA by enzyme-linked immunosorbent assay (ELISA) (fig. S4, A and B) and did not interfere with NKG2D binding to MICA (fig. S5, A to C). Antibody-mediated targeting of the MICA and MICB $\alpha 3$ domain could thus specifically inhibit proteolytic shedding of these NKG2D ligands.

We selected mAb 7C6 for further experiments because it was most effective in stabilizing MICA and MICB on the surface of tumor cells (fig. S3, B and C). NKG2D is an important receptor for NK cell-mediated cytotoxicity, and we found that the 7C6 mAb (with human immunoglobulin G1 Fc region hIgG1) enabled strong NK cell-mediated killing of human tumor cells, including tumor cell lines not targeted by NK cells in the absence of this antibody (Fig. 1E and figs. S6A and S7). Human NK cells also produced higher amounts of interferon- γ (IFN- γ) when cocultured with tumor cells in the presence of the 7C6-hIgG1 mAb (fig. S6B). The 7C6 antibody also inhibited MICA and MICB shedding by short-term human melanoma (24) cell lines generated from metastatic lesions (fig. S8, A to C). These results demonstrate that a MICA $\alpha 3$ domain-specific antibody could enhance the function of human NK cells against tumor cells.

Although only primates have *MICA* and *MICB* genes (1), human MICA is recognized by the murine NKG2D receptor (fig. S9), which enabled preclinical testing in syngeneic, fully immunocompetent mouse tumor models. We introduced the *MICA* cDNA with a lentiviral vector into murine B16F10 melanoma and CT26 colon cancer cell lines and tested the activity of the 7C6 antibody in lung metastasis models. Treatment with 7C6 antibody (mouse immunoglobulin G2a Fc region, mIgG2a) strongly reduced the number of lung metastases formed by B16F10-MICA tumor cells (Fig. 2, A and B, and fig. S10, A and B). Shed MICA concentrations were high in sera of mice treated with an isotype control antibody but became undetectable in mice treated with 7C6 mAb (Fig. 2C). The 7C6 mAb also demonstrated efficacy in a lung metastasis model with CT26 cells expressing MICA (Fig. 2D) and could be detected on the surface of B16F10-MICA cells in subcutaneous tumors (fig. S11, A and B). Also, increased MICA expression was detected on the surface of B16F10-MICA tumor cells when mice were treated with 7C6-mIgG2a compared to isotype control antibody (fig. S11C). Interestingly, endogenous anti-MICA antibodies naturally arose in mice inoculated with MICA-expressing tumor cells (fig. S11D). Murine IgG1 was the predominant isotype for these antibodies (fig. S11E), an isotype associated with poor antitumor activity (25). These endogenous antibodies did not affect detection of recombinant MICA by ELISA (fig. S11F), did not slow tumor growth (fig. S11G), and moderately inhibited detection of shed MICA in serum samples (fig. S11H). Accordingly, 7C6 treatment inhibited growth of subcutaneous B16F10-MICA melanomas more effectively in B cell-deficient mice (*Igh*^{−/−}) that were unable to mount such an antibody response (fig. S11, I and

¹Department of Cancer Immunology and Virology, Dana-Farber Cancer Institute, 450 Brookline Avenue, Boston, MA 02215, USA. ²Harvard Medical School, 25 Shattuck Street, Boston, MA 02115, USA. ³Department of Biostatistics and Computational Biology, Dana-Farber Cancer Institute, 450 Brookline Avenue, Boston, MA 02215, USA. ⁴Department of Medical Oncology, Dana-Farber Cancer Institute, 450 Brookline Avenue, Boston, MA 02215, USA. ⁵Department of Surgery, Brigham and Women's Hospital, 75 Francis Street, Boston, MA 02115, USA. *Present address: Novartis Institutes for Biomedical Research, 250 Massachusetts Avenue, Cambridge, MA 02139, USA. †Corresponding author. Email: kai_wucherpfennig@dfci.harvard.edu

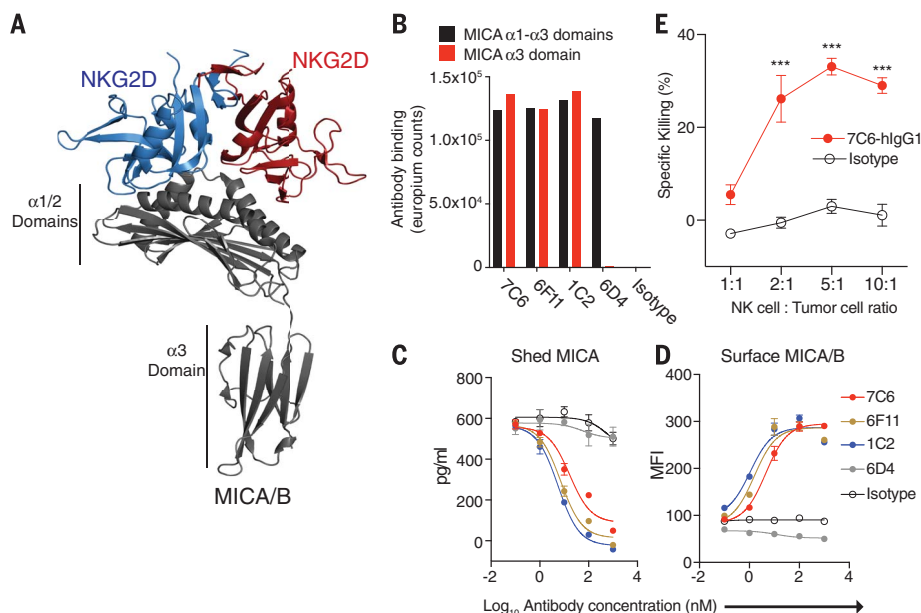


Fig. 1. MICA and MICB α 3 domain-specific antibodies inhibit shedding and stabilize the protein on the surface of human tumor cells for recognition by NK cells. (A) Illustration of MICA protein bound to a NKG2D homodimer (Protein Data Bank 1HYR). MICA is colored in gray and the NKG2D homodimer in blue and red. The NKG2D homodimer binds to the α 1 and α 2 domains; the α 3 domain is the site of proteolytic cleavage. (B) Binding of mAbs to immobilized MICA α 3 domain or MICA α 1 to α 3 domains detected with a fluorescence-based ELISA (one representative of three independent experiments). (C and D) A375 cells were treated for 24 hours with the indicated mAbs. (C) MICA α 3 domain-specific mAbs (7C6, 6F11, 1C2) inhibit MICA release into the supernatant, as quantified by sandwich ELISA; mAb 6D4 binds outside the MICA α 3 domain and thus does not inhibit shedding. Data show mean \pm SD for triplicate measurements from one representative of three independent experiments. (D) MICA α 3 domain-specific mAbs stabilize MICA surface expression, as determined by flow cytometry using phycoerythrin (PE)-labeled 6D4 mAb. MFI, mean fluorescence intensity. Data show mean \pm SD for triplicate measurements from one representative of three independent experiments. (E) Human NK cells exhibit cytotoxicity against A375 cells in the presence of 7C6-hlgG1 antibody (66.7 nM) but not isotype control antibody. Mean \pm SD for quadruplicate measurements. *** P < 0.001 calculated by two-way analysis of variance (ANOVA) and Bonferroni's post hoc test. Representative of three independent experiments (each experiment was done with different human NK cell donors).

J). The efficacy of the 7C6 mAb was restricted to subcutaneous tumors that expressed full-length MICA or MICB; no therapeutic effect was observed for tumors that secreted the extracellular domain of MICA or that lacked these NKG2D ligands (Fig. 2E). Furthermore, 7C6 mAb inhibited MICA and MICB shedding but did not promote clearance of secreted MICA protein (fig. S12A). These results demonstrate that a mAb that inhibited MICA and MICB shedding had antitumor activity in fully immunocompetent mouse models.

Antibody-mediated depletion revealed that NK cells, but not CD8 T cells, were essential for the therapeutic activity of 7C6 mAb against lung metastases (Fig. 2F and fig. S12B). Furthermore, therapeutic efficacy was lost in perforin (*Prf1*)-but not IFN- γ (*Ifng*)-deficient mice, indicating that NK cell-mediated cytotoxicity represented an essential mechanism (Fig. 2G and fig. S12C). Treatment with 7C6 mAb was associated with tumor cell apoptosis and a substantial reduction of tumor cell load within lung tissue (fig. S13, A to E). The MICA antibody also had activity against

established metastases. Treatment was delayed until day 7, when metastases were detectable, and 7C6-mIgG2a reduced serum MICA concentrations and the number of lung metastases while enhancing infiltration of lung tissue by activated NK cells (fig. S14, A to D).

We next examined the changes in gene expression by NK cells induced by MICA antibodies. Human NK cells cocultured with 7C6-hlgG1-pretreated human A375 melanoma cells up-regulated genes associated with NK cell activation and effector functions (fig. S15, A and B). It was previously reported that tumors are infiltrated by group 1 innate lymphoid cells (ILCs), which are composed of NK cells and innate lymphoid cells 1 (ILC1) (26). We sorted group 1 ILCs from metastatic lung tissue by flow cytometry for single-cell RNA sequencing (RNA-seq); these tissue-infiltrating group 1 ILCs expressed CD69, a tissue residency marker, whereas blood group 1 ILCs (likely NK cells) were low in CD69 (fig. S16A). Single-cell RNA-seq demonstrated major differences in the composition and activation state of group 1 ILCs

between 7C6-mIgG2a and isotype control treatment groups. In 7C6-mIgG2a-antibody treated mice, most group 1 ILCs (63.2%) were NK cells with a gene expression signature associated with activation and cytotoxicity, including expression of eomesodermin (EOMES), granzyme A (GZMA), granzyme B (GZMB), and perforin 1 (PRF1) (Fig. 3, A and B, and fig. S17, A and B). By notable contrast, a large fraction of cells (49.4%) in isotype control antibody-treated mice were ILC1 with a gene expression signature associated with cytokine and chemokine signaling and inflammation, including expression of the CXCR3 and CXCR6 chemokine receptors and lymphotxin β (LTB) (Fig. 3, A and B, and fig. S18, A and B) (26). We also identified ILC1 in lung tissue of naïve mice that had not been injected with tumor cells (fig. S19, A and B), indicating that ILC1 originated from a lung-resident cell population. Taken together, these data indicated that treatment with this MICA antibody resulted in a notable activation of tissue-infiltrating NK cells and expression of cytotoxicity genes.

Using flow cytometry, we validated key findings from the single-cell RNA-seq study. Lung-infiltrating NK cells were identified using EOMES and CD49b as markers, whereas lung-resident ILC1 were positive for CD49a, CD226, CXCR3, and CXCR6 (fig. S20A). Staining for GZMA allowed identification of activated NK cells that also expressed EOMES and CD49b (fig. S20A). Quantification of EOMES⁺ GZMA⁺ cells demonstrated an approximately fourfold increase of these activated NK cells (adjusted for tumor burden) on days 4, 7, and 11 in 7C6-mIgG2a-treated mice compared to isotype control antibody-treated mice with lung metastases (Fig. 3C and fig. S20C). Also, the presence of lung metastases increased absolute numbers of lung-resident NK cells and ILC1 as shown by comparison of naïve mice and isotype control antibody-treated mice with lung metastases (figs. S16B and S20B). ILC1 expressed higher amounts of NKG2D at the protein level, but not at the mRNA level, compared to NK cells (Fig. 3B and fig. S20A). Also, surface levels of NKG2D were higher among tissue-infiltrating NK cells than blood NK cells (figs. S16C and S21A). However, NKG2D surface levels were substantially reduced among tissue-resident NK cells and ILC1 in tumor-bearing mice compared to naïve mice, even when tumor cells did not express MICA (figs. S21, A and B, and S16C), suggesting that signals from the tumor microenvironment (such as transforming growth factor- β) contributed to lower NKG2D levels within metastases (27, 28).

NK cells are regulated by multiple activating and inhibitory receptors, and both NKG2D and CD16 Fc receptors strongly modulate NK cell functions (29). We introduced two mutations into the 7C6-hlgG1 and mIgG2b heavy chains [aspartate to alanine at position 265 (D265A) and asparagine to alanine at position 297 (N297A), or DANA] to abrogate binding to activating Fc receptors (25). 7C6-DANA mutant antibodies did not bind to the activating Fc receptor expressed by NK cells (CD16a) but retained MICA

binding (fig. S22, A to D). The 7C6-mIgG2b-DANA mutant antibody inhibited MICA shedding to the same extent as nonmutated mIgG2b and mIgG2a forms (fig. S23, A and B). Pretreatment of A375 cells with the 7C6-hIgG1-DANA mutant mAb induced killing by human NK cells, and this effect was blocked with an NKG2D-blocking mAb. This result demonstrates that inhibition of MICA shedding could induce NK cell-mediated cytotoxicity in the absence of Fc receptor engagement (Fig. 3D and fig. S23C). The 7C6-DANA mutant antibody also had therapeutic activity in the B16F10-MICA lung metastasis model, and therapeutic benefit was lost when a NKG2D-blocking antibody was administered (fig. S23, D and E).

These results demonstrate that inhibition of MICA and MICB shedding by 7C6 restored NKG2D-mediated tumor immunity.

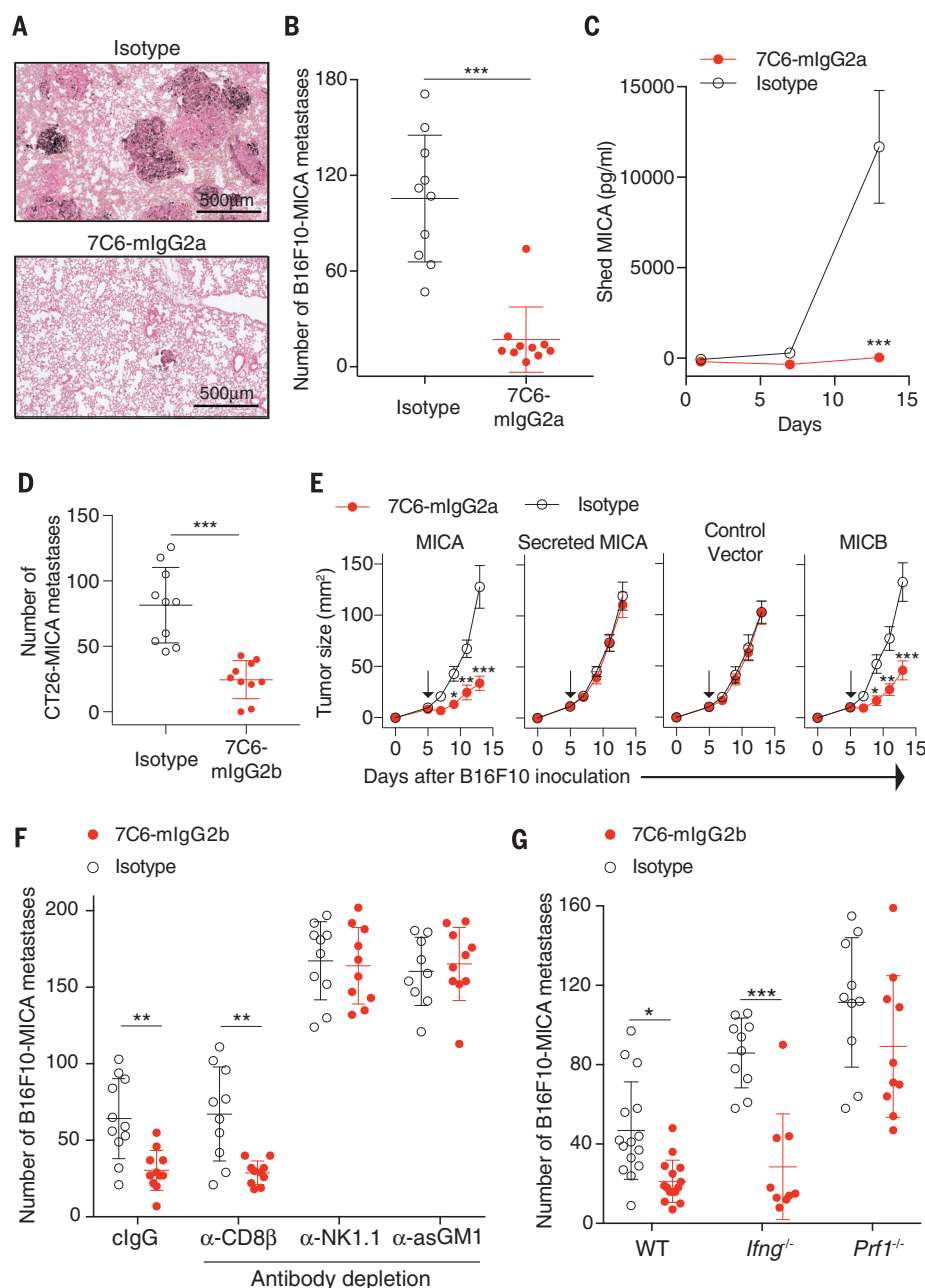
Engagement of multiple activating receptors enhances NK cell effector functions (29, 30). 7C6 mAb with a fully functional Fc region (hIgG1) triggered stronger cytotoxicity by human NK cells than the 7C6-hIgG1-DANA mutant (Fig. 3D). We also addressed the contribution of NKG2D and CD16 Fc receptors to NK cell functions *in vivo* by transfer of wild-type (WT) or mutant NK cells into *Rag2^{-/-} Il2rg^{-/-}* mice that were T cell and NK cell deficient. The most consistent reduction in the number of lung metastases was observed after transfer of WT NK cells. The therapeutic

effect was maintained (but more variable) after transfer of NK cells deficient in either NKG2D (*Klrk1^{-/-}*) or CD16 (*Fcgr3a^{-/-}*). By notable contrast, antibody treatment was ineffective after transfer of NK cells that lacked both NKG2D and CD16 receptors, although shed MICA was still reduced (Fig. 3E and fig. S12D). NKG2D and CD16 Fc receptors were also both required for optimal inhibition of subcutaneous tumor growth (fig. S24, A and B). These data demonstrate that 7C6 mAb activated NK cells through two important receptors, the NKG2D and CD16 Fc receptors.

In the syngeneic tumor models described above, *MICA* and *MICB* gene expression was induced by a heterologous promoter. However,

Fig. 2. Antitumor activity of antibodies that inhibit MICA and MICB shedding.

(A to C) C57BL/6 mice were injected intravenously with B16F10-MICA cells and treated with 7C6-mIgG2a, 7C6-mIgG2b, or isotype control antibodies (200 μ g per injection) on days 1, 2, 7, and 10. (A) Histological analysis (Fontana-Masson staining) of lung tissue demonstrated an apparent reduction in the number and size of metastases in mice that were treated with the MICA antibody (representative of five mice). (B) MICA antibody treatment reduced the number of superficial lung metastases counted by stereomicroscopy on day 14. Data indicate mean \pm SD of pooled data from two independent experiments. (C) Serum concentrations of shed MICA. Data show mean \pm SEM for five mice per group and one representative of two independent experiments. (D) 7C6-mIgG2b antibody had activity against CT26-MICA lung metastases (intravenous injection of tumor cells into Balb/c mice; antibody injection on days 1, 2, 7, and 14; lung metastases counted on day 21). Data indicate mean \pm SD of pooled data from two independent experiments. (E) Analysis of therapeutic activity of 7C6-mIgG2a antibody against subcutaneous B16F10 tumors that expressed full-length MICA or MICB or a secreted form of MICA, or were transduced with control vector. Tumor cells were inoculated into *Igh^{-/-}* mice; treatment with 7C6-mIgG2a or isotype control antibodies was started on day 5 (arrows) and repeated at every tumor measurement. Data show mean \pm SEM for 10 mice per group pooled from two independent experiments. (F and G) Efficacy of 7C6 antibody treatment required NK cells and their cytotoxic function. Same experimental design as in (A) to (C). (F) Quantification of pulmonary metastases in mice that were CD8 T cell depleted (α -CD8 β) or NK cell depleted (α -NK1.1 and α -asGM1). Data indicate mean \pm SD pooled from two independent experiments. (G) Mice deficient for PRF1-mediated cytotoxicity, but not IFN- γ production, were unresponsive to 7C6 mAb treatment. Data indicate mean \pm SD pooled from two independent experiments. * P < 0.05, ** P < 0.01, and *** P < 0.001, calculated by unpaired Student's *t* test (B) and (D) and two-way ANOVA and Bonferroni's post hoc test (C) and (E) to (G).



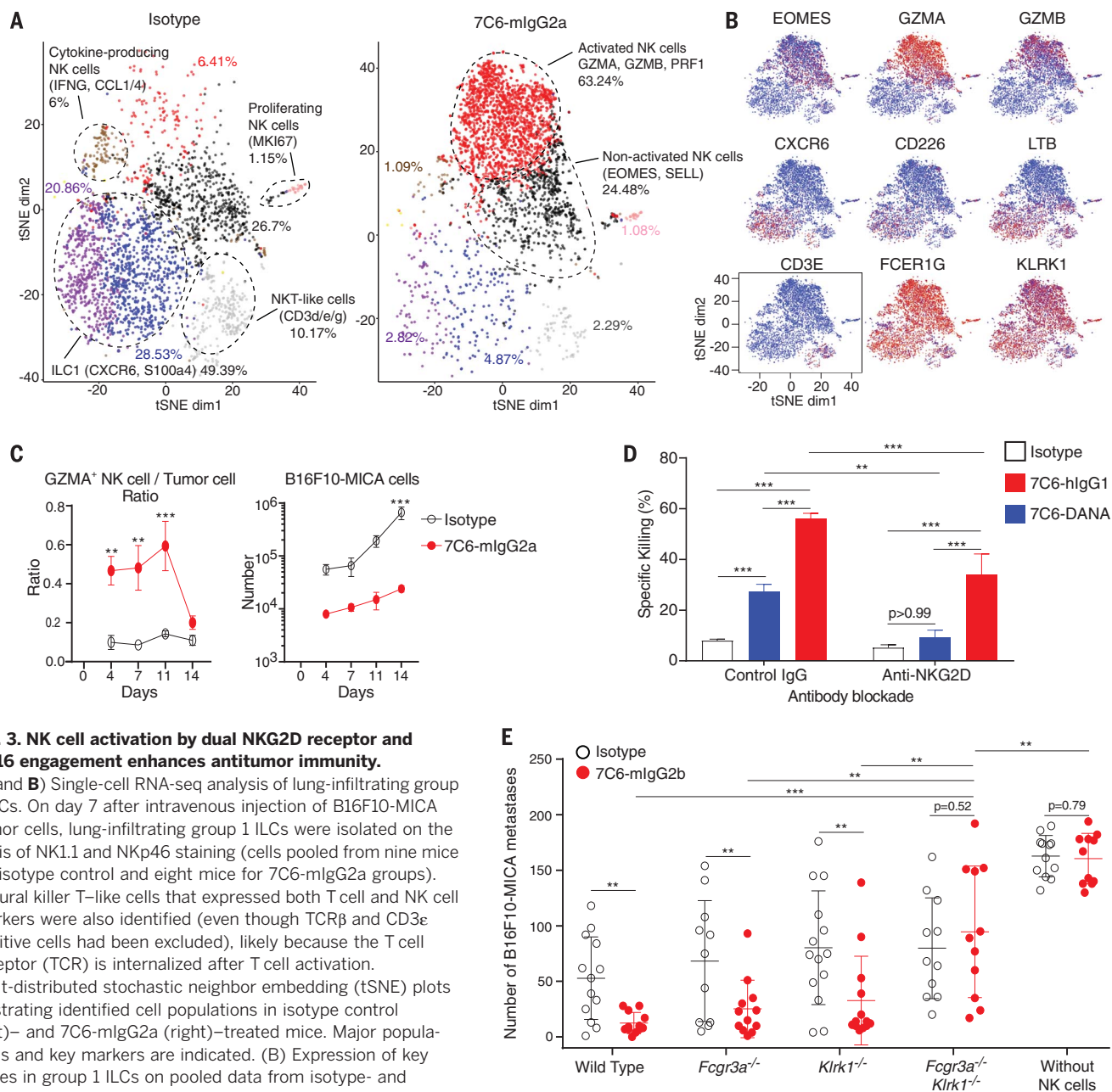


Fig. 3. NK cell activation by dual NKG2D receptor and CD16 engagement enhances antitumor immunity.

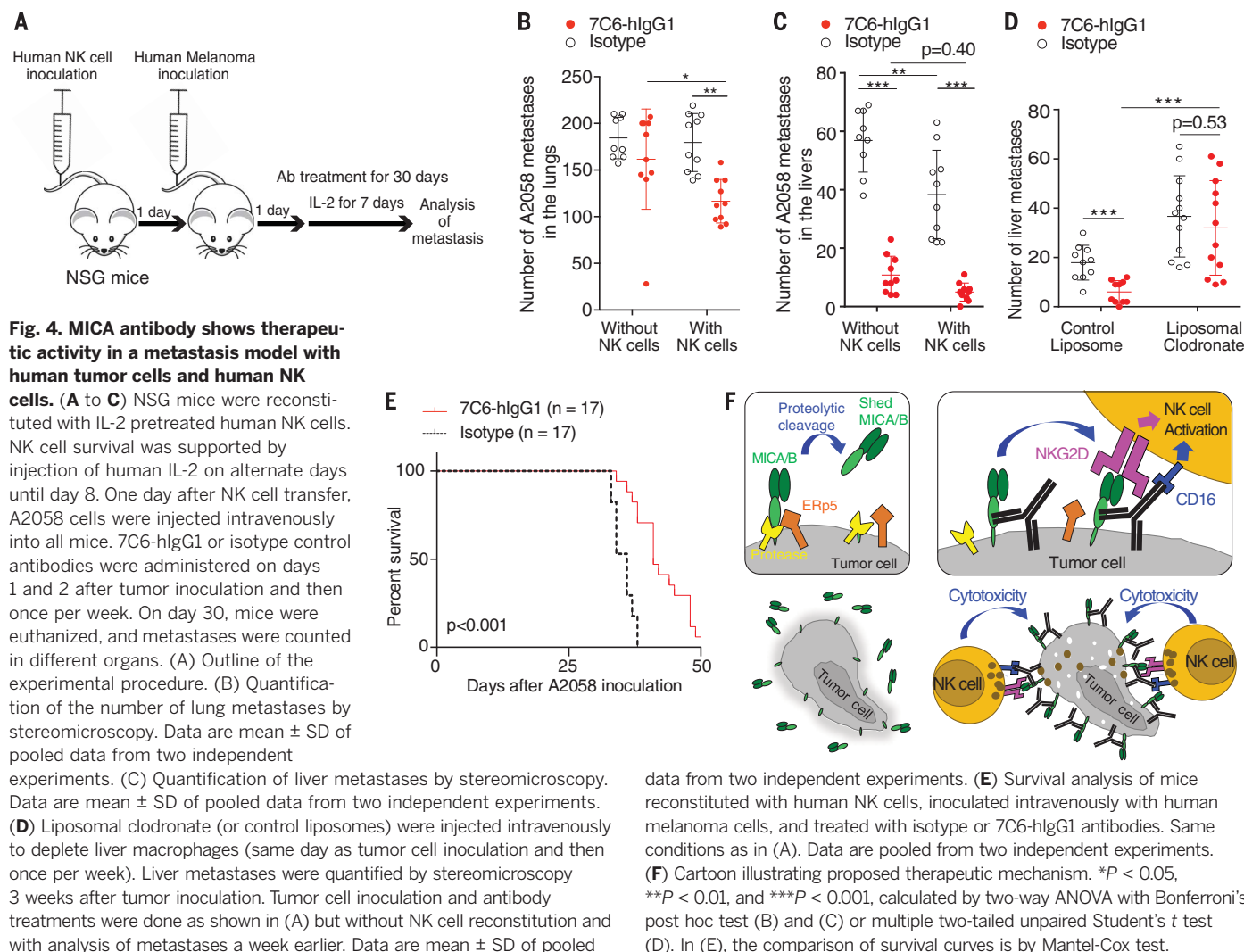
(A and B) Single-cell RNA-seq analysis of lung-infiltrating group 1 ILCs. On day 7 after intravenous injection of B16F10-MICA tumor cells, lung-infiltrating group 1 ILCs were isolated on the basis of NK1.1 and NKP46 staining (cells pooled from nine mice for isotype control and eight mice for 7C6-mIgG2a groups). Natural killer T-like cells that expressed both T cell and NK cell markers were also identified (even though TCR β and CD3 ϵ positive cells had been excluded), likely because the T cell receptor (TCR) is internalized after T cell activation. (A) t-distributed stochastic neighbor embedding (tSNE) plots illustrating identified cell populations in isotype control (left)– and 7C6-mIgG2a (right)–treated mice. Major populations and key markers are indicated. (B) Expression of key genes in group 1 ILCs on pooled data from isotype- and 7C6-mIgG2a-treated groups. FCER1G, Fc epsilon receptor gamma chain. (C) Fluorescence-activated cell sorting analysis of lung-infiltrating activated NK cells (EOMES⁺ GZMA⁺) across indicated time points relative to tumor burden (five mice per group and time point). Data indicate mean \pm SEM; days 7 and 14 are representative of two independent experiments. (D) Contribution of NKG2D and Fc receptor activation to NK cell-mediated cytotoxicity. A375 cells were treated for 48 hours with indicated antibodies and then cocultured for 4 hours with human NK cells in a ⁵¹Cr-release assay. The 7C6-hlgG1-DANA mutant lacked binding to activating Fc receptors. NKG2D recognition was blocked with anti-NKG2D mAb 1D11. Data indicate mean \pm SD and one

representative of three independent experiments. (E) Both NKG2D and CD16 receptors contribute to therapeutic activity of MICA antibody. *Rag2*^{-/-} *Il2rg*^{-/-} mice were reconstituted with WT NK cells or NK cells mutant for NKG2D (*Klrk1*) and/or CD16 (*Fcgr3a*) genes. Mice were then injected intravenously with B16F10-MICA cells and treated with 7C6-mIgG2b or isotype control antibodies, and lung metastases were quantified on day 14. Data indicate mean \pm SD of pooled data from three independent experiments. ***P* < 0.01 and ****P* < 0.001, calculated by two-way ANOVA with Bonferroni's post hoc test (C) and (D) or multiple two-tailed unpaired Student's *t* test (E).

in human cancers, *MICA* and *MICB* gene expression is endogenously activated in response to malignant transformation (7). To test this therapeutic concept with human cancer cells and NK cells, NOD-*scid*IL2Rg^{null} (NSG) mice were reconstituted with human NK cells, followed by

injection of human A2058 melanoma cells (Fig. 4A). IL-2 was injected every other day for a week to support NK cell survival. Inoculation of A2058 cells by an intravenous route resulted not only in lung metastases but, surprisingly, also widespread metastases in many other organs (fig.

S25C). Significantly fewer lung metastases were present in mice reconstituted with human NK cells and treated with 7C6-hlgG1 mAb (Fig. 4B and fig. S25A). Antibody treatment also reduced the spread of metastases to many other organs (fig. S25, C to E). Metastases were particularly



prominent in the liver and caused liver damage, as measured by a serum biomarker (alanine transaminase activity). Interestingly, 7C6-hlgG1 treatment substantially reduced the number of liver metastases and prevented liver damage even without NK cell transfer (Fig. 4C and fig. S26A). Liver-resident F4/80^{high} macrophages (Kupffer cells) that expressed activating Fc receptors (fig. S26B) had higher surface levels of the CD80 activation marker in 7C6-hlgG1 treated mice (fig. S26C). Macrophage depletion with clodronate liposomes abrogated the therapeutic activity of 7C6-hlgG1 antibody against liver metastases (Fig. 4D) but had no negative effect on therapeutic efficacy in the lung metastasis model in immunocompetent mice (fig. S27). Human macrophages cultured *in vitro* express MICA and MICB, and treatment with acetylated low-density lipoproteins, a model of foam cells present in atherosclerotic lesions, increased MICA and MICB expression (31). Treatment with 7C6-hlgG1 antibody inhibited MICA shedding and increased MICA and MICB surface levels on macrophages (fig. S28, A to C). These mechanisms account for the significant survival benefit of

7C6-hlgG1 treatment in this humanized metastasis model (Fig. 4E). These data demonstrate the therapeutic activity of a MICA $\alpha 3$ domain-specific antibody in a humanized metastasis model by activating NK cells and macrophages in an organ-dependent manner.

We found that MICA and MICB $\alpha 3$ domain-specific antibodies substantially increased the density of the stimulatory MICA and MICB ligands on the surface of tumor cells, reduced shed MICA amounts, and induced NK cell-mediated tumor immunity. This therapeutic strategy restores the function of an activating immune pathway that promotes clearance of stressed and transformed cells (Fig. 4F). We propose that the association between MICA and MICB shedding and cancer progression is primarily due to the loss of immunostimulatory NKG2D ligands on the tumor cell surface, although shed MICA may also be a relevant contributing factor. Interestingly, shedding of the high-affinity murine MULT-1 ligand of NKG2D enhances antitumor immunity by inhibiting chronic NKG2D engagement of intra-tumoral NK cells by myeloid cells that express RAE-1, a murine NKG2D ligand (32). Soluble

data from two independent experiments. (E) Survival analysis of mice reconstituted with human NK cells, inoculated intravenously with human melanoma cells, and treated with isotype or 7C6-hlgG1 antibodies. Same conditions as in (A). Data are pooled from two independent experiments. (F) Cartoon illustrating proposed therapeutic mechanism. * $P < 0.05$, ** $P < 0.01$, and *** $P < 0.001$, calculated by two-way ANOVA with Bonferroni's post hoc test (B) and (C) or multiple two-tailed unpaired Student's t test (D). In (E), the comparison of survival curves is by Mantel-Cox test.

MICA and MICB have a substantially lower affinity for the NKG2D receptor than MULT-1, which may explain why shed MICA and MICB do not have such a stimulatory function (7). Given that MICA and MICB are widely expressed in human cancers, MICA and MICB antibodies may hold promise for both solid and hematological malignancies (14, 33–36). Such antibodies could be used in combination with established therapies that induce or enhance MICA and MICB expression through genomic damage pathways, including local radiation therapy or antibody-drug conjugates that deliver toxic payloads to tumor cells (4). MICA antibodies are also of considerable interest as a combination partner with other immunotherapies to activate NK cells and enhance cytotoxic T cell function for protective antitumor immunity.

REFERENCES AND NOTES

1. D. H. Raulet, S. Gasser, B. G. Gowen, W. Deng, H. Jung, *Annu. Rev. Immunol.* **31**, 413–441 (2013).
2. P. Vantourout et al., *Sci. Transl. Med.* **6**, 231ra49 (2014).
3. S. Bahram, M. Bresnahan, D. E. Geraghty, T. Spies, *Proc. Natl. Acad. Sci. U.S.A.* **91**, 6259–6263 (1994).

4. S. Gasser, S. Orsulic, E. J. Brown, D. H. Raulet, *Nature* **436**, 1186–1190 (2005).
5. L. L. Lanier, *Cancer Immunol. Res.* **3**, 575–582 (2015).
6. Y. Hayakawa *et al.*, *J. Immunol.* **169**, 5377–5381 (2002).
7. S. Bauer *et al.*, *Science* **285**, 727–729 (1999).
8. V. Groh *et al.*, *Nat. Immunol.* **2**, 255–260 (2001).
9. B. K. Kaiser *et al.*, *Nature* **447**, 482–486 (2007).
10. P. Boutet *et al.*, *J. Immunol.* **182**, 49–53 (2009).
11. V. Groh, J. Wu, C. Yee, T. Spies, *Nature* **419**, 734–738 (2002).
12. I. Waldhauer *et al.*, *Cancer Res.* **68**, 6368–6376 (2008).
13. L. Raffaghello *et al.*, *Neoplasia* **6**, 558–568 (2004).
14. M. Jinushi *et al.*, *Proc. Natl. Acad. Sci. U.S.A.* **105**, 1285–1290 (2008).
15. S. Holdenrieder *et al.*, *Int. J. Cancer* **118**, 684–687 (2006).
16. Y. Koguchi *et al.*, *Cancer Res.* **75**, 5084–5092 (2015).
17. J. D. Wu *et al.*, *J. Clin. Invest.* **114**, 560–568 (2004).
18. G. Chitadze *et al.*, *Int. J. Cancer* **133**, 1557–1566 (2013).
19. F. Q. Yang *et al.*, *Actas Urol. Esp.* **38**, 172–178 (2014).
20. L. Huergo-Zapico *et al.*, *Cancer Immunol. Immunother.* **61**, 1201–1210 (2012).
21. X. Wang *et al.*, *Biochem. Biophys. Res. Commun.* **387**, 476–481 (2009).
22. P. Li *et al.*, *Nat. Immunol.* **2**, 443–451 (2001).
23. V. Groh, A. Steinle, S. Bauer, T. Spies, *Science* **279**, 1737–1740 (1998).
24. B. Izar *et al.*, *Pigment Cell Melanoma Res.* **29**, 656–668 (2016).
25. F. Nimmerjahn, J. V. Ravetch, *Science* **310**, 1510–1512 (2005).
26. Y. Gao *et al.*, *Nat. Immunol.* **18**, 1004–1015 (2017).
27. J.-C. Lee, K.-M. Lee, D.-W. Kim, D. S. Heo, *J. Immunol.* **172**, 7335–7340 (2004).
28. A. Clayton *et al.*, *J. Immunol.* **180**, 7249–7258 (2008).
29. E. O. Long, H. S. Kim, D. Liu, M. E. Peterson, S. Rajagopalan, *Annu. Rev. Immunol.* **31**, 227–258 (2013).
30. Y. T. Bryceson, M. E. March, H.-G. Ljunggren, E. O. Long, *Blood* **107**, 159–166 (2006).
31. S. Ikeshita, Y. Miyatake, N. Otsuka, M. Kasahara, *Exp. Mol. Pathol.* **97**, 171–175 (2014).
32. W. Deng *et al.*, *Science* **348**, 136–139 (2015).
33. J. Zhang, F. Basher, J. D. Wu, *Front. Immunol.* **6**, 97 (2015).
34. C. S. Vetter *et al.*, *J. Invest. Dermatol.* **118**, 600–605 (2002).
35. D. Pende *et al.*, *Cancer Res.* **62**, 6178–6186 (2002).
36. G. Liu *et al.*, *J. Clin. Invest.* **123**, 4410–4422 (2013).

ACKNOWLEDGMENTS

We thank H.-J. Kim for providing *Rag2^{-/-} γc^{-/-}* mice, C. Sharma for providing the HEPG2 and MDA-MB-231 cell lines, and M. J. Smyth for providing the RMA-S parental cell line. We thank D. Neuberg for advice regarding statistical analyses. **Funding:** L.F.d.A. was supported by a Friends for Life Neuroblastoma Fellowship; D.P. is a Cancer Research Institute–Robertson Foundation Fellow; R.E.T. was supported by an Agency for Science, Technology, and Research (A*STAR) Graduate Fellowship; A.M.L. was supported by a Cancer Immunology Training Grant (T32 CA207021); S.B. was supported by a U.S. Department of Defense fellowship (DOD CA150776); K.F.M. was supported by an American Society of Clinical Oncology Young Investigator Award, a Prostate Cancer Foundation Young Investigator Award, and a National Cancer Institute (NCI) T32 grant; K.W.W. was supported by a grant from NCI (R01 CA173750); and K.W.W. and G.D. were supported by a grant from the Melanoma Research Alliance. **Author contributions:**

K.W.W. and G.D. conceived the study; L.F.d.A., G.D., and K.W.W. designed experimental approaches and interpreted the data; L.F.d.A. characterized antibodies reported in this study and performed therapy as well as mechanistic experiments; R.E.T., Y.L., and L.F.d.A. performed flow cytometry experiments; D.P. analyzed RNA-seq data; S.B. generated some of the recombinant MICA proteins and the B16F10-MICB cell line; A.M.L., D.T., and G.-C.Y. generated single-cell RNA-seq data; B.F. and K.F.M. isolated the first MICA antibody; C.J.H. contributed to early stages of this project; S.K. performed in vivo studies; J.W.P. purified recombinant MICA and MICB proteins; C.Y. provided primary human melanoma cell lines and helped with the design of in vitro functional assays; F.S.H. contributed clinical expertise; and L.F.d.A. and K.W.W. wrote the paper. **Competing interests:** The technology has been licensed by the Dana-Farber Cancer Institute to a pharmaceutical company. B.F., K.F.M., C.J.H., J.W.P., F.S.H., G.D., and K.W.W. are inventors on the relevant patent applications (WO 2014144791 A3, WO 2015179627 A1). **Data and materials availability:** Materials reported in this study are available through a materials transfer agreement with the Dana-Farber Cancer Institute and by contacting K.W.W. RNA-seq data are deposited in the Gene Expression Omnibus database under accession number GSE109542.

SUPPLEMENTARY MATERIALS

www.sciencemag.org/content/359/6383/1537/suppl/DC1
Materials and Methods
Figs. S1 to S28
References (37–39)

8 June 2017; resubmitted 18 December 2017
Accepted 1 February 2018
10.1126/science.aao0505

VIRAL EVOLUTION

Destabilizing mutations encode nongenetic variation that drives evolutionary innovation

Katherine L. Petrie,^{1,2*} Nathan D. Palmer,¹ Daniel T. Johnson,¹ Sarah J. Medina,¹ Stephanie J. Yan,¹ Victor Li,¹ Alita R. Burmeister,³ Justin R. Meyer^{1*}

Evolutionary innovations are often achieved by repurposing existing genes to perform new functions; however, the mechanisms enabling the transition from old to new remain controversial. We identified mutations in bacteriophage λ 's host-recognition gene *J* that confer enhanced adsorption to λ 's native receptor, LamB, and the ability to access a new receptor, OmpF. The mutations destabilize λ particles and cause conformational bistability of *J*, which yields progeny of multiple phenotypic forms, each proficient at different receptors. This work provides an example of how nongenetic protein variation can catalyze an evolutionary innovation. We propose that cases where a single genotype can manifest as multiple phenotypes may be more common than previously expected and offer a general mechanism for evolutionary innovation.

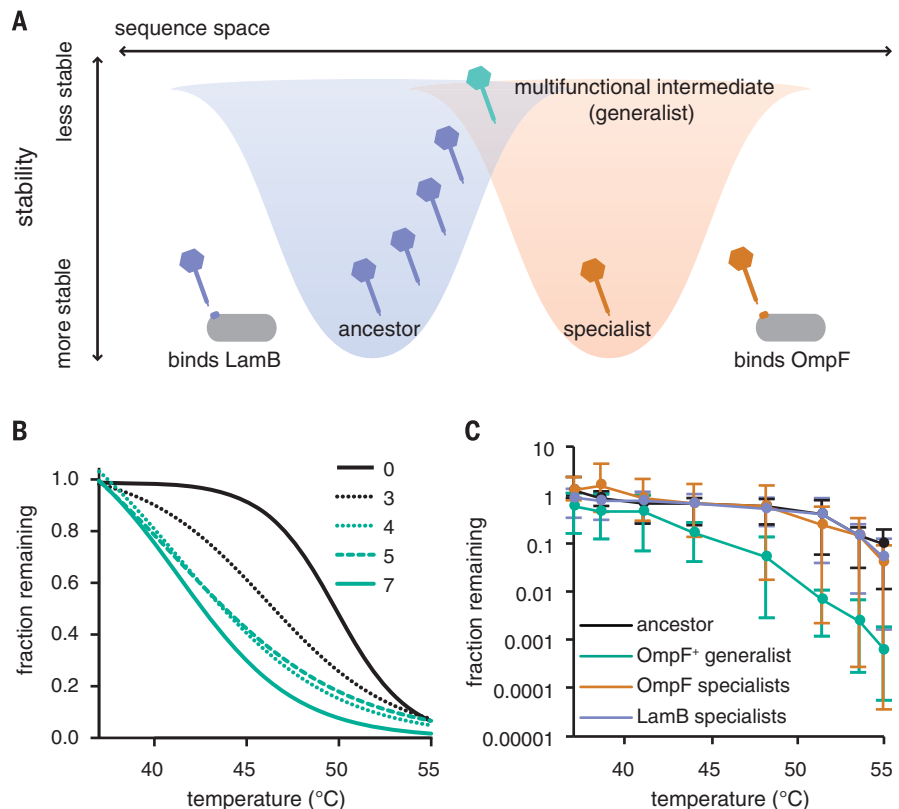
The tree of life is punctuated with numerous biological innovations, but explaining the origin of novelty has been problematic. Natural selection, the predominant theory for adaptation, is unable to explain how mutations encode new function (1, 2). This dilemma is epitomized by the progress made in understanding the evolution of the model virus bacteriophage λ . Under typical laboratory conditions, λ evolves to exploit a new receptor (OmpF) (3). This inno-

vation is achieved through four mutations in its host-recognition gene, *J* (3). The mutations evolve by natural selection because they accelerate adsorption to the original receptor (LamB) (4) and later are coopted for OmpF function (3). Remaining to be explained is how *J* mutations improve LamB adsorption and open access to OmpF. Here we report studies of the molecular mechanisms of *J* mutations and offer an answer to the question of how novelty arises.

Protein functional evolution is typically thought to occur through gene duplication and divergence (5). This model cannot explain λ 's evolution because the *J* gene did not duplicate (3). Instead, λ evolved a promiscuous *J* protein capable of using LamB and OmpF receptors, which then diverged into two receptor specialists (6). The leading explanation for the evolution of promiscuity is through protein-destabilizing mutations that cause structural disorder, allowing proteins to occupy multiple conformations (7–10). Once a promiscuous protein is evolved, additional evolutionary refinement of specific function leads to specialization and restabilization (8, 9, 11) (Fig. 1A).

We tested this hypothesis by measuring the thermostability of five λ genotypes that only varied in the number of *J* mutations. Each strain was genetically engineered with mutations that have been observed to evolve on the path to OmpF⁺ (3). Thermostability was assessed by measuring the temperature dependence of phage survival after 1 hour of exposure to multiple temperatures, ranging from λ 's natural 37°C to a destabilizing 55°C. The number of mutations and the degree of sensitivity were correlated [Spearman's $r = 0.90$, $P = 0.0167$; Fig. 1B and fig. S1 (12)]. One caveat is that nonsynonymous mutations tend

Fig. 1. Evolutionary innovation through functional bistability. (A) Schematic overview of λ evolution. Mutations to improve ancestral receptor binding reduce stability until a critical mutation produces a multifunctional genotype. Further evolution can restabilize the protein. (B) Temperature sensitivity of genotypes with indicated numbers of mutations relative to the ancestor. Some have more than four mutations because λ often evolves additional mutations before achieving OmpF use. The y axis shows the fraction of infectious particles remaining after incubation. Curves are logistic models fit to data from multiple trials; fig. S1 shows all data (12). OmpF⁺ phages are shown in teal, and LamB-reliant genotypes are shown in black. (C) Temperature sensitivity of the ancestor, an OmpF⁺ generalist, and the generalist's specialist descendants. Bars indicate the data range; fig. S2 shows all data.



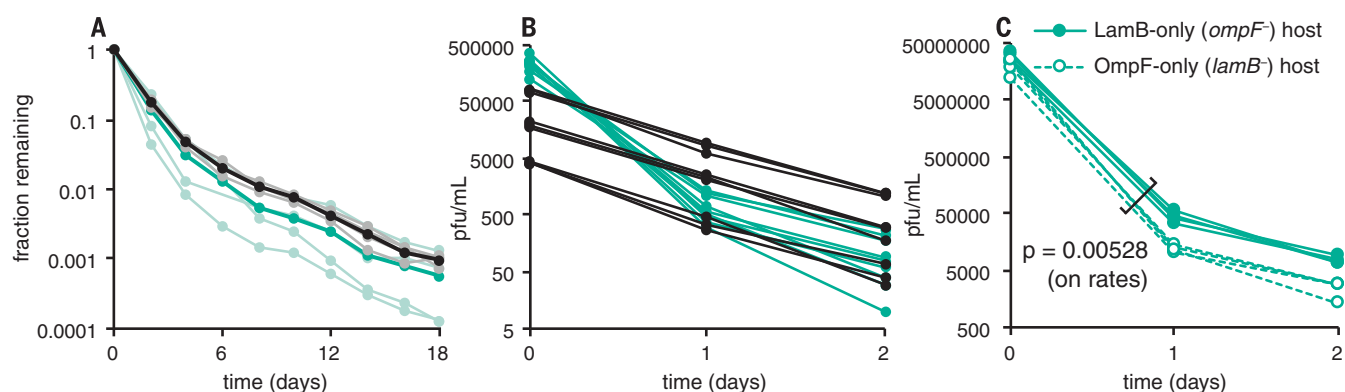


Fig. 2. Decay rate heterogeneity. Decay of ancestor (black) or OmpF⁺ generalist (teal) phage over (A) 18 days or (B) 2 days. Four replicates (pale) and the average (bold) are shown in (A). Individual replicates are shown in (B).

(C) Number of phage particles able to form plaques on LamB-only (solid) or OmpF-only (dashed) bacterial lawns after 2 days. Individual replicates are shown. pfu, plaque forming units.

to destabilize proteins (11), so this relationship is also expected under a null model of protein mutagenesis.

We tested whether additional *J* mutations that cause specialization restabilize the protein. We measured the thermostability of the ancestral λ and an OmpF⁺ generalist variant, as well as 10 of the generalist's descendants that evolved to specialize on either LamB or OmpF (table S1) (6). The null expectation is that all specialists should lose stability because each evolved additional *J* mutations; however, none did. In fact, five out of five LamB specialists and three out of five OmpF specialists regained ancestral stability (fig. S2). On average, the specialists were significantly more stable than the OmpF⁺ generalist [Fisher's method, $X^2(4) = 22.6$, $P = 0.0001$] and indistinguishable from the ancestor [Fisher's method, $X^2(4) = 5.56$, $P = 0.234$] [Fig. 1C; comparisons made at 51.4°C (12)].

An additional investigation of λ particle decay yielded a surprising discovery. We studied the temporal dynamics of the most and least stable strains observed (ancestor and seven mutations; Fig. 1B) decaying at 37°C for 18 days (Fig. 2A). The seven-mutation OmpF⁺ generalist phage decayed at a faster rate, but, unexpectedly, both genotypes decayed at decreased rates over time. If phage stocks contained just a single phage phenotype, then all particles should share a common half-life. Instead, a model of fast-decaying and slow-decaying subpopulations fits the data better than a model of single exponential decay [fig. S3 and table S3 (12)]. Thus, despite originating from an isogenic stock, λ particles exhibit phenotypic heterogeneity: Some are stable and some are unstable. In line with this observation was the previous discovery that genetically identical λ particles can have different rates of LamB adsorption as well (13).

Destabilized promiscuous intermediates may facilitate innovation by permitting proteins to flexibly accommodate different ligands (11, 14), or they may produce polypeptide chains that are sensitive to contingent folding processes that result in multiple isoforms with different capacities (9, 15). Sometimes, the energy barrier between

these isoforms may be high enough to prevent their refolding, making the protein appear conformationally bistable (9, 16). The repeated observations of nongenetic phenotypic heterogeneity suggest that this mechanism may be acting during λ evolution.

To test whether the heterogeneity in decay was related to the mutations spurring the innovation, we reexamined decay dynamics (12). First, we studied whether the accelerated OmpF⁺ decay is due to the emergence of a new, fast-decaying phenotypic class. We found that the decay rate of this strain was significantly faster during the first day of incubation than the second (t test, $t_8 = -14.2$, $P < 0.000001$); there was no significant change in the ancestral λ decay rate over 2 days ($t_8 = -1.35$, $P = 0.214$) (Fig. 2B). This pattern is consistent with a new fast-decaying subgroup that is mostly lost within the first day. Next, we predicted that the newly evolved unstable subgroup was composed of OmpF⁺ particles. We repeated the decay experiment with the OmpF⁺ strain, but we quantified the number of OmpF-binding and LamB-binding particles by plating subsamples on hosts that express only OmpF (*ompF*) or only LamB (*ompF*) (12). The number of particles that produced infections on OmpF lawns declined significantly faster than the number on LamB lawns (t test, $t_3 = -7.31$, $P = 0.00528$; Fig. 2C), indicating that among genetically identical λ particles, we observed unstable OmpF⁺ and stable LamB-reliant particles. We confirmed that the increased frequency of LamB-reliant particles was due to nongenetic heterogeneity and not genetic changes by regrowing LamB-reliant phages and showing that nearly all cultures regained function on OmpF [fig. S4 (12)]. We also confirmed that the instability was not due to proteinase sensitivity [fig. S5 (12)].

Further confirmation that only a fraction of particles can exploit OmpF was gained through an OmpF⁺ pull-down experiment in which λ s that bind OmpF were selectively removed (12). If all λ particles are equivalent, then this assay would not affect the frequency of remaining particles that exploit LamB or OmpF. However, if there is heterogeneity, then we would expect

a decline in the ratio of OmpF⁺ to LamB⁺ particles. OmpF pull-downs preferentially depleted λ s that could form plaques on the OmpF lawns (t test, $t_2 = -5.15$, $P = 0.0357$; Fig. 3A). As a control, we confirmed that this depletion by binding was greater than the decay observed when the incubation was done with no complementary receptors (t test, $t_3 = -4.14$, $P = 0.0255$; Fig. 3B).

Taken together, our results indicate that *J* mutations that move λ toward innovation destabilize the phage and allow it to access multiple phenotypes. We reason that this observed heterogeneity originates from the stochastic folding of individual *J* proteins, because *J* mutations alone are sufficient to alter the heterogeneity. However, because we studied the whole phage, we are unable to confirm whether the heterogeneity is entirely explained by *J* protein variation or whether it stems from an interaction between *J* and the rest of the particle.

Next, we studied how natural selection promotes the evolution of nongenetic phenotypic heterogeneity. We hypothesized that the OmpF⁺ subpopulation is a by-product of selection for improved LamB adsorption and a result of protein misfolding. To test this, we compared the adsorption rates of an OmpF⁺ genotype and its OmpF⁻ progenitor, which is one mutation removed from OmpF function (3). As expected, even the last mutation required for the innovation improved binding to the original receptor (t test, $t_4 = 11.7$, $P = 0.0003$; Fig. 3C). Next, we predicted that the LamB-reliant fraction of OmpF⁺ λ particles should have a faster adsorption rate on LamB than the misfolded OmpF⁺ particles. We measured the adsorption to LamB of the entire population versus that of the LamB-reliant subpopulation by removing OmpF⁺ particles with the OmpF pull-down technique. The pull-down technique enriched the unbound fraction for particles that were 13.4% faster at adsorbing to LamB (t test, $t_8 = 2.77$, $P = 0.0244$; Fig. 3D), indicating that there is a cost for producing the subpopulation of OmpF⁺ particles. This demonstrates that a single gene can evolve to improve two functions simultaneously by expressing multiple forms, even if the functions are antagonistic.

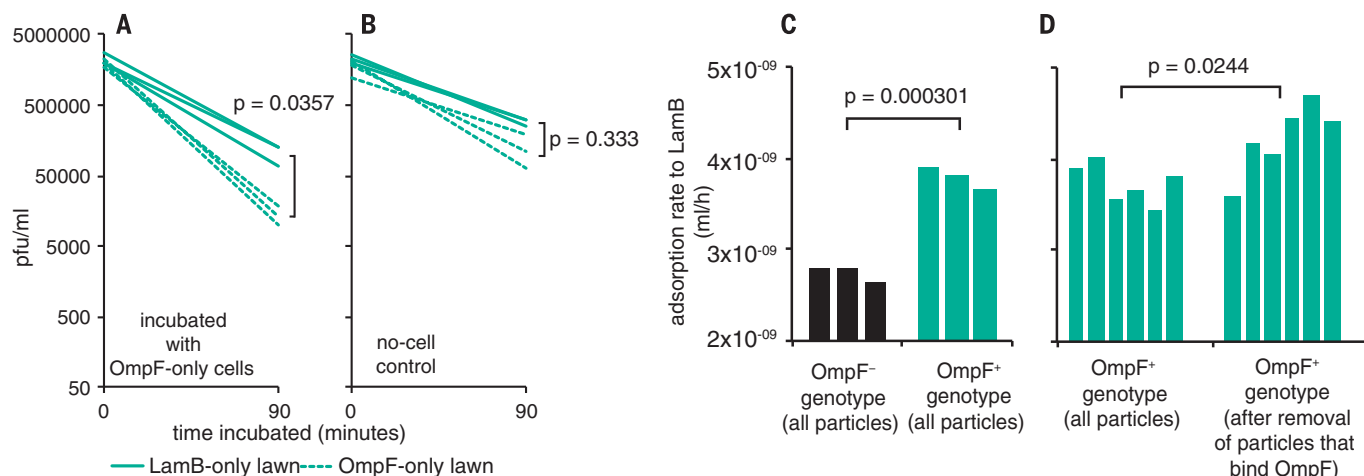


Fig. 3. Isolation and properties of λ subpopulations. A phage pull-down assay shows the number of phage particles capable of infecting LamB-only (solid) or OmpF-only (dashed) hosts before and after incubation (A) in the presence of OmpF-only cells or (B) alone (in the absence of cells). (C) Adsorption

rate to LamB before or after OmpF innovation; genotypes differ by one mutation. (D) LamB adsorption rate of the entire OmpF+ culture compared with that of the LamB-faithful subpopulation. *P* values are from paired *t* tests [(A) and (B)] or standard *t* tests [(C) and (D)]. h, hours.

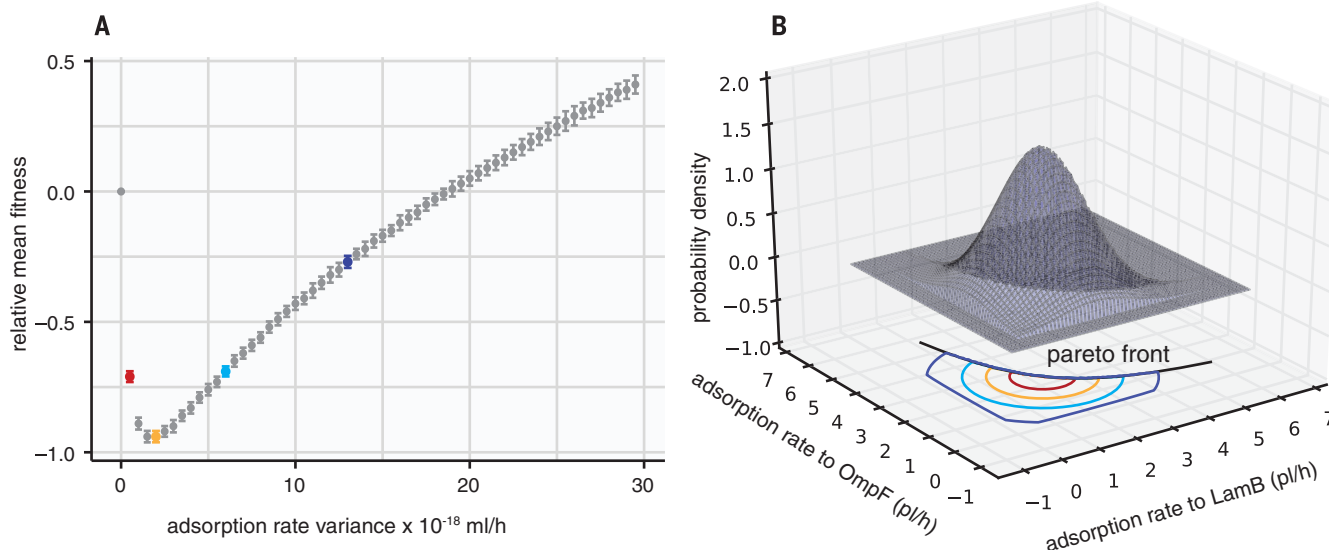


Fig. 4. The fitness of ensembles of phenotypes. (A) Population fitness as a function of phenotypic variance. (B) Example of bivariate normal distribution of phenotypes constrained by a convex Pareto front (19). The variance of the colored points in (A) is the parameter

used to calculate corresponding colored outlines in (B). The outlines represent the largest variance at which 50% of the population is contained. Error bars in (A) represent numerical error in estimating the integrals.

Nongenetic phenotypic heterogeneity may arise by chance, or it could evolve by natural selection if a distribution of phenotypes confers higher fitness than a single type. We tested this by mathematical evaluations of the fitness of generalist λ s that only vary in the width of their adsorption rate distributions. We assumed that the λ particles' adsorption rates to LamB and OmpF are normally distributed but constrained by a trade-off curve (6) and adsorption rates ≥ 0 . We found that small variances resulted in substantial loss of mean population fitness; however, at large variances, this cost was recouped, and fitness exceeded that at zero variance [Fig. 4 (12)].

We show that the OmpF innovation evolved by violating the “one sequence, one structure” dogma (17) with a DNA sequence that encodes

multiple protein forms. This allowed the virus to simultaneously optimize binding to its original receptor and experiment with new functions. Nongenetic heterogeneity in gene expression levels is predicted to facilitate evolutionary novelty (18); here, we extend this hypothesis to the expressed molecules themselves and demonstrate the role of nongenetic heterogeneity in action. Our mathematical model establishes circumstances where nongenetic heterogeneity is adaptive, and thus this mechanism is more likely than if heterogeneity evolved by chance alone.

REFERENCES AND NOTES

1. S. Gavrillets, in *Evolution: The Extended Synthesis*, M. Pigliucci, G. B. Müller, Eds. (MIT Press, 2010), pp. 45–79.
2. H. DeVries, *Species and Varieties, Their Origin by Mutation* (Open Court Publishing Company, 1904).
3. J. R. Meyer et al., *Science* **335**, 428–432 (2012).
4. A. R. Burmeister, R. E. Lenski, J. R. Meyer, *Proc. Biol. Sci. R.* **283**, 20161528 (2016).
5. S. Ohno, *Evolution by Gene Duplication* (Springer, 1970).
6. J. R. Meyer et al., *Science* **354**, 1301–1304 (2016).
7. N. Tokuriki, D. S. Tawfik, *Science* **324**, 203–207 (2009).
8. M. Münz, J. Hein, P. C. Biggin, *PLOS Comput. Biol.* **8**, e1002749 (2012).
9. T. Sikosek, H. S. Chan, *J. R. Soc. Interface* **11**, 20140419 (2014).
10. E. Dellus-Gur et al., *J. Mol. Biol.* **427**, 2396–2409 (2015).
11. N. Tokuriki, D. S. Tawfik, *Curr. Opin. Struct. Biol.* **19**, 596–604 (2009).
12. Supplementary materials.
13. R. Gallet, T. Lenormand, I.-N. Wang, *Evolution* **66**, 3485–3494 (2012).
14. T. Zou, V. A. Risso, J. A. Gavira, J. M. Sanchez-Ruiz, S. B. Ozkan, *Mol. Biol. Evol.* **32**, 132–143 (2015).
15. L. C. James, D. S. Tawfik, *Trends Biochem. Sci.* **28**, 361–368 (2003).
16. J. F. Sinclair, M. M. Ziegler, T. O. Baldwin, *Nat. Struct. Biol.* **1**, 320–326 (1994).

17. S. C. Goodchild, P. M. G. Curmi, L. J. Brown, *Biophys. Rev.* **3**, 143–153 (2011).
18. A. Eldar, M. B. Elowitz, *Nature* **467**, 167–173 (2010).
19. O. Shoval *et al.*, *Science* **336**, 1157–1160 (2012).

ACKNOWLEDGMENTS

We thank A. Gupta and A. Tripathi for help in the laboratory.

Funding: K.L.P. is supported by the ELSI Origins Network, funded by the John Templeton Foundation. A.R.B. was supported by the

U.S. NSF (award DGE-1424871). The ideas expressed herein are not necessarily those of the funders. **Author contributions:** K.L.P. and J.R.M. conceived the project, N.D.P. developed mathematical models, all authors ran experiments, and J.R.M. and K.L.P. wrote the manuscript. **Competing interests:** The authors have none. **Data and materials availability:** Data are deposited at <https://doi.org/10.5061/dryad.fj852>. Biological material is available from J.R.M. under a material transfer agreement with UC San Diego (<http://blink.ucsd.edu/research/conducting-research/mta/index.html>).

SUPPLEMENTARY MATERIALS

www.sciencemag.org/content/359/6383/1542/suppl/DC1
Materials and Methods
Supplementary Text
Figs. S1 to S6
Tables S1 to S6
References (20–37)

12 October 2017; accepted 8 February 2018
10.1126/science.aar1954

CONGRATULATIONS to the 2018 Canada Gairdner Award Laureates

2018 JOHN DIRKS CANADA GAIRDNER GLOBAL HEALTH AWARD



Alan D. Lopez, AC, PhD, FAHMS
*Melbourne Laureate Professor,
Rowden-White Chair of Global Health
and Burden of Disease Measurement,
University of Melbourne*



Christopher J.L. Murray, MD, DPhil
*Director of the Institute for Health Metrics
and Evaluation (IHME); Professor of
Global Health, University of Washington*

Awarded “for their ground-breaking work in
conceptualizing and quantifying the Global
Burden of Disease”

2018 CANADA GAIRDNER INTERNATIONAL AWARD



Davor Solter, MD, PhD
*Emeritus Member and Director, Max
Planck Institute of Immunobiology
and Epigenetics; Visiting International
Professor, Siriraj Center for Excellence in
Stem Cell Research, Mahidol University;
Visiting Professor, University of Zagreb
Medical School*



**Professor Azim Surani, PhD,
FMedSci, FRS**
*Director of germline and epigenetic
research, Wellcome Trust/Cancer
Research UK Gurdon Institute, University
of Cambridge*

Awarded “for their discovery of mammalian
genomic imprinting that causes parent-of-origin
specific gene expression and its consequences
for development and disease”

2018 CANADA GAIRDNER WIGHTMAN AWARD



**Frances A. Shepherd, OC, OOnt, MD,
FRCPC, FASCO**
*Medical oncologist, Princess Margaret
Cancer Centre, University Health
Network; Professor of Medicine,
University of Toronto*

Awarded “for her global leadership in oncology
which has contributed significantly to improving
survival outcomes of lung cancer patients worldwide”

2018 CANADA GAIRDNER INTERNATIONAL AWARD



Peter Hegemann, MD, PhD
*Hertie Professor for Neurosciences,
Experimental Biophysics, Department of
Biology, Humboldt-Universität zu Berlin*



Karl Deisseroth, MD, PhD
*D.H. Chen Professor of Bioengineering
and Psychiatry, Stanford University;
Investigator, Howard Hughes Medical
Institute*



Edward S. Boyden, PhD
*Professor, Departments of Biological
Engineering and Brain and Cognitive
Sciences, Media Lab and McGovern
Institute, MIT*

Awarded “for the discovery of light-gated ion
channel mechanisms, and for the discovery
of optogenetics, a technology that has
revolutionized neuroscience”



CELEBRATING EXCELLENCE

CONVENING LEADERS

INSPIRING THE NEXT GENERATION

gairdner.org

@gairdnerawards

Revolutionizing your confocal imaging.

ZEISS LSM 880 with Airyscan

// INNOVATION
MADE BY ZEISS

Your new standard for fast and gentle confocal imaging

Discover ZEISS LSM 880 with Airyscan: this unique confocal laser scanning microscope delivers perfect optical sections with 120 nm resolution in x/y and 350 nm in z. You get 4–8× higher sensitivity for gentle superresolution imaging. Use the additional Fast mode with acquisition speeds of 27 fps (at 480 × 480 pixels) to follow even the most dynamic processes in your samples.

www.zeiss.com/lsm880





The Next Benchmark

The new refrigerated Centrifuge 5910 R

The Centrifuge 5910 R sets the next benchmark in versatility, capacity and user convenience.

Its main swing-bucket rotor holds both conical tubes and plates – no need to change rotor buckets or adapters. This improves handling and saves time.

- > Max. capacity: 4 x 750 mL or 36 x 50 mL conical
- > Excellent rotor versatility
- > Modern operating system with outstanding functionality
- > Advanced temperature management that keeps your samples safe



www.eppendorf.com/next-benchmark

Eppendorf® and the Eppendorf Brand Design are registered trademarks of Eppendorf AG, Germany. All rights reserved, including graphics and images. Copyright © 2018 by Eppendorf AG.



Expertise on every level

to craft science and technology
solutions in life science

Supelco.

Trusted Analytical
Products

Milli-Q®

Pioneering Lab
Water Solutions

Sigma-Aldrich®

State-of-the-Art Lab &
Production Materials

BioReliance®

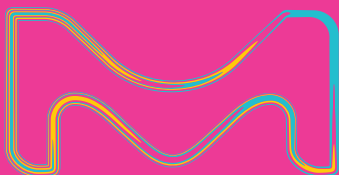
Expert Pharma & Biopharma
Manufacturing & Testing Services

SAFC®

Tailored Pharma & Biopharma
Raw Material Solutions

Millipore®

Proven Preparation,
Separation, Filtration
& Testing Products



MilliporeSigma has brought together the world's
leading Life Science brands, so whatever your life
science problem, you can benefit from our expert
products and services.

To find out how MilliporeSigma can help you work,
visit [SigmaAldrich.com/advancinglifescience](https://www.sigmaaldrich.com/advancinglifescience)

#howwesolve

**The life science business of Merck KGaA,
Darmstadt, Germany operates as
MilliporeSigma in the U.S. and Canada.**

MilliporeSigma, the vibrant M, Milli-Q, Millipore, SAFC, BioReliance,
Supelco and Sigma-Aldrich are trademarks of Merck KGaA, Darmstadt,
Germany or its affiliates. All other trademarks are the property of their
respective owners. Detailed information on trademarks is available via
publicly accessible resources.

© 2018 Merck KGaA, Darmstadt, Germany and/or its affiliates.
All Rights Reserved.

**MILLIPORE
SIGMA**

Every shade of brilliance

for creative science and technology
solutions in life science

Millipore®

Proven Preparation,
Separation, Filtration
& Testing Products

BioReliance®

Expert Pharma & Biopharma
Manufacturing & Testing Services

Sigma-Aldrich®

State-of-the-Art Lab &
Production Materials

Supelco®

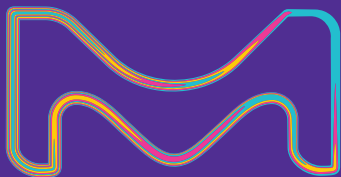
Trusted Analytical
Products

Milli-Q®

Pioneering Lab
Water Solutions

SAFC®

Tailored Pharma & Biopharma
Raw Material Solutions



MilliporeSigma has brought together the world's leading Life Science brands, so whatever your life science problem, you can benefit from our expert products and services.

To find out how MilliporeSigma can help you work, visit SigmaAldrich.com/advancinglifescience

#howwesolve

The life science business of Merck KGaA, Darmstadt, Germany operates as MilliporeSigma in the U.S. and Canada.

MilliporeSigma, the vibrant M, Milli-Q, Millipore, SAFC, BioReliance, Supelco and Sigma-Aldrich are trademarks of Merck KGaA, Darmstadt, Germany or its affiliates. All other trademarks are the property of their respective owners. Detailed information on trademarks is available via publicly accessible resources.

© 2018 Merck KGaA, Darmstadt, Germany and/or its affiliates. All Rights Reserved.

**Millipore
Sigma**

Culture, Food, and Renewable Resources • Anthropology • Astronomy • Atmospheric and Hydrospheric Sciences • Biological Sciences • Chemistry • Dentistry • Oral Health Sciences • Education • Engineering • General Interest in Science • Geology and Geography • History and Philosophy of Science • Information and Technology • Information, Computing, and Communication • Linguistics • Language Sciences • Mathematics • Medical Sciences • Neuroscience • Pharmaceutical Sciences • Physics • Psychology • Social, Economic, and Political Sciences • Social Impact • Space • Statistics • Agriculture, Food, and Renewable Resources • Anthropology • Atmospheric and Hydrospheric Sciences • Biological Sciences • Chemistry • Dentistry • Oral Health Sciences • Education • Engineering • General Interest in Science • Geology and Geography • History and Philosophy of Science • Information and Technology • Information, Computing, and Communication • Linguistics • Language Sciences • Mathematics • Medical Sciences • Neuroscience • Pharmaceutical Sciences • Physics • Psychology • Social, Economic, and Political Sciences • Social Impact • Space • Statistics



**AAAS MEMBERSHIP.
MAKE THE CONNECTION.**

Join AAAS Sections.
They are the foundation
of your AAAS membership

- Be a subject-matter expert.
- Represent your discipline.
- Network with leaders in your field.

aaas.org/sections

AMERICAN ASSOCIATION FOR THE ADVANCEMENT OF SCIENCE

NEW! 3-axis Micromanipulator

- Quiet linear resolution
- 25 mm travel in all 3 axes
- Sub-micron resolution
- User selectable angles
- Compact ROE controller

(TRIO shown with
Sutter IPA headstage)



TRIO™

The new TRIO™-245 from Sutter Instrument is a highly stable 3-axis manipulator with 25 mm of travel on each axis and a synthetic 4th axis that can be set as any angle between 0 and 90 degrees. The lead-screw drive offers improved stability. The compact design of the integrated ROE controller requires minimal bench space and provides quiet, fan-free operation.

SUTTER INSTRUMENT®

PHONE: +1.415.883.0128 | FAX: +1.415.883.0572
EMAIL: INFO@SUTTER.COM | WWW.SUTTER.COM

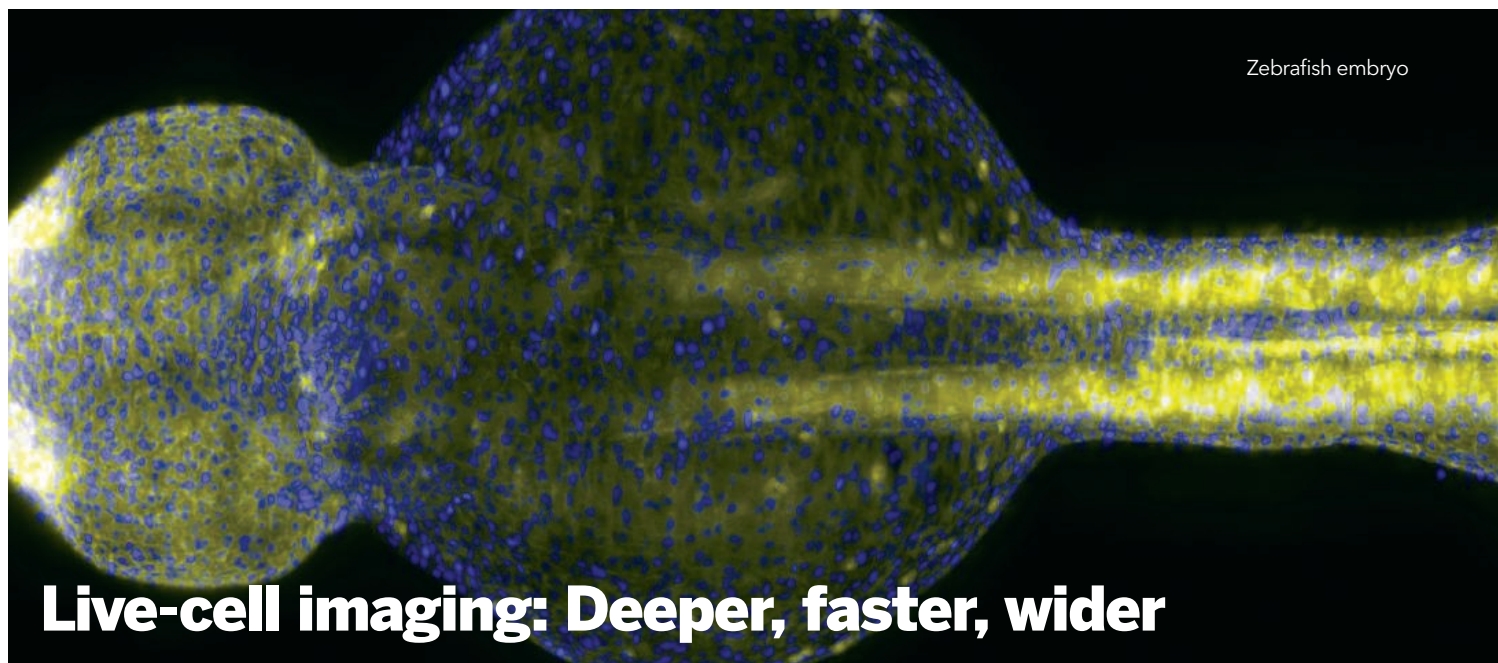
**Submit Your Research for
Publication in *Science Robotics***

ScienceRobotics.org

Science Robotics
AAAS

Send pre-submission inquiries
and expressions of interest to
sciroboteditors@aaas.org.





Zebrafish embryo

Live-cell imaging: Deeper, faster, wider

The field of live-cell imaging has expanded greatly in recent years, but still faces many challenges, such as how to improve spatial and temporal resolution as well as how to keep cells healthy for extended periods of time. Recent developments in multiphoton microscopy, light-sheet microscopy, and Raman microscopy may hold the key to overcoming these issues. **By Amber Dance**

In just 20 hours, a zebrafish embryo advances from a single cell to a 20,000-cell organism capable of twitching its tail. Philipp Keller, as he began his Ph.D. in 2005, wanted to watch how that complexity is built up in such a short time. With embryonic cells migrating as fast as several microns per second, he needed high-speed video that could capture the process.

The answer was light-sheet microscopy, says Keller, now a biologist and physicist at **Janelia Research Campus** near Ashburn, Virginia. The concept is simple, even if the internal optics are not: Illuminate an entire plane of the sample at one time, take a widefield image, then move the plane. This method obtains 3D, live volumes much faster than the point-by-point scanning of a typical confocal microscope. It also exposes individual cells to less toxic light than other techniques do. Thus, light-sheet systems have become the next wave in live-cell imaging for many scientists interested in high-speed cellular activities, such as the firing of neurons or the flowing of blood cells. Other techniques advancing in the live-imaging space include multiphoton microscopy and label-free processes such as Raman microscopy and third harmonic generation imaging.

"Live-cell imaging is—and has always been—the ultimate thing you can do with a microscope," says Christian Hellriegel, an applications specialist at **ZEISS Microscopy** in Jena, Germany. It goes beyond the structure of life and gets to biological processes, including how cells or molecules move, how cells respond to their environment or neighbors, and how the brain works or how injuries heal, he says.

Companies and scientists are developing an array of options, all of which boil down to the following trifecta, says Chris Xu, an applied physicist at **Cornell University** in Ithaca, New York: "Everybody wants to go deeper, everybody wants to go faster, everybody wants to go wider."

Deeper: Multiphoton imaging

To achieve greater depth in microscopy, one solution is multiphoton imaging, says Julian Burke, chief scientific officer of **Leica Microsystems**, in Cambridge, United Kingdom. Leica just launched SP8 DIVE, a multicolor two-photon system that looks deeply into live tissues. The trick is that instead of one photon, it uses two longer-wavelength photons to excite the fluorophore. Those red-der, longer light waves can penetrate deeper into tissues—up to 500 microns at optimal conditions, says Burke—because they're less likely to be scattered by the tissue itself. They're also less toxic and less likely to bleach fluorophores, he adds.

David Monchaud, a chemist at the **University of Burgundy** in France, was drawn to multiphoton imaging for its precision, sensitivity, and ability to image living cells. He studies DNA and RNA quadruplexes, nucleic acid structures that were first visualized via confocal microscopy in fixed, dead cells. Using multiphoton microscopy, he could confirm that quadruplexes exist in living cells, indicating they likely have some function there. "This microscopy was invaluable," says Monchaud.

If two photons are good, might three be better? That's what Xu is investigating. By requiring three photons—of very long wavelength—to activate a fluorophore, he can peer even deeper into a living sample. In 2017, he reported visualization of mouse neurons firing at a depth of 1 millimeter. The microscope could image right through the dense, light-scattering white matter, a feat no prior microscope could achieve, says Xu. Several labs are using the technology to study topics such as cell migration and neuroscience, he says.

Upcoming features

Molecular biology: PCR anniversary—May 11 ■ Proteomics: Big data sharing—June 15 ■ Genomics: Pharmacogenomics—September 28

Faster: Sheets of light

Multiphoton imaging still relies on slow point-scanning, though. “Speed and depth is always the trade-off,” says Xu. And Keller wanted his entire zebrafish embryo scanned in 60–90 seconds, so light-sheet microscopy was the answer.

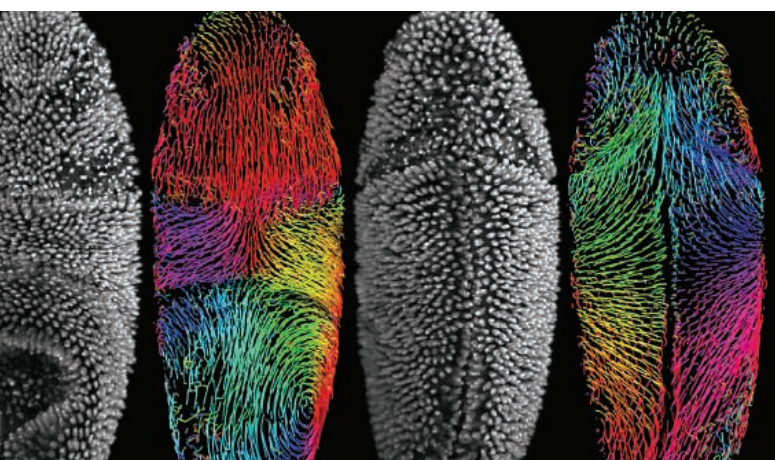
While light-sheet microscopy is an old idea—scientists at ZEISS Microscopy and collaborators first came up with it in 1903—only in this century has the convergence of fluorescent labels that work to process image volumes combined to make light-sheet mainstream. The ZEISS Lightsheet Z.1 microscope includes a life-support chamber that can hold entire organisms—a fruit fly or even a small octopus, for example—dangling in front of the objective, and permits easy rotation for a better point of view.

A 2008 version of Keller’s light-sheet microscope, called digitally scanned laser light-sheet fluorescence microscopy (DSLIM), gave him the speed he craved: 1.5 billion voxels per minute. The design differs from that of a conventional commercial microscope: Keller placed the laser and objective lens at right angles to each other atop a table; then he embedded zebrafish embryos in agarose in a sample tube between the two. He translocated the sample back and forth through the light sheet to hit all planes. He could observe never-before-seen instances of zebrafish embryo development, and the formation of germ layers.

Since then, Keller has updated the technology. One issue was that if a sample is large or opaque, the light sheet might not reach all the way through it. To deal with this, Keller developed SiMView: He doubled the light sheets and cameras to collect four images within 20 milliseconds or less, because each camera can focus on the two sheets in rapid succession.

Another issue he tackled was anisotropy, that is, the fact that a single objective will typically give better resolution in the lateral xy direction than in the axial z direction. To create a 3D image with equal resolution at any viewing angle—a technology called IsoView—Keller doubled the number of cameras and sheets again to four, and digitally combined those images.

IMAGE: JANELIA RESEARCH CAMPUS, HOWARD HUGHES MEDICAL INSTITUTE



Live imaging and computational tracking of cells in an entire developing *Drosophila* embryo undergoing gastrulation (shown are views of the dorsal and ventral sides of the embryo). The nuclei-labeled embryo was imaged with SiMView light-sheet microscopy and computationally reconstructed with the TGMM cell-lineaging framework.

At the **National Institute of Biomedical Imaging and Bioengineering** in Bethesda, Maryland, microscopist Hari Shroff is also interested in developmental neuroscience. In collaboration with scientists at Yale University in New Haven, Connecticut, and the Sloan-Kettering Institute in New York, he’s imaging how the brain of a nematode develops.

“The worm embryo: It’s hard to image, and it’s very sensitive to light,” says Shroff. “You really have to be fast.”

He and his colleagues wanted to avoid the classic light-sheet arrangement in which the sample is embedded in a tube of agarose and surrounded by lasers and cameras. Instead, they preferred to put the worm embryos on standard glass coverslips.

To get the incoming light sheet and observing objectives at right angles to each other, Shroff’s solution was to tilt each by 45 degrees from vertical. The apparatus looks much like a standard microscope, except for the two askew objectives aimed at one stage. The sample stays stationary, and the light sheet from one objective and the other detection objective move in tandem. The system is called inverted selective plane illumination microscopy (iSPIM).

Like Keller, Shroff also dealt with the anisotropy issue, but he didn’t add any more objectives to do it. He simply set each to either produce a light sheet or collect an image, and to alternate between the two. First, objective A produces the sheet and objective B the image, then they swap. The researchers called this arrangement symmetrical dual-view iSPIM (diSPIM).

But Shroff and colleagues weren’t finished. In another version they call triple-view SPIM, they added an extra objective below the coverslip, to collect extra output and improve spatial resolution at no cost to speed, and with no added dose of light. Finally, the researchers experimented with performing diSPIM with a mirrored coverslip. This creates a “virtual image” beyond the looking glass, as if the sample and the light sheets were doubled. With the right algorithms to make sense of it all, Shroff and his team can pull information from those reflections. The result is more sensitive imaging at twice the speed, all for the cost of an aluminum-coated coverslip.

Wider: Living, moving landSCAPEs

Elizabeth Hillman, a biomedical engineer at **Columbia University** in New York, has developed a light-sheet technique that uses only a single objective to both produce the light sheet and to collect all the signals from the sample—which could be an entire, freely moving organism. The system uses a mirror to sweep the light—and the focal point of the camera—through a sample. She refers to her system as “swept confocally-aligned planar excitation” (SCAPE) microscopy.

As with other new light-sheet techniques, SCAPE has the advantage of tremendous speed. With newer cameras, Hillman is imaging more than 100 volumes of sample per second. That allows her to image the cells of awake, moving creatures, such as the flashing neurons of crawling fly larvae or the beating hearts of twitching zebrafish, without the problem of blurring when the animal moves. “We’re going so fast that we can see timing information no one’s ever seen before.” **cont.>**

Featured participants

California Institute of Technology
mr.caltech.edu

Columbia University
www.columbia.edu

Cornell University
www.cornell.edu

**Hunter College, City University
of New York**
www.hunter.cuny.edu

Imperial College London
www.imperial.ac.uk

Janelia Research Campus
www.janelia.org

Leica Microsystems
www.leica-microsystems.com

**National Institute of Biomedical
Imaging and Bioengineering**
www.nibib.nih.gov

Osaka University
www.osaka-u.ac.jp/en

University of Burgundy
en.u-bourgogne.fr

ZEISS Microscopy
www.zeiss.com/microscopy/us/
home.html

It's easy to adapt the SCAPE objective to a variety of sample types, says Hillman. The cells or organisms could be in a plate or dish, or in the head of a mouse; it doesn't matter.

Columbia has licensed the SCAPE technology to Leica, though Burke is not certain when Leica's SCAPE system will be available. Leica has also licensed another sheet-sweeping technology, the oblique plane microscopy (OPM) developed by Chris Dunsby, a biomedical optics researcher at **Imperial College London**.

Dunsby's goal was to perform light-sheet microscopy with a single objective, while maintaining good resolution. His technique uses three microscopes in succession to magnify the sample, capture light from the tilted plane, and sweep the light sheet.

The complete setup offers high-speed, 3D imaging with subcellular resolution, says Dunsby. For example, he's used it along with a calcium-tracking dye in cardiac muscle cells from a rat, to image the sparks and waves of calcium ions that can trigger deadly arrhythmias during heart failure. "We were able to see for the first time, in 3D, where calcium waves come from in cardiac myocytes," he explains.

OPM also works in multiwell plates. Dunsby and colleagues used it to measure glucose uptake, indicated by a fluorescent biosensor, in multicellular kidney cell spheroids. Imaging 42 wells took 9 minutes.

What's next?

SCAPE and OPM complement each other nicely, says Burke, and Leica plans to combine the two in an upcoming product.

What's next for live-cell imaging? "I don't think we have explored the full capabilities of light sheet yet," says Hellriegel. For example, he suggests that superresolution techniques might be incorporated into light-sheet imaging.

Burke predicts more fluorescent proteins and dyes that indicate cellular events (e.g., neurotransmission) will make real-time, rapid imaging appealing to many scientists. He also anticipates that faster, more sensitive cameras will be needed—and developed—for speedy imaging.

Labels and the lack thereof

Sometimes, scientists don't want to use fluorescent tags. For one thing, it can be tricky to introduce them into samples. It's also hard to be certain that the fluorophore accurately reflects the location and activity of the target protein. The label might not find the protein efficiently, or might photobleach over time.

Biophysicist Hyungsik Lim at **Hunter College, City University of New York**, uses third harmonic generation (THG) microscopy to image myelin—the "insulation" around nerve "wires"—in live cultures and tissues without adding any labels. THG generates a signal when the energy from three incoming photons is combined into one outgoing photon. The technique is particularly sensitive to boundaries where the refractive index of a tissue changes, such as those between aqueous solutions and lipid- or protein-rich structures, such as myelin.

Another option is Raman microscopy, a scanning version of Raman spectroscopy, says Katsumasa Fujita, an applied scientist at **Osaka University** in Japan, who is introducing Raman to the microscopy world. Raman spectroscopy relies on the incoming light of a single wavelength to excite the molecules in a sample. The photons that make up this light bounce, or scatter, off the molecules in the sample, mostly at the same wavelength they had coming in. But every so often (about one in 100 million photons), a photon will bounce off with a different wavelength, shifted to a lower, more reddish frequency. The frequency of the shifted light depends on the molecule it scattered from. In this way, Raman spectroscopy can identify the components of a sample.

Under the life-science microscope, Raman scattering works in a similar way, providing a profile of the component molecules in a specimen—whether it is DNA, protein, or lipid. However, it can't distinguish much beyond that; for example, it can't tell one kinase from another.

Meanwhile, researchers at Columbia University in New York are working on a way to add dozens of color labels to Raman-imaged cells. Traditional fluorescence imaging maxes out at around five colored labels, because the broad ranges of wavelengths emitted by the fluorophores overlap, points out biophysical chemist Wei Min. But the wavelengths emitted in Raman spectroscopy fall into a much tighter range, so it ought to be possible to use many more colors without that overlap.

A former postdoc of Min's, Lu Wei, now a chemistry professor at the **California Institute of Technology** in Pasadena, took on the challenge. She and her colleagues designed 24 different fluorescent dyes by varying the triple carbon-carbon bonds, triple carbon-nitrogen bonds, and isotope content to create different colors.

Now, Wei and Min are working on more colors and methods to link the dyes to specific biomolecules or organelles of interest—Min thinks 50 or more colors should be possible.

Amber Dance is a freelance writer living in Los Angeles.



35-mm Imaging Dish
ibidi's μ -Dish 35-mm Quad is a four-compartment cell culture dish that guarantees brilliant optical quality. The subdivisions enable up to four parallel, individual experiments in one dish, where applications such as transfection,

immunofluorescence staining, and live-cell imaging can be conveniently performed. Quad is the ideal solution for scientists who conduct simultaneous, multiplex analysis of different cell lines or apply distinct experimental conditions. The subdivisions not only save time, but also decrease experimental costs by reducing the cell numbers and reagents needed. Its unique ibidi Polymer Coverslip Bottom guarantees superior optics for high-end microscopy. Excellent phase contrast is provided by the centered plate construction. This Ph+ (Phase Contrast +) feature avoids any meniscus effect and facilitates homogenous cell growth.

ibidi

For info: 844-276-6363
www.ibidi.com

Apoptosis/Necrosis Detection Kit

Enzo Life Science's GFP-CERTIFIED Apoptosis/Necrosis Detection Kit detects four distinct cell states: viable cells, early apoptotic cells, late apoptotic cells, and necrotic cells. Plasma membrane integrity and the display of phosphatidylserine on the plasma membrane's extracellular face are both hallmarks of apoptosis, and are used in this kit to distinguish apoptosis from necrosis. The kit features true multiplexing capabilities with green fluorescent protein (GFP) and other green fluorescent probes, and is optimized for both fluorescence microscopy and flow cytometry applications. It is validated for use with live or postfixed cells in conjunction with probes, and identifies each stage with high specificity, sensitivity, and convenience. The transition from apoptosis to necrosis is a loosely defined continuum that is crucial for understanding the development, homeostasis, and pathogenesis of different diseases; it is necessary to identify the various stages of this process to truly understand the role it plays in fields such as cancer and neuroscience research, drug discovery, and more.

Enzo Life Sciences

For info: 800-942-0430
www.enzolifesciences.com

Spinning Disk Confocal Superresolution Microscope

With resolving power that surpasses the limits of conventional optical microscopes, the Olympus IXplore SpinSR10 imaging system balances speed, resolution, and efficiency in a single, flexible platform. A high frame rate and 120-nm XY resolution enable researchers to observe the fine details and workings of internal cellular structures while offering the ability to switch between superresolution, confocal, and widefield imaging modes. The SpinSR10 can quickly image as deep as 100 μ m into regions that can be hard to access using traditional superresolution methods. A suite of features helps minimize phototoxicity and photobleaching when capturing 3D images, prolonging the viability of live cells during time-lapse imaging. Researchers get these benefits without having to change their existing fluorescence-labeling protocols—

so live-cell, superresolution images can be captured using conventional fluorescent dyes.

Olympus

For info: 781-419-3900

www.olympus-lifescience.com/advanced-imaging-solutions/spinsr10

Plate Reader

The EnSight Multimode Plate Reader is a benchtop system that offers well-imaging along with label-free and labeled detection technologies. Its imaging module and easy-to-use Kaleido 2.0 data acquisition and analysis software allow you to image a 384-well plate in less than 5 min., a two-color image in around 6 min., and a three-color image in around 7 min. With its image cytometry capabilities, you can quickly and easily generate per-cell data, whether you're using fixed or live cells, performing end-point assays, or taking kinetic measurements over time—opening up a broad range of cell-based applications. The system's speed makes it ideal for assay optimization and for assessing cell-based assay quality to reveal cell-seeding errors, improper liquid handling, and bacterial contamination. You can use ready-made, click-and-go protocols or build your own from the toolbox, and the plate stacker gives you the convenience of walkaway operation.

PerkinElmer

For info: 800-762-4000

www.perkinelmer.com/ensight/index.html

Live-Cell Incubator Imager

Etaluma's high-resolution, versatile, and compact inverted LS Microscopes (Lumascopes) actually fit inside your incubator, giving you stable temperatures and CO₂ levels throughout your assays. They perform three-color fluorescence, phase-contrast, and brightfield microscopy, and can accommodate 1.25–100X objectives. Choose from an automated XY stage with autofocus in Z (LS720) or a manual stage (LS620) and get images, time-lapse series, and videos recorded directly to your computer. These fully functioning microscopes empower users to visualize cells from microplates, dishes, flasks, slides, microfluidic chips, or custom labware. Their quality is comparable to that of traditional, high-cost microscopes—you can finally get the big picture without the big-ticket price.

Etaluma

For info: 760-298-2355

www.etaluma.com/live-cell

Digital Imaging System

The CELENA S is a small, powerful digital imaging system that simplifies imaging and data analysis. Integrating advanced precision optics, a highly sensitive scientific-grade complementary metal oxide semiconductor (CMOS) camera, and a computer with user-friendly software, it allows researchers to capture vivid, publication-quality images with ease. Interchangeable objectives and filter cubes accommodate a wide range of imaging needs. Researchers can use the CELENA S for multiple applications, such as capturing and analyzing multicolor fluorescence images, live-cell imaging, and automated cell counting. The new onstage incubation system features an environmental chamber, temperature controller, and gas mixer. Researchers can control temperature, humidity, and gas content with precision. Live cells can be monitored with the time-lapse function or the growth monitor.

Logos Biosystems

For info: +82-(31)-478-4185

logosbio.com/digital_microscope/CELENA_S/features.php

Electronically submit your new product description or product literature information! Go to www.sciencemag.org/about/new-products-section for more information.

Newly offered instrumentation, apparatus, and laboratory materials of interest to researchers in all disciplines in academic, industrial, and governmental organizations are featured in this space. Emphasis is given to purpose, chief characteristics, and availability of products and materials. Endorsement by *Science* or AAAS of any products or materials mentioned is not implied. Additional information may be obtained from the manufacturer or supplier.

Step up your job search with *Science* Careers



- Access thousands of job postings
- Sign up for job alerts
- Explore career development tools and resources



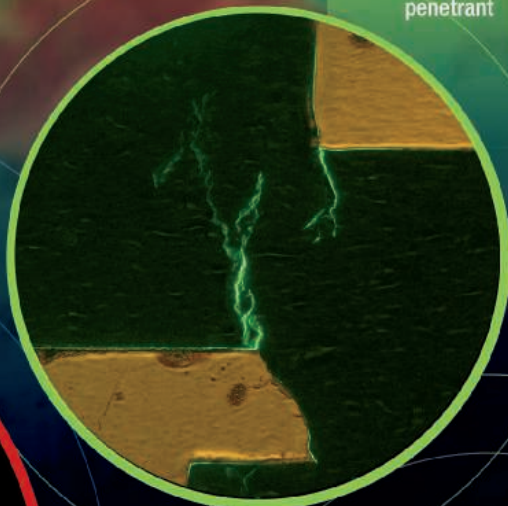
Search jobs on **ScienceCareers.org** today

there's more to see...

WITH FLUORESCENCE

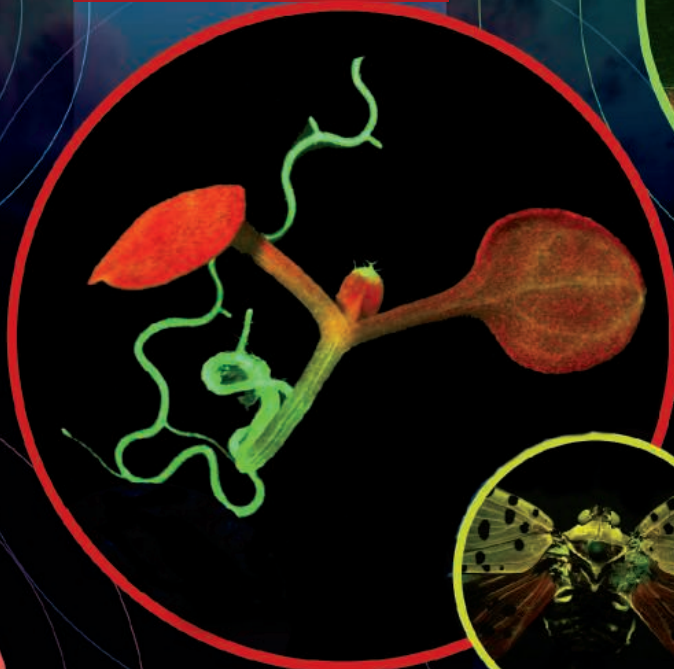
INDUSTRY

Crack feature,
fluorescent
penetrant



LIFE SCIENCE

Arabidopsis sp. expressing green
fluorescent protein (GFP) in roots



FORENSIC SCIENCE

'Dust bunny' under
blue excitation



PHOTOGRAPHY

Inchworm on leaf,
fluorescence, Maine



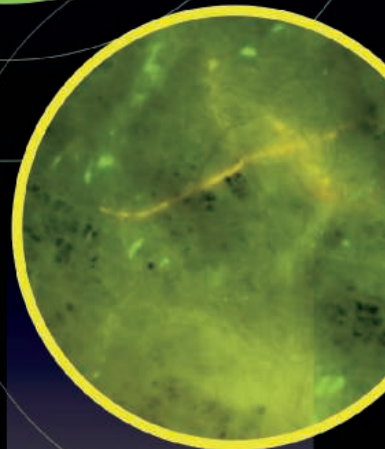
ENTOMOLOGY

Natural fluorescence of a
Leafhopper



ENVIRONMENTAL SCIENCE

Microplastics in the oceans
and water supplies, the food
chain, and consumer prod-
ucts have become pervasive.



PRACTICAL SOLUTIONS FOR VIEWING AND PHOTOGRAPHING FLUORESCENCE

NIGHTSEA

Fluorescence Viewing Systems

Fluorescence has diverse applications in science, education, art, forensic sciences, industry and more. NIGHTSEA provides complete solutions – light sources and matched filters – for viewing and imaging fluorescence. With both off-the-shelf and customized equipment Fluorescence Viewing Systems have helped thousands of customers around the world enter this hidden spectral realm.



**CONTACT US FOR
MORE INFORMATION...**

**Electron
Microscopy
Sciences**

P.O. Box 550 • 1560 Industry Rd.
Hatfield, Pa 19440
Tel: (215) 412-8400
Fax: (215) 412-8450
email: sgkcck@aol.com
or stacie@ems-secure.com
www.emsdiasum.com



Astronomy at Peking University

PKU astronomy encompasses the Department of Astronomy (DoA) and the Kavli Institute for Astronomy and Astrophysics (KIAA), the latter being jointly supported by PKU and the Kavli Foundation, USA. With DoA and KIAA working closely, PKU astronomy has established a high-level international research team through worldwide recruitment. It currently has 25 faculty members (30% are non-Chinese), 30 postdoctoral fellows (60% are non-Chinese), 104 undergraduate students and 59 graduate students. The research includes four major areas of astrophysics: (1) cosmology, galaxy formation and evolution; (2) interstellar medium, stellar and planetary systems; (3) gravitational physics and high-energy phenomena; and (4) computational astrophysics. Recent years have witnessed a number of research findings with considerable international impact.

In 2014, Prof. Fukun Liu and his colleagues found a pair of supermassive black holes in an ordinary galaxy for the first time. This discovery was praised for “really changing the way we think about the universe, and opening up whole new areas for astronomers to study” by international colleagues.

In 2015, Prof. Xuebing Wu’s team discovered the most luminous quasar with a central black hole mass of 12 billion solar masses in the early Universe, the most massive black hole discovered at redshift greater than 6. This finding seriously challenged black hole formation and galaxy evolution theories. Published in *Nature*, it was selected as one of the top 10 major scientific achievements of the year in China.

In 2016, Prof. Subo Dong discovered the most luminous supernova ever seen, which may lead to new ideas and new ob-

servations of the whole class of superluminous supernovae. Published in *Science*, it was selected as one of the top 10 achievements in astronomical science and technology of the year in China.

In 2015-2016, former PhD student Chengyuan Li published two papers in *Nature*: after finding that intermediate-age star clusters can be composed of a single-generation stellar population, he and his colleagues discovered young populations of stars within globular clusters that have apparently formed from gas flowing in from outside of the clusters themselves.

More achievements are demonstrated by the many prestigious projects and awards, such as the National Key Program for Science and Technology Research and Development sponsored by the Ministry of Science and Technology (MOST) of China, and the Group Innovation Award granted by the National Science Founda-

tion of China. The PKU astronomy group also plays significant roles in the majority of large astronomical research facilities and initiatives involved by China, including NGPS, LAMOST, FAST, QTT, JCMT, TMT, SKA, etc., and serves as key coordinator for the China-US ‘10+10’ program in astronomy, which promotes scientific cooperation and exchange in astronomy between 10 United States universities and 10 Chinese universities.

PKU has become one of the most important platforms for cultivating talent and conducting cutting-edge scientific research in astronomy, generating impact around the world.

Feel free to contact us:

Tel: +86-10-6275-6630

Email: shuyan@pku.edu.cn

<http://kiaa.pku.edu.cn/>

<http://vega.bac.pku.edu.cn/astro/astro.htm>

Credit: ESA - C. Carreau.



Credits: Zhaoyu Li. The background images are from NASA/JPL-Caltech and Misti Mountain Observatory



Credit: ESA/Hubble & NASA. Acknowledgment: Judy Schmidt (geckzilla.com)



Credit: Beijing Planetarium / Jin Ma



Energy and Resources Engineering at Peking University



The Department of Energy and Resources Engineering (DERE) at Peking University, committed to cutting-edge research on engineering problems related to energy and environment, has a reputation for its research on the development of unconventional fossil energy and renewable energy sources, as well as on the cyclic utilization of resources.

Professor Dongxiao Zhang, the dean of the college, is leading his team to conduct fundamental research on the mechanisms and technologies

of unconventional oil and gas development, such as shale gas/oil, coal bed methane and natural gas hydrate. Professor Hailong Lu and his group are dedicated to the fundamental studies of the physical and chemical properties of natural gas hydrates for the development of production and survey technology, providing strong technical support for China's first production test of marine gas hydrate in the South China Sea.

DERE has developed several new energy sources such as new solar cells,

lithium battery materials, biomass fuel, and microorganisms (including microalgae) as single-cell factories for biofuels. Xiaowei Zhan and his team created a brand-new nonfullerene acceptor system, the Fused-ring Electron Acceptor (FREA), which is recognized as the best-performing nonfullerene acceptor system and has been adopted by many research groups across the world to fabricate high-performance organic photovoltaics (OPV) with efficiencies exceeding 14%, far superior to fullerene-based OPV (11-12%). The emergence of such a high-performance fullerene acceptor as FREA has begun to marginalize previously predominant acceptors in OPV, inaugurating a new era of OPV technology.

DERE is pioneering new environmental techniques and unconventional resources utilization. Hao Wang and his group has made a breakthrough by developing a nanoscale detection method, i.e. Joints of Interfaces, on the triple-phase contact lines and detected dynamic nanoscale information which was urgently needed for long-standing debates. They created self-driven and aligned moving contact lines on both solid and solution surfaces, which can

be used in systems to achieve fast, environmentally friendly, and large-scale fabrication of materials like solar perovskites. They have also developed a smart bubbling scrubber that allows fume gas to be quickly cleaned through interaction with bubbles. Professor Xidong Wang, chair of DERE, is conducting research on the efficient recycling of solid waste resources and residual energy. Various environmentally-friendly material products, by coupling waste resources and residual energy, have been researched, invented, and widely used in industrial production.

DERE has established many laboratories, such as the Beijing Key Laboratory for Advanced Battery Materials and the Beijing Key Laboratory of Solid Waste Utilization, in order to facilitate interdisciplinary research on energy and resources. Outstanding scholars in relevant research areas are warmly welcome to contact DERE at PKU. Feel free to contact us at:

<http://en.coe.pku.edu.cn/Energy-Resources-Engineering/index.htm>

Tel: +86-10-82529077

Fax: +86-10-82529010

Email: gnyx@pku.edu.cn

Space Sciences at Peking University

The discipline of space sciences was initiated at Peking University in 1959, only two years after the successful launch of the first manmade spacecraft that marked the start of the space era. Peking University has listed space science as one of its key cross-disciplinary sciences. The Institute of Space Sciences and Applied Technology (ISPAT) offers undergraduate and graduate programs in five major fields of space sciences: solar and heliospheric physics, magnetospheric physics, ionospheric and upper atmospheric physics, space weather, and space exploration.

ISPAT has been conducting high-impact research. For instance, ISPAT is undergoing a NSFC (National Natural Science Foundation of China) Creative Research Group project, led by Prof. Qiugang Zong, to comprehensively investigate the acceleration, transportation, and effects of energetic particles in solar-terrestrial space. ISPAT has achieved a number of scientific breakthroughs in the field of space physics: the discovery of the unusual, isotropic superhalo electrons in the interplanetary space

that are probably originated from the magnetic reconnections in solar nano/micro-flares, the establishment of the double-component theory of kinetic turbulence in the solar wind, the proposal of the fast acceleration mechanism of inner-magnetospheric particles via ULF waves, the discovery of the sudden flux drop and subsequent dropout echo of the outer radiation belt electrons that are triggered by interplanetary shocks, the proposal of the drift-echo mechanism to account for a zebra-like pattern of inner radiation belt elections, the discovery of an inverted V-type spectral structure that is generated by the upflowing oxygen ions while accelerated along the magnetic field in the polar regions, etc.

On the other hand, ISPAT has been conducting the design and development of space-borne instrumentation. For instance, the particle radiation detector on board the China-Brazil Earth Resources Satellite has successfully probed the inner radiation belt by monitoring the radiation environment inside the spacecraft. Recently, the Imaging Electron Spectrometer (IES),

developed by ISPAT, has been flown on one Beidou Navigation Satellite, to monitor the outer radiation belt and especially explore the wave-particle resonance interactions.

In May 2017, Peking University established the Center of Planetary and Space Sciences upon ISPAT, aiming to provide a world-class research and education platform for space sciences.

ISPAT will expand its efforts in all fields of space sciences, in order to explore the heliosphere - the home of human beings in the universe. Specifically, ISPAT will explore the acceleration and transport of energetic particles from the Sun and in the heliosphere, the solar origin and interplanetary transport of solar wind and coronal mass ejections, as well as the interactions between solar wind and interstellar wind at the outer heliosphere and beyond. It will also conduct comparative planetology studies, especially aiming to investigate the loss of planetary atmosphere and the origin and evolution of planetary magnetic field/magnetosphere.

Since the space-borne instrumen-

tation is a major pacing factor of space sciences, ISPAT will focus on the design and development of the new-generation instrumentation and technology, including the multi-pitch-grid Energetic Neutral Atom Imager that provides the unique way to observe the physics processes in space plasma. ISPAT will also continue participating in China's Mars and Jupiter Exploration Programs, as well as the prospective Magnetosphere-Ionosphere-Thermosphere Coupling Exploration Program (PI: Prof. Suiyan Fu from ISPAT).

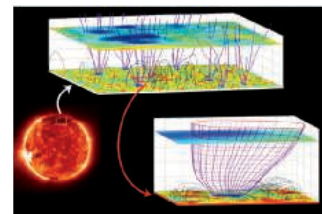
For more information, please refer to:

<http://www.space.pku.edu.cn/en/>

Or Contact Prof. Qiugang ZONG

Email: qgzong@pku.edu.cn,

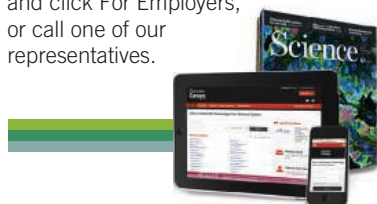
Tel: +86-10-62767422



Science Careers

SCIENCE CAREERS ADVERTISING

For full advertising details, go to ScienceCareers.org and click For Employers, or call one of our representatives.



AMERICAS

+1 202 326-6577
+1 202 326-6578
advertise@sciencecareers.org

EUROPE, INDIA, AUSTRALIA, NEW ZEALAND, REST OF WORLD

+44 (0) 1223 326527
advertise@sciencecareers.org

CHINA, KOREA, SINGAPORE, TAIWAN, THAILAND

+86 131 4114 0012
advertise@sciencecareers.org

JAPAN

+81 3-6459-4174
advertise@sciencecareers.org

CUSTOMER SERVICE

AMERICAS

+1 202 326-6577

REST OF WORLD

+44 (0) 1223 326528

advertise@sciencecareers.org

All ads submitted for publication must comply with applicable U.S. and non-U.S. laws. *Science* reserves the right to refuse any advertisement at its sole discretion for any reason, including without limitation for offensive language or inappropriate content, and all advertising is subject to publisher approval. *Science* encourages our readers to alert us to any ads that they feel may be discriminatory or offensive.

ScienceCareers

FROM THE JOURNAL SCIENCE AAAS

ScienceCareers.org

Advance
your career
with expert
advice from
Science
Careers.



Download Free Career Advice Booklets!
ScienceCareers.org/booklets

Featured Topics:

- Networking
- Industry or Academia
- Job Searching
- Non-Bench Careers
- And More



ScienceCareers

FROM THE JOURNAL SCIENCE AAAS



Nanjing Agricultural University Welcomes Talents from All Over the World

Nanjing Agricultural University (NAU) sincerely invites you to join us in teaching and research.

About us

Nanjing Agricultural University is a university under the administration of the Ministry of Education and has been selected and included in the National "Double World-Class" University Construction Initiative. In the fourth-round national first-level discipline evaluation in 2017, it had four disciplines listed in Class A+, ranking itself the 11th of the top universities in China. In the ESI rankings, it had seven disciplines ranked among the top 1% worldwide, and two of the disciplines, Agricultural Science and Plant & Animal Science, among the top 1‰. The US News 2018 has listed NAU the top 9 among the Best Global Universities of Agricultural Sciences.

Fields of research

The fields of research you are invited to join in are:

Agricultural Sciences including :

Crop Science, Horticulture, Agricultural Resources & Environment, Plant Protection, Animal Husbandry, Veterinary Science, Fisheries Science, and Grass Science;

Science and Technology including :

Biology, Ecology, Environmental Science & Engineering, Food Science & Engineering, Landscape Architecture, Agricultural Engineering, Bioinformatics, and Computer Science & Technology;

Humanities and Social Sciences including :

Management, Economics, Sociology, Legal Science, History, Literature, and Linguistics.

You are also welcome to join us in the following

Interdisciplinary Subjects :

Genomics & Phenomics, Microorganism-Botany-Pest Interactions, Food Nutrition and Human Health, Agricultural Equipment Engineering, Agricultural Informatics, and so on.

Position requirements

Doctorate recipients from world famous universities; post-doctor researchers from famous research institutes; and talents with professional titles of associate professor, professor or other higher titles, from world-famous higher institutions or research institutes, and with outstanding teaching and research achievements.

NAU will offer you a benefits package which is competitive among the universities in the local area and which will be negotiated in person.

Talent introduction policy

You will enjoy a talent allowance equivalent to those for the Zhongshan Scholars of NAU who are Zhongshan Distinguished Professor, Zhongshan Professor, Zhongshan Fellow, and Zhongshan Young Scholar, according to your qualities for recruitment; or we may talk and agree on your annual salary.

Specific conditions of your research team, laboratory, graduate students to supervise, accommodation, and employment of your spouse are to be discussed in person.

Note: The Zhongshan Scholars is an NAU-developed open initiative to support career development and

academic innovation for leading scientists of today and tomorrow, and it is a major initiative to construct a world-class university and to establish world-class disciplines, so as to realize NAU's strategy of rejuvenation by talents. Recruitment is divided into four categories: Zhongshan Distinguished Professor, Zhongshan Professor, Zhongshan Fellow and Zhongshan Young Scholar. Special talent allowance is provided for these outstanding scientists.

Application documents

Please prepare and email to rcb@njau.edu.cn the following documents for your qualification:

- a detailed CV, starting from your undergraduate education till the time of your application, including periods of continuous education, working experience, publications, research projects hosted or participated in, and certificates of awards.
- photocopies of diplomas, certificate of doctor's degree, and certificate of current employment
- Full texts of five representative papers published in the past five years.

Contacts:

Ms. Liu Hongmei

Telephone:

+86-25-84399039

Email address:

rcb@njau.edu.cn



Changsha University

Dedicated for Regional First-Class University with Global Intelligence

Faculty Opportunities in Changsha University

Located in the culture-steeped city of Changsha, capital of Hunan Province, Changsha University (CCSU), is proudly designated as application-oriented university in Industry-College Cooperation Program of National "Thirteenth Five-Year Plan". Qualified as newly authorized postgraduate program construction unit in Hunan province and the only municipal-level university in Changsha, CCSU functions with both provincial and municipal funding and is principally directed by municipal administration. Boasted 133 hectares garden-like campus, CCSU runs 15 schools (departments) with 43 undergraduate programs and attracts 1,020 faculty members and over 14,000 full-time students. With decades of dedication, a multi-disciplinary development vision in CCSU has been generally realized featuring diverse and collaborated structure comprehensively spanning science, engineering, law, management, humanities and arts, which prominently underpinned by engineering application programs with strong wing support from programs in cultural creativity and modern service fields. To further sail for excellence in both research and innovation, we earnestly seek for qualified candidates worldwide, offering favorable environment and facilities, internationally competitive salaries and benefits.

Recruitment Disciplines

Architecture, Civil Engineering, Transport Engineering, Management Science and Engineering, Mechanical Engineering, Material Science and Engineering, Computer Science and Technology, Software Engineering, Information and Communication Engineering, Control Science and Engineering, Electrical Engineering, Electronic Science and Technology, Surveying and Mapping Science and Technology, Bioengineering, Mathematic, Biology, Chemistry, Business Management, Theoretical Economics, Applied Economics, Law, Chinese Language and Literature, Foreign Language and Literature, Journalism, Art Theory, Design Art, Drama, Film and Television Studies, Animations, Digital Media and Art, Music and Dance, Politics, Philosophy, Chinese History, Social Science, Physical Science, Psychology, Education.

Requirements, Remuneration and Benefits

Positions	Requirements and Qualifications	Remuneration and Benefits
Leading Scholars	1. Under the age of 55; 2. Qualified to be listed in National "Thousand Talents Plan" (Long Term), China National Funds for Distinguished Young Talents; professors or scholars of the equivalent academic achievements from elite international universities or institutes; senior technical or managerial specialist with leadership experience from world-renowned enterprises or institutions.	1. Research startup fund: RMB 5,000,000 or above for natural sciences; RMB 1,500,000 for social sciences; 2. Housing allowance: RMB 2,000,000. 3. Annual salary (pre-tax): RMB 1,000,000 or above.
Academic Leaders	1. Under the age of 53; 2. Qualified to be listed in National "Thousand Talents Plan" for Young Professionals, National Science Foundation for Outstanding Youth Program; associate professors or scholars of the equivalent or above academic achievements from elite international universities or institutes; senior technical or managerial specialists from world-renowned enterprises or institutions.	1. Research startup fund: RMB 2,000,000 or above for natural sciences; RMB 800,000 for social sciences; 2. Housing allowance: RMB 1,200,000. 3. Annual salary (pre-tax): RMB 600,000 or above.
Academic Backbones	1. Under the age of 48; 2. Elite Chinese young scholars; assistant professors or scholars of the equivalent or above academic achievements from elite international universities or institutes; intermediate technical or managerial specialists from world-renowned enterprises or institutions.	1. Research startup fund: RMB 1,000,000 or above for natural sciences; RMB 500,000 for social sciences; 2. Housing allowance: RMB 800,000. 3. Annual salary (pre-tax): RMB 450,000 or above.
Excellent Doctors and Post Doctoral Fellows	1. Post-doctor or Ph.D holder, under the age of 35. The age limit for candidates with consecutively 3+ years 'working experience' in field-relevant industries or enterprises extends to 38 years. 2. Comparatively strong and promising research capacity.	1. Research startup fund: RMB 100,000-150,000 for natural sciences; RMB 60,000-80,000 for social sciences; 2. Housing allowance: RMB 250,000-500,000. 3. Annual salary (pre-tax): RMB 120,000 or above.
1. Individual treatment for candidate with outstanding achievements is negotiable; 2. Special treatment for academic team recruitment is negotiable.		

Application

Please log in <http://rszp.ccsu.cn/zpsys> to submit your applications. This advertisement is valid permanently for elite talents and overseas doctors.

Contact Us

Website: <http://www.ccsu.cn/>
Contact Person: Xiaopeng Nan
Address: No. 98, Hongshan Road, Changsha, 410022, Hunan Province, China

Email: changshaxy@163.com
Tel: 0086-731-8426-1360



Southwest Jiaotong University, Chengdu, China Invites Applications for Academic Positions

Southwest Jiaotong University (SWJTU), founded in 1896, is one of the oldest institutions of high learning in China. In its proud legacy of 120 years, the University has been dedicated to Chinese higher education and has proudly nurtured generations of engineering and scientific leaders. As the most comprehensive leading research university in transportation, SWJTU is world-renowned for pioneering the Chinese railway transportation engineering and industry, and for its leading contributions to the development of Chinese high-speed rail system. For its sustained excellence and prominence, the University is placed among the key, elite multidisciplinary "211" and "985" Tier-1 universities directly administered by the Chinese Ministry of Education. We offer comprehensive education and research programs in 19 faculties and institutes/centers, covering diverse disciplines in engineering, sciences, arts, and management leading from undergraduate to doctoral degrees. The University boasts 2,600 outstanding academic staffs, 15 doctoral/ 43 master/ 75 undergraduate programs and 11 post-doctoral stations, supported by more than 30 cutting edge key laboratories at the national and provincial levels.

Located strategically in Chengdu, the capital of Sichuan province—the China's dynamically growing West, SWJTU is blessed with rich heritage, unparallel vibrancy, and a beautiful campus.

"Prosperous and plentiful ever now and then, the City flourishes in hibiscus blossoms in no end," as so known, Chengdu has been long renowned for its historical and cultural heritage, and for its natural beauty and abundance. As a major cultural and economical center and a transportation hub, the City offers first-class cultural experience, education, employment, cuisine and living environment. Leveraging on these unique advantages and the University's strengths, SWJTU is vigorously implementing its strategic plan "Developing and Strengthening SWJTU: Attracting and Cultivating Talents". We earnestly look forward to your joining our legacy and contributing to the University's continuing excellence.

More information is available at <http://www.swjtu.edu.cn/>

Openings in

Civil Engineering/Surveying Science and Engineering/Mechanical Engineering
Science of Transportation and Logistics/ Science of Information and Communication
Electrical Engineering/Computer Science and Technology
Materials Science and Technology/Mechanics/ Management Science and Technology
Managing Technology and Innovation/Environmental Science/Architecture
Physics Science/ Mathematics Science/Life Science/Medical Science
Chemical Science/Humanities and Social Science

Salary and Fringe Benefits

Salary will be highly competitive, commensurate with qualifications and experiences. The University offers a comprehensive fringe benefit package for eligible appointees, including relocation allowances, subsidy of rental residence, start-up funds for research. The University is committed to proving assistance in establishing scientific platform and research group as well as international-level training and promotion. The University also assists the eligible appointees in child education. Special arrangements are open for discussion for exceptional appointees.

How to Apply

Interested candidates should send a full resume, copies of academic credentials, a publication list with abstracts of selected publications, a research plan, a teaching statement, together with names of three references to Human Resources Department Southwest Jiaotong University Western Park of High-Tech Zone Chengdu, Sichuan Province, China 611756

Tel: +86-28-66366202

Email: talent@swjtu.edu.cn

For inquiries, please contact Ms. Ye Zeng or Mr. Jian Wu at the above addresses.

乡愁，
是那一汪大海，
我在这头，
家人在那头。

千万个
不回的理由，
难抵
一个归根的念头。

Nostalgia,
is like an ocean,
I am here,
the family is over there.

Thousands of reasons
to stay abroad,
but one decision to
return to the roots.

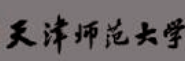
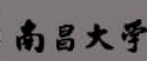
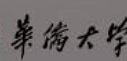
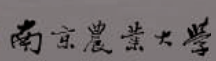
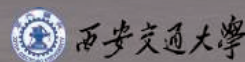
Overseas Scholar's Visit to Top Chinese Universities —— Chinese Universities Forums

For more information, please check www.edu.cn/zqx



- 10,000+ academic job vacancies in China
- Free one-to-one consultation service

Send your CV to
consultant@acabridge.edu.cn





Are you conducting research that is both environmentally and socially relevant? Are you an excellent researcher with forward-thinking ideas and an inter- or transdisciplinary research approach?

If yes, we would like to invite you to apply for the

Robert Bosch Junior Professorship “Research into the Sustainable Use of Natural Resources”

together with a German university or research institution of your choice. Applicants of all nationalities are welcome.

Areas addressed

We are looking for an outstanding young scientist who wants to find new approaches to clarify and tackle global challenges with regard to the sustainable use of natural resources. The research should focus on developing and emerging countries.

We are especially interested in applications that also consider human behaviour in this context. Research approaches may be based in the humanities, the social, or the natural sciences.

Scope

The successful applicant will be awarded a grant worth up to 1 million euros for a five year period in order to set up a research group in a German university or research institution.

The funds can be allocated flexibly towards covering salaries and research costs.

Candidate profile

- excellent doctorate degree, completed no more than 5 years prior to the application deadline of 13 May 2018 (adjusted for documented parental leave)
- compelling independent past scientific achievements and publications in peer-reviewed journals
- international research experience
- excellent proficiency in English
- non-German applicants should be prepared to learn German

The application deadline is **13 May 2018**.

For further information and to apply please visit

www.bosch-stiftung.de/juniorprofessorship

myIDP: A career plan customized for you, by you.



For your career in science, there's only one **Science**



Recommended by
leading professional
societies and the NIH

Features in myIDP include:

- Exercises to help you examine your skills, interests, and values.
- A list of 20 scientific career paths with a prediction of which ones best fit your skills and interests.
- A tool for setting strategic goals for the coming year, with optional reminders to keep you on track.
- Articles and resources to guide you through the process.
- Options to save materials online and print them for further review and discussion.
- Ability to select which portion of your IDP you wish to share with advisors, mentors, or others.
- A certificate of completion for users that finish myIDP.

Visit the website and start planning today!

myIDP.sciencecareers.org

Science Careers

In partnership with:





ÉCOLE POLYTECHNIQUE
FÉDÉRALE DE LAUSANNE

Faculty Position in Extreme Environments at the Ecole polytechnique fédérale de Lausanne (EPFL)

The EPFL School of Architecture, Civil and Environmental Engineering (ENAC) invites applications for the Ingvar Kamrad Chair, a tenured Associate or Full Professor position in its Institute of Environmental Engineering (IIE). The appointee will join the newly formed EPFL Centre for Changing Alpine and Polar Environments (CAPE), based in Sion, Switzerland, and contribute to research and teaching activities within IIE. This appointment is one of several CAPE professorships, and offers unrivalled collaboration opportunities at the local and European levels. The appointee will also participate (and represent EPFL) in the Swiss Polar Institute, which promotes collaborative research within Switzerland and internationally.

The holder of this Chair will be an internationally recognized scholar in quantifying impacts of climate change on frozen water resources at large scales in Alpine and Polar environments. This area of activity is interpreted broadly, and potentially considers ice physics and dynamics, remote sensing of polar caps/glaciers and interpretation of physical changes, physically based and data-intensive modelling of mountain/polar hydrological systems, snow physics, and implications for mountain/polar water resources.

In this context, we seek an outstanding individual who will lead an internationally recognized research program that leverages the opportunities offered by CAPE/EPFL. The professor will be committed to excellence in research and in undergraduate and graduate level teaching, and will contribute to the teaching program in Environmental Engineering at EPFL, which views basic and translational research as the foundation for environmental adaption and engineering design.

With its main campus located in Lausanne and its developing antennae in neighbouring cantons in Switzerland, EPFL is a growing and well-funded institution

fostering excellence and diversity. It is well equipped with experimental and computational infrastructure, and offers a fertile environment for research collaboration between different disciplines. The EPFL environment is multilingual and multicultural, with English serving as a common interface. EPFL offers internationally competitive start-up resources, salaries, and benefits.

The following documents are requested in PDF format: cover letter including a statement of motivation, curriculum vitae, publications list, concise statements of research and teaching interests (3-5 pages) as well as the names and addresses, including emails, of at least five references (may be contacted at a later stage). Applications should be uploaded to the EPFL recruitment web site:

<https://facultyrecruiting.epfl.ch/position/10972780>

Formal evaluation of the applications will begin on **May 1, 2018** and the search will continue until the position is filled.

Further enquiries should be made to the Chair of the Search Committee:

Prof. D. Andrew Barry

Director of the Environmental Engineering Institute

E-mail: extreme-environments@epfl.ch

For additional information on EPFL:

<http://www.epfl.ch>; <http://enac.epfl.ch>; <https://valais.epfl.ch/Home>

EPFL is an equal opportunity employer and a family friendly university.

ScienceCareers

FROM THE JOURNAL SCIENCE AAAS

Follow us for jobs, career advice & more!



@ScienceCareers



/ScienceCareers



Science Careers

ScienceCareers.org



St. Jude Children's
Research Hospital

ALSAC • Danny Thomas, Founder

Bioinformatics Research Scientist Pathology & Developmental Neurobiology

St. Jude Children's Research Hospital is a world-renowned institution that is recognized as one of the best places to work in the nation. Currently, a Bioinformatics Research Scientist position is available in the laboratories of Drs. Charles Mullighan, MBBS, MD (Pathology) and Paul Northcott, PhD (Developmental Neurobiology). This joint position offers an unrivaled opportunity to be embedded in an environment leading integrated genomic and experimental studies in childhood brain tumors and leukemia.

The successful applicant will be part of the recently established St. Jude Epigenetic Collaborative project examining the role of epigenomic and transcriptional alteration in pediatric cancer. This will involve interaction with world leaders in the field including Scott Armstrong (Dana Farber), David Allis (Rockefeller), Tom Muir (Princeton) and Charles Roberts (St. Jude). You will be involved in the integrative epigenomic and transcriptomic analysis of large cancer genomic datasets from patients with childhood brain cancers and leukemia and engineered models of pediatric cancer.

To learn more and apply, visit: <http://bit.ly/stjudesciencemag>

*St. Jude Children's Research Hospital
is an Equal Opportunity Employer.*



By Malin L. Nording

Figuring out how I belong

I was confused. I knew what was expected in theory, but I couldn't seem to grasp the reality of it. As a recently appointed assistant professor applying for university funds to buy a new piece of equipment, for example, I proudly listed all of my collaborations with other departments, certain that this would help my chances. When I found out that I didn't get the funding, I learned the hard way that the decision was made only by faculty members within my own department, so outside collaborations weren't a selling point. I felt so ashamed for not understanding the unspoken terms, and for giving my colleagues the false impression that I knew what I was doing.

It wasn't always like this. In the Swedish village where I grew up, I was proud to be the class bookworm. As a student and postdoc, it was exciting to satisfy challenging (yet clear) expectations. When I became a faculty member, I was full of passion and confidence and was eager to fit in and measure up.

But faced with the politics of being an assistant professor, I couldn't discern what was expected of me. I couldn't understand the implicit messages, which led to embarrassing mistakes such as the equipment funding incident. Another time, I enthusiastically developed a new course to fill a gap I had noticed in the curriculum. But the subject area was not a good match for my department, I realized after doing the work, so I didn't get any credit. There were also smaller incidents: simple things like not understanding which meetings I was supposed to attend and who to go to for advice.

Every time something like this happened, it stripped away a piece of my self-worth. My passion for science faded, and I did not feel like I belonged anymore. The more overwhelming that feeling became, the more I distanced myself and my research group from the rest of the department. Hiding my shame was a way to survive. But without a connection with my fellow faculty members, I crumbled.

After almost 3 years, when things seemed as dark as they could possibly be, I found a potential escape: a 3-year international career grant from the Swedish Research Council. I would be able to keep my appointment at my home institution and continue as thesis adviser for my students while working elsewhere. My department head was supportive, and I worked out strategies for staying connected with my research group while I was away. Whatever the drawbacks might be, I was convinced that



“When I became a faculty member, I was ... eager to fit in and measure up.”

of struggling to read hidden signals and fearing that I've missed some crucial details, I'm spending my energy on expanding my skill set.

I intend to carry this new confidence back to my home institution when I return in a few months. I'm facing a very empty lab, but now I know how I want to contribute to my academic community. In addition to my chemistry research, I'm committed to fostering an open, supportive, inclusive environment like the one I've experienced during my stay abroad. I also have a newfound determination to clarify expectations before they become a problem. And when I make mistakes in spite of all my efforts, instead of hiding them in shame, I will accept them and, most importantly, share and learn from them. ■

Malin L. Nording is an assistant professor at Umeå University in Sweden and a Marie Skłodowska-Curie International Career Grant Fellow at the University of California, Davis.